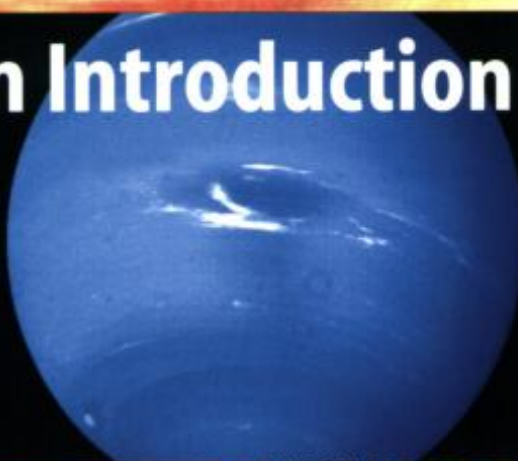


GIANT PLANETS OF OUR SOLAR SYSTEM

An Introduction



Patrick Irwin



Springer

Copyrighted Material

PRAXIS

Giant Planets of Our Solar System

An Introduction

Patrick G. J. Irwin

Giant Planets of Our Solar System

An Introduction



Springer

Published in association with
Praxis Publishing
Chichester, UK



Dr Patrick G. J. Irwin
Atmospheric, Oceanic, and Planetary Physics
Clarendon Laboratory
Oxford
UK
and
St Anne's College
Oxford
UK

SPRINGER-PRAXIS BOOKS IN ASTRONOMY AND PLANETARY SCIENCES
SUBJECT ADVISORY EDITORS: Dr Philippe Blondel, C.Geol., F.G.S., Ph.D., M.Sc., Senior Scientist,
Department of Physics, University of Bath, Bath, UK; John Mason, M.Sc., B.Sc., Ph.D.

ISBN 3-540-31317-6 Springer-Verlag Berlin Heidelberg New York

Springer is part of Springer-Science + Business Media (springeronline.com)

Bibliographic information published by Die Deutsche Bibliothek

Die Deutsche Bibliothek lists this publication in the Deutsche Nationalbibliografie;
detailed bibliographic data are available from the Internet at <http://dnb.ddb.de>

Library of Congress Control Number: 2005938845

Apart from any fair dealing for the purposes of research or private study, or criticism or review, as permitted under the Copyright, Designs and Patents Act 1988, this publication may only be reproduced, stored or transmitted, in any form or by any means, with the prior permission in writing of the publishers, or in the case of reprographic reproduction in accordance with the terms of licences issued by the Copyright Licensing Agency. Enquiries concerning reproduction outside those terms should be sent to the publishers.

© Praxis Publishing Ltd, Chichester, UK, 2003

Reprinted with corrections and issued as an abridged paperback, 2006

Printed in Germany

The use of general descriptive names, registered names, trademarks, etc. in this publication does not imply, even in the absence of a specific statement, that such names are exempt from the relevant protective laws and regulations and therefore free for general use.

Cover design: Jim Wilkie

Project management: Originator Publishing Services, Gt Yarmouth, Norfolk, UK

Printed on acid-free paper

Contents

Preface	xi
Acknowledgements	xiii
Abbreviations	xv
List of figures	xix
List of tables	xxiii
List of colour plates	xxv
1 Introduction	1
1.1 The giant outer planets.	1
1.2 Observed atmospheres of the giant planets	5
1.2.1 Jupiter	5
1.2.2 Saturn	8
1.2.3 Uranus	9
1.2.4 Neptune	11
1.3 Satellites of the outer planets.	12
1.4 Exploration of the outer planets.	13
1.5 Organization of book	14
1.6 References	15
1.7 Bibliography.	15
2 Formation of the giant planets	17
2.1 Formation of the universe and primordial constituents	17
2.2 Formation of the stars and evolution of the interstellar medium.	18

2.3	Formation of the protosolar nebula	21
2.3.1	Collapse of the interstellar cloud	21
2.3.2	Formation of circumstellar disc	23
2.4	Formation of the Jovian planets and comets.	28
2.4.1	Core accretion model.	28
2.4.2	Gravitational instability model.	32
2.5	Formation of Jovian satellites	32
2.6	Bulk composition of the outer planets and isotope ratios.	33
2.6.1	Constraints on formation: D/H ratio	33
2.6.2	Constraints on formation: Nitrogen	39
2.7	Interiors of the giant planets	39
2.7.1	Gravitational data.	39
2.7.2	Magnetic field data	42
2.7.3	Internal structure of Jupiter and Saturn	42
2.7.4	Internal structure of Uranus and Neptune	45
2.8	Migration and extrasolar planets	47
2.9	References	48
2.10	Bibliography.	51
3	Evolution processes in outer planet atmospheres	53
3.1	Introduction	53
3.2	Thermal escape.	53
3.2.1	Jeans' formula	53
3.2.2	Diffusion and limiting flux	55
3.2.3	Hydrodynamic escape	58
3.3	Impacts with comets and planetesimals	59
3.4	Internal differentiation processes.	59
3.4.1	Effective radiating temperature of planets	60
3.5	Evolution of the giant planet atmospheres	62
3.5.1	Jupiter	62
3.5.2	Saturn	63
3.5.3	Uranus and Neptune.	64
3.6	References	65
3.7	Bibliography.	65
4	Vertical structure of temperature, composition, and clouds.	67
4.1	Pressure and temperature profiles	67
4.1.1	Pressure	67
4.1.2	Temperature	68
4.1.3	Secondary effects on temperature/pressure profiles	73
4.1.4	Temperature/pressure profiles of the outer planets	76
4.2	Vertical mixing–eddy mixing coefficients.	77
4.3	Composition profiles – general considerations	81
4.3.1	Disequilibrium species	81
4.3.2	Photolysis	84

4.3.3	Condensation	89
4.3.4	Extraplanetary sources	91
4.4	Composition and cloud profiles of the giant planets	92
4.4.1	Jupiter	92
4.4.2	Saturn	103
4.4.3	Uranus	110
4.4.4	Neptune	116
4.5	References	125
4.6	Bibliography	131
5	Dynamical processes	133
5.1	Introduction	133
5.2	Mean circulation of the giant planet atmospheres	133
5.2.1	Equations of motion	135
5.2.2	Mean zonal motions in the giant planet atmospheres	141
5.3	Eddy motion in the giant planet atmospheres	147
5.3.1	Turbulence in the giant planet atmospheres	147
5.3.2	Waves in the giant planet atmospheres	151
5.3.3	Vortices in the giant planet atmospheres	156
5.4	Mean and eddy circulation of the giant planet atmospheres	158
5.4.1	Tropospheric circulation	158
5.4.2	Stratospheric and upper tropospheric circulation	163
5.5	Meteorology of Jupiter	164
5.5.1	General circulation and zonal structure	164
5.5.2	Storms and vortices	169
5.5.3	Waves	173
5.6	Meteorology of Saturn	177
5.6.1	General circulation and zonal structure	177
5.6.2	Storms and vortices	179
5.6.3	Waves	180
5.7	Meteorology of Uranus	183
5.7.1	General circulation and zonal structure	183
5.7.2	Storms and vortices	184
5.7.3	Waves	185
5.8	Meteorology of Neptune	185
5.8.1	General circulation and zonal structure	185
5.8.2	Storms and vortices	187
5.8.3	Waves	190
5.9	References	191
5.10	Bibliography	196
6	Radiative transfer processes in outer planetary atmospheres	197
6.1	Introduction	197
6.2	Interaction between electromagnetic radiation and particles	198
6.2.1	Fermi's golden rule	198

6.2.2	Electric and magnetic moments	199
6.3	Molecular spectroscopy: vibrational–rotational transitions	200
6.3.1	Molecular vibrational energy levels	200
6.3.2	Molecular rotational energy levels	201
6.3.3	Rotational transitions	203
6.3.4	Vibration–rotation bands	204
6.3.5	Inversion bands and inversion-doubling	208
6.3.6	Diatom homonuclear molecules	208
6.3.7	Line-broadening	209
6.3.8	Giant planet gas transmission spectra	211
6.4	Radiative transfer in a grey atmosphere	212
6.4.1	Nadir viewing	213
6.4.2	Net flux and disc-averaging	216
6.4.3	Limb-viewing	218
6.4.4	Radiative balance	220
6.4.5	Local thermodynamic equilibrium	221
6.4.6	Transmission calculations	222
6.5	Scattering of light by particles	225
6.5.1	Rayleigh or dipole scattering	226
6.5.2	Mie theory	227
6.5.3	Non-spherical particles	228
6.5.4	Analytical forms of phase functions	229
6.6	Radiative transfer in scattering atmospheres	229
6.6.1	Plane-parallel approximation	230
6.6.2	Spherical atmospheres and limb-viewing: Monte Carlo simulations	232
6.7	Giant planet spectra	233
6.7.1	General features of giant planet spectra: UV to microwave	233
6.7.2	Near-IR and visible reflectance spectra	234
6.7.3	Thermal-IR spectra	236
6.7.4	Microwave spectra	241
6.8	Appendix	242
6.8.1	Planck function	242
6.9	References	244
6.10	Bibliography	245
7	Sources of remotely sensed data on the giant planets	247
7.1	Introduction	247
7.2	Measurement of visible, IR, and microwave spectra	248
7.2.1	Detection of IR radiation	248
7.2.2	Radiometers/photometers	249
7.2.3	Grating spectrometers	250
7.2.4	Michelson interferometers	251
7.2.5	Detection of microwave radiation	254
7.3	Ground-based observations of the giant planets	255

7.3.1	Terrestrial atmospheric absorption	255
7.3.2	Angular resolution	257
7.3.3	Brightness	260
7.4	Ground-based visible/IR observatories	261
7.4.1	European Southern Observatory (ESO) – Very Large Telescope (VLT)	263
7.4.2	The Mauna Kea observatories	265
7.4.3	Other major observatories	268
7.5	Airborne visible/IR observations	268
7.5.1	Kuiper Airborne Observatory	269
7.6	Ground-based microwave observatories	270
7.6.1	The Institut de RadioAstronomie Millimétrique (IRAM)	271
7.6.2	Very Large Array (VLA)	272
7.6.3	Very Large Baseline Array (VLBA)	273
7.6.4	Berkeley Illinois Maryland Association (BIMA)	274
7.6.5	Owens Valley Radio Observatory (OVRO)	274
7.6.6	Nobeyama Millimeter Array (NMA)	275
7.7	Space-based telescopes	276
7.7.1	HST	277
7.7.2	ISO	279
7.7.3	Submillimeter Wave Astronomy Satellite (SWAS)	283
7.8	Flyby spacecraft	284
7.8.1	<i>Pioneer</i>	286
7.8.2	<i>Voyager</i>	288
7.8.3	<i>Ulysses</i>	292
7.9	Orbiting spacecraft	292
7.9.1	<i>Galileo</i>	292
7.9.2	<i>Cassini/Huygens</i>	300
7.10	Retrievals	303
7.10.1	Exact, least squares, and Backus–Gilbert solution	306
7.10.2	Linear optimal estimation	307
7.10.3	Non-linear optimal estimation	309
7.10.4	Joint retrievals	309
7.11	References	309
7.12	Bibliography	310
Index	313

Preface

I can remember it vividly. I was eleven and standing on a cold, windy hill with one of my mother's friends who had offered to let me view the planets through his telescope. It was only a small telescope, but through it I was able to see the disc of Jupiter with the two dark strips of the equatorial belts together with Jupiter's Galilean moons. As for Saturn, the sight of it hanging there in space surrounded by its fabulous ring system quite took my breath away. This experience, amongst others, fostered a life-long interest and enthusiasm in physics and in the planets of our Solar System, especially the giant planets. Ten years later I found myself as a research student in Oxford studying the atmosphere of Mars. Twenty years later I found myself on a beach in Florida, watching the launch of the *Cassini/Huygens* mission to Saturn, carrying with it the CIRS instrument that I had helped to design and build. I am now fortunate enough to be involved in several space missions to the planets, and the study of planetary atmospheres continues to fascinate and inspire me.

This book is aimed at 3rd to 4th year undergraduates of physics and astronomy and 1st year postgraduate students of planetary physics. I hope it may also serve as a handy reference for researchers. One of the difficulties I had in compiling the book was in peeling away some of the jargon used in the scientific literature that assumed prior knowledge but which was actually sometimes rather arcane. Hence, wherever possible I have tried to approach all of the fields that make up this book from the starting point of an undergraduate with a good grasp of physics but no prior specialist knowledge. Furthermore, I have tried to include references to the major books and papers in the various fields which should allow an interested reader to explore further should they wish to. For the chapters dealing with current and future projects I have also included a number of website addresses which were very helpful in writing these chapters. In many areas presented in this book the opinion of the scientific community is still split and thus research is actively on-going. In such cases I have tried to objectively present both sides of the arguments and I apologise for any bias that may, or may not, have crept in. In other cases, such as formation models,

there are a wide range of results and simulations and thus it should be remembered that there is considerable variance about the mean view that I have tried to present.

I hope my reader finds this book useful, and while I can't offer the exhilaration of viewing a planet for the first time on a cold, windy hillside, I hope he or she will share my enthusiasm for this fascinating area of astronomy.

Acknowledgements

I would like first of all to thank both my sub-department of Atmospheric, Oceanic, and Planetary Physics and St Anne's College for granting me sabbatical leave to write this book between March and December 2002. I would also like to thank the UK Particle Physics and Research Council (PPARC) for supporting my group's research into the atmospheres of the giant planets, some results of which are presented in this book. I would then like to thank all of my colleagues who have assisted me in collecting and collating the material that I have presented in this book including, in no particular order: Therese Encrenaz, Emmanuel Lellouch, Andy Ingersoll, Kevin Baines, Sushil Atreya, Bill Hubbard, Larry Sromovsky, Augustin Sanchez-Lavega, Maarten Roos-Serote, Imke de Pater, Dave Jewitt, Don Yeomans, Mark McCaughrean, Tristan Guillot, Franck Hersant, Uwe Fink, Jacques Sauval, Ashwin Vasavada, Erich Karkoschka, Glenn Orton, Julianne Moses, Gary Davis, Bruno Bézard, and David Andrews. I would also like to thank my Oxford colleagues Peter Read and Steve Lewis for many long and illuminating discussions on planetary dynamics which were of enormous value in completing Chapter 5. I would especially like to thank my other Oxford colleagues Thierry Fouchet and Fred Taylor who both kindly reviewed large sections of this book and who made many helpful comments and suggestions. I am also very grateful to Clive Horwood and John Mason of Springer-Praxis who also reviewed this book and helped me to mould it into its final form. I would very much like to thank the various authors, journals, space agencies, and websites whose figures are reproduced in this book. Full acknowledgement has been given in all cases and every effort has been made in gaining permission. Finally I would like to thank my wife and young family for putting up with Dad often having to work late and occasionally being a little grumpy!

To my wife Dunja,
and to Benjamin and Samuel, my two little boys.

Abbreviations

AAO	Anglo-Australian Observatory
ACP	Aerosol Collector and Pyrolyzer (<i>Huygens</i>)
ACS	Advanced Camera for Surveys (HST)
ALICE	Ultraviolet Image Spectrometer (<i>Rosetta</i>)
AUI	Associated Universities, Inc.
BDRF	bidirectional reflectivity
BIMA	Berkeley Illinois Maryland Association
CAPS	<i>Cassini</i> Plasma Spectrometer
CARMA	Combined Array for Research in Millimeter wave Astronomy
CDA	Cosmic Dust Analyzer (<i>Cassini</i>)
CELT	Californian Extremely Large Telescope
CFHT	Canada–France–Hawaii Telescope
CIA	collision induced absorptions
CIRS	Composite InfraRed Spectrometer (<i>Cassini</i>)
CNRS	Centre National de la Recherche Scientifique
COBE	Cosmic Background Explorer
CONCERT	Comet Nucleus Sounding Experiment by Radiowave Transmission (<i>Rosetta</i>)
COROT	COncvection ROTation and Transits
COSIMA	Cometary Secondary Ion Mass Analyzer (<i>Rosetta</i>)
DALR	dry adiabatic lapse rate
DISR	Descent Imager and Spectral Radiometer (<i>Huygens</i>)
DWE	Doppler Wind Experiment (<i>Huygens</i>)
ECCM	equilibrium cloud condensation model
ELT	Extremely Large Telescope
ESO	European Southern Observatory
EUV	extreme ultraviolet
EZ	Equatorial Zone

f.s.h.	fractional scale height
FOV	field of view
FTS	Fourier-Transform Spectrometer
FUV	far ultraviolet
GCM	General Circulation Model
GCMS	Gas Chromatograph and Mass Spectrometer (<i>Huygens</i>)
GCR	Galactic Cosmic Ray
GDS	Great Dark Spot (<i>Neptune</i>)
GIADA	Grain Impact Analyzer and Dust Accumulator (<i>Rosetta</i>)
GPMS	Galileo Probe Man Spectrometer
GRS	Great Red Spot (<i>Jupiter</i>)
HAD	Galileo Probe Helium Abundance Detector
HASI	Huygens Atmospheric Structure Instrument (<i>Huygens</i>)
HGA	High Gain Antenna
HIFI	Heterodyne Instrument for the Far Infrared (<i>Herschel</i>)
HST	Hubble Space Telescope
IAU	International Astronomical Union
IGN	Instituto Geográfico Nacional
ING	Isaac Newton Group of Telescopes
IPD	interplanetary dust
IR	infrared
IRAC	Infrared Array Camera (SIRTF)
IRAM	Institut de Radio Astronomie Millimétrique
IRIS	Infrared Interferometer Spectrometer (<i>Voyager</i>)
IRS	Infrared Spectrograph (SIRTF)
IRTF	Infrared Telescope Facility
ISIM	Integrated Science Instrument Module (JWST)
ISM	Interstellar Medium
ISO	Infrared Space Observatory
ISO-SWS	ISO Short Wavelength Spectrometer
ISO-LWS	ISO Long Wavelength Spectrometer
ISS	Imaging Science Subsystem (<i>Voyager</i> , <i>Cassini</i>)
ITCZ	Intertropical Convergence Zone
JAC	Joint Astronomy Centre (UK, Holland, and Canada)
JPL	Jet Propulsion Laboratory (NASA)
JWST	James Webb Space Telescope
KAO	Kuiper Airborne Observatory
KBO	Kuiper belt objects
LBT	Large Binocular Telescope
LBTI	Large Binocular Telescope Interferometer
LTE	local thermodynamic equilibrium
MAG	Dual Technique Magnetometer (<i>Cassini</i>)
MAMA	multi-anode microchemical array (HST)
MIDAS	Microwave Imaging Dust Analysis System (<i>Rosetta</i>)
MIMI	Magnetospheric Imaging Instrument (<i>Cassini</i>)

MIPS	Multiband Imaging Photometer (SIRTF)
MIRI	Mid-Infrared Instrument (JWST)
MIRO	Microwave Instrument for the <i>Rosetta</i> orbiter
MPG	Max Planck Gesellschaft
NAOJ	National Astronomical Observatory of Japan
NEB	North Equatorial Belt (Jupiter)
NEP	noise equivalent power
NER	noise equivalent radiance
NFR	Net Flux Radiometer (<i>Galileo</i>)
NICMOS	Near Infrared Camera and Multi-Object Spectrometer (HST)
NIMS	Near Infrared Mapping Spectrometer (<i>Galileo</i>)
NIR	near-infrared
NIRCam	Near Infrared Camera (JWST)
NIRSpec	Near Infrared Spectrograph (JWST)
NMA	Nobeyama Millimeter Array
NOAO	National Optical Astronomy Observatories
NPS	North Polar Spot (Saturn)
NRAO	National Radio Astronomy Observatory
NTB	North Tropical Belt (Jupiter)
NTropZ	North Tropical Zone (Jupiter)
NTT	New Technology Telescope
OCIW	Observatories of the Carnegie Institution of Washington
OSIRIS	Optical, Spectroscopic, and Infrared Remote Imaging System (<i>Rosetta</i>)
OVRO	Owens Valley Radio Observatory
OWL	OverWhelmingly Large Telescope
PACS	Photodetector Array Camera and Spectrometer (<i>Herschel</i>)
PHOT	ISO photopolarimeter
PPR	Photopolarimeter–Radiometer (<i>Galileo</i>)
PPS	Photopolarimeter Subsystem (<i>Voyager</i>)
PSF	point spread function
QBO	quasi-biennial oscillation (Earth)
QQO	quasi-quadrennial oscillation (Jupiter)
ROSINA	<i>Rosetta</i> Orbiter Spectrometer for Ion and Neutral Analysis
RPWS	Radio and Plasma Wave Science (<i>Cassini</i>)
RSP	Remote Sensing Platform (<i>Galileo</i>)
RSS	Radio Science Instrument (<i>Cassini</i>)
RTG	radioisotope thermoelectric generators
s.v.p.	saturated vapour pressure
SALR	saturated adiabatic lapse rate
SEB	South Equatorial Belt (Jupiter)
SEST	Swedish ESO Submillimetre Telescope
SIM	Space Interferometry Mission
SIRTF	Space Infrared Telescope Facility
SIS	superconductor–insulator–superconductor

xviii Abbreviations

SPF	South Polar Feature (Neptune)
SPIRE	Spectral and Photometric Imaging REceiver (<i>Herschel</i>)
SPW	South Polar Wave (Neptune)
SSI	Solid State Imaging (<i>Galileo</i>)
SSP	Surface Science Package (<i>Huygens</i>)
STB	South Temperate Belt (Jupiter)
STIS	Space Telescope Imaging Spectrograph (HST)
STP	standard temperature and pressure
STZ	South Temperate Zone (Jupiter)
SWAS	Submillimeter Wave Astronomy Satellite
SWS	ISO Short Wavelength Spectrometer
TPF	Terrestrial Planet Finder
UKIRT	United Kingdom Infrared Telescope
UV	ultraviolet
UVIS	Ultraviolet Imaging Spectrometer (<i>Cassini</i>)
UVS	Ultraviolet Spectrometer (<i>Voyager</i>)
v.m.r.	volume mixing ratio
VEEGA	Venus–Earth–Earth–Gravity-Assist (<i>Galileo</i>)
VIMS	Visible and Infrared Mapping Spectrometer (<i>Cassini</i>)
VIRTIS	Visible and Infrared Thermal Imaging Spectrometer (<i>Rosetta</i>)
VISTA	Visible and Infrared Telescope for Astronomy
VLA	Very Large Array
VLBA	Very Large Baseline Array
VLT	Very Large Telescope (ESO)
VLTI	Very Large Telescope Interferometer
VLST	Very Large Telescope – Survey Telescope
VVEJGA	Venus–Venus–Earth–Jupiter–Gravity-Assist (<i>Cassini</i>)
WF/PC	Wide Field/Planetary Camera (HST)
YSO	young stellar objects

Figures

1.1	The giant planets as observed by the <i>Voyager</i> spacecraft together with the Earth for comparison	2
1.2	Total thermal infrared radiation flux emitted by the giant planets as a function of latitude.	4
1.4	Jovian zonal nomenclature.	6
2.1	Molecular cloud Barnard 68 observed by the ESO Very Large Telescope	22
2.2	Hubble Space Telescope image of a young circumstellar disc (Orion 114-426) in the Orion nebula	24
2.3	Wide-field medium-resolution false-colour near-IR image of HH212	26
2.4	Variation of nebula pressure in circumstellar disc above ecliptic plane	27
2.5	The Oort comet cloud	31
2.7	Measured D/H ratios of the giant planets, meteorites, and comets	36
2.8	Definition of the planetographic and planetocentric latitude systems	41
2.9	Interior models of Jupiter and Saturn	43
2.10	Interior models of Uranus and Neptune	46
4.1	Equatorial temperature/pressure profiles of the giant planet atmospheres	72
4.2	Variation of molecular heat capacity of molecular hydrogen with temperature	74
4.3	Variation of eddy mixing and molecular diffusion coefficients with height in the giant planet atmospheres	81
4.4	UV cross sections of different gases relevant to giant planet atmospheres	87
4.5	Methane photochemistry paths.	88
4.6	<i>Voyager 1</i> image of Jupiter.	93
4.7	Equilibrium cloud condensation model of Jupiter's atmosphere.	94
4.8	Observed and modelled abundance profiles in the atmosphere of Jupiter	95
4.9	Relative cloud profile of Jupiter deduced from the <i>Galileo</i> probe nephelometer experiment cloud results.	100
4.12	<i>Galileo</i> /SSI images of a convective storm and the associated lightning in Jupiter's atmosphere	101
4.13	Mean observed/modelled cloud profiles of the giant planets	102

xx Figures

4.15	Image of Saturn recorded by the HST/WFPC-2 instrument in 1990	103
4.16	Equilibrium cloud condensation model of Saturn's atmosphere	104
4.17	Observed and modelled abundance profiles in the atmosphere of Saturn	108
4.20	Equilibrium cloud condensation model of Uranus' atmosphere	111
4.21	Observed and modelled abundance profiles in the atmosphere of Uranus	114
4.22	Neptune observed by <i>Voyager 2</i> in 1989	117
4.23	Observed and modelled abundance profiles in the atmosphere of Neptune	118
4.24	Equilibrium cloud condensation model of Neptune's atmosphere	118
4.25	Close up of Neptune's methane clouds showing shadows cast by them on the main cloud deck beneath	123
5.1	Conversion of thermal energy into kinetic energy by a Carnot heat engine	134
5.2	Zonal wind structure of the giant planets	142
5.3	Zonal wind structure of the giant planets superimposed onto representations of their visible appearance	143
5.4	Canonical zonal flow diagram of Jupiter	144
5.5	Regime diagram of the main characteristic atmospheric motion as a function of the Richardson number (<i>Ri</i>)	148
5.6	Taylor–Proudman columns and differential cylinders	159
5.7	Stability of zonal structure of Jupiter and Saturn	160
5.8	Vortex tube stretching associated with Taylor–Proudman columns	161
5.9	Mosaic of four HST/WFPC-2 images of Jupiter showing the evolution of the Shoemaker–Levy 9 G impact site in 1994	165
5.10	<i>Voyager 1</i> image of Jupiter's Great Red Spot and one of the STBs White Ovals in 1979	166
5.12	Southern hemisphere of Jupiter observed by <i>Cassini</i> /ISS in December 2000	167
5.13	Multispectral images of Jupiter observed by <i>Cassini</i> /ISS on 8 October 2000, as it approached Jupiter during its flyby	168
5.14	<i>Voyager 1</i> image of a Brown Barge on Jupiter	170
5.15	The merger of the White Ovals from 1997 to 2000 observed by HST	172
5.16	Mesoscale waves in Jupiter's atmosphere recorded by <i>Galileo</i> /SSI	174
5.17	Standard Saturnian zonal nomenclature	178
5.18	Mosaic of five HST images of Saturn recorded between 1996 and 2000, showing the opening of Saturn's rings	178
5.21	Saturn's North Polar Hexagon, North Polar Spot, and the 'Ribbon Wave'	181
5.22	The 'Ribbon Wave' cloud structure in Saturn's atmosphere observed by <i>Voyager</i>	182
5.24	Three HST/WFPC-2 images of Uranus recorded in 1994 in a methane absorption band	185
5.25	Detail of the GDS and DS2 observed by <i>Voyager 2</i> in 1989	188
5.26	HST image of a new 'Great Dark Spot', located at a latitude of 32°N in the northern hemisphere of the planet Neptune recorded in 1994	189
6.1	Population of rotational energy states	204
6.2	Measured line strengths at 296 K in the rotation band of CO	205
6.3	Measured line strengths at 296 K in the ν_2 vibration–rotation band of CO ₂	206
6.4	Vibrational modes of CO ₂	207
6.5	Mid to far-IR transmission of tropospheric and stratospheric gases for a solar composition path	212
6.6	Near-IR transmission of tropospheric gases for a solar composition path	213

6.7	Radiative transfer in a grey plane-parallel atmosphere	214
6.8	Calculated nadir transmission weighting functions for Jupiter	216
6.9	Variation of peak of calculated transmission weighting function with wavelength for Jupiter	217
6.10	Calculated nadir and disc-averaged weighting functions for Jupiter at 600 cm^{-1}	219
6.11	Calculated limb weighting functions for Jupiter at 600 cm^{-1}	220
6.12	Scattering angle definition	226
6.13	Mie scattering calculation of Q_{ext} as a function of wavelength	228
6.14	Examples of different Henyey–Greenstein phase functions	230
6.15	Measured and calculated geometric albedo spectra of the giant planets	234
6.16	Calculated thermal emission spectra of the giant planets for nadir viewing	236
6.17	Calculated thermal emission spectra of the giant planets on a log scale	237
6.18	Calculated brightness temperature spectra of the giant planets	238
6.19	Overlap spectral regions between thermal emission and reflected sunlight for the giant planets	239
6.20	Microwave and radio-emission disc-averaged spectra of the giant planets	242
6.21	Appearance of Jupiter at 2.0, 3.56, and 6.14 cm as observed by the VLA	243
7.1	Grating spectrometer layout	250
7.2	Michelson interferometer layout	252
7.3	Transmission of Earth's atmosphere from ground to space (vertical path)	256
7.4	Comparative sizes of the giant planets and the Earth	257
7.5	Relative apparent sizes of the giant planets as seen at opposition from the Earth with a telescope of ‘perfect’ resolution	257
7.6	Relative appearance of the giant planets as seen at opposition from the Earth with good ‘seeing’ of approximately 1 arcsec resolution	258
7.7	Calculated disc-integrated irradiance spectra of the giant planets in the visible and near-IR as seen from the Earth at opposition	262
7.8	Calculated disc-integrated irradiance spectra of the giant planets in the mid- to far-IR as seen from the Earth at opposition	262
7.9	The European Southern Observatory Very Large Telescope (VLT)	264
7.10	Schematic design of VLT site	265
7.11	Mauna Kea site in Hawaii	266
7.12	Schematic design of the Keck Observatory, Hawaii	267
7.13	The Kuiper Airborne Observatory (KAO) aircraft	269
7.14	The KAO telescope looking through the aperture in the aircraft’s side	270
7.15	The IRAM millimetre array at the Plateau de Bure Observatory, France	272
7.16	The Very Large Array (VLA) in New Mexico	273
7.17	The Berkeley Illinois Maryland Association (BIMA) millimetre array at Hat Creek, California	274
7.18	The Owens Valley Radio Observatory (OVRO) millimetre array in Bishop, California	275
7.19	The Nobeyama Millimeter Array (NMA) in Japan	276
7.20	The Hubble Space Telescope in orbit about the Earth	277
7.21	Orbit of the Infrared Space Observatory (ISO) about the Earth	279
7.22	Schematic design of ISO	280
7.23	Disc-integrated spectra of the giant planets recorded by ISO/SWS	282
7.24	Disc-integrated spectra of Jupiter and Saturn recorded by ISO/LWS	283

xxii **Figures**

7.25	Disc-integrated spectra of the giant planets recorded by both ISO/SWS and ISO/LWS, plotted together on a log-scale	284
7.26	<i>Pioneer 10 and 11</i> spacecraft	287
7.27	<i>Pioneer 10 and 11</i> trajectories	287
7.28	<i>Voyager 1 and 2</i> spacecraft	289
7.29	<i>Voyager 1 and 2</i> trajectories	290
7.30	Current position of <i>Pioneer</i> and <i>Voyager</i> spacecraft	291
7.31	<i>Voyager/IRIS</i> instrument	292
7.32	<i>Voyager/IRIS</i> radiance spectra of the giant planets	293
7.33	<i>Voyager/IRIS</i> average spectra of the giant planets expressed as brightness temperatures	294
7.34	<i>Galileo</i> spacecraft	294
7.35	<i>Galileo</i> interplanetary trajectory	295
7.36	<i>Galileo</i> prime mission orbital design	296
7.37	Near-IR Mapping Spectrometer (NIMS)	298
7.38	<i>Galileo</i> probe descent trajectory	299
7.39	<i>Cassini</i> interplanetary trajectory	301
7.40	<i>Cassini</i> spacecraft	302
7.41	CIRS instrument	304
7.42	CIRS focal plane pointing and FOV	305

Tables

1.1	Observed properties of the giant planets and Earth	3
1.2a	Major satellites of Jupiter	8
1.2b	Major satellites of Saturn	9
1.2c	Major satellites of Uranus	11
1.2d	Major satellites of Neptune	12
1.2e	Properties of Pluto and Charon	13
2.1	Solar System abundances of the elements	20
2.2a	Bulk composition of the Jovian planets (relative to H ₂)	34
2.2b	Bulk composition of the Jovian planets (as mole fractions)	35
2.3	Solar System D/H ratios	35
2.4	Gravitational and magnetic properties of Earth and giant planets	42
3.1	Calculated exospheric escape times for the giant planets, Earth, Titan, and Triton	56
3.2	Thermal balance of the Earth and giant planets	61
4.1	Mean pressure/temperature properties of the giant planet atmospheres	68
4.2	Measured estimates of the eddy mixing coefficient in the giant planet atmospheres	79
4.3	Refractive index parameters and depolarization factors for giant planet gases	85
4.4	Pressure level of unit optical depth for Rayleigh scattering in the giant planet atmospheres	86
4.5	Coefficients <i>A</i> and <i>B</i> for various sublimation and vaporization curves relevant to giant planet atmospheres	90
4.6	Composition of Jupiter	96
4.7	Composition of Saturn	106
4.8	Composition of Uranus	113
4.9	Composition of Neptune	120
5.1	Instability criteria	149

xxiv **Tables**

6.1	Symmetry classifications of molecules relevant to giant planets	201
7.1	La Silla telescopes	263
7.2	Mauna Kea telescopes	267
7.3	Receivers available at the VLA	273
7.4	Spatial resolutions of terrestrial and earth-orbiting telescopes at the giant planets	285
7.5	Conversion of angular resolution to spatial resolution as a function of distance	286

Colour plates (between pages 166 and 167)

- 1.3** Jupiter as observed by *Cassini* in December 2000.
- 1.5** Saturn as observed by the Hubble Space Telescope (HST) in December 1994.
- 1.6** Uranus observed by *Voyager 2* in 1986.
- 1.7** Neptune as observed by *Voyager 2* in 1989.
- 2.6** Plan view of known trans-Neptunian object orbits in the Kuiper–Edgeworth belt.
- 4.10** False colour image of the GRS constructed from near-IR data recorded in 1996 by *Galileo*/NIMS.
- 4.11** False colour picture of a convective thunderstorm 10,000 km (6,218 miles) northwest of the GRS recorded by *Galileo*/SSI in June 1996.
- 4.14** *Galileo* NIMS images of Jupiter recorded in September 1996.
- 4.18** False colour image of Saturn recorded by HST in 1998.
- 4.19** Uranus observed by *Voyager 2* in 1986.
- 5.11** Cloud features on Jupiter observed by *Cassini*/ISS in 2000/2001.
- 5.19** False colour image of Saturn recorded by *Voyager 1* in 1980.
- 5.20** Highly enhanced image of Saturn's cloud features observed by *Voyager 2*.
- 5.23** HST/NICMOS false colour image of Uranus recorded in 1998.
- 5.27** False colour images of Neptune recorded in 1998.
- 5.28** Cylindrical map of Neptune between 90°S and 90°N from *Voyager 2* data.

1

Introduction

1.1 THE GIANT OUTER PLANETS

The giant outer planets: Jupiter, Saturn, Uranus, and Neptune (Figure 1.1) are by far the largest planetary bodies in the Solar System and together comprise 99.56% of the planetary mass. Although very far from the Earth, the enormous physical size of Jupiter and Saturn meant that these planets were easily visible to the ancients. However the other two ‘giants’, Uranus and Neptune, are significantly smaller and so much further from the Earth that they were unknown before the advent of telescopes, although Uranus is in fact just visible to the naked eye. Uranus was discovered by accident in 1781 by William Herschel (1738–1822) (later Sir William Herschel). Perturbations in the observed orbit of Uranus led John Couch Adams (1819–1892) and Urbain Jean Joseph Le Verrier (1811–1877) to independently predict the presence of a further planet, and Neptune was subsequently discovered close to its predicted position by Johann Gottfried Galle (1812–1910) in 1846. The mean observable properties of the outer planets are listed in Table 1.1.

All the giant planets are observed to rotate very rapidly, and the shape of the planets distort under the centrifugal forces which arise. Hence all the giant planets are noticeably oblate, especially Jupiter and Saturn, with the pole-to-pole diameter being significantly less than the equatorial diameter. Another key difference between the inner terrestrial planets, such as the Earth, and the giant planets is that the latter have surprising low densities, roughly equivalent to water, and similar to that of the Sun which has a density of 1.41 g cm^{-3} . Hence while we know that the Earth is a rocky body, the outer planets must be composed of much lighter material. In fact the giant planets are now known not to have a solid rocky ‘surface’ at all, but instead are gaseous in nature throughout.

Considering the mass, radius, and density of the giant planets they can be seen to divide naturally into two pairs: Jupiter and Saturn, composed primarily of hydrogen and helium and sometimes known as the ‘gas giants’; and Uranus and Neptune,

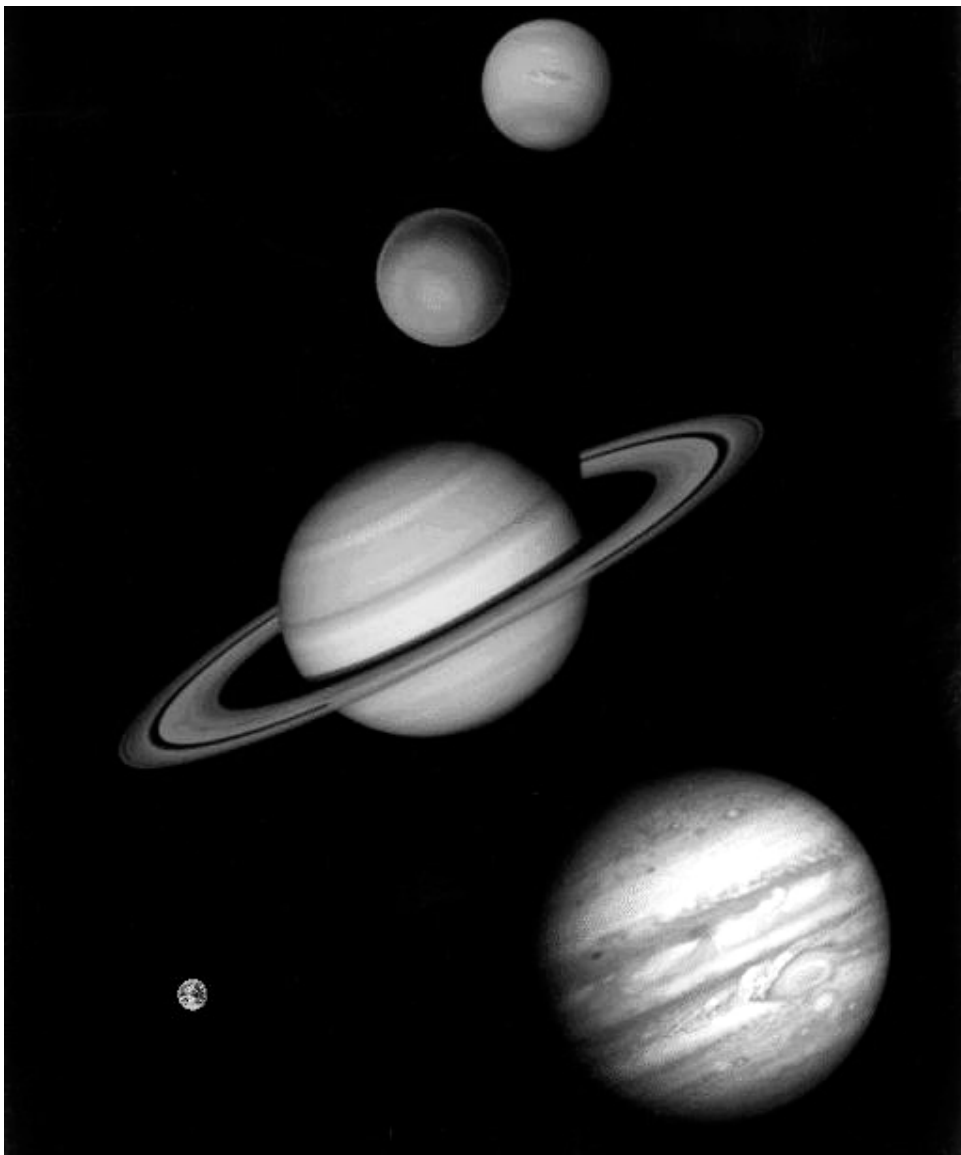


Figure 1.1 The giant planets as observed by the *Voyager* spacecraft together with the Earth for comparison.

Courtesy of NASA.

composed primarily of ices such as water and methane and sometimes known as the ‘ice giants’. Jupiter and Saturn both have a radius in the range 60,000–72,000 km, while Uranus and Neptune are somewhat smaller with a radius of approximately 25,000 km. These are respectively 10 times, and 4 times the radius of the Earth. By

Table 1.1. Observed properties of the giant planets and Earth.

Property	Earth	Jupiter	Saturn	Uranus	Neptune
Solar distance (AU) [†]	1.0	5.2	9.5	19.2	30.1
Sidereal orbital period (years)	1.0	11.9	29.5	84	165
Orbital eccentricity	0.017	0.048	0.056	0.046	0.009
Equatorial radius R_e (km) [‡]	6,378.0	71,492	60,268	25,559	24,764
Eq. radius relative to Earth	1.0	11.2	9.4	4.0	3.9
Oblateness $(R_e - R_p)/R_e$	0.000 34	0.065	0.098	0.023	0.017
Mass (10^{24} kg)	5.97	1,898.8	568.5	86.625	102.78
Mass (Relative to Earth)	1.0	318	95	14.5	17.1
Mean density (g cm^{-3})	5.515	1.33	0.70	1.27	1.76
Sidereal day	23 h 56 m	9 h 55 m (System III)	10 h 39 m (System III)	17 h 14 m	16 h 6 m
Eq. surface gravity at 1 bar (m s^{-2})	9.81	23.1	9.1	8.7	11.0
Escape velocity (km s^{-1})	11.2	58.6	33.1	21.1	23.3
Obliquity	23.5°	3°	27°	98°	29°
Equilibrium radiating temperature T_E (K)	255	110	82	58	47
Mean temperature at 1 bar (K)	288	167	138	79	70
Bolometric temperature* T_B (K)	255	124	95	59	59
Emitted/absorbed flux ratio	1.0	1.67	1.78	1.06	2.52

[†] 1 AU is one astronomical unit, the mean distance of the Earth from the Sun equal to 1.496×10^8 km.

[‡] The equatorial radii quoted refer to the 1 bar pressure level. References are given in Table 2.4.

* The bolometric temperature is the temperature of a black body sphere which would radiate heat to space at the same rate as that observed for the planet.

comparison, the radius of the Sun is ten times larger than Jupiter at 696,265 km. The mass of Uranus and Neptune are similar to each other at around $15 M_{\oplus}$ (where M_{\oplus} is the mass of the Earth), while the masses of Jupiter ($318 M_{\oplus}$) and Saturn ($95 M_{\oplus}$) are substantially different indicating that Jupiter is much more compressed than Saturn, given their similar size. Although the giant planets are truly massive, their combined mass is still only 0.1% of the solar mass which is estimated to be 1.9891×10^{30} kg. However, while most of the Solar System mass is accounted for by the Sun, its combined spin angular momentum and orbital momentum about the Solar System barycentre accounts for only 1% of that of the total Solar System. Instead, most of the Solar System angular momentum is accounted for by the giant planets, with the orbital angular momentum of Jupiter and Saturn contributing 85%. This counter-intuitive observation provides major constraints on models of Solar System formation as we shall see in Chapter 2.

The atmospheres of the giant planets are found to be meteorologically active and highly convective with the exception of Uranus which seems to have a somewhat sluggish atmospheric circulation. A clear indication of convective activity can be seen from observing the mean temperatures of the giant planets. The solar irradiance drops with the inverse square of distance from the Sun, and thus the calculated

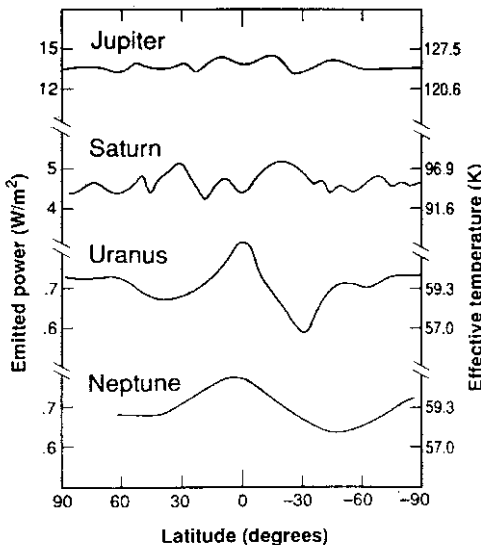


Figure 1.2 Total thermal infrared radiation flux (W m^{-2}) emitted by the giant planets as a function of latitude (Ingersoll, 1990). While some belt/zone variations are visible, the emitted flux is to a first approximation independent of latitude. The radiation is emitted predominantly from the 0.3–0.5 bar pressure levels. On the right-hand axis the radiative flux has been converted to brightness temperature (the temperature of a black body that would emit the same flux).

Reprinted with permission from Ingersoll (1990). Copyright 1990 American Association for the Advancement of Science.

effective radiating temperatures (the temperature at which the absorbed solar radiation is balanced by the emitted thermal radiation of the planet, discussed in Chapter 3) also decreases with distance from the Sun. While the observed mean *bolometric temperatures* (the mean temperatures at which the planets actually radiate) are indeed found to decrease with distance, the bolometric temperature exceeds the effective radiation temperature for all the giant planets except Uranus. Hence all the giant planets except Uranus radiate significantly more radiation than they receive from the Sun indicating a substantial internal heat source. The absorbed solar fluxes vary from a maximum at the sub-solar point to zero at the limb, while the emitted thermal fluxes are found to a first order to be independent of latitude and longitude and are shown as a function of latitude in Figure 1.2. The ratios of emitted to absorbed fluxes are listed in Table 1.1. As can be seen, both Jupiter and Saturn have significant internal heat sources. However, Uranus and Neptune which are otherwise so similar are found to be very different in this regard with Uranus having almost no internal heat source, and Neptune a very large supply giving it the highest flux ratio of all the giant planets. As we shall see in Chapter 3, this internal heat is thought for all the giant planets except Saturn to be residual heat left over from the formation of the planet which is slowly radiating away to space as the planets contract via the *Kelvin–Helmholtz* mechanism. For example the radius of

Jupiter is estimated to be currently shrinking by approximately 1 mm yr^{-1} . The emitted flux of Saturn is thought to be too high for the source to be residual formation heat since this is estimated to have radiated away almost 2 billion years ago. Instead the source is thought to arise due to internal differentiation of helium. We will return to this topic in Chapter 3.

1.2 OBSERVED ATMOSPHERES OF THE GIANT PLANETS

The observable atmospheres of the giant planets are dominated by molecular hydrogen and helium, in proportions roughly similar to that found in the Sun. The abundance of ‘heavy’ elements (which in this context refers to elements heavier than helium) is found, or estimated, to be approximately 3 times solar for Jupiter, 5 times solar for Saturn, increasing to 20–30 times solar for Uranus and Neptune. As we shall see in Chapter 2, the generally favoured interpretation of this and the mean size and density measurements, is that the outer planets accreted originally from icy planetesimals and became so massive that they were able to gravitationally attract hydrogen (H_2) and helium (H) from the solar nebula. It would appear that Jupiter and Saturn grew large enough, and rapidly enough to capture a huge mass of hydrogen and helium, while Uranus and Neptune were not able to attract so much. Hence the abundance of icy materials is higher in Uranus and Neptune than in Jupiter and Saturn. In the upper, cooler parts of the giant planet atmospheres which are actually observable, these heavy elements are mainly present in their fully reduced form and thus after H_2 and He , the next most abundant molecules inferred or measured (prior to any condensation) are, in decreasing order, water (H_2O), methane (CH_4), ammonia (NH_3), and hydrogen sulphide (H_2S). In fact, the upper atmospheres of the giant planets are so cold that H_2O , H_2S , and NH_3 condense at various levels forming the cloud decks observed on these giant planets. The upper atmospheres of Uranus and Neptune are so cold that even CH_4 condenses.

The observed atmospheres of the giant planets reveal many very interesting properties which will be briefly described here, and expanded upon in Chapters 2 to 5.

1.2.1 Jupiter

Through a telescope, Jupiter appears as a dusky ochre-coloured oblate planet with dark horizontal stripes aligned parallel to the equator. Two of these dark ‘belts’ are especially clear on either side of the brighter equatorial ‘zone’, with other thinner ‘belts’ seen closer to the poles. In fact the atmosphere of Jupiter has the most colour contrast of any atmosphere in the Solar System, including that of the Earth’s (Dowling, 1997), and a recent image of Jupiter recorded by the *Cassini* spacecraft in 2000 is shown in Figure 1.3 (colour plate). The general belt/zone structure appears to be very stable and a universally accepted naming scheme is shown in Figure 1.4. Although the general structure is long lived, the contrast of the different features

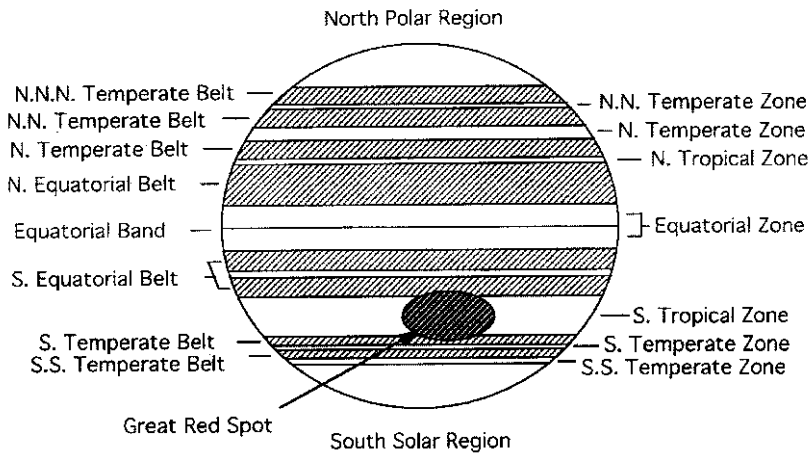


Figure 1.4 Jovian zonal nomenclature (Irwin, 1999).

Reprinted with kind permission of Kluwer Academic Publishers.

varies with time. These changes are usually gradual although the South Equatorial Belt (SEB) often displays dramatic outbursts of cloud activity (Dowling, 1997; Rogers, 1995). The belt/zone structure is generally thought to be formed by a global circulation system that upwells moist air in the ‘zones’ forming bright cloudy regions and subsides in the belts forming relatively cloud-free regions which appear dark in the visible wavelengths. The upper observable cloud deck is almost certainly composed of ammonia crystals, although as we shall see in Chapter 4 these appear to be modified in some way such that their pure spectral features are usually masked. Above the main cloud decks, various processes such as photochemistry act to create hydrocarbon haze particles, of uncertain composition, which gradually settle down through the atmosphere and are eventually pyrolysed and destroyed.

In addition to the general zonal structure, Jupiter is found to have a number of large oval structures or vortices. Unlike three-dimensional turbulence where one expects a large eddy to split up into smaller ones (for example a smoke ring rapidly dissipates), weather systems are governed predominantly by two-dimensional turbulence which has the counter-intuitive property that smaller eddies merge into larger ones by a process known as *backwards energy cascade*. The most famous of these ovals is the Great Red Spot (GRS). The GRS is a vast anticyclonic weather system which is currently $\sim 20,000$ km wide in the east–west direction and $\sim 12,000$ km in the north–south making it large enough that the Earth would easily fit in the middle! Winds in the centre of the spot are light but increase rapidly towards the edge reaching speeds of 100 m s^{-1} . The GRS appears to be extremely long lived. Robert Hooke (1635–1703) first reported a large spot in 1665 and ‘Hooke’s spot’ was subsequently observed intermittently from 1664 to 1701. Although this may have been the GRS itself, continuous observations of the current GRS can be traced back only to 1831 (Dowling, 1997; Simon-Miller *et al.*, 2002). Indeed it has been argued that Hooke’s spot became unstable and dissipated,

only for the current GRS to form later (Simon-Miller *et al.*, 2002). The current GRS has undergone numerous changes since observations began. For example it became nearly invisible in the 1860s, but within 10 years was very prominent again. It was particularly prominent during the *Pioneer* and *Voyager* flybys. In addition the GRS is shrinking in the longitudinal direction. A hundred years ago the east–west diameter of the spot was \sim 46,000 km, almost twice as wide as it is today. If the GRS continues to shrink in the east–west direction at the current rate then by 2040 the spot will be circular. We shall see in Chapter 5 that such a configuration is thought unlikely to be stable and thus the GRS may actually break up and disappear in our lifetime, perhaps to spawn the generation of a new great oval!

Other well-known ovals include the South Temperate Belt-South (STBs) White Ovals and the North Equatorial Belt-North (NEBn) Brown Barges. The current STBs White Ovals initiated as a disturbance in the South Temperate Zone (STZ) in 1939 and coalesced into three white coloured ovals. Two of these ovals merged together in 1998, and in March 2000, the two remaining ovals merged to form a single white oval. While 90% of the Jovian vortices are anticyclonic, only 10% are cyclonic and the most well-known of these are the NEBn Brown Barges which appear at the boundary between the NEB and the North Tropical Zone (NTropZ).

We shall see in Chapter 5 that the winds on the giant planets blow almost entirely in the zonal direction (i.e., east to west, or west to east), and the winds alternate in direction in association with the belts and zones. The zonal wind speed on Jupiter varies particularly rapidly with latitude and is puzzlingly strong at the equator, reaching speeds of 100 m s^{-1} in the eastward direction. The equatorial region of Jupiter is thus super-rotating (i.e., rotates faster than the bulk of the planet), a state which is extremely difficult to simulate with numerical models pointing to considerable underlying complexity as we shall see in Chapter 5. Observations of ovals and other atmospheric features by early astronomers such as Jean-Dominique (a.k.a. Gian-Domenico) Cassini (1625–1712) had to be referred to a longitude system and since, because of the fast equatorial prograde zonal winds, the equator rotates at a noticeably faster rate than the rest of the planet, two conventions arose. The System I frame referred to features at equatorial latitudes within 10° of the equator, while the System II frame referred to all other latitudes. Both systems have since been superseded by System III which is referenced to the bulk rotation of the interior as inferred from radio observations of the rotation of the magnetosphere.

Jupiter is accompanied by four large moons, known as the Galilean satellites, after their discoverer Galileo Galilei (1564–1642), which are closely aligned with the equatorial plane of Jupiter. Their alignment and the observed compositional differences (Section 1.3) suggest that these were formed at the same time as Jupiter, from the protoJupiter accretion disc. Jupiter also has a number of much smaller satellites which inhabit various eccentric and inclined orbits. These are probably captured planetesimals. The larger satellites of Jupiter, with a radius greater than 100 km, are listed in Table 1.2a. Finally, Jupiter has a small ring which was first observed by *Voyager 1* in 1979.

Table 1.2a. Major satellites of Jupiter.

Satellite	Mass (kg)	Radius (km)	Density (g cm ⁻³)	P (days)	A_G	R (10 ³ km)	e	i (°)
Io	8.9×10^{22}	1815	3.55	1.77	0.61	422	0.004	0.04
Europa	4.8×10^{22}	1569	3.01	3.55	0.64	671	0.009	0.47
Ganymede	14.8×10^{22}	2631	1.95	7.15	0.42	1070	0.002	0.21
Callisto	10.7×10^{22}	2400	1.86	16.69	0.20	1883	0.007	0.51
Amalthea	7.2×10^{18}	~100	1.72	0.50	0.05	181	0.003	0.40

P is the orbital period, A_G is the geometric albedo, R is the semi-major axis orbital radius, e is the orbital eccentricity, and i is the inclination of orbit to the planet's equator.

Only satellites with a mean radius greater than 100 km have been included.

1.2.2 Saturn

Through a telescope, and ignoring Saturn's magnificent ring system, the observable 'surface' of Saturn appears much blander than that of Jupiter with less banding and fewer ovals seen, although the predominant pale ochre colour is similar. Like Jupiter, Saturn also has a significant internal heat source. However, although this is a greater fraction of the total heat emitted, the combined total is much smaller than that of Jupiter. Hence the atmosphere is thought to be less meteorologically active than Jupiter's since the heating rate driving it is less. In addition, any convective structures that are present are more masked by overlying haze due to the colder temperatures found in the upper observable part of Saturn's atmosphere. These cooler temperatures mean that the expected upper cloud deck of ammonia ice (Chapter 4) occurs deeper in the atmosphere than in Jupiter's. In addition, the lower gravitational acceleration of Saturn means that the atmosphere is more vertically extended, and thus the absorption by upper atmospheric haze is enhanced.

Although generally more quiescent than Jupiter, major convective-type events are occasionally observed in Saturn's brighter zonal regions (outlined in Chapter 5). These are known as 'brightenings' or 'Great White Spots' and have been observed intermittently since 1793. Recent 'brightenings' occurred in the Equatorial Zone in 1990 and 1994 and were observed with the Hubble Space Telescope (HST) (Figure 1.5, colour plate). What appears to be happening in these events is that some kind of disturbance deep below the visible cloud/haze top of Saturn, triggers rapid, possibly thunderstorm-style, deep vertical convection, and the resultant formation of thick, very high ammonia clouds. These clouds are subsequently torn apart by the zonal wind flow shear and dissipate over a timescale of a few months.

The zonal wind system of Saturn is similar to that of Jupiter's with the wind direction alternating in association with the belts/zones. However the widths of Saturn's belts/zones are greater than those of Jupiter and the equatorial jet is found to be very much stronger and blows at a very rapid 500 m s^{-1} in the prograde direction relative to the interior System III rotation rate. Thus the equatorial zone of Saturn appears to be even more super-rotating than that of Jupiter.

The satellite system of Saturn is rather different to that of Jupiter and Table 1.2b

Table 1.2b. Major satellites of Saturn.

Satellite	Mass (kg)	Radius (km)	Density (g cm ⁻³)	P (days)	A_G	R (10 ³ km)	e	i (°)
Mimas	4.6×10^{19}	196	1.44	0.94	0.5	186	0.020	1.53
Enceladus	7.4×10^{19}	250	1.13	1.37	1.0	238	0.005	0.00
Tethys	7.4×10^{20}	530	1.19	1.89	0.9	295	0.000	1.86
Dione	1.1×10^{21}	560	1.43	2.74	0.7	377	0.002	0.02
Rhea	2.5×10^{21}	765	1.33	4.52	0.7	527	0.001	0.35
Titan	1.4×10^{23}	2,575	1.89	15.95	0.21	1,222	0.029	0.33
Hyperion	1.7×10^{19}	~130	1.85	21.28	0.3	1,481	0.104	0.43
Iapetus	1.9×10^{21}	730	1.15	79.33	0.2	3,561	0.028	14.72
Phoebe	4.0×10^{17}	110	0.07	550.48R	0.06	12,952	0.163	177
Janus	—	~100	—	0.69	0.8	151	0.007	0.14

P is the orbital period, A_G is the geometric albedo, R is the semi-major axis orbital radius, e is the orbital eccentricity, and i is the inclination of orbit to the planet's equator.

R is the retropart.

Only satellites with a mean radius greater than 100 km have been included.

lists those satellites with a radius greater than 100 km. Most of the satellites are somewhat smaller than the Galilean satellites with the exception of Rhea, Iapetus, and most notably Titan. Titan is the second largest satellite in the Solar System (after Ganymede) with a radius of 2,575 km and a substantial atmosphere composed mainly of N₂ with a surface pressure of ~1.5 atm. However, while its composition and surface pressure look similar to the Earth's, its surface temperature of ~90 K is extremely cold. The surface of Titan is obscured by atmospheric hazes, although recent ground-based and orbital telescopes have detected surface features in the near-infrared (NIR). The satellite will be the target of the *Huygens* probe which will parachute down through Titan's atmosphere soon after *Cassini/Huygens'* arrival in the Saturnian system in 2004.

The ring system of Saturn is the most stunning of all the giant planets. It is now known that all the giant planets have ring systems, which may form either from the tidal disruption of captured satellites, which subsequently spread and are dissipated or absorbed by the planet over time, or by the sputtering of particles from the surfaces of satellites. While the very thin ring first observed by the *Voyager* space-craft around Jupiter is thought to be due to sputtering, the massive ring system of Saturn can only have formed from the tidal disruption of a satellite and will thus eventually dissipate. Hence it is purely serendipitous that Saturn's ring system should be so spectacular at this particular moment in the Solar System's history.

1.2.3 Uranus

Uranus and Neptune are a good deal smaller than their larger siblings Jupiter and Saturn, and a good deal more dense being composed mostly of icy materials with a much less massive envelope of molecular hydrogen/helium. The greeny-blue colour

of Uranus, and blue colour of Neptune arises from the greater abundance of red-absorbing methane in the observable atmospheres of these planets, and also to the nature of the particles comprising the main observable cloud deck of these planets which preferentially absorb wavelengths longer than $0.6\text{ }\mu\text{m}$ (Figure 1.6, colour plate).

The observable atmospheres of both Uranus and Neptune are much colder than Jupiter and Saturn, and so ammonia is expected to condense deep in the atmosphere, but at levels still accessible to microwave remote sensing. However the deep abundance of ammonia inferred from ground-based microwave observations is so low that it would seem that most of the ammonia combines at even deeper levels with other molecules to form perhaps aqueous-ammonia or ammonium hydrosulphide (NH_4SH) clouds, well below the main observed upper cloud deck. The composition of the main cloud deck is unknown, but is most probably H_2S . Above this main cloud deck, a second thinner cloud deck of CH_4 ice is observed.

The atmospheric circulation of all the giant planets is driven by both solar and internal heating. However, for Uranus the mean global internal heat flux is at most 6% of the solar flux and thus the dominant circulation must be that forced by the uneven distribution of sunlight over the planet, by which the atmosphere attempts to revert to a barotropic state (temperature constant on constant-pressure surfaces). This thermal forcing is complicated by the fact that Uranus' large obliquity of 98° means that during the course of its orbit Uranus receives direct sunlight over both poles, as well as the equator. In fact, even though both poles experience a night that is half a Uranian year long, on average they receive 50% more sunlight per unit area than the equator. The *Voyager 2* flyby in 1986 occurred soon after the Northern Winter Solstice when the South Pole was facing almost directly towards the Sun and the North Pole was in complete darkness. If there were no meridional circulation, we would have expected there to have been a significant pole-to-pole temperature gradient of the order of 10 K. However the IR spectrometer on *Voyager 2* found there to be almost no temperature difference and hence the atmosphere appears to efficiently redistribute the absorbed solar heat. Uranus will reach its Northern Spring Equinox in 2007.

Although only a very low-contrast belt/zone structure is seen on Uranus, the planet does have a distinctive zonal wind structure which may be estimated from thermal measurements and also cloud tracking as is used for the other giant planets. Even though the convective overturning of Uranus' atmosphere appears sluggish, occasional convective-type white clouds are intermittently observed and may result from deep convection cells transporting CH_4 -rich air high into the atmosphere where it condenses. Similar cloud events are seen in the atmosphere of Neptune although these have much higher contrast and appear to be much more vigorous. The zonal wind structure of Uranus shows none of the rapid latitudinal structure associated with belts and zones seen on Jupiter and Saturn. Instead the structure appears fairly symmetric with mid-latitude winds blowing at 200 m s^{-1} in the prograde direction and equatorial winds blowing at 100 m s^{-1} in the retrograde direction, opposite to that of Jupiter and Saturn.

The large obliquity of Uranus may be evidence of an off-centre impact of a single

Table 1.2c. Major satellites of Uranus.

Satellite	Mass (kg)	Radius (km)	Density (g cm ⁻³)	P (days)	A_G	R (10 ³ km)	e	i (°)
Ariel	1.35×10^{21}	579	1.66	2.52	0.34	191	0.003	0.3
Umbriel	1.17×10^{21}	586	1.39	4.14	0.18	266	0.005	0.36
Titania	3.52×10^{21}	790	1.70	8.71	0.27	436	0.002	0.14
Oberon	3.01×10^{21}	762	1.62	13.46	0.24	584	0.001	0.10
Miranda	6.93×10^{19}	240	1.20	1.41	0.27	129	0.003	4.2

P is the orbital period, A_G is the geometric albedo, R is the semi-major axis orbital radius, e is the orbital eccentricity, and i is the inclination of orbit to the planet's equator.

Only satellites with a mean radius greater than 100 km have been included.

planet-sized body into Uranus towards the end of its accretion phase. The fact that Uranus' compact and regular satellite and ring system closely shares this obliquity suggests that the unusual spin vector was imparted early, some 4.6 Gyr ago. It has even been speculated that this cataclysmic event may have extinguished the internal heat source by effectively turning the planet inside-out causing the planet to release most of its internal energy soon after formation, rather than gradually like the other giant planets! The larger satellites of Uranus (radius > 100 km) are listed in Table 1.2c.

1.2.4 Neptune

Although Neptune is further from the Sun than Uranus, and thus receives less sunlight, its bolometric temperature is very similar to that of Uranus indicating a strong source of internal heat. In fact its ratio of emitted thermal/absorbed solar flux is the highest of any of the giant planets. Neptune appears bluer than Uranus and has some of the most active meteorology and global variability of any of the giant planets (Figure 1.7, colour plate).

The vertical cloud structure appears to be similar to that of Uranus. Again ground-based microwave spectra indicate very little NH₃ at the expected NH₃ condensation level suggesting that it combines with either H₂O or H₂S well below the observable cloud decks. Instead the main cloud deck is again probably composed of H₂S. A thinner CH₄ haze is found at higher altitudes. Like Uranus, no clear belt/zone structure is evident but a number of storm systems were observed by *Voyager 2* in 1989 including the 'Great Dark Spot' (GDS) at southern mid-latitudes. The GDS may have had a similar structure to Jupiter's GRS but it was short lived and had disappeared by the time of new HST observations in 1994. By 1995 a new dark spot had appeared at northern mid-latitudes. These features are dark probably because of either a darkening or deepening of the main H₂S cloud top at 3.8 bar. In addition several smaller white clouds are intermittently seen all over the planet, but mainly at mid-latitudes, and allow the estimation of zonal wind speed. The general structure of this seems similar to that of Uranus in that rather than a series of alternating

Table 1.2d. Major satellites of Neptune.

Satellite	Mass (kg)	Radius (km)	Density (g cm ⁻³)	P (days)	A_G	R (10 ³ km)	e	i (°)
Triton	2.15×10^{22}	1,353	2.07	5.88R	0.7	355	0.000	157.3
Nereid	2.06×10^{19}	170	1.00	360.14	0.4	5,513	0.751	27.6
Larissa	–	~100	–	0.55	0.06	74	0.001	0.2
Proteus	–	~200	–	1.12	0.06	118	<0.001	0.55

P is the orbital period, A_G is the geometric albedo, R is the semi-major axis orbital radius, e is the orbital eccentricity, and i is the inclination of orbit to the planet's equator.
Only satellites with a mean radius greater than 100 km have been included.

easterlies and westerlies as is found on Jupiter and Saturn, the winds are strongly retrograde at the equator and then reverse direction slowly to become strongly prograde at latitudes of approximately 70° before returning to 0 at the poles. However the strength of the zonal winds on Neptune greatly exceeds those found on Uranus with the retrograde equatorial jet reaching speeds of 400 m s⁻¹, while the prograde sub-polar jets are estimated to reach 200 m s⁻¹. Hence Neptune has the largest range of atmospheric rotation periods of any of the giant planets. Why the equatorial jets of Jupiter and Saturn should be prograde, and those of Uranus and Neptune are retrograde is a mystery that will be returned to in Chapter 5.

Neptune's satellite system is less compact and organized than Uranus and the largest satellite, Triton is in highly inclined orbit as can be seen in Table 1.2d which lists the larger Neptunian satellites with a radius greater than 100 km. *Voyager 2* observed Triton to have an extremely thin N₂ atmosphere.

1.3 SATELLITES OF THE OUTER PLANETS

The satellites of the giant planets are believed to have formed in two ways: (1) formation in a circumplanetary accretion disc (accretion discs are discussed in Chapter 2) at the same time as the planet; and (2) later capture of remaining planetesimals in the solar system. Satellites formed by the first mechanism are expected to lie in the equatorial plane of the planet and to have near-circular orbits. Satellites formed by the second mechanism may have any inclination, and are likely to have eccentric orbits.

The satellites of the giant planets show just this dichotomy as can be seen in Tables 1.2a–d. We will see in Chapter 2 that those satellites which formed directly from the circumplanetary accretion disc should have compositional differences which reflect the temperature distribution of the disc during the period in which the satellites were forming. This is particularly clear for the Galilean satellites of Jupiter (Io, Europa, Ganymede and Callisto) where clear density and thus compositional differences are observed with the inner satellites containing less H₂O and other volatiles than the outer satellites. To capture interplanetary planetesimals into the

Table 1.2e. Properties of Pluto and Charon.

Body	Mass (kg)	Radius (km)	Density (g cm ⁻³)	P (days)	A_G	R (10 ³ km)	e	i (°)
Pluto	1.5×10^{22}	1151	1.1	—	0.3	—	—	—
Charon	3.3×10^{21}	593	3.8	6.39	0.5	19.6	<0.001	99.0

P is the orbital period, A_G is the geometric albedo, R is the semi-major axis orbital radius, e is the orbital eccentricity, and i is the inclination of orbit to the planet's equator.

eccentric orbits seen requires some kind of friction, which suggests either aerocapture or that the planetesimals were braked by passing through the dense circumplanetary accretion disc and were thus captured early in the planet's formation. Presumably the composition of these captured satellites has not varied much since the beginning of the Solar System and so they are very interesting bodies to examine to understand the composition of early planetesimals. The clearest candidate for a captured satellite is Triton, whose physical characteristics are thought to be similar to Pluto and Charon (listed in Table 1.2e) and to the Kuiper belt objects discussed in Chapter 2.

1.4 EXPLORATION OF THE OUTER PLANETS

How do we know what we do know about the giant planets? The basic mass, density, and size parameters given in Table 1.1 were established from ground-based visible observations of the planets, their orbits around the Sun, and also the orbits of their satellites around them. We shall see in Chapter 2 that even this very simple data leads to profound implications for the internal structure of the giant planets.

Information on the temperature, composition, and cloud structure of the giant planets may be determined from ground-based observations at ultraviolet (UV)/visible through to infrared (IR) and microwave wavelengths in a number of spectral windows where the absorption of the Earth's atmosphere is low (Chapter 7). Absorption features of many molecules are observed in these spectra which may be used to constrain composition and at certain wavelengths dominated by absorption features of well-mixed gases such as H₂, H, and CH₄, thermal-IR and microwave observations of the 'brightness temperature' may be used to infer atmospheric temperatures over a wide range of pressure levels. Another technique that is sometimes used is stellar occultation. Occasionally the planets move in front of a star as seen from certain points on the Earth, and observations of the star's light curve during one of these occultations provides unique information on the upper atmospheres of these planets.

Such ground-based observations have recently been improved by the advent of adaptive optics, together with data processing techniques such as speckle imaging and deconvolution (discussed in Chapter 7), which have greatly increased the spatial resolution. In addition, earth-orbiting telescopes such as the HST and the Infrared

Space Observatory (ISO) are capable of not only greater spatial resolution (owing to the lack of an intervening, turbulent terrestrial atmosphere), but are also unencumbered by terrestrial absorptions and so may measure the entire visible and IR spectrum and also the UV spectrum which contains additional information on composition and clouds.

Together with continually improving telescopic observations from the ground or Earth orbit, observations of the giant planets entered the space age on 3 December 1973 when *Pioneer 10* became the first spacecraft to fly by a giant planet, Jupiter. Spacecraft remote observations of planetary atmospheres from UV to far-IR wavelengths offer excellent spatial resolution and unrivalled phase-angle coverage (the angle between the direction of the Sun and the direction of observation) of these atmospheres. Remote observations by subsequent missions: *Pioneer 11*, *Voyagers 1* and *2*, *Galileo*, and *Cassini/Huygens*, have greatly increased our knowledge of the atmospheres of the giant planets, and in the case of *Cassini/Huygens* will continue to do so when the *Cassini* spacecraft goes into orbit around Saturn in 2004 and subsequently deploys the *Huygens* entry probe into the atmosphere of Titan. In addition to remote observations, it is possible to record the strength of the radio signal broadcast by these spacecraft as they go behind or come out from behind the planets in their orbital trajectory, and such radio-occultations provide highly precise measurements of the vertical density profile, and thus thermal structure. Furthermore the *Galileo* mission included an entry probe which parachuted through the atmosphere of Jupiter on 7 December 1995 providing the first ever *in situ* measurements of the atmosphere of a giant planet.

1.5 ORGANIZATION OF BOOK

This book is aimed at final year physics/astronomy undergraduates and first year postgraduate students of planetary physics. Knowledge of basic physics is assumed, but no previous atmospheric physics knowledge is needed. Formulae are derived where possible or referred to if not.

In Chapter 2 we will look at theories of formation of the giant planets which may be used to interpret their physical and compositional differences and in Chapter 3 we will review how the atmospheres of these planets may have evolved with time. In Chapter 4 we will review what is known about the vertical temperature, composition, and cloud structure of the planets and in Chapter 5 we will look in detail at the meteorology and dynamical processes taking place. Since the only giant planet where *in situ* measurements have been made is Jupiter, most of what we know about the giant planets comes from remote sensing via measurements of the UV, visible, IR, and microwave spectra as we mentioned in the previous section. Hence in Chapter 6 we will examine the observed spectra of the planets and review the physics of the observed spectral features and radiative transfer processes. Finally, in Chapter 7 we will review the sources of information that have been used to construct our current understanding of the atmospheres of these planets and

outline how these remotely sensed spectra may be inverted via retrieval theory in order to estimate the physical conditions in these atmospheres.

1.6 REFERENCES

- Dowling, T. E. (1997) Jupiter: Atmosphere. *Encyclopaedia of the Planetary Sciences*. Chapman & Hall, London.
- Ingersoll, A.P. (1990) Atmospheric dynamics of the outer planets. *Science*, **248**, 308–315.
- Irwin, P. G. J. (1999) Cloud structure and composition of Jupiter’s atmosphere. *Surveys in Geophysics*, **20**, 505–535.
- Rogers, J. H. (1995) *The Giant Planet Jupiter*. Cambridge University Press, Cambridge, UK.
- Simon-Miller, A. A., P. J. Gierasch, R. F. Beebe, B. Conrath, F. M. Flasar, R. K. Achterberg, and the *Cassini* CIRS Team (2002) New observational results concerning Jupiter’s Great Red Spot. *Icarus*, **158**, 249–266.

1.7 BIBLIOGRAPHY

- Beatty, J. K. and A. Chaikin (eds) (1998) *The New Solar System* (4th Edition). Sky Publishing, Cambridge, MA.
- de Pater, I. and J. J. Lissauer (2001) *Planetary Sciences*. Cambridge University Press, Cambridge, UK.
- Encrenaz, T., J.-P. Bibring, and M. Blanc (1995) *The Solar System* (2nd Edition). Springer, Berlin.
- Jones, B. W. (1999) *Discovering the Solar System*. John Wiley & Sons, Chichester, UK.
- Miner, E. D. (2000) *Uranus: The planet, rings and satellites* (2nd Edition). Springer–Praxis, Chichester, UK.
- Miner, E. D. and R. R. Wessen (2002) *Neptune: The Planet, Rings and Satellites*. Springer–Praxis, Chichester, UK.
- Rogers, J. H. (1995) *The Giant Planet Jupiter*. Cambridge University Press, Cambridge, UK.
- Shirley, J. H. and R. W. Fairbridge (eds) (1997) *Encyclopaedia of the Planetary Sciences*. Chapman & Hall, London.
- Weissman, P. R., L.-A. McFadden, and T. V. Johnson (eds) (1999) *Encyclopedia of the Solar System*. Academic Press, San Diego, CA.

2

Formation of the giant planets

2.1 FORMATION OF THE UNIVERSE AND PRIMORDIAL CONSTITUENTS

According to current cosmological theories, approximately 14 billion years ago, the universe was created at a single point in space–time in the ‘Big Bang’. As the universe expanded and cooled, numerous particle physics processes and particle–antiparticle annihilations (Krane, 1996) occurred. After about $t = 6$ s the universe consisted of some number N protons, N electrons, $0.16N$ neutrons, 10^9N photons, and 10^9N neutrinos, all at a temperature of approximately 10^{10} K.

As protons and neutrons collided with each other it was possible to form deuterium nuclei via the reaction



However, interactions with photons with energy greater than 2.22 MeV can break up these deuterium nuclei via the reverse reaction. Hence the universe had to cool to about 9×10^8 K before significant numbers of neutrons could stably combine with protons in this way. At about the same time, the deuterons formed could engage in further reactions such as



with an energy of formation of 5.49 MeV, and



with an energy of formation of 6.26 MeV. Both these reactions have energies well above the threshold of deuteron formation and thus photons not energetic enough to break up deuterons would certainly not have been energetic enough to destroy these nuclei.

The final steps in initial nuclei formation were:



and



There are no stable nuclei with molecular weight 5 and thus no further reactions involving single nucleons were possible. Further reactions involving other nuclei did occur, but their products made up only a very small fraction of the final number of nuclei produced which was dominated by ${}^1\text{H}$ and ${}^4\text{He}$. By $t = 250$ s, the original $0.16 N$ neutrons had decayed to about $0.12 N$, and these combined with $0.12 N$ protons to form very nearly $0.06 N$ ${}^4\text{He}$ nuclei (i.e., the amount of ${}^2\text{H}$, ${}^3\text{H}$ which rapidly decays to ${}^3\text{He}$, ${}^4\text{He}$, and heavier nuclei left over was very small) via the reactions listed above. Hence after this time the universe contained $0.82 N$ nuclei, of which 7.3% were ${}^4\text{He}$ and 92.7% were protons. This translates to a helium mass fraction of about 24%. While ${}^3\text{He}$ and ${}^3\text{H}$ can be produced by fusion in stars, ${}^2\text{H}$ is not produced in significant quantities by any cosmic process that has occurred since the Big Bang, although it is destroyed via stellar fusion. Hence the deuterium nuclei present in the universe now are truly *primordial*, and the primordial value of D/H is estimated (from observing absorption lines in the spectra of very distant, first generation stars [Burles and Tytler, 1988]) to be $(3.4 \pm 0.25) \times 10^{-5}$.

As time progressed, the universe expanded and cooled until at about $t = 700,000$ yr, the energy of the photons had reduced to such a level that the nuclei could combine with the electrons to form neutral atoms. At this point the universe became transparent to electromagnetic radiation and astronomy could begin. Residual photons at this time typically had ultraviolet (UV) wavelengths, but as the universe has since expanded these have become considerably red-shifted to the microwave part of the electromagnetic spectrum. This residual radiation from the Big Bang is called the cosmic microwave background radiation and was first observed in 1967 by Arno Penzias and Robert Wilson. The cosmic microwave background radiation is found to be almost entirely isotropic (i.e., has almost the same intensity in all directions) and is consistent with black body, or cavity radiation with a temperature of 2.7 K. Although it was not identified until 1967, the microwave ‘hiss’ of the cosmic microwave background radiation is actually responsible for the familiar white noise seen on television screens between channels.

2.2 FORMATION OF THE STARS AND EVOLUTION OF THE INTERSTELLAR MEDIUM

As the universe further cooled and expanded, fluctuations in density initiated the condensation of galaxies and the formation of first-generation stars. Such density variations appear to have been present from the earliest stages of formation and were first detected as ripples in the cosmic microwave background radiation by the *Cosmic Background Explorer (COBE)* spacecraft, launched in 1989. The early, massive first-generation stars had very short lifetimes and ended in Type II supernovae, spreading

their fused and remaining unfused molecules into the material occupying the gaps between the stars known as the Interstellar Medium (ISM). Hence the composition of this medium changed over time, with the D/H ratio slowly reducing as deuterium was ‘burnt’ in stars and the He/H ratio increasing for the same reason. In addition of course, the abundance of heavy elements (where the term ‘heavy’ denotes atoms heavier than He) increased as more and more hydrogen and then helium was fused in stars. Subsequent stars typically had lower mass and longer lives and shed their atmospheres more gently into the ISM when they died. The $^{15}\text{N}/^{14}\text{N}$ ratio of the material in the ISM is a good indicator of how much the material has evolved, since ^{15}N comes mainly from early primary production in stars ending in Type II supernovae, while ^{14}N comes mainly from second-generation lower-mass, longer-lived stars. Hence we expect the abundance of ^{14}N to build up over time and the $^{15}\text{N}/^{14}\text{N}$ ratio to slowly reduce.

Hence all the atoms of our world, and indeed our bodies, such as carbon, oxygen, nitrogen etc., were all produced in the cores of ancient stars which have long since perished and given up fractions of their atmosphere to the ISM. A review of the chemistry taking place in the ISM and particularly molecular clouds is given by Fraser *et al.* (2002). The estimated abundance, relative to hydrogen, of different elements in the Solar System has been the subject of many studies over the years (Cameron, 1982; Anders and Grevesse, 1989; Grevesse and Sauval, 1998). The most recent estimates of Grevesse and Sauval (1998) are given in Table 2.1. These estimated ‘solar’ abundances have changed significantly over the years and thus when the abundances of elements in the giant planet atmospheres are referred to in various papers in terms of their ratio to solar abundance, the source of the solar data needs to be clarified.

The molecular form of the elements in the current ISM may be inferred from spectroscopic measurements and modelling. Oxygen is thought to be mostly found within molecules of water ice and carbon mainly within molecules of CO and some CH₄. Nitrogen is assumed to be mainly in the form of N₂, although this molecule can not be spectroscopically detected (Chapter 6), and sulphur is thought to exist mainly within H₂S molecules. Ion–molecule reactions forming water molecules directly from the atoms in the ISM would have enriched the deuterium abundance, such that the D/H ratio in water molecules of the presolar cloud was increased to something like 7.3×10^{-4} . All recent comets coming from the Oort cloud (see Section 2.4.1) have been observed to have a D/H ratio of 3×10^{-4} in their water molecules which has implications for how they formed as we shall see later in Section 2.6.1. For reference the D/H ratio in the Earth’s oceans is $\sim 1.5 \times 10^{-4}$. This is greater than would be expected if all the earth’s water came from the local solar nebula at the time of formation, but less than if it all came from comets as has sometimes been suggested. A combination of the two sources thus seems most likely.

Table 2.1. Solar System abundances of the elements.

Atomic number	Name	Atomic weight	Mass fraction	Number of atoms X/H	X/H ₂ (A&G 1989)	Ratio (new/old)
1	Hydrogen	H	1.008	0.708768	1.000	1.000
2	Helium	He	4.0026	0.2275034	0.09772	0.1954
8	Oxygen	O	15.9994	0.007603	6.761×10^{-4}	0.001352
6	Carbon	C	12.0111	0.002797	3.311×10^{-4}	6.623×10^{-4}
10	Neon	Ne	20.179	0.001706	1.202×10^{-4}	2.405×10^{-4}
26	Iron	Fe	55.847	0.001242	3.162×10^{-5}	6.325×10^{-5}
7	Nitrogen	N	14.0067	8.19×10^{-4}	8.318×10^{-5}	1.664×10^{-4}
14	Silicon	Si	28.086	7.17×10^{-4}	3.631×10^{-5}	7.262×10^{-5}
12	Magnesium	Mg	24.305	6.5×10^{-4}	3.802×10^{-5}	7.604×10^{-5}
16	Sulphur	S	32.06	3.57×10^{-4}	1.585×10^{-5}	3.170×10^{-5}
28	Nickel	Ni	58.71	7.34×10^{-5}	1.778×10^{-6}	3.557×10^{-6}
18	Argon	Ar	39.948	7.06×10^{-5}	2.512×10^{-5}	5.024×10^{-5}
20	Calcium	Ca	40.08	6.31×10^{-5}	2.239×10^{-6}	4.477×10^{-6}
13	Aluminium	Al	26.9815	5.86×10^{-5}	3.090×10^{-6}	6.181×10^{-6}
11	Sodium	Na	22.9898	3.38×10^{-5}	2.089×10^{-6}	4.179×10^{-6}
15	Phosphorus	P	31.00	7.91×10^{-6}	3.631×10^{-7}	7.262×10^{-7}
32	Germanium	Ge	72.71	2.18×10^{-7}	4.266×10^{-9}	8.532×10^{-9}
36	Krypton	Kr	83.903	1.2×10^{-7}	2.042×10^{-9}	4.083×10^{-9}
54	Xenon	Xe	131.28	1.37×10^{-8}	1.479×10^{-10}	2.958×10^{-10}
33	Arsenic	As	75.00	1.24×10^{-8}	2.344×10^{-10}	4.688×10^{-10}

Data mainly after Grevesse and Sauval (1998). (A&G 1989) denotes data from Anders and Grevesse (1989).

2.3 FORMATION OF THE PROTOSOLAR NEBULA

2.3.1 Collapse of the interstellar cloud

Our Solar System formed at the edge of our galaxy in one of its spiral arms about 4.6 billion years ago (as determined by radioisotope dating analysis). During this time the Solar System has completed approximately 20 orbits about the galactic centre. Since the formation of the galaxy, the composition of the local ISM had been evolving and at the time the Solar System formed was composed of approximately 71% by mass of hydrogen, 27% helium, and 2% ‘heavy’ elements (i.e., elements with molecular weight greater than He). About 1% of the heavy elements are thought to have existed in a condensed ‘dust’ phase.

The density and temperature of the ISM varies considerably with position. The denser parts having a temperature of the order of 10 K, and a density of typically $10^{-14} \text{ kg m}^{-3}$, from which the pressure can be calculated to be $3.5 \times 10^{-10} \text{ Pa}$. The pressure in these ‘dense molecular clouds’ is thus considerably less than the best modern laboratory vacuum! These dense clouds typically have a size of a few light years across and thus contain enough mass to form many hundreds of stars. Figure 2.1 shows just such a dense molecular cloud, Barnard 68, observed in 1999 by the ESO Very Large Telescope (VLT). At visible wavelengths, the opacity of dust in these clouds is sufficient to obscure the light of stars behind the cloud. However, since the dust grains are small, the opacity decreases rapidly with wavelength (as we shall see in Section 6.5) such that at near-infrared (NIR) wavelengths the cloud becomes almost transparent. Under certain circumstances these dense molecular clouds may become unstable to gravitational collapse leading to the formation of stars as we shall now see.

Jeans theory of collapse

The conditions for gravitational collapse of dense molecular clouds were first considered by Sir James Jeans in 1917. Ignoring all other forces, an isothermal cloud of mass M and temperature T will undergo gravitational collapse if its gravitational potential energy is greater than its internal thermal energy. The thermal energy of a cloud is given roughly by

$$E_T = Nk_B T = \frac{M}{\mu m_H} k_B T \quad (2.6)$$

where μ is the mean molecular weight of the material in cloud, m_H is the mass of a hydrogen atom, N is the total number of molecules in the cloud, and k_B is the Boltzmann constant.

The gravitational binding energy of a cloud of radius R is given by

$$E_G \approx \frac{GM^2}{R} \quad (2.7)$$

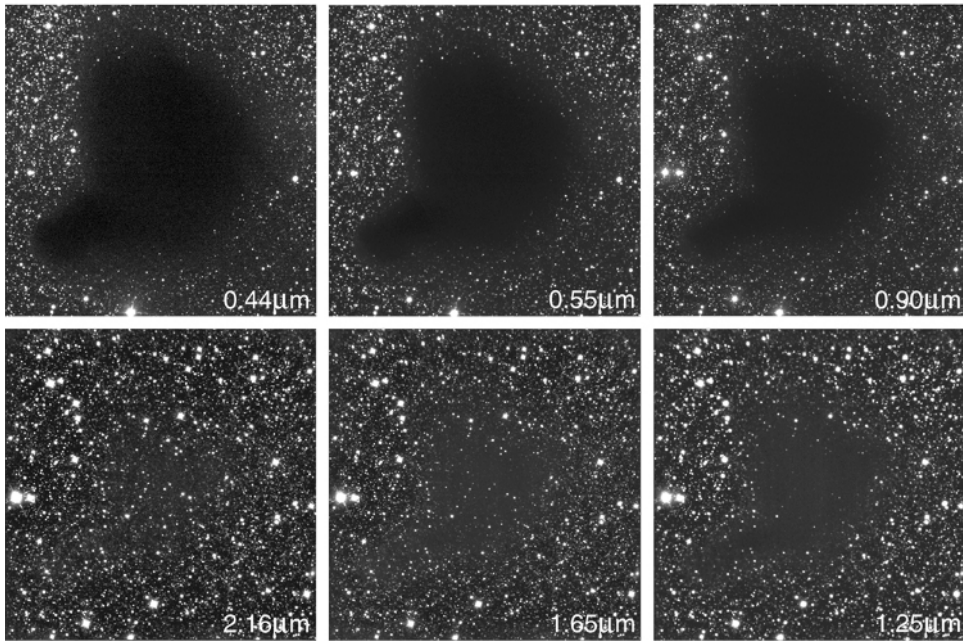


Figure 2.1 Molecular cloud Barnard 68 observed by the ESO Very Large Telescope at a range of visible and near-infrared wavelengths between 0.44 and 2.16 μm .

Credit European Southern Observatory.

and hence an interstellar cloud should collapse if $E_G > E_T$, or

$$\frac{GM^2}{R} > \frac{Mk_B T}{\mu m_H}. \quad (2.8)$$

Assuming that the cloud has a uniform density ρ , its mean radius will be

$$R = \left(\frac{3M}{4\pi\rho} \right)^{1/3}. \quad (2.9)$$

Substituting for R in Eq. 2.8, and rearranging, we obtain Jeans' expression for the minimum mass of cloud of temperature T and density ρ that will collapse

$$M_J = \frac{1}{\rho^{1/2}} \left(\frac{k_B T}{G\mu m_H} \right)^{3/2}. \quad (2.10)$$

Substituting a temperature of 10 K, and a density of $10^{-14} \text{ kg m}^{-3}$, we find that $M_J \approx 10^{29} \text{ kg}$, or approximately $0.1 M_\odot$ (where M_\odot is the mass of the Sun), and from Eq. 2.9, $R = 1.4 \times 10^{14} \text{ m}$ (or 0.015 light years, or $\sim 1,000 \text{ AU}$). Hence according to Jeans' theory, the denser parts of the ISM should be unstable to Jean's collapse. However this theory ignores effects such as magnetic fields and

gas flow in the clouds which oppose the collapse. Thus, in reality it appears that in most cases some sort of external compression is also required such as collision between two clouds, impact of a shock wave from a nearby, exploding star, or the action of spiral density wave that sweeps through the galaxy (Jones, 1999).

Once the whole cloud starts to contract, the denser parts of the cloud contract more quickly and thus the cloud quickly fragments, with each cloud fragment condensing to form its own star system. Thus new stars form in clusters as is observed.

2.3.2 Formation of circumstellar disc

As each cloud fragment collapses, the gravitational binding energy is released as thermal energy. In the initial stages the temperature rise is small since the opacity of the nebula is very thin and thus this energy efficiently radiates away. However, the centre of the nebula is predicted to collapse more quickly than the edge, and once its density increases to the point where it starts to become opaque, the temperature rise is rapid. Although this rise in temperature tends to slow the rate of collapse, the temperature of the central ‘protostar’ still continues to rise until the temperature of the core is sufficient to initiate fusion.

The whole cloud fragment will have some net rotation. Hence as the cloud collapses, the inner parts will begin to rotate more rapidly by conservation of angular momentum. Material on or near the net rotation axis will fall freely towards the centre whereas the infall elsewhere is moderated by the centrifugal force. Hence a circumstellar disc forms in the plane perpendicular to the rotation axis. Approximately 50% of young stellar objects (YSO) that have been observed to date are surrounded by disc- or ring-like structures (Drouart *et al.*, 1999; André and Montmerle, 1994). There are 4 classes of these:

- (1) Class 0. The youngest class of YSO with a large mass of circumstellar material ($0.5 M_{\odot}$ or more) and a lifetime of approximately 10,000 yr (M_{\odot} is the current mass of the Sun).
- (2) Class I. Mass $\sim 0.1 M_{\odot}$, lifetime around 100,000 yr, extending up to few 1,000 AU across.
- (3) Class II. Mass $\sim 0.01 M_{\odot}$, lifetime around 1 million yr and optically thick at $10 \mu\text{m}$ with excess thermal emission.
- (4) Class III. Optically thin at $10 \mu\text{m}$, and radially more compact at around 100 AU.

These observations are consistent with the evolutionary scenario where a massive envelope (Class 0) rapidly collapses to form a protostar in a timescale of only 100,000 years, together with an extended disc of mass between 0.01 and $0.1 M_{\odot}$ (Class I and Class II) which evolves over a timescale of 1 million to 10 million years into a less massive disc with lower density (Class III). The upper bound of the estimated disc masses is consistent with a theoretical upper mass of $\sim 0.3 M_{\odot}$ derived from stability arguments of Shu *et al.* (1990). Particularly clear examples of these circumstellar discs are seen in the Orion Nebula. Here several such nebulae are seen in front of a glowing background interstellar cloud which is lit by the light of

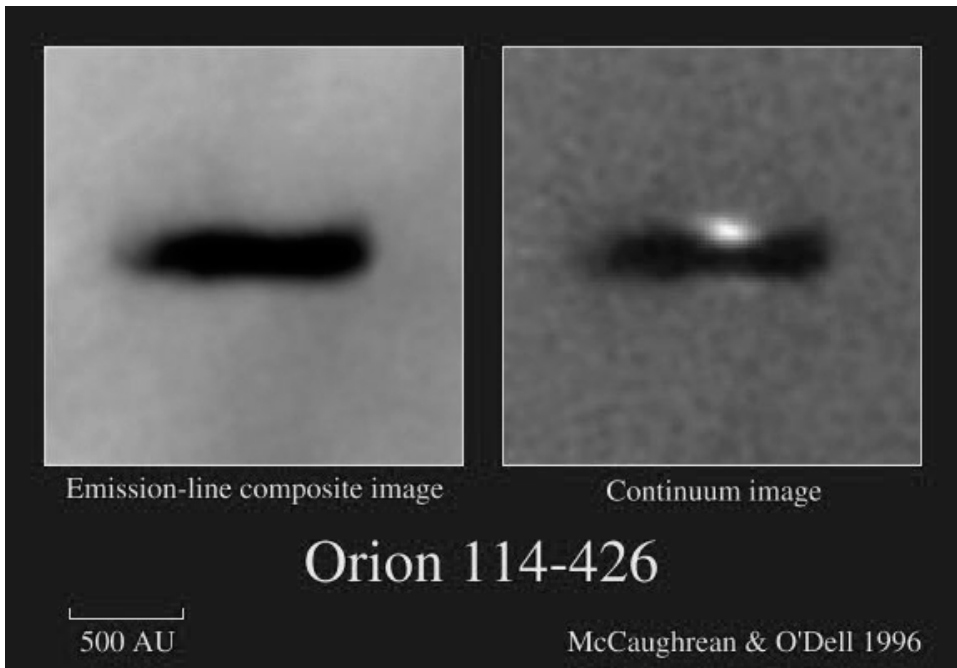


Figure 2.2 Hubble Space Telescope image of a young circumstellar disc (Orion 114-426) in the Orion Nebula (after McCaughrean and O'Dell, 1996). The left-hand panel shows an emission-line composite, made by combining data from three narrow-band filters centred on bright emission lines from the nebula, namely [OIII] (blue), Halpha (green), and [NII] (red). The strong emission lines provide a bright background which reveals the circumstellar discs as silhouettes around their young stars. The right-hand panel shows the corresponding continuum image taken through the medium bandwidth F547M filter. The central star shows up most clearly in the right-hand panel, and a faint reflection nebula is also seen above and below the plane of the silhouette disk.

Courtesy of Mark McCaughran and the *Astronomical Journal*.

stars already created (Figure 2.2) (McCaughrean and O'Dell, 1996; McCaughrean *et al.*, 1998). As can be seen, the circumstellar disc is of the order of 1,000 AU across. This formation scenario requires a mechanism for disc dispersal on timescales of 1 million to 10 million years. Solar mass stars cannot easily blow away dense circumstellar discs and thus accretion onto the star seems more likely. However in order for this accretion to proceed, some way is needed of losing or redistributing the angular momentum.

By conservation of angular momentum, one would expect the nebula to rotate fastest towards the centre and thus the protoSun should initially have been rotating very rapidly. However, the Sun now contains only 1% of the Solar System angular momentum (0.5% in spin, and 0.5% in orbital rotation of the Sun about the Solar System barycentre, which is just outside of the Sun) with the bulk (85%) now contained in the orbital angular momenta of Jupiter and Saturn. Hence to explain

the current state of the Solar System, a means is needed whereby the circumstellar disc was accreted or dissipated and where most of the protoSun's angular momentum was lost. Two key processes have been identified:

- (1) *Turbulence.* Conditions in the early circumstellar disc are likely to have been very turbulent. This turbulence would have led to a net transfer of mass outward in the outer part of the disc, and inwards towards the protoSun nearer the centre. Associated with this mass flow would have been a net transfer of angular momentum from the protoSun to the disc. The transfer of angular momentum would have caused the disc to spread further and further out into space, reducing its density. In the inner disc, the mass loss would have been towards the protoSun and also to space via outflow along the rotation axis, in collimated jets which are observed in protostellar nebulae as shown in Figure 2.3 (McCaughrean *et al.* 1994). These polar jets are probably collimated both by the dense circumstellar disc itself and by the magnetic field of the protostars. They are seen to be episodic in nature, which is consistent with them being fed by turbulent infall of the inner circumstellar disc. However, while this bipolar outflow would have carried off as much as 10% of the nebula mass, it would not have accounted for much of the angular momentum.
- (2) *T-tauri phase.* The Sun is currently about half way through its *main sequence* (Lewis, 1995). Just prior to the main sequence phase, a period called the *T-tauri phase* (named after a star currently observed in the constellation of Taurus) occurs which is marked by a considerable outflow of gas in the solar wind, and also high UV radiation. For a star with the mass of the Sun, this period would have lasted about 10 million years and would have led to the Sun losing about 10% of its mass, and a significant proportion of its angular momentum. As we shall see later, the high solar wind associated with this phase would have swept away any remaining fragments of the solar nebula and thus the timing has profound implications on the formation of the giant planet atmospheres.

Observations of YSOs suggest that the Sun had accreted most of its mass very rapidly within about 100,000 yr of the start of collapse. At this stage the Sun was surrounded by a circumstellar disc. The inner part of the disc would have been very hot due to a combination of opacity, turbulent frictional heating, and solar luminosity. Temperatures out to approximately 1 AU probably exceeded 2,000 K, evaporating almost every solid constituent. Further out, temperatures reduced with distance from the Sun and thus the 'condensation line' (i.e. the distance from the Sun that different minerals and ices would have condensed from the nebula) occurred at varying distances from the Sun, with more volatile materials condensing further from the Sun than less volatile materials. As time progressed, and the disc cooled and spread out, these condensation lines would have moved inwards towards the Sun at a rate governed by both the radiative heat loss to space and the frictional heating generated by turbulence. Not all parts of the disc may have been dominated by turbulence however. In the outer disc, beyond perhaps 50 AU the nebula density is predicted to have been so low that turbulence would not have been able to play such an important role. In this low-turbulence region, material would rotate about

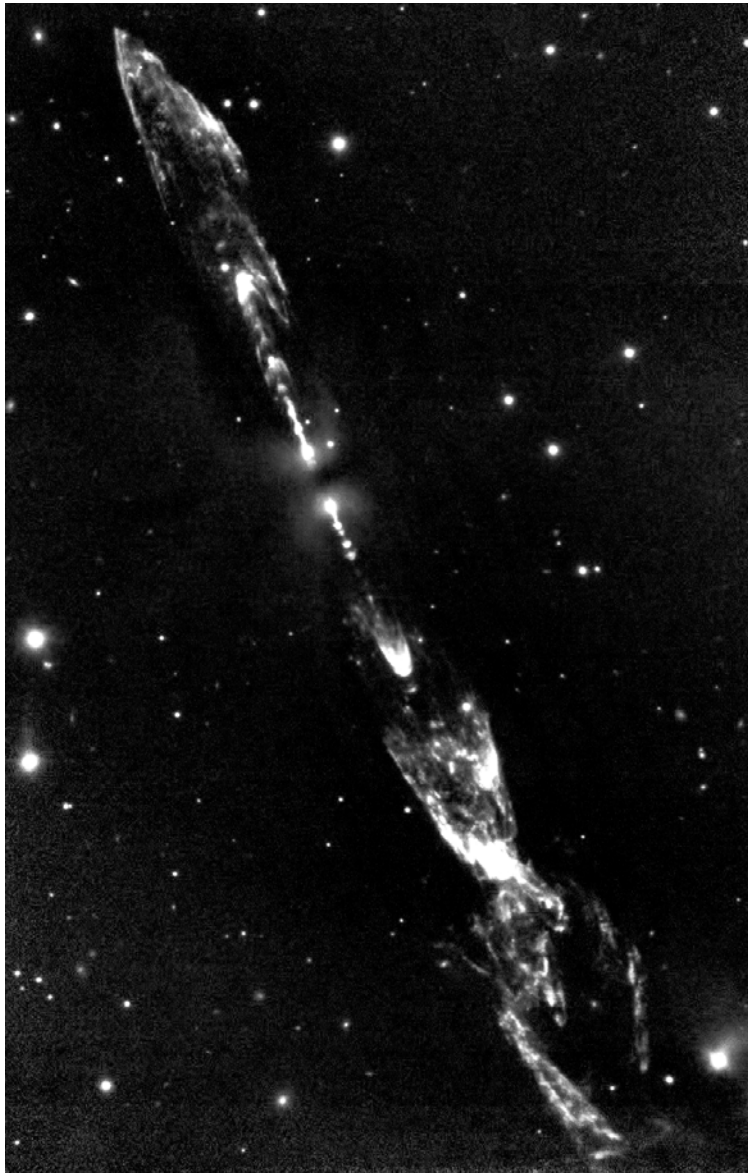


Figure 2.3 Wide-field, medium-resolution near-IR (molecular hydrogen line at $2.122\text{ }\mu\text{m}$) image of HH212. Data taken in December 1996 using the Calar Alto 3.5-m telescope in Spain. The image shows the bi-polar jet from the formation of a star near the centre of the frame and hence the circumstellar disc appears to be almost edge-on. Material can be seen to be ejected in pulses and there is a clear symmetry between the pulses in the upper and lower jets. The episodic nature of the outflow seen points to the turbulent nature with which material falls from the circumstellar disc onto the central star.

Courtesy of Mark McCaughrean.

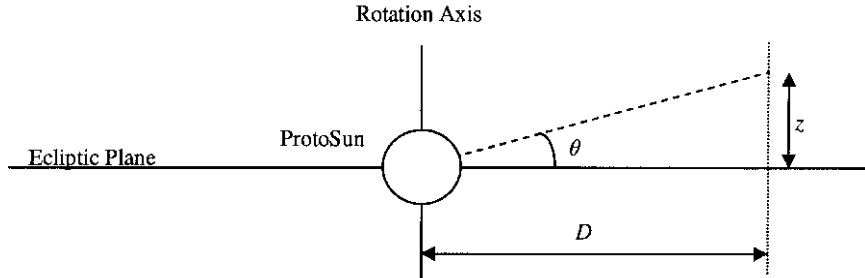


Figure 2.4 Variation of nebula pressure in circumstellar disc above ecliptic plane.

the protostar with a period governed by Kepler's orbital laws and thus this part of the nebula is called the Keplerian disc. Such two-component circumstellar discs have recently been observed (Drouart *et al.*, 1999; Guilloteau *et al.*, 1997). Hence while we expect the material in the inner turbulent disc to have undergone significant mixing and thermal reprocessing, material in the outer Keplerian disc will have been largely unmixed, and unprocessed from its presolar form.

The structure of the gaseous part of the nebula would have been determined via hydrostatic equilibrium and centrifugal forces in the radial direction, but by hydrostatic forces only in the direction parallel to the rotation axis (Figure 2.4). Collapse in this direction stops when the pressure gradient force equals the gravitational force, i.e.,

$$g_z = g \sin \theta \approx \frac{GM_S z}{D^3} \quad (2.11)$$

where D is the distance to the protostar, z is the height of a parcel of gas above the disc plane, M_S is the mass of the protostar, and θ is the angular elevation of the parcel above the disc plane as seen from the protostar. Assuming hydrostatic equilibrium, the change in pressure between heights z and $z + dz$ above the disc plane is given by

$$dp = -\rho g_z dz = \left(-\frac{p\mu}{RT} \right) \left(\frac{GM_S z}{D^3} \right) dz \quad (2.12)$$

where μ is the molecular weight of the gas and R is the gas constant, and hence in equilibrium

$$p_z = p_c \exp \left(-\frac{z^2}{H^2} \right) \quad (2.13)$$

where H is the *scale height* given by

$$H = \left(\frac{2RTD^3}{\mu GM_S} \right)^{1/2} \quad (2.14)$$

This structure is very different to that formed by the dust grains in the nebula. The condensed dust/ice grains were initially only 1–30 μm across and the grains tended to settle on the ecliptic plane as a result of the net gravitational field and gas drag.

Settling increased as the disc turbulence diminished and the dust grains grew. The dust sheet was probably of the order of 10,000 km thick near the Sun, increasing slightly with distance (Jones, 1999).

2.4 FORMATION OF THE JOVIAN PLANETS AND COMETS

2.4.1 Core accretion model

Concentration of the solid material into a sheet in the disc plane increased the chances of collision. For small grains, Van der Waal's attractive forces could act between grains in similar orbits, causing grains to collide with low collision speeds, and leading them to stick together in a process called coagulation. While the relative velocities between grains in nearby orbits reduced with distance from the Sun, so did the collision probability since the nebula density decreased with distance. Hence the coagulation time increased with distance except at the condensation line of H₂O or the 'ice line' where there would have been a small step-like increase superimposed on the general decreasing trend. Hence it is estimated that by the time bodies could have grown to 10 mm at 30 AU, bodies at 5 AU would have grown to 0.1–10 km in size, large enough to be called *planetesimals*. Conditions in this early nebula are likely to have remained highly turbulent and evidence for this comes from the recent detection of crystalline silicates in comets coming from the Oort cloud. These comets are thought to have originally condensed in the cooler outer nebula near the orbits of Uranus and Neptune. They were thus expected to have a very low abundance of crystalline silicates since these minerals have high condensation temperatures and are thus expected to have condensed close to the Sun, not in the outer Solar System. Detection of such minerals in these comets thus suggests considerable mixing between material that originally condensed close to the Sun and that which condensed further away.

The formation of the giant planets from planetesimals and Nebula gas is generally thought to have occurred in three phases (Pollack *et al.*, 1996) as outlined below.

Phase 1

Once planetesimals started to reach a size of the order of 10 km, their gravitational attractive forces started to become significant. This increased the collision rate between planetesimals and led to the growth of larger planetesimals at the expense of smaller ones. This was a runaway process and led to the formation of a number of *embryos* in a timeframe of perhaps 500,000 years after the formation of the Sun. The embryos accounted for 90% of the original mass in the local *feeding zone*, which formed an annular strip covering a small range of heliocentric distances centred on the embryo. The remaining 10% of the solid material in each feeding zone was composed of a swarm of very much smaller planetesimals. Solar nebula models predict that both the embryo masses and the widths of the feeding zones increased with distance, with a sharp increase at the water ice condensation line (Jones, 1999).

Typical modelled embryo masses at 1 AU are of the order of $0.1 M_{\oplus}$ (where M_{\oplus} is the mass of the Earth), while at 5 AU they are of the order of $10 M_{\oplus}$. While it is tempting to think that this is due to the presence of ices as well as refractory elements in the outer parts of the dust sheet, and hence a greater density of solid material, this is in fact not quite correct. The embryo formation process initially requires low-speed collisions between planetesimals in near-identical orbits and these conditions are more easily met in the outer, more slowly rotating part of the nebula, than the inner more rapidly rotating, turbulent part. An additional effect is that at greater distances from the Sun, the tidal disruption forces are less which also allows embryos to form more easily. Hence the calculated widths of the feeding zones are modelled to increase with distance and thus the predicted embryo masses, and their separations, are larger.

Phase 2

Once the embryos predicted to form in the outer Solar System reached a mass of the order of $10 M_{\oplus}$, they started being able to trap the nebula gas itself, and any remaining planetesimals. This second very slow stage of accretion lasted between 1 and 10 million years and led to the accumulation of a considerable envelope of gas and ice about the initial primary ice core. Eventually the mass of some of the planets reached a critical mass which was so high that the remaining nebula gas became unstable to hydrodynamical collapse, leading to the final phase of formation.

Phase 3

Once the critical mass was reached, any remaining nebula gas hydrodynamically collapsed onto the planet. This is modelled to have been a very rapid phase lasting perhaps 30,000 yr for Jupiter and 20,000 yr for Saturn. Since the time for the accretion of the critical mass is predicted to have increased with distance from the Sun, due to the decrease in nebula density, it would appear that Uranus and Neptune never accreted enough mass to leave phase 2. The energy released by the accretion of the giant planets would have raised the internal temperatures of the planets, including the new gaseous envelopes significantly. Hence most of the icy planetesimals would have dissolved into the envelopes, with only the more rocky materials accreting onto the cores. The heat released by this accretion would also have initiated substantial convection in the envelopes, further inhibiting accretion on to the core.

The timing of these phases is critical in explaining the nature of the Jovian planets. Jupiter is predicted to have reached phase 3 about 1.5 million years after the formation of the Sun, and Saturn after something like 11 million years (Hersant *et al.*, 2001). These times are very much model-dependent and are constantly being revised. What is generally accepted with these models however, is that before Uranus and Neptune could reach their critical mass, the remnants of the circumsolar disc were finally dissipated when the Sun entered its T-tauri phase after about 16 million years (Drouart *et al.*, 1999). The high solar wind associated with this phase effectively swept all remaining gas out of the solar nebula and shut off the gas-capture

process. Hence the bulk differences between the giant outer planets, and indeed the inner terrestrial planets, are very elegantly explained with this model.

A recent observation which supports this timescale of giant planet formation is of the protoplanetary disc around a nearby pre-main-sequence star (Brittain and Rettig, 2002). The abundance of CO (and presumably other gases) in the inner part of this disc, which is estimated to be 5–10 million years old, appears to be very low out to a distance of approximately 17 AU, but is substantial at larger distances. This suggests that the inner stellar system has already been substantially cleared of gas. However H_3^+ emission is also detected from the star system. While it is theoretically possible that such emission comes from the inner edge of the circumstellar disc near 17 AU this seems unlikely since the inferred abundance of CO at this distance should very efficiently destroy all H_3^+ molecules. Instead it is suggested that the H_3^+ emission comes from the auroral regions of one or more giant planets that have already formed at distances less than 17 AU from the star. This suggestion is consistent with the observation that the only H_3^+ emission observed anywhere in our own Solar System comes from the auroral regions of our own giant planets.

Although some of the planetesimals remaining in the nebula would have continued to be captured (as indeed they are today with Jupiter capturing Comet Shoemaker–Levy 9 in 1994), most remaining planetesimals would have been ejected from the Solar System by the gravitational perturbations to their orbits exerted by the giant planets. All planetesimals in the Jupiter–Saturn region are predicted to have been accumulated or ejected completely. Planetesimals in the Uranus–Neptune region however would have been less violently ejected and are thought to have formed the Oort cloud which is believed to exist as a spherical shell of small, irregularly shaped bodies orbiting the Sun well beyond the main planets. The existence of this cloud was postulated in 1950 by the Dutch astronomer Jan Hendrik Oort (1900–1992) who noticed that no comet had ever been observed with an orbit indicating that it came from interstellar space, and that the orbits of most long-period comets had aphelia (greatest distance from the Sun) of about 50,000 AU, and no preferred direction. Hence Oort proposed that long-period comets come from objects uniformly spread around the Sun at about this aphelia distance which are perturbed by tiny effects such as gravitational tides exerted by stars in the galactic disc and in the galactic core. Estimates for the mass of material in the Oort cloud vary from about 40 M_\oplus to perhaps the mass of Jupiter and most Oort cloud objects are thought to orbit at a distance of between 10,000 and 20,000 AU from the Sun although the cloud extends outwards as far as perhaps 50,000 to 70,000 AU (Figure 2.5).

Beyond the orbit of Neptune, the probability of embryo formation appears to have been too small to form a giant planet, perhaps due to the lack of turbulent mixing at this distance. Instead, the remaining planetesimals in this region, which form the Kuiper–Edgeworth belt, are probably relatively unevolved examples of the planetesimals that originally existed in this region. The Kuiper–Edgeworth belt is named after Gerard Peter Kuiper (1905–1973) and Kenneth Essex Edgeworth (1880–1972) who independently suggested the presence of small planetary bodies beyond the orbit of Pluto and Neptune respectively. The Kuiper–Edgeworth belt

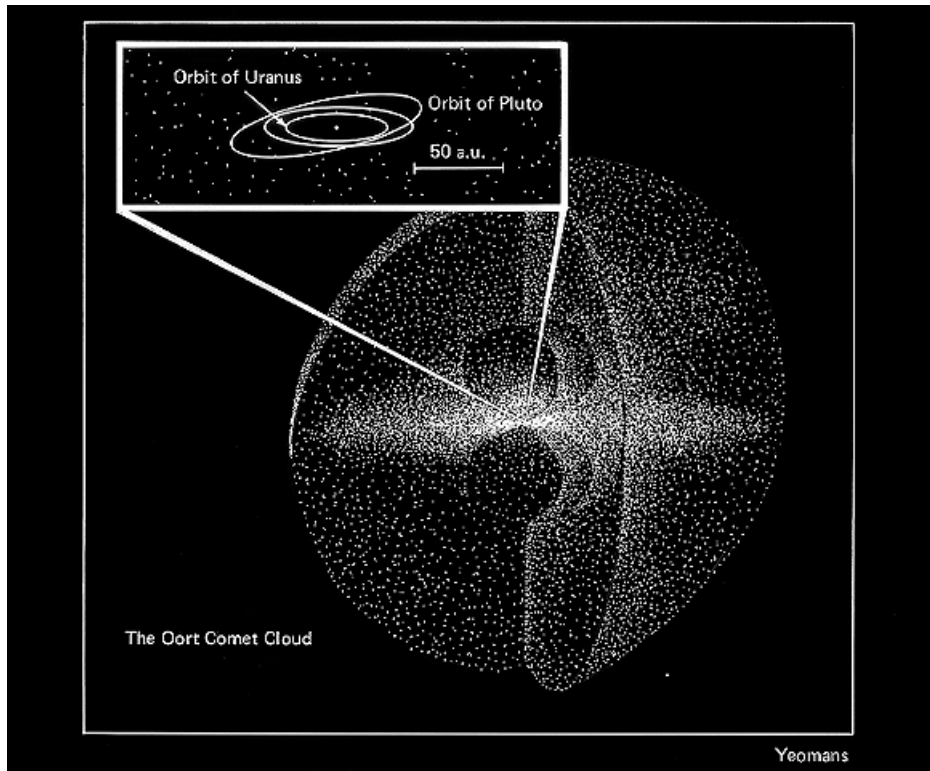


Figure 2.5 The Oort comet cloud.

Courtesy of Donald Yeomans, Jet Propulsion Laboratory.

(often just called the Kuiper belt) extends from the orbit of Neptune at 30 AU out to approximately 50 AU and is thought to contain at least 70,000 ‘trans-Neptunians’ or Kuiper belt objects (KBOs) with diameters exceeding 100 km, concentrated near the ecliptic plane. New KBOs are continually being discovered and the total now stands at around 300 (Figure 2.6, colour plate). It is thought that the Kuiper belt may extend further and merge with the Oort cloud at a distance of roughly 1,000 AU. The high eccentricity of Pluto’s orbit, and the high inclination of Triton’s orbit about Neptune (indicating that it is probably a captured satellite, rather than forming from the circumplanetary disc as discussed in Section 2.5) suggest that both these bodies may in fact themselves be KBOs. This conclusion is supported by the recent discovery of several KBOs with diameters of the order of 1,000 km.

Finally, this mode of formation is consistent with almost all of the planets spinning in the same direction as their orbital motion (prograde). The obliquities of the planets probably arose from off-centre collisions between planetesimals and perhaps embryos towards the end of formation although they may also have arisen due to spin–orbit resonances (Ward and Hamilton, 2002). One particularly extreme case is Uranus which has an obliquity of 98° and thus spins almost on its side. Such a

large obliquity could have arisen from several cumulative off-centre impacts, or conceivably a single massive impact towards the end of formation.

2.4.2 Gravitational instability model

While the core accretion model is the most generally accepted model of planet formation, alternative explanations exist. In particular it has been proposed that giant planets may collapse directly from the disc in the early period of the circumstellar disc evolution via gravitational instability (Boss, 1998). While these models address certain deficiencies in the core accretion model, they suffer from the major drawback that the condensed planets would all have near-solar composition (which as we shall see later in this chapter does not appear to be the case) unless their outer gas-rich layers were somehow removed, or they subsequently incorporated large masses of icy planetesimals. However such models have some advantages, in particular their ability to account for the ‘Hot Jupiters’ currently being discovered in close orbit about other stars (Section 2.8). Future observations of circumstellar discs and extrasolar planets, may help to discriminate between these two theories.

2.5 FORMATION OF JOVIAN SATELLITES

Material captured by the giant planets during phases 1 and 2 of the core accretion model would have been captured predominantly in the equatorial plane, and prior to accretion would have formed a circumplanetary disc in exactly the same way as a circumstellar disc of material formed about the Sun. These discs would also have had significant variations of temperatures with distance both due to heating from the central hot planets (generated by the release of gravitational energy by accretion), and by turbulent mixing. Planetesimals captured early in these discs would probably have been disrupted by turbulence and collisions with other planetesimals, and hence the current satellites probably reformed from material that had been disrupted by accretion into the circumplanetary disc and had been thermally reprocessed by the radial temperature gradient. Such a model explains why most of the satellites about the giant planets are in the equatorial plane of the planet. It also explains why for Jupiter, the composition of the Galilean satellites (Io, Europa, Ganymede, and Callisto) vary greatly with distance from Jupiter. Satellites of the giant planets which are not in the equatorial plane are thought to be objects captured after most of the protoplanet disc had been dissipated.

Some theories suggest that the giant planets probably moved towards the Sun by a few AU during their formation, both due to gas drag with the nebula, and due to the loss of momentum arising from them ejecting substantial numbers of planetesimals to interstellar space for Jupiter and Saturn, and to the Oort cloud for Uranus and Neptune. However the conclusion of inward migration is by no means clear and there is some indication that Neptune actually migrated outwards as we shall discuss later in Section 2.8.

2.6 BULK COMPOSITION OF THE OUTER PLANETS AND ISOTAPE RATIOS

Using the estimated Solar System elemental abundances given in Table 2.1, we can calculate the expected composition of an atmosphere of solar abundance assuming a cold dense atmosphere where all elements appear in the fully hydrogenated form. The expected solar composition abundances of the most abundant molecules (relative to H₂) are compared to those actually measured or estimated in the giant planet atmospheres in Table 2.2a. The sources of these data will be reviewed in Chapter 4. The same abundances, expressed as volume mixing ratios (or mole fractions), are listed in Table 2.2b. As can be seen, the atmospheres of the giant planets have compositions somewhat different to a pure solar mixture and in particular the proportion of heavy elements increases as we move outwards through the Solar System. This variation in composition provides strong constraints on formation theories as we shall now see.

2.6.1 Constraints on formation: D/H ratio

As the presolar cloud collapsed into a circumstellar disc, incoming material arriving from the presolar cloud will have been subjected to appreciable reprocessing both through the collapse process itself, and through shocking as the material entered the dense nebula. Both these effects are likely to have been more substantial near the Sun and less important at greater distances. Older models suggested that the water molecules in the ices were completely dissociated by this process and then recombined. This theory may be tested by examining the D/H ratio of the various bodies currently in the Solar System. As we mentioned earlier, deuterium is a truly primordial isotope, which was created just after the Big Bang and has not been produced since.

After H₂ and He, the most abundant molecule in the ISM, and thus the presolar cloud, is H₂O, either in the gaseous, or condensed phases. In dense, neutral media such as the solar nebula, fractionation of D and H in water occurs through reactions between the gas phases



At higher temperatures the D/H ratio in molecular hydrogen and water is the same, but at lower temperatures ($T < 500$ K), deuterium becomes concentrated in water (Drouart *et al.*, 1999). Similar fractionation occurs in molecules such as CH₃D and NH₂D. While the equilibrium D/H ratio in water and other molecules increases rapidly as the temperature drops, the rate of isotopic exchange between neutral molecules in the nebula falls rapidly, and effectively disappears for $T < 200$ K. This means that the enrichment factor $f_{\text{H}_2\text{O}} = (\text{D}/\text{H})_{\text{H}_2\text{O}}/(\text{D}/\text{H})_{\text{H}_2}$ in water molecules equilibrating with molecular hydrogen in the solar nebula is unlikely to be greater than 3. For the model where water molecules reformed from the dissociation products of formation, the ratio would be close to 1.0. However, the $(\text{D}/\text{H})_{\text{H}_2\text{O}}$ ratio of some Solar System objects is found to be greatly in excess of the theoretical

Table 2.2a. Bulk composition of the Jovian planets (relative to H₂).

Solar fraction <i>f</i>	Jupiter		Saturn		Uranus		Neptune	
	fraction <i>f</i>	<i>f</i> /solar	fraction <i>f</i>	<i>f</i> /solar	fraction <i>f</i>	<i>f</i> /solar	fraction <i>f</i>	<i>f</i> /solar
H ₂	1.0	1.0	1.0	1.0	1.0	1.0	1	1
He	0.1954	0.157	0.8	0.13	0.67	0.18	0.18	0.92
H ₂ O	1.352 × 10 ⁻³	~6 × 10 ⁻⁴	~0.44	2 × 10 ⁻⁷	0.00	?	?	?
CH ₄	6.623 × 10 ⁻⁴	2.1 × 10 ⁻³	3.17	4.5 × 10 ⁻³	6.8	0.019	29	40
Ne	2.405 × 10 ⁻⁴	2.46 × 10 ⁻⁵	0.1	?	?	?	?	?
NH ₃	1.664 × 10 ⁻⁴	7.1 × 10 ⁻⁴	4.27	>1.1 × 10 ⁻⁴	>0.66	?	?	?
H ₂ S	3.170 × 10 ⁻⁵	8.1 × 10 ⁻⁵	2.56	?	?	?	?	?
Ar	5.024 × 10 ⁻⁶	1.81 × 10 ⁻⁵	3.6	?	?	?	?	?
PH ₃	7.262 × 10 ⁻⁷	6.94 × 10 ⁻⁷	0.96	7.94 × 10 ⁻⁶	10.9	?	?	?
GeH ₄	8.532 × 10 ⁻⁹	8.1 × 10 ⁻¹⁰	0.1	2 × 10 ⁻⁹	0.23	?	?	?
Kr	4.083 × 10 ⁻⁹	8.69 × 10 ⁻⁹	2.13	?	?	?	?	?
Xe	2.958 × 10 ⁻¹⁰	8.74 × 10 ⁻¹⁰	2.95	?	?	?	?	?
AsH ₃	4.688 × 10 ⁻¹⁰	8.1 × 10 ⁻¹⁰	1.73	2.3 × 10 ⁻⁹	4.27	?	?	?

Solar composition is assumed to be as estimated by Grevesse and Sauval (1998) and listed in Table 2.1.

Table 2.2b. Bulk composition of the Jovian planets (as mole fractions).

	Solar mole fraction	Jupiter	Saturn	Uranus	Neptune
H ₂	0.835	0.864	0.883	0.834	0.829
He	0.163	0.136	0.115	0.15	0.15
H ₂ O	1.1×10^{-3}	$>5 \times 10^{-4}$	$>1.8 \times 10^{-7}$?	?
CH ₄	5.5×10^{-4}	1.8×10^{-3}	4.0×10^{-3}	0.016	0.022
Ne	2.0×10^{-4}	2.1×10^{-5}	?	?	?
NH ₃	1.4×10^{-4}	6.1×10^{-4}	$>9.7 \times 10^{-5}$?	?
H ₂ S	2.6×10^{-5}	7×10^{-5}	?	?	?
Ar	4.2×10^{-6}	1.6×10^{-5}	?	?	?
PH ₃	6.1×10^{-7}	6×10^{-7}	7×10^{-6}	?	?
GeH ₄	7.1×10^{-9}	7×10^{-10}	1.8×10^{-9}	?	?
Kr	3.4×10^{-9}	7.5×10^{-9}	?	?	?
Xe	2.5×10^{-10}	7.5×10^{-10}	?	?	?
AsH ₃	3.9×10^{-10}	7×10^{-10}	1.8×10^{-9}	?	?

Table 2.3. Solar System D/H ratios.

Molecule	Species	Value ($\times 10^{-5}$)	Reference
Protosolar	H ₂	2.1 ± 0.4	Geiss and Gloeckler (1998)
Protosolar	H ₂ O	~ 70	Deloule <i>et al.</i> (1998), Mousis <i>et al.</i> (2000)
Comets	H ₂ O	~ 30	Balsiger <i>et al.</i> (1995) Eberhardt <i>et al.</i> (1995) Bockelée-Morvan <i>et al.</i> (1998) Meier <i>et al.</i> (1998)
Earth	H ₂ O	14.9 ± 0.3	Lécuyer <i>et al.</i> (1998)
Jupiter	H ₂	2.2 ± 0.35	Lellouch <i>et al.</i> (2001)
Saturn	H ₂	$1.70^{+0.75}_{-0.45}$	Lellouch <i>et al.</i> (2001)
Uranus	H ₂	$5.5^{+3.5}_{-1.5}$	Feuchtgruber <i>et al.</i> (1999)
Neptune	H ₂	$6.5^{+2.5}_{-1.5}$	Feuchtgruber <i>et al.</i> (1999)

limit of 3 times the protosolar (D/H)_{H₂} ratio as can be seen in Table 2.3 and Figure 2.7. This suggests that some other interaction must have taken place to increase the f_{H₂O} ratio.

While the enrichment factor f_{H₂O} may not exceed ~ 3 for neutral molecule–molecule interactions, other interactions may occur in the ISM which lead to different enrichments. If the ISM is partially ionized (which is often the case) then ion–molecule reactions can occur where the additional ionization energy serves to get over the activation energy of the fractionation reactions and hence leads to much greater levels of enrichment. In recent formation models (Drouart *et al.*, 1999; Mousis *et al.*, 2000) it is assumed that while water ice is probably vaporized when it enters the inner part of the circumstellar disc (out to distances of 30–50 AU) it is

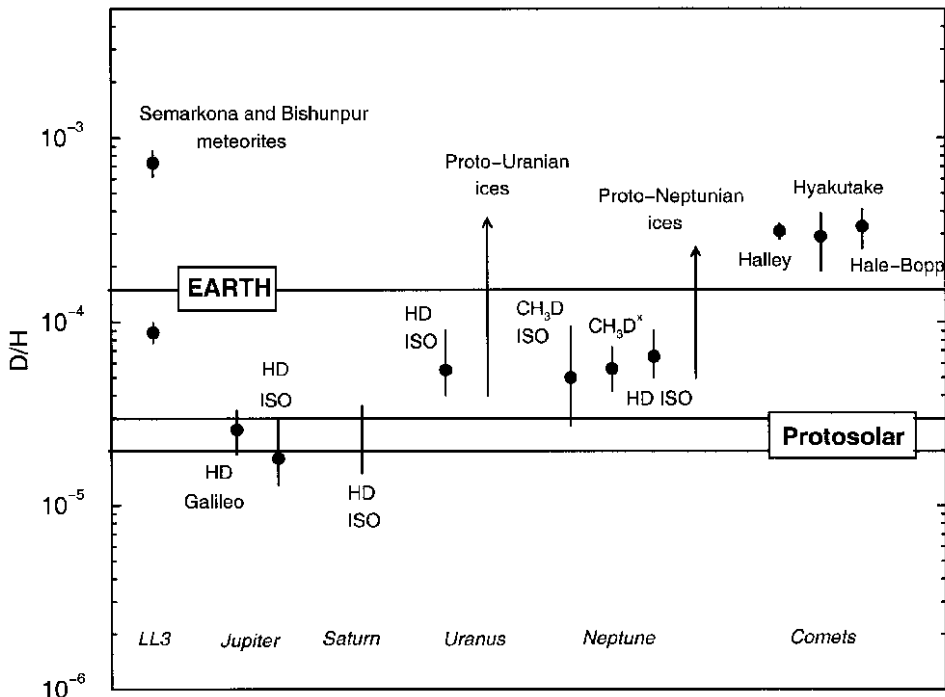


Figure 2.7 Measured D/H ratios of the giant planets, meteorites, and comets.

From Hersant *et al.* (2001). Reprinted with permission from the *Astrophysical Journal*.

not actually dissociated and thus retains its pristine, high $f_{\text{H}_2\text{O}}$ ratio. Subsequent neutral gas interactions with molecular hydrogen in the hot inner nebula quickly reduce the $f_{\text{H}_2\text{O}}$ to 1, but further from the Sun the predicted ratio tends to 1 more slowly, due to the lower temperatures and turbulent mixing in the nebula between low- f ice water near the sun and high- f ice further out. The initial degree of D-enrichment of the presolar ice grains may be indicated by measurements of the composition of Semarkona and Bishunpur LL3 meteorites which are thought to have originally condensed at around 3 AU from the Sun. Water is incorporated as clays in these meteorites and these are found to be composed of two components: roughly 15% has $f_{\text{H}_2\text{O}}$ equal to approximately 25, while the remainder has $f_{\text{H}_2\text{O}}$ equal to approximately 3. This observation is consistent with the idea of mixing between pristine unvaporized presolar ice grains with $f_{\text{H}_2\text{O}} = 25$, together with water that has equilibrated with the local solar nebula.

Using this initial value of $f_{\text{H}_2\text{O}}$, and making reasonable assumptions about the nebula cooling rate, and the degree of turbulent mixing, the formation of models by Drouart *et al.* (1999) and Mousis *et al.* (2000), predict that by the time that Uranus, Neptune, and the comets were forming in the outer solar nebula, the mean D-enrichment of the water molecules could have fallen to approximately 10 which is

what is observed in the Halley, Hyakutake, and Hale–Bopp comets. The D/H ratio observed in the molecular hydrogen outer envelopes of the giant planets comes not only from the D/H of the molecular hydrogen in the presolar cloud but also through mixing and equilibration with the D-enriched water ices making up the planet. For Jupiter and Saturn, the mass of hydrogen far outweighs that of ice and thus the D/H ratio should be representative of the presolar ratio in molecular hydrogen. For Uranus and Neptune however, the observed ratio is much higher and if we assume that the atmospheres have thoroughly mixed throughout their whole depth, and the D/H exchanged between water and molecular hydrogen, then providing we know the relative masses of hydrogen and ice, we can calculate the D/H ratio of the pre-Neptune, pre-Uranus ices. The relative masses may be calculated from interior models, and recent estimates of the mass of hydrogen in these planets is $4.2 M_{\oplus}$ for Uranus and $3.2 M_{\oplus}$ for Neptune (Podolak *et al.*, 2000; Mousis *et al.*, 2000), already mentioned earlier. Using these values, the f_{H_2O} enrichment of the pre-Neptune and pre-Uranus ices is consistent with the cometary value of 10. Similar arguments may be used to estimate the presolar D-enrichment in HCN and subsequent evolution.

In addition to accumulating hydrogen, helium, and water, the outer planets are also observed to have accumulated significant quantities of other ‘heavy’ elements such as carbon, nitrogen, and sulphur. The predominant presolar nebula form of these elements is in uncondensed, gaseous molecules (C as CO or CH_4 , N mainly as N_2 with perhaps 10% as NH_3/HCN , and S as H_2S), and thus a solar composition abundance of these constituents might be expected. However the ratio of these elements with respect to hydrogen is found to be significantly supersolar with values of approximately $3\times$ the solar value for Jupiter for C/H, N/H, S/H, Ar/H, Kr/H, and Xe/H. The C/H ratio is estimated to increase to $3\text{--}6\times$ the solar value for Saturn and of the order of $20\times$ the solar value for Uranus and Neptune. Hence these molecules cannot have been accreted from their gaseous phase but instead must have been concentrated in some way. Current theories suggest that significant quantities of these molecules were incorporated into water ice which then accreted in phase 1 and 2 to produce the observed enhancement. However there is considerable disagreement as to the form of the ice.

A number of laboratory experiments have been conducted to assess how well presolar nebula gases may be trapped by water ice. At very low temperatures ($T < 100$ K), water condenses as *amorphous* ice, and laboratory experiments have shown that to trap the quantities of heavy elements observed in Jupiter’s atmosphere, the ice formation temperature must have been as low as 30 K (Bar-Nun *et al.*, 1988; Owen *et al.*, 1999). This is much lower than the predicted nebula temperatures at 5–6 AU during the time that Jupiter formed and suggests that either: (i) the presolar ice grains (which are almost certainly amorphous) never vaporized in the Jupiter region (i.e., the nebula was much colder than is currently modelled); or (ii) that Jupiter originally formed as far out as 30 AU and later migrated in. The latter possibility seems unlikely owing to the excessively long formation time of a Jupiter-sized planet at this distance and the difficulty in moving the planet in by almost 25 AU. The former scenario does not seem to tie in with the good evidence for high

inner solar nebula temperatures and evidence of mixing (crystalline silicates in comets). An alternative explanation has been put forward which utilizes crystalline water ice. Here the water ice is assumed to be vaporized on entry into the nebula and then subsequently re-condenses at the ‘ice line’. The partial pressure of water vapour in the nebula was low and thus water initially condensed at about 150 K. Further cooling would have led to more and more water vapour molecules condensing onto the ice grains as the temperature dropped. Water condensing at 150 K is necessarily *crystalline* and as such may trap other gas molecules either as hydrates or molecules such as ammonia ($\text{NH}_3\text{-H}_2\text{O}$) would have formed at approximately 85 K at pressures of the 10^{-8} bar) or clathrate–hydrates for other molecules where molecules of other gases are trapped in ‘cages’ of water molecules (Gautier *et al.*, 2001a, b). There are two classes of clathrate–hydrate depending on the number of water molecules in each cage to the number of trapped molecules. The ratio is 5.75 for class I and 5.66 for class II. As the temperature dropped, more and more ice condensed onto the grains until the temperature was so low that amorphous ice started to form. However, since the saturated vapour pressure decreases exponentially as the temperature reduces it can be seen that the bulk of the condensed ice grains must have been crystalline. Laboratory studies have shown that the heavy molecules in the solar nebula could be trapped in clathrate–hydrates in quantities needed to account for the observed enrichments of the outer planets at far higher temperatures than would be needed to trap equivalent amounts in amorphous ice (Gautier *et al.*, 2001a, b). The clathrate–hydrate formation scenario is consistent with the current turbulent Solar System models and is also consistent with recent observations of a circumstellar disc where 90% of the ice is observed to be crystalline in a region whose temperature is 30–60 K (Mousis *et al.*, 2000). It also provides a good explanation of the low Jovian Ne/H ratio since neon is poorly trapped in clathrates. The Jovian N/H ratio is consistent with $\text{N}_2/\text{NH}_3 > 10$ in the presolar cloud which seems plausible, although Owen *et al.* (2001) argue that the observed high abundance of N in Jupiter’s atmosphere supports the cold amorphous ice model and thus that Jupiter contains a large fraction of material incorporated as planetesimals formed at $T < 50$ K. Clearly there is much work still to be done to determine which of these formation views is correct. The main failure of the clathrate–hydrate scenario is that it predicts a Jovian S/H ratio far in excess of that observed. Attempts to explain this by H_2S corroding Fe alloy grains in the inner nebula, with this depleted sulphur gas being turbulently mixed out to Jupiter, are disputed. A clear difference is that many more water molecules are required to trap a guest molecule in a clathrate–hydrate structure than in amorphous ice and thus the model predicts the Jovian O/H ratio to be $> 9.4 \times$ the solar value. Unfortunately water condenses below the observable part of the Jovian atmosphere and thus the deep abundance is not currently known, although it can be inferred from determinations of the abundance of CO and may be accessible by future gravitational measurements. Recent modelling of the observed deep tropospheric abundance of CO (Bézard *et al.*, 2002) suggests that the Jovian O/H ratio is in the range 0.2–9× the solar value, with a preferred value of 3× the solar value. Hence this study would appear to argue against the clathrate model.

2.6.2 Constraints on formation: Nitrogen

Since the Jovian atmosphere is almost entirely captured solar nebula gas, it is expected that the $^{15}\text{N}/^{14}\text{N}$ ratio of the Sun and Jupiter are the same. The upper value of this ratio has been measured in the solar wind to be $\leq 2.8 \times 10^{-3}$ (Hashizume *et al.*, 2000). The $^{15}\text{N}/^{14}\text{N}$ ratio in ammonia on Jupiter is estimated from Infrared Space Observatory Short Wavelength Spectrometer (ISO/SWS) observations (Fouchet *et al.*, 2000) to be $(1.9_{-1.0}^{+0.9}) \times 10^{-3}$ and an analysis of the Galileo probe mass spectrometer measurements (Owen *et al.*, 2001) yields an estimate of $(2.3 \pm 0.3) \times 10^{-3}$. Both measurements are consistent with the solar wind estimate.

The $^{15}\text{N}/^{14}\text{N}$ ratio in HCN in the current local ISM is estimated to be $(2.2 \pm 0.5) \times 10^{-3}$ (Dahmen *et al.*, 1995). As mentioned earlier the $^{15}\text{N}/^{14}\text{N}$ is expected to reduce over time as the ^{15}N produced by early Type II supernovae is diluted with ^{14}N coming from the death of longer lived, intermediate-mass stars. Hence we would expect that the $^{15}\text{N}/^{14}\text{N}$ ratio should have been higher in molecules such as NH_3 and HCN in the presolar cloud than in the current ISM. The $^{15}\text{N}/^{14}\text{N}$ ratio in HCN for comet Hale–Bopp was estimated to be roughly 3×10^{-3} (Jewitt *et al.*, 1997) which, assuming the ratio for this comet is representative of the protosolar value, is consistent with this expectation. We also expect that the $^{15}\text{N}/^{14}\text{N}$ ratio in molecules such as HCN and NH_3 in the ISM was higher than in N_2 due to the same ion–molecule reactions which appear to increase the D/H ratio. Hence the lower $^{15}\text{N}/^{14}\text{N}$ ratio found in ammonia in Jupiter’s atmosphere, and in the solar wind, suggest that nitrogen was captured by the Sun and by Jupiter mainly in the form of N_2 and not as NH_3 or HCN (Owen *et al.*, 2001).

2.7 INTERIORS OF THE GIANT PLANETS

Much of what has been outlined previously regarding the formation of the planets is based not only upon their current atmospheric composition but also on what we know about the interiors of the giant planets. How can we tell what the conditions are in the interior of the giant planets, well below the visible cloud decks? There are a number of techniques, most notably the details of the gravitational field and estimation of the planets’ moment of inertia as we shall now see.

2.7.1 Gravitational data

The shape of the Earth and the other terrestrial planets are well approximated by spheres and thus the gravitational acceleration all over the surface points almost exactly towards the centre of the planet. However, as we have seen the outer planets spin very rapidly, and since the interiors of these planets are essentially fluid, the planets bulge out at the equator in response to the centrifugal force.

This non-sphericity means that the shape of the gravitational field is modified from the spherical form with which we are more accustomed.

In general the gravitational acceleration at some point in a gravitational field is given by the gradient of the gravitational potential function U ,

$$\mathbf{g} = -\nabla U, \quad (2.16)$$

and outside a planet U satisfies Laplace's equation,

$$\nabla^2 U = 0. \quad (2.17)$$

In spherical polar coordinates, Laplace's equation has a number of well-known solutions. If we limit ourselves to solutions which are axially symmetric (i.e., those that do not depend on the azimuth angle) then we find

$$U = \sum_{n=0}^{\infty} (A_n r^n + B_n r^{-(n+1)}) P_n(\cos \theta) \quad (2.18)$$

where θ is the zenith angle and P_n are Legendre polynomials. If we further limit ourselves to solutions which possess north/south symmetry (which all the giant planets have) then we only need consider even powers of n . Additionally we may put $A_n = 0$, since the potential must tend to zero as r tends to infinity. Adding in centripetal effects we obtain (Lindel *et al.*, 1985)

$$U(r, \phi) = -\frac{GM}{r} \left[1 - \sum_{n=1}^{\infty} J_{2n} \left(\frac{R}{r} \right)^{2n} P_{2n}(\sin \phi) \right] - \frac{1}{2} \Omega^2 r^2 \cos^2 \phi \quad (2.19)$$

where ϕ is the *planetocentric* latitude which is $(90 - \theta)^\circ$ and Ω is the spin angular velocity. Taking the gradient of Equation 2.19 we obtain an expression for the gravitational acceleration as a function of radial distance r and planetocentric latitude ϕ in the radial direction

$$g_r(r, \phi) = -\frac{GM}{r^2} \left(1 - \sum_{n=1}^{\infty} (2n+1) J_{2n} \left(\frac{R}{r} \right)^{2n} P_{2n}(\sin \phi) \right) + \frac{2}{3} \Omega^2 r [1 - P_2(\sin \phi)] \quad (2.20)$$

and in the latitudinal direction

$$g_\phi(r, \phi) = -\frac{GM}{r^2} \left(\sum_{n=1}^{\infty} J_{2n} \left(\frac{R}{r} \right)^{2n} \frac{dP_{2n}(\sin \phi)}{d\phi} \right) - \frac{1}{3} \Omega^2 r \frac{dP_2(\sin \phi)}{d\phi} \quad (2.21)$$

and the total gravity is $g = \sqrt{(g_r^2 + g_\phi^2)}$. For the approximately spherical terrestrial planets the so-called ‘ J -coefficients’ are negligible and thus $g_r \gg g_\phi$. However, the oblateness of the outer planets means that J -coefficients are substantial and thus the ‘surface’ gravitational field does not point directly towards the centre of the planet, but is instead displaced by a small angle ψ where $\psi = \arctan(g_\phi/g_r)$ which varies with ϕ . This offset leads to a second definition of latitude and longitude, the *planetographic* system. The planetographic latitude is defined as the inclination of the local normal to the equatorial plane. This is equal to $\phi_g = \phi + \psi$ and is shown in

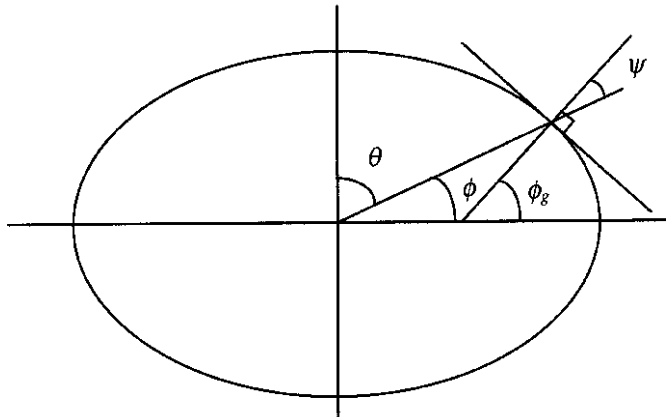


Figure 2.8 Definition of the planetographic and planetocentric latitude systems. Here ϕ is the planetocentric latitude, and ϕ_g is the planetographic latitude.

Figure 2.8. The curve described by the limb of a planet is, to a first approximation an ellipse and thus the planetocentric and planetographic latitudes are more simply related by

$$\tan \phi_g = \left(\frac{R_e}{R_p} \right)^2 \tan \phi \quad (2.22)$$

where R_e and R_p are the equatorial and polar radii respectively. The other difference between the planetocentric and planetographic systems is that while planetocentric longitudes run eastwards, planetographic longitudes run in the direction opposite to the rotation. Hence for planets which have prograde spins, the longitudes run westwards, while for planets with retrograde spins such as Venus and Uranus, they run eastwards.

Measurements of the J -coefficients of the giant planets, by observing the gravitational perturbations acting on satellites, rings, and passing spacecraft, can be used to determine the distribution of mass in the interior. In addition to the J -coefficients themselves, we can tell even more about the interior of the planets if we can measure, or estimate, the polar moment of inertia C . To directly measure C requires that we observe the precession of the rotation axis which is not possible for the giant planets. However, C may be calculated if we can measure the mass M of the planet, its equatorial radius R_e , its sidereal rotation period T , and the J_2 coefficient. This calculation assumes that the interior of the planet is in hydrostatic equilibrium (i.e., that the interior has no shear strength and responds to tidal forces essentially as a liquid). The moment of inertia ratio C/MR_e^2 is particularly useful since it indicates the degree of mass concentration towards the centre. For a hollow sphere the ratio is $2/3$ while for a sphere with uniform density it is 0.4 (Jones, 1999). For a sphere where all the mass is at the centre it is 0 . The gravitational constants of the giant planets are listed in Table 2.4.

Table 2.4. Gravitational and magnetic properties of Earth and the giant planets.

Planet	Equatorial radius R_e (km)	$J_2(\times 10^{-2})$	$J_4(\times 10^{-4})$	$J_6(\times 10^{-4})$	C/MR^2	Magnetic dipole moment (A m^2)
Earth	6,378	1.901	0.00161	?	0.3308	7.9×10^{22}
Jupiter	71,492	1.4697(1)	-5.84(5)	0.31(20)	0.264	1.54×10^{27}
Saturn	60,268	1.6332(10)	-9.19(40)	1.04(50)	0.21	4.6×10^{25}
Uranus	25,559	0.3513(3)	-0.318(5)	?	0.23	3.8×10^{24}
Neptune	24,764	0.3538(9)	-0.380(1)	?	0.29	2.0×10^{24}

Source of gravity data: Jupiter, Campbell and Synott (1985); Saturn, Campbell and Anderson (1989); Uranus, French *et al.* (1988); Neptune, Owen *et al.* (1991). Moment of inertia and magnetic data after Table 4.2 of Jones (1999).

2.7.2 Magnetic field data

Magnetic fields are caused by electrical currents in the centres of the planets and thus much can be learned about the planetary interiors by looking at the B -fields. The mechanism by which planets create magnetic fields is not well understood. The centres of the planets are thought to be electrically conducting and convective. Any stray magnetic fields that might be present will modify the motion of moving electrical charges and will thus induce electrical currents which will themselves generate their own magnetic field. What appears to happen is that some kind of positive feedback mechanism then acts to increase the strength of the magnetic field in a particular direction which encourages the currents to flow in one particular sense. This magneto-hydrodynamic effect, called the *self-exciting dynamo*, is thought to be responsible for generating the magnetic fields of all the planets (Jones, 1999). Since viscous dissipation tends to reduce the field over time, internal rotational energy must be continually ‘tapped’ by the magnetic field in order to sustain it. To do this, most models of the process require that the axis of the magnetic field is not coincident with the rotational axis (Cowling theorem) and this appears to be the observed case for all the planets with the one exception of Saturn. Even when a field is ‘stable’, as it is for the Earth, we observe that in fact it evolves and varies over time and even undergoes complete reversals. Hence the generation of the magnetic field can be seen to be a dynamic and ongoing process. The mean dipole moment of the giant planets’ magnetic fields are listed in Table 2.4.

The internal currents generating the magnetic field are distributed, and hence the field is not a simple dipole, but has higher terms (just like the J -coefficients for gravity fields). Hence observation of the shape of the magnetic field can be used to map the current flows in the interior.

2.7.3 Internal structure of Jupiter and Saturn

The mean internal structures of Jupiter and Saturn are shown in Figure 2.9. Jupiter is significantly oblate (0.065), and its estimated moment of inertia ratio (C/MR_e^2) of

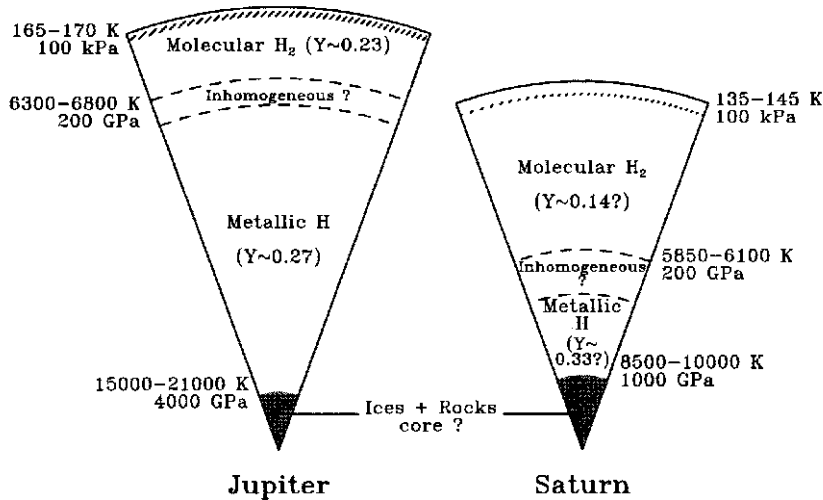


Figure 2.9 Interior models of Jupiter and Saturn.

From Guillot (1999b). Reprinted with permission of the American Association for the Advancement of Science. Copyright 1999.

0.264 indicates a significant concentration of mass towards the centre of the planet. Saturn is even more oblate (0.098) and in fact is the most oblate body in the Solar System. Its moment of inertia ratio of 0.21 is the lowest of all the planets suggesting even greater mass concentration. These figures, together with the measured J -coefficients of the gravitational field may be fitted with internal models that model how the density, pressure, temperature, and composition vary with depth. Hydrostatic equilibrium is assumed, and from the fitted pressure-density profile, conclusions may be drawn about the internal structure (Guillot, 1999a, b). Internal modelling studies suggest that Jupiter is significantly heavier than would be expected were the elements to be present in solar abundance. The mass of heavy elements (i.e., those with mass greater than helium) is estimated to be approximately $15 M_{\oplus}$ which is three times more than would be expected if Jupiter had a solar composition. Saturn is estimated to be even more enriched in heavy elements containing as much as $29 M_{\oplus}$, whereas only $1 M_{\oplus}$ would be expected if Saturn had a solar composition.

If Saturn is so much less massive than Jupiter, why is its volume approximately the same and thus its density so low? Hydrogen is a light and compressible substance and its compressibility is found to be little affected by temperature (provided that the temperature is not too big). Hence a low-temperature sphere of hydrogen with a mass similar to Jupiter's, has a *characteristic radius* which is nearly independent of total mass and interior temperature (Hubbard, 1997a). In other words, hydrogen is so compressible that a large increase in mass produces almost no change in radius. For a pure-hydrogen planet in the giant planet mass range the characteristic radius is 80,000 km, for a pure-helium planet it is 35,000 km, and for a ‘heavy’ elements planet it is typically 25,000 km. For an approximately solar composition, the characteristic radius would be 70,000 km, close to the observed radii of both Jupiter and Saturn.

Pressures and temperatures rise quickly towards the centre of both planets and at temperatures greater than around 3,000 K and pressures greater than around 1.4 Mbar, hydrogen is thought to change to an electron-degenerate state of pressure-ionized protons and electrons called ‘metallic-hydrogen’. Recently, experiments have been done in the laboratory using shock-compression of hydrogen samples with gas-guns and lasers which have confirmed this transition (Nellis, 2000; Cauble *et al.*, 2000; Nellis *et al.*, 1995). The phase transition appears to be continuous rather than first-order and thus there is probably not a sharp boundary between the two phases in the interiors of these planets (Nellis, 2000). Rather, molecular hydrogen begins to dissociate at ~ 0.4 Mbar and is completely dissociated at ~ 3 Mbar. The mid-point pressure of 1.4 Mbar corresponds to a fractional radius of 0.9 for Jupiter and 0.5 for the much less compressed Saturn (Nellis, 2000). The transition region between molecular and metallic hydrogen is thus predicted to occur at a depth of $\sim 7,000$ km for Jupiter and $\sim 30,000$ km for Saturn. Thus the overwhelming bulk of Jupiter’s hydrogen is thought to exist in the metallic phase.

Saturn’s low moment of inertia requires a high degree of differentiation (i.e., concentration towards the centre of the heavy elements). Approximately $5 M_{\oplus}$ are thought to reside in the molecular mantle, with the remainder in the metallic region and possibly in a dense core. Jupiter’s higher moment of inertia implies less differentiation and it is estimated that perhaps $5 M_{\oplus}$ resides in a dense core (although whether a dense core exists at all is debatable), with the remaining $10 M_{\oplus}$ of heavy elements evenly distributed throughout the hydrogen/helium envelope. These estimates are consistent with the formation model scenario outlined earlier, where an icy embryo forms first which then attracts further ice and gas before entering the final runaway gas collapse phase. Clearly Saturn was able to acquire less hydrogen and helium during this final stage which accounts for its lighter mass, and greater heavy element enrichment compared with Jupiter.

The estimated interior convective velocities and the calculated conductivity of metallic-hydrogen are more than adequate to sustain a magneto-hydrodynamic dynamo of the size needed to account for Jupiter’s very powerful magnetic field, especially since the conducting metallic region extends over 90% of the planetary radius. The convective timescale is estimated to be of the order 100 yr, and thus changes in the field are likely to occur on this timescale also. Long-term monitoring of the magnetic field may eventually provide clues on the deep currents. Charged particles from the solar wind and other sources become trapped and accelerated in this field leading to powerful synchrotron radio wave emission at decametric wavelengths which are detected at Earth and led to the first measurements of the internal bulk rotation rate (System III). This was observable since Jupiter’s magnetic field is sufficiently misaligned with respect to the rotation axis that diurnal changes in the radio wave emission are easily detectable.

In Saturn the observed heat flux must similarly drive convection in most of the liquid interior. However it is possible that compositional differences across the metallic/molecular hydrogen phase boundary might inhibit convection and thus transport of heat across this stably-stratified boundary might be via conduction. This might explain why Saturn’s magnetic field is so closely aligned (to within 1°)

with the rotation axis since the non-axially symmetric parts of the magnetic field generated via the magneto-hydrodynamic dynamo in the convective interior of the metallic-hydrogen zone (which only accounts for 50% of the radius) may be screened out by a stably stratified conducting layer at the top of this region. The smaller size of the metallic-hydrogen conducting core may also explain why the magnetic field of Saturn is generally weaker than Jupiter's, and why the higher order field components are more greatly reduced (Nellis, 2000; Hubbard, 1997b). The close alignment between the magnetic and rotation axes make it difficult to determine Saturn's magnetic field rotation period from the Earth, and thus this was not determined until the *Pioneer 11* flyby in 1979 (Russell and Luhmann, 1997).

The magnetosphere of Jupiter, where Jupiter's magnetic field dominates over the interplanetary magnetic field, is vast and if visible would have a diameter exceeding that of the Moon as seen from the Earth. This great size is due not only to the high strength of Jupiter's magnetic field but also due to the low density of the solar wind at 5 AU and the additional source of charged particles from Io which resides within the magnetosphere. The magnetosphere of Saturn is much smaller.

2.7.4 Internal structure of Uranus and Neptune

While Jupiter and Saturn have many similarities with each other, they are both very different to Uranus and Neptune, which form a separate pair of planets. The mean internal structures of Uranus and Neptune are shown in Figure 2.10. The small radii of Uranus and Neptune tell us immediately that although hydrogen and helium account for the bulk of the molecules in the observable atmosphere, the planets cannot be predominantly composed of hydrogen and helium since the density would then be far too low. Instead their radius is close to the characteristic radius of icy materials and thus these planets are thought to be composed predominantly of ice, with only a thin outer envelope of hydrogen and helium. It would be possible to match the planet's mean density by having a hydrogen atmosphere over a small rocky core, but this would have a moment of inertia much smaller than that observed, so this possibility must be discounted. Of course, the 'ices' occurring in the high-pressure, high-temperature interior of Uranus and Neptune would actually exist as a hot molecular fluid, not the solid cold ice that we are more familiar with. Interior models of these planets suggest that their interiors are rather homogeneous and there is no hard evidence for a dense rocky core. This suggests that the accumulation of these planets was slow, allowing internal heat to radiate away and thus that the ice-rock planetesimals have not been subsequently differentiated.

The high pressure–temperature environments of the internal regions of Uranus and Neptune have been experimentally modelled by 'synthetic Uranus' models where a liquid solution of water, ammonia, and isopropanol (with 'solar' molar abundances of H, O, C, and N) is subjected to single and double shockwave experiments conducted up to 2.2 Mbar and $T > 4,000$ K (Hubbard, 1997c, d; Radousky *et al.*, 1990). The compression curves derived from these experiments (i.e., the relationship between pressure and fluid density) closely match those required by interior models of these planets to match the observed density and J -coefficients, again suggesting

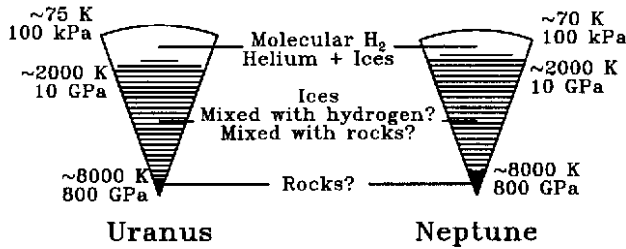


Figure 2.10 Interior models of Uranus and Neptune.

From Guillot (1999b). Reprinted with permission of the American Association for the Advancement of Science. Copyright 1999.

that the bulk of these planets are made of icy materials. For the outer part of the atmosphere at pressures less than 100 kbar, the modelled compression curve matches that of nebular hydrogen and helium. In fact the ‘mantle’ material, if it has a solar composition of heavy elements, should actually be composed of about 40% water ice, 25% methane ice, approximately 25% iron and rocks, with ammonia making up part of the remaining 10%. The abundance of rocky material would make this material denser than that modelled in the mantle and assumed by the ‘synthetic Uranus’ models. Hence to reduce the density of the mantle material to that required by interior models requires either that the rocks and iron differentiate from the icy material in the mantle and form a rocky core, of which there is currently no evidence, or that sufficient low-density material such as hydrogen and helium is also mixed throughout the mantle to offset the effect of the denser rocks. Roughly $1\text{--}2 M_{\oplus}$ of hydrogen/helium would be required to do this (Hubbard, 1997d).

The hydrogen-rich outer layer appears to be rather thin and comprises no more than 15% (3,500 km) of the radius for Neptune (amounting to $0.5\text{--}1.0 M_{\oplus}$) and 20% (5,000 km) of the radius for Uranus (amounting to less than $3 M_{\oplus}$). Hence Uranus and Neptune appear to be only slightly evolved from the original embryos that gravitationally swept up the gas in the outer parts of the protosolar nebula during phase 2 of formation. As mentioned earlier, the longer time required to accrete planets at greater distances from the Sun meant that Uranus and Neptune appear never to have reached phase 3 of formation before the T-tauri phase of the Sun swept the Solar System clean of any remaining nebula gas.

A small fraction of the hydrogen in the envelopes of these planets may have resulted from the decomposition of hydrogen-bearing ices in the interior. However, the He/H_2 ratio in Uranus’ atmosphere is found to be very close to the solar value and hence this fraction is probably very small. The high abundance of methane (20–30 times greater than would be expected for a solar C/H fraction) in the observable atmospheres of these planets however is good evidence of the presence of an enormous ice reservoir beneath the hydrogen-rich envelope, and considerable mixing between the two which also explains the high D/H ratio in H_2 found for these planets. Given the other similarities between Uranus and Neptune, we might then expect the Neptunian He/H_2 ratio to be similar to that of Uranus. However the initial estimates of the He/H_2 ratio were supersolar which is

somewhat puzzling. These ratios were determined from the infrared spectra of the planets recorded by *Voyager 2* and the analysis made the assumption that there was no N₂ in the atmosphere (Conrath *et al.*, 1991). However the detection at microwave wavelengths of HCN in the stratosphere of Neptune (and not in the stratosphere of Uranus), suggests that there may in fact be N₂ in the Neptunian atmosphere. A more recent study suggests that a mole fraction of only 0.3% of N₂ would be sufficient to reduce the He/H₂ ratio inferred from the far-IR spectrum of Neptune to that of Uranus (Conrath *et al.*, 1993). One possibility is that the stratospheric N₂ of Neptune comes from nitrogen exospherically lost from the atmosphere of Neptune's moon Triton. However it would appear that this process has difficulty in matching the amounts of N₂ required. An alternative, probably more plausible explanation is that N₂ is dredged up from the interior of Neptune via the vigorous convection known to exist on that planet. We will return to the question of nitrogen in Neptune's atmosphere in Chapter 4.

2.8 MIGRATION AND EXTRASOLAR PLANETS

The scenario of Solar System formation presented in this chapter is the 'best average' of a number of scientific studies that have been conducted to explain the observed properties of the Solar System. However there is a wide variation about the mean, since Solar System formation models are by their very nature somewhat chaotic in their behaviour, particularly with respect to the gravitational interactions between planetesimals (Bryden *et al.*, 2000a). Also we saw earlier that the generally accepted core accretion model is not universally accepted, and that an alternative gravitation instability model has some advantages. A particular problem of the core accretion model is that while it explains the properties of our Solar System very well, it is not so successful in explaining the properties of the planets now being regularly discovered around other stars. The majority of these *extrasolar* planets discovered to date are predominantly of Jovian mass size, and orbit typically within 1 AU of the star. It is not known if this is in fact the general structure of solar systems since the observational techniques used to date are more able to detect heavy, close planets than lighter, more distant planets and thus there is a clear observational bias. However, the fact that there are so many stellar systems with giant planets close to the star poses a considerable challenge to Solar System formation theories.

The giant planets are probably unlikely to be at the same distance from the Sun as when they initially formed due to gravitational and frictional interactions. The proposed gravitational ejection of planetesimals mentioned in Section 2.4.1 would be expected to extract energy from the planet's motion and cause them to migrate towards the Sun. The action of friction between the embryos and the turbulent disc early in the Solar System history is more difficult to quantify. It was mentioned earlier in Section 2.3.2 that material in the inner disc is thought to have moved in towards the Sun, while at greater distances, the disc would have spread out and dissipated. The critical radius separating these two mean motions is estimated to be at around 10 AU (Ida *et al.*, 2000). Hence a proto-Neptune,

forming at a distance somewhat greater than 10 AU, would be expected to have been drawn outwards (Bryden *et al.*, 2000b) and this migration appears to be supported by the observation of a considerable proportion of trans-Neptunian objects in the Kuiper–Edgeworth belt orbiting in a 3 : 2 resonance with Neptune at approximately 40 AU (i.e., they orbit twice for every three orbits of Neptune). These objects are sometimes known as *plutinos*, since Pluto is considered to be one of them. The fact that few objects are found at the 2 : 1 resonance distance of approximately 48 AU is interpreted as being due to the migration having occurred over a timescale of between 1 million and 10 million years (Ida *et al.*, 2000) with Neptune migrating a distance of something like 8 AU away from the Sun.

Extrasolar planetary systems with close Jovian planets or ‘Hot Jupiters’ offer clear evidence that either our current formation models are somehow wrong or that in many cases, giant planets forming within the critical radius of the disc migrate inwards. Such planets would gravitationally eject or capture all terrestrial planets in the so-called ‘habitable zone’ of the inner Solar System where surface temperatures would allow the presence of liquid water and thus, perhaps, the evolution of life. Keeping giant planets at distances greater than ~ 5 AU not only allows the development of an inner Solar System like that in our Solar System, but also efficiently expels small planetesimals that would otherwise swarm in this region, continually bombarding the inner planets and impeding the evolution of life. Hence the ‘smooth’ evolution of life on Earth actually required the presence of Jupiter, but not too close! Hence it is of great interest to the Astrobiology community to determine whether or not there are other planetary systems with characteristics more like ours, and in June 2002, the announcement of the discovery of a giant extrasolar planet in a circular orbit of radius 3.65 AU about the star HD 190360 A was made by the Geneva Observatory.

2.9 REFERENCES

- Anders, E. and N. Grevesse (1989) Abundances of the elements: Meteoritic and solar. *Geochimica et Cosmochimica Acta*, **53**, 197–214.
- André, Ph. and T. Montmerle (1994) From T tauri stars to protostars: Circumstellar material and young stellar objects in the ρ Ophiuchi cloud. *Astrophys. J.*, **420**, 837–862.
- Balsiger, H., K. Altwegg, and J. Geiss (1995) D/H and $^{18}\text{O}/^{16}\text{O}$ ratio in hydronium ion and in neutral water from in situ ion measurements in comet P/Halley. *J. Geophys. Res.*, **100**, 5827–5834.
- Bar-Nun, A., I. Kleinfeld, and E. Kochavi (1988) Trapping of gas mixtures by amorphous water ice. *Physical Review B*, **38**, 7749–7754.
- Bézard, B., E. Lellouch, D. Strobel, J.-P. Maillard, and P. Drossart (2002) Carbon monoxide on Jupiter: Evidence for both internal and external sources. *Icarus*, **159**, 95–111.
- Bockelée-Morvan, D., D. Gautier, D. C. Lis, K. Young, J. Keene, T. Phillips, T. Owen, J. Crovisier, P. F. Goldsmith, E. A. Bergin, D. Despois, and A. Wooten (1998) Deuterated water in Comet C1996 B2 (Hyukutake) and its implications for the origin of comets. *Icarus*, **133**, 147–162.

- Boss, A. P. (1998) Evolution of the solar nebula. IV. Giant gaseous protoplanet formation. *Astrophys. J.*, **503**, 923–937.
- Brittain, S. D. and T. W. Rettig (2002) CO and H₃⁺ in the protoplanetary disk around the star HD141569. *Nature*, **418**, 57–59.
- Bryden, G., M. Rozyczka, D. N. C. Lin, and P. Bodenheimer (2000a) On the interaction between protoplanets and protostellar disks. *Astrophys. J.*, **540**, 1091–1101.
- Bryden, G., D. N. C. Lin, and S. Ida (2000b) Protoplanetary formation. I. Neptune. *Astrophys. J.*, **544**, 482–495.
- Burles, S. and D. Tytler (1988) *Proceedings of the Second Oak Ridge Symposium on Atomic and Nuclear Astrophysics* (edited by P. Mezzacappa, p. 113). Institute of Physics, Bristol.
- Cameron, A. G. W. (1982) Elemental and nuclidic abundances in the solar system. In *Essays in Nuclear Astrophysics* (edited by C. A. Barnes, D. D. Clayton, and D. N. Schramm, pp. 23–43). Cambridge University Press, Cambridge, UK.
- Campbell, J. K. and J. D. Anderson (1989) Gravity field of the Saturnian system from Pioneer and Voyager tracking data. *Astron. J.*, **97**, 1485–1495.
- Campbell, J. K. and S. P. Synott (1985) Gravity field of the Jovian system from Pioneer and Voyager tracking data. *Astron. J.*, **90**, 364–372.
- Cauble, R., P. M. Celliers, G. W. Collins, L. B. da Silva, D. M. Gold, M. E. Foord, K. S. Budil, R. L. Wallace, and A. Ng (2000) Equation of state and material property measurements of hydrogen isotopes at the high-pressure, high-temperature, insulator-metal transition. *Astrophys. J. Suppl.*, **127**, 267–273.
- Conrath, B. J., D. Gautier, G. F. Lindal, R. E. Samuelson, and W. A. Shaffer (1991) The helium abundance of Neptune from Voyager measurements. *J. Geophys. Res.*, **96**, 18 907–18 919.
- Conrath, B. J., D. Gautier, T. C. Owen, and R. E. Samuelson (1993) Constraints on N₂ in Neptune's atmosphere from Voyager measurements. *Icarus*, **101**, 168–172.
- Dahmen, G., T. L. Wilson, and F. Matteucci (1995) The nitrogen isotope abundance in the galaxy. 1: The galactic disk gradient. *Astron. and Astrophys.*, **295**, 194–198.
- Deloule, E., J.-C. Doukhan, and F. Robert (1998) Interstellar hydroxyls in meteorite chondrules: Implications for the origin of water in the inner solar system. *Geochim. Cosmochim. Acta*, **62**, 3367–3378.
- Drouart, A., B. Dubrulle, D. Gautier, and F. Robert (1999) Structure and transport in the solar nebula from constraints on deuterium enrichment and giant planets formation. *Icarus*, **140**, 129–155.
- Eberhardt, P., M. Reber, D. Kranyakowsky, and R. R. Hodges (1995) The D/H and ¹⁸O/¹⁶O ratios in water from Comet P/Halley. *Astron. Astrophys.*, **302**, 301–316.
- Feuchtgruber, H., E. Lellouch, B. Bézard, Th. Encrenaz, Th. de Graauw, and G. R. Davis (1999) Detection of HD in the atmospheres of Uranus and Neptune: A new determination of the D/H ratio. *Astron. and Astrophys.*, **341**, L17–L21.
- Fouchet, T., E. Lellouch, B. Bézard, T. Encrenaz, P. Drossart, H. Feuchtgruber, and T. de Graauw (2000) ISO-SWS observations of Jupiter: Measurement of the ammonia tropospheric profile and the ¹⁵N/¹⁴N isotopic ratio. *Icarus*, **143**, 223–243.
- Fraser, H. J., M. R. S. McCoustra, and D. A. Williams (2002) The molecular universe. *Astronomy and Geophysics*, **43**, 210–218.
- French, R. G., J. L. Elliot, L. M. French, J. A. Kangas, K. J. Meech, M. E. Ressler, M. W. Buie, J. A. Frogel, J. B. Holberg, J. J. Fuensalida, and M. Joy (1988) Uranian ring orbits from earth-based and Voyager occultation observations. *Icarus*, **73**, 349–378.

- Gautier, D., F. Hersant, O. Mousis, and J. I. Lunine (2001a) Enrichments in volatiles in Jupiter: A new interpretation of the *Galileo* measurements. *Astrophys. J.*, **550**, L227–L230.
- Gautier, D., F. Hersant, O. Mousis, and J. I. Lunine (2001b) Erratum: Enrichments in volatiles in Jupiter. *Astrophys. J.*, **559**, L183–L183.
- Geiss, J. and G. Gloeckler (1998) Abundances of deuterium and helium-3 in the protosolar cloud. *Space Sci. Rev.*, **84**, 239–250.
- Grevesse, N. and A. J. Sauval (1998) Standard solar composition. *Space Sci. Rev.*, **85**, 161–174.
- Guillot, T. (1999a) A comparison of the interiors of Jupiter and Saturn. *Plan. Spac. Sci.*, **47**, 1183–1200.
- Guillot, T. (1999b) Interiors of giant planets inside and outside the Solar System. *Science*, **286**, 72–77.
- Guilloteau, T., A. Dutrey, and F. Gueth (1997) Disks and outflows as seen from the IRAM interferometer. In *Herbig-Haro flows and the Birth of Low Mass Stars* (edited by B. Reithpurth and C. Bertout, pp. 365–380). International Astronomical Union Symposium No. 182, Kluwer Academic, Dordrecht, The Netherlands.
- Hashizume, K., M. Chaussidon, B. Marty, and F. Robert (2000) Solar wind record on the Moon: Deciphering presolar from planetary nitrogen. *Science*, **290**, 1142–1145.
- Hersant, F., D. Gautier, and J-M Huré (2001) A two-dimensional model of the primordial nebula constrained by D/H measurements in the solar system: Implications for the formation of the giant planets. *Astrophys. J.*, **554**, 391–407.
- Hubbard, W. B. (1997a) Jupiter: Interior structure. *Encyclopaedia of the Planetary Sciences*. Chapman & Hall, London.
- Hubbard, W. B. (1997b) Saturn: Interior structure. *Encyclopaedia of the Planetary Sciences*. Chapman & Hall, London.
- Hubbard, W. B. (1997c) Uranus: Interior structure. *Encyclopaedia of the Planetary Sciences*. Chapman & Hall, London.
- Hubbard, W. B. (1997d) Neptune: Interior structure. *Encyclopaedia of the Planetary Sciences*. Chapman & Hall, London.
- Ida, S., G. Bryden, D. N. C. Lin, and H. Tanaka (2000) Orbital migration of Neptune and orbital distribution of trans-neptunian objects. *Astrophys. J.*, **534**, 428–445.
- Jewitt, D. C., H. E. Matthews, T. Owen, and R. Meier (1997) Measurement of $^{12}\text{C}/^{13}\text{C}$, $^{14}\text{N}/^{15}\text{N}$, $^{32}\text{S}/^{34}\text{S}$ in Comet Hale-Bopp (C/1995 O1). *Science*, **278**, 90–93.
- Jones, B. W. (1999) *Discovering the Solar System*. John Wiley & Sons, Chichester, UK.
- Krane, K. (1996) *Modern Physics* (2nd Edition). John Wiley & Sons, Chichester, UK.
- Lécuyer, C., Ph. Gillet, and F. Robert (1998) The hydrogen isotope composition of sea water and the global water cycle. *Chem. Geol.*, **145**, 249–261.
- Lellouch, E., B. Bézard, T. Fouchet, H. Feuchtgruber, T. Encrenaz, and T. de Graauw (2001) The deuterium abundance in Jupiter and Saturn from ISO-SWS observations. *Astron. and Astrophys.*, **670**, 610–622.
- Lewis, J. S. (1995) *Physics and Chemistry of the Solar System*. Academic Press.
- Lindal, G., D. Sweetnam, and V. Eshleman (1985) The atmosphere of Saturn: An analysis of the *Voyager* radio occultation measurements. *Astronomical J.*, **90**, 1136–1146.
- McCaughrean, M. J. and C. R. O'Dell (1996) Direct imaging of circumstellar disks in the Orion Nebula. *Astronomical J.*, **111**, 1977.
- McCaughrean, M. J., J. T. Rayner, and H. Zinnecker (1994) Discovery of a molecular hydrogen jet near IC 348. *Astrophysical J.*, **436**, L189–L192.

- McCaughrean, M. J., H. Chen, J. Bally, E. Erickson, R. Thompson, M. Rieke, G. Schneider, S. Stolovy, and E. Young (1998) High-resolution near-infrared imaging of the Orion 114-426 Silhouette Disk. *Astrophys. J.*, **492**, 157.
- Meier, R., T. Owen, H. E. Matthews, D. C. Jewitt, D. Bockelée-Morvan, N. Biver, J. Crovisier, and D. Gautier (1998) A determination of the HDO/H₂O ratio in Comet C/1995 O1 (Hale-Bopp). *Science*, **279**, 842.
- Mousis, O., D. Gautier, D. Bockelée-Morvan, F. Robert, B. Dubrulle, and A. Drouart (2000) Constraints on the formation of comets from D/H ratios measured in H₂O and HCN. *Icarus*, **148**, 513–525.
- Nellis, W. J. (2000) Metallization of fluid hydrogen at 140 GPa (1.4 Mbar): Implications for Jupiter. *Plan. Space Sci.*, **48**, 671–677.
- Nellis, W. J., M. Ross, and N. C. Holmes (1995) Temperature measurements of shock-compressed liquid hydrogen: Implications for the interior of Jupiter. *Science*, **269**, 1249–1252.
- Owen, W. M., R. M. Vaughan, and S. P. Synnott (1991) Orbits of the six new satellites of Neptune. *Astron. J.*, **101**, 1511–1515.
- Owen, T., P. R. Mahaffy, H.B. Niemann, S. Atreya, and M. Wong (2001) Protosolar nitrogen. *Astrophys. J.*, **553**, L77–L79.
- Owen, T., P. Mahaffy, H. B. Niemann, S. Atreya, T. Donahue, A. Bar-Nun, and I. de Pater (1999) A low-temperature origin for the planetesimals that formed Jupiter. *Nature*, **402**, 269–270.
- Podolak, M., J. I. Podolak, and M.S. Marley (2000) Further investigations of random models of Uranus and Neptune. *Planet. Space Sci.*, **48**, 143–151.
- Pollack, J. B., O. Hubickyj, P. Bodenheimer, J. J. Lissauer, M. Podolak, and Y. Greenzweig (1996) Formation of the giant planets by concurrent accretion of solids and gas. *Icarus*, **124**, 62–85.
- Radousky, H. B., A. C. Mitchell, and W. J. Nellis (1990) Shock temperature measurements of planetary ices – NH₃, CH₄, and ‘synthetic Uranus’. *J. Chem. Phys.*, **93**, 8235–8239.
- Russell, C. T. and J. G. Luhmann (1997) Saturn: Magnetic field and magnetosphere. *Encyclopaedia of the Planetary Sciences*. Chapman & Hall, London.
- Shu, F. H., S. Tremaine, F. C. Adams, and P. Ruden (1990) Sling amplification and eccentric gravitational instabilities in gaseous disks. *Astrophys. J.*, **358**, 495–514.
- Ward, W. and D. P. Hamilton (2002) The obliquities of the giant planets. Paper presented at *Eurojove: Jupiter after Galileo and Cassini, Lisbon, June 2002*.

2.10 BIBLIOGRAPHY

- Beatty, J. K. and A. Chaikin (eds) (1998) *The New Solar System* (4th Edition). Sky Publishing, Cambridge, MA.
- Clark, S. (2000) *Extrasolar Planets*. Springer–Praxis, Chichester, UK.
- Davies, J. (2001) *Beyond Pluto*. Cambridge University Press, Cambridge, UK.
- de Pater, I. and J. J. Lissauer (2001) *Planetary Sciences*. Cambridge University Press, Cambridge, UK.
- Encrenaz, T., J.-P. Bibring, and M. Blanc (1995) *The Solar System* (2nd Edition). Springer, Berlin.
- Jones, B. W. (1999) *Discovering the Solar System*. John Wiley & Sons, Chichester, UK.

- Shirley, J. H. and R. W. Fairbridge (eds) (1997) *Encyclopaedia of the Planetary Sciences*. Chapman & Hall, London.
- Weissman, P. R., L.-A. McFadden, and T. V. Johnson (eds) (1999) *Encyclopaedia of the Solar System*. Academic Press, London.

The following websites are also useful.

Kuiper belt objects:

<http://www.ifa.hawaii.edu/faculty/jewitt/kb.html>
<http://www.nineplanets.org/kboc.html>

Oort cloud:

<http://www.nineplanets.org/kboc.html>
<http://www.solarviews.com/eng/oort.htm>

3

Evolution processes in outer planet atmospheres

3.1 INTRODUCTION

Subsequent to their formation from the collapse of the solar nebula, the atmospheres of all the planets, including the giant planets, have (to a greater or lesser extent) evolved over time through the action of a number of possible processes including thermal escape, cometary bombardment, and internal differentiation. In this chapter we will outline the principle evolution mechanisms and estimate their effects on the present day composition of the giant planet atmospheres.

3.2 THERMAL ESCAPE

3.2.1 Jeans' formula

In the upper atmospheres of planets, the density becomes very low, and the temperature becomes very high due to absorption of solar ultraviolet (UV) light and, for the giant planets, other sources such as the viscous damping of vertically propagating gravity waves (Young *et al.*, 1997; Matcheva and Strobel, 1999). Hot, fast-moving molecules may escape should their kinetic energy (in the vertical direction) exceed their gravitational potential energy, i.e.,

$$\frac{1}{2}mv^2 > \frac{GMm}{a} \quad (3.1)$$

where M is the mass of the planet, G is the gravitational constant, m is the mass of the molecule, v is its velocity in the upward direction, and a is the planetary radius at the altitude of the thermosphere. Since the gravitational acceleration at radius a is given by $g = GM/a^2$, this condition may be rewritten as

$$\frac{1}{2}v^2 > ga \quad (3.2)$$

or

$$v > \sqrt{2ga}. \quad (3.3)$$

Molecules moving upwards with speeds in excess of this calculated *escape velocity* will however only escape if they do not collide with any other molecules on the way. Hence substantial escape of molecules only occurs when the vertically integrated density of air molecules above a certain *critical level* z_c accounts for one mean free path, i.e.,

$$\int_{z_c}^{\infty} \sigma n_a(z) dz = 1 \quad (3.4)$$

where $n_a(z)$ is the number density profile of *all* molecules and σ is the collisional cross section. Assuming the atmosphere to be in hydrostatic equilibrium (Section 4.1.1) such that $n_a(z) = n_a(z_c) \exp(-z/H_{ca}^*)$, where H_{ca}^* is the mean atmospheric number density scale height discussed in Section 3.2.2, Equation 3.4 may be integrated to give

$$\int_{z_c}^{\infty} \sigma n_a(z) dz = \sigma n_a(z_c) \int_{z_c}^{\infty} e^{-z/H_{ca}^*} dz = \sigma n_a(z_c) H_{ca}^* = 1. \quad (3.5)$$

For the giant planet atmospheres, the most abundant molecule in the upper atmosphere is atomic hydrogen, and thus it is this molecule which largely determines the altitude of the critical level, otherwise known as the *exobase*. Assuming a Maxwell–Boltzmann distribution of speeds, the probability that a molecule of molecular weight m will have a speed in the range c to $c + dc$ is given by

$$P(c) dc = 4 \left(\frac{\alpha^3}{\pi} \right)^{1/2} c^2 \exp(-\alpha c^2) dc \quad (3.6)$$

where $\alpha = m/2RT$, R is the gas constant, and T is the temperature. For such a gas, the number of molecules passing upwards through unit area per second at the exobase with speeds in the range c to $c + dc$ is then given by the well-known kinetic theory (Flowers and Mendoza, 1970) expression

$$dF = \frac{1}{4} n(z_c) c P(c) dc. \quad (3.7)$$

Assuming that all such molecules with speed greater than the escape velocity $v_e = \sqrt{2ga}$ will escape the atmosphere, we may integrate Equation 3.7 to calculate the flux of escaping molecules, known as the *Jeans flux*

$$\begin{aligned} F_{Jea} &= n(z_c) \left(\frac{\alpha^3}{\pi} \right)^{1/2} \int_{v_e}^{\infty} c^3 \exp(-\alpha c^2) dc \\ &= \frac{1}{2} n(z_c) \left(\frac{\alpha}{\pi} \right)^{1/2} \left(v_e^2 + \frac{1}{\alpha} \right) \exp(-\alpha v_e^2) \end{aligned} \quad (3.8)$$

or

$$F_{Jea} = \frac{n(z_c) U}{2\sqrt{\pi}} (1 + \lambda) \exp(-\lambda) \quad (3.9)$$

where the most probable speed $U = \sqrt{2RT/m}$ and the escape parameter λ is defined as $\lambda = v_e^2/U^2$.

The rate at which the concentration of molecules is reduced may then be calculated by considering that the total number of molecules per unit area above the exobase (and thus which may escape) is given by $N = n(z_c)H_c^*$ where H_c^* is the number density scale height of the escaping molecule or atom at the critical level. Thus expressing the Jeans flux as $F_{Jea} = \beta n(z_c)$ we obtain

$$F_{Jea} = \left(\frac{\partial N}{\partial t} \right)_{Jea} = -\frac{\beta}{H_c^*} N \quad (3.10)$$

which may be integrated to give

$$N = N_0 \exp\left(-\frac{\beta}{H_c^*} t\right). \quad (3.11)$$

From this expression we can see that there is a *characteristic escape time* for thermal escape given by $\tau_e = H_c^*/\beta$. Alternatively, we can define a mean velocity at which molecules or atoms escape upwards from the exobase, known as the *expansion velocity* given by $v_{ex} = H_c^*/\tau_e = \beta$. The calculated escape times for various gases in the atmospheres of the giant planets, the Earth, and also Titan and Triton are listed in Table 3.1. As can be seen, compared to the smaller planets, the masses of the giant planets are so large, and their exospheric temperatures so cool, that negligible exospheric escape is calculated and thus these planets have effectively lost none of their atmospheres. This is not the case for the Earth, Titan, and Triton where significant loss of the lighter atoms is calculated and whose atmospheres have thus significantly evolved over time. The relatively unevolved atmospheres of the giant planets thus offer a unique picture of the composition of the solar nebula at the time of the planets' formation, provided that no other processes have acted to modify the composition. We shall return to this in Sections 3.3 and 3.4.

3.2.2 Diffusion and limiting flux

For planets such as the Earth, and giant planet satellites such as Titan and Triton, where exospheric escape is of importance, the rate of exospheric escape is actually limited by the rate at which molecules may be transported to the exobase from below by processes such as diffusion (Chamberlain and Hunten, 1987) and their approach is reproduced here for the reader's convenience.

Suppose a minor constituent has a density distribution $n_i(z)$ in an atmosphere where its density distribution in diffusive equilibrium would be $n_{iE}(z)$, then by the process of molecular diffusion there will be an upward flux equal to

$$\phi_i = n_i w_i = -D_i n_{iE} \frac{\partial(n_i/n_{iE})}{\partial z} \quad (3.12)$$

Table 3.1. Calculated exospheric escape times for the giant planets, Earth, Titan and Triton.

	Earth	Jupiter	Saturn	Uranus	Neptune	Titan	Triton
R_0 (km)	6,378	71,492	60,268	25,559	24,764	2,575	1,353
z_c (km)	500	2000	2000	2000	2000	1000	300
T (K)	1480	700	420	700	700	300	300
g_0 (m s^{-2})	9.81	23.1	9.1	8.7	11	1.41	0.78
v_{esc} (km s^{-1})	10.77	56.6	32.5	20.3	22.4	2.28	1.31
$\tau(\text{H})$ (yrs)	5.6×10^{-4}	$2.6 \times 10^{11.2}$	1.2×10^{59}	1.5×10^9	2.6×10^{12}	1.2×10^{-4}	1.7×10^{-4}
$\tau(\text{He})$ (yrs)	1.1×10^{-2}	$2.2 \times 10^{47.1}$	2.2×10^{256}	3.0×10^{54}	9.3×10^{67}	5.7×10^{-4}	1.3×10^{-4}
$\tau(\text{C})$ (yrs)	5.5×10^{17}	1.4×10^{1430}	1.1×10^{784}	8.6×10^{176}	6.3×10^{217}	5.5×10^{-1}	5.7×10^{-4}
$\tau(\text{N})$ (yrs)	5.5×10^{21}	8.9×10^{1669}	1.1×10^{916}	4.2×10^{207}	2.2×10^{235}	3.62	9.4×10^{-4}
$\tau(\text{O})$ (yrs)	5.6×10^{25}	5.6×10^{1509}	1.1×10^{1048}	2.2×10^{238}	7.6×10^{292}	24.3	1.6×10^{-3}
$\tau(\text{Ar})$ (yrs)	2.1×10^{74}	5.8×10^{4787}	5.0×10^{2632}	1.8×10^{607}	8.2×10^{743}	5.5×10^{11}	1.8
$\tau(\text{Kr})$ (yrs)	9.8×10^{163}	5.4×10^{10064}	3.1×10^{5538}	1.7×10^{1284}	2.6×10^{1571}	2.0×10^{31}	2.5×10^6

NB. R_0 is the equatorial radius at the 1 bar pressure level, and z_c is the altitude of the critical level above R_0 .

where D_i is the molecular diffusion coefficient for the i th gas and w_i is the mean effective vertical speed. From kinetic theory considerations, the coefficient of diffusion for a single gas may be shown to be

$$D_i = \frac{1}{3} \lambda_i \bar{c}_i \quad (3.13)$$

where

$$\bar{c}_i = \left(\frac{8RT}{\pi m_i} \right)^{1/2}$$

is the mean speed of the molecules of molecular weight m_i and $\lambda_i = 1/\sqrt{2n}\sigma_i$ is the mean free path where σ_i is the collision cross section. Hence the coefficient may be written as $D_i = \bar{c}_i/3\sqrt{2n}\sigma_i$ or more generally in the semi-empirical form

$$D_i = \frac{b_i}{n} = \frac{A_i T^{S_i}}{n} \quad (3.14)$$

where b_i is the *binary collision parameter* which is expressed in terms of the coefficients A_i and S_i which are fitted to experimental data.

For an atmosphere in hydrostatic equilibrium (Section 4.1.1), the pressure distribution $p(z)$ is given by $p = p_0 e^{-z/H}$ where the scale height to a first approximation is $H = RT/\bar{m}g$ (assuming negligible variation of temperature with height) and \bar{m} is the mean molecular weight. Similarly, it is straightforward to show that the number density $n_{iE}(z) = p(z)/kT$, has a similar distribution given by

$$n_{iE} = n_0 e^{-z/H^*} \quad (3.15)$$

where H^* is the number density scale height given by

$$\frac{1}{H^*} = \frac{1}{H_i} + \frac{1}{T} \frac{dT}{dz}. \quad (3.16)$$

Substituting $n_{iE}(z)$ into Equation 3.12 we obtain

$$\phi_i = -n_i D_i \left(\frac{1}{n_i} \frac{dn_i}{dz} + \frac{1}{H_i} + \frac{1}{T} \frac{dT}{dz} \right) \quad (3.17)$$

or

$$\phi_i = n_i W_i = n_i D_i \left(\frac{1}{H_i^*} - \frac{1}{H_{iE}^*} \right) \quad (3.18)$$

where we have also equated the flux to the product of the number density times the mean vertical flux velocity w_i . A mean estimate for the diffusion time is given by the expression $\tau_i \sim H_i^*/w_i$ or, since w_i is of the order of D/H , $\tau_i \sim H^2/D_i$.

Defining the *volume mixing ratio*, or *mole fraction*, of the i th element as $f_i = n_i/n_a$, and differentiating we obtain

$$\frac{1}{f_i} \frac{df_i}{dz} = \frac{1}{n_i} \frac{dn_i}{dz} - \frac{1}{n_a} \frac{dn_a}{dz}. \quad (3.19)$$

Substituting this into Equation 3.17 we get

$$\phi_i = \phi_L - D_i n_a \frac{df_i}{dz} \quad (3.20)$$

where the *limiting flux* ϕ_L , is given by

$$\phi_L = -n_i D_i \left(\frac{1}{n_a} \frac{dn_a}{dz} + \frac{1}{H_i} + \frac{1}{T} \frac{dT}{dz} \right). \quad (3.21)$$

Hence the exospheric loss is in fact moderated by the rate at which molecules may diffuse up to the exobase. This consideration is of particular importance for estimating the rate of escape of H and H₂ from the atmospheres of Titan and Triton. Note that in Equations 3.20 and 3.21, the eddy diffusion coefficient should also be added to the molecular diffusion coefficient to give total ‘diffusion’. Eddy diffusion is discussed in the next chapter.

3.2.3 Hydrodynamic escape

We saw earlier that only light atoms can escape in significant amounts by Jeans’ escape mechanism from the atmospheres of Titan and Triton. However if the flux of light atoms is large then heavier atoms may also be driven off by ‘blowoff’ (Chamberlain and Hunten, 1987). Substituting the empirical expression for the diffusion coefficient (Equation 3.14) into the diffusion equation (Equation 3.17) we have

$$\phi_i = -n_i \frac{b}{n} \left(\frac{1}{n_i} \frac{dn_i}{dz} + \frac{1}{H_i} + \frac{1}{T} \frac{dT}{dz} \right) \quad (3.22)$$

where b is the empirical binary collision parameter. This equation may be rearranged to give

$$\frac{dn_i}{dz} = -\left(\frac{\phi_i n}{b} + \frac{n_i}{H_i} + \frac{n_i}{T} \frac{dT}{dz} \right). \quad (3.23)$$

This equation assumes that the individual gases may be treated separately. However, if two gases are considered, moving with different fluxes of respectively ϕ_1 and ϕ_2 , then their combined diffusion equations, ignoring the dT/dz terms which are found to be negligible (Chamberlain and Hunten, 1987), are

$$\begin{aligned} \frac{dn_1}{dz} &= -\frac{n_1}{H_1} + \frac{1}{b} (n_1 \phi_2 - n_2 \phi_1) \\ \frac{dn_2}{dz} &= -\frac{n_2}{H_2} + \frac{1}{b} (n_2 \phi_1 - n_1 \phi_2). \end{aligned} \quad (3.24)$$

With a bit of manipulation, the flux ϕ_2 of the heavier gas of molecular weight M_2 , blown by a flux ϕ_1 of lighter gas molecules of molecular weight M_1 , may be shown to be

$$\phi_2 = \frac{f_2}{f_1} \phi_1 \left(\frac{M_c - M_1}{M_c - M_2} \right) \quad (3.25)$$

where f_n is the mole fraction of component n and

$$M_c = M_1 + \frac{kT\phi_1}{bgf_1}$$

is called the *crossover mass* and represents the heaviest species which can be removed in this way. This effect is clearly negligible in the giant planet atmospheres since the Jeans flux of even the lightest atom, hydrogen, is so low.

3.3 IMPACTS WITH COMETS AND PLANETESIMALS

Planets have undergone significant bombardment by comets and planetesimals in the past, and in fact, as the collision of Comet Shoemaker–Levy 9 with Jupiter in 1994 showed, these impacts are an ongoing process in the evolution of planetary atmospheres. During such an impact, in addition to introducing new material to the planet from the planetesimal itself such as ‘soot’ and trace species (discussed in Chapters 4 and 5), a small fraction of the planet’s atmosphere may be driven off if it acquires sufficient kinetic energy to escape the planet’s gravity.

We can make a simple calculation of the rate at which the atmosphere is ejected in this way. Suppose an impactor of radius R and speed v_s strikes an atmosphere of density σ_a per unit area above the level where the impactor’s energy is spent. The kinetic energy acquired by the air through which the comet passes may be estimated to be roughly

$$E = \frac{1}{2}\pi R^2 \sigma_a v_s^2. \quad (3.26)$$

Assuming all this energy is converted to eject a mass M_e of atmosphere at the escape velocity v_e , we can obtain an upper estimate of the atmospheric mass loss

$$M_e = \frac{\pi R^2 \sigma_a v_s^2}{v_e^2}. \quad (3.27)$$

This process, unlike thermal escape and hydrodynamic escape, does not discriminate with respect to mass and hence does not cause fractionation of species. However, its effect on the evolution of the giant planet atmospheres is likely to be very small due to the large escape velocities of these planets.

3.4 INTERNAL DIFFERENTIATION PROCESSES

The final way in which composition of the outer planet atmosphere may evolve is through differentiation where heavier materials preferentially fall towards the centre of the planet decreasing their abundance in the exterior. This is a separate effect to the initial differentiation of the giant planets arising from the different phases of their growth described in Chapter 2. This secondary differentiation is inhibited by convection which tends to make the interior of the planets well-mixed and

homogeneous. If differentiation does occur however it should be observable both via observed depletions in the outer parts of the atmosphere and through the additional source of internal heat that such gravitational settling would release. To evaluate the degree of internal heating, currently active in the interiors of the giant planets, we need to compare their current observed bolometric temperatures with those expected were the planets to be in thermal equilibrium with the incident solar radiation.

3.4.1 Effective radiating temperature of planets

The Sun radiates essentially as a black body, with an effective surface temperature $T_S = 5,750$ K, and radius $R_S = 700,000$ km. Applying Stefan–Boltzmann’s law we find that the total power radiated by the sun in all directions is

$$E_S = \sigma(4\pi R_S^2)T_S^4 = 3.8 \times 10^{26} \text{ W} \quad (3.28)$$

where σ is the Stefan–Boltzmann constant. The flux of sunlight (W m^{-2}) arriving at a planet at distance D from the Sun is simply this power divided by the surface area of a sphere of radius equal to the distance to the Sun, i.e.,

$$F_S = \sigma \left(\frac{R_S}{D} \right)^2 T_S^4. \quad (3.29)$$

At the Earth’s distance from the Sun the solar constant F_S is equal to 1.37 kW m^{-2} . The total amount of sunlight absorbed by the planet is then equal to

$$P_{abs} = (1 - A_B)\pi R_P^2 F_S \quad (3.30)$$

where R_p is the planetary radius, πR_P^2 is the projected disc area, and A_B is the *Bond Albedo* which is the fraction of sunlight reflected by the planet in all directions. Assuming no other sources of heat, in order for the temperature of the planet to be in equilibrium, this absorbed power must be balanced by the thermal radiation emitted to space. Since the observable temperatures of the giant planets are so much smaller than the Sun’s, the Planck functions of incident solar and emitted thermal radiation show negligible overlap and thus the two fluxes may be considered separately. The total power emitted by the planet to space is equal to its total surface area multiplied by the infrared (IR) flux $F_{IR} = \sigma T_E^4$, i.e.,

$$P_{emm} = 4\pi R_P^2 F_{IR}. \quad (3.31)$$

Equating the total absorbed power to the emitted power we find

$$\sigma(4\pi R_P^2)T_E^4 = (1 - A_B)\pi R_P^2 F_S \quad (3.32)$$

and rearranging for T_E , the *effective radiating temperature*, we obtain

$$T_E = \left(\frac{(1 - A_B)}{4\sigma} F_S \right)^{1/4} \quad (3.33)$$

Table 3.2. Thermal balance of the Earth and giant planets.

	Earth	Jupiter	Saturn	Uranus	Neptune
D (AU)	1	5.20	9.56	19.22	30.11
Solar flux F_S (W m^{-2})	1370.0	50.66	14.99	3.71	1.51
Geometric Albedo A_G	0.3?	0.274	0.242	0.215	0.215
Bond Albedo A_B	0.4	0.343	0.342	0.300	0.290
Absorbed flux	205.5	8.32	2.47	0.65	0.27
$F_{ab}((1 - A_B) \times F_S/4)$					
Observed F_{IR}	205.5	13.89	4.40	0.69	0.72
Energy balance (F_{IR}/F_{ab})	1.0	1.67	1.78	1.06	2.61
T_E (K)	255	109.5	82.4	58.2	46.6
T_{IR} (K)	255	124.4	95.0	59.1	59.3
$F_{int}(F_{IR} - F_{ab})$	0.0	5.57	1.93	0.04	0.45

Adapted from Table 7 of Pearl and Conrath (1991).

or by substituting F_S from Equation 3.29

$$T_E = T_S \left(\frac{(1 - A_B)R_S^2}{4D^2} \right)^{1/4}. \quad (3.34)$$

For the Earth, T_E is estimated to be approximately 255 K. The mean *surface* temperature on the Earth is fortunately significantly higher due to the Greenhouse Effect provided by the IR absorptivity of carbon dioxide and water vapour.

The albedo used here for effective radiating temperature calculations is the *Bond Albedo* (or *Planetary Bolometric Albedo*) and is defined as the fraction of incident solar radiation scattered in all directions. When measuring the reflectivity of planets, in particular the giant planets, all we see is the radiation reflected in the direction back to Earth. If the Earth, Sun, and planet are all in the same line, the albedo measured is called the *Geometric Albedo*. Should the surface of the planet reflect light equally well in all directions (and thus be a perfect *Lambert Reflector*) then the Bond and Geometric Albedos are in fact identical. Otherwise, they differ depending upon the scattering properties of the planet's surface or cloud layers.

The measured albedos and thermal IR fluxes of the giant planets are listed in Table 3.2. The data in this table shows that the calculated effective radiating temperatures of all the Jovian planets except Uranus are significantly smaller than the observed bolometric temperatures. This implies therefore that these planets have internal sources of heat which may come from three possible sources:

- (1) Residual heat of formation arising from the continued cooling, and shrinking of the planets via the *Kelvin–Helmholtz* mechanism.
- (2) Fractionation in the interior, with heavy elements settling towards the centre and converting gravitational energy into thermal energy.
- (3) Radioisotope heating.

The contribution of all these sources to the observed bolometric temperatures of the giant planets will now be discussed.

3.5 EVOLUTION OF THE GIANT PLANET ATMOSPHERES

3.5.1 Jupiter

The bolometric temperature of Jupiter (124 K) is consistent with that expected by the planet radiating its primordial heat to space continually since formation via the Kelvin–Helmholtz mechanism. The interior heat flux remains sufficiently high to keep the liquid metallic interior highly convective with the result that most of the planet mixes thoroughly on a timescale of the order of 100 years. As we saw in Chapter 2, this vigorous convection of the metallic-hydrogen interior easily accounts for Jupiter’s very high magnetic field.

The phase transition between molecular- and metallic-hydrogen may however have an effect upon the atmospheric abundances in the observable atmosphere. Some calculations suggest that solar abundances of helium cannot be dissolved in metallic-hydrogen under current Jovian temperature conditions at the lowest pressure where metallic-hydrogen exists. Droplets of liquid helium would form in these regions and drop towards the centre of the planet converting their gravitational energy into thermal energy and reducing the abundance of helium in the observable atmosphere. However these solubility calculations are highly model-dependent and thus it is not clear whether or not there has been significant depletion of helium. The current helium mass fraction of 0.238 (von Zahn *et al.*, 1998) is almost the same as the current observable solar value although the primordial helium fraction is believed to have been larger, perhaps 0.275 (Grevesse and Sauval, 1998). Hence Jupiter’s atmosphere could be depleted if the Sun underwent a similar process of helium separation over time with the Sun fusing helium in its core. The atmospheric depletion of Neon observed by the *Galileo* entry probe would be consistent with helium differentiation since Neon is highly soluble in liquid helium. However the low abundance of Neon may also be explained by the clathrate–hydrate theory of formation outlined in Chapter 2 since Neon is not easily trapped in clathrates.

The deep circulation of interior is not well understood. Most models assume that the molecular and metallic regions are homogeneous (i.e., well mixed) since Jupiter and Saturn are still emitting more energy than they receive from the Sun which implies active convection at great depth. This is a good assumption provided that the hydrogen–helium mix is sufficiently opaque such that convective heat transfer is more efficient than radiative heat transfer. This is almost certainly true in the metallic-hydrogen region which is thought to be highly opaque to thermal photons, but not particularly conductive for a metal. However in the molecular-hydrogen region some models suggest that the opacity may be sufficiently small at kilobar pressure levels to allow the presence of a thin radiative zone, which would serve as a barrier to convection. This may also occur in Saturn. Likewise the molecular–metallic interface (Figure 2.9), if it exists as a discrete phase boundary,

may also act as a barrier (Hubbard, 1997a), although recent laboratory experiments (Nellis, 2000) suggest that the molecular–metallic phase boundary is in fact somewhat smooth as was noted in Chapter 2. In these ‘barrier’ regions, stable to convection, the fluid interior would be stably stratified. If there were negligible turbulent eddy mixing (see Chapter 4) then gravitational settling of the heavier molecules towards the base of the layer may occur in these regions. Hence a composition gradient would be set up, leading to a net transfer of molecules between the well-mixed convective layers above and below the stable region, and thus leading to long-term evolution of the composition of the observed atmosphere. In reality, interior models suggest that it is very unlikely that eddy mixing is so low that gravitational settling occurs. However these ‘barrier’ regions may have an effect on the observed composition in another way. Eddy mixing is not as efficient at transporting material as convective mixing and thus if the material above and below the convective ‘barrier’ initially has different composition then the barrier would greatly inhibit the transfer of material across it and thus compositional differences may be maintained over long periods of time. During the formation of the giant planets deeper material is thought, from the core accretion model, to have been more icy than material accreted later, which contained proportionally more and more nebula gas. If the whole interior was convectively unstable then these differences would be rapidly eliminated. However the presence of convective barriers may mean that the material above and below the barriers has still not come to equilibrium today and thus that the composition of the observable atmosphere may still be evolving.

3.5.2 Saturn

The current Saturn thermal flux is 1.9 W m^{-2} . Although this is smaller than the corresponding figure for Jupiter, this is due to Saturn’s much lower mass and in fact, unlike Jupiter, most models suggest that the figure is too large to be explained by the Kelvin–Helmholtz mechanism alone. Cooling via the Kelvin–Helmholtz mechanism decreases exponentially over time and for Saturn is predicted by most models to have mostly disappeared after approximately 2.5 billion years. Hence an additional source of heat seems to be required, which is released later, during the planet’s evolution as it cools to lower temperatures. Although Saturn has more rocky material than Jupiter, radioactive heating from the $\sim 29 M_{\oplus}$ of heavy material in Saturn would account for no more than 1% of this, and may be discounted. One possibility is that, like Jupiter, at the lower temperatures found in the metallic-hydrogen region of Saturn, helium becomes slightly immiscible and droplets of helium form which ‘rain out’ towards the centre. This gradual precipitation, with resultant release of gravitational energy would account for the additional internal heat source, and is also consistent with estimates of the He/H_2 ratio of 0.13 which is significantly smaller than the ratio of 0.157 measured in Jupiter’s atmosphere.

Saturn may also have a radiative zone in its molecular-hydrogen region, and together with the possible convective barrier at the metallic–molecular-hydrogen

boundary (Figure 2.9), these may act to inhibit the transfer of material between the interior and exterior of the planet. The extent of this is unknown.

3.5.3 Uranus and Neptune

Uranus radiates at most only 6% more energy than it receives from the Sun and its internal heat flux is estimated to be less than 0.04 W m^{-2} . Hence to a first approximation it has almost no internal heat source at all, although by the Kelvin–Helmholtz mechanism as much as 1 W m^{-2} would currently be expected. This low value of Uranus' internal flux is extremely puzzling, especially when it is considered that Neptune, which is otherwise very similar to Uranus, has a very strong internal heat source. In fact Neptune's total thermal emission to space is almost equal to that of Uranus' (their bolometric temperatures are approximately equal), even though Neptune is much further from the Sun.

Uranus is estimated to include as much as $4 M_{\oplus}$ of rocky materials and assuming that this rock is heated by radioactive decay at the same rate as terrestrial rocks, then a flux of 0.02 W m^{-2} is calculated (Hubbard, 1997b), which is a substantial fraction of that estimated.

There is no consensus on why Uranus' flux is so low. One suggestion is that chemical composition gradients, such as that at 5,000 km depth at the ice/hydrogen–helium interface (Figure 2.10) may act as a convection barrier and thus inhibit the transport of heat from the planet's hot interior. However, why this might happen in Uranus' atmosphere, and not in Neptune's is unclear. Another possibility is that towards the end of its formation, Uranus suffered a cataclysmic off-centre impact with another planet-sized body. Such an impact would account for Uranus' abnormally high obliquity and compact, equatorially aligned satellite system formed out of collision debris. It might also have had the effect of greatly accelerating the release of internal heat by effectively turning the planet inside out! Neptune on the other hand may have suffered much more centred impacts and thus rather than turn the planet on its side, the collision energy would have been converted into additional internal heat which would explain Neptune's high internal heat source. It should be remembered that these 'giant collision' theories are highly speculative and indeed Uranus' high obliquity could have been imparted by several off-centre collisions with much smaller bodies during formation and not necessarily a single giant collision.

Although methane and water in the deep interior should dissociate at the high temperatures and pressures found there, it does not appear that the hydrogen this releases permanently escapes the interior and mixes with the nebular hydrogen in the outer hydrogen–helium envelope since the observed He/H_2 ratio is close to the solar value. There is however good evidence of considerable mixing of the nebula hydrogen with this dissociated hydrogen since the $(\text{D}/\text{H})_{\text{H}_2}$ ratio is observed to be high, as was discussed in Chapter 2. The case for Neptune is similar although initial estimates of the He/H_2 ratio were supersolar which was very puzzling. It may be possible that the vigorous convection in Neptune's atmosphere, consistent with its high internal heat flux, brings substantial quantities of N_2 to the observable atmosphere which has a substantial effect on the He/H_2 ratio detection technique

employed by *Voyager 2*. As little as 0.3% abundance of N₂ reduces the estimated He/H₂ ratio to that of Uranus as we saw in Chapter 2.

Although Uranus' internal heat source appears very low, and thus vertical convection is presumably sluggish, the atmosphere is still very dynamic and the circulation efficiently redistributes relatively warm polar air over the planet. During the *Voyager 2* flyby, Uranus was close to Northern Winter Solstice with the South Pole permanently in sunlight and the North Pole permanently in darkness. If there were no atmospheric motion then we would have expected the South Pole to become very much warmer than the North, perhaps by as much as 7°C or 7K. However, *Voyager 2* found almost no difference at the 0.5–1 bar pressure level indicating a very dynamic circulation. The dynamics of Neptune's atmosphere were observed by *Voyager 2* to be even more vigorous, with winds approaching speeds of 400 m s⁻¹, as we shall see in Chapter 5. Subsequent observations of these planets from the ground and from Earth-orbiting telescopes have confirmed the dynamic nature of these planetary atmospheres.

3.6 REFERENCES

- Chamberlain, J. W. and D. M. Hunten (1987) *Theory of Planetary Atmospheres. An Introduction to Their Physics and Chemistry* (2nd Edition). Academic Press, San Diego, CA.
- Flowers, B. H. and E. Mendoza (1970) *Properties of Matter*. John Wiley & Sons, Chichester, UK.
- Grevesse, N. and A. J. Sauval (1998) Standard solar composition. *Space Sci. Rev.*, **85**, 161–174.
- Hubbard, W. B. (1997a) Jupiter: Interior structure. *Encyclopaedia of the Planetary Sciences*. Chapman & Hall, London.
- Hubbard, W. B. (1997b) Uranus. *Encyclopaedia of the Planetary Sciences*. Chapman & Hall, London.
- Matcheva, K. I. and D. F. Strobel (1999) Heating of Jupiter's thermosphere by dissipation of gravity waves due to molecular viscosity and heat conduction. *Icarus*, **140**, 328–340.
- Nellis, W. (2000) Metallization of fluid hydrogen at 140 GPa (1.4 Mbar): Implications for Jupiter. *Plan. Space. Sci.*, **48**, 671–677.
- Pearl, J. C. and B. J. Conrath (1991) The albedo, effective temperature, and energy balance of Neptune, as determined from Voyager data. *J. Geophys. Res.*, **96**, 18921–18930.
- Young, L. A., R. V. Yelle, R. Young, A. Seiff, and D. B. Kirk (1997) Gravity waves in Jupiter's thermosphere. *Science*, **276**, 108–111.
- Von Zahn, U., D. M. Hunten, and G. Lehmacher (1998) Helium in Jupiter's atmosphere: Results from the Galileo probe helium interferometer experiment. *J. Geophys. Res.*, **103**, 22815–22829.

3.7 BIBLIOGRAPHY

- Andrews, D. G. (2000) *An Introduction to Atmospheric Physics*. Cambridge University Press, Cambridge, UK.
- Atreya, S. K. (1986) *Atmospheres and Ionospheres of the Outer Planets and Their Satellites*. Springer, Berlin.

- Chamberlain, J. W. and D. M. Hunten (1987) *Theory of Planetary Atmospheres. An Introduction to Their Physics and Chemistry* (2nd Edition). Academic Press, London.
- Houghton, J. T. (1986) *The Physics of Atmospheres* (2nd Edition). Cambridge University Press, Cambridge, UK.
- Shirley, J. H. and R. W. Fairbridge (eds) (1997) *Encyclopaedia of the Planetary Sciences*. Chapman & Hall, London.
- Weissman, P. R., L.-A. McFadden, and T. V. Johnson (eds) (1999) *Encyclopaedia of the Solar System*. Academic Press, London.

4

Vertical structure of temperature, composition, and clouds

4.1 PRESSURE AND TEMPERATURE PROFILES

Much of what we know about the giant planets comes from observations of the conditions in the upper parts of their molecular-hydrogen/helium envelopes. Remote sounding and *in situ* observations of the vertical profiles of pressure, temperature, and composition provide constraints on vertical motion, mixing, heat sources, deep composition, and photochemistry. These observations are complemented by observations of vertical cloud structure.

4.1.1 Pressure

In planetary atmospheres, where vertical wind velocities are generally very much less than horizontal velocities, the assumption of hydrostatic equilibrium is very accurate. Thus the vertical pressure difference across a slab of air of density ρ and thickness dz subject to a gravitational acceleration g is

$$dp = -\rho g dz. \quad (4.1)$$

Assuming the air behaves as an ideal gas, the density may be determined from the temperature T and pressure p as

$$\rho = \frac{\bar{m}p}{RT} \quad (4.2)$$

where R is the molar gas constant and \bar{m} is the mean molecular weight of the atmosphere. Substituting for ρ in Equation 4.1 and integrating (assuming T is constant with height) we obtain

$$p = p_0 e^{-z/H} \quad (4.3)$$

where p_0 is the pressure where $z = 0$, and $H = RT/\bar{m}g$ is known as the *scale height*. As we saw in Chapter 2, the giant planets are significantly oblate and rapidly

Table 4.1. Mean pressure/temperature properties of the giant planet atmospheres.

Planet	Location	T (K)	c_p (J kg^{-1})	g (m s^{-2})	Γ_d (K km^{-1})	H (km)
Jupiter	Equator (1 bar)	163	10,998	23.1	2.10	25.5
	Pole (1 bar)	163	10,998	26.9	2.45	21.9
Saturn	Equator (1 bar)	135	10,658	9.1	0.85	54.5
	Pole (1 bar)	135	10,658	12.1	1.13	41.0
Uranus	Equator (1.5 bar)	87.5	8,643	8.7	1.01	32.8
	Pole (1.5 bar)	87.5	8,643	8.9	1.03	32.3
Neptune	Equator (1.5 bar)	107.5	8,187	11.0	1.34	29.1
	Pole (1.5 bar)	107.5	8,187	11.4	1.39	28.0

rotating. Thus the net gravitational acceleration (which includes the centripetal acceleration) varies significantly with latitude as does the scale height. This can be seen in Table 4.1.

4.1.2 Temperature

Lower troposphere

In the lower troposphere of the outer planets the air is heated both from the interior and, in the upper levels, from absorbed sunlight. If the infrared (IR) optical depth to space is high, then the heat may not escape radiatively, and instead the air rises convectively in order to transfer the heat upwards. This region of the atmosphere is called the troposphere (after the Greek word for ‘turning’). As the air parcels rise they expand and, assuming negligible thermal contact with neighbouring air masses, they cool adiabatically to give a temperature profile which may be calculated as follows. Consider a parcel of air moving vertically containing 1 mole of gas. If we assume that there is no net exchange of heat between the parcel and its surroundings, then the expansion may be considered to be adiabatic and reversible, and hence isentropic, i.e.,

$$dS = \left(\frac{\partial S}{\partial T} \right)_p dT + \left(\frac{\partial S}{\partial p} \right)_T dp = 0 \quad (4.4)$$

or

$$dS = C_p \frac{dT}{T} - \left(\frac{\partial V}{\partial T} \right)_p dp = 0 \quad (4.5)$$

where C_p is the molar heat capacity at constant pressure of the parcel and where the second partial derivative has been replaced using one of Maxwell’s relations (Finn, 1993). Assuming the gas is ideal, we may calculate $\partial V/\partial T$ from the ideal gas equation $pV = RT$ and derive

$$C_p \frac{dT}{T} = \frac{R}{p} dp \quad (4.6)$$

where R is again the molar gas constant. Substituting for dp from the hydrostatic equation (Equation 4.1) we find

$$C_p \frac{dT}{dz} = -\bar{m}g \quad (4.7)$$

where \bar{m} is the mean molecular weight of the atmosphere and thus

$$\frac{dT}{dz} = -\frac{\bar{m}}{C_p} g = -\frac{g}{c_p} = -\Gamma_d \quad (4.8)$$

where c_p is the *specific* heat capacity at constant pressure ($\text{J kg}^{-1} \text{K}^{-1}$), and Γ_d is called the *dry adiabatic lapse rate* (DALR).

In parts of the atmosphere where the air contains volatiles, upward motion of air parcels and cooling causes the condensation of cloud particles and the subsequent release of latent heat which causes the temperature to drop more slowly with height. For air at temperature T , where several gas components are saturated, the saturated adiabatic lapse rate (SALR) may be shown to be (Andrews, 2000; Atreya, 1986)

$$\Gamma_s = -\frac{g}{c_p} \frac{\left[1 + \frac{1}{RT} \sum L_i x_i \right]}{\left[1 + \frac{1}{\bar{m} c_p T^2} \sum \frac{L_i^2 x_i}{R} \right]} \quad (4.9)$$

where L_i is the *molar* latent heat of vaporization (or sublimation) of the i th condensing component, R is the molar gas constant, \bar{m} is the mean molecular weight of the air (excluding condensates) and x_i is the saturated volume mixing ratio (or *mole fraction*) of the i th component defined as $x_i = p_i/p$, where p is the total pressure and p_i is saturation vapour pressure of the constituent at the local temperature. In the terrestrial atmospheres, Γ_s is usually significantly less than Γ_d (e.g., for the Earth, $\Gamma_s = 6\text{--}9 \text{ K km}^{-1}$, while $\Gamma_d \sim 9.8 \text{ K km}^{-1}$). For Jupiter and Saturn, the difference is usually small since the volume mixing ratios of condensing species is small. However for Uranus and Neptune, the abundance of condensing species is much higher and thus significant differences between Γ_d and Γ_s exist at levels of major cloud formation. A major difference between giant planet atmospheres and the terrestrial atmosphere is that condensing species in the giant planet atmospheres (H_2O , NH_3 , CH_4 etc.) are all *heavier* than the bulk of the hydrogen–helium air. The opposite is true for the Earth’s atmosphere where water vapour is lighter than the bulk of the nitrogen–oxygen atmosphere. Hence ‘moist’ air is naturally buoyant in the terrestrial atmosphere and tends to rise, whereas ‘moist’ air is naturally dense in giant, planet atmospheres and tends to sink. Hence while clouds may arise in the Earths atmosphere simply due to moist, buoyant air rising to its condensation level, the formation of clouds in the giant planet atmospheres is more complicated. Another difference is that c_p , and thus Γ_d , can vary significantly with height, especially at cold temperatures where, as we will see in Section 4.1.3, the heat capacity is a strong function of the temperature and the ortho : para ratio of molecular hydrogen. This effect is difficult to observe in the warmer tropospheres of Jupiter and Saturn but is significant in the atmospheres of Uranus and Neptune. These latter planets have the

additional complication that methane, which has a significant abundance, freezes out at roughly 1 bar. This leads to significant changes in both c_p and the mean molecular weight of the atmosphere.

In addition to single condensate clouds, two-component clouds may also form in the atmospheres of the giant planets of which the most important is probably solid ammonium hydrosulphide NH_4SH which may form by the reaction



The formation of the cloud releases additional heat which affects the lapse rate and it may be shown that the equation for the SALR rate must be modified to (Atreya, 1986)

$$\Gamma_s = -\frac{g}{c_p} \frac{\left[1 + \frac{1}{RT} \left(\sum L_i x_i + \frac{2(x_{\text{NH}_3} \cdot x_{\text{H}_2\text{S}})}{(x_{\text{NH}_3} + x_{\text{H}_2\text{S}})} L_{\text{NH}_4\text{SH}} \right) \right]}{\left[1 + \frac{1}{mc_p T^2} \left(\sum \frac{L_i^2 x_i}{R} + \frac{2(x_{\text{NH}_3} \cdot x_{\text{H}_2\text{S}})}{(x_{\text{NH}_3} + x_{\text{H}_2\text{S}})} L_{\text{NH}_4\text{SH}} \cdot B_{\text{NH}_4\text{SH}} \right) \right]} \quad (4.11)$$

where x_{NH_3} is the saturated partial pressure of ammonia above solid NH_4SH particles, $x_{\text{H}_2\text{S}}$ is the saturated partial pressure of hydrogen sulphide above the same particles, the molar heat of formation $L_{\text{NH}_4\text{SH}} = 46,025.0 \text{ J mol}^{-1}$ and $B_{\text{NH}_4\text{SH}}$ is a constant of the reaction rate equation (see Section 4.3.3) whose value is $10,833.6 \text{ K}^{-1}$.

Upper troposphere and stratosphere

At higher levels in the atmosphere, the opacity of the overlying air becomes progressively smaller and thus radiation becomes more efficient than convection at transporting heat. Hence at these levels the temperature profile is determined by radiative equilibrium. Consider a very thin layer of opacity ε high in the atmosphere with negligible atmospheric opacity above it. The atmosphere below this layer effectively emits as a black body of temperature equal to the bolometric temperature T_B . Hence the heating rate of the thin layer per unit area is simply εT_B^4 . However, heat from this layer may be emitted both upwards and downwards and thus in equilibrium, assuming Kirchoff's law, we find

$$\varepsilon \sigma T_B^4 = 2\varepsilon \sigma T_S^4. \quad (4.12)$$

Thus the limiting temperature of the thin slab, known as the *stratospheric temperature* is given by

$$T_S = \frac{T_B}{2^{1/4}} \approx 0.841 T_B. \quad (4.13)$$

With more detailed analysis it can be shown that the temperature in the upper atmosphere should tend gradually to this stratospheric temperature via the Milne–Eddington equation (Atreya, 1986)

$$T_S^4 = \frac{T_B^4}{4} (2 + 3\tau) \quad (4.14)$$

where τ is the IR optical thickness between the layer and space, known as the IR *optical depth*. Calculating $T_S(\tau)$ from Equation 4.14 we find that the rate of increase of temperature with depth as we go down through the atmosphere is initially small and much less than the DALR. Hence the upper atmosphere is convectively stable since parcels displaced vertically will tend to return to their original altitudes. However since τ increases quickly with depth in the atmosphere, the radiative equilibrium vertical temperature gradient increases rapidly until, at some point, it exceeds the DALR. Such a temperature gradient is highly unstable and convection in the atmosphere quickly reduces the temperature gradient to the DALR. The boundary between the convective and radiative regions is known as the *radiative–convective boundary*.

According to Equation 4.14, the temperature in the upper atmosphere should tend to a constant value in the absence of other sources of heat. However when we look at the temperature profiles of the planets it is found that the temperatures decrease with height to roughly the stratospheric temperature at a certain level known as the *tropopause* (after the Greek words for ‘turning’ and ‘stop’) and then increase again. The region above the tropopause where temperature increases with height is very stable to convection and is known as the *stratosphere*, since the air forms stably stratified layers. The region between the tropopause and the radiative–convective boundary is known as the *upper troposphere*. This is actually a slight misnomer since the lapse rate in this region is less than the DALR and the region is thus also stable to convective overturning, although turbulent overturning is important (NB, eddy mixing, discussed in Section 4.2 is found to be at a minimum at the tropopause so this is perhaps not such a misleading word after all!). Unforced convective overturning only occurs in the atmosphere below the radiative–convective boundary, in the *lower troposphere*.

The increase of temperature with height in the stratosphere implies the presence of additional energy sources. These sources include:

- (1) absorption of ultraviolet radiation from the Sun via gaseous photodissociation reactions;
- (2) absorption of sunlight by stratospheric aerosols; and
- (3) absorption of near-IR sunlight by methane gas absorption bands.

To achieve thermal balance these sources of energy must be transported or radiated away. The stratospheres of all the giant planets appear to be close to radiative equilibrium and the cooling of the lower stratosphere appears to be due mainly to the thermal emission from ethane and acetylene molecules, with the upper stratosphere cooled by methane emission in the case of Jupiter and Saturn (Yelle *et al.*, 2001). Acetylene and ethane are photochemical products derived from the photolysis of methane and are observed in the stratospheres of all the giant planets with the exception of Uranus where only acetylene has so far been detected, although ethane is expected. Thus the temperature structure in the stratospheres of the giant planets depends critically on the vertical distribution of photochemical products in the same way that the stratospheric temperature profile of the Earth depends critically on the abundance of another photochemical product, ozone. The stratospheres of Mars and

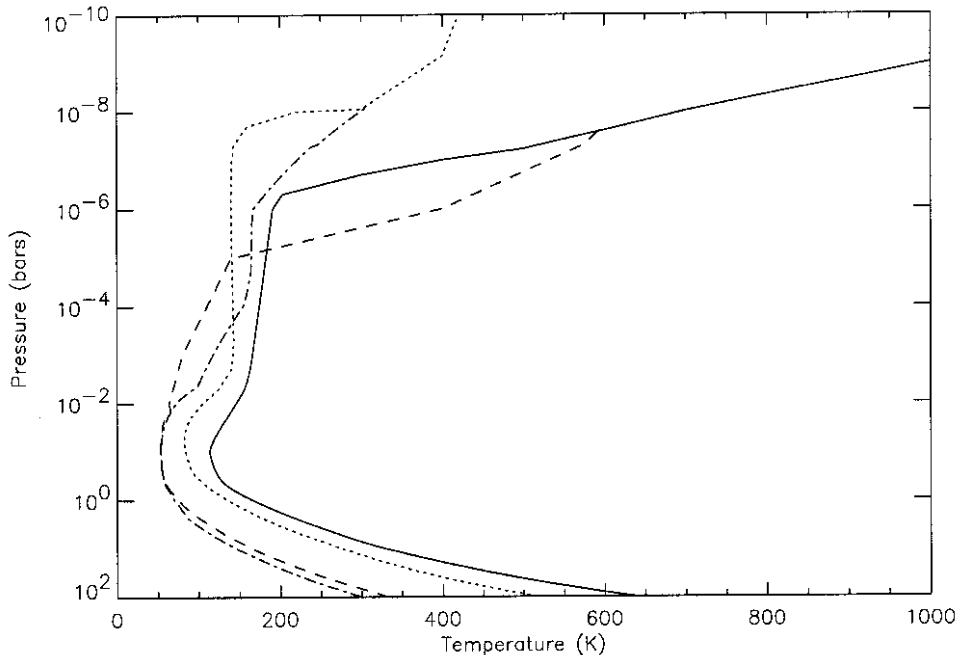


Figure 4.1 Equatorial temperature/pressure profiles of the giant planet atmospheres. Jupiter: solid line, Saturn: dotted line, Uranus: dashed line, Neptune: dot-dashed line.

Venus which do not contain significant quantities of photochemical products such as ozone do not have nearly so well a defined tropopause. Hence in a peculiar way the terrestrial stratosphere has, in this sense, more in common with the stratospheres of the giant planets than it does with the stratospheres of the other terrestrial planets (Yelle *et al.*, 2001)! From Figure 4.1 it can be seen that the stratospheric temperatures of all the giant planets are rather similar which is puzzling considering that the solar flux at Neptune is 33 times smaller than at Jupiter (Table 3.2). Chamberlain and Hunten (1987) note that this may be due to the positioning of the main ethane and acetylene absorption bands with respect to the Planck function at the stratospheric temperature. Although these gases are not very abundant in the stratosphere, their absorption bands overlap with the Planck function much better than the main ν_4 methane band at $7.7\text{ }\mu\text{m}$ and this is why the stratospheric temperatures depend so critically on their abundances. At 150 K , the Planck function peaks at $19\text{ }\mu\text{m}$, and only slightly overlaps with the main acetylene band at $13.7\text{ }\mu\text{m}$ and even less with the main ethane band at $12.2\text{ }\mu\text{m}$. If the stratosphere cools, this overlap rapidly disappears, effectively shutting off the cooling to space by ethane and acetylene. Hence the stratospheric temperatures of the giant planets would appear to be almost ‘thermostatted’ by the presence of these molecules.

At even higher altitudes, significant ionization of the atmosphere is allowed via solar extreme-ultraviolet (EUV) photons, and bombardment with charged particles

from the solar wind and cosmic rays. The breaking of gravity waves vertically propagating from the troposphere may also be important. A description of the ionospheres of the outer planets is beyond the scope of this book but are well described by Atreya (1986).

4.1.3 Secondary effects on temperature/pressure profiles

Heat capacity and ortho/para hydrogen

We saw earlier that the lapse rate in the troposphere depends on c_p and g . The gravitational acceleration g is a function of latitude on all the giant planets, while c_p is dominated by the heat capacity of both helium (which is monatomic and thus has only translational degrees of freedom leading to $C_p = 2.5R\text{ J mol}^{-1}\text{ K}^{-1}$, where $C_p = C_v + R$) and molecular hydrogen which is a diatomic molecule and thus also has rotational degrees of freedom. For Jupiter and Saturn the contribution of other molecules to the mean heat capacity in the observable atmosphere is negligible. However for Uranus and Neptune, the heat capacity of methane and water vapour are also important considerations below their respective condensation levels.

The rotation of linear molecules may be modelled by the motion of a rigid rotator. From quantum mechanics (Rae, 1985) the allowed energy levels of such a rotator are

$$E_l = \frac{\hbar^2}{2I} l(l+1) \quad (4.15)$$

where l is an integer, I is the moment of inertia, and \hbar is Planck's constant divided by 2π . Equation 4.15 may conveniently be re-expressed as $E_l = l(l+1)k_B\Phi_R$ where k_B is the Boltzmann constant, and $\Phi_R = \hbar^2/2k_B I$ is known as the *rotational temperature*. These rotational energy levels are degenerate with a degeneracy factor $g_l = (2l+1)$, and thus the rotational partition function is

$$Z_{rot} = \sum_{l=0,1,\dots} (2l+1) \exp[-l(l+1)\Phi_R/T]. \quad (4.16)$$

Assuming that the rotational energy of diatomic molecules is independent of their translational energy, the contribution to the heat capacity may be simply added to the translational heat capacity at constant volume $C_v = 3R/2$. The contribution of rotational energy to the molar internal energy U_{rot} is

$$U_{rot} = RT^2 \frac{d(\ln Z_{rot})}{dT} \quad (4.17)$$

and the contribution to the molar heat capacity at constant volume is $C_v = dU/dT$. Using this expression for the partition function we can calculate the rotational heat capacity as a function of temperature for H₂ (where $\Phi_R = 85\text{ K}$) shown in Figure 4.2 (solid line). As can be seen the rotational contribution to the molar heat capacity at constant volume tends to $R\text{ (J mol}^{-1}\text{ K}^{-1}\text{)}$ for temperatures well above the rotational temperature and tends to zero for $T \ll \Phi_R$. Although the predicted heat capacity using this formula agrees well with the measured rotational heat capacity for linear

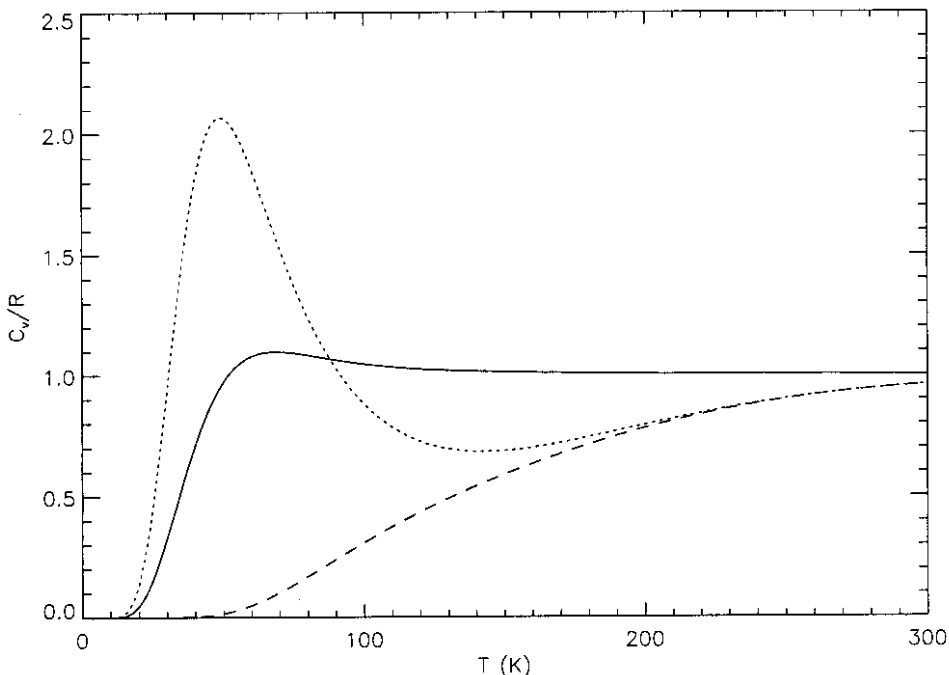


Figure 4.2 Variation of molar heat capacity at constant volume of molecular hydrogen with temperature. Solid line is the expected curve from using the expression for the partition function of Equation 4.16. The dotted line is the heat capacity calculated from the revised partition function of Equation 4.18. This is the curve measured in the presence of a catalyst. For cases where ortho:para equilibration is so slow that the ortho/para ratio may be considered to be frozen at its high-temperature 3:1 ratio, the dashed line is obtained from Equation 4.19, in good agreement with measurement.

molecules such as CO and NO (adjusting the rotation temperature appropriately), something strange is found to happen for molecular hydrogen. If hydrogen at room temperature is cooled fairly rapidly and its heat capacity measured as a function of temperature, the dashed curve of Figure 4.2 is obtained which is clearly rather different to that expected. Even more puzzling is that if this experiment is done very slowly, or in the presence of a catalyst such as activated charcoal, the dotted curve is obtained! What can be going on?

Although the theory outlined above is satisfactory for heteronuclear diatomic molecules such as CO and NO, it is not applicable for homonuclear diatomic molecules such as H₂ where the two nuclei are identical. The nuclei of the H₂ molecule are protons, which are fermions and must thus be described by antisymmetric wavefunctions. Thus the wavefunction of the molecule must change if the two protons are interchanged. The wavefunction may in fact be separated into the product of a ‘rotation part’ and a ‘spin part’. The rotation part describes the rotation of the two nuclei round each other and it is found that the states $l = 0, 2, 4, \dots$ have even exchange parity, while the $l = 1, 3, \dots$ have odd exchange

parity. Hence the even, symmetric rotation states must have odd, antisymmetric spins with total spin $S = 0$ in order for the total wavefunction to be antisymmetric, and likewise the odd, asymmetric rotational states must have even, parallel spins with total spin $S = 1$. Hydrogen molecules with spins antiparallel ($S = 0, l = 0, 2, 4, \dots$) are known as para-hydrogen, while hydrogen molecules with spins parallel ($S = 1, l = 1, 3, \dots$) are known as ortho-hydrogen. The $S = 0$ state can be shown to be a singlet state, whilst the $S = 1$ state is a triplet state.

Because there is such a fundamental difference between ortho- and para-hydrogen, a simple summing over the rotational states in Equation 4.16 is incorrect. Instead, assuming that the hydrogen is in thermal equilibrium, the partition function is given by

$$Z_{\text{rot}} = \sum_{\text{even}} (2l + 1) \exp[-l(l + 1)\Phi_R/T] + 3 \sum_{\text{odd}} (2l + 1) \exp[-l(l + 1)\Phi_R/T]. \quad (4.18)$$

The heat capacity derived from this partition function accurately fits the dotted curve of Figure 4.2 – where hydrogen is slowly cooled in the presence of a catalyst to ensure equilibrium. What can be said about the remaining curve however? It turns out that conversion between ortho- and para-hydrogen via collision processes is actually quite difficult, since to change l by ± 1 requires that the total spin is also changed which is not easy unless there is a third body, such as a surface, to take away the spin. Hence ortho- and para-hydrogen behave almost as different gases and may be treated quasi-separately. At high temperatures, the sums in Equation 4.18 are both equal and thus high temperature ($T \gg \Phi$), thermally equilibrated hydrogen has an ortho:para ratio of 3:1, or equivalently a para-H₂ fraction $f_p = 0.25$. Room temperature is ‘high’ in this case. Thus the heat capacity of hydrogen which is cooled rapidly enough such that negligible ortho:para conversion occur will have a heat capacity given by

$$C_v = 0.75C_{v,\text{ortho}} + 0.25C_{v,\text{para}} \quad (4.19)$$

where the ortho part is obtained from the rigid rotor partition function (Equation 4.16) summed only over odd l , and the para part is obtained also from Equation 4.16 by summing only over even l . In the giant planet atmospheres, air upwelling from the deep interior will have the deep ortho:para ratio of 3:1 and this ratio will slowly change as ortho para conversion proceeds at a rate governed mainly by the availability of aerosol surfaces to exchange spin angular momentum with (Massie and Hunten, 1982; Fouchet *et al.*, 2003). Hence a measurement of the f_p ratio in the giant planet atmospheres provides information on the rate of vertical upwelling and on the presence of catalytic aerosol surfaces. Observations of this fraction will be discussed later. An additional effect of so-called ‘lagged’ ortho:para conversion is that the latent heat release can act to stabilize the vertical profile of temperature and thus inhibit convection.

Molecular weight

The scale height of an atmosphere depends on temperature, gravity, and also the mean molecular weight. If no condensation occurs and the atmosphere is well mixed

then the molecular weight remains constant. However, the condensation of non-negligible constituents such as water vapour or, for Uranus and Neptune, methane, leads to significant vertical variation of the molecular weight and thus the density and scale height.

4.1.4 Temperature/pressure profiles of the outer planets

The temperature/pressure profiles observed and inferred in the upper parts of the outer planet atmospheres in the equatorial regions were shown previously in Figure 4.1. The stratospheric temperatures calculated from Equation 4.13 are 104.6, 79.9, 49.7, and 49.9 K respectively for Jupiter, Saturn, Uranus, and Neptune, and it can be seen that the observed tropopause temperatures are indeed close to these values. Below the radiative–convective boundary, the temperature profiles are observed to follow an adiabatic lapse rate, and in this figure the SALRs have been assumed. For Jupiter and Saturn it is not possible to determine the hydrogen ortho : para ratio from the measured lapse rate since the heat capacities (and hence lapse rates) of both equilibrium and frozen (3 : 1) hydrogen are indistinguishable at the observable tropospheric temperatures of these planets (Figure 4.2). However, Uranus and Neptune are much colder and so there is a big difference between the two calculated lapse rates. The atmospheric circulation of Uranus is apparently very sluggish and as we shall see in Section 4.3.1, the ortho : para ratio is found to be roughly in equilibrium. However, the observed lapse rate is more consistent with the frozen 3 : 1 ortho : para ratio. It has been suggested that the two observations may be compatible if in general the ortho : para ratio is equal to the equilibrium value at a particular level, but vertical displacements are small and rapid enough such that negligible ortho : para redistribution occurs during the motion of individual parcels and the transfer of heat. Thus

$$C_v = (1 - f_{eqm})C_{v,ortho} + f_{eqm}C_{v,para} \quad (4.20)$$

where

$$f_{eqm} = \frac{\sum_{even}(2l+1)\exp[-l(l+1)\Phi_R/T]}{\sum_{even}(2l+1)\exp[-l(l+1)\Phi_R/T] + 3\sum_{odd}(2l+1)\exp[-l(l+1)\Phi_R/T]}. \quad (4.21)$$

This ‘intermediate’ hydrogen (de Pater and Massie, 1985) has a very similar heat capacity to frozen 3 : 1 ortho : para ratio hydrogen and may thus explain why the observed lapse rate on Uranus is more consistent with frozen hydrogen than with equilibrium hydrogen.

All the planets have clearly defined upper tropospheres which start at approximately 500–600 mbar for Jupiter, 400–500 mbar for Saturn, and 1–2 bars for both Uranus and Neptune. The tropopauses occur at 100, 60, 100, and 50 mbar respectively. The stratospheric temperatures in Saturn’s atmosphere are generally lower than those found in Jupiter’s which might be expected from Saturn’s increased

distance from the Sun. However, the stratospheric temperatures of Uranus and Neptune are noticeably and puzzlingly different. Although the temperature profiles of these planets are similar in the lower troposphere, the stratospheric temperatures in the 10–0.01 mbar pressure region is of the order of 40 K warmer in Neptune’s atmosphere than in Uranus’. The difference may be due to the abundance of stratospheric hazes (see Section 4.4.4) which perhaps absorb more sunlight in Neptune’s atmosphere than in Uranus’. Some absorption of solar radiation by stratospheric aerosols in Uranus’ atmosphere does occur however, leading to the small temperature maxima observed by *Voyager 2* radio-occultation in Uranus’ atmosphere near 10 mbar.

4.2 VERTICAL MIXING–EDDY MIXING COEFFICIENTS

In Chapter 2 we outlined the bulk composition of the outer gaseous envelopes of the giant planets. These compositions refer to the ‘deep’ atmosphere although this refers to pressures only up to 10–20 bar for Jupiter and Saturn and up to approximately 100 bar for Uranus and Neptune. In the upper, observable parts of the atmosphere, the composition of certain gas species vary as a function of height due to processes such as photochemistry and condensation. As we have seen in Section 4.1.3 for ortho-/para-hydrogen the composition is also a function of the rate at which air is uplifted from the warm interior since if the upwelling is rapid enough, non-equilibrium ‘quenched’ molecules may be present. Hence the rate of vertical motion has a major effect on the vertical profiles of composition, and also cloud structure.

Air parcels may be transported vertically in atmospheres by three main mechanisms:

- (1) convection;
- (2) atmospheric waves; and
- (3) turbulence.

To understand how these processes affect the measured abundance profiles, consider the continuity equation in the vertical direction (Yung and DeMore, 1999; Atreya, 1986) for a certain gas species which has a number density n_i

$$\frac{\partial n_i}{\partial t} + \frac{\partial \phi_i}{\partial z} = P_i - L_i \quad (4.22)$$

where ϕ_i is the vertical flux of molecules, P_i is the chemical production rate and L_i is the chemical loss rate. If the mean vertical wind speed w is known at a certain location, then the vertical flux of molecules is simply $\phi_i = n_i w$. For the organized belt/zone circulation of Jupiter where zones are interpreted as regions of general upwelling and belts are regions of general subsidence, the mean vertical wind may sometimes be calculated from departures of the temperature from the radiative equilibrium temperature (Gierasch *et al.*, 1986, Conrath *et al.*, 1998). However,

even on these general flows, there are superimposed smaller convective events, such as isolated convective plumes observed in Jupiter's North Equatorial Belt, and a good deal of turbulence which tends to mix the air vertically even in regions which from dynamical models (Chapter 5) appear to be regions of general uplift and subsidence only. Hence to understand the effects of these processes on the vertical abundance profiles, we need a more general way to parameterize the vertical flux of molecules.

According to *Prandtl's mixing length theory* (Holton, 1992), a parcel of air displaced vertically will carry the mean abundances of its original level for a characteristic distance l' analogous to the mean free path in molecular diffusion. This displacement will create a turbulent fluctuation in the composition of the new level whose magnitude will depend on l' and on the vertical gradient of the mean composition. Thus, the process is very similar to molecular diffusion and may be modelled in the same way if we define an eddy-mixing coefficient K , analogous to the molecular diffusion coefficient D . Using such a model, the vertical flux of species i may be calculated as being due both to molecular and eddy diffusion via an equation very similar to Equation 3.17

$$\phi_i = n_i \left[-D_i \left(\frac{1}{n_i} \frac{\partial n_i}{\partial z} + \frac{1}{H_i} + \frac{1}{T} \frac{\partial T}{\partial z} \right) - K \left(\frac{1}{n_i} \frac{\partial n_i}{\partial z} + \frac{1}{H_a} + \frac{1}{T} \frac{\partial T}{\partial z} \right) \right] \quad (4.23)$$

where D_i is the molecular diffusion coefficient of the i th component, T is the temperature, H_i and H_a are the pressure scale heights of the i th species and bulk atmosphere respectively ($H_i = RT/m_i g$, $H_a = RT/\bar{m}g$), and K is the eddy diffusion coefficient determined via observation. When molecular diffusion dominates, each species tends to its own profile with its own scale height. When eddy diffusion dominates, the gas is well mixed and has a single bulk scale height. The level where molecular diffusion becomes dominant is called the *homopause*.

In the stratospheres of the outer planets it is thought that the principal mechanism for eddy mixing is the dissipation and break-up of vertically propagating gravity waves. The kinetic energy of non-dissipative waves should remain constant and this is by simple analysis proportional to ρv^2 where ρ is the density and v is the amplitude of the velocity. Thus the amplitude of these waves should be roughly proportional to $\rho^{-0.5}$ or equivalently $n^{-0.5}$ where n is the number density (Andrews *et al.*, 1987). Hence the amplitude of these waves grows rapidly with height and eventually becomes so high that the wave is unstable to either convective instability or shear instability. The resulting turbulence leads to the wave 'breaking' and turbulent mixing of the air. Such waves are generated in the troposphere due to convective turbulence, or for the terrestrial planets the deflection of air over surface features. Small amplitude waves clearly travel higher into the stratosphere before breaking than high amplitude waves and thus waves break at a range of altitudes in the stratosphere providing a source of eddy mixing throughout the region. Gravity waves will be discussed in more detail in Chapter 5. By mixing length theory (Holton, 1992) the eddy mixing coefficient should be proportional to the mean mixing length and thus we expect that K is proportional to the amplitude of the breaking gravity waves and thus $K \propto n^{-0.5}$. In the troposphere, convective processes dominate and

Table 4.2. Measured estimates of the eddy mixing coefficient in the giant planet atmospheres.

Planet	K ($\text{cm}^2 \text{s}^{-1}$)	Density (cm^{-3})	Pressure (bar)	Altitude (km)
Jupiter	$1.4_{-0.7}^{+0.8} \times 10^6$	1.4×10^{13}	10^{-6}	385 (homopause)
	4.6×10^2	9.3×10^{18}	0.14	40 (troposphere)
	1.5×10^4	2.4×10^{19}	0.42	20 (troposphere)
Saturn	$1.7_{-1.0}^{+4.3} \times 10^8$	1.2×10^{11}	5×10^{-9}	1140 (homopause)
	$\leq (3.5\text{--}8.7) \times 10^3$	1.1×10^{19}	0.13	80 (troposphere) (40°N , 12°N)
Uranus	$(5\text{--}10) \times 10^3$	$(2\text{--}1) \times 10^{15}$	$(4\text{--}2) \times 10^{-5}$	354–390 (homopause)
Neptune	$(3\text{--}10) \times 10^6$	$\sim 10^{13}$	2×10^{-7}	585–610 (homopause)

Adapted from Atreya *et al.* (1999).

thus it is assumed that K is either roughly a constant, or increases linearly with density. Hence the functional dependence of $K(z)$ in the atmosphere is usually parameterized as

$$K(z) = K_H \left[\frac{n_H}{n(z)} \right]^\gamma \quad P \leq P_T, \quad (4.24)$$

$$K(z) = K_T(n/n_0) \quad \text{or} \quad K(z) = K_T \quad P > P_T \quad (4.25)$$

where P_T is the pressure at the tropopause, $n(z)$ is the total number density, n_H is $n(z)$ at the homopause, K_H is the associated eddy mixing coefficient, and γ is a coefficient close to 0.5 (Atreya, 1986). Note that this formulation allows for a discontinuity in $n(z)$ at the tropopause. Typical estimated values of $K(z)$ at different levels for the outer giant planets are listed in Table 4.2.

From the previous chapter we saw that the molecular diffusion coefficient may be calculated as

$$D_i = \frac{1}{3\sqrt{2n}\sigma_i} \bar{c}_i \quad (4.26)$$

and thus D_i varies with density as n^{-1} . However since K varies typically as $n^{-0.5}$ it can be seen that although K dominates at higher pressures in the *homosphere*, it increases more slowly with height than D_i and hence at some altitude for a given species D_i becomes greater and dominates at all higher altitudes. It should be noted that the homopause level, where $D_i = K$, is actually dependent on the molecule under consideration. For the giant planets, it is presumed, unless stated otherwise, that by the word homopause we mean the *methane* homopause. The time constant for reaching diffusive equilibrium by the two processes are $\tau_D = H_a^2/D_i$ and $\tau_K = H_a^2/K$ respectively, via reasoning introduced in Section 3.2.2.

The effect of eddy mixing on vertical profiles may conveniently be explained using the example of ammonia on Jupiter and Saturn. Ammonia should condense at approximately 700 mbar for Jupiter and 1.8 bars for Saturn and above that, in the absence of eddy mixing, the partial pressure initially follows the saturated vapour pressure curve. At higher altitudes, solar ultraviolet (UV) radiation photolyses

ammonia and leads to an even greater rate of decrease of abundance with height. If the eddy mixing coefficient is high, then more ammonia would be expected at the photolysis altitudes because fresh ammonia is transported there faster than it can be photolysed. Conversely if the eddy mixing coefficient is low, then very little ammonia is expected at the photolysis altitudes since the new ammonia will be photolysed as fast as it can arrive there. Hence by measuring the ammonia mixing ratio profile, we can estimate the value of $K(z)$ in the upper troposphere. Another good indicator of the upper tropospheric eddy mixing coefficient for Jupiter and Saturn is the vertical profile of phosphine, which is also photolysed in the region of the tropopause. The profiles of ammonia and phosphine may be estimated from thermal-IR and near-IR remotely sensed measurements for Jupiter and Saturn, but not for Uranus and Neptune where the abundances are too low. At higher altitudes, methane photochemistry becomes important which produces hydrocarbons such as ethane and acetylene. Measurements of the vertical distribution of these gases may be derived from thermal-IR measurements for *all* of the giant planets and used to infer the value of $K(z)$ at these altitudes. Finally, estimates of the value of $K(z)$ at the methane homopause may be made from observations at two UV wavelengths (Atreya, 1986): Lyman- α (1216 Å), and Helium 584 Å. The Jovian planets are relatively bright at Lyman- α wavelengths primarily through the resonance scattering of incident sunlight by hydrogen atoms. Methane is a strong UV absorber and hence only those hydrogen atoms that are above the methane homopause level may contribute to this radiation. Hence for atmospheres with large eddy diffusion coefficients (high homopause), fewer hydrogen atoms may contribute to the resonance scattering, thus the measured intensity is less. Similarly helium atoms in the Jovian planets resonantly scatter photons at 584 Å. However in this case, as $K(z)$ increases, the measured intensity increases (rather than decreases as it does for Lyman- α) since the abundance of helium at the top of the homosphere is greater. However to interpret the He 584 Å observations, independent measurements of the temperature in the scattering region are also required which are difficult to estimate.

A combination of many of these measurements has been used to estimate the variation of $K(z)$ with pressure for all of the giant planets which are shown in Figure 4.3 (Fouchet *et al.*, 2003) where the estimates from Table 4.2 (Atreya *et al.*, 1999) are also shown as cross symbols. Also plotted as dotted lines are the profiles of molecular diffusion coefficients for methane calculated from the semi-empirical formula (Moses *et al.*, 2000)

$$D_{CH_4} = \frac{2.3 \times 10^{17} T^{0.765}}{n} \quad (4.27)$$

where the temperature profiles shown in earlier Figure 4.1 have been used. The greater rate of increase with height of D than K is clearly seen, and the level where the curves meet is the methane homopause. It can be seen that the methane homopause occurs at a pressure of approximately 10^{-8} bar for both Jupiter and Saturn, indicating active vertical eddy mixing. Turbulence in Neptune's stratosphere is less active with the methane homopause at 10^{-6} bar. The vertical mixing in

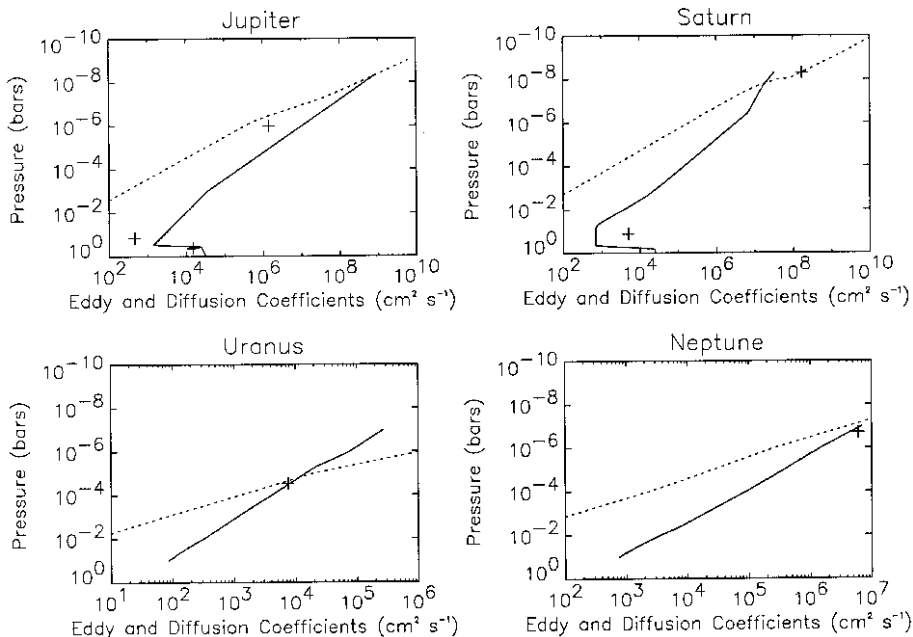


Figure 4.3 Variation of eddy mixing and molecular diffusion coefficients with height in the giant planet atmospheres. Solid lines are eddy diffusion coefficient profiles (from Fouchet *et al.*, 2003). Dotted lines are the molecular diffusion coefficients of methane calculated from Equation 4.27. Cross symbols are estimates of eddy diffusion coefficients from Table 4.2.

Uranus' atmosphere can be seen to be particularly sluggish with the homopause at $\sim 10^{-5}$ bar.

4.3 COMPOSITION PROFILES – GENERAL CONSIDERATIONS

Now that we have discussed the vertical structure of planetary atmospheres in terms of temperature, pressure, and vertical mixing, we are in a position to discuss and interpret the vertical composition profiles of the outer planets.

4.3.1 Disequilibrium species

The most stable equilibrium chemical form that different elements exist in depends upon the temperature, and on the abundance of other molecules and atoms with which reactions can occur. Similarly, the equilibrium ortho : para ratio of hydrogen is a function of temperature. The rate at which equilibrium is reached depends upon the temperature, density, and sometimes the presence of catalysing aerosols. Hence in rapidly overturning atmospheres, the composition of air which has been rapidly uplifted from warmer, denser levels may be partially ‘quenched’ at its deeper

equilibrium composition. Measurement of the abundances of so-called ‘disequilibrium’ species thus provides information on the upwelling rates, and hence on the vertical circulation, and is a very important diagnostic tool in understanding the circulation of the giant planet atmospheres.

Nitrogen and carbon

The molecular forms of carbon and nitrogen are good examples of disequilibrium species in giant planet atmospheres. The chemical form of nitrogen and carbon that is observed depends upon the following equilibrium reactions:



Above about 1,000 K, the right-hand side of these reactions dominates, whereas at lower temperatures the left-hand side dominates. Hence in the observable, cool parts of the giant planet atmospheres we do not expect to see much CO or N₂ unless vertical transport is particularly vigorous. This conclusion seems to be true for all of the giant planets with the notable exception of Neptune where there is evidence that small quantities of both molecules are present in the observable atmosphere suggesting rapid upwelling which is consistent with Neptune’s observed high internal heat source.

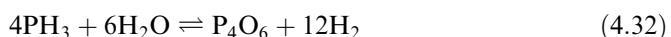
Carbon dioxide may also appear in disequilibrium in the upper atmosphere through the reaction



although carbon dioxide has not been detected in the tropospheres of any of the giant planets.

Germane, arsine, and phosphine

The abundances of phosphine, arsine, and germane in the atmospheres of Jupiter and Saturn are higher than would be expected if the atmospheres were in chemical equilibrium. These gases are assumed to be produced by equilibrium chemistry at P ~ 1 kbar and T ~ 1,000 K and to slowly convert at the cold temperatures found in the upper parts of these atmospheres to the chemical forms given below, with a timescale of the order of 100 days (the chemistry here is highly complicated and there are lots of intermediate steps. The reader is referred to Atreya (1986) for more details).



Measurements of the vertical profiles of these species provide constraints in the eddy mixing coefficient as mentioned earlier. Mapping the spatial abundance of these materials provides information on the general upwelling/downwelling motions.

Ortho-/para-hydrogen

We have seen already that molecular hydrogen may exist in two distinct ortho- and para-states. At high temperatures (T greater than roughly 300 K) the para-H₂ fraction f_p is 0.25, and this equilibrium value increases as the temperature decreases as may be determined from Equation 4.21. The ortho : para ratio as a function of height may be measured from far-IR collision-induced and quadrupole absorptions (the nature of dipole and quadrupole absorption lines are discussed in Chapter 6), and also from visible hydrogen quadrupole absorption lines in the atmosphere of the giant planets. Any departure of the measured para-H₂ fraction from the equilibrium value calculated from Equation 4.21 using the local temperature provides information on the vigorousness of vertical convection with more convectively active atmospheres having f_p closer to the deep value of 0.25 than to the equilibrium value. However, the conversion of ortho- to para-hydrogen is catalysed by the presence of aerosols as mentioned in Section 4.1.3 and thus knowledge of the aerosol distribution is essential to understanding the f_p profile. The average ortho/para fraction in the upper tropospheres of the giant planets has been estimated from *Voyager IRIS* far-IR data by Conrath *et al.* (1998). We will see in Chapter 5 that the latitudinal variation of f_p and T provides diagnostic information on the convection and vertical transport in the giant planet atmospheres at these pressure levels.

More recently the para-H₂ fraction has been estimated in the lower stratospheres at the 1 and 10 mbar levels by Fouchet *et al.* (2003) from Infrared Space Observatory Short Wavelength Spectrometer (ISO/SWS) observations of the far-IR hydrogen quadrupole lines. For Jupiter, the stratospheric f_p is found to be similar to the tropopause value and does not vary between the two pressure levels. Fouchet *et al.* (2003) propose that ortho/para conversion is mainly accomplished through the catalytic effects of aerosols, and thus since the Jovian stratosphere is relatively clear, the stratospheric f_p value is frozen at its tropopause value. For Saturn they find that while f_p has the same value at both 1 and 10 mbar levels, this value is higher than the tropopause value, but lower than the equilibrium value. They propose that some catalysis has occurred on lower stratospheric equatorial haze which is observed to be confined below 10 mbars. For Uranus, the f_p value is found to be close to equilibrium value at both altitudes and thus decreases with height as the temperature increases. Uranus is estimated to have a high abundance of very small aerosols at these altitudes (Pollack *et al.*, 1987) which would appear to efficiently catalyse the conversion. The eddy mixing coefficient is also very small and thus the air is relatively stagnant. For Neptune, f_p is also found to decrease with height in the stratosphere, but is significantly greater than the local equilibrium para-H₂ fractions. Although the optical depth of Neptune's stratospheric hazes is estimated to be greater than those of Uranus, the particle sizes are estimated to be rather larger (Pryor *et al.*, 1992) and thus the number density of aerosols is less, leading to presumably less efficient catalysis. In addition the eddy mixing coefficient in Neptune's atmosphere is 10 times greater than in Uranus' atmosphere leading to rapid vertical transport of high- f_p air from the tropopause.

4.3.2 Photolysis

Photodissociation of molecules by solar UV radiation is an extremely important driver on the composition profiles measured in the upper parts of the giant planet atmospheres. It is beyond the scope of this book to provide a detailed exposition on the finer points of this topic and the reader is referred to books such as Atreya (1986) for a more complete discussions. Here we shall limit ourselves to the main photochemical reactions governing the upper atmospheric composition profiles of important giant planets gases. However before we can discuss photodissociation, we must briefly introduce Rayleigh scattering, and how it affects the flux of UV photons reaching the upper atmospheres of the giant planets.

Rayleigh scattering

Photolysis of different molecules requires UV photons of different frequencies. For example photolysis of methane requires photons with wavelengths less than 160 nm, whereas photolysis of ammonia, phosphine, and hydrazine requires photons in the wavelength range 160–230 nm. Solar photons with wavelengths less than 160 nm are dominated by Lyman- α emission at 121.6 nm. However the penetration of UV photons into planetary atmospheres is regulated by the Rayleigh scattering of the air molecules, which is strongly wavelength dependent. In general, the Rayleigh scattering cross-sectional area per dipole is given by (Goody and Yung, 1989)

$$\sigma_R = \frac{8\pi}{3} \left(\frac{2\pi}{\lambda} \right)^4 |\alpha|^2 \quad (4.34)$$

where α is the polarizability which relates the electric dipole induced on a molecule or atom by the local electric field strength $\mathbf{p} = \alpha \mathbf{E}_{\text{Local}}$, and λ is the wavelength. It can immediately be seen that shorter wavelength photons are much more efficiently scattered than longer wavelength photons and indeed this is why the Earth's sky is blue! For atoms and molecules where the polarizability is independent of the molecule's orientation with respect to the incident electric field, the polarizability is related to the refractive index m via the equation

$$\alpha = \frac{m - 1}{2\pi N} \quad (4.35)$$

where N is the number of molecules per unit volume. Hence substituting into Equation 4.34 we find

$$\sigma_R = \frac{32\pi}{3\lambda^4} \frac{(m - 1)^2}{N^2}. \quad (4.36)$$

For all but spherical top molecules (Chapter 6), the polarizability is not actually independent of the molecule's orientation with respect to the incident electric field and thus Equation 4.36 must be modified to

$$\sigma_R = \frac{32\pi}{3\lambda^4} \frac{(m - 1)^2}{N^2} f_{\text{anisotropic}} \quad (4.37)$$

Table 4.3. Refractive index parameters and depolarization factors for giant planet gases.

Molecule	A	B (m ²)	Δ
He	3.48×10^{-5}	2.3×10^{-15}	0
H ₂	13.58×10^{-5}	7.52×10^{-15}	0.02
CH ₄	42.7×10^{-5}	10.0×10^{-5}	0.02
N ₂	29.06×10^{-5}	7.7×10^{-5}	0.03

Data from Allen (1976).

where $f_{\text{anisotropic}}$ is a parameter describing the non-isotropy of the atom or molecule (Goody and Yung, 1989). Assuming that a number of atoms/molecules are randomly orientated with respect to the incident electric field, the correction factor $f_{\text{anisotropic}}$ may be shown to be equal to

$$f_{\text{anisotropic}} = \frac{3(2 + \Delta)}{(6 - 7\Delta)} \quad (4.38)$$

where Δ is known as the depolarization factor which may be measured in the laboratory and which is listed in Table 4.3 for relevant Jovian gases. The refractive indices of hydrogen, helium, and methane at standard temperature and pressure (STP) may be calculated from the semi-empirical formula

$$m - 1 = A(1 + B/\lambda^2). \quad (4.39)$$

Values of the coefficients A and B are also listed in Table 4.3. Since m is close to 1.0 and since from the Clausius–Mossotti relation (Hecht, 1998) we expect $m^2 - 1$ to vary linearly with N , we may use m evaluated at STP in Equation 4.37 provided N is also calculated at STP. In practice for the giant planet atmospheres where the composition is dominated by near-solar hydrogen–helium, it is found that Equation 4.37 may be reasonably accurately approximated by (Atreya, 1986)

$$\sigma_R = \frac{7.5 \times 10^{-17}}{\lambda^4} \quad (4.40)$$

where the wavelength λ is assumed to be expressed as Å, and where the calculated cross section is in units of m². The pressure level of unit optical depths at different UV wavelengths for the giant planets is listed in Table 4.4 where it can be seen that longer UV wavelengths travel to much deeper levels than shorter wavelengths.

Photodissociation of important giant planet gases

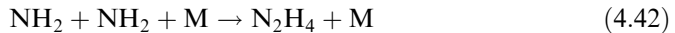
Now that we have seen how Rayleigh scattering affects the incident fluxes of UV photons we will discuss the photodissociation of the three most important photo-active gases in the upper tropospheres and stratospheres of the giant planets, namely: ammonia, phosphine, and methane.

Table 4.4. Pressure level of unit optical depth for Rayleigh scattering in the giant planet atmospheres.

Planet	1000 Å	2000 Å	3000 Å
Jupiter	10 mbar	200 mbar	1000 bar
Saturn	6 mbar	80 mbar	400 mbar
Uranus	5 mbar	70 mbar	300 mbar
Neptune	6 mbar	90 mbar	400 mbar

Ammonia

If ammonia is transported to sufficiently high altitudes in an atmosphere (where pressures are of the order of 100 mbar) then it may be photodissociated to form hydrazine (N_2H_4) via the reactions:



where M is any other molecule. Hence we expect the abundance of ammonia to decrease above the 100 mbar level. In fact, the ammonia decreases at lower altitudes also, due to vertical eddy mixing, and as we saw in Section 4.2, the rate of decrease with height is thus determined by the strength of sunlight and the degree of eddy mixing.

Hydrazine itself may also be photolysed into other products and the photo-absorption cross sections of ammonia, hydrazine, and phosphine are shown in Figure 4.4. Hydrazine should condense at the temperatures found in Jupiter and Saturn's upper troposphere and the resultant ice particles may thus be a constituent of the hazes found in the upper tropospheres of these planets.

Phosphine

Photolysis of phosphine may lead to the formation of diphosphine P_2H_4 via the reactions:



The main pressure level of photolysis is again around 100 mbar and thus the abundance of phosphine is expected to decrease throughout the upper troposphere and lower stratosphere of Jupiter and Saturn with a scale height governed by the vertical eddy mixing coefficient and the solar insolation. Phosphine has not been observed in the atmospheres of Uranus and Neptune due, most likely, to their low IR brightnesses at wavelengths where phosphine has strong absorption features rather than an absence of the molecule itself.

If temperatures are low enough for the diphosphine to condense, then this may provide an extra source of haze materials in the upper troposphere of Jupiter and

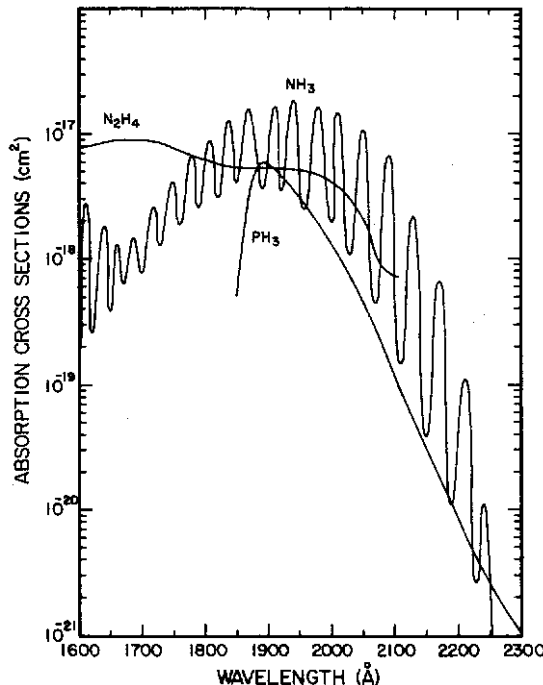


Figure 4.4 UV cross sections of different gases relevant to giant planet atmospheres.

From Atreya (1986).

Saturn. However, if the diphosphine does not condense then further reactions are possible which, provided that the levels of scavenging molecules such as acetylene (C_2H_2) and ethylene (C_2H_4) are not too high, give rise to the production of the solid phosphorus allotrope $P_4(s)$. The $P_4(s)$ allotrope is bright red and it has been suggested that this product might be able to explain the red coloration of Jupiter's Great Red Spot (GRS). However this identification is highly speculative and unproven.

Unfortunately, insufficient thermodynamic data exists for diphosphine to predict whether or not it does actually condense in the upper tropospheres of Jupiter and Saturn.

Methane

Methane photochemistry is highly complicated with a number of possible branch reactions shown in Figure 4.5.

From Table 4.4, we can see that the UV photons (mainly Lyman- α at 121.6 nm) capable of initiating methane photolysis subject to Rayleigh scattering alone may penetrate to pressures of only 10 mbar in the atmospheres of all the giant planets. However, the photoabsorption cross section of methane is very high and thus the

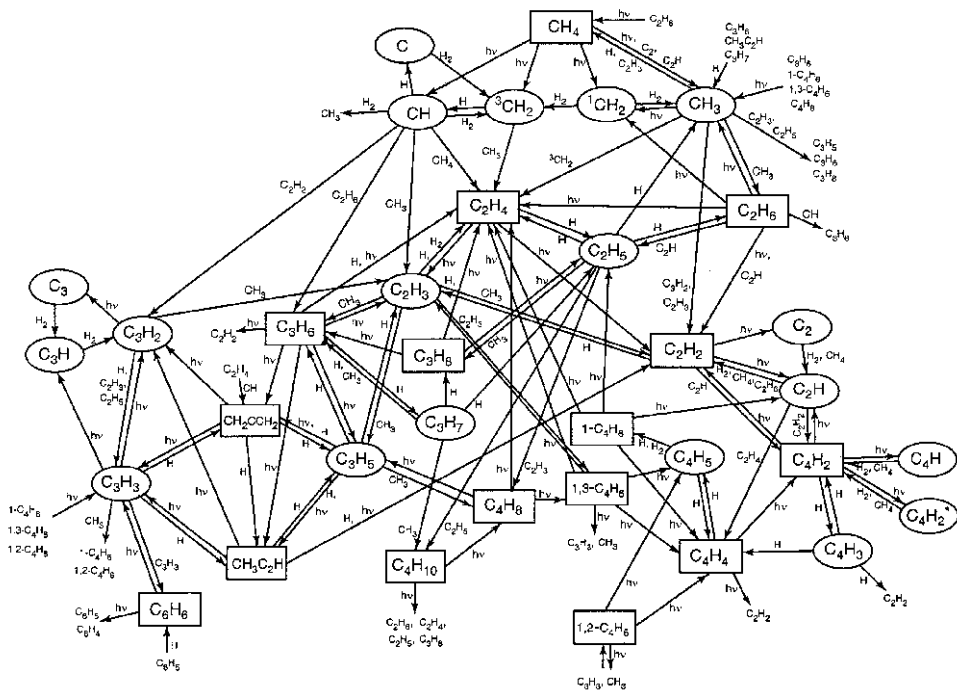


Figure 4.5 Methane photochemistry paths.

From Moses *et al.* (2000). Reprinted with kind permission of Elsevier.

peak level of methane photodissociation is actually at even higher levels (depending on the methane abundance) and for Jupiter extends between 0.1 μ bar and 0.1 mbar. While this is the main region of methane photodissociation, to combine the resulting products into hydrocarbons requires a number of two-body and three-body reactions which are only efficient at higher pressures (0.1 mbar and higher). The main resultant products of methane photodissociation are acetylene (C_2H_2), ethane (C_2H_6), and polyacetylenes ($C_{2n}H_2$). The intermediate molecule ethylene (C_2H_4) is more unstable but has been detected in the atmosphere of Jupiter. Further reactions are possible leading to more complicated molecules such as methyl-acetylene (CH_3C_2H) and benzene (C_6H_6) which have been detected in some of the giant planet atmospheres. The intermediate product CH_3 has now also been detected in all the giant planet atmospheres except Uranus.

Haze particles similar to terrestrial ‘smog’ are probably produced at these altitudes by further complex chemical reactions that produce long-chain polymers that ultimately form aerosol particles. Both the hydrocarbons and the hazes spread vertically to other pressure levels through eddy mixing. At deeper pressures, the haze particles may also start to coagulate and settle gravitationally through the atmosphere. Eventually the photochemical products will reach the deep warm atmosphere where they are pyrolysed back into methane again.

4.3.3 Condensation

As material is transported upwards through the troposphere, temperatures drop and for some gases the partial pressure becomes equal to the saturated vapour pressure. Assuming the presence of cloud condensation nuclei, which appear abundant in the giant planet atmospheres, cloud layers may form and the gaseous abundance of the condensing molecules above the condensation level is determined by the saturated vapour pressure. For simple liquid–vapour and solid–vapour transitions, the condensation levels of clouds may be easily estimated from simple thermodynamics.

The *Clausius–Clapeyron* equation which governs how pressure p and temperature T vary along a 1st order phase transition is given by (Finn, 1993)

$$\frac{dp}{dT} = \frac{\Delta S}{\Delta V} \quad (4.45)$$

where ΔS is the change in entropy of a certain quantity of material changing phase, and ΔV is the associated change in volume. For the liquid–vapour and solid–vapour phase boundaries, where the volume of the gas phases greatly exceeds that of the liquid or solid phases, ΔV is approximately the volume of the gas phase alone and thus Equation 4.45 is well approximated by

$$\frac{dp}{dT} = \frac{Lp}{RT^2} \quad (4.46)$$

where the ideal gas equation has been assumed and where L is the latent heat of vaporization *per mole* and R is the molar gas constant. If L is assumed to be constant with temperature then this equation may be simply integrated to give

$$\ln p = A - \frac{L}{RT} = A - \frac{B}{T} \quad (4.47)$$

where A and B are constants which may be fitted to the measured saturated vapour pressure curves. More generally, the latent heat L varies with temperature which also introduces extra terms into Equation 4.47. However, these are secondary effects and for the case of giant planet atmospheres where many constituents may condense and whose phase boundaries have not been measured with very great precision, they are usually neglected. The fitted coefficients A and B for a number of 1st order phase transitions relevant to the giant planet atmospheres are listed in Table 4.5.

In addition to the simple condensation of vapour into liquid or solid aerosols, more complex two-component reactions may occur such as the formation of solid ammonium hydrosulphide (Equation 4.10). The thermodynamics of this are more complicated, but the variation of the vapour pressure of both reactants with temperature may be adequately approximated by a similar equilibrium constant equation to Equation 4.47

$$\ln(p_{\text{NH}_3}) + \ln(p_{\text{H}_2\text{S}}) = 34.15 - \frac{10,833.6}{T} \quad (4.48)$$

where p_{NH_3} and $p_{\text{H}_2\text{S}}$ are the partial pressures (in bars) of NH_3 and H_2S respectively. Clearly to solve this equation we need additional information which comes from the

Table 4.5. Coefficients A and B for various sublimation and vaporization curves relevant to giant planet atmospheres.

Gas	A_{ice}	B_{ice}	T_{triple}	A_{liq}	B_{liq}
NH ₃	17.347	3930.6	195.45	11.901	2850.4
H ₂ O	17.477	6164.65	273.16	14.149	5257.2
H ₂ S	12.884	2702.4	187.65	11.347	2411.4
CH ₄	10.682	1163.8	90.65	9.382	1045.5
C ₂ H ₂	14.636	2757.7	191.65	—	—
C ₂ H ₆	—	—	90.0	10.685	1959.6
C ₂ H ₄	—	—	104.14	10.831	1822.4
C ₄ H ₂	16.284	4366.7	238.25	11.137	3144.6
CH ₃ C ₂ H	—	—	170.45	11.884	2803.6
PH ₃	10.057	18.65.9	140.65	—	—

NB, the form of C₃H₄ found in the atmospheres of the giant planets is as above, CH₃C₂H, known as methyl acetylene (or alternatively propyne). The alternative isomer of C₃H₄, called allene (or alternatively propadiene) is not found.

fact that we know that one molecule of NH₃ reacts with one molecule of H₂S to form NH₄SH. Hence if by substituting the uncondensed values of p_{NH_3} and p_{H_2S} into Equation 4.48 we find that the left-hand side exceeds the right-hand side and we solve for the amount Δ by which we need to reduce both p_{NH_3} and p_{H_2S} , i.e.,

$$\ln(p_{NH_3} - \Delta) + \ln(p_{H_2S} - \Delta) = 34.15 - \frac{10,833.6}{T}. \quad (4.49)$$

To a first-order approximation the general shape of the abundance profile of a condensable species may be determined by considering a parcel of deep air which is lifted right up through the atmosphere without mixing with surrounding air. At first the mixing ratio remains fixed at its deep level but at a certain level it becomes equal to the saturated volume mixing ratio (v.m.r.) and thus the gas starts to condense. Moving the parcel to higher altitudes – and thus lower temperatures – more and more of the gas condenses to form aerosols and thus the mixing ratio profile follows the saturated v.m.r. curve. At the tropopause, the temperature stops decreasing with height and instead starts to rise again. However if we assume that cloud particles condensed at lower altitudes are not carried with the parcel but instead fall through the atmosphere, then the v.m.r. can not rise again above the tropopause by re-evaporation of the aerosols but instead remains fixed at the tropopause value. Hence the tropopause acts as a ‘cold trap’ to molecules that condense in the troposphere and limits the stratospheric abundances. The altitude where the deep fixed v.m.r. meets the saturated v.m.r. curve determines the base level of the condensed cloud. Clearly if the deep v.m.r. is higher then the cloud base pressure is higher and vice versa.

In reality, mixing of the rising air parcels with descending dry air, both vertically and horizontally, means that the v.m.r. profile derived from spatially averaged remotely sensed data is usually substantially subsaturated even in areas of

localised rapid convection. Hence while this model is useful for estimating the approximate level of the cloud bases, and thus where the volatile species starts to condense, it does not model well the rate of decrease of gas abundance with height. In addition the technique gives no indication on the vertical extent or optical thickness of the cloud. These depend on two things: (1) the rate of uplift, or vertical mixing; and (2) the rate of formation of cloud aerosols and their size which governs how quickly they fall back down through the atmosphere towards warmer regions where they may again evaporate. Thus accurately estimating the vertical distribution of the cloud particle density (sometimes expressed in terms of a *cloud scale height* analogous to the pressure scale height mentioned earlier) and the cloud particle size distribution, both vital parameters to know if remote sensing observations are to be used to interpret cloud structure, is an extremely difficult microphysical problem.

As air is uplifted from the deep atmosphere, in addition to the observable clouds of material such as water and ammonia, a number of rather exotic layers may form at deeper pressures. For example, in Jupiter's atmosphere, clouds of magnesium silicates are predicted to condense near 2,000 K, and clouds of silver and gold are predicted to condense in thin layers near 1,000 K!

4.3.4 Extraplanetary sources

The ISO mission discovered the presence of gaseous H₂O in the stratospheres of all four giant planets (Feuchtgruber *et al.*, 1997). Since the tropopause of these planets are very cold, there is effectively a ‘cold trap’ which, in the absence of any other sources, should keep the stratospheric water abundance very low, as discussed in the last section. The fact that significant levels of water exist at these levels, and in addition oxygenated species such as CO₂, suggests that there is an external source of oxygen. The source of this stratospheric H₂O and CO₂ was initially thought to be due to the arrival of interplanetary icy micrometeoroids, and a flux of approximately 10⁶ molecule cm⁻² s⁻¹ was modelled to be required for all four giant planets. Species such as CO and CO₂ may be contributed to directly from these micrometeoroids or through subsequent reactions between water vapour and stratospheric hydrocarbons. Note that the presence of CO does not on its own suggest external sources, since rapid convection from the interior may inject this disequilibrium species into the stratosphere. The presence of stratospheric CO₂ however, does imply the stratospheric water vapour.

Although an approximately similar flux rate of Interplanetary Dust (IPD) was required for all four giant planets, Feuchtgruber *et al.* (1997) noted that Jupiter and Saturn actually required a flux approximately 10 times greater than Uranus and Neptune. It was initially suggested that this might be due to variations in the IPD density as a function of distance from the Sun. However it is now thought that the differences are due to additional sources of water. For Saturn, the extra source would appear to be the erosion of ring material which becomes ionized and then spirals into the atmosphere along connecting magnetic field lines causing increased abundances of water at mid-latitudes (Prangé *et al.*, 1998). For Jupiter, the extra source of water,

and CO₂, would appear to have been the collision of Comet Shoemaker–Levy 9 (SL9) with Jupiter in 1994, which injected large abundances of oxygen-rich molecules into the stratosphere (Lellouch *et al.*, 2002). While the latitude dependence of Jovian stratospheric water remains unclear, the abundance of stratospheric CO₂ is observed to decrease by a factor of 7 from the southern mid-latitudes, where SL9 struck, to northern mid-latitudes. Whether the latitudinal variation of stratospheric water is similar will require further observations.

4.4 COMPOSITION AND CLOUD PROFILES OF THE GIANT PLANETS

Now that we have described the various processes affecting the vertical composition and cloud profiles of the giant planet atmospheres, we will now review the most recent measurements of these profiles from remote and *in situ* observations.

4.4.1 Jupiter

Composition profiles

The bulk composition of Jupiter (Figure 4.6) was discussed in Chapter 2. Of all the giant planets it is the one that most closely approximates to a protosolar composition, but even here the abundance of heavy elements such as carbon, sulphur, and nitrogen is found to be roughly three times greater than would be expected in a purely solar composition atmosphere. This is consistent with the core accretion theory that Jupiter initially formed from icy planetesimals which then formed an embryo big enough to gravitationally attract the surrounding nebula gas.

When we talk about the ‘deep’ compositions, which are listed in Tables 2.2a and 2.2b, it is worth clarifying how ‘deep’ we really mean. Jupiter is the only giant planet from which *in situ* measurements of the atmospheric composition have been made by the *Galileo* entry probe in 1995. These measurements extend down to pressures of approximately 20 bar. While this is very high compared to remotely sensed IR and microwave observations which extend down to 10 bar at most, it is still only scraping the surface of the enormous Jovian atmosphere. Hence all we can really measure is the composition of the top of the molecular-hydrogen region. Any composition gradients that may occur in radiative zones, or at the metallic-/molecular-hydrogen phase boundary are very difficult to detect and may only be inferred from interior models matching the observed oblateness, rotation rate, and gravitational *J*-coefficients.

Figure 4.7 shows the results of a calculation using an equilibrium cloud condensation model (ECCM) of Jupiter. In these models (Lewis, 1995; Atreya, 1986), a parcel of air is raised upwards and if the partial pressure of a gas exceeds the saturated vapour pressure (s.v.p.), the excess is assumed to condense as cloud droplets and be lost from the parcel. Here the temperature profile observed in the upper troposphere has been extended downwards towards the interior along the

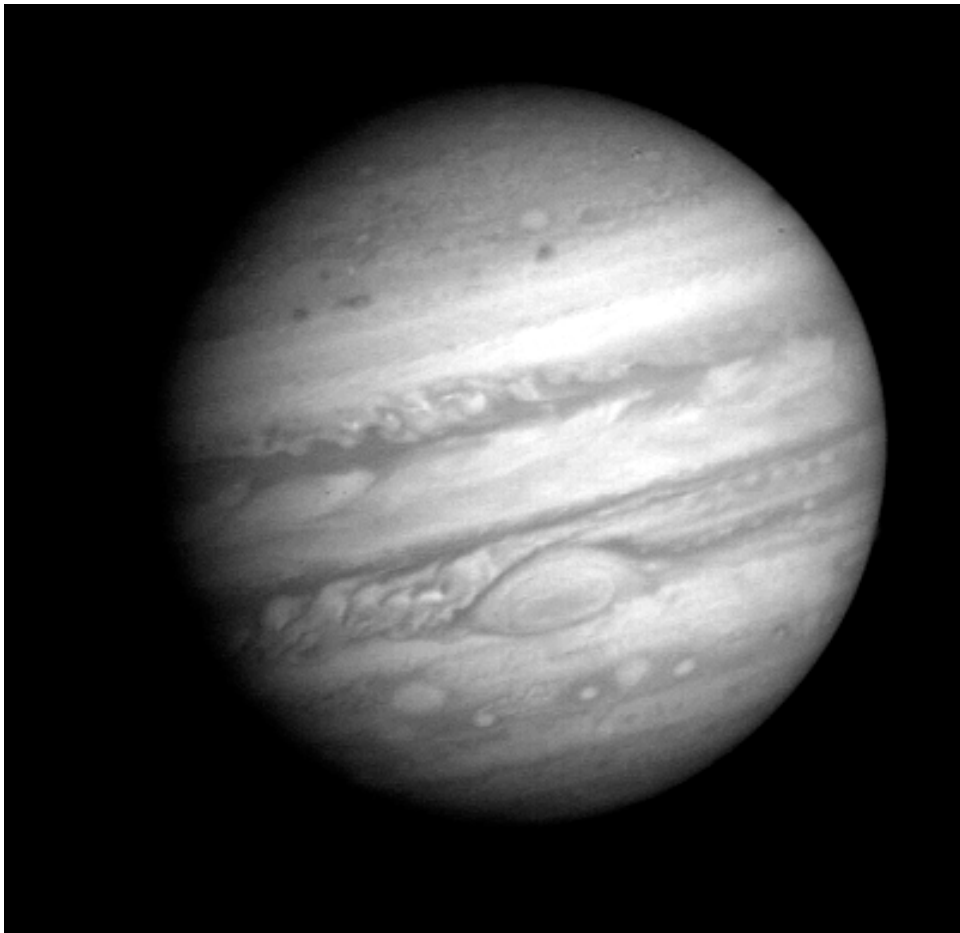


Figure 4.6 *Voyager 1* image of Jupiter. The Great Red Spot (GRS) is clearly visible near the centre of the image.

Courtesy of NASA.

SALR consistent with the condensation of water, NH_4SH , and NH_3 clouds at the different levels shown in the figure. The temperature profile that is calculated assuming a DALR is shown as the dotted line for comparison. The deep abundances of O, N, and S (relative to H) are assumed to be $3\times$ the solar value, and C/H is set at $3.17\times$ the solar value. The lapse rates calculated at different altitudes in the troposphere are also shown in Figure 4.7. The DALR can be seen to increase with height, due almost entirely to the decrease of the molecular hydrogen heat capacity with height as the temperature falls. The slight reduction in gravitational acceleration with height tends to decrease the lapse rate but this effect is small. When condensation is included, the SALR can be seen to be significantly smaller than the DALR

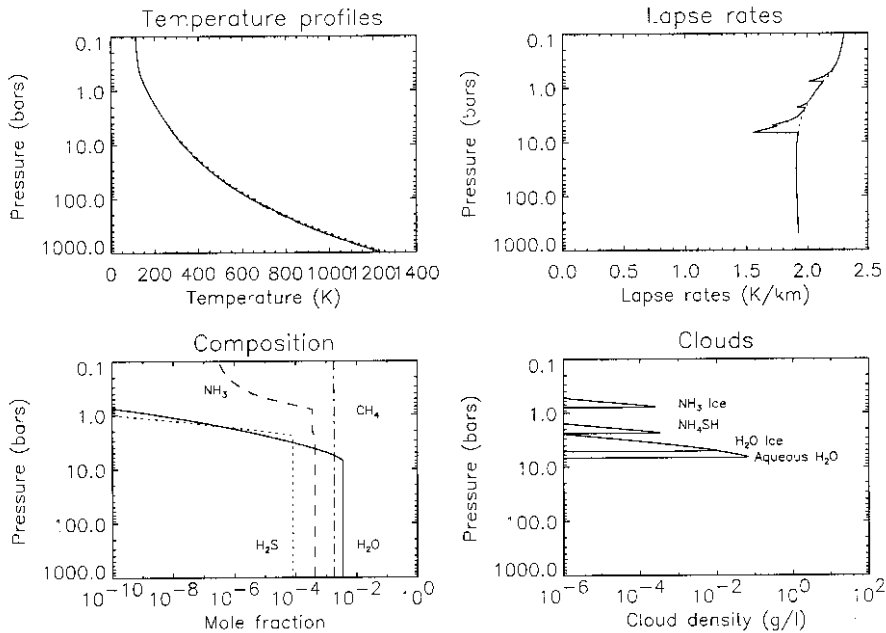


Figure 4.7 Equilibrium cloud condensation model of Jupiter's atmosphere. (1) Top left. Temperature profile follows SALR below radiative-convective boundary. Dotted line follows DALR below 1 bar level. (2) Top right. Variation of calculated lapse rates with height. Dotted line is DALR, solid line is SALR. (3) Bottom left. Composition profiles: H₂O (solid), H₂S (dotted), NH₃ (dashed), CH₄ (dot-dashed). (4) Bottom right. Cloud densities: H₂O cloud (water, then ice) at ~7 bar, NH₄SH at ~2 bar, and NH₃ ice at ~0.7 bar. Assumed composition: O/H, N/H, S/H = 3× the solar value C/H = 3.17× the solar value.

near the bases of the main clouds due to the release of latent heat, although the resultant differences in the calculated dry and saturated temperature profiles can be seen to be small since the main condensates have small initial abundances. The abundance profiles of NH₃, H₂S, H₂O, and CH₄ are calculated by limiting the partial pressures to the s.v.p. when condensation occurs. Associated cloud densities are also shown in the diagram. We will discuss the calculated cloud profiles in the next section.

While such ECCM models are useful for estimating the basic tropospheric abundance profiles of condensing molecules, observations of the composition profiles are rather different as can be seen in Figure 4.8 where the composition profiles of other species are also shown. Sources of estimated Jovian composition data and references are listed in Table 4.6. In particular, analysis of the 5-μm part of the IR spectrum measured by *Voyager*, and more recently *Galileo*, has found water to be significantly less abundant than expected. This is probably due to this spectral region being most sensitive to cloud-free areas which appear to be volatile depleted regions either due to subsidence or column-stretching as we shall see

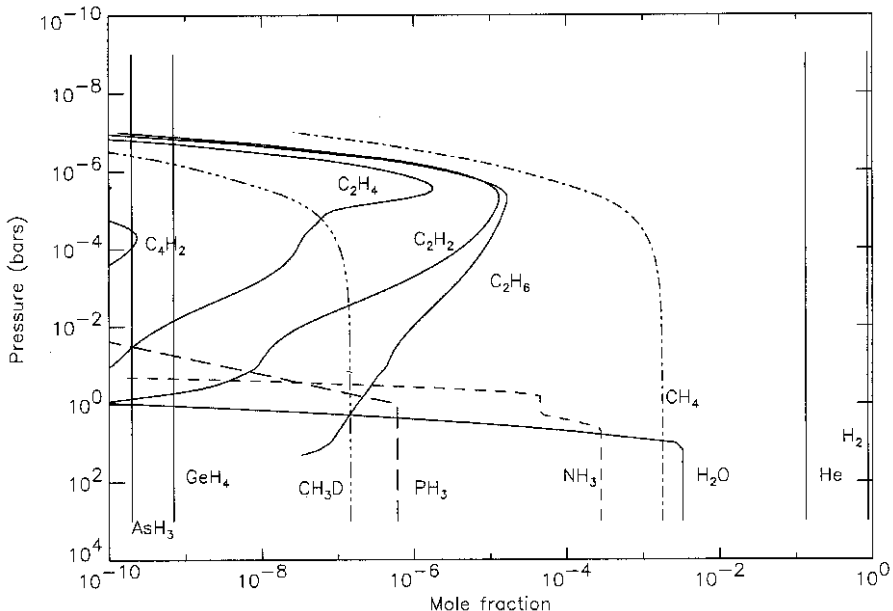


Figure 4.8 Observed and modelled abundance profiles in the atmosphere of Jupiter.

in Chapter 5. Typical levels of saturation in the 5 bar region are found to be of the order of 10%. It was hoped that the question of the deep abundance of water would have been answered by the *Galileo* entry probe. However, the probe descended through just such a cloud-free 5-μm-bright region and so its estimates of volatile abundances are similarly depleted! The probe mass spectrometer found that the abundance of water increased with depth and had reached a value of $\sim 0.5 \times$ the solar value at 19 bar. A similar depleted profile was inferred from the probe's Net Flux Radiometer. Presumably the water vapour profile in upwelling, cloudy regions is similar to the calculated ECCM case but until estimates of water vapour can be made in such regions we can not be sure.

The ammonia profile is expected to have two ‘knees’ since the abundance is first expected to be depleted at the level of the ammonium hydrosulphide cloud layer at around 1–2 bar and then to remain fixed until the formation of an ammonia ice cloud at 700–500 mbar. Such a profile is consistent with ground-based microwave observations of the disc-averaged spectrum where the deep ammonia abundance was estimated to be roughly $2 \times$ the solar value. However, like water, ammonia is observed to be severely depleted in 5-μm hotspot areas both from measurements of the near-IR and 5-μm spectrum and also from the *in situ* observations of the *Galileo* entry probe. However, one surprising result of the probe analysis was that although the ammonia abundance was found to be severely depleted above about 2 bar, it increased rapidly with depth to a maximum value of almost $4 \times$ the solar value. de Pater *et al.* (2001) have reanalysed their ground-based disc-averaged microwave spectra in terms of this new estimated ammonia profile (assuming it to

Table 4.6. Composition of Jupiter.

Gas	Mole fraction	Measurement technique	Reference
He	0.136	<i>Galileo</i> Probe GPMS and HAD	Von Zahn <i>et al.</i> (1998), Niemann <i>et al.</i> (1998)
NH ₃	4.4×10^{-4} at deep levels decreasing to 1.3×10^{-4} near 1-bar level 2.2×10^{-4} at $p > 2$ bar $(2.5\text{--}3.4) \times 10^{-4}$ at $p > 2$ bar decreasing to $(3\text{--}3.8) \times 10^{-5}$ at $p < 1.5$ bar Sub-saturated in upper troposphere $(7 \pm 1) \times 10^{-4}$ at $p > 7$ bar, $(6.1 \pm 2.8) \times 10^{-4}$ in 8.6–12.0 bar region 2.5×10^{-4} at $p > 5$ bar, falling to 1.5×10^{-4} at 2.5 bar and then declining rapidly with height ~10% relative humidity ~ 3.5×10^{-4} at $p > 5$ bar, reducing to ~ 2.5×10^{-5} between 2 and 0.5 bar and falling with f.s.h. of 0.15 above ~ 2.8×10^{-4} at $p > 5$ bar reducing to ~ 4.5×10^{-5} between 2 and 0.5 bar and falling with f.s.h. of 0.15 above 3.1 $\times 10^{-4}$ (5–8 bar)	Ground-based microwave Radio occultation Ground-based microwave <i>Voyager</i> Mid-IR <i>Galileo</i> Probe signal and GPMS <i>Galileo</i> Probe NFR <i>Galileo</i> NIMS 5-μm ISO/SWS 10 μm <i>Galileo</i> NIMS 5-μm ISO/SWS 10 μm	
			Irwin <i>et al.</i> (1998), Roos-Serote <i>et al.</i> (1998) Fouchet <i>et al.</i> (2000)
H ₂ S	Never detected 6.7×10^{-5} ($p > 16$ bar)	Ground-based 5 μm <i>Galileo</i> Probe GPMS	Bézard <i>et al.</i> (2002) de Pater <i>et al.</i> (1991) Niemann <i>et al.</i> (1998)
H ₂ O	5.2×10^{-4} at 19 bar and increasing 1.7×10^{-9} ($p < 10$ mbar)	<i>Galileo</i> Probe GPMS ISO/SWS	Niemann <i>et al.</i> (1998), Atreya <i>et al.</i> (1999) Lellouch <i>et al.</i> (1997)
CH ₄	1.81×10^{-3}	<i>Galileo</i> Probe GPMS	Niemann <i>et al.</i> (1998)

CH ₃ D	3.5×10^{-7} $(1.2\text{--}2) \times 10^{-7}$ 1.8×10^{-7}	<i>Voyager</i> 5 μm ISO/SWS Ground-based 5-μm	Kunde <i>et al.</i> (1982) Lellouch <i>et al.</i> (2001) Bézard <i>et al.</i> (2002)
PH ₃	6×10^{-7} (5–8 bar) f.s.h. above 1 bar level = 0.3 f.s.h. above 1 bar level = 0.27 Not detected	<i>Voyager</i> 5 μm <i>Voyager</i> mid-IR <i>Galileo</i> near-IR (NIMS) Ground-based millimetre	Kunde <i>et al.</i> (1982) Carlson <i>et al.</i> (1993) Irwin <i>et al.</i> (1998) Weisstein and Serabyn (1994)
AsH ₃	$\sim 7 \times 10^{-10}$ (5–8 bar) 2.4×10^{-10} (5–8 bar) f.s.h. above 1 bar level ~ 0.7	Ground-based 5-μm Ground-based 5-μm	Noll <i>et al.</i> (1989) Bézard <i>et al.</i> (2002)
GeH ₄	7×10^{-10} (5–8 bar) 4.5×10^{-10} (5–8 bar) f.s.h. above 1 bar level ~ 1.6	<i>Voyager</i> 5-μm Ground-based 5-μm	Kunde <i>et al.</i> (1982) Bézard <i>et al.</i> (2002)
CO	1.6×10^{-9} (5–8 bar)	Ground-based 5-μm	Noll <i>et al.</i> (1988)
HCN	$(0.9\text{--}3.6) \times 10^{-9}$ (upper troposphere) Not detected	Ground-based mid-IR Ground-based sub-mm	Tokunaga <i>et al.</i> (1981) Davis <i>et al.</i> (1997)
N ₂	—	—	—
C ₂ H ₆	3.5×10^{-6} (~ 10 mbar)	Mid-IR	Moses <i>et al.</i> (2002)
C ₂ H ₂	3.5×10^{-8} (~ 10 mbar)	Mid-IR	Moses <i>et al.</i> (2002)
C ₄ H ₂	$\sim 10^{-12}$ (~ 10 mbar)	Modelled	Moses <i>et al.</i> (2002)
C ₂ H ₄	3×10^{-10} (~ 10 mbar)	Mid-IR and modelled	Moses <i>et al.</i> (2002)
CH ₃ C ₂ H	2×10^{-10} (~ 10 mbar)	Mid-IR and modelled	Moses <i>et al.</i> (2002)
CO ₂	3.5×10^{-10} ($p < 10$ mbar)	ISO/SWS	Encrenaz (1999)

apply globally) and have found that it is also consistent with their spectra. If the estimated 5- μm hotspot ammonia profile is really representative of the globally averaged ammonia profile, then some means of globally depleting the abundance of ammonia in the upper troposphere of Jupiter is required. de Pater *et al.* (2001) suggest that more ammonia might dissolve in the aqueous ammonia cloud than is currently expected (laboratory data does not exist at Jovian temperatures and so must be extrapolated from room temperature measurements), or alternatively that more than one ammonia molecule combines with each hydrogen sulphide molecule to produce products such as ammonium sulphide $(\text{NH}_4)_2\text{S}$ (where each H_2S molecule combines with two NH_3 molecules). Alternatively it is possible that more ammonia may adsorb onto the solid NH_4SH particles than is currently estimated. At higher altitudes, analysis of mid-IR spectra show that the ammonia abundance in the upper troposphere decreases much more rapidly with height than would be expected from saturation alone, both because of horizontal averaging, and also because ammonia is photolysed at roughly 100 mbar and vertical mixing brings this further ammonia-depleted air to lower altitudes. At these altitudes (\sim 400 mbar), mid-IR observations by *Cassini* have revealed a clear latitudinal variation in ammonia abundance which matches well the observed belt/zone structure with moist air rising in the zones and descending in the belts. This belt/zone difference is also apparent in ground-based microwave images (de Pater *et al.*, 2001; de Pater, 1986) shown in Figure 6.21.

Although phosphine does not condense in the Jovian atmosphere, its abundance is found to decrease rapidly above the 1-bar level due to photodissociation near the tropopause and vertical mixing. Its ‘deep’ abundance is estimated to be approximately solar which is a little puzzling since the X/H ratio of almost every other element appears to be \sim 3. Of course, since phosphine is a disequilibrium species, the deep bulk P/H ratio may well be higher. The abundance of phosphine from *Cassini* observations also appears to vary with latitude in a manner just described for ammonia. In addition there has recently been some indication of increased abundance over the GRS from *Cassini* observations although this has not been confirmed. In addition to phosphine, the other main disequilibrium species observed are germane (GeH_4) and arsine (AsH_3). The detected tropospheric (5–8 bar) mole fractions are approximately 4.5×10^{-10} and 2.4×10^{-10} respectively and indicate rapid vertical uplifting. Unfortunately how the abundances of germane and arsine vary with height has not been discernable from measurements made to date. Similarly, a higher than expected level of carbon monoxide has also been detected in the 5–8 bar region with a v.m.r. of approximately 1×10^{-9} , which requires an internal source. However, the abundance of CO in the stratosphere has recently been found to be even higher than that found in the troposphere, rising to perhaps 4×10^{-9} just above the tropopause (Bézard *et al.*, 2002). This observation requires an external source of CO in addition to the internal source and, like Noll *et al.* (1997), Bézard *et al.* (2002) conclude that this may be formed by shock chemistry from the infall of kilometre- to sub-kilometre-size Jupiter family comets.

In the stratosphere, the photolysis products of methane are observed with the

peak v.m.r.s of the main products, ethane and acetylene, observed towards the lower part of the main photolysis region between 1 μ bar and 0.1 mbar. Smog-like haze particles are probably also produced at these altitudes by further complex chemical reactions. Both the hydrocarbons and the hazes spread vertically to other pressure levels through eddy mixing. The abundances of ethane and acetylene are estimated in this lower region (1–10 mbars) to be 3.5×10^{-6} and 3.5×10^{-8} respectively. The hydrocarbon abundances decrease with increasing pressure due to vertical mixing and conversion back to methane. Water vapour has recently been observed in the stratospheres of all the giant planets as outlined in Section 4.3.4. The abundances are listed in Tables 4.6–4.9.

Clouds and hazes

If we follow a parcel of Jovian air, with the assumed ‘deep’ composition, travelling up through the atmosphere with its temperature decreasing adiabatically, three main cloud decks are calculated to form by an ECCM. Atreya *et al.* (1999) calculate the following cloud layers:

- (1) An aqueous ammonia cloud blending into a water ice cloud at higher levels based at approximately 7 bar with a maximum column density of $\sim 1,000 \text{ kg m}^{-2}$.
- (2) A solid ammonium hydrosulphide cloud based at 2.5 bar with a maximum column density of 22 kg m^{-2} .
- (3) An ammonia ice cloud based at 0.8 bar with a maximum column density of 12 kg m^{-2} .

While the cloud bases calculated by an ECCM are fairly reliable, the cloud densities are likely to greatly exceed the actual mass density of the condensed clouds since they neglect the precipitation (and thus re-evaporation) of condensed aerosols and also horizontal mixing with nearby dry air.

In reality, the Jovian cloud structure in the troposphere appears to be much more complicated than this, and a post-*Voyager* review was made by West *et al.* (1986). The only *in situ* measurements that have been made with the *Galileo* entry probe are ambiguous since the probe sampled an unrepresentative 5- μ m hotspot which had abnormally low cloud cover and low abundance of volatiles (we will return to the phenomenon of 5- μ m hotspots in Chapter 5). The cloud structure measured by the *Galileo* probe nephelometer experiment was found to be very tenuous with a main cloud layer based at 1.4 bar, a thinner cloud below at 1.6 bar, and the suggestion of a cloud based at 0.4 bar (Figure 4.9). The three clouds have tentatively been identified as NH₄SH, water ice, and NH₃ ice respectively, but they are at higher altitudes than expected. As we shall see in Chapter 5 these hotspots have been modelled either as regions of extremely rapid downdraft or more recently, and probably more plausibly, as part of an atmospheric wave system where the air column is vertically stretched and compressed with the hotspots occurring at the stretching phase. Both explanations are consistent with the low volatile abundances and low cloud cover. However while it is easy to reconcile the puzzling probe results with our expected cloud model, wide-area visible and near-IR measurements by the

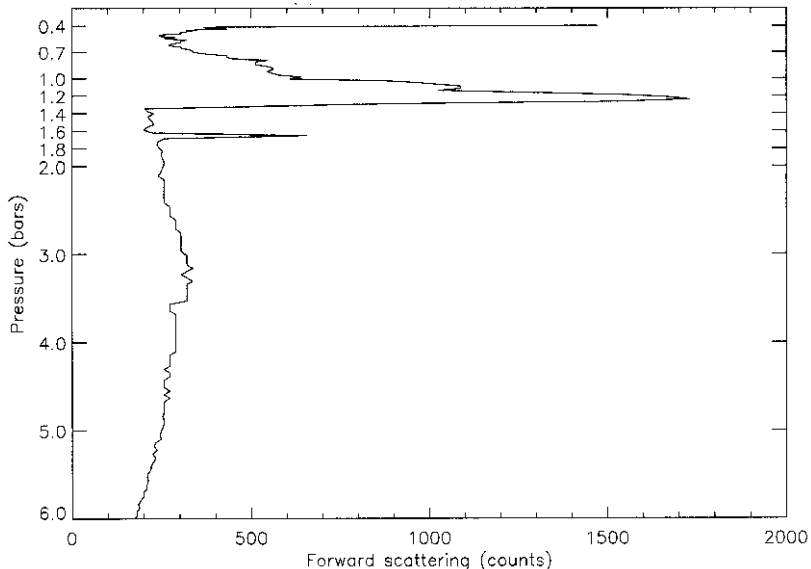


Figure 4.9 Relative cloud profile of Jupiter deduced from the *Galileo* probe nephelometer experiment cloud results.

From Ragent *et al.* (1998).

Galileo orbiter also reveal a structure apparently inconsistent with expectations. For a long time, the main cloud deck responsible for the albedo contrasts was thought to be ammonia ice with a base at about 0.7 bar. However, recent estimates (Irwin *et al.*, 2001; Banfield *et al.*, 1998; Irwin and Dyudina, 2002) suggest that the main cloud deck responsible has a base near 1 bar and is considerably vertically extended, merging with photochemically produced hazes in the upper troposphere. While this cloud is probably some form of ammonia, it would seem to be inconsistent with pure ammonia ice since this would sublime at 1 bar unless the N/H ratio was significantly supersolar at these altitudes, which as we saw in the last section does not seem to be the case. Instead it has been suggested that this cloud might perhaps be the top of the NH₄SH cloud, or that the ammonia ice particles are contaminated, perhaps by haze material, which increases their sublimation temperature. Such a modification would be consistent with the previous lack of observation of ammonia ice spectral features throughout the IR spectrum of Jupiter except in small, localized regions of rapid uplift (Figure 4.10, colour plate) which condense pure ammonia ice particles at high altitudes (Baines *et al.*, 2002). Although Brooke *et al.* (1998) find that the 3-μm part of the ISO-SWS disc-averaged spectrum is well modelled with the inclusion of ammonia ice particles, Irwin *et al.* (2001) point out that this introduces erroneous features in other parts of the IR spectrum. However, some preliminary results from *Cassini/CIRS* (Wong *et al.*, 2003) report a more wide-area detection of ammonia ice absorption, assuming non-spherical ammonia ice particles, at 10 μm in the thermal-IR in the North Tropical Zone (NTropZ) at

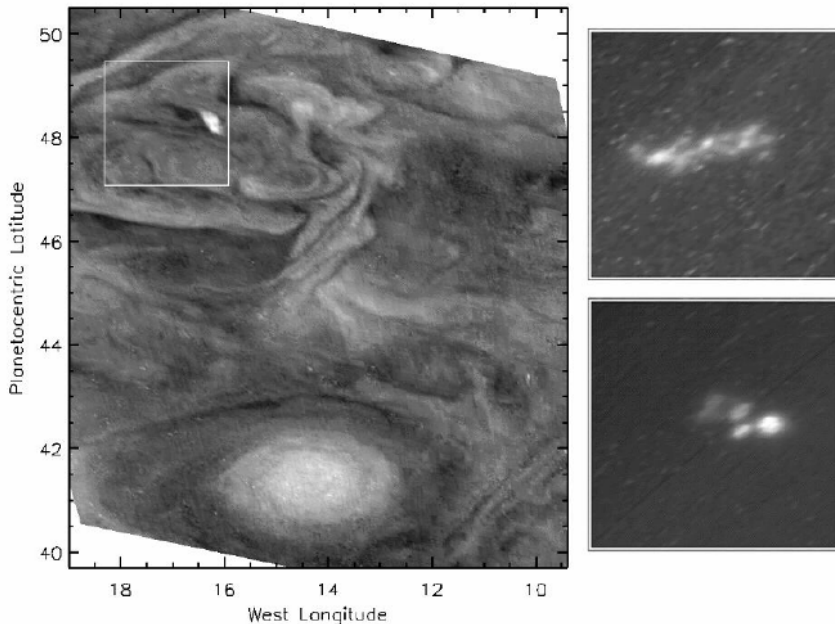


Figure 4.12 *Galileo/SSI* images of a convective storm (left panel) and the associated lightning (right panels) in Jupiter's atmosphere. The left-hand image shows the day-side view of a storm cloud while the right-hand images show a close-up of lightning strikes from the storm some 2 hours later when the feature had rotated around to the nightside. The two lightning images were taken about 4 minutes apart. The day-side image was recorded at 727 nm, while the night images were recorded with a 'red' filter to improve the throughput.

Courtesy of NASA.

latitudes between 22° and 25°N . Clearly this remains an area of active research. At deeper levels, there is now increasing evidence for the detection of a deep water cloud at roughly 5 bar. This has been detected both by 5- μm measurements (Nixon *et al.*, 2001) and by visible/near-IR observations of Jovian thunderstorm clouds, which have bases in excess of 4 bar (Figure 4.11, colour plate) and have clearly detected lightning activity (Banfield *et al.*, 1998; Little *et al.*, 1999; Gierasch *et al.*, 2000; Dyudina and Ingersoll, 2002) shown in Figure 4.12. In addition, the possible spectral absorption of water ice has now been observed in *Voyager* far-IR spectra (Simon-Miller *et al.*, 2000) which suggests that water ice particles may be lifted up to pressures less than 1 bar. Figure 4.13 shows a summary of the estimated cloud structure of Jupiter and of the other giant planets.

At higher altitudes, above the radiative–convective boundary but below the tropopause, the 'ammonia' cloud appears to blend into the haze layers formed possibly by the dissociation products of ammonia and phosphine, and also methane haze products settling from the stratosphere. The upper tropospheric haze layers are seen mostly over the GRS and the northern edge of the Equatorial Zone (EZ) where they appear much more zonally spread out than the convective clouds seen in the troposphere (Figure 4.14, colour plate). The main altitude of

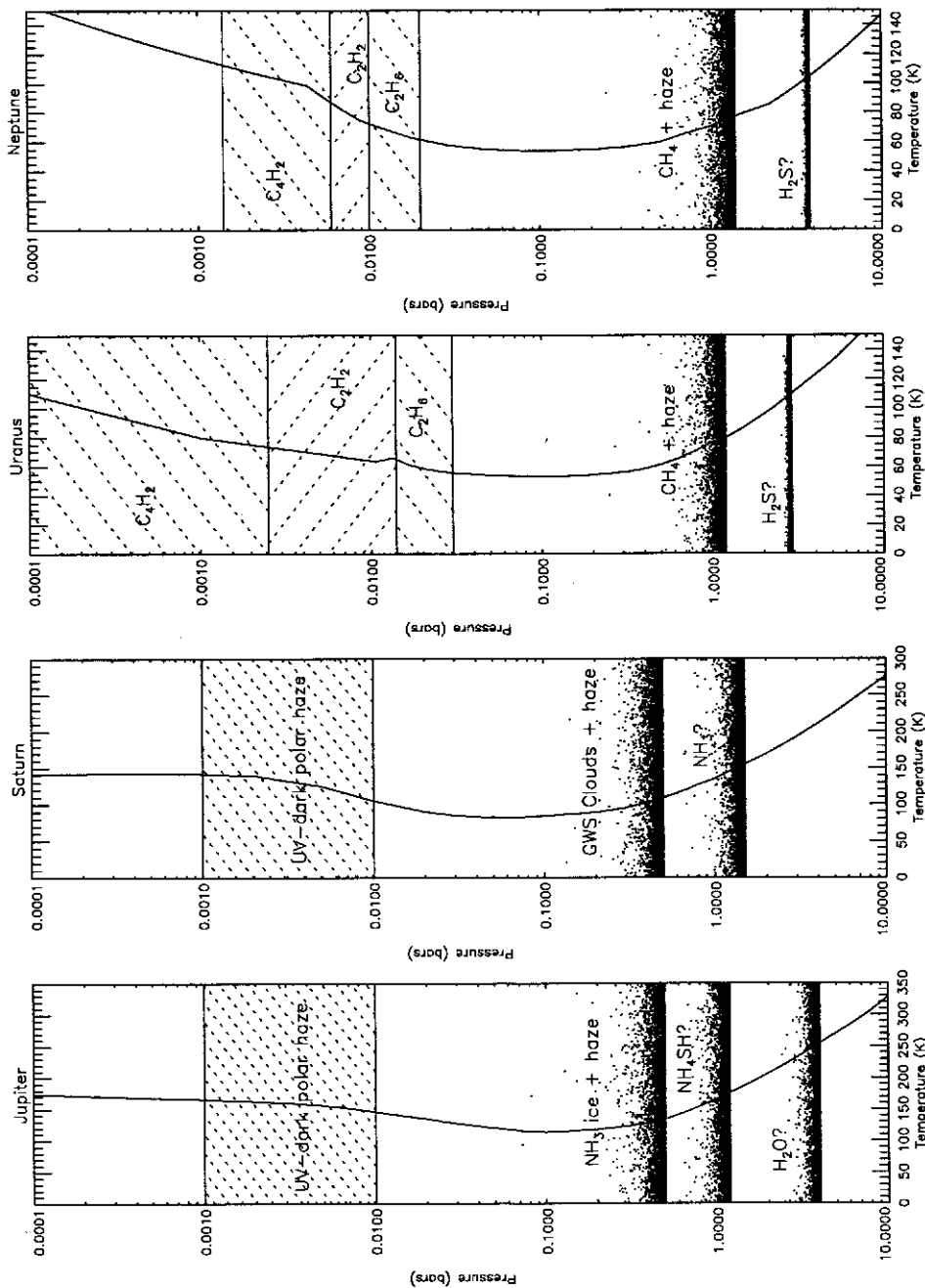


Figure 4.13 Mean observed/modelled cloud profiles of the giant planets.

ammonia photodissociation occurs in the 30–300 mbar region for ammonia, and peaks at the 80 mbar pressure level for phosphine. The main photochemical product of ammonia is likely to be hydrazine which should form ice particles that slowly settle through the atmosphere and are pyrolysed at deeper levels. Similarly diphosphine particles may also be present in the upper tropospheric hazes. In addition, red phosphorus P₄(s) may also be produced, as mentioned in Section 4.3.2.

Observations of stratospheric hazes have been made both from ground-based methane band measurements (West, 1979a, b; West and Tomasko, 1980) and more recently from *Galileo* (Rages *et al.*, 1999). Such observations are described more fully in the context of Saturn's stratospheric hazes (Section 4.4.2). These hazes may be produced from the higher mass photolysis products of methane. However the stratospheric aerosols of Jupiter (and Saturn) in the polar regions are found to be highly UV-absorbing and very different from those seen at other latitudes. In these regions it would appear that haze production results from a different mechanism, possibly by charged particles from the solar wind and magnetosphere which travel down the magnetic field lines to strike air molecules in the upper atmosphere causing ionization.

4.4.2 Saturn

Composition profiles

Tables 2.2a and 2.2b list the 'deep' composition of the Saturnian atmosphere. Like Jupiter there is good evidence that Saturn (Figure 4.15) initially formed from icy planetesimals before reaching sufficient mass to collapse and condense the solar nebula in its feeding zone. The fact that Saturn is much less massive than Jupiter suggests that it was able to attract a smaller mass of H₂ and He from the nebula, and thus the mixing ratios of the heavier elements (X/H) are expected to be correspond-

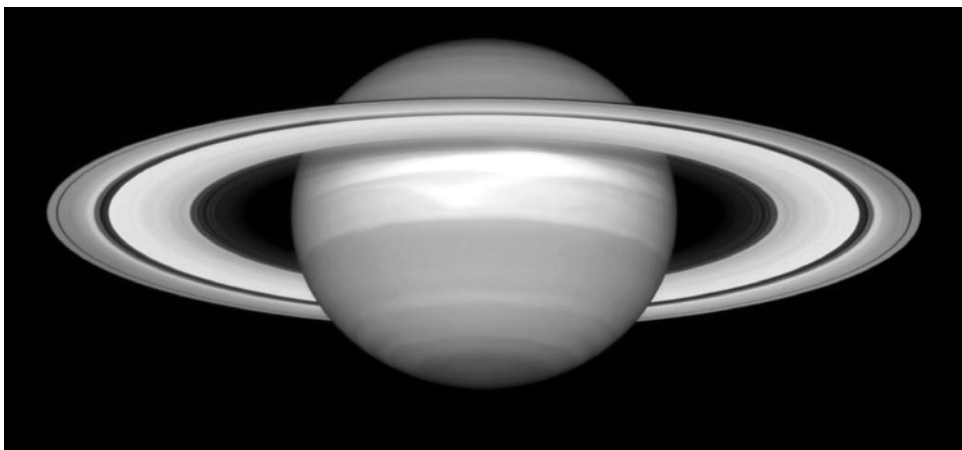


Figure 4.15 Image of Saturn recorded by the HST/WFPC-2 instrument in 1990.

Courtesy of NASA.

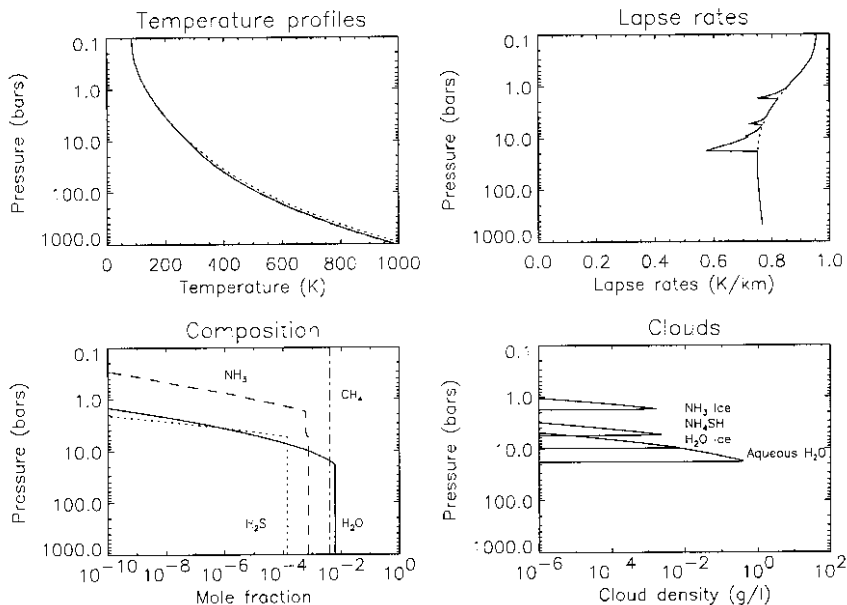


Figure 4.16 Equilibrium cloud condensation model of Saturn's atmosphere (as Figure 4.7). Calculated cloud layers: H_2O cloud (water, then ice) at ~ 18 bar, NH_4SH at ~ 5 bar and NH_3 ice at ~ 1.8 bar. Assumed composition: O/H, N/H, S/H = $5 \times$ the solar value, C/H = $6.8 \times$ the solar value.

ingly higher. The observed estimated value of the deep C/H ratio of $\sim 6 \times$ the solar value (Courtin *et al.*, 1984; de Graauw *et al.*, 1997) is thus entirely consistent with this expectation. Similarly the deep abundance of ammonia has been estimated from ground-based microwave observations to be approximately $2\text{--}3 \times$ the solar value (de Pater and Massie, 1985), although 5- μm observations suggest a lower value, and the estimated abundance of phosphine from sub-millimetre observations suggest that the deep P/H ratio is $5\text{--}10 \times$ the solar value (Orton *et al.*, 2000, 2001). A more precise estimate of the bulk methane abundance should result from combined *Cassini/CIRS* nadir- and limb-retrievals when *Cassini* goes into Saturn orbit in 2004.

The troposphere of Saturn is colder than that of Jupiter and thus the condensation levels of different tropospheric gases is correspondingly lower. Figure 4.16 shows the results of calculation of a Saturn ECCM. The deep abundances of O, N, and S (relative to H) are assumed to be $5 \times$ the solar value, and C/H is set at $6.8 \times$ the solar value. It can be seen that water vapour should start to condense near 18 bar and thus the composition of this molecule falls rapidly with height and has a v.m.r. of only 2×10^{-7} at a pressure of 3 bar. The ammonia v.m.r. remains fixed until approximately 5 bar where it is partially depleted by the formation of a putative NH_4SH cloud. Just as for Jupiter, the ammonia v.m.r. in this model is expected to remain fixed until the ammonia cloud condensation level of approximately 1.8 bar, and to then fall rapidly above this due to the same combination of condensation, photolysis, and mixing which defines Jupiter's ammonia profile.

Estimates of the Saturn composition profiles actually measured (and references thereto) are listed in Table 4.7 and best fit profiles are shown in Figure 4.17. The abundance of water at 3 bar is found to be similar to that calculated from the ECCM. Ammonia however is again found to be less abundant than predicted by the ECCM with an estimated deep mole fraction from 5- μm observations (Noll and Larson, 1990; de Graauw *et al.*, 1997) of only $\sim 0.7 \times$ the solar value. The variation of ammonia above the condensation level is more difficult to detect than for Jupiter since the spectral absorption features generated above the 1 bar level in the mid-IR are swamped by the high abundances of phosphine. An ammonia profile with approximately 50% humidity is consistent with measurements (de Graauw *et al.*, 1997). The phosphine profile appears to be fixed up to a pressure level of ~ 600 mbar and falls rapidly above this due to photodissociation and mixing. Significant levels of CO are detected in the troposphere (of the order of 10^{-9} if uniformly mixed according to Noll and Larson, 1990) which indicates rapid upwelling and vertical mixing. Indeed the inferred stratospheric eddy mixing coefficient profile is found by some studies (Atreya *et al.*, 1999) to be much greater than that of Jupiter's. This mixing may arise from gravity waves generated in the convective troposphere. It is presumed that since CO is found, N₂ may also present in the stratosphere although this is impossible to detect directly. However, at the time of writing this book, photochemical products such as HCN, which are observed in Neptune's atmosphere indicating N₂, have not been observed in Saturn's atmosphere. In addition to the aforementioned disequilibrium species PH₃ and CO, arsine and germane are also observed in the Saturnian atmosphere but at higher v.m.r.s (both are estimated to be 2.3×10^{-9}) than seen in Jupiter's atmosphere, consistent with the generally increased abundance of heavy elements in Saturn's atmosphere compared with Jupiter's.

In the upper stratosphere, methane photochemistry produces hydrocarbons such as ethane and acetylene whose abundances may be estimated from mid-IR spectroscopy. In addition to the general micrometeoroid source of stratospheric oxygen discussed in Section 4.3.4, an additional source of stratospheric water in Saturn's atmosphere appears to be material falling from the rings onto the planet at specific latitudes (magnetically connected to rings). Although it is difficult to measure the latitudinal variation of water vapour, it is possible to observe a decrease in hydrocarbon abundance at certain latitudes. This could be due to reactions between water and hydrocarbons which lead to other, so far undetected molecules. This may be an indirect signature of water from the rings.

Clouds and hazes

Using an ECCM, and assuming all heavy elements are enriched to $\sim 5 \times$ the solar value, Atreya *et al.* (1999) predict the same three main cloud decks to occur in Saturn's atmosphere as are expected in the Jovian atmosphere. However since the Saturnian temperatures are lower the clouds are based at correspondingly deeper levels. Hence Atreya *et al.* (1999) find that an aqueous ammonia cloud (blending into a water ice cloud at higher levels) is expected to start condensing near 20 bar with a column density of $12,000 \text{ kg m}^{-2}$, followed by an ammonium hydrosulphide cloud at

Table 4.7. Composition of Saturn.

Gas	Mole fraction	Measurement technique	Reference
He	0.115	<i>Voyager</i> far-IR	Conrath and Gautier (2000)
NH ₃	3×10^{-4} ($p > 3$ bar) $< 3 \times 10^{-4}$ (deep) 1.1×10^{-4} (deep) 50% humidity	Ground-based microwave Ground-based 5-μm ISO 5-μm ISO mid-IR	de Pater and Massie (1985) Noll and Larson (1990) de Graauw <i>et al.</i> (1997) de Graauw <i>et al.</i> (1997)
H ₂ S	Never detected	Ground-based microwave	de Pater <i>et al.</i> (1991)
H ₂ O	2.3×10^{-7} (upper troposphere) (2–23) × 10 ⁻⁹ ($p < 0.3$ mbar)	ISO-SWS 5-μm ISO-SWS	de Graauw <i>et al.</i> (1997) Feuchtgruber <i>et al.</i> (1997)
CH ₄	$\sim 5 \times 10^{-3}$	<i>Voyager</i> mid-IR	Courtin <i>et al.</i> (1984)
CH ₃ O	$(3.3 \pm 1.5) \times 10^{-7}$	Ground-based 5-μm	Noll and Larson (1990)
PH ₃	1×10^{-6} for $p < 400$ mbar $(7^{+3}_{-2}) \times 10^{-6}$ for $p > 400$ mbar 5×10^{-6} 3×10^{-6} (upper troposphere cut off at 100 mbar) 7.4×10^{-6} at 645 mbar, 4.3×10^{-7} at 150 mbar	Ground-based 5-μm	Noll and Larson (1990) de Graauw <i>et al.</i> (1997) Weissstein and Serabyn (1994) Orton <i>et al.</i> (2000, 2001)
AsH ₃	3×10^{-9} (troposphere) 2.3×10^{-9} (stratosphere)	Ground-based 5-μm ISO-SWS 5-μm	Noll and Larson (1990) de Graauw <i>et al.</i> (1997)

GeV ₄	$(4 \pm 4) \times 10^{-10}$ (troposphere) 2.3×10^{-9} (troposphere)	Ground-based 5-μm ISO-SWS 5-μm	Noll and Larson (1990) de Graauw <i>et al.</i> (1997)
CO	1×10^{-9} (if uniformly mixed), 2.5×10^{-8} (if in stratosphere only at $p < 80$ mbar) $< 10^{-7}$ (stratosphere) 2.1×10^{-9}	Ground-based 5-μm ISO-SWS 5-μm	Noll and Larson (1990) Rosenqvist <i>et al.</i> (1992) de Graauw <i>et al.</i> (1997)
HCN	—	—	—
N ₂	—	—	—
C ₂ H ₆	4.5×10^{-6} ($p < 10$ mbar)	ISO-SWS mid-IR	de Graauw <i>et al.</i> (1997)
C ₂ H ₂	4×10^{-6} (0.1 mbar), 3×10^{-7} (1 mbar)	ISO-SWS mid-IR	de Graauw <i>et al.</i> (1997)
C ₄ H ₂	1×10^{-10} ($p < 10$ mbar)	ISO-SWS mid-IR	de Graauw <i>et al.</i> (1997)
C ₂ H ₄	—	—	—
CH ₃ C ₂ H	7×10^{-10} ($p < 10$ mbar)	ISO-SWS mid-IR	de Graauw <i>et al.</i> (1997)
CO ₂	3.4×10^{-10} ($p < 10$ mbar)	ISO-SWS mid-IR	de Graauw <i>et al.</i> (1997)

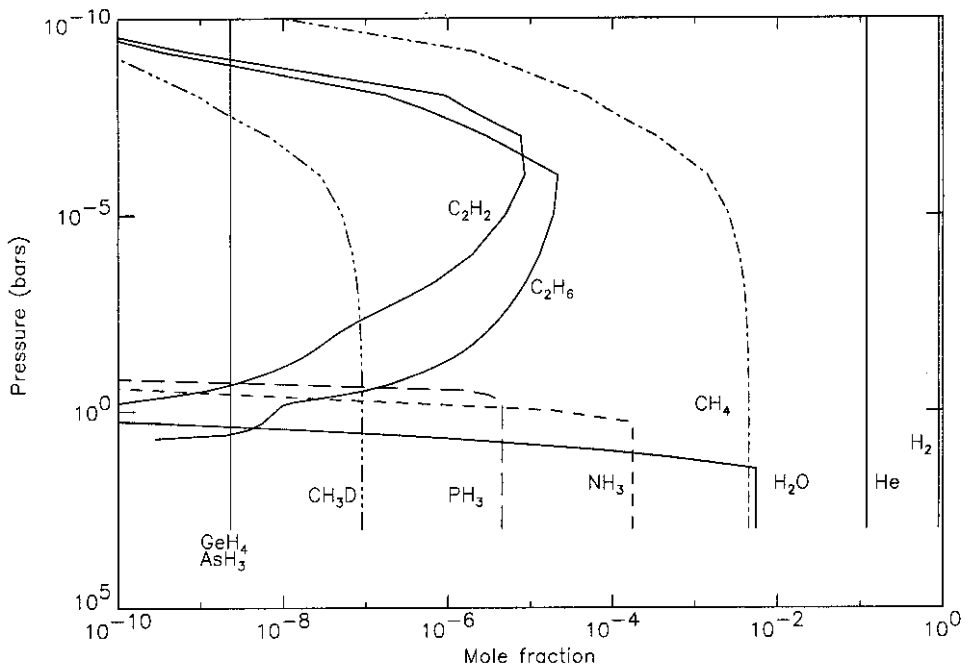


Figure 4.17 Observed and modelled abundance profiles in the atmosphere of Saturn.

~ 6 bar with a column density of 200 kg m^{-2} , and an ammonia ice cloud at 1.8 bar with a column density of $\sim 100 \text{ kg m}^{-2}$ (again these cloud densities are greatly overestimated but they do provide a guide for the *relative* maximum cloud thicknesses). Hence part of the reason that the visible cloud features of Saturn have a lower contrast than those of Jupiter is that the main cloud decks lie at deeper pressures in Saturn's atmosphere compared with Jupiter's. Fewer measurements of the Saturnian cloud structure have been made than for Jupiter, and thus this is a major goal for the *Cassini/Huygens* mission in 2004. However, a number of estimates have been made from ground-based telescopes, the Hubble Space Telescope (HST), and *Voyager* imaging observations which are summarized in Figure 4.13. While to a first order the presumed ECCM cloud structure is roughly consistent with the measured abundances of water vapour and ammonia, observations suggest that, like Jupiter, the depletion in abundance of these volatiles appears to occur at deeper pressures and higher temperatures than predicted by a simple ECCM. For example, ground-based microwave observations by de Pater and Massie (1985), suggest that, globally, ammonia is depleted between 3 and 1.5 bar which would push the NH_3 cloud to higher altitudes and reduce its opacity. Indeed, cloud models of Saturn that are consistent with measured visible and near-IR reflectance spectra place a thin haze layer at roughly 500 mbar and a deeper optically thick cloud top at 1.5 bar (de Graauw *et al.*, 1997). The other factor contributing to the low contrast appearance of Saturn's belts and zones is that Saturn's

pressure scale height is more than twice that of Jupiter. Assuming that the tropospheric haze has roughly the same density in both atmospheres, the column abundance of haze above the ammonia condensation level is estimated to be 5 times greater in Saturn's atmosphere than in Jupiter's, leading to lower contrast of convective cloud features (Smith *et al.*, 1981). The discrete cloud features that are observed appear to be the tops of active convection systems that push their way up into the overlying semitransparent tropospheric haze region.

Just as in Jupiter's atmosphere, molecules such as ammonia and phosphine are probably photolysed near the tropopause, contributing to the production of upper tropospheric haze, and likewise in the stratosphere, the photolysis of methane leads to detectable levels of ethane, acetylene, and other hydrocarbon products. These products diffuse downwards, and heavier hydrocarbons may perhaps condense near the tropopause where the temperatures are lowest. The highest concentrations of these smog products might thus be expected at the sub-solar latitude which varies during the period of Saturn's orbit from 26.7°N to 26.7°S (Beebe, 1997). During the *Voyager* flybys, Saturn's year was just entering northern spring and thus this simple model would predict that the haze would be thickest over the equator. However, measurements by *Voyager* in the UV (Smith *et al.*, 1982) found the stratospheric haze to be thickest over the North Pole, moderately thick in northern mid-equatorial latitudes, and almost absent at southern mid-latitudes (the South Pole was in darkness at the time). This north/south asymmetry was also observed in ground-based observations in the near-IR methane absorption bands (West *et al.*, 1982) and would thus seem at odds with the simple photolysed methane haze model. Further analysis of the *Voyager* data (West *et al.*, 1983) suggested that three types of haze are present:

- (1) a high altitude (above 10 mbar level) UV absorbing stratospheric haze at polar latitudes;
- (2) a lower stratospheric haze (below 10 mbar level) at equatorial latitudes; and
- (3) a tropospheric haze component.

Ground-based observations of the reflection spectrum of Saturn have been made from near-IR to visible wavelengths for almost 20 years (West *et al.*, 1982; Karkoschka and Tomasko, 1992; Ortiz *et al.*, 1993, 1995, 1996) and have been extended into the UV by HST (Karkoschka and Tomasko, 1993). The vertical and horizontal haze structure may be inferred from these observations of the reflection spectrum as follows. At visible continuum wavelengths, reflection from clouds and hazes at all levels is seen, whilst in the near-IR methane-absorption bands, only light reflected from the upper haze layers may be seen which appear *bright* against a *dark* background. In the UV, Rayleigh scattering from the air molecules becomes important and thus, as for the near-IR methane absorption bands only light reflected from the upper atmosphere is seen. However, since Rayleigh scattering from the air molecules is conservative, high altitude hazes appear *dark* against a *bright* background. Hence images of giant planets at UV and methane-absorption wavelengths should, to a first approximation, be complementary and thus any differences that are

present may be used to infer particle size and absorption properties. Karkoschka and Tomasko (1993), from just such a study, suggest that there are two types of haze: a tropospheric haze spread between the tropopause and the expected ECCM base of the ammonia cloud at 1.8 bar, and a separate stratospheric haze. The tropospheric haze appears to be composed of particles of approximately $1.5\text{ }\mu\text{m}$ radius and is probably associated with the ammonia cloud (although no ammonia ice absorption features have been observed to date). The stratospheric haze particles appear to be substantially smaller with a radius of only $0.15\text{ }\mu\text{m}$. The tropospheric haze was found to be thickest over the Equatorial Zone (EZ) and in general seemed correlated with the belt/zone structure. However, the stratospheric haze was found to be most abundant over the North Pole (the South Pole was in shadow in 1993) and highly UV-absorbing. At mid-latitudes the stratospheric haze almost disappeared but then rose again slightly at the equator. The stratospheric aerosols are thus thought to be produced directly from gas by auroral processes in the polar regions, as is the case for Jupiter. At the equator, the stratospheric aerosols may derive directly from photochemical products of methane, or they may perhaps arise through the ‘overshooting’ of tropospheric particles. This latter interpretation is perhaps supported by the observation of Ortiz *et al.* (1993, 1995, 1996) that the brightness of the EZ in near-IR methane-absorption bands increased dramatically from 1991 to 1992 and appeared to be decaying in 1993, suggesting an increase in the optical depth and/or height of the tropospheric haze. This period was just after the ‘Equatorial Disturbance’ (or Great White Spot) of 1990. The 1994 Equatorial Disturbance was shown earlier in this book in Figure 1.5. At continuum wavelengths a north/south asymmetry was observed with the southern hemisphere appearing darker at longer wavelengths suggesting smaller particle size in the tropospheric haze. These latitudes had just emerged from the shadow of the rings which may have had an effect. The distribution of clouds and hazes observed by HST in 1998 is shown in Figure 4.18, colour plate.

The nature of the tropospheric haze particles is puzzling. Simplistically one would expect these to be composed predominantly of ammonia, although as is the case on Jupiter (except recently for a small localized upwelling), there has been no spectroscopic identification of pure ammonia ice. One suggestion that has been made is that the ammonia crystals become coated with stratospheric haze material settling down from above. Unfortunately the low column amounts of stratospheric haze except at the poles seem to rule this explanation out. Perhaps the thermal history of the tropospheric particles hides their identity, or perhaps the photochemical products of ammonia and phosphine produced near the tropopause combine with ammonia ice in some way to produce a hybrid particle.

4.4.3 Uranus

Composition profiles

In Chapter 2 we saw that the observable deep atmosphere of Uranus (Figure 4.19, colour plate) has much higher levels of methane than Jupiter and Saturn, and a much

greater D/H ratio. The methane v.m.r. was estimated to be 2.3% from *Voyager 2* radio-occultation measurements (Lindal *et al.*, 1987), although more recent ground-based visible hydrogen quadrupole measurements suggest a figure closer to 1.6% (Baines *et al.*, 1995b). Hence the C/H ratio appears to be between 30 and 40× the solar value. This, and other indicators, suggest that the hydrogen–helium atmosphere observed is merely a thin shell, accounting for only 20% of the radius and 20% of the mass, and that the bulk of Uranus is composed of ice, albeit hot and fluid.

The troposphere of Uranus (and Neptune) is much colder than that of Jupiter and Saturn. Abundances of condensable species such as water are also much higher. Hence ECCM calculations predict that clouds such as water and NH₄SH condense at much deeper levels as can be seen in Figure 4.20. The deep abundances are here assumed to be: O/H = 100× the solar value, N/H = the solar value, S/H = 10× the solar value, and C/H = 29× the solar value. The reasons for these assumptions are outlined in the next paragraph. Water is expected to condense at very deep levels, with methane condensing near 1.5 bar. Considering their measured (or assumed) high abundances, the SALR can be seen to be very different from the DALR and thus the dry and wet temperature profiles are substantially different. The sharp variation in the dry adiabatic lapse rate at 1.5 bar is due to the reduction in

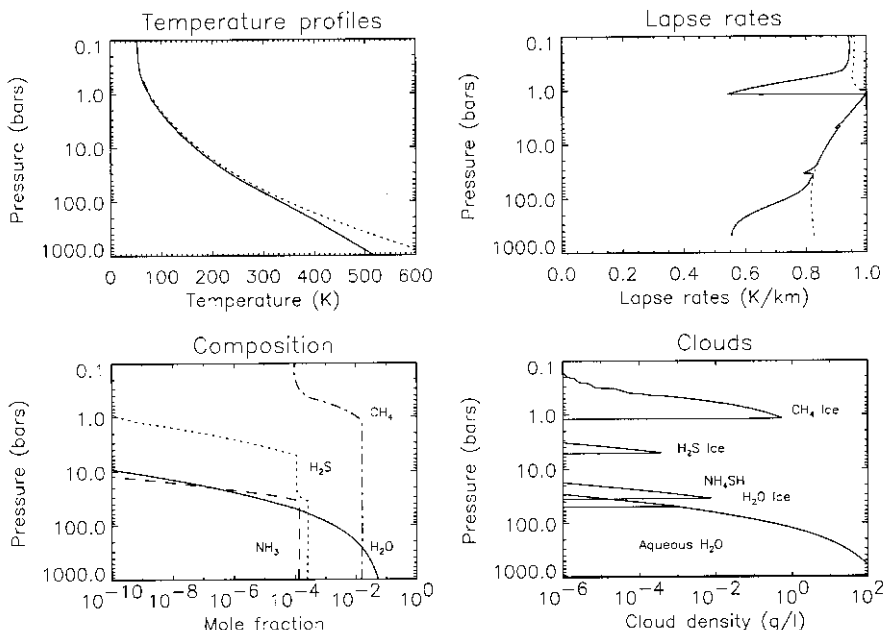


Figure 4.20 Equilibrium cloud condensation model of Uranus' atmosphere (as Figure 4.7). Calculated cloud layers: H₂O cloud (water, then ice) at $p > 1,000$ bar, NH₄SH at ~ 40 bar, H₂S ice at ~ 5 bar, and CH₄ ice at ~ 1.2 bar. Assumed composition: O/H = 100× the solar value, N/H = the solar value, S/H = 10× the solar value, C/H = 29× the solar value.

atmospheric heat capacity caused by the condensation of methane. It should also be noted that the sudden change in the mean molecular weight at this cloud base (and at the base of the deeper water cloud) causes a substantial change in the pressure scale height. The ortho-/para-hydrogen was here assumed to be in the ‘intermediate’ state outlined in Section 4.1.3.

Because the observable atmosphere of Uranus (and Neptune) is extremely cold, unlike Jupiter and Saturn it is difficult to determine composition profiles using thermal-IR spectroscopy because the emitted spectrum has such low power. Hence we know a lot less about the composition of the atmospheres of Uranus and Neptune than we do about the atmospheres of Jupiter and Saturn. What has been determined about Uranus’ composition is outlined in Table 4.8 and Figure 4.21. Methane is indeed found to condense near the 1.5 bar level and the v.m.r. drops very rapidly with height above this level reaching a minimum of approximately $(0.3\text{--}1) \times 10^{-4}$ at the tropopause. In the stratosphere, photodissociation of methane occurs between 0.1 and 1 mb, giving rise to hydrocarbon products. Acetylene (C_2H_2) has been detected by ISO (Encrenaz *et al.*, 1998) with a maximum v.m.r. of 4×10^{-7} peaking at the 0.1 mbar pressure level. The v.m.r. of methane at the same altitude may not exceed 3×10^{-6} and photochemical models suggest that ethane must be present at the same altitude with a v.m.r. of 3×10^{-6} , although this and other hydrocarbon species so far remain undetected.

Ground-based microwave observations of Uranus between 1 mm and 20 cm indicate that both ammonia and water vapour are substantially subsolar (by a factor of several hundred) down to pressures of approximately 50 bar. The low abundance of water vapour is not surprising since it is expected to have mostly condensed by 100 bar, but the low abundance of ammonia is very surprising, especially when the abundance of methane is so high, and when both Jupiter and Saturn have significant quantities of ammonia. It would appear that almost all the available ammonia must react with H_2S to form NH_4SH at levels of approximately 40 bar, or that substantial quantities are incorporated into massive aqueous ammonia clouds at deep levels. The microwave observations suggest that H_2S is much more abundant than in the atmospheres of Jupiter and Saturn at levels of $(10\text{--}30)\times$ the solar value. To account for the massive depletion of ammonia via the formation of an NH_4SH cloud, the ratio of S/N must be greater than $5\times$ the solar value. Ground-based microwave observations have also revealed that the deep abundance of ammonia that is present appears to vary with latitude by almost an order of magnitude with higher levels detected at equatorial latitudes. Such a variation may be indicative of a large scale Hadley cell with air rising at the equator and descending at the poles (de Pater *et al.*, 1991). Higher in the atmosphere, the meridional circulation seems to be somewhat different with upwelling at mid-latitudes and subsidence at the poles and equator (Chapter 5). If cloud absorption is neglected, the observed microwave spectra suggest that the atmospheric temperature profile becomes isothermal at depth (de Pater *et al.*, 1989). Such a profile would be consistent with Uranus having a very low internal heat flux since the atmospheric dynamics would then be driven primarily by absorbed sunlight. However the observed spectrum may also be explained by the presence of a deep, very optically

Table 4.8. Composition of Uranus.

Gas	Mole fraction	Measurement technique	Reference
He	0.15 ($p < 1$ bar) f_{H_2} , fraction of H ₂ with equal ortho/para	<i>Voyager</i> far-IR Ground-based visible hydrogen quadrupole	Conrath <i>et al.</i> (1987) Baines <i>et al.</i> (1995b)
NH ₃	Solar/(100–200), $p < 10$ –20 bar (10–30) × the solar value $> 5 \times$ the solar value	Ground-based microwave Ground-based microwave Ground-based microwave	de Pater and Massie (1985) de Pater <i>et al.</i> (1991) de Pater <i>et al.</i> (1991)
H ₂ S		ISO/SWS	Feuchtgruber <i>et al.</i> (1997)
S/N			Lindal <i>et al.</i> (1987) Baines <i>et al.</i> (1995b)
H ₂ O	$(6\text{--}14)} \times 10^{-9}$ ($p < 0.03$ mbar)	Radio-occultation Ground-based visible hydrogen quadrupole	
CH ₄	0.023 ($p > 1.5$ bar) 0.016 ($p > 1.5$ bar)	ISO/SWS	Encrenaz <i>et al.</i> (1998)
	$(0.3\text{--}1)} \times 10^{-4}$ at tropopause, $< 3 \times 10^{-6}$ at 0.1 mbar	Ground-based 6100–6700 cm ⁻¹ Ground-based 1–1.5 mm	
CH ₃ D/CH ₄	$3.6^{+3.6}_{-2.4} \times 10^{-4}$		
PH ₃	$< 4 \times 10^{-8}$ (stratosphere) $< 10^{-8}$ (troposphere) $< 5 \times 10^{-7}$ (troposphere)	—	—
AsH ₃	—	—	Rosenqvist <i>et al.</i> (1992)
GeH ₄	—	—	Marten <i>et al.</i> (1993)
CO	—	—	Encrenaz <i>et al.</i> (1996)
HCN	—	—	—
N ₂	—	—	—
C ₂ H ₆	3×10^{-6} at 0.1 mbar	Modelled	Encrenaz <i>et al.</i> (1998)
C ₂ H ₂	10^{-8} 4×10^{-7} at 0.1 mbar	<i>Voyager</i> UV ISO/SWS	Yelle <i>et al.</i> (1989) Encrenaz <i>et al.</i> (1998)
C ₄ H ₂	—	—	—
C ₂ H ₄	—	—	—
CH ₃ C ₂ H	—	—	—
CO ₂	—	—	—

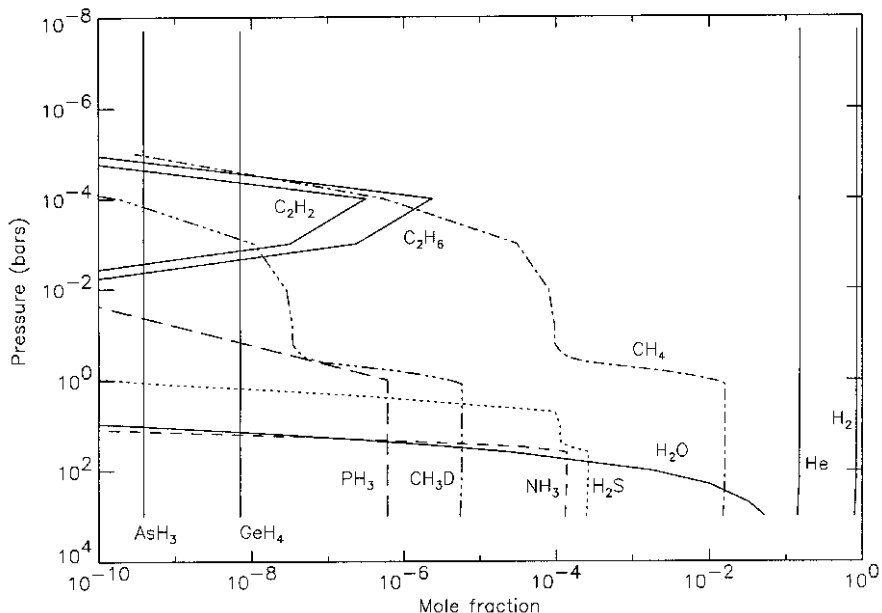


Figure 4.21 Observed and modelled abundance profiles in the atmosphere of Uranus.

thick cloud such as the expected water cloud. Hence whether or not the deep atmosphere of Uranus is really isothermal is debatable. In Figure 4.20 we have assumed that the temperature profile follows a SALR at depth.

The low IR flux of Uranus means that spectral features of possible disequilibrium species such as phosphine, germane, and arsine are not currently observable in the mid-IR, even if they are there. Although phosphine does have features in the very far-IR between 1 and 1.5 mm, it is expected to condense at the tropopause in Uranus' very cold atmosphere. Ground-based observations of these absorption lines suggest $P/H < 4 \times$ the solar value although we might expect the deep P/H ratio to be somewhat higher given the high C/H ratio. Its low abundance suggests sluggish vertical mixing in Uranus' atmosphere. This conclusion is supported by the absence of observable CO absorption features (suggesting the v.m.r. of this molecule in the troposphere is $< 10^{-7}$ – 10^{-8}) and also by the observation that the ortho-/para-hydrogen ratio appears to be close to equilibrium at all levels. The time constant for ortho-/para-hydrogen conversion depends on the aerosol abundances, which act to catalyse the reaction, but is likely to be of the order of several years, which places an important constraint on the vertical mixing time scale. To date, only one observation of the 5-μm spectrum has been made (Orton and Kaminski, 1989) but the signal to noise ratio was too high to enable the measurement of the deep abundance of molecules such as PH_3 . New 5-μm observations are planned in the near future.

Clouds and hazes

Using the ECCM described earlier, a massive water cloud is expected to condense anywhere between 100–1,000 bar (the exact level depends on the H₂O/H₂ ratio and the deep temperature profile, both of which are uncertain); an ammonia hydro-sulphide cloud somewhere around 40 bar; either an ammonia ice cloud or a hydrogen sulphide ice cloud somewhere around 8 bar (which depends on whether the deep v.m.r. of ammonia is greater than or less than that of hydrogen sulphide, assuming that the minor species is effectively mopped up in the NH₄SH cloud leaving just the more abundant species to condense at lower temperatures); and a methane ice cloud at approximately 1.5 bar (de Pater *et al.*, 1991). As has already been discussed, the apparent depletion of tropospheric ammonia suggest that almost all the ammonia which is not dissolved in an aqueous ammonia cloud at deeper levels reacts with H₂S to form NH₄SH leaving an H₂S cloud to condense near 8 bar.

Observationally only two convective cloud decks are actually observed in the Uranian atmosphere (Figure 4.13), a thin cloud near the 1.5 bar level, and an optically thick cloud beneath with a cloud top at approximately 2.7–3.1 bar (detected using observations of the hydrogen 4-0 and 3-0 quadrupole lines, and CH₄ at 6,818 Å (Baines and Bergstrahl, 1986; Baines *et al.*, 1995b). The observed abundance of methane rapidly reduces with height at the 1.5-bar level indicating that this is indeed the methane cloud. However the optical depth of the methane cloud is found to be very thin ($0.4 < \tau < 0.7$) at low latitudes which indicates either very weak vertical mixing at this level or that particles rapidly grow and precipitate in this cloud leading to low visible reflectance. The opacity of the methane ‘haze’ is found to increase to approximately 2.4 at 65°S in Uranus’ ‘bright’ South Polar zone and the mean particle size in the methane layer is estimated to be of the order of 1 μm at all latitudes observed (Rages *et al.*, 1991). The lower cloud is probably the top of the expected hydrogen sulphide cloud although no positive spectral identification has been made. All we do know is that the aerosols in this cloud appear bright in the blue–green but darken significantly at wavelengths longer than 0.6 μm (Baines and Smith, 1990; Baines and Bergstrahl 1986). This, combined with the methane gas becoming increasingly absorbed at longer wavelengths in the visible spectrum leads to Uranus’ dominant blue–green colour. The identity of this chromophore material is unknown but may arise from ‘tanning’ of aerosols by incident UV sunlight.

As mentioned earlier, the methane observed in the stratosphere arrives there almost entirely through eddy mixing from the tropopause. Although small convective clouds are seen (Karkoschka, 1998) these are not as bright as the small clouds seen on Neptune. The northern (currently dark) hemisphere appears to be more active than the south, and the tops of these discrete clouds are estimated to be at approximately 0.5 bar with particle sizes of the order of 1 μm, similar to the properties of the methane haze layer. Hence, like Neptune, these clouds are thought to be convective methane cumulus clouds. However, unlike Neptune (as we will see), these clouds are not thought to be vigorous enough to penetrate the tropopause and thus increase the stratospheric methane to levels greater than the tropopause saturated

v.m.r. In fact, the stratospheric abundance of methane in Uranus' stratosphere is the lowest of any of the giant planets, indicating very weak vertical mixing. Methane photochemistry which is important between 10 and 0.1 mbar is expected to produce hydrocarbons such as ethane (C_2H_6), acetylene (C_2H_2), ethylene (C_2H_4), and poly-acetylenes ($C_{2n}H_2$, $n = 2, 3, 4$), although to date only acetylene has been observed. These products diffuse through the atmosphere via eddy mixing, but unlike Jupiter and Saturn, where the products diffuse through the tropopause without further processing, the temperature in Uranus' stratosphere is so low that these products actually condense to form stratospheric hydrocarbon haze layers at lower altitudes. Diacetylene ice (C_4H_2) is expected to start condensing at $p > 0.1$ mbar, acetylene ice at $p > 2.5$ mbar, and ethane-ice haze at $p > 15$ mbar. Once haze particles start to condense, they begin to coalesce to form larger particles which may then gravitationally settle out of the atmosphere. Hence the haze layers gradually thin out at pressures greater than roughly 30 mbar. The mean haze particle size is estimated to be of the order of $0.1\text{ }\mu\text{m}$ (West *et al.*, 1991) and the visible optical depth of the combined haze layers is estimated to be very low at only 0.01. The main component of the haze is modelled to be acetylene ice although the haze particles are found not to be the pure white hydrocarbon condensates that are expected, but instead are quite dark (imaginary refractive index of 0.01 in visible). The cause of this may possibly be UV-induced polymerization or ‘tanning’, which appears consistent with the dark particles that are also found in Neptune’s stratosphere. The sub-micron size of the haze particles means that they precipitate out of the stratosphere only very slowly on timescales of 10–100 years. Eventually they reach the troposphere where they are evaporated and eventually pyrolysed back to methane at sufficiently high temperatures. No very great change in the stratospheric haze optical depth with latitude has been found, which is in stark contrast to the stratospheric hazes of Jupiter and Saturn which are strongly UV absorbing near the poles. Presumably auroral processes are not so important in Uranus’ atmosphere.

4.4.4 Neptune

Composition profiles

Neptune is the most remote and most difficult to observe of the giant planets (Figure 4.22). The mean composition profiles of tropospheric and stratospheric gases in Neptune’s atmosphere are shown in Figure 4.23. Just like Uranus, Neptune appears to have a higher abundance of methane in its lower atmosphere than Jupiter and Saturn, and a much greater D/H ratio. *Voyager* radio-occultation profiles and ground-based observations of hydrogen quadrupole lines indicate a deep methane v.m.r. of 2.2% (Baines and Hammel, 1994), indicating a C/H enrichment of $\sim 40\times$ the solar value. Since interior models of Neptune suggest that it contains a greater proportion of heavy elements than Uranus, it is likely that the Neptune CH_4 mixing ratio is indeed greater than that of Uranus. Again the hydrogen–helium atmosphere observed is merely a thin shell, accounting for roughly 15% of the radius and 6% of the mass.

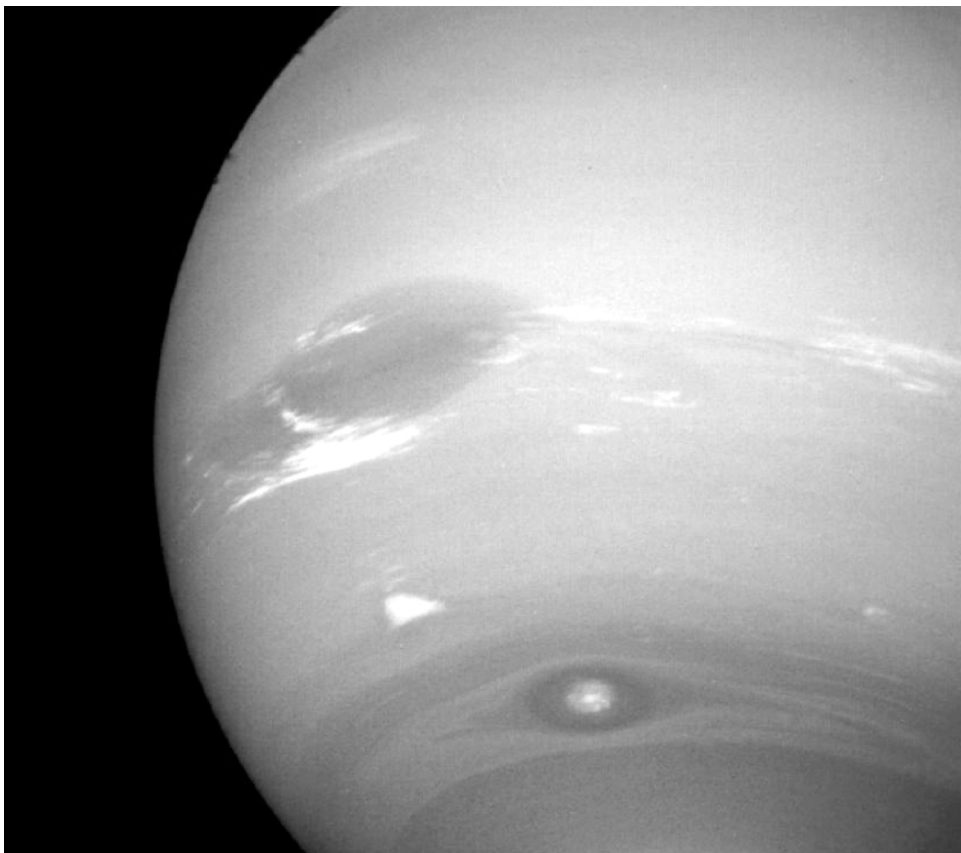


Figure 4.22 Neptune observed by *Voyager 2* in 1989.

Courtesy of NASA.

As for Uranus, ECCM calculations predict that clouds such as water and NH_4SH condense at very deep levels as can be seen in Figure 4.24 with methane condensing near 2 bar. The deep abundances are here assumed to be: O/H = $100 \times$ the solar value, N/H = the solar value, S/H = $10 \times$ the solar value, and C/H = $40 \times$ the solar value. The low N/H value and the choice of the other abundances will be discussed further in the next paragraph. Considering the measured (or assumed) high abundances of condensable species, the SALR can be seen to be very different from the DALR and thus the dry and wet temperature profiles are substantially different. The ortho-/para-hydrogen was again assumed to be in the ‘intermediate’ state outlined in Section 4.1.3.

Observations of Neptune’s composition profiles are listed in Table 4.9. Ground-based microwave observations suggest that the atmosphere of Neptune is, like Uranus, greatly depleted in ammonia by a factor of roughly 100 relative to the solar value, down to levels of approximately 50 bar. This suggests again that large

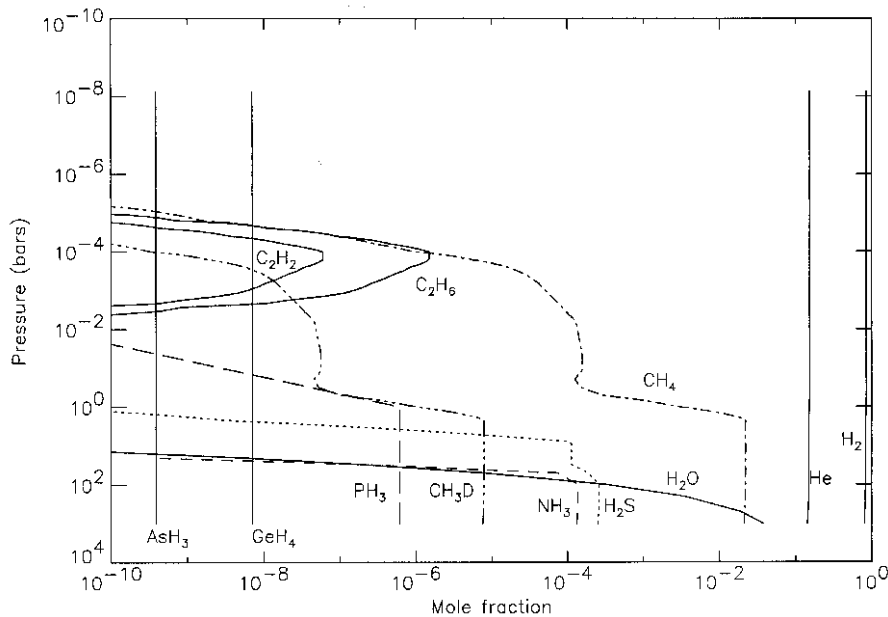


Figure 4.23 Observed and modelled abundance profiles in the atmosphere of Neptune.

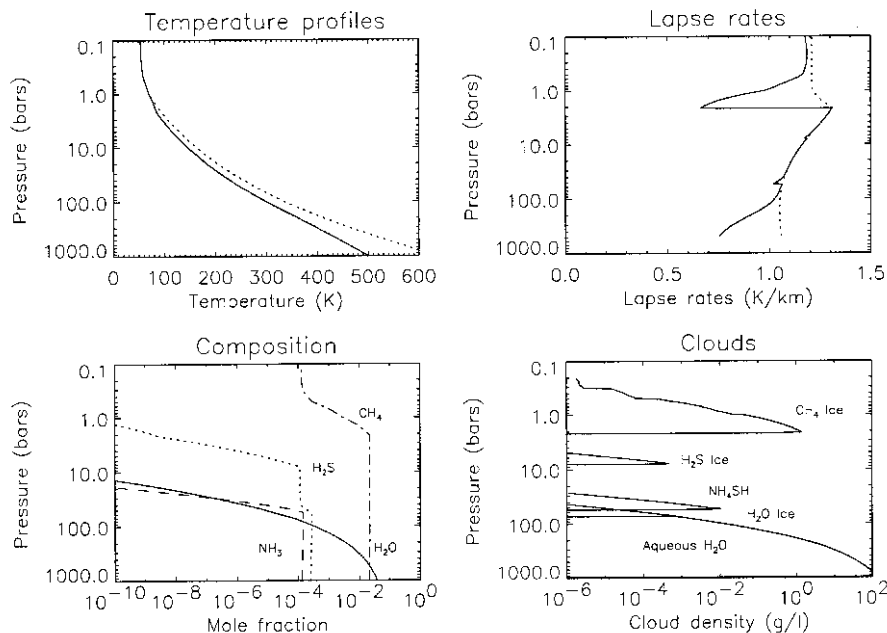


Figure 4.24 Equilibrium cloud condensation model of Neptune's atmosphere (as Figure 4.7). Calculated cloud layers: H_2O cloud (water, then ice) at $p > 1,000$ bar, NH_4SH at ~ 50 bar, H_2S ice at ~ 8 bar, and CH_4 ice at ~ 2 bar. Assumed composition: O/H = 100 × the solar value, N/H = the solar value, S/H = 10 × the solar value, C/H = 40 × the solar value.

quantities of ammonia may be locked up in an aqueous ammonia cloud, or that the abundance of H₂S exceeds that of NH₃ by a factor of at least 5 and thus that the formation of an NH₄SH cloud at ~ 40 bar effectively removes all remaining ammonia from the atmosphere. The H₂S abundance is estimated from these ground-based microwave studies to be $(10\text{--}30) \times$ the solar value. However, alternative explanations exist. For example it may just be that Neptune (and Uranus) are nitrogen-poor since formation as N₂ is not efficiently trapped in amorphous ice unless the ice-formation temperature is very cold (see Chapter 2). However, this would not be the case if the alternative clathrate-hydrate ice formation model is used. It would also appear unlikely, that Jupiter and Saturn should be nitrogen-rich, and Uranus and Neptune nitrogen-poor if these planets formed in the neighbourhood of their current distances from the Sun. Instead we would have to form Jupiter and Saturn initially at the edge of the Solar System (at ~ 30 AU) migrating inwards, and form Uranus and Neptune at 5–10 AU migrating outwards. Although at first sight this appears unlikely, the possibility cannot be ruled out! Another explanation for the low abundance of ammonia in Neptune's atmosphere is that nitrogen may instead be mostly in the form of N₂ in the observable atmosphere which is difficult to detect spectroscopically. This scenario is consistent with the observed levels of stratospheric HCN (v.m.r. $\sim 3 \times 10^{-10}$) which is most likely formed from the photolysis by-products of CH₄ and nitrogen atoms. High levels of molecular nitrogen, a disequilibrium species in the observable atmosphere of Neptune, suggests rapid convection which is consistent with Neptune's strong internal heat flux, the non-equilibrium ortho-H₂:para-H₂ ratio determinations (Conrath *et al.*, 1998), and with the presence of significant levels of tropospheric and stratospheric CO, whose v.m.r. has been estimated from millimetre and UV reflectance observations to be of the order of 1.0×10^{-6} . If a significant fraction of nitrogen in Neptune's atmosphere does exist mostly in the form of N₂ and not ammonia, then this may explain why the He/H₂ ratio derived from *Voyager* far-IR measurements exceeds the solar value, an observation which is almost impossible to theoretically explain. Assuming an N₂ v.m.r. of only 0.3% (which is equivalent to an N/H value of $\sim 40 \times$ the solar value) reduces the derived He/H₂ ratio to the solar value, which is much more plausible and is also consistent with the Uranian estimate. Once transported to the stratosphere, the rate of production of nitrogen atoms from N₂ molecules is thought to be controlled by the rate of Galactic Cosmic Ray (GCR) impacts (Lellouch *et al.*, 1994). Clearly N₂ is very much a disequilibrium species in the cold reducing atmosphere of Neptune, and thus as fast as it may be uplifted, a certain fraction per second will convert to NH₃. Why then do we still not see much ammonia in Neptune's atmosphere? It is likely that ammonia formed from N₂ at pressures less than ~ 40 bar will react with H₂S (which appears to be more abundant in the Neptune and Uranus atmospheres by a factor S/N > 5) to form NH₄SH. Alternatively NH₃ formed at pressures less than ~ 8 bar, should freeze out to form ammonia crystals. It is interesting to note that the *Voyager* 2 radio-occultation experiment estimated the ammonia v.m.r. at ~ 130 K and 6 bar to be 6×10^{-7} , which is close to the s.v.p. of ammonia under those conditions, suggesting the presence of ammonia crystals. An alternative source of nitrogen atoms in the atmosphere of Neptune may be from

Table 4.9. Composition of Neptune.

Gas	Mole fraction	Measurement technique	Reference
He	0.19 ($p < 1$ bar) 0.15 if N ₂ v.m.r is 0.003	<i>Voyager</i> far-IR <i>Voyager</i> far-IR	Conrath <i>et al.</i> (1991) Conrath <i>et al.</i> (1993)
f_{eH_2} fraction of H ₂ with eqm ortho/para	$0.63 < f_{eH_2} \leq 1.0$	Ground-based visible hydrogen quadrupole	Baines <i>et al.</i> (1995b)
NH ₃	Solar/(100–200), $p < 10$ –20 bar 6×10^{-7} (saturated) at ~ 130 K, 6 bar May be supersaturated (w.r.t. to NH ₄ SH) at $p < 20$ –25 bar. Hence greater than Uranus $(10$ –30) \times the solar value. Same as for Uranus	Radio occultation Ground-based microwave	Lindal <i>et al.</i> (1992) de Pater <i>et al.</i> (1991)
H ₂ S	$> 5 \times$ the solar value	Ground-based microwave	de Pater <i>et al.</i> (1991)
S/N	Up to $440 \times$ the solar value	Modelled to allow 1 ppm of CO	Lodders and Fegley (1994)
H ₂ O	< 100 –200 \times the solar value $(1.7$ –4.1) $\times 10^{-9}$ ($p < 0.6$ mbar)	Interior models ISO-SWS	Poddak and Marley (1991) Feuchtgruber <i>et al.</i> (1997)
CH ₄	~ 0.01 ($p > 1.5$ bar) 0.02 ($p > 1.5$ bar) 0.022 ($p > 1.5$ bar) 3.5×10^{-4} (stratosphere)	Radio occultation Radio occultation Ground-based visible reflectance	Tyler <i>et al.</i> (1989) Lindal <i>et al.</i> (1992) Baines and Hammel (1994)
CH ₄ /CH ₃ D	$6^{+6}_{-4} \times 10^{-4}$ $(3.6 \pm 0.5) \times 10^{-4}$	Ground-based 6100–6700 cm ⁻¹ Ground-based mid-IR	de Bergh <i>et al.</i> (1990) Orton <i>et al.</i> (1992)

PH ₃	No evidence of strong supersaturation, deep abundance unmeasurable	Ground-based 1–1.5 mm	Encrenaz <i>et al.</i> (1996)
AsH ₃	–	–	–
GeH ₄	–	–	–
CO	(6.5 ± 3.5) × 10 ⁻⁷ (stratosphere). Seems present in troposphere too (1.2 ± 0.4) × 10 ⁻⁶ (0.6–1.5) × 10 ⁻⁶ (0.5–2 bar) (0.7–1.3) × 10 ⁻⁶ (troposphere) 2.7 × 10 ⁻⁷ (30–80 mbar) < 1 × 10 ⁻⁶ (6 × 10 ⁻⁷ preferred) (3 ± 1.5) × 10 ⁻¹⁰ (stratosphere) (1.0 ± 0.3) × 10 ⁻⁹ (0.003–30 mbars. Confined to stratosphere) (3.2 ± 1.5) × 10 ⁻¹⁰ at 2 mbars. Approximately constant with height. Condenses at 3 mbars < 0.6%, 0.3% preferred.	Ground-based 1–1.3 mm Ground-based 1 mm Ground-based 2.6 mm Ground-based 0.87 mm UV reflectance HST Ground-based 1–1.5 mm Ground-based 1–1.3 mm Ground-based 1 mm Ground-based 1.1 mm	Rosenqvist <i>et al.</i> (1992) Marten <i>et al.</i> (1993) Guilloteau <i>et al.</i> (1993) Naylor <i>et al.</i> (1994) Courtin <i>et al.</i> (1996) Encrenaz <i>et al.</i> (1996) Lellouch <i>et al.</i> (1994) <i>Voyager</i> far-IR <i>Voyager</i> mid-IR <i>Voyager</i> mid-IR – – – – – ISO/SWS
HCN	(1.0 ± 0.3) × 10 ⁻⁹ (0.003–30 mbars. Confined to stratosphere)	–	Rosenqvist <i>et al.</i> (1992) Marten <i>et al.</i> (1993)
N ₂	–	–	Conrath <i>et al.</i> (1993)
C ₂ H ₆	1.5 × 10 ⁻⁶ (stratosphere)	–	Bézard and Romani (1991)
C ₂ H ₂	6 × 10 ⁻⁸ (stratosphere)	–	Bézard and Romani (1991)
C ₄ H ₂	–	–	–
C ₂ H ₄	–	–	–
CH ₃ C ₂ H	–	–	–
CO ₂	6 × 10 ⁻⁸ ($p < 5$ mbar)	–	Feuchtgruber <i>et al.</i> (1997)

atoms escaping from neighbouring Triton which are then captured by Neptune. Opinion is currently split on which source of atomic nitrogen is the most important, although both may be significant (Marten *et al.*, 1993; Lellouch *et al.*, 1994).

Of the other possible tropospheric species, H₂O, AsH₃, GeH₄, and PH₃, only PH₃ has any spectral thermal-IR features in regions of the spectrum where the extremely cold Neptune atmosphere emits in any strength. Even a solar abundance of phosphine is predicted to condense at Neptune's tropopause. To date no phosphine has been detected, although ground-base millimetre studies suggest that the possibility of supersaturation is very small (Encrenaz *et al.*, 1996). The formation theory of Neptune suggests that the bulk H₂O/H₂ fraction must be several hundred times the solar ratio and models suggest that just such a large fraction is necessary to account for the high abundance of CO detected (Lodders and Fegley, 1994).

The abundance of methane in the stratosphere, estimated to be 3.5×10^{-4} , is greater than the saturated vapour pressure of methane at the tropopause of Neptune which is $(1-3) \times 10^{-5}$. The implication of this is that methane must be transported to the stratosphere not just as a gas, but also as ice crystals from the troposphere which subsequently sublime at the higher stratospheric temperatures. It has been proposed that the high internal heat flux of Neptune drives moist convection which produces convection cells vigorous enough to punch their way up through the tropopause and into the stratosphere. There is good observational evidence of localized, high, thick methane clouds and other transient storms, especially at mid-latitudes, which are considered to be sufficiently vigorous to lift methane ice crystals to the stratosphere. The shadows cast by these clouds on the underlying main 3.8 bar cloud deck were occasionally observed during the *Voyager 2* flyby (Figure 4.25), and were used to determine their cloud-top altitudes, which were found to be near the 1-bar level. This is consistent with them being composed of methane crystals. Once in the stratosphere, methane is photolysed at high altitudes to form hydrocarbons. The only hydrocarbons that have been detected so far are ethane and acetylene with v.m.r.s of 1.5×10^{-6} and 6×10^{-8} respectively (Bézard and Romani, 1991). Both stratospheric water ($\sim 3 \times 10^{-9}$ at $p < 0.6$ mbar) and CO₂ (6×10^{-8} at $p < 5$ mbar) have been detected by ISO-SWS, indicating an external source of oxygen, probably via the continuing capture of interplanetary dust (Feuchtgruber *et al.*, 1997).

Clouds and hazes

To first order, the composition and pressure levels of the major cloud layers are similar to those of Uranus. Cloud layers of CH₄, H₂S, or NH₃, NH₄SH, and H₂O (ice and aqueous) are expected at about 2, 8, 50, and greater than 50 bar respectively. The H₂O cloud in particular is likely to be extremely massive, and heavily precipitating since the deep O/H ratio is thought to be several hundred times greater than the solar ratio. Again, as for Uranus, only two cloud decks are actually observed (Figure 4.13), a thin cloud near the 1.5 bar level ($\tau \sim 0.1$), and an optically thick cloud

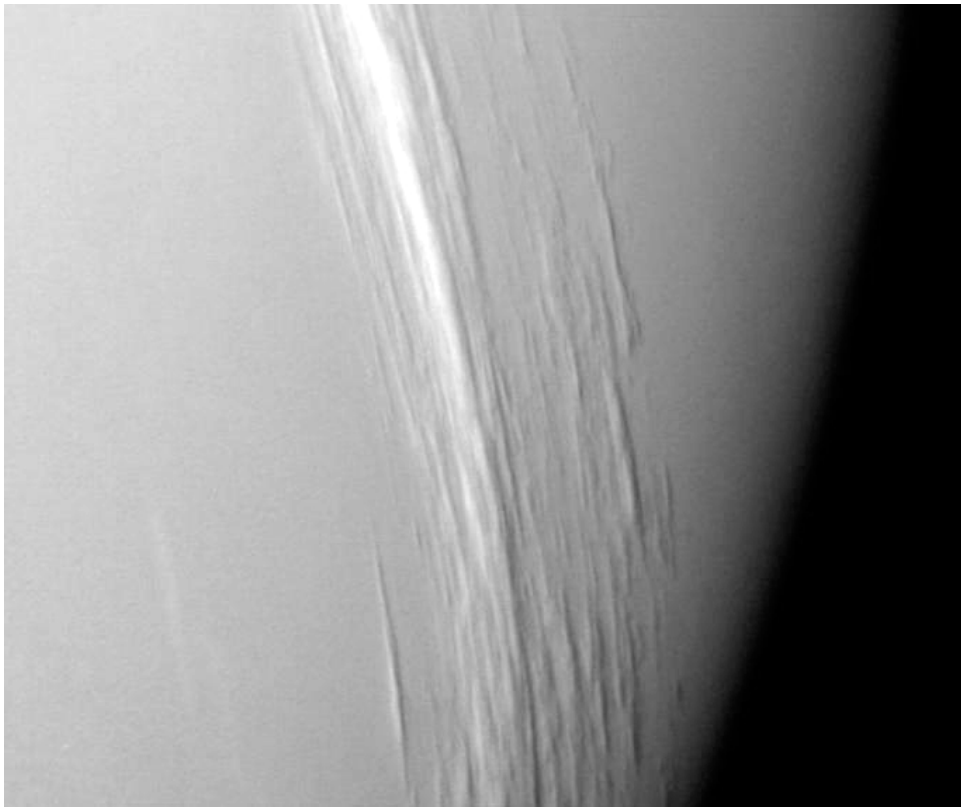


Figure 4.25 Close up of Neptune's methane clouds showing shadows cast by them on the main cloud deck beneath.

Courtesy of NASA.

beneath with a cloud top at ~ 3.8 bar (detected using observations of the hydrogen 4-0 and 3-0 quadrupole lines, and CH_4 at $6,818 \text{ \AA}$ (Baines and Hammel, 1994; Baines *et al.*, 1995a)). The observed abundance of methane rapidly reduces with height at the 1.5-bar level indicating that this is indeed the methane cloud. However the optical depth is again very much less than that predicted by ECCM models. It is thought that the particle growth in this cloud is likely to be very rapid and thus that 'rain drops' rapidly form which drop back through to below the condensation level, thus keeping the visible and near-IR optical depth of this cloud low. The deeper thick cloud is most likely the top of the expected H_2S cloud, although it has an unexpectedly strong absorption at red wavelengths which contributes to Neptune's blue colour. Clearly Neptune's main cloud deck is more red-absorbing than Uranus' since Neptune appears significantly bluer than Uranus (Baines and Bergstrahl 1986; Baines *et al.*, 1995a). The blueness of the deep cloud is puzzling since the coloration is not experimentally observed in H_2S and NH_3 ices. Irradiated frosts do have a dip in reflectance at $0.6 \mu\text{m}$, but the albedo recovers at longer wavelengths,

whereas the observed clouds are dark for $\lambda > 0.7 \mu\text{m}$. An alternative interpretation is that the 3.8 bar cloud is partially transparent (Sromovsky *et al.*, 2001) and thus that the properties may have more to do with the wavelength dependence of scattering efficiency.

Higher up in the stratosphere, methane is photolysed into hydrocarbons which diffuse down through the atmosphere and freeze out as haze layers as the temperature decreases towards its minimum of 50 K at the tropopause. Using photochemical models and estimated eddy mixing coefficients to calculate hydrocarbon v.m.r. profiles consistent with measurements, it is predicted that C_4H_2 condenses at $p > 2 \text{ mbar}$, C_2H_2 condenses at $p > 6 \text{ mbar}$, and C_2H_6 condenses at $p > 10 \text{ mbar}$ (Baines *et al.*, 1995a). The Neptunian hydrocarbon hazes appear to be more abundant and optically thicker than their counterparts in the Uranian atmosphere, and indeed absorption of sunlight by these aerosols may explain why the lower stratosphere of Neptune is some 40 K warmer than Uranus. It is estimated that 6–14% of the incident solar UV and visible flux is absorbed by stratospheric hazes. However, other sources of heating are possible, such as tidal heating by Triton, or the breaking of vertically propagating gravity waves generated in the more vigorous Neptunian troposphere. The mean particle size of the stratospheric hazes is estimated to be $0.2 \mu\text{m}$, and the average visible optical depth (619 nm) is estimated to be 0.025 (Pryor *et al.*, 1992; Baines *et al.*, 1995a). Particle formation requires the presence of foreign condensation nuclei or ions. At lower stratospheric altitudes these are provided by hazes ‘drizzling’ down from above, but at the highest altitudes the likely sources of condensation nuclei and ions, such as meteoritic material or UV and cosmic ray ionization, are limited. Hence it is likely that the hydrocarbon vapours may become significantly supersaturated before condensation starts. Indeed it has been postulated that haze formation may be episodic with partial pressures slowly rising to levels greatly in excess of the s.v.p., triggering the onset of condensation and rapid formation of haze particles, which reduce the supersaturation level to 1.0 and then fall down through the atmosphere. A particularly curious feature of Neptune’s stratospheric aerosols is that their reflectance appears to be correlated with the solar activity (Baines *et al.*, 1995a; Baines, 1997), whereas no such correlation is seen in Uranus’ stratosphere which is otherwise so similar. It has been proposed that over time the hydrocarbon aerosol particles of both Uranus and Neptune are ‘tanned’ by radiation from the Sun which makes them more absorbing, and that the rate of ‘tanning’ depends on the solar activity. On Neptune, the higher optical depth of stratospheric hazes means they contribute more to the disc-integrated reflectivity, and the particles sizes are large enough ($0.2 \mu\text{m}$) that tanned particles fall reasonably quickly through the atmosphere to be replaced by fresh white particles which themselves slowly tan. Hence there is a fair degree of correlation between solar activity and disc-averaged reflectivity. On Uranus, however, the haze particle size is estimate to be only of the order of $0.1 \mu\text{m}$ and thus these particles remain much longer in the stratosphere before settling. It is thus proposed that the haze particle residence time is a sufficiently large fraction of the solar cycle period of $\sim 11 \text{ yr}$ on Uranus that there is not such a strong tracking between mean aerosol brightness and reflectivity. In addition the haze optical

depth on Uranus is lower than on Neptune and thus any variable stratospheric haze reflectivity that might be present contributes a smaller fraction of the total disc reflectance. Neptune is the only planet whose mean albedo appears linked to solar activity. There are some problems with this theory, not least of which is its apparent inconsistency with the episodic haze formation scenario outlined earlier. However it is an intriguing possibility.

4.5 REFERENCES

- Allen, C. W. (1976) *Astrophysical Quantities* (3rd Edition). Athlone Press, University of London, London.
- Andrews, D. G. (2000) *An Introduction to Atmospheric Physics*. Cambridge University Press, Cambridge, UK.
- Andrews, D. G., J. R. Holton, and C. B. Leovy (1987) *Middle Atmosphere Dynamics*. Academic Press, London.
- Atreya, S. K. (1986) *Atmospheres and Ionospheres of the Outer Planets and Their Satellites*. Springer, Berlin.
- Atreya, S. K., M. H. Wong, T. C. Owen, P. R. Mahaffy, H. B. Niemann, I. de Pater, P. Drossart, and Th. Encrenaz (1999) A comparison of the atmospheres of Jupiter and Saturn: Deep atmospheric composition, cloud structure, vertical mixing, and origin. *Plan. Space Sci.*, **47**, 1243–1262.
- Baines, K. H. (1997) Neptune: Atmosphere. *Encyclopaedia of the Planetary Sciences*. Chapman & Hall, London.
- Baines, K. H. and J. T. Bergstrahl (1986) The structure of the Uranian atmosphere: Constraints from the geometric albedo spectrum and H₂ and CH₄ line profiles. *Icarus*, **65**, 406–441.
- Baines, K. H. and H. Hammel (1994) Clouds, hazes, and stratospheric methane abundance in Neptune. *Icarus*, **109**, 20–39.
- Baines, K. H. and W. H. Smith (1990) The atmospheric structure and dynamical properties of Neptune derived from ground-based and IUE spectrophotometry. *Icarus*, **85**, 65–108.
- Baines, K. H., H. B. Hammel, K. A. Rages, P. N. Romani, and R. E. Samuelson (1995a) Clouds and hazes in the atmosphere of Neptune. In *Neptune and Triton* (edited by D. P. Cruikshank, M. S. Matthews, and A. M. Schumann, pp. 489–546). University of Arizona Press, Tucson, AZ.
- Baines, K. H., M. E. Mickelson, L. E. Larson, and D. W. Ferguson (1995b) The abundances of methane and ortho/para hydrogen on Uranus and Neptune: Implications of new laboratory 4-0 H₂ quadrupole line parameters. *Icarus*, **144**, 328–340.
- Baines, K. H., R. W. Carlson, and L. W. Kamp (2002) Fresh ammonia ice clouds in Jupiter: Spectroscopic identification, spatial distribution, and dynamical implications. *Icarus*, **159**, 74–94.
- Banfield, D., P. J. Gierasch, M. Bell, E. Ustinov, A. P. Ingersoll, A. R. Vasavada, R. West, and M. J. S. Belton (1998) Jupiter's cloud structure from Galileo imaging data. *Icarus*, **135**, 230–250.
- Beebe, R. F. (1997) Saturn: Atmosphere. *Encyclopaedia of the Planetary Sciences*. Chapman & Hall, London.
- Bézard, B. and P. Romani (1991) Hydrocarbons in Neptune's stratosphere from Voyager infrared observations. *J. Geophys. Res.*, **96**, 18961–18975.

- Bézard, B., E. Lellouch, D. Strobel, J.-P. Maillard, and P. Drossart (2002) Carbon monoxide on Jupiter: Evidence for both internal and external sources. *Icarus*, **159**, 95–111.
- Brooke, T. Y., R. F. Knacke, T. Encrenaz, P. Drossart, D. Crisp, and H. Feuchtgruber (1998) Models of the ISO 3 micron reflection spectrum of Jupiter. *Icarus*, **136**, 1–13.
- Carlson, B., A. Lacis, and W. Rossow (1993) Tropospheric gas composition and cloud structure of the Jovian North Equatorial Belt. *J. Geophys. Res.*, **98**, 5251–5290.
- Cassini, C. F. (1666) Of a permanent spot in Jupiter: By which is manifested the conversion of Jupiter about his own axis. *Philos. Trans. R. Soc. London*, **1**, 143–145.
- Chamberlain, J. W. and D. M. Hunten (1987) *Theory of Planetary Atmospheres. An Introduction to Their Physics and Chemistry* (2nd Edition). Academic Press, San Diego, CA.
- Conrath, B. J. and D. Gautier (2000) Saturn helium abundance: A reanalysis of Voyager measurements. *Icarus*, **144**, 124–134.
- Conrath, B. J., D. Gautier, R. Hanel, G. Lindal, and A. Marten (1987) The helium abundance of Uranus from Voyager measurements. *J. Geophys. Res.*, **92**, 15003–15010.
- Conrath, B. J., D. Gautier, G. F. Lindal, R. E. Samuelson, and W. A. Shaffer (1991) The helium abundance of Neptune from Voyager measurements. *J. Geophys. Res.*, **96**, 18907–18919.
- Conrath, B. J., D. Gautier, T. C. Owen, and R. E. Samuelson (1993) Constraints on N₂ in Neptune's atmosphere from Voyager measurements. *Icarus*, **101**, 168–172.
- Conrath, B. J., P. J. Gierasch, and E. A. Ustinov (1998) Thermal structure and para hydrogen fraction on the outer planets from Voyager IRIS measurements. *Icarus*, **135**, 501–517.
- Courtin, R., D. Gautier, A. Marten, B. Bézard, and R. Hanel (1984) The composition of Saturn's atmosphere at northern temperate latitudes from Voyager IRIS spectra: NH₃, PH₃, C₂H₂, C₂H₆, CH₃D, CH₄, and the Saturnian D/H isotopic ratio. *Astrophys. J.*, **287**, 899–916.
- Courtin, R., D. Gautier, and D. Strobel (1996) The CO abundance on Neptune from HST observations. *Icarus*, **123**, 37–55.
- Davis, G. R., D. A. Naylor, M. J. Griffin, T. A. Clark, and W. S. Holland (1997) Broadband submillimeter spectroscopy of HCN, NH₃ and PH₃ in the troposphere of Jupiter. *Icarus*, **130**, 387–403.
- de Bergh, C., B. L. Lutz, T. Owen, J. Brault, and J. Chauville (1986a) Monodeuterated methane in the outer solar system. II: Its detection on Uranus at 1.6 microns. *Astrophys. J.*, **311**, 501–510.
- de Bergh, C., B. L. Lutz, T. Owen, and J.-P. Maillard (1986b) Monodeuterated methane in the outer solar system. IV: Its detection and abundance on Neptune. *Astrophys. J.*, **355**, 661–666.
- de Graauw, Th., H. Feuchtgruber, B. Bézard, P. Drossart, Th. Encrenaz, D. A. Beintama, M. Griffin, A. Heras, M. Kessler, K. Leech, E. Lellouch, P. Morris, P. R. Roelfsema, M. Roos-Serote, A. Salama, B. Vandenbussche, E. A. Valentijn, G. R. Davis, and D. A. Naylor (1997) First results of ISO-SWS observations of Saturn: Detection of CO₂, CH₃C₂H, C₄H₂ and tropospheric H₂O. *Astron. Astrophys.*, **321**, L13–L16.
- de Pater, I. (1986) Jupiter's zone-belt structure at radio wavelengths. *Icarus*, **68**, 344–365.
- de Pater, I. and S. Massie (1985) Models of millimetre-centimetre spectra of the giant planets. *Icarus*, **62**, 143–171.
- de Pater, I., P. N. Romani, and S. K. Atreya (1989) Uranus' deep atmosphere revealed. *Icarus*, **82**, 288–313.
- de Pater, I., P. N. Romani, and S. K. Atreya (1991) Possible microwave absorption by H₂S gas in Uranus' and Neptune's atmospheres. *Icarus*, **91**, 220–233.

- de Pater, I., D. Dunn, P. N. Romani, and K. Zahnle (2001) Reconciling Galileo probe data and ground-based radio observations of ammonia on Jupiter. *Icarus*, **149**, 66–78.
- Dyudina, U. and A. P. Ingersoll (2002) Monte Carlo radiative transfer modelling of lightning observed in Galileo images of Jupiter. *Icarus* (submitted).
- Encrenaz, Th. (1999) The planet Jupiter. *Astron. Astrophys. Rev.*, **9**, 171–219.
- Encrenaz, Th., E. Serabyn, and E. W. Weistein (1996) Millimeter spectroscopy of Uranus and Neptune: Constraints on CO and PH₃ tropospheric abundances. *Icarus*, **124**, 616–624.
- Encrenaz, Th., H. Feuchtgruber, S. K. Atreya, B. Bézard, E. Lellouch, J. Bishop, S. Edgington, Th. de Graauw, M. Griffin, and M. F. Kessler (1998) ISO observations of Uranus: The stratospheric distribution of C₂H₂ and the eddy diffusion coefficient. *Astron. Astrophys.*, **333**, L43–L46.
- Fegley, B. Jr. and K. Lodders (1994) Chemical models of the deep atmospheres of Jupiter and Saturn. *Icarus*, **110**, 117–154.
- Feuchtgruber, H., E. Lellouch, T. de Graauw, B. Bézard, T. Encrenaz, and M. Griffin (1997) External supply of Oxygen to the atmospheres of the Giant Planets. *Nature*, **389**, 159.
- Finn, C. B. P. (1993) *Thermal Physics* (2nd Edition). Chapman & Hall, London.
- Folkner, W. M., R. Woo, and S. Nandi (1998) Ammonia abundance in Jupiter's atmosphere derived from the attenuation of the Galileo probe's radio signal. *J. Geophys. Res.*, **103**, 22847–22855.
- Fouchet, T., E. Lellouch, B. Bézard, T. Encrenaz, P. Drossart, H. Feuchtgruber, and T. de Graauw (2003) ISO-SWS observations of Jupiter: Measurement of the ammonia tropospheric profile and the ¹⁵N/¹⁴N isotopic ratio. *Icarus*, **143**, 223–243.
- Fouchet, T., E. Lellouch, and H. Feuchtgruber (2003) The hydrogen ortho-to-para ratio in the stratospheres of the giant planets. *Icarus*, **161**, 127–143.
- Gierasch, P. J., B. J. Conrath, and J. A. Magalães (1986) Zonal mean properties of Jupiter's upper troposphere from Voyager infrared observations. *Icarus*, **67**, 456–483.
- Gierasch, P. J., A. P. Ingersoll, D. Banfield, S. P. Ewald, P. Helfenstein, A. Simon-Miller, A. Vasavada, H. H. Breneman, D. A. Senske, and the Galileo Imaging Team (2000) Observation of moist convection in Jupiter's atmosphere. *Nature*, **403**, 628–630.
- Goody, R. M. and Y. L. Yung (1989) *Atmospheric Radiation. Theoretical Basis*, (2nd Edition). Oxford University Press, Oxford, UK.
- Guilloteau, S., A. Dutrey, A. Marten, and D. Gautier (1993) CO in the troposphere of Neptune: Detection of the J = 1 – 0 line in absorption. *Astron. Astrophys.*, **279**, 661–667.
- Hecht, E. (1998) *Optics*, (3rd Edition). Addison-Wesley, Reading, MA.
- Holton, J. R. (1992) *An Introduction to Dynamical Meteorology* (3rd Edition). Academic Press, London..
- Hooke, R. (1665) A spot in one of the belts of Jupiter. *Philos. Trans. R. Soc. London*, **1**, 3.
- Irwin, P. G. J. and U. Dyudina (2002) The retrieval of cloud structure maps in the equatorial region of Jupiter using a principal component analysis of Galileo/NIMS data. *Icarus*, **156**, 52–63.
- Irwin, P. G. J., A. L. Weir, S. E. Smith, F. W. Taylor, A. L. Lambert, S. B. Calcutt, P. J. Cameron-Smith, R. W. Carlson, K. Baines, G. S. Orton, P. Drossart, T. Encrenaz, and M. Roos-Serote (1998) Cloud structure and atmospheric composition of Jupiter retrieved from Galileo near-infrared mapping spectrometer real-time spectra. *J. Geophys. Res.*, **103**, 23001–23021.
- Irwin, P. G. J., A. L. Weir, F. W. Taylor, S. B. Calcutt, and R. W. Carlson (2001) The origin of belt/zone contrasts in the atmosphere of Jupiter and their correlation with 5-micron opacity. *Icarus*, **149**, 397–415.
- Karkoschka, E. (1998) Clouds of high contrast on Uranus. *Science*, **280**, 570–572.

- Karkoschka, E. and M. G. Tomasko (1992) Saturn's upper troposphere 1986–1989. *Icarus*, **97**, 161–181.
- Karkoschka, E. and M. G. Tomasko (1993) Saturn's upper atmospheric hazes observed by the Hubble Space Telescope. *Icarus*, **106**, 428–441.
- Kunde, V., R. Hanel, W. Maguire, D. Gautier, J. P. Baluteau, A. Marten, A. Chedin, N. Husson, and N. Scott (1982) The tropospheric gas composition of Jupiter's North Equatorial Belt (NH_3 , PH_3 , CH_3D , GeH_4 , H_2O) and the Jovian D/H ratio. *Astrophys. J.*, **263**, 443–467.
- Lellouch, E., P. Romani, and J. Rosenqvist (1994) The vertical distribution and origin of HCN in Neptune's atmosphere. *Icarus*, **108**, 112–136.
- Lellouch, E., H. Feuchtgruber, Th. de Graauw, B. Bézard, and M. Griffin (1997) ESA-SP **419**, 131.
- Lellouch, E., B. Bézard, T. Fouchet, H. Feuchtgruber, T. Encrenaz, and Th. de Graauw (2001) The deuterium abundance in Jupiter and Saturn from ISO/SWS observations. *Astron. Astrophys.*, **670**, 610–622.
- Lellouch, E., B. Bézard, J. I. Moses, G. R. Davis, P. Drossart, H. Feuchtgruber, E. A. Bergin, R. Moreno, and T. Encrenaz (2002) The origin of water vapor and carbon dioxide in Jupiter's stratosphere. *Icarus*, **159**, 112–131.
- Lewis, J. S. (1995) *Physics and Chemistry of the Solar System*. Academic Press, London.
- Lindal, G. F. (1992) The atmosphere of Neptune: An analysis of radio occultation data acquired with Voyager 2. *Astronomical J.*, **103**, 967–982.
- Lindal, G. F., G. E. Wood, G. S. Levy, J. D. Anderson, D. N. Sweetnam, H. B. Hotz, B. J. Buckles, D. P. Holmes, P. E. Doms, V. R. Eshleman, G. L. Tyler, and T. A. Croft (1981) The atmosphere of Jupiter: An analysis of the Voyager radio occultation measurements. *J. Geophys. Res.*, **86**, 8721–8727.
- Lindal, G. F., J. R. Lyons, D. N. Sweetnam, V. R. Eshleman, D. P. Hinson, and G. L. Tyler (1987) The atmosphere of Uranus: Results of radio occultation measurements with Voyager 2. *J. Geophys. Res.*, **92**, 14987–15001.
- Little, B., C. D. Anger, A. P. Ingersoll, A. R. Vasavada, D. A. Senske, H. H. Breneman, W. J. Borucki, and the Galileo SSI team (1999) Galileo images of lightning on Jupiter. *Icarus*, **142**, 306–323.
- Lodders, K. and B. Fegley Jr (1994) The origin of carbon monoxide in Neptune's atmosphere. *Icarus*, **112**, 368–375.
- Massie, S. T. and D. M. Hunten (1982) Conversion of para- and ortho-hydrogen in the Jovian planets. *Icarus*, **49**, 213–226.
- Marten, A., D. Gautier, T. Owen, D. B. Sanders, H. E. Matthews, S. K. Atreya, R. P. J. Tilanus, and J. R. Deane (1993) First observations of CO and HCN on Neptune and Uranus at millimeter wavelengths and their implications for atmospheric chemistry. *Astrophys. J.*, **406**, 285–297.
- Moses, J. I., B. Bézard, E. Lellouch, G.R. Gladstone, H. Feuchtgruber, and M. Allen (2000) Photochemistry of Saturn's atmosphere. I: Hydrocarbon chemistry and comparisons with ISO observations. *Icarus*, **143**, 244–298.
- Moses, J. I., T. Fouchet, R. V. Yelle, A. J. Friedson, G. S. Orton, B. Bézard, P. Drossart, G. R. Gladstone, T. Kostiuk, and T. A. Livengood (2003) The stratosphere of Jupiter. *Jupiter*, in preparation, Cambridge University Press, Cambridge, UK.
- Naylor, D. A., G. R. Davis, M. J. Griffin, T. A. Clark, D. Gautier, and A. Marten (1994) Broad-band spectroscopic detection of the CO $J = 3 - 2$ tropospheric absorption in the atmosphere of Neptune. *Astron. Astrophys.*, **291**, L51–L53.

- Niemann, H. B., S. K. Atreya, G. R. Carignan, T. M. Donahue, J. A. Haberman, D. N. Harpold, R. E. Hartle, D. M. Hunten, W. T. Kasprzak, P. R. Mahaffy, T. C. Owen, and S. H. Way (1998) The composition of the Jovian atmosphere as determined by the Galileo probe mass spectrometer. *J. Geophys. Res.*, **103**, 22831–22845.
- Nixon, C. A., P. G. J. Irwin, S. B. Calcutt, F. W. Taylor, and R. W. Carlson (2001) Atmospheric composition and cloud structure on Jovian 5-micron hotspots from analysis of Galileo NIMS measurements. *Icarus*, **150**, 48–68.
- Noll, K. S. and H. P. Larson (1990) The spectrum of Saturn from 1990 to 2230 cm⁻¹: Abundances of AsH₃, CH₃D, CO, GeH₄, NH₃, and PH₃. *Icarus*, **89**, 168–189.
- Noll, K. S., R. F. Knacke, T. R. Geballe, and A. T. Tokunaga (1988) The origin and vertical distribution of carbon monoxide in Jupiter. *Astrophys. J.*, **324**, 1210–1218.
- Noll, K. S., T. R. Geballe, and R. F. Knacke (1989) Arsine in Saturn and Jupiter. *Astrophys. J.*, **338**, L71–L74.
- Noll, K. S., D. Gilmore, R. F. Knacke, M. Womack, C. A. Griffith, and G. Orton (1997) Carbon monoxide in Jupiter after Comet Shoemaker-Levy 9. *Icarus*, **126**, 324–335.
- Ortiz, J. L., F. Moreno, and A. Molina (1993) Absolutely calibrated CCD images of Saturn at methane band and continuum wavelengths during its 1991 opposition. *J. Geophys. Res.*, **98**, 3053–3063.
- Ortiz, J. L., F. Moreno, and A. Molina (1995) Saturn 1991–1993: Reflectivities and limb-darkening coefficients at methane bands and nearby continua—Temporal changes. *Icarus*, **117**, 328–344.
- Ortiz, J. L., F. Moreno and A. Molina (1996) Saturn 1991–1993: Clouds and haze. *Icarus*, **119**, 53–66.
- Orton, G. S., and C. D. Kaminski (1989) An exploratory 5-micron spectrum of Uranus. *Icarus*, **77**, 109–117.
- Orton, G. S., J. H. Lacy, J. M. Achtermann, P. Parmar, and W. E. Blass (1992) Thermal spectroscopy of Neptune: The stratospheric temperature, hydrocarbon abundances, and isotopic ratios. *Icarus*, **100**, 541–555.
- Orton, G., E. Serabyn and Y. Lee (2000, 2001) Vertical distribution of PH₃ in Saturn from observations of its 1-0 and 3-2 rotational lines. *Icarus*, **146**, 48–59. Corrigendum: *Icarus*, **149**, 489–490, 2001.
- Peek, B. M. (1958) *The planet Jupiter*. Faber & Faber, London.
- Podolak, M. and M. Marley (1991) Interior model constraints on super-abundances of volatiles in the atmosphere of neptune. *Bull. Am. Ast. Soc.*, **23**, 1164.
- Pollack, J. B., K. Rages, S. K. Pope, M. G. Tomasko, P. N. Romani, and S. K. Atreya (1987) Nature of the stratospheric haze on Uranus: Evidence for condensed hydrocarbons. *J. Geophys. Res.*, **92**, 15037–15065.
- Prangé, R., T. Fouchet, and R. Courtin (1998) FUV remote sensing of the atmosphere of Saturn with HST: Polar haze and latitudinal dependence of water abundance. In *The Jovian System after Galileo. The Saturnian System before Cassini-Huygens* (pp. 25–26). International Symposium, Nantes, France, 11–15 May 1998.
- Pryor, W. R., R. A. West, K. E. Simmons, and M. Delitsky (1992) High-phase-angle observations of Neptune at 2650 and 7500 Å: Haze structure and particle properties. *Icarus*, **99**, 302–317.
- Rae, A. I. M. (1985) *Quantum Mechanics*. Adam Hilger, Bristol.
- Ragent, B., D. S. Colburn, K. A. Rages, T. C. D. Knight, P. Avrin, G. S. Orton, P. A. Yanamandra-Fisher, and G. W. Grams (1998) The clouds of Jupiter: Results of the Galileo Jupiter Mission Probe Nephelometer Experiment. *J. Geophys. Res.*, **103**, 22891–22909.

- Rages, K., R. Beebe, and D. Senske (1999) Jovian stratospheric hazes: The high phase angle view from Galileo. *Icarus*, **139**, 211–226.
- Rages, K., J. B. Pollack, M. G. Tomasko, and L. R. Doose (1991) Properties of scatterers in the troposphere and lower stratosphere of Uranus based on Voyager imaging data. *Icarus*, **80**, 359–376.
- Rogers, J. H. (1995) *The Giant Planet Jupiter*. Cambridge University Press, Cambridge, UK.
- Roos-Serote, M., P. Drossart, T. Encrenaz, E. Lellouch, R. W. Carlson, K. Baines, L. Kamp, R. Mehlman, G. S. Orton, S. Calcutt, P. Irwin, F. Taylor, and A. Weir (1998) Analysis of Jupiter NEB hotspots in the 4–5 mm range from Galileo/NIMS observations: Measurements of cloud opacity, water and ammonia. *J. Geophys. Res.*, **103**, 23023–23041.
- Rosenqvist, J., E. Lellouch, P. N. Romani, G. Paubert, and T. Encrenaz (1992) Millimeter-wave observations of Saturn, Uranus, and Neptune: CO and HCN on Neptune. *Astrophys. J.*, **392**, L99–L102.
- Simon-Miller, A. A., B. Conrath, P. J. Giersch, and R. F. Beebe (2000) A detection of water ice on Jupiter with Voyager IRIS. *Icarus*, **145**, 454–461.
- Smith, B. A., L. Soderblom, R. Beebe, J. Boyce, G. Briggs, A. Bunker, S. A. Collins, C. J. Hansen, T. V. Johnson, J. L. Mitchell, R. J. Terrile, A. F. Cook, J. Cuzzi, J. B. Pollack, G. E. Danielson, A. P. Ingersoll, M. E. Davies, G. E. Hunt, H. Masursky, E. Shoemaker, D. Morrison, T. Owen, C. Sagan, J. Veverka, R. Strom, and V. E. Suomi (1981) Encounter with Saturn: Voyager 1 imaging science results. *Science*, **212**, 163–191.
- Smith, B. A., L. Soderblom, R. Batson, P. Bridges, J. Inge, H. Masursky, E. Shoemaker, R. Beebe, J. Boyce, G. Briggs, A. Bunker, S. A. Collins, C. J. Hansen, T. V. Johnson, J. L. Mitchell, R. J. Terrile, A. F. Cooke, J. Cuzzi, J. B. Pollack, G. E. Danielson, A. P. Ingersoll, M. E. Davies, G. E. Hunt, D. Morrison, T. Owen, C. Sagan, J. Veverka, R. Strom, and V. E. Suomi (1982) A new look at the Saturn system: The Voyager 2 images. *Science*, **215**, 504–537.
- Sromovsky, L. A., A. D. Collard, P. M. Fry, G. S. Orton, M. T. Lemmon, M. G. Tomasko, and R. S. Freedman (1998) Galileo probe measurements of thermal and solar radiation fluxes in the Jovian atmosphere. *J. Geophys. Res.*, **103**, 22929–22977.
- Sromovsky, L. A., P. M. Fry, T. E. Dowling, K. H. Baines, and S. S. Limaye (2001) Coordinated 1996 HST and IRTF imaging of Neptune and Triton. II: Implications of disk-integrated photometry. *Icarus*, **149**, 435–458.
- Tokunaga, A. T., S. C. Beck, T. R. Geballe, J. H. Lacy, and E. Serabyn (1981) The detection of HCN on Jupiter. *Icarus*, **48**, 283–289.
- Tyler, G. L., D. N. Sweetnam, J. D. Anderson, S. E. Borutzki, J. K. Campbell, V. R. Esheleman, D. L. Gresh, E. M. Gurrola, D. P. Hinson, N. Kawashima, E. R. Kursinski, G. S. Levy, G. F. Lindal, J. R. Lyons, E. A. Marouf, P. A. Rosen, R. A. Simpson, and G. E. Wood (1989) Voyager radio science observations of Neptune and Triton. *Science*, **246**, 1466–1473.
- Weast, R. C. (ed.) (1975) *Handbook of Chemistry and Physics* (56th Edition). CRC Press, Cleveland, OH.
- Weisstein, E. W. and E. Serabyn (1994) Detection of the 267 GHz $J = 1 - 0$ rotational transition of PH₃ in Saturn with a new fourier transform spectrometer. *Icarus*, **109**, 367–381.
- West, R., K. Baines, and J. Pollack (1991) Clouds and aerosols in the Uranian atmosphere. In *Uranus* (edited by J. Bergstrahl, E. D. Miner and M. S. Matthews). University of Arizona Press, Tucson, AZ.
- West, R. A. (1979a) Spatially resolved methane band photometry of Jupiter. II: Analysis of the SEB and STrZ reflectivity. *Icarus*, **38**, 34–53.

- West, R. A. (1979b) Spatially resolved methane band photometry of Jupiter. I: Absolute reflectivity and CTL variations in the 6190, 7250 and 8900Å bands. *Icarus*, **38**, 12–33.
- West, R. A. and M. G. Tomasko (1980) Spatially resolved methane band photometry of Jupiter. III: Cloud vertical structures for several axisymmetric bands and the GRS. *Icarus*, **41**, 278–292.
- West, R. A., M. G. Tomasko, M. P. Wijensinghe, L. R. Doose, H. J. Reitsema, and S. M. Larson (1982) Spatially resolved methane band photometry of Saturn. I: Absolute reflectivity and centre to limb variations in 6190-, 7250-, and 8900-Å bands. *Icarus*, **51**, 51–64.
- West, R. A., M. Sato, H. Hart, A. L. Lane, C. W. Hord, K. E. Simmons, L. W. Esposito, D. L. Coffeen, and R. B. Pompfrey (1983) Photometry and polarimetry of Saturn at 2640 and 7500 Å. *J. Geophys. Res.*, **88**, 8679–8697.
- West, R. A., D. F. Strobel, and M. G. Tomasko (1986) Clouds, aerosols and photochemistry in the Jovian atmosphere. *Icarus*, **65**, 161–217.
- Westphal, J. A., W. A. Baum, A. P. Ingersoll, C. D. Barnet, E. M. De Jong, G. E. Danielson, and J. Caldwell (1992) Hubble Space Telescope observations of the 1990 equatorial disturbance on Saturn: Images, albedoes and limb-darkening. *Icarus*, **100**, 485–498.
- Wong, M. H., G. L. Bjoraker, M. D. Smith, F. M. Flasar, and C. A. Nixon (2003a) Identification of the 10-μm ammonia ice feature on Jupiter. *Plan. Space Sci.* (submitted).
- Wong, M. H., S. K. Atreya, P. R. Mahaffy, H. B. Niemann, and T. C. Owen (2003b) Comparison of updated Galileo probe entry site condensable volatile profiles with the entraining downdraft model. *Icarus* (submitted).
- Yelle, R. V., J. C. McConnel, D. R. Strobel, and L. R. Doose (1989) The far ultraviolet reflection spectrum of Uranus: Results from the Voyager encounter. *Icarus*, **77**, 439–456.
- Yelle, R. V., C. Griffith, and L. A. Young (2001) Structure of the Jovian stratosphere at the Galileo Probe Entry Site. *Icarus*, **152**, 331–346.
- Yung, Y. L. and W. B. DeMore (1999) *Photochemistry of Planetary Atmospheres*. Oxford University Press, Oxford, UK.
- von Zahn, U., D. M. Hunten, and G. Lehmacher (1998) Helium in Jupiter's atmosphere: Results from the Galileo probe Helium Interferometer experiment. *J. Geophys. Res.*, **103**, 22815–22829.

4.6 BIBLIOGRAPHY

- Andrews, D. G. (2000) *An Introduction to Atmospheric Physics*. Cambridge University Press, Cambridge, UK.
- Atreya, S. K. (1986) *Atmospheres and Ionospheres of the Outer Planets and Their Satellites*. Springer, Berlin.
- Beatty, J. K. and A. Chaikin (eds) (1998) *The New Solar System* (4th Edition). Sky Publishing, Cambridge, MA.
- Bergstrahl, J., E. D. Miner, and M. S. Matthews (eds) (1991) *Uranus*, University of Arizona Press, Tucson, AZ.
- Cruikshank, D. P., M. S. Matthews, and A. M. Schumann (eds) (1995) *Neptune and Triton*. University of Arizona Press, Tucson, AZ.
- Encrenaz, T., J.-P. Bibring, and M. Blanc (1995) *The Solar System* (2nd Edition). Springer, Berlin.
- Gehrels, T. (ed.) (1976) *Jupiter*. University of Arizona Press, Tucson, AZ.

- Gehrels, T. and M. S. Matthews (eds) (1984) *Saturn*. University of Arizona Press, Tucson, AZ.
- Houghton, J. T. (1986) *The Physics of Atmospheres*, (2nd Edition). Cambridge University Press, Cambridge, UK.
- Lewis, J. S. (1995) *Physics and Chemistry of the Solar System*. Academic Press, London.
- Shirley, J. H. and R. W. Fairbridge (eds) (1997) *Encyclopaedia of the Planetary Sciences*. Chapman & Hall, London.
- Weissman, P. R., L.-A. McFadden and T. V. Johnson (eds) (1999) *Encyclopaedia of the Solar System*. Academic Press, London.

NASA Planetary images in this chapter were mostly downloaded from:

<http://photojournal.jpl.nasa.gov/>

5

Dynamical processes

5.1 INTRODUCTION

In Chapter 4 we discussed the vertical profiles of temperature, pressure, composition, and clouds of the giant planet atmospheres, and also briefly discussed transport mechanisms such as convection and eddy mixing. Of course the real atmospheres of planets are three-dimensional and thus to fully understand the observations of ground-based telescopes and spacecraft missions, we need to understand how planetary atmospheres move and how heat and material are transported, not just vertically but horizontally as well. In this chapter we will consider the basic equations of fluid motion in rotating planetary atmospheres and see how these theoretical considerations relate to the observed winds, clouds, and storm systems observed in the atmospheres of the giant planets.

5.2 MEAN CIRCULATION OF THE GIANT PLANET ATMOSPHERES

The deep interiors of the giant planets are fluid as was discussed in Chapter 2. As the planets gradually contract, heat is released via the Kelvin–Helmholtz mechanism and this heat is believed to be transported outwards mainly via convection currents, although at certain depths, conduction and radiation may become more important. In the absence of heat being removed from the top of the convective cells, parcels of air cool adiabatically as they rise and then heat adiabatically as they descend by *exactly the same amount* and the temperature profile should thus be a perfect adiabat. Of course in the upper, optically thin, observable atmosphere, some heat is lost near the top of the atmosphere by infrared (IR) radiation, cooling the air more than it would do by adiabatic expansion alone. Hence in a convective atmosphere where heat is being transported radially outwards, the temperature profile must on average be slightly sub-adiabatic, although the actual difference is in reality

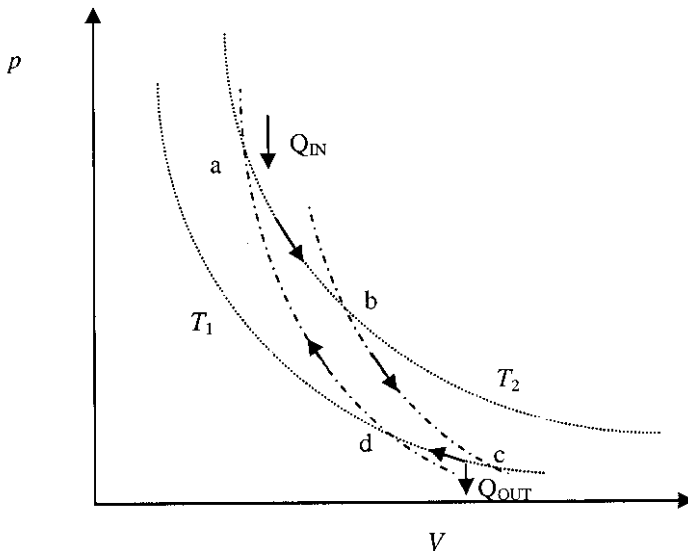


Figure 5.1 Conversion of thermal energy into kinetic energy by a Carnot heat engine moving along path abcd. The dotted lines are isotherms and dash-dotted lines are adiabats. The area of enclosed loop is proportional to the rate at which thermal energy is converted into work.

almost undetectable since the heat flow is negligible compared to the atmospheric heat capacity. Hence the deep interiors of the giant planets to all intents and purposes may be considered to be perfectly adiabatic and thus perfectly *barotropic* (i.e., there are no temperature gradients on constant pressure surfaces).

In the upper layers of the planetary atmospheres, where the atmosphere starts to become optically thin, the heating of the lower atmosphere both through absorption of sunlight, and by absorption of internal energy, provides a source of kinetic energy for atmospheric motion through a number of cycles akin to that of a heat engine shown in Figure 5.1. Consider local heating of the atmosphere. Air near the bottom of the atmosphere is heated quasi-isothermally which (in regions where free or forced convection occur) causes the air to rise and cool adiabatically. The air then radiates energy to space in the IR at the top of the atmosphere (where it is optically thin) causing it to cool further before it descends again and heats adiabatically until it reaches the bottom of the atmosphere and the cycle repeats. The integrated area of the p/V cycle is the work done per cycle, or equivalently is proportional to the rate at which thermal energy is converted into kinetic energy on a local scale. On a larger scale, solar heating is strongest at sub-solar latitudes and least near the poles (except for Uranus which spins on its side and where the sub-solar latitude varies between the equator and poles during the course of a Uranian year). Hence, in the absence of atmospheric motion, the tropics would become warmer than the poles. Such differential heating creates pressure gradients and atmospheres in general respond to this by moving in such a way as to minimize the temperature differences over the planet and become barotropic. Atmospheric motions are found to efficiently counter-

balance differential solar heating on all of the giant planets. Even Uranus, which for large fractions of its orbit receives sunlight at either the North or South Pole only, has negligible equator-to-pole temperature difference at levels where $p > 0.5$ bar. In addition to this differential solar heating, all of the giant planets with the exception of Uranus, have large internal heat sources resulting from Kelvin–Helmholtz contractions and internal differentiation. It would appear that the circulations of the giant planet atmospheres are arranged such that more of this internal energy is released away from the subsolar latitudes since the net thermal emission to space is found to be almost independent of latitude as was discussed in Chapter 1.

Before we can go on to describe the general circulations of the giant planets further we need to outline some basic atmospheric dynamics.

5.2.1 Equations of motion

Navier–Stokes equation

The fundamental equation governing the motion of air in a planetary atmosphere is the *Navier–Stokes* equation. Consider a parcel of air of volume $\delta V = \delta x \delta y \delta z$ and density ρ . From Newton’s 2nd law, $\mathbf{F} = m\mathbf{a}$ and thus

$$\mathbf{F} = (\rho \delta V) \frac{d\mathbf{V}}{dt} \quad (5.1)$$

where \mathbf{V} is the velocity vector. There are three main forces that may act on air parcels in a non-rotating planetary atmosphere: gravity, the pressure gradient force, and friction. Incorporating these forces leads to the Navier–Stokes equation in an inertial frame

$$\frac{d\mathbf{V}}{dt} = \mathbf{g}_i - \frac{1}{\rho} \nabla p + \frac{\eta}{\rho} \nabla^2 \mathbf{V} \quad (5.2)$$

where η is the viscosity and \mathbf{g}_i is the gravitational acceleration excluding centrifugal forces. In reality of course, planets rotate and thus to describe atmospheric motion we need to re-express this equation in a form suitable for a rotating frame of reference. A vector \mathbf{A} in frame S_R which is rotating at an angular velocity $\boldsymbol{\Omega}$ with respect to a stationary inertial frame S_I will have a component of motion $\boldsymbol{\Omega} \times \mathbf{A}$ in the stationary frame S_I . Hence differentiating \mathbf{A} with respect to time in the two frames leads to

$$\left(\frac{d\mathbf{A}}{dt} \right)_{S_I} = \left(\frac{d\mathbf{A}}{dt} \right)_{S_R} + \boldsymbol{\Omega} \times \mathbf{A}. \quad (5.3)$$

Putting $\mathbf{A} = \mathbf{r}$ we find

$$\mathbf{V}_I = \mathbf{V}_R + \boldsymbol{\Omega} \times \mathbf{r}, \quad (5.4)$$

and putting $\mathbf{A} = d\mathbf{r}/dt$ we have

$$\left(\frac{d\mathbf{V}_I}{dt} \right)_{S_I} = \left(\frac{d\mathbf{V}_R}{dt} \right)_{S_R} + \boldsymbol{\Omega} \times \mathbf{V}_R. \quad (5.5)$$

Combining the two we have given the expression

$$\left(\frac{d\mathbf{V}_I}{dt} \right)_{S_I} = \left(\frac{d\mathbf{V}_R}{dt} \right)_{S_R} + 2\boldsymbol{\Omega} \times \mathbf{V}_R + \boldsymbol{\Omega} \times (\boldsymbol{\Omega} \times \mathbf{r}) \quad (5.6)$$

which may be substituted into the Navier–Stokes equations to give

$$\left(\frac{d\mathbf{V}_R}{dt} \right)_{S_R} = -\frac{1}{\rho} \nabla p + 2\mathbf{V}_R \times \boldsymbol{\Omega} + \mathbf{g}_i - \boldsymbol{\Omega} \times (\boldsymbol{\Omega} \times \mathbf{r}) + \frac{\eta}{\rho} \nabla^2 \mathbf{V}_R \quad (5.7)$$

or more conveniently

$$\frac{d\mathbf{V}}{dt} = \mathbf{g} - \frac{1}{\rho} \nabla p + 2\mathbf{V} \times \boldsymbol{\Omega} + \frac{\eta}{\rho} \nabla^2 \mathbf{V} \quad (5.8)$$

where the velocity, and differentiation are assumed to be with respect to the rotating plane, and where $\mathbf{g} = \mathbf{g}_i - \boldsymbol{\Omega} \times (\boldsymbol{\Omega} \times \mathbf{r})$ is the local effective gravity which includes the centrifugal force.

Equation 5.8 can be seen to be almost identical to the equation in the inertial frame with the exception that \mathbf{g} is modified as just described and the new equation also has an additional term $2(\mathbf{V} \times \boldsymbol{\Omega})$ which arises due to the so-called *Coriolis force*. This is an apparent force experienced by objects moving in a rotating frame which, since it acts at right angles to the velocity, gives rise to circular motion. Near the equator, or at all latitudes on a slowly-rotating planet such as Venus, the Coriolis force is small and in such conditions the primary circulation tends to be a simple *Hadley cell* circulation whereby air rises at the equator, moves polewards at high altitude before descending and then returning to the equator at low altitude. For slowly-rotating planets such as Venus the descending part of the circulation is at the poles themselves and the Hadley cell is thus global in extent. However, for the Earth and the giant planets, the Coriolis force becomes significant quite close to the equator and thus air is deflected eastwards as it moves towards the poles at high altitude, and deflected westwards as it returns to the equator at low altitudes. The Coriolis force modification to the terrestrial equatorial Hadley cell, which extends from the equator to latitudes of approximately $\pm 30^\circ$, thus forces the low altitude, equatorward air to be deflected towards the west, giving rise to the easterly ‘Trade Winds’ at sub-equatorial latitudes. As mentioned, the Hadley cell breaks down at latitudes of approximately $\pm 30^\circ$ on the Earth, and for the more rapidly rotating giant planets, this critical latitude limit is substantially smaller.

To solve the Navier–Stokes equation for planetary atmospheres where the Coriolis force is important, which is clearly the case in the rapidly-rotating giant planet atmospheres, we first need to split up \mathbf{V} into its three components (u, v, w), where u is the velocity east/west in the x -direction, v is the velocity north/south in the y -direction, and w is the vertical velocity in the z -direction. Using these components we find that for a spherical planet, following the approach of Houghton (1986),

$$\frac{d\mathbf{V}}{dt} = \left(\frac{du}{dt} - \frac{uv \tan \phi}{R} + \frac{uw}{R} \right) \mathbf{i} + \left(\frac{dv}{dt} - \frac{u^2 \tan \phi}{R} + \frac{vw}{R} \right) \mathbf{j} + \left(\frac{dw}{dt} - \frac{u^2 + v^2}{R} \right) \mathbf{k} \quad (5.9)$$

where ϕ is the latitude and R is the planetary radius. Similarly the Coriolis force term may be rewritten as

$$2\mathbf{V} \times \boldsymbol{\Omega} = 2\Omega(v \sin \phi - w \cos \phi)\mathbf{i} - 2\Omega u \sin \phi \mathbf{j} + 2\Omega_u \cos \phi \mathbf{k}. \quad (5.10)$$

For the significantly oblate giant planets, Equation 5.10 must be expressed in terms of the planetographic latitude ϕ_g (introduced earlier in Chapter 2), not the planetocentric latitude. The modifications to Equation 5.9 for the oblate giant planets are more complicated, but fortunately the differences are in terms which are usually neglected since in practice it is found to be very difficult to solve the Navier–Stokes equation explicitly. Instead a number of reasonable and justifiable approximations are made. First of all, it is found to be a good approximation to assume that the wind speeds are much less than the radius of the planet, and thus that the $1/R$ terms in Equation 5.9 may be ignored. Secondly, it is assumed that the vertical wind speeds are very much less than the horizontal wind speeds. This is found to be a good approximation since the action of gravity in the vertical direction keeps departures from hydrostatic equilibrium small and frictional forces are usually negligible which means that horizontal winds, once initiated, tend to blow relatively freely. Finally it is found that the vertical component of $2\mathbf{V} \times \boldsymbol{\Omega}$, and the vertical component of friction may both be neglected compared to the gravitational acceleration \mathbf{g} . Making these approximations to the Navier–Stokes equation and resolving into components we derive the *momentum equations*:

$$\frac{du}{dt} - fv + \frac{1}{\rho} \frac{\partial p}{\partial x} = F^{(x)} \quad (5.11)$$

$$\frac{dv}{dt} + fu + \frac{1}{\rho} \frac{\partial p}{\partial y} = F^{(y)} \quad (5.12)$$

$$\frac{dw}{dt} + \frac{1}{\rho} \frac{\partial p}{\partial z} + g = 0 \quad (5.13)$$

where $f = 2\Omega \sin \phi_g$ is called the Coriolis parameter and we have written the components of friction acting in the x - and y -directions explicitly. In most cases the vertical accelerations of the winds are also negligible compared to the local gravitational acceleration and thus Equation 5.13 may be well approximated by the hydrostatic equation

$$\frac{\partial p}{\partial z} = -g\rho. \quad (5.14)$$

Further approximations may be made to these equations, including the *geostrophic approximation* which is relevant to giant planet dynamics.

Geostrophic approximation

For large-scale motion away from the planetary surface (always obeyed by the giant planets!) the frictional forces are to a first approximation negligible. Furthermore,

for steady motion with small curvature $d\mathbf{V}/dt$ is also negligible and hence the horizontal momentum equations reduce to:

$$fv = \frac{1}{\rho} \frac{\partial p}{\partial x} \quad (5.15)$$

and

$$fu = -\frac{1}{\rho} \frac{\partial p}{\partial y}. \quad (5.16)$$

These are the *geostrophic equations* and lead to the familiar situation on the Earth of winds blowing along isobars, with (for prograde spinning planets) anticlockwise motion about centres of low pressure (cyclones) in the northern hemisphere, and clockwise motion about cyclones in the southern hemisphere. To make this geostrophic approximation we need to ensure that the acceleration terms in the momentum equations are much less than the Coriolis terms and we define the *Rossby number* (Ro) to be the ratio of the acceleration to Coriolis terms for which an approximate expression is

$$Ro \approx \frac{U^2/L}{fU} = \frac{U}{fL} \quad (5.17)$$

where U is the mean wind speed and L is the typical horizontal dimension of motion. The geostrophic approximation is then valid, and thus Coriolis forces are dominant, if $Ro \ll 1$. For the giant planets, the Rossby number is estimated to be of the order of 10^{-2} (Chamberlain and Hunten, 1987) and thus to a first approximation the atmospheric flows of these planets should be geostrophic.

Thermal Wind Equation

To use the geostrophic equation to analyse flow in a planetary atmosphere, we need to know the three-dimensional pressure field. Whilst this can be measured for the Earth's atmosphere, it is almost impossible to derive from remote sensing observations of the giant planets. However, remote sensing observations can derive the three-dimensional temperature field and, if we know the wind speeds at a certain pressure level by, for example, tracking discrete cloud features at the cloud tops, then the wind speeds at all other levels can be estimated from the *Thermal Wind Equation*.

To derive the Thermal Wind Equations, the hydrostatic equation $dp = -\rho g dz$, must first be rearranged to give

$$\frac{1}{\rho} = -g \left(\frac{\partial z}{\partial p} \right)_{x,y,t} \quad (5.18)$$

which may be substituted in the geostrophic equations. Hence for the meridional component of the geostrophic equation (Equation 5.15) we have, using the above expression for $1/\rho$ together with the cyclical relation,

$$fv = \frac{1}{\rho} \frac{\partial p}{\partial x} = -g \left(\frac{\partial p}{\partial x} \right) \left(\frac{\partial z}{\partial p} \right) = g \left(\frac{\partial z}{\partial x} \right)_{p,y,t}. \quad (5.19)$$

Similarly the zonal component of the geostrophic equation may be rearranged to give

$$fu = -g \left(\frac{\partial z}{\partial y} \right)_{p,x,t}. \quad (5.20)$$

The density of the atmosphere is given by $\rho = \bar{m}p/RT$, where \bar{m} is the mean molecular weight of the air and R is the molar gas constant. Substituting this into the hydrostatic equation we find

$$g \left(\frac{\partial z}{\partial p} \right)_{x,y,t} = -\frac{1}{\rho} = -\left(\frac{RT}{\bar{m}p} \right) \quad (5.21)$$

which may be differentiated with respect to x , holding p constant, to give

$$g \frac{\partial^2 z}{\partial x \partial p} = \left(\frac{R}{\bar{m}p} \right) \left(\frac{\partial T}{\partial x} \right)_p. \quad (5.22)$$

Similarly, if we differentiate the meridional component of the geostrophic equation (Equation 5.19) with respect to p , holding x constant we find

$$f \left(\frac{\partial v}{\partial p} \right)_x = g \frac{\partial^2 z}{\partial p \partial x} \quad (5.23)$$

and thus equating Equation 5.22 and Equation 5.23 we derive

$$f \left(\frac{\partial v}{\partial p} \right)_x = \left(\frac{R}{\bar{m}p} \right) \left(\frac{\partial T}{\partial x} \right)_p \quad (5.24)$$

or

$$f \left(\frac{\partial v}{\partial p} \right)_x = \frac{1}{\rho T} \left(\frac{\partial T}{\partial x} \right)_p. \quad (5.25)$$

A similar manipulation of the zonal wind component (Equation 5.16) of the geostrophic wind equation leads to

$$f \left(\frac{\partial u}{\partial p} \right)_y = -\frac{1}{\rho T} \left(\frac{\partial T}{\partial y} \right)_p. \quad (5.26)$$

These are the *Thermal Wind Equations*. It should be noted that in deriving these equations we assumed that only temperature varied with horizontal location and that the molecular weight of the atmosphere remained constant. This is not in general true, especially for planets that have large fractions of condensable gases such as Uranus and Neptune and in these situations the thermal wind equation needs to be slightly modified.

Vorticity equation

The final concept needed to understand the general horizontal motions in giant planet atmospheres is the concept of vorticity ω which is defined simply enough as the curl of the velocity vector

$$\omega = \nabla \times \mathbf{V} \quad (5.27)$$

Vorticity is important since it (and properties derived from it) is conserved under certain conditions. The physical meaning of vorticity is that it is a measure of the spin of a fluid flow at any particular point and as such tells us something about the angular momentum of the fluid flow. For velocities measured in a frame rotating with constant angular velocity $\boldsymbol{\Omega}$ we know that

$$\mathbf{V}_I = \mathbf{V}_R + \boldsymbol{\Omega} \times \mathbf{r}. \quad (5.28)$$

Taking the curl of both sides we find

$$\boldsymbol{\omega}_I = \boldsymbol{\omega}_R + 2\boldsymbol{\Omega}. \quad (5.29)$$

For the special case of horizontal flow only, which very well approximates to the conditions in giant planet atmospheres where the zonal and meridional velocities greatly exceed vertical velocities, $\mathbf{V} \sim (u, v, 0)$, and $\boldsymbol{\omega}_R \sim (0, 0, \zeta)$ where ζ , known as the *relative vorticity*, is equal to

$$\zeta = \frac{\partial v}{\partial x} - \frac{\partial u}{\partial y}. \quad (5.30)$$

Substituting for $\boldsymbol{\omega}_R$ in Equation 5.29 we then find

$$\boldsymbol{\omega}_I = (0, 2\Omega \cos \phi_g, \zeta + 2\Omega \sin \phi_g) \quad (5.31)$$

or

$$\boldsymbol{\omega}_I = (0, 2\Omega \cos \phi_g, \zeta + f). \quad (5.32)$$

A *vorticity equation* may be derived from the x and y components of the momentum equations expressed in whatever coordinates are most convenient and taking into account any suitable approximations. For example, differentiating Equation 5.11 with respect to y and differentiating Equation 5.12 with respect to x and subtracting (ignoring frictional forces) we find that, assuming pressure and density do not vary with horizontal position and that there are no vertical motions (Houghton 1986),

$$\frac{d_h}{dt}(\zeta + f) = -(\zeta + f) \left(\frac{\partial u}{\partial x} + \frac{\partial v}{\partial y} \right) \quad (5.33)$$

where

$$\frac{d_h}{dt} = \frac{\partial}{\partial t} + u \frac{\partial}{\partial x} + v \frac{\partial}{\partial y}. \quad (5.34)$$

If the flow can be considered to be two-dimensional and non-divergent (i.e., the vertical velocities are negligible) it can be seen from Equation 5.33 that the quantity $\zeta + f$, known as the *absolute vorticity*, is conserved. We will see in Section 5.3.2 that this conservation law is the central restoring force which supports *Rossby* or *Planetary* waves. A less stringent approximation is to assume that the air has roughly constant density and temperature for which the mass continuity equation

$$\partial \rho / \partial t + \nabla \cdot (\rho \mathbf{V}) = 0 \quad (5.35)$$

becomes simply $\nabla \cdot \mathbf{V} = 0$. Substituting this into Equation 5.33 we find

$$\frac{d_h}{dt}(\zeta + f) = -(\zeta + f)\frac{\partial w}{\partial z} \quad (5.36)$$

from which it may be deduced that (Houghton, 1986)

$$\frac{d_h}{dt}\left(\frac{\zeta + f}{h}\right) = 0 \quad (5.37)$$

where h is the separation between material levels in the fluid. The quantity $(\zeta + f)/h$ is a simplified form of the *potential vorticity*, and its conservation is analogous to the conservation of angular momentum. When a parcel is vertically stretched (and hence made thinner by conservation of mass) it rotates faster to maintain its angular momentum in the same way as an ice skater spins faster when they draw their arms inwards. The most general form of the potential vorticity is Ertel's potential vorticity which is defined as

$$q_E = \frac{\zeta}{\rho} \cdot \nabla \theta \quad (5.38)$$

where θ is the potential temperature defined later in Section 5.3.1. This quantity may be calculated from the temperature/pressure maps fitted to measured data and since q_E is conserved (under frictionless, non-diabatic heating cases) maps of this quantity may also be used as a tracer for atmospheric motion. A more approximate expression for potential vorticity is the quasi-geostrophic expression described for example by Andrews (2000).

Taylor–Proudman theorem

Another form of the vorticity equation is derived by Chamberlain and Hunten (1987) (p. 106, Equation 2.6.4) in isobaric coordinates for steady, slow motions in a frictionless atmosphere with acceleration terms and quadratic terms being negligible:

$$\frac{\partial(\zeta + f)}{\partial t} \approx -f \nabla_p \cdot \mathbf{V} = 0 \quad (5.39)$$

where ∇_p is the gradient along isobars and $\mathbf{V} = (u, v, 0)$. Again, applying the continuity equation, this relation implies that $\partial \omega / \partial p = 0$, where $\omega = dp/dt$ is the equivalent of vertical velocity in pressure coordinates. This implies that ω equals a constant and the only physical solution is that $\omega = 0$ and thus that, to a first approximation, all steady motions in a rotating atmosphere with zero viscosity must be barotropic. This is a fundamental conclusion and is equivalent to the *Taylor–Proudman theorem* in hydrodynamics which we shall come across again later.

5.2.2 Mean zonal motions in the giant planet atmospheres

All the giant planets are found to have a very stable, zonal banded structure of cloud opacity and wind structure with the winds blowing strongly in the east–west direction with very little mean meridional motion. The fact that these planets have

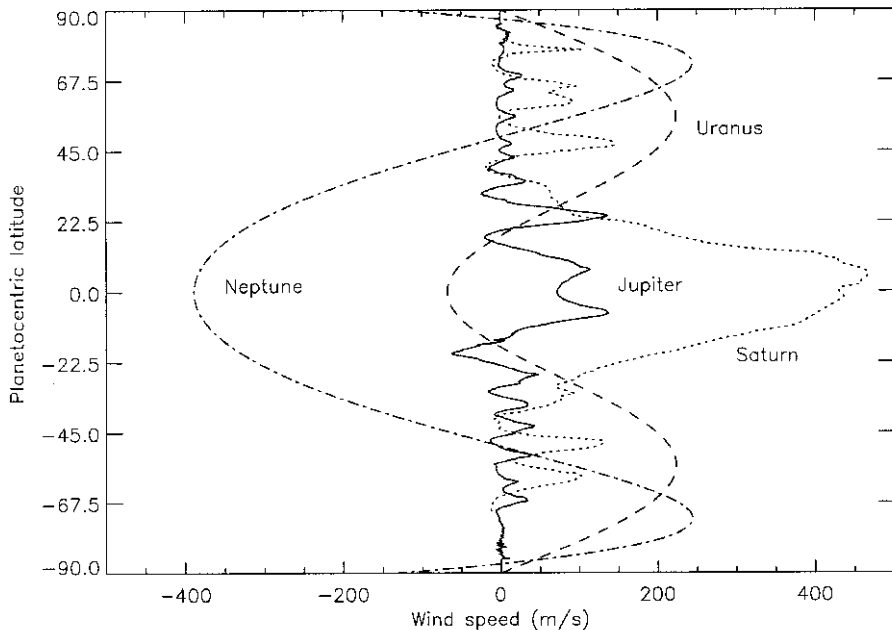


Figure 5.2 Zonal wind structure of the giant planets. Solid line: Jupiter, dotted line: Saturn, dashed line: Uranus, dot-dashed line: Neptune. The sources of these wind speeds are: Jupiter – Vasavada (2002), Porco *et al.* (2003); Saturn – Sanchez-Lavega *et al.* (2000); Uranus – Hammel *et al.* (2001); Neptune – Stromovsky *et al.* (1993).

such different solar flux and internal energy forcings suggests that the zonal structure derives from the nature of these planetary atmospheres themselves, together with their rapid rotation, rather than due to the method of forcing. The measured zonal wind speeds at the cloud tops for the four giant planets are shown in Figure 5.2 together with images of the mean visible appearance in Figure 5.3 upon which have been superimposed the wind speeds in terms of degrees longitude per rotation of the planet. It can be seen that there is very close north/south symmetry in the wind structure for all four planets. For Jupiter, the wind variations are closely associated with visible cloud features where cyclonic vorticity shear regions ($du/dy < 0$, or anticlockwise relative rotation in the northern hemisphere) are seen as visibly dark, relatively cloud-free ‘belts’, while anticyclonic vorticity shear regions ($du/dy > 0$, or clockwise rotation in the northern hemisphere) are seen as visibly bright cloudy ‘zones’. The mean cloudiness of the belts/zones is confirmed by observations of the thermal emission at $5\text{ }\mu\text{m}$, where the cloud-free belts allow radiance to escape from the warm 5–8 bar pressure levels underneath, while the cloudy zones appear dark. Hence the visible and near-IR albedo is closely anticorrelated with the $5\text{ }\mu\text{m}$ brightness (Irwin *et al.*, 2001). The belt/zone structure of Saturn appears much blander than that of Jupiter due to the greater obscuration by tropospheric haze (Chapter 4), but there appears to be a more fundamental difference in that there is

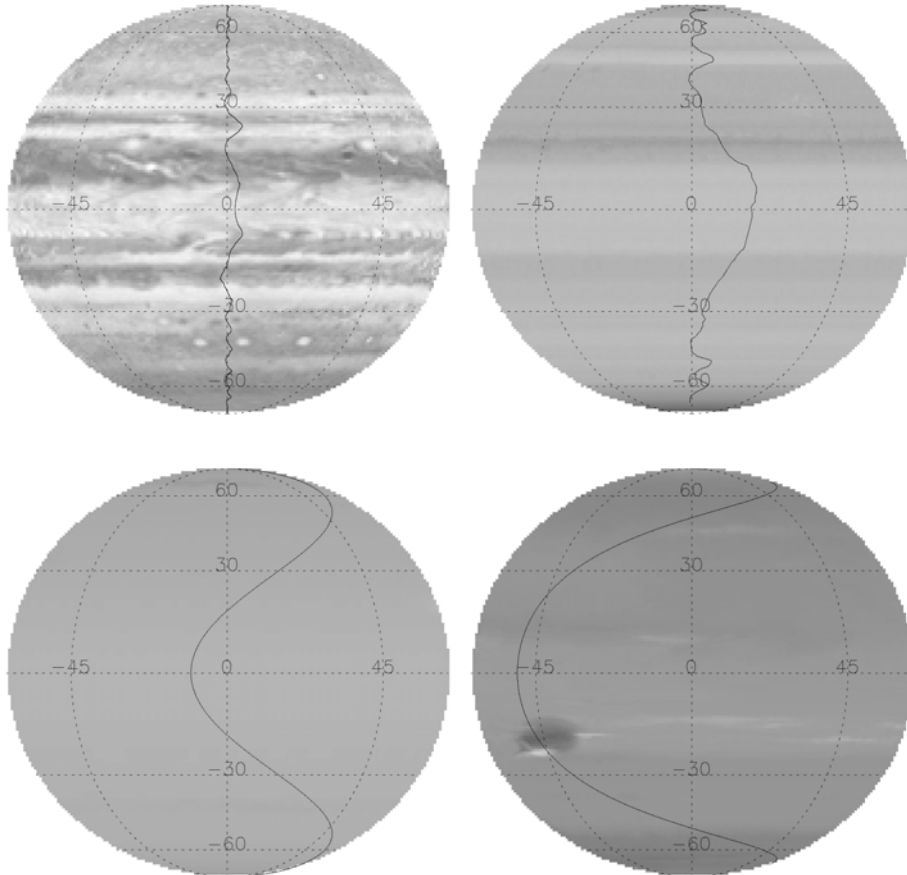


Figure 5.3 Zonal wind structure of the giant planets superimposed onto representations of their visible appearance. The wind speeds have been converted into degrees longitude/rotation of the planet. Note that the figures in the discs refer to degrees latitude and longitude, and not to wind speed.

Planetary images based on NASA data and processed by James Hastings-Trew and Björn Jónsson (<http://www.media.is/~bjj>).

less correspondence between wind shear and albedo. In fact, the Saturn belts/zones appear better correlated with the mean zonal wind than they do with the wind shear. The appearance of Saturn in the 5- μm window has also recently been recorded from ground-based observations. While there is a greater component of reflected sunlight in Saturn's 5- μm spectrum, the observed radiance is, like Jupiter, principally due to thermal emission of the deep atmosphere especially at the long wave end of the window at 5.2 μm (Yanamandra-Fisher *et al.*, 2001). However, unlike Jupiter there is observed to be little correlation between the 5.2- μm brightness and the visible albedo although the main bright 5- μm band seen between 38°S and 49°S does seem to coincide with an eastward jet. Since the 5- μm observations map the total cloud opacity above the 5-bar level on Saturn there again seems to be less, or perhaps

a different correlation between cloud opacity and zonal wind flow. Investigating this further will be a major goal of the forthcoming *Cassini/Huygens* mission which arrives in Saturn orbit in 2004.

Measurements of the mean thermal emission as a function of latitude by *Voyager* (and more recently *Cassini* for Jupiter) may be used to calculate the zonal thermal vertical wind shears which, combined with the measured cloud top winds (assuming the pressure level of this is accurately known) can be used to calculate the zonal wind speed as a function of height. On all four giant planets, the zonal winds are found to decay with height to zero within about 3–4 scale heights of the cloud tops. The nature of the frictional force that this braking implies is not clear, although it is believed that the breaking of gravity waves or eddy motions may play a role. The latitude dependence of temperature in the upper troposphere may also be used to deduce meridional motion. Latitude bands with warmer than average temperatures imply horizontal convergence and thus presumably subsidence below, while cooler latitudes imply divergence and thus upwelling from below. On Jupiter it is found that anticyclonic, more cloudy latitudes, are cooler in the upper troposphere while cyclonic, less cloudy latitudes, are warmer leading to the canonical view of the flow in the Jovian atmosphere, shown in Figure 5.4, that zones are regions of moist, upwelling air and belts are regions of subsiding, dry air. Recent *Cassini* observations suggest that this view may in fact be the wrong way round since convective clouds are found to occur exclusively in belts, and not zones. Unfortunately the picture for Saturn is again not quite so clear-cut. However

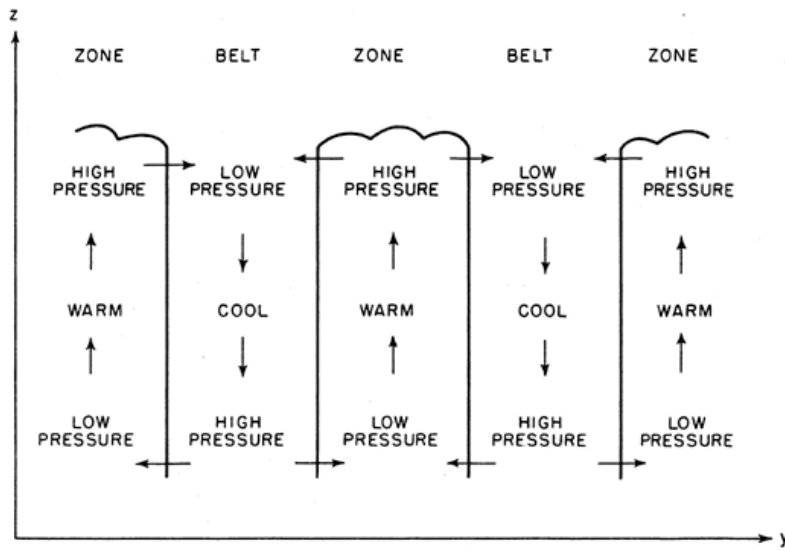


Figure 5.4 Stone's (1976) canonical zonal flow diagram of Jupiter where bright 'zones' are regions of upwelling and thus divergence at the top of the atmosphere, and 'belts' are regions of convergence and subduction. While this model fits well with the Jovian cloud structure and zonal winds, it less successfully models the flows in the other giant planet atmospheres.

From Stone (1976). Reprinted by permission of the University of Arizona Press. © Arizona Board of Regents.

one similarity between the zonal wind structure of Jupiter and Saturn is that the equatorial jet appears to have ‘horns’ in that the wind speed first initially increases away from the equator before rapidly diminishing. Such a structure is consistent with a small Hadley cell centred at the equator where air rising at the equator (and thus forming the zone’s bright clouds) then moves polewards at the cloud tops and picks up zonal speed due to the conservation of angular momentum, or equivalently the conservation of vorticity, before descending at the edges of the zone.

Jupiter and Saturn have similar zonal wind patterns, with a strong eastward, or *prograde*, jet at the equator and rapidly varying wind direction towards both poles. At the equator, the air is effectively rotating faster than the bulk of the planet and thus is described as ‘super-rotating’. How such a state might be driven is extremely puzzling since it can be proved that no axisymmetric (i.e., zonal-mean) process can lead to such a state. Instead, non-linear wave interactions are required such as diffusive small-scale eddies, or gravity/Kelvin/Rossby waves discussed later. The nature of the super-rotation of the equatorial atmospheres of Jupiter and Saturn, and indeed the observed super-rotation of the slowly rotating worlds of Venus and Titan is an area of very active research.

The zonal wind profiles of Uranus and Neptune are completely different to those of Jupiter and Saturn, having a very smooth, slow variation of zonal wind speed with latitude, and *retrograde* equatorial jets. Uranus has a particularly bland appearance in the visible with a hint of brighter albedoes at the equator and poles and darker albedoes in mid-latitudes where the winds are eastward. Neptune also seems to show the same correspondence. The wind shear is anticyclonic at mid-latitudes and cyclonic at the poles, suggesting upwelling at mid-latitudes and subsidence at the equator and poles. This view is supported by *Voyager* and more recently the Hubble Space Telescope (HST) observations of these planets which show convective activity in the upper methane cloud layers at just these darker mid-latitudes. In addition, measurements of the zonal temperature structure show the upper troposphere to be warm at the equator and poles but cooler at mid-latitudes, which fits nicely with this picture. Hence the brighter albedoes observed at the equator and poles are believed to be due partly to the concentration of upper tropospheric haze in the convergence zones above the poles and equator and also partly due to either the cloud-top pressure or colour of the main presumed H₂S cloud. Why the atmospheric circulations of Uranus and Neptune should be so different to Jupiter and Saturn is not known.

An indicator of vertical and meridional flow in the atmospheres of the giant planets is the variation in the observed para-H₂ fraction, or f_p . The simultaneous variation of f_p and temperature with latitude and over a small height region of approximately 1 scale height width centred approximately at 300 mbar has been calculated from *Voyager* IRIS measurements by Conrath *et al.* (1998) for all four giant planets. More recent analysis of the far-IR hydrogen quadrupole lines observed by the Infrared Space Observatory Short Wavelength Spectrometer (ISO/SWS) has allowed disc-averaged estimates of the stratospheric f_p value at 1 and 10 mbar as well (Fouchet *et al.*, 2003). For Jupiter, the upper tropospheric temperatures are found to be cool above zones and warm above belts while f_p is found to be low and high

respectively supporting the view of uplift and subsidence. The picture for Saturn is not so clear since considerable north/south asymmetry is apparent showing that this planet is more affected by seasonal forcing. However, some regions of low temperatures, such as at 60°S have low f_p indicating upwelling and others which have higher than average temperature such as at 15°S have higher f_p . The upper tropospheric temperatures of Uranus have the variation mentioned earlier in that the coolest temperatures are found above mid-latitudes. There was also substantial seasonal asymmetry at these upper tropospheric pressures with the temperatures considerably warmer in the south at the time of the *Voyager* observations. The para- H_2 fraction is found to be lowest at southern latitudes and highest at northern latitudes suggesting upwelling in the south and subsidence in the north. Finally, Neptune has a more symmetric temperature structure which is coolest at mid-latitudes. These regions correspond to low f_p which is consistent with the model that these are regions of rapid uplift.

For many years, the jets were assumed to be confined to the upper weather layer of the atmosphere and not extend into the interior. The generally accepted explanation of the observed belts and zones (discussed earlier and shown in Figure 5.4) is that, due to unspecified frictional drag processes in anticyclonic shear regions where the Coriolis force is balanced by high pressures (assuming the geostrophic approximation), the flow is divergent within the clouds and at the cloud tops, but convergent beneath. Therefore, anticyclonic regions were preferentially heated from below by latent heat release (Ingersoll, 1990). This heating would act to sustain the anticyclone by heating the core, and from the Thermal Wind Equation increasing the anticyclonicity with altitude, thus causing more divergence in the clouds. This explanation is certainly consistent with the zonal cloud structure on Jupiter, but is far less successful in explaining the belt/zone structure of the other planets. It also suffers from further flaws: (1) it does not actually explain the banded appearance of the planets since it works equally well for isolated anticyclonic spots as it does for extended anticyclonically sheared zones; and (2) it relies on difficult-to-observe (and estimate) processes such as frictional drag and latent heat release. One aspect of this picture that can easily confuse is that on the Earth we are familiar with anticyclones (high pressure regions) being regions of downwelling, cloud free air, while cyclones (low pressure regions) are regions of upwelling, cloudy air. This is clearly the opposite of what is found on the giant planets! However it must be remembered that the Earth has a definite lower boundary and thus it is the frictional forces near the ground that cause convergence at the base of low pressures and divergence at the base of high pressures. On the giant planets there is no such lower boundary and thus the nature of any deep frictional forces responsible for any meridional flow is unclear. However, the giant planets do appear to have an upper boundary in that the zonal winds are found to decay with height presumably due to some kind of frictional damping. If this is also the main source of the friction driving the meridional circulations then the ‘highs’ and ‘lows’ on the giant planets have friction at their tops rather than at their bottoms, which would account for their inverted properties relative to their terrestrial cousins.

For all the giant planets, although there is evidence for significant turbulence

and wave activity, the zonal winds appear to be extremely stable, and have not altered greatly since observations of these planets began. In order to investigate the stability, driving, and dissipation of the zonal mean circulation, we need to introduce the basic theory of eddy motion in the giant planet atmospheres.

5.3 EDDY MOTION IN THE GIANT PLANET ATMOSPHERES

The basic motion of the giant planet interiors is almost certainly barotropic up to pressure levels where the visible and thermal-infrared optical depth of the atmosphere becomes small enough to allow both solar heating and radiation to space. Hence while horizontal temperature variations are observed on the giant planets at pressures less than about 1 bar, temperature variations are observed to decrease at higher pressures and presumably rapidly diminish to zero in the deep atmosphere. The dominating barotropic nature of the flow, combined with the large Coriolis forces on the giant planets, low viscosity, and the absence of significant surface friction, seems to result in a simple zonal circulation for all four giant planets. However, while the molecular viscosity is low, turbulence in the atmosphere leads to considerable eddy viscosity. This, together with differential solar heating, leads to time-varying eddy motions (where by eddy motion we technically mean anything departing from the mean flow) including turbulence, large-scale vortices, and waves which will be discussed below.

5.3.1 Turbulence in the giant planet atmospheres

Although the atmospheres of these planets are very deep, the magnitude of the gravitational force greatly exceeds anything else, and so the flow is to a first approximation two-dimensional. Under such conditions, any turbulence that is generated in the flow has the counter-intuitive property of being converted into larger and larger scale eddies. This is exactly the opposite of what occurs in more familiar three-dimensional turbulence, where turbulence cascades into smaller and smaller scales, a classic example being the break-up and dispersion of a smoke ring. The process is called the backwards energy cascade (Charney, 1971) and has fundamental consequences for planetary atmospheres. Turbulence in a planetary atmosphere may arise through a number of mechanisms such as static instability, where the atmosphere is unstable to convective overturning, or in cases where there is excessive horizontal or vertical wind shear. In general, it is found that once turbulence is initiated, the associated energy may be dissipated due to friction, or transfer of energy to the mean flow. It can be shown (Andrews *et al.*, 1987) that many forms of turbulence will persist provided that a quantity known as the *Richardson Number* (Ri), is less than approximately one, where

$$Ri = \frac{gS}{T(\partial u / \partial z)^2}. \quad (5.40)$$

Here g is the gravitational acceleration, S is the static stability described below, T is the temperature, and u is the zonal (east–west) wind. In addition to assessing

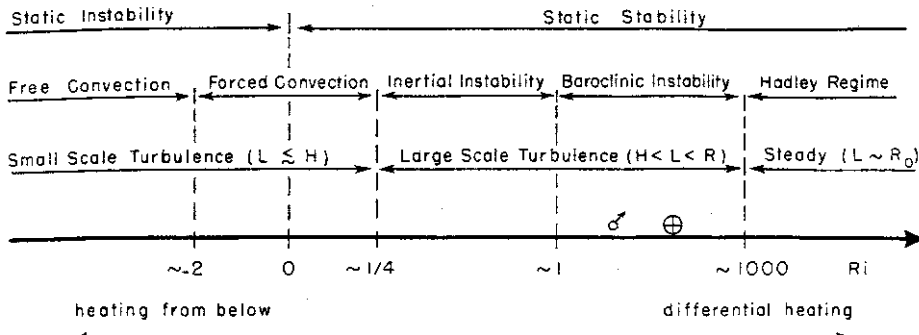


Figure 5.5 Stone's (1976) regime diagram of the main characteristic atmospheric motion as a function of the Richardson number (Ri).

From Stone (1976). Reprinted by permission of the University Arizona Press. © Arizona Board of Regents.

turbulence, the Richardson Number provides a very useful measure of the dominant heat transporting modes on planets as described by Stone (1976). Negative values of Ri (hence persistent turbulence) are associated with static instability and free convection. Large positive numbers are associated with Hadley cell circulations. A summary diagram of the different heat transfer modes associated with different Ri on the giant planets is shown in Figure 5.5 from Stone (1976).

For the giant planets, assuming geostrophic conditions and barotropic flow, turbulent eddies are predicted to grow and absorb smaller disturbances until their size reaches the *Rhines length* L_β (Rhines, 1973, 1975)

$$L_\beta = 2\pi \sqrt{\frac{2U}{\beta}}, \quad (5.41)$$

where U is the mean wind speed and the β -parameter is defined in Equation 5.46, when the disturbance is converted to planetary waves and the backwards energy cascade terminates. Thus eddies have a maximum scale, and this is likely to be related to the zonal structure scale. This property provides one link between U and L for the giant planets but another condition is required to uniquely determine both the length and velocity scales. The other condition may be provided by the *radius of deformation*, which is the length scale at which Coriolis effects become significant, described in Section 5.3.2, and which is found to be similar to the width of the zones on Jupiter (Gierasch and Conrath, 1993), although this conclusion depends on the assumed static stability.

We will now outline some of the instability mechanisms which may, or may not, be responsible for turbulence in the giant planet atmospheres, and which are also summarized for convenience in Table 5.1 after Stone (1976).

Static instability

The simplest form of instability is static instability whereby the temperature decreases with height more rapidly than the adiabatic lapse rate. The static

Table 5.1. Instability criteria (from Stone, 1976).

Dynamical mode (source)	Criteria for instability	Structure	Characteristic horizontal scale	Characteristic timescale
Barotopic instability	$\frac{d^2u}{dy^2} > \beta$	3-D	$\pi \left(\frac{u}{\beta} \right)^{1/2}$	$\frac{10}{(u\beta)^{1/2}}$
Baroclinic instability	$Ri > 0.84$	3-D	$2 \frac{u}{f} (1 + Ri)^{1/2}$	$\frac{3}{f} (1 + Ri)^{1/2}$
Inertial instability	$0 < Ri < 1$	Axially symmetric	$2 \left(\frac{u}{\beta} \right)^{1/2} \left(\frac{Ri^2}{1 - Ri} \right)^{1/4}$	$\frac{1}{f} \left(\frac{Ri^2}{1 - Ri} \right)^{1/2}$
	or			
	$f - \frac{du}{\partial y} < 0$			
Radiative instability	(See p. 151)	Axially symmetric	$2 \frac{(\alpha g H^2 S)^{1/4}}{\beta^{1/2}}$	$\frac{\tau}{2} \alpha HS$
Free convection	$S < 0$	3-D	$\sim H$	$\sim (\alpha g S)^{-1/2}$

α is the thermal expansion coefficient ($= 1/T$) and τ is the radiative relaxation time (from Stone, 1976).

stability S of an atmosphere is defined as the rate of change of potential temperature with height

$$S = \frac{\partial \theta}{\partial z}. \quad (5.42)$$

The potential temperature is defined as the equivalent temperature of an air parcel if it is compressed or expanded adiabatically (along a dry adiabat) to a reference pressure p_0 , usually 1 bar, and may be shown to be equal to

$$\theta = T \left(\frac{p_0}{p} \right)^{R/C_p} \quad (5.43)$$

where R is the universal molar gas constant and C_p is the molar heat capacity at constant pressure. In an atmosphere where the temperature T falls with height at the dry adiabatic lapse rate, the potential temperature is constant with height and thus S is zero. For an atmosphere which is diabatically heated by, say, direct absorption of sunlight through gas absorption or aerosol absorption, the temperature falls less quickly with height and may, as in the stratospheres of the giant planets, actually rise. In such cases S is positive, and the atmosphere is convectively stable. A parcel displaced vertically and adiabatically will be cooler, and so less buoyant than the surrounding air, and will thus sink back to its original level (in fact it may oscillate about its original level as we shall see in Section 5.3.2). If S is negative, then the temperature falls with height more quickly than the lapse rate. Such a situation is unstable since a parcel displaced vertically and adiabatically will be warmer, and so more buoyant than the surrounding air and will thus continue to rise. Whether the atmosphere actually turns over or not depends on the magnitude of the instability

and the viscosity of the air (Chamberlain and Hunten, 1987). Clearly static instability dominates for $Ri < 0$.

Kelvin–Helmholtz instability

Another source of turbulence is vertical wind shear, and examples are Kelvin–Helmholtz instabilities which occur for $0 < Ri < 0.25$. Such instability accounts for the formation of waves on the surface of the sea, and also for the so-called ‘Mackerel Skies’ seen in upper cloud layers of the Earth during the approach of bad weather.

Inertial instability

Inertial instability arises from mismatches between the pressure gradient force and centrifugal forces for a parcel displaced radially in an axisymmetric vortex (Andrews *et al.*, 1987), and are found to be important for atmospheres where $0.25 < Ri < 1$. They are driven primarily by the vertical eddy stresses associated with the vertical wind shear of thermal winds and transport heat both down the horizontal temperature gradient and vertically upwards thereby increasing both the static stability of the atmosphere and Ri .

Inertial instability has been proposed as a mechanism to account for the formation of banded structures in giant planet atmospheres since it leads to axisymmetric (i.e., independent of longitude) motions, consistent with the banded structure (Stone, 1976). Inertial instability may also explain the cloud structure on smaller scales such as in the Great Red Spot (GRS) since a second condition for inertial instability is that the absolute vorticity is negative, i.e.,

$$f - \frac{\partial u}{\partial y} < 0 \quad (5.44)$$

or equivalently that the potential vorticity changes sign. It can be seen that the second condition for inertial instability favours regions of anticyclonic vorticity. Hence in such anticyclonic eddies, inertial instability may create turbulence and thus enhanced cloudiness, as is observed.

Barotropic instability

The word *barotropic* refers to cases where there are no temperature gradients on constant pressure surfaces (i.e., there is no differential heating). This means that the basic zonal winds do not vary with height as can be understood from the Thermal Wind Equations. Under such conditions, instabilities arise mainly through excessive horizontal curvature of the basic flow profile (Andrews *et al.*, 1987). For barotropic waves in a shallow-atmospheric flow where the height of the lower boundary is fixed, it may be shown (Houghton, 1986) that the condition for instability is the *Rayleigh*–

Kuo criterion which states that barotropic waves confined within a certain latitude band are stable unless the quantity

$$\beta - \frac{d^2\bar{u}}{dy^2} \quad (5.45)$$

changes sign somewhere within the latitude band, where the beta-parameter (β) is the latitudinal gradient of planetary vorticity defined as

$$\beta = \frac{df}{dy} \approx \frac{2\Omega \cos \phi_g}{R} \quad (5.46)$$

where R is the planetary radius at the latitude in question. The barotropic instability condition is equivalent to saying that the meridional gradient of potential vorticity must change sign somewhere in a domain. While this may appear similar to inertial instability, barotropic instability is fundamentally different, not least because the Richardson Number for barotropic conditions is poorly defined since the vertical wind shear in Equation 5.40 is zero.

Baroclinic instability

The word *baroclinic* refers to cases where temperature *does* vary on constant pressure surfaces. From the Thermal Wind Equation this implies that the zonal winds *do* vary with height. Hence baroclinic instabilities depend, broadly speaking, on the vertical curvature of the flow. However the flow under baroclinic conditions may also have large horizontal curvature and thus under these conditions, the relevant instability criterion is the *Charney–Stern* criterion (Andrews *et al.*, 1987) which states that a shallow-atmosphere baroclinic wave confined within a certain latitude band is stable unless the quantity

$$\beta - \frac{d^2\bar{u}}{dy^2} - \rho_0^{-1}(\rho_0 \varepsilon \bar{u}_z)_z \quad (5.47)$$

changes sign, where $\varepsilon(z) = f_0^2/N_B^2(z)$ and N_B is the Brunt–Väisälä frequency defined in Section 5.3.2. Baroclinic instabilities give rise to the mid-latitude storms seen in the Earth’s atmosphere but their importance in the Jovian atmospheres is unclear. Baroclinic instabilities are important for $Ri > 0.84$.

Radiative instability

This is a possible mechanism which has been proposed to account for the banded structure of the giant planets. If, in a condensing region of the atmosphere, the condensate enhances the greenhouse effect, then the increased thermal blanketing heats the atmosphere further thus enhancing the vertical convection via positive feedback. Latitudinal temperature differences would then drive strong zonal winds from the thermal wind equation.

5.3.2 Waves in the giant planet atmospheres

We saw in the previous section that turbulent motion arises when parcels that are deflected from their original positions feel forces which pull them further from their

equilibrium positions. In some circumstances however, displaced parcels may feel forces that return them to their equilibrium positions. Such forces give rise to a wide range of wave motions which are clearly observed in all planetary atmospheres, including those of the giant planets.

The two main properties of planetary atmospheres that may lead to waves (ignoring sound waves) are vertical stratification and the rotation of the atmosphere (Andrews *et al.*, 1987). *Internal gravity* waves result directly from stable stratification, while larger scale *inertio-gravity* waves result from a combination of stratification and Coriolis effects. *Planetary*, or *Rossby* waves, result from the polar gradient in planetary vorticity (the β -effect) and the conservation of potential vorticity. To deal with the whole spectrum of waves fully is beyond the scope of this book and the reader is referred to books such as Andrews (2000), Houghton (1986), Andrews *et al.* (1987), or Holton (1992). Historically the equations of motion have first been linearized by separating parameters such as pressure and wind into their mean and perturbation components, and then looking for waves with small enough amplitude that the linearizing approximation still holds. This *linear wave theory* is explored in detail by Andrews *et al.* (1987). A wide spectrum of waves is predicted under different assumed conditions including waves that are free to travel in all directions and others which are trapped in certain latitude bands. A particularly important example of the latter for study of giant planet dynamics are the so-called *equatorially-trapped* waves (Andrews *et al.*, 1987; Allison, 1990). More recently, advances in computation have made it possible to search for wave motion in the full non-linear Navier–Stokes equations, and thus look for waves with large amplitudes (Dowling *et al.*, 1998). However in this section we will summarize the main features of the linear waves which are predicted to occur under different conditions in giant planet atmospheres.

Gravity waves and radius of deformation

Consider a parcel of air at a certain height and at the same temperature as the surroundings T_0 , which is moved vertically and adiabatically from its equilibrium position by a small distance δz . If no condensation occurs then the new temperature of the parcel will be $T_1 = T_0 - \Gamma_d \delta z$ where Γ_d is the dry adiabatic lapse rate (DALR). The temperature of the surrounding atmosphere however will be $T_{e1} = T_0 + (dT/dz) \delta z$, where dT/dz is the background lapse rate. If the two are different the parcel will feel a buoyancy force of

$$F = \rho_1 V \frac{d^2(\delta z)}{dt^2} = gV(\rho_{e1} - \rho_1) \quad (5.48)$$

where ρ_1 is the density of the parcel, ρ_{e1} is the density of the environmental air at the same altitude, and V is the parcel's volume. Hence the parcel's acceleration is given by

$$\frac{d^2(\delta z)}{dt^2} = g \left(\frac{\rho_{e1}}{\rho_1} - 1 \right) = g \left(\frac{T_1}{T_{e1}} - 1 \right). \quad (5.49)$$

where on the right-hand side we have substituted the expression for density in terms of temperature and pressure assuming that the gas is ideal. Substituting for T_1 and T_{e1} in terms of lapse rates and displacements and rearranging we find

$$\frac{d^2(\delta z)}{dt^2} = -\frac{g}{T_0} \left(\frac{dT}{dz} + \Gamma_d \right) \delta z \quad (5.50)$$

or

$$\frac{d^2(\delta z)}{dt^2} + N_B^2 \delta z = 0 \quad (5.51)$$

where

$$N_B^2 = \frac{g}{T_0} \left(\frac{dT}{dz} + \Gamma_d \right). \quad (5.52)$$

In a statically stable atmosphere, N_B^2 is positive and thus Equation 5.51 represents simple harmonic oscillation of the parcel about its equilibrium position. The oscillation angular frequency N_B is known as the *buoyancy*, or *Brunt–Väisälä* frequency. If N_B^2 is negative, then the solution of Equation 5.51 is exponential in z , and thus the atmosphere is unstable. It can be shown (Andrews, 2000) that Equation 5.52 may be further simplified to a form incorporating the potential temperature and static stability

$$N_B^2 = \frac{g}{\theta_0} \left(\frac{d\theta}{dz} \right) = \frac{gS}{\theta_0}. \quad (5.53)$$

If the horizontal direction is also considered, it is easily shown that these gravity waves propagate horizontally as well as vertically (Andrews, 2000; Houghton, 1986). Vertical perturbations in the lower troposphere, such as those generated by convection, may initiate such oscillations in the stable part of the atmosphere above the radiative–convective boundary. The resulting waves propagate both horizontally and vertically, where their amplitude is found to increase exponentially with height as the atmosphere becomes less and less dense. Small-scale, high-frequency waves do not feel the effects of the Coriolis force and are called internal gravity waves. Larger-scale, lower-frequency waves however are affected by the planet's rotation and are called inertio-gravity waves. The length scale at which Coriolis effects become important is defined by the *Radius of Deformation*, $a = c/f$, (sometimes called the *Rossby Radius*), where c is the phase speed of the wave and f is the Coriolis parameter (Gill, 1982). It should be noted that there is not a single radius of deformation, but in fact an individual deformation radius for every particular class and mode of wave since the phase speed c depends on wavenumber, and also on the vertical stratification through the Brunt–Väisälä frequency. For atmospheres where the geostrophic approximation applies it is found that the energy of short-wavelength disturbances is mainly in the form of kinetic energy, while the energy of long-wavelength disturbances is mainly in the form of potential energy. Both are equal at the scale of the radius of deformation. This scale is also sometimes called the *Synoptic Scale*. The radius of deformation may also be thought of as the ‘preferred’ horizontal length of disturbances, in the sense that waves arising from

baroclinic instabilities (Section 5.3.1) grow most rapidly (and are thus most visible) when their horizontal dimension is of this radius. For a continuously stratified atmosphere, a useful expression for the mean radius of deformation (Gierasch and Conrath, 1993) is $a = N_B H/f$, where H is the scale height of the atmosphere.

Gravity waves are thought to be the dominant source of vertical eddy mixing in the stratospheres of the giant planets. At very high altitudes the waves ‘break’, as described in Chapter 4, much as surface water waves break when they reach beaches. At altitudes where the gravity waves break, the momentum of the wave is transferred to the momentum of the mean flow.

Kelvin waves

Kelvin waves are a special class of gravity waves which are found to move eastwards relative to the mean zonal flow (but only at latitudes close to the equator). Air moving in the atmospheres of rotating planets is affected by the Coriolis force which, for prograde-spinning planets, deflects the air to the right in the northern hemisphere and to the left in the southern hemisphere. Consider a pressure disturbance moving eastwards relative to the mean zonal flow which is symmetric about the equator. The Coriolis force is zero at the equator but increases with latitude. Hence the part of the disturbance to the north of the equator is deflected south, while that to the south of the equator is deflected north, which by conservation of mass increases the pressure at the equator. Eventually the equatorial pressure rises to a level sufficient to balance the Coriolis ‘compression’ and the disturbance spreads latitudinally again before the cycle repeats. These equatorially-trapped *Kelvin* waves are observed in the Earth’s atmosphere and may also be important at equatorial latitudes in the giant planets. This description is very simplistic and more detailed treatments are summarized by Allison (1990) and Andrews *et al.* (1987). The amplitude of these waves is calculated to diminish away from the equator with an exponential decay length L_{eq} , known as the *equatorial deformation radius*

$$L_{eq} = \left(\frac{2c}{\beta_{eq}} \right) \quad (5.54)$$

where c is the phase speed. A key diagnostic feature of equatorially-trapped Kelvin waves is that the meridional velocity across the equator is zero.

Rossby or Planetary waves

We saw in Section 5.2.1 that potential vorticity is conserved by an atmosphere where friction and diabatic heating are negligible. Consider a parcel of air of height h at some latitude ϕ in the northern hemisphere which initially has zero relative vorticity ζ . Suppose the parcel is displaced northwards. From Section 5.2.1 we know that its potential vorticity $(\zeta + f)/h$ must be conserved. However, the Coriolis parameter f increases as the parcel moves north and thus the absolute vorticity ζ must decrease in order to compensate. Hence, the parcel gains negative (clockwise) *relative* vorticity. Similarly a parcel displaced southwards gains positive (anticlockwise) relative

vorticity. This conservation mechanism gives rise to *Rossby*, or *Planetary* waves at latitudes where the air stream is moving in the eastward direction. Air deflected to the south will gain positive relative vorticity and thus turn towards the left and then northwards. After crossing the starting latitude, the air will gain negative relative vorticity and thus turn towards the right and then southwards and so on, setting up a stable wave. To outline how we may show this analytically, consider the momentum equations in pressure coordinates for a frictionless flow, where vertical motion is neglected (Houghton, 1986):

$$\left(\frac{\partial}{\partial t} + u \frac{\partial}{\partial x} + v \frac{\partial}{\partial y} \right) u - fv = -g \frac{\partial z}{\partial x}, \quad (5.55)$$

$$\left(\frac{\partial}{\partial t} + u \frac{\partial}{\partial x} + v \frac{\partial}{\partial y} \right) v - fu = g \frac{\partial z}{\partial y}. \quad (5.56)$$

Differentiating Equation 5.56 with respect to x and differentiating Equation 5.55 with respect to y and then subtracting gives another form of the vorticity equation

$$\left(\frac{\partial}{\partial t} + u \frac{\partial}{\partial x} + v \frac{\partial}{\partial y} \right) \zeta + v \frac{df}{dy} = 0. \quad (5.57)$$

We now substitute the following mean and perturbation values: $u = \bar{u} + u'$, $v = v'$, $\zeta = \zeta'$, and define a perturbation stream function $u' = -\partial\psi/\partial y$ and $v' = -\partial\psi/\partial x$ such that $\zeta' = \nabla^2\psi$. The *perturbation form* of Equation 5.57 is then

$$\left(\frac{\partial}{\partial t} + \bar{u} \frac{\partial}{\partial x} \right) \nabla^2\psi + \beta \frac{\partial\psi}{\partial x} = 0. \quad (5.58)$$

This is a wave equation and assuming a wave solution of the form $\psi = Ae^{i(\omega t+kx+ly)}$, and substituting this into Equation 5.58 we may then derive the dispersion relation

$$c = -\frac{\omega}{k} = \bar{u} - \frac{\beta}{k^2 + l^2}. \quad (5.59)$$

This expression shows that wave motion is indeed possible, and that the waves move westward relative to the zonal flow. Clearly if the zonal flow is eastward with a speed equal to this phase speed, then the Rossby wave appears stationary. The analysis may be extended to the vertical dimension also but this is beyond the scope of this book. Instead the reader is referred to more specialized texts such as Andrews (2000), Houghton (1986), or Andrews *et al.* (1987). For Rossby waves it can be seen that the meridional velocity variations are non-zero.

A combination of westward moving Rossby waves, and eastward moving gravity waves, including equatorially-trapped Kelvin waves is believed to be responsible for the *quasi-biennial oscillation* (QBO) observed in the Earth's stratosphere at equatorial latitudes. Here the mean zonal winds (between 15 and 200 mbar) are found to vary quasi-periodically between eastward and westward flow with a period of about 28 months. In periods of eastward flow near the bottom of the stratosphere, equatorially trapped mixed Rossby–gravity waves may propagate vertically upwards and dump their energy into an upper westward flow. As a

result of this energy dumping, the region of westward flow gradually moves down. When the westward flow region reaches the bottom of the stratosphere, only Kelvin waves may propagate vertically upwards. These establish an eastward flow in the upper stratosphere where they break, which subsequently slowly moves down over time as more and more energy is dumped there. Eventually the eastward flow reaches the bottom of the stratosphere and mixed Rossby–gravity waves begin to propagate vertically again and thus the cycle repeats itself. A similar process may be responsible for the quasi-quadrennial oscillation (QJO) observed in the equatorial stratosphere of Jupiter. This is discussed further in Section 5.5.3.

5.3.3 Vortices in the giant planet atmospheres

In addition to turbulence and waves, the giant planet atmospheres exhibit one more, very distinctive planetary scale motion peculiar to them: long-lived vortices, or oval circulations such as the GRS on Jupiter, and the dark spots on Neptune. Such systems typically appear at latitudes of large horizontal wind shear and appear to be very stable. In one respect their presence is expected from two-dimensional turbulence since any small vortices generated in such shear regions between the belts and zones are expected to merge with other vortices and grow. However what is not clear is by what instability mechanism these vortices are initiated, and how they are maintained once they are established. In particular it is not clear whether they draw their energy directly from the zonal flow or through some other mechanism such as, for example, moist convection.

A fundamental clue to the nature of the large ovals comes from examining the distribution of cyclones and anticyclones across the planet. The geostrophic equations derived in Section 5.2.1 are completely symmetric with respect to the sign of the vorticity and thus, if the atmospheres of the giant planets were purely geostrophic, we might expect that cyclonic ovals were equally numerous as anti-cyclonic ones. In fact, almost all observed ovals on the giant planets are anticyclonic. For example, on Jupiter, 90% of all ovals are anticyclones. Why might such an asymmetry arise? One way of achieving such an asymmetry is to include centrifugal forces. Consider the acceleration of air moving with speed V in a circle of radius R . Starting with the horizontal momentum equations, and ignoring friction, we find that (Chamberlain and Hunten, 1987; Holton, 1992; Houghton, 1986)

$$\frac{V^2}{R} = -fV + \frac{1}{\rho} \frac{\partial p}{\partial R}. \quad (5.60)$$

Equation 5.60 may be solved for V to give

$$V = -\frac{fR}{2} \pm \left(\frac{f^2 R^2}{4} + \frac{R}{\rho} \frac{\partial p}{\partial R} \right)^{1/2}. \quad (5.61)$$

This is the *gradient wind approximation* and by convention V is taken as positive for cyclonic motion and negative for anticyclonic motion, and R is positive and measured from the centre of curvature. This equation has one cyclonic solution

(low pressure in the centre and thus $\partial p / \partial R$ is positive), but three anticyclonic solutions, two of which have high pressures in the centre of the cyclone, but one that has low pressure at the centre. Hence by including the acceleration term, the symmetry between cyclones and anticyclones is broken although it is not known if this also accounts for the observed cyclonic/anticyclonic asymmetry on the giant planets. Another reason for the greater number of anticyclones than cyclones might be that anticyclones are more stable under Jovian conditions and thus that cyclones rapidly become disrupted and break up. One reason for this may be that cyclones are more susceptible than anticyclones to moist convection (Dowling, 1997). The extra mass of an anticyclone depresses the atmospheric layers beneath it whereas cyclones have the opposite effect and can raise deep moist air beyond its lifting condensation level. Hence moist convection may be triggered which, if vigorous enough, may disrupt organized cyclonic circulation.

Much modelling has been done on long-lived eddies, and in addition laboratory studies have been conducted with rotating annulus experiments to simulate a range of driving conditions (Read, 1986; Read and Hide, 1983, 1984). The GRS on Jupiter is the largest of the long-lived anticyclones observed on the giant planets and the way it is driven and sustained is the source of much debate. There are at least four possible driving mechanisms that have been considered:

- (1) barotropic shear;
- (2) baroclinic shear;
- (3) local forcing (e.g. moist convections, ortho/para conversion); and
- (4) capture and absorption of smaller eddies.

Unfortunately the precise forcing mechanism is unclear, although the capture of smaller eddies would lead to the deposition of their momentum in the outer annulus of the spot, whose observed width of roughly 300–500 km is consistent with the smallest scale of observed eddies, and may be equal to the radius of deformation for Jupiter. While many studies concentrate on how such flows may be maintained against dissipation, another possibility is that the GRS is a ‘free mode’ of the Jovian circulation system and thus needs very little driving against dissipative effects. If frictional forces on the giant planets really are as low as they appear, then such vortices may appear spontaneously and be naturally long-lived (Lewis, 1988). Hence, for example, the GRS can be considered to be a giant ‘flywheel’ which, rather than being difficult to drive, is actually rather difficult to stop!

While some vortices such as the GRS certainly appear to be isolated, other examples of ovals such as the White Ovals and Brown Barges of Jupiter discussed in Section 5.5.2, often appear in regular chains suggesting a link with planetary-scale Rossby waves, perhaps through the Rhines effect. Another example is the North Polar Spot (NPS) on Saturn and its associated Polar Hexagon Wave. While at first glance it appears as though the wave arises through deflection of the mean flow around the NPS, followed by subsequent oscillation, it may be that the NPS is just a manifestation of a global series of cyclones and anticyclones at this latitude with an accompanying, apparently wave-like flow around them.

5.4 MEAN AND EDDY CIRCULATION OF THE GIANT PLANET ATMOSPHERES

5.4.1 Tropospheric circulation

We have seen that the zonal wind circulation of the giant planets is very vigorous. What is not so clear however, is how deep these zonal winds extend and in this section we will review some of the modelling work that has been done to understand the mean circulation of the giant planet atmospheres.

Shallow-layer models

If the interior of the giant planets were all rotating at the same internal System III rotation rate then the deep atmosphere may be reasonably approximated as a fixed lower surface, since the interior is adiabatic and has a huge mass. Any ‘weather’ arising from differential heating and cooling is likely to be confined to the surface layers. Such shallow-layer models, adapted from terrestrial models, have provided a reasonable first analysis model for interpreting the dynamics of the giant planet atmospheres (Williams and Robinson, 1973; Williams, 1978, 1979, 1986). In such models, belts and zones appear spontaneously and there are examples of the kind of vortices found on the giant planets. However a problem is that such models constantly need ‘pumping’ of energy to keep them going, and the calculated outward thermal flux greatly exceeds that actually observed.

Deep models

While shallow-layer models are reasonably simple, and are clearly applicable to the atmospheres of the terrestrial planets, the shallow weather layer theory of Jovian dynamics has suffered two setbacks since space age observation of the planetary atmospheres began. First of all, it is observed that although they experience differential solar heating, the giant planets have very little temperature variation with latitude, and any latitudinal variation that is present rapidly diminishes as the pressure increases. If the zonal winds really were confined to the surface weather layer, then there must be a large thermal wind shear below the cloud tops, and from the Thermal Wind Equation an accompanying large variation in temperature with latitude, particularly for Saturn and Neptune which have such high zonal winds. The low temperature variation actually observed clearly suggest that the zonal wind structure is deep. For Saturn, the zonal winds are estimated to extend to pressures of at least 10 bar (Smith *et al.*, 1981). Similar low-temperature variations are found at Jupiter, and in addition, radio tracking of the *Galileo* entry probe allowed the direct determination of the deep wind structure at the edge of the 5- μm hotspot it entered. Rather than decrease with depth, the winds were found to initially increase with depth and then tend to a constant value. The second major problem with the shallow weather layer model is that for Jupiter and Saturn (but not Uranus and Neptune) the rapidly varying zonal wind structure gives wind curvatures at the eastward jets which violate the barotropic instability, or Rayleigh–Kuo, criterion that $\beta - u_{yy}$ should not

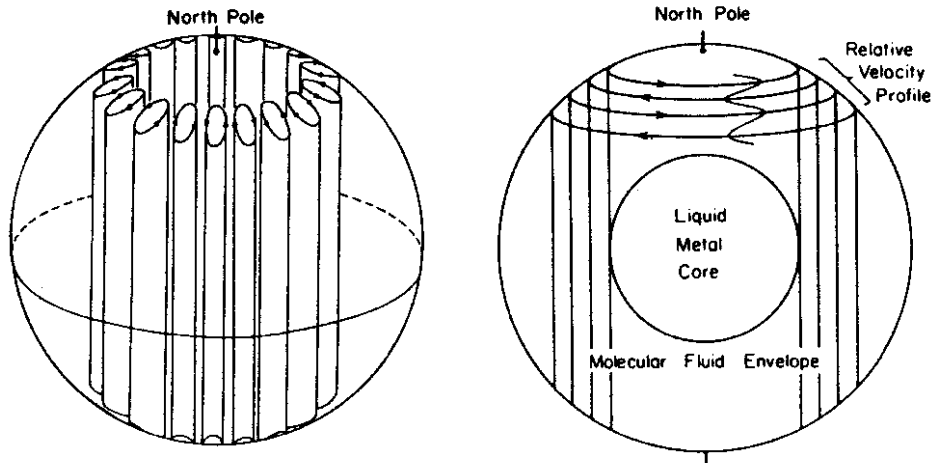


Figure 5.6 Taylor–Proudman columns and differential cylinders.

From Ingersoll and Pollard (1982). Reprinted with permission from Elsevier.

change sign. Since the zonal wind structure in fact appears very stable, this violation would suggest that the physical assumptions used in deriving the criterion are invalid for Jovian atmospheres. Hence the zonal winds of the giant planets would appear to be deep, not shallow, and several other features in the giant planet atmospheres, discussed later, suggest significant coupling between the surface weather layer and the deep interior. Hence a more complete picture of the giant planet atmospheres would appear to require the consideration of deep interior flows also.

One effect of the giant planets rapid rotation on the interior fluid dynamics is the suppression of motion parallel to its rotation axis, known as the Taylor–Proudman effect (Busse, 1976; Ingersoll and Pollard, 1982) introduced earlier. This tends to force the fluid to move as semi-rigid columns that are aligned with the rotation axis as shown in Figure 5.6. A remarkable experiment was performed on *Spacelab 3* in 1985 (Hart *et al.*, 1986) where a liquid confined between two hemispherical surfaces was spun about its own axis, and an electrostatic field was used to simulate gravity. Under certain conditions a clear ‘banana-cell’ convection flow was seen. The oblate-spheroidal shape of planets cause these columns to stretch as they move towards or away from the rotation axis and, via the conservation of angular momentum this vortex tube stretching effect is suggested to give rise to Rossby waves. An obvious consequence of this model is that the atmospheric motions should be symmetric about the equator, which to a very good approximation they are. Thus to explain the zonal structure of the giant planet atmospheres it is possible to imagine the Taylor–Proudman columns organizing themselves into a number of concentric cylinders, all rotating at slightly different rates. This theory elegantly explained the symmetric zonal structure of the giant planets, and was also consistent with the findings of the *Voyager* missions, that the zonal structure broke down at high latitudes and was replaced by chaotic overturning. The latitude where this occurred was found to be close to that where a cylinder just touching the

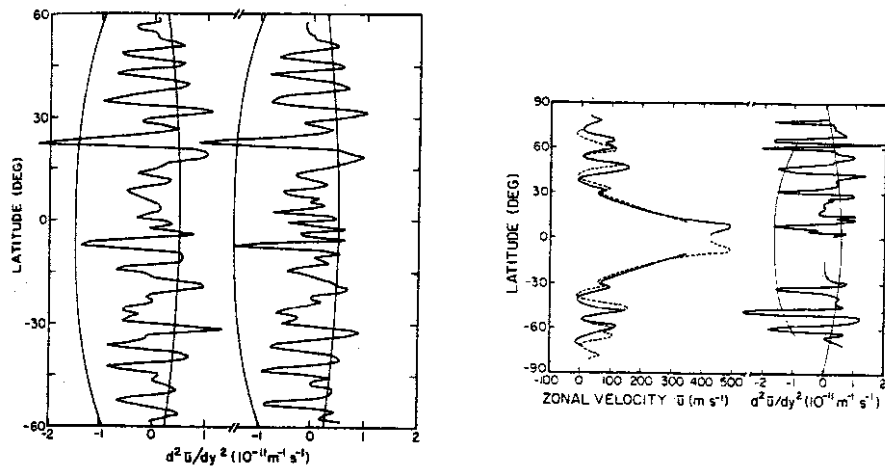


Figure 5.7 Stability of zonal structure of Jupiter and Saturn assuming: (1) a shallow layer and barotropic instability; and (2) assuming deep Taylor–Proudman columns (Ingersoll and Pollard, 1982). The left-hand figure shows the curvature of the zonal winds of Jupiter derived from both *Voyager 1* and *2* data. The barotropic stability curves are the smooth curves for positive values of $d^2 u / dy^2$, and it can be seen that the winds on Jupiter clearly exceed this curve at several points. The winds do seem stable with respect to the deep Taylor–Proudman model however, since the curvature is rarely more negative than the second stability curve shown, derived by Ingersoll and Pollard (1982). Similar results are shown on the right-hand side of the figure for the zonal winds measured on Saturn by *Voyagers 1* and *2*.

Reprinted with permission of Elsevier.

metallic–molecular boundary was predicted to intersect the surface spheroid. This critical latitude is at approximately 40–45° for Jupiter and 65° for Saturn. It is interesting to note from Figure 5.2 that both Jupiter and Saturn have three eastward jets between the equator and these latitudes (Smith *et al.*, 1982). Polewards of this latitude, less organized motion would be expected since the Taylor–Proudman columns could not pass right through the planet but instead would intersect the metallic-/molecular-hydrogen phase boundary. An additional advantage of this model is that the stability criterion of zonal flow is different from the barotropic instability criterion mentioned earlier, and is found to be better satisfied by the zonal flows of all the giant planets (Ingersoll and Pollard, 1982) as can be seen in Figure 5.7 for the case of Jupiter and Saturn. However this model, while very elegant, has suffered a setback following the recent Jupiter flyby by *Cassini/Huygens*. The *Cassini* ISS camera has now found organized, long-lived zonal motion extending all the way to the poles, and high-latitude organized symmetric polar motion has also been observed on Saturn by *Voyager* and ground-based observations. There is also a problem that very different behaviour is expected either side of the critical latitude in that, on the equatorward side, northern motion stretches the columns, but on the poleward side, northern motion compresses the columns (Figure 5.8). Such differential behaviour in the atmospheric flow is not

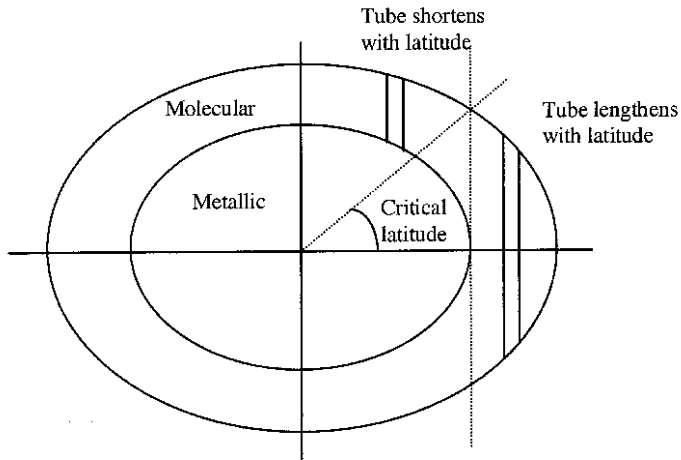


Figure 5.8 Vortex tube stretching associated with Taylor–Proudman columns. Columns intersecting at latitudes less than the critical latitude pass right through from north to south. Motion of the column towards the rotation axis stretches the column. Columns at latitudes poleward of the critical latitude do not pass through to the other hemisphere. Furthermore, motion of the column towards the rotation axis *compresses* the column. Hence this model would suggest very different atmospheric flow on either side of the critical latitude which is not actually seen on any of the giant planets.

observed. Although these observations present a problem to the Taylor–Proudman column theory, it remains an attractive and intriguing possibility and it is hence of great interest to determine how deep the winds on the giant planets actually extend. Coherently organized internal motion of the kind just described will create perturbations in the gravitational equipotential ‘surface’ of the planets which will affect the gravitational J -coefficients. For Neptune, which has a very broad and rapidly rotating zonal structure, the measured J_4 -coefficients have been found to be inconsistent with Taylor–Proudman columns extending throughout the planet and instead, the winds are concluded to be limited at most to the outer hydrogen–helium shell (Hubbard, 1997). However, this does not discount the Taylor–Proudman theory since for Neptune (and Uranus) the transition to the icy interior, which should present the same boundary to Taylor–Proudman columns as the transition from molecular- to metallic-hydrogen does in Jupiter and Saturn, occurs just a few thousand kilometres below the cloud tops. Planets such as Jupiter and Saturn have a much finer zonal structure and thus the effects of such columns (if they exist) will only be apparent in the higher order J -coefficients which have not yet been accurately measured. Future missions will need to fly much closer to these planets if these coefficients are to be determined (Hubbard, 1999).

One-and-a-half-layer models

We have seen that the apparently deep nature of the zonal flow argues against shallow-layer models of the giant planets in favour of perhaps a system of

co-rotating cylinders. However this deep-atmosphere theory is apparently cast into doubt by the absence of a difference in atmospheric flow at the latitude cylinder tangential to the metallic-/molecular-hydrogen boundary, and the observation of zonal jets extending polewards of the critical latitudes. Hence the real flow of these planets would appear to be more complicated than either of these more simple approaches and ideally a fully three-dimensional model of atmospheric flow needs to be constructed to investigate the dynamics of the giant planets. Unfortunately, to model numerically the entire three-dimensional flow of the interiors and observable atmospheres of the giant planets is completely beyond the scope of today's computers and will continue to be impractical for many years to come. However, since the deep interiors of the giant planets are almost certainly barotropic, and since the surface layers exhibit many similarities with shallow-layer models, it may well be that these planets can be represented by models that have deep barotropic flows up to nearly the observable levels, capped by a statically stable layer that is driven by turbulent energy, injected from below (Leovy, 1986). One way of representing this idea is to use 'one-and-a-half'-layer models, where the deep atmospheric flow is represented as latitudinal variations in the height of a lower boundary layer. These height variations may be determined by tracking the vorticity of features on the edge of anticyclones such as the GRS which have significant north/south motion and assuming that the potential vorticity $q = (\zeta + f)/h$ is conserved. Hence the effective height h of the weather layer may be determined by observing the variation in the vorticity of the flow (Dowling and Ingersoll, 1988, 1989). One-and-a-half-layer models with lower topography determined in this way are able to simulate the zonal flow of Jupiter (and other planets) and mimic the spontaneous formation and growth of large oval circulations. However, like shallow-layer models, they have the disadvantage that they need to be continuously forced in order to maintain the flow, and thus seem to lack the principal energy source that maintains the zonal circulations of these planets.

The idea of a thin stable surface layer on top of barotropic but differentially rotating interior cylinders also provides one explanation for how Jupiter, Saturn, and Neptune, which have significant internal heat sources but differential solar heating, all radiate approximately equally in all directions. The solar heating will be maximum at equatorial latitudes and this will tend to increase the static stability of the air and thus reduce the amount of internal heat that is convectively transported. Conversely, solar heating is minimum at the poles which will tend to make the atmosphere neutrally statically stable and thus convection will be uninhibited. Hence more internal heat is radiated at the poles than the equator, counteracting the differential absorption of sunlight. However, the fact that Uranus, which also has significant differential solar heating but negligible internal heat, also radiates equally in all directions suggests that reality may once again be more complicated!

Eddy–mean interactions

The interaction between the zonal mean flow and waves/vortices is currently unclear and opinion is divided between two main points of view. Some scientists believe that

the zonal motions are in effect a free-mode of a low-viscosity atmospheric circulation driven directly by internal energy and absorbed sunlight, and hence that the observed eddy motion is a result of turbulence at the belt/zone boundaries and thus that the eddies draw their energy from the mean flow. The alternative point of view is that it is the eddies which primarily draw their energy from internal sources and absorbed sunlight, and that it is these eddies which then drive the zonal flow and the large vortices.

One feature of the atmospheres of Jupiter and Saturn which argues in favour of the zonal winds being driven by eddies (which includes wave motion) is the super-rotation of the equatorial zones of these planets. Another argument in favour of eddy driving came from the analysis of the motion of eddies observed in *Voyager 1* and 2 images of Jupiter by Beebe *et al.* (1980) and Ingersoll *et al.* (1981). In these studies, observation of the motion of individual clouds allowed the estimation of the Reynolds Stress $\bar{u}'\bar{v}'$ which is the average northwards transport of momentum by eddies. (NB, here the zonal and meridional winds have been split into their zonal-mean and transient, or eddy, components: $u = \bar{u} + u'$, $v = \bar{v} + v'$.) Ingersoll *et al.* (1981) found that the eddies were pumping momentum into the jets and thus sustaining them. However, this scenario has been cast into doubt by Sromovsky *et al.* (1982) who found that Ingersoll *et al.*'s (1981) conclusion was probably caused by a biased sampling of prominent eddy cloud features. A more uniform spatial sampling shows no evidence for eddy pumping although the topic is still hotly debated. Of course, if the eddies drive the jets then that begs the question what drives the eddies! One possibility is that eddies may be produced by baroclinic instability, which releases stored potential energy set up by horizontal temperature gradients (Ingersoll, 1990). However, the only temperature variations that have been observed are associated with the jets, and it is not tenable to believe that the jets sustain the eddies which then sustain the jets! Another possibility is that the smallest eddies derive their energy by moist convection and latent heat release as suggested by Ingersoll *et al.* (2000).

5.4.2 Stratospheric and upper tropospheric circulation

The temperatures in the upper tropospheres of the giant planets have been estimated from thermal-IR observations approximately at $18\text{ }\mu\text{m}$ (555 cm^{-1}), both by space-craft and ground-based observations in the case of Jupiter. Zonal contrast is clearly seen and applying the Thermal Wind Equation, the zonal wind structure is predicted to decay to zero at approximately 3–4 scale heights above the cloud tops. The source of the friction implied is probably due to eddy motions or gravity wave breaking as was mentioned earlier. The temperatures in the stratosphere at $\sim 20\text{ mbar}$ may be estimated from observations in the methane ν_4 vibration–rotation band at $7.7\text{ }\mu\text{m}$ ($1,300\text{ cm}^{-1}$). A number of two-dimensional radiative–dynamical models have been constructed to estimate how the atmosphere responds to solar irradiation and thermal cooling to space. These models have been used to calculate the long-term meridional flow structures in the stratospheres of the giant planets which match the estimated stratospheric temperatures. Conrath *et al.* (1990) considered direct heating of the stratosphere through absorption of visible and near-IR solar irradiation by

methane gas alone, and predicted that the *residual mean* circulation (or *diabatic circulation*) in the stratospheres of all giant planets had air rising near the sub-solar latitude (where the solar flux is highest) and descending near the poles. A similar residual circulation is observed in the Earth's stratosphere and is known as the *Brewer–Dobson* circulation. Air rising at the sub-solar latitude means that Conrath *et al.*'s calculations are seasonally dependent for Saturn, Uranus, and Neptune, but less so for Jupiter whose obliquity is close to zero. West *et al.* (1992) challenged Conrath *et al.*'s findings for the case of Jupiter since the absorption of UV sunlight by stratospheric hazes near the pole had been neglected in Conrath's model. In West's model, air rose over the poles above the ~ 10 mbar level and descended at the equator! However, at lower altitudes air descended over both poles, as in Conrath's model. Hence air drifted equatorwards above the 10 mbar level and polewards below it. However, these models are highly dependent on the assumed gas and haze absorption coefficients, and a more recent study of the Jovian atmosphere by Moreno and Sedano (1997), based upon West's model but with revised haze and methane absorption characteristics, has a meridional flow structure closer to Conrath *et al.*'s calculations. For Saturn, the role of UV-absorbing polar stratospheric hazes may also affect the calculations of Conrath *et al.*, but for Uranus and Neptune, which do not have UV-absorbing polar stratospheric hazes, Conrath *et al.*'s model would seem to be reliable.

These residual mean calculations are useful in understanding mean stratospheric meridional flow, but they represent time-averages over long periods and do not necessarily model how tracers are actually transported in the stratosphere. In particular they neglect horizontal eddy diffusion processes that can transport material meridionally in much shorter time periods. This was well demonstrated by the collision of Comet Shoemaker–Levy 9 into Jupiter's atmosphere in 1994 (Figure 5.9). All the models of the Jovian stratospheric circulation mentioned predict that air moves poleward between the 100 and 10 mbar pressure levels and thus the sooty debris of the impact deposited at these altitudes at 45°S was expected to drift towards the South Pole (Friedson *et al.*, 1999). Instead the debris (observed at 230 nm by HST) drifted towards the equator and had reached a latitude of 20°S by 1997. In addition, trace constituents introduced by the comet such as HCN and CO₂ were observed to cross the equator into the northern hemisphere (West, 1999; Lellouch *et al.*, 2002).

5.5 METEOROLOGY OF JUPITER

5.5.1 General circulation and zonal structure

Jupiter emits 1.67 times more radiation than it receives from the Sun indicating a substantial internal heat source, and hence presumably vigorous convection. The zonal structure of Jupiter appears to be neutrally stable with well-defined belts and zones summarized in Figure 1.4 and reviewed in great detail by Rogers (1995). In fact this canonical stable belt/zone structure is a little misleading since

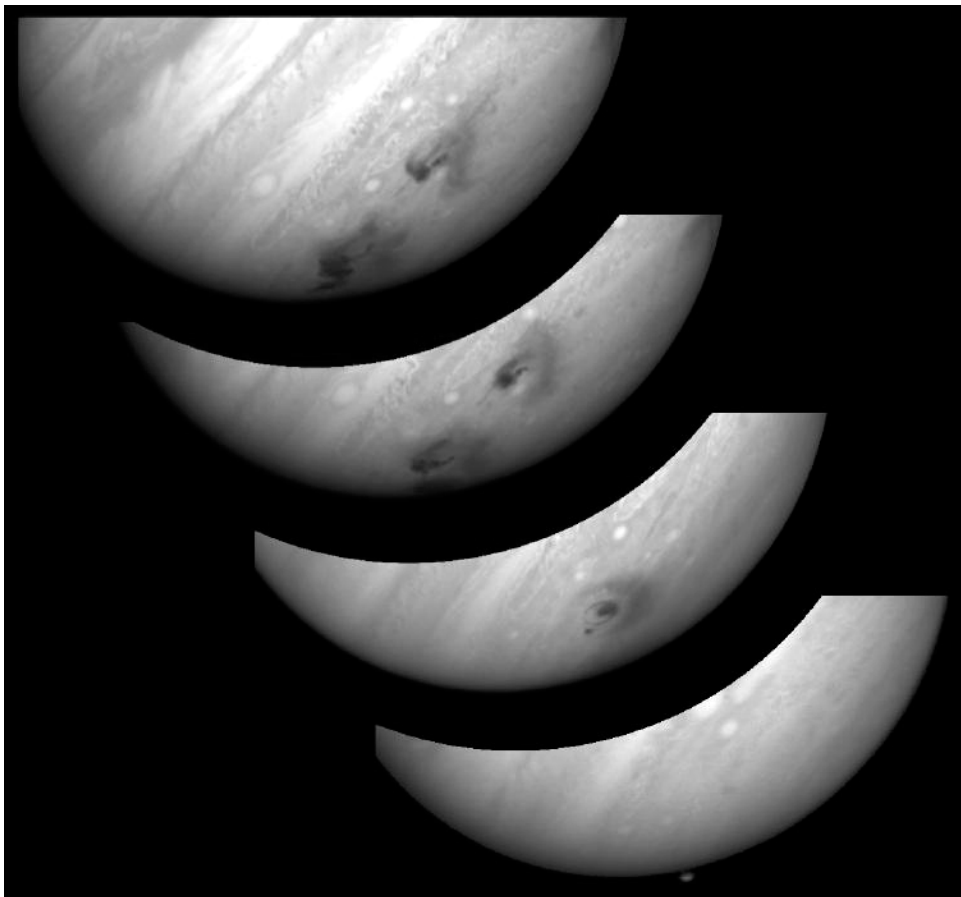


Figure 5.9 Mosaic of four HST/WFPC-2 images of Jupiter showing the evolution of the Shoemaker-Levy 9 G impact site in 1994. The images from lower right to upper left show: (1) the impact plume at 7:38 UT on 18 July (about 5 minutes after the impact); (2) the fresh impact site an hour and a half later at 9:19 UT; (3) the G impact site after evolution by the winds of Jupiter (left), along with the L impact (right), taken at 6:22 UT on 21 July (3 days after the G impact and 1.3 days after the L impact); and (4) further evolution of the G and L sites due to winds and an additional impact (S) in the G vicinity, taken at 8:08 UT on 23 July (5 days after the G impact).

Courtesy of NASA.

the dark belts occasionally brighten and the bright zones occasionally darken with typical timescales ranging from days to years. However, since the advent of space missions, it has become clear that the zonal wind structure associated with the bands is much more invariant, and that the atmospheric motion may best be referred to as fast-moving ‘jet streams’ seen in the zonal wind flow. Belts and zones occur in pairs, or domains, to the north and south of the equatorial zone, with the belt bounded by an eastward flowing jet stream on the side closest to the equator, and a westward



Figure 5.10 *Voyager 1* image of Jupiter's Great Red Spot and one of the STBs White Ovals in 1979.

Courtesy of NASA.

flowing jet stream on the poleward side. Thus the belts are regions of cyclonic vorticity and the zones anticyclonic vorticity as described earlier. Sandwiched within this general zonal flow structure are several short- and long-lived ovals, of which the largest and most long-lived are the GRS shown in Figure 5.10 which lies at 22°S (planetographic) between the South Equatorial Belt (SEB) and South Tropical Zone (STropZ), and the South Temperate Belt-South (STBs) White Ovals which lie at 32.6°S (planetographic) between the South Temperate Belt and the South Temperate Zone (STZ). A summary of Jupiter's visible cloud features is shown in Figures 5.11 (colour plate) and 5.12 and its appearance at visible, UV, and near-IR wavelengths is shown in Figure 5.13.

As mentioned previously, there is a clear correlation between cloud opacity and latitudinal wind shear with anticyclonic latitudes appearing bright at visible wave-

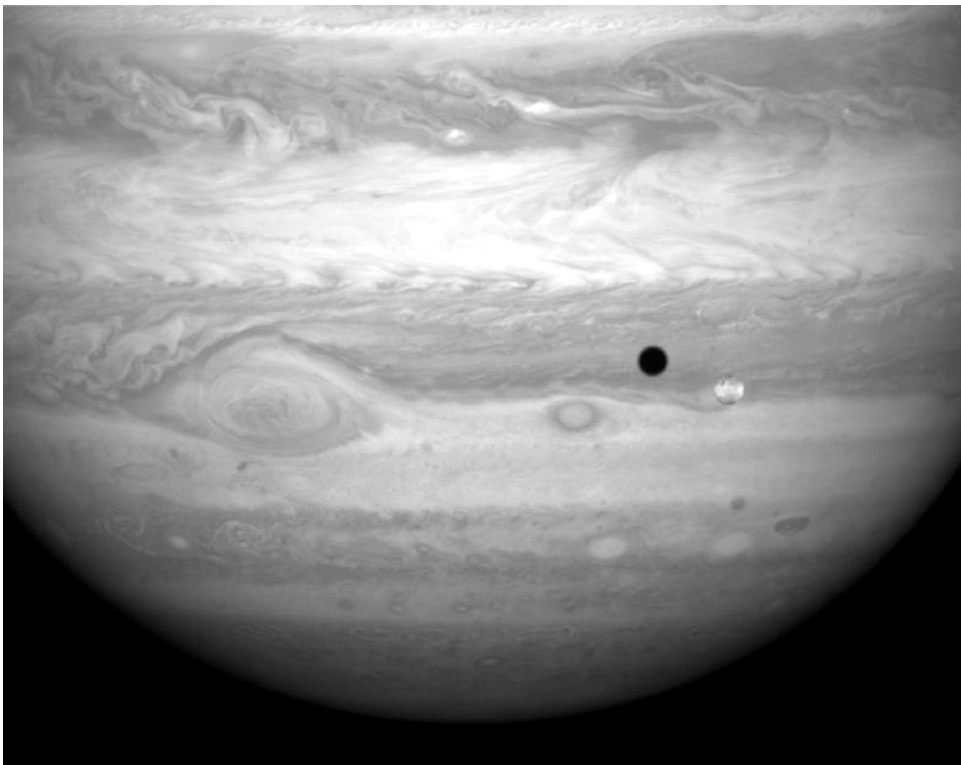


Figure 5.12 Southern hemisphere of Jupiter observed by *Cassini*/ISS in December 2000. The Galilean satellite Io is visible in the middle right together with its shadow. The image shows several of the main cloud features of Jupiter. The GRS is clearly visible, together with small SSTB White Ovals to the south. The turbulence in the EZ is clear, as are two of the dark plumes on its northern edge. In the NEB, a bright white transitory convective cloud is clearly seen in the process of being torn apart by the horizontal wind shear.

Courtesy of NASA.

lengths and dark at $5\text{ }\mu\text{m}$, and cyclonic latitudes appearing dark at visible wavelengths but bright at $5\text{ }\mu\text{m}$. This correlation becomes less clear at certain near-IR and visible wavelengths where the atmosphere is more opaque and thus where most of the observed reflection comes from the upper troposphere. This is probably because the small aerosols detected near the tropopause are transported horizontally from zone to belt on a short timescale compared to the rainout time. The origin of the colours, or *chromophores*, observed in the Jovian atmosphere have always been a source of much speculation. Pure water, ammonium hydrosulphide, and ammonia condensates produced in the laboratory are all pure white, so the yellow–ochre appearance of Jupiter has always been intriguing. The red appearance of the GRS is often ascribed to triclinic phosphorus $\text{P}_4(\text{s})$ and candidates for the various yellow, red, and brown colours seen elsewhere are allotropes of sulphur, or hydrocarbon ‘smog’ particles produced by photolysis in the stratosphere. However, it should be

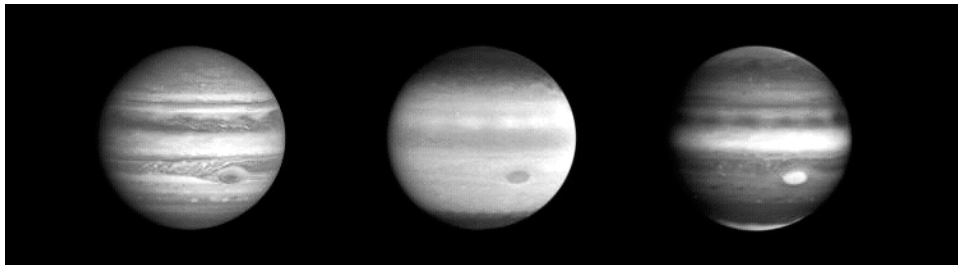


Figure 5.13 Three images of Jupiter observed by *Cassini/ISS* on 8 October 2000, as it approached Jupiter during its flyby. The image on the left was taken through the blue filter and appears similar to Jupiter's visible appearance. The middle image is recorded in the ultraviolet. At this wavelength light is Rayleigh-scattered from the upper atmosphere and the disk appears bright unless there are high abundances of upper tropospheric and stratospheric hazes. The strong haze absorption near the poles is clearly visible as is the increased haze abundance over the EZ. A wavelike pattern is also seen at the northern edge of this haze which appears correlated with the plumes/hotspots seen in the blue image. The image to the right is recorded in the near-IR at $0.89\text{ }\mu\text{m}$ where methane absorption is strong and so only light scattered by high altitude hazes is visible. This image is almost the negative of the UV image at equatorial latitudes although the anticorrelation breaks down at polar latitudes indicating the peculiar properties of the aerosols near the poles. The high haze opacity over the GRS is clearly visible.

Courtesy of NASA.

remembered that the pictures of Jupiter, and the other giant planets, that we have all become accustomed to are heavily enhanced and colour-stretched. The 'true' appearance of the giant planets is much blander, and indeed it can be argued that the apparent redness of the GRS has more to do with how the human eye perceives colour in different lighting conditions than with a real intrinsic redness (Young, 1985)!

The zonal structure of Jupiter was observed by the *Voyager* spacecraft up to latitudes of $\pm 60^\circ$ (Smith *et al.*, 1979a, b), and the organized zonal structure appeared to diminish towards the pole and be replaced by more chaotic motion. Such an observation was consistent with the model of Ingersoll and Pollard (1982) that the zonal flow of Jupiter arises from the flow of the interior, organizing itself into a series of differentially rotating concentric cylinders. However, more recent observations of the zonal winds by *Cassini/ISS* (Vasavada, 2002; Porco *et al.*, 2003) reveal the organized zonal flow to extend all the way to $\pm 70^\circ$, and to still possess north/south symmetry which presents a considerable problem for the cylinder model. Thermal measurements by both *Voyager* (Hanel *et al.*, 1979a, b) and more recently *Cassini* indicate that these winds decay with height and tend to zero within 3–4 scale heights of the cloud tops.

Long-term imaging of Jupiter at $18\text{ }\mu\text{m}$ (Orton *et al.*, 1994) and $7.4\text{ }\mu\text{m}$ (Orton *et al.*, 1991) sounding the 250 mbar and 20 mbar levels respectively have yielded unique information on seasonal variability, albedo correlation, and wave motion in the Jovian atmosphere. Although Jupiter has very small obliquity, clear seasonal varia-

tions are seen at both pressure levels, especially at high latitudes. At the 250 mbar level the seasonal maxima/minima occur roughly 2 years after the solstices. Such a time lag is expected since the atmosphere has a finite heat capacity and the solar heating is balanced by increased radiation to space at a later date. The radiative time constant (Chapter 6) at 250 mbars is estimated (Orton *et al.*, 1994) to be 6×10^7 s or 1.9 years which is consistent with the observations. A seasonal cycle is also seen at 20 mbar, but at this altitude there appears to be no lag between the solstice and maximum temperature which is inconsistent with radiative equilibrium models, and suggests that additional factors affect the stratospheric temperatures. Periods of upper tropospheric equatorial cooling in 1980 and 1992 coincided with a visible whitening of the Equatorial Zone (EZ), consistent with an episode of increased upwelling and condensation of cloud particles. However, the equatorial cooling observed in 1988 did not correspond to any albedo change. Interesting variability in the strong prograde jet at 20°N was observed between 1984 and 1990 where, from the Thermal Wind Equation it appeared that the jet went from a condition where it decayed with height, to one where it remained almost constant with height! During this period the North Temperate Belt (NTB) brightened in the middle of 1987 and then darkened in 1990 during a major outbreak of white and dark spots in the STB. In addition the North Equatorial Belt (NEB) broadened to the north in 1988 and then receded in 1999 leaving an array of Dark Barges and White Ovals (Orton *et al.*, 1994). Whether or not these changes were caused or influenced by the apparent change of vertical structure of the 20°N jet is not known, although it would certainly appear to be an interesting area of study.

5.5.2 Storms and vortices

The atmosphere of Jupiter contains numerous examples of large, long-lived ovals of which almost 90% are anticyclonic as was discussed earlier in Section 5.3.3. Stable cyclones do exist however and the most prominent are the ‘Brown Barges’ which appear at the northern edge of the NEB at 16°N (Figure 5.14). The strong cyclonic shear found at this latitude may help to stabilize the Brown Barges which are observed to be dark at visible wavelengths, but bright in the IR suggesting that they are regions of reduced cloud cover and subsidence. Analysis of the cloud-top wind vectors observed by *Voyager* noted earlier, suggests that the small-scale eddies in general pump energy into the mean zonal flow and large-scale eddies (Ingersoll *et al.*, 1981). However this conclusion is challenged on sampling grounds (Sromovsky *et al.*, 1982). In addition, the driving force behind the small-scale eddies is unclear although it has been suggested that moist convection may be the ultimate source (Ingersoll *et al.*, 2000). It will be interesting to see if analysis of the *Cassini*/ISS data currently being conducted leads to the same conclusion.

The largest visible oval is the GRS which is a huge anticyclonic vortex centred at $22.4^\circ \pm 0.5^\circ\text{S}$ (planetographic) and has a constant latitudinal extent of 11° or 12,000 km, and a longitudinal extent of currently 17° or 20,000 km. Winds in the vortex rise to over 100 m s^{-1} in the outer annulus, but the centre is found to be quiescent and also roughly 8 K cooler than the surrounding cloud tops. Applying

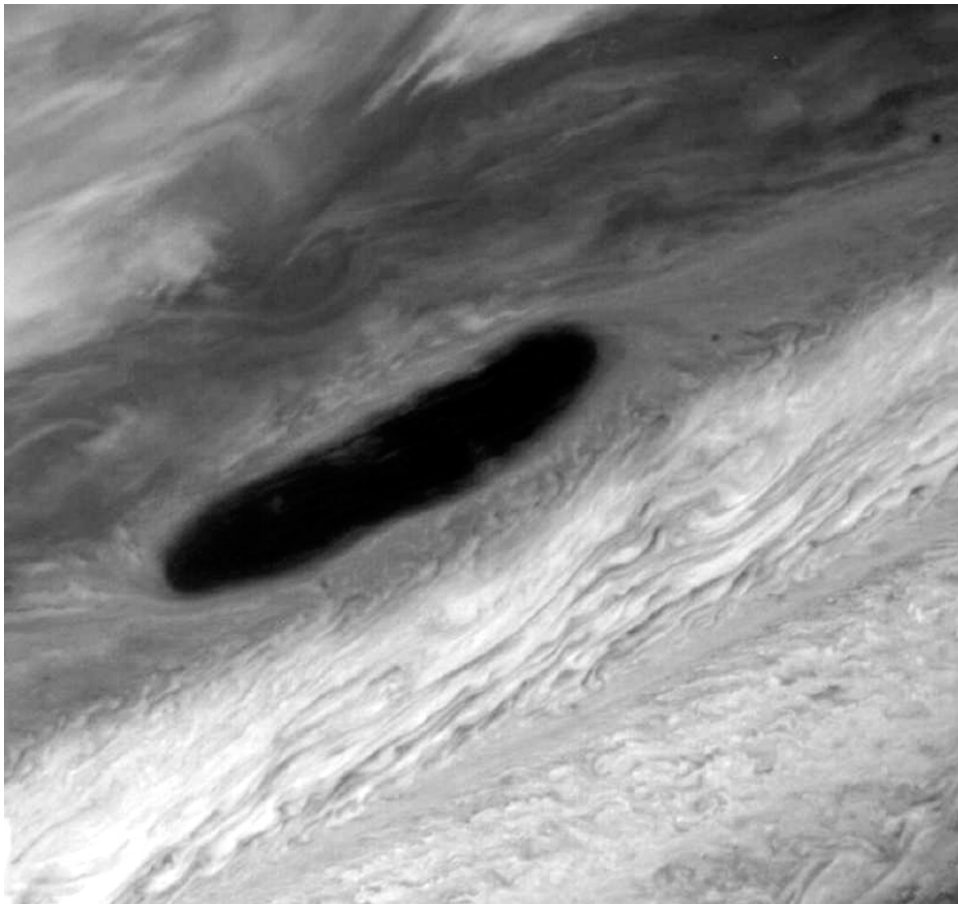


Figure 5.14 *Voyager 1* image of a Brown Barge on Jupiter.

Courtesy of NASA.

the Thermal Wind Equation, this implies that the wind speed should decrease with depth into the atmosphere and thus that the GRS is probably only 200 km thick, which is tiny compared to its horizontal dimensions. Clouds in the centre of the spot are found to be very thick and high and also tilt slightly from the north to south and more subtly from east to west. The GRS thus resembles a ‘tilted pancake’ (Simon-Miller *et al.*, 2002; West, 1999) and is quite unlike a terrestrial hurricane with which it is often compared (West, 1999), whose breadths are 20–30 times their heights. The thick clouds and low upper tropospheric temperatures imply upwelling in the centre of the GRS, and at the edges, high 5- μm emissions indicate low cloud opacity and thus subsidence, again unlike a hurricane where subsidence takes place in the central eye. The GRS appears to be very long-lived, although the visibility of the spot changes greatly with time and was particularly clear during the *Pioneer* encounters. However, at other times, such as during SEB disturbances, the spot almost disap-

pears. A large spot at the current GRS latitude was first observed in 1665 by Robert Hooke, and a year later by Cassini (Simon-Miller *et al.*, 2002). However, it is not clear whether the current GRS is actually the same spot since continuous observations can only be traced back to 1830, 120 years after the last sighting of Hooke's Spot. Today's GRS is observed to be gradually shrinking in the longitudinal direction at a rate of 0.193° per year (Simon-Miller *et al.*, 2002) which translates to 4,000 km between the time of the *Voyager* flyby and current observations. In addition, the winds in the collar have increased since the *Voyager* flyby. If the current rate of shrinking continues then by around the year 2040 the GRS will be perfectly circular. A circular aspect ratio is believed to be an unstable configuration for such a large anticyclone and hence it is possible that the GRS may actually disappear 40 years from now! Rogers (1995) has proposed that this may be what happened to Hooke's Spot (which was reported to be roughly circular) in around 1700 and that the current GRS formed from a belt-wide disturbance (rather like the formation of the STBs White Ovals in 1939) at about the same time and has been continuously shrinking in the longitudinal direction ever since. Its formation may even have been fed by its predecessor, Hooke's Spot! The quiescent conditions at the centre of the GRS may mean that air is trapped inside it for substantial periods of time which may lead to the production of the characteristic red chromophore which gives the GRS its apparent reddish colour. An alternative explanation is that the clouds seen in the centre of the GRS have much higher cloud tops than anywhere else on the planet, suggesting vigorous convection. Hence high levels of gases such as phosphine may be present whose photolysis may lead to the production of triclinic red phosphorus P₄(s).

The STBs White Ovals are the most prominent storm systems after the GRS. The current oval system first appeared in 1939 when a wavy disturbance appeared in the STB, although similar ovals had previously been seen at this latitude. This disturbance developed into 6 pinched regions that were labelled A to F. These eventually coalesced into the 3 White Ovals labelled BC, DE, FA sandwiched between the STZ and STB and which were observed during the *Voyager* flybys in 1979. More recently, two of these ovals merged together in 1998, and in March 2000 the resultant two remaining ovals coalesced to form a single White Oval (Figure 5.15). How long the single surviving White Oval will last remains to be seen.

The region to the north-west of the GRS is a region of cyclonic vorticity and appears to be particularly chaotic and rapidly changing. Small bright clouds regularly appear which have been widely interpreted as thunderstorm clouds, and the base of the clouds appear to be at pressures greater than 4 bar (Banfield *et al.*, 1998 and Figure 4.11) suggesting a moist convective cumulus cloud rising from the base of the expected water cloud. In addition, the spectral signature of ammonia ice has been detected in these bright white clouds indicating rapid updrafts and formation of pure white ammonia crystals (Baines *et al.*, 2002 and Figure 4.10). The absence of ammonia ice features elsewhere, except in the NEB plumes, indicates that these crystals are rapidly modified or coated in some way as to hide their pure spectral signature. A number of thunderstorms have now been observed on Jupiter at latitudes of cyclonic shear (Little *et al.*, 1999; Gierasch *et al.*, 2000) by

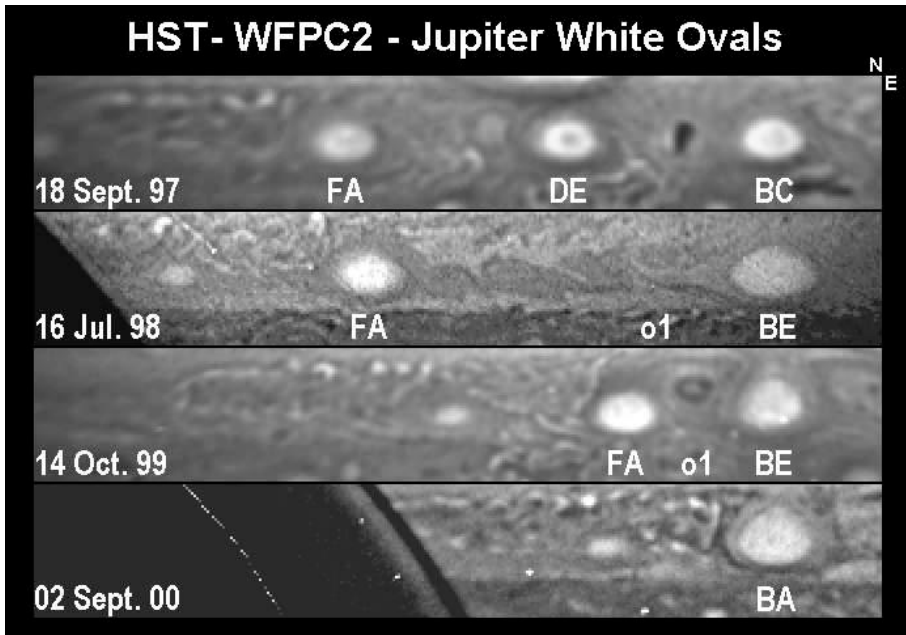


Figure 5.15 The merger of the White Ovals from 1997 to 2000 observed by HST.

Courtesy of NASA.

observing their flashes on the night-side (Figure 4.12). The size of lightning spots in the images suggests that they result from point sources within or below the expected water cloud and their intensity suggests that the lightning strikes are much more energetic than the average terrestrial lightning bolt. Although cyclonic shear latitudes are generally cloud-free regions, higher occurrence of lightning flashes is not thought to be purely an observational effect in that the flashes are simply more visible where there are no clouds! Instead, modelling of the scattering properties of the thunderstorm, and other clouds, indicates that deep flashes occurring in zones would also be visible. Hence the correlation suggests that regions of cyclonic shear are simply more susceptible to moist convection, as was mentioned in Section 5.3.3. The moist convection scenario is also supported by an indication of increased water humidity in these areas (Roos-Serote *et al.*, 2000). Although the *Galileo* entry probe descended in just such a cyclonic shear zone at 6.5°N, no lightning was detected within 10,000 km and indeed the nearest lightning strike detected in images was observed at 8.6°N.

At higher altitudes, in the stratosphere, other transient spot-like features have been noted by HST, *Galileo*/SSI, and *Cassini*/ISS at UV wavelengths sounding approximately the 1-mbar level in the polar regions. These wavelengths are sensitive to the abundances of stratospheric hazes and the ovals appear with sizes comparable to the GRS. An example of such a UV spot can be seen in the middle, UV image of Figure 5.13 (on the top right-hand limb). What these spots are is not

known, although recent observations by *Cassini*/ISS should be able to shed some light on them (Porco *et al.*, 2003). Further towards the poles, *Cassini*/CIRS appeared to detect possible increased abundances of stratospheric acetylene in diametrically opposed spots at $\sim \pm 80^\circ$. However, this deduction is highly dependent on the assumed stratospheric temperature structure, and it could be that rather than the abundance of acetylene being higher, the local stratospheric temperatures may instead be higher. The location of the ‘acetylene’ spots lies within the polar auroral ovals, and appear to be coincident with an area of enhanced X-ray emission observed in December 2000 by the Chandra X-Ray Telescope, launched into Earth orbit in July, 1999. Interestingly, during the *Cassini* flyby, the *Cassini*/ISS instrument recorded the birth, development, and subsequent decay of a large dark UV spot at a latitude of 60°N with a total lifetime of approximately two months (Porco *et al.*, 2003). This spot was also found to lie within the main auroral oval strongly suggesting a link with auroral processes.

5.5.3 Waves

The Jovian atmosphere contains numerous examples of waves on a wide range of length scales. At the smallest scale, Flasar and Gierasch (1986) discovered waves in the equatorial region in *Voyager* images travelling east–west at the cloud tops with wavelengths of ~ 300 km, gathered together in wave packets of length $\sim 1,300$ km in the meridional direction and 3,000–13,000 km in the zonal direction. These were interpreted as equatorially trapped modes with smaller gravity waves superimposed on them, generated by Kelvin–Helmholtz instabilities, and were most apparent at the edges of the equatorial jet at $\pm 8^\circ$. A more recent observation of these waves is shown in Figure 5.16. The interpretation of these features led to the suggestion of a statically stable duct beneath the NH_3 cloud deck and this hypothesis was later supported by the *Galileo* probe temperature measurements (Seiff *et al.*, 1998), although the *Galileo* probe entered a 5- μm hotspot which may not be very representative of the mean near-equatorial conditions. At larger, planetary scales, waves have been detected in both thermal maps of Jupiter (Orton *et al.*, 1991, 1994; Deming *et al.*, 1989, 1997; Magalhães *et al.*, 1989, 1990) and in the planetary variation of cloud opacity as determined by the 5- μm emission (Harrington *et al.*, 1996; Ortiz *et al.*, 1998).

A near-stationary wavenumber-9 wave was discovered by Magalhães *et al.* (1989, 1990) from *Voyager* IRIS data in the upper troposphere at 270 mbar near 15°N , and a similar wavenumber-11 wave was observed at 20°N at 45 μm (which sounds down to 1 bar in the absence of clouds). Similar wavenumber-10 waves were observed by Deming *et al.* (1989) from ground-based observations at 8–13 μm , both at 20°N and at the equator. Ground-based observations at 7.8 μm (Orton *et al.*, 1991) sounding the 20-mbar temperature found near-stationary waves at $\pm 20^\circ$ which were interpreted as planetary waves generated by instabilities in the strong cloud-top prograde jets at $\pm 18^\circ$. The near-stationary appearance of these waves with respect to System III implies some sort of dynamical link with the interior bulk rotation of the planet. Observations by Orton *et al.* (1994) at 18 μm which sound

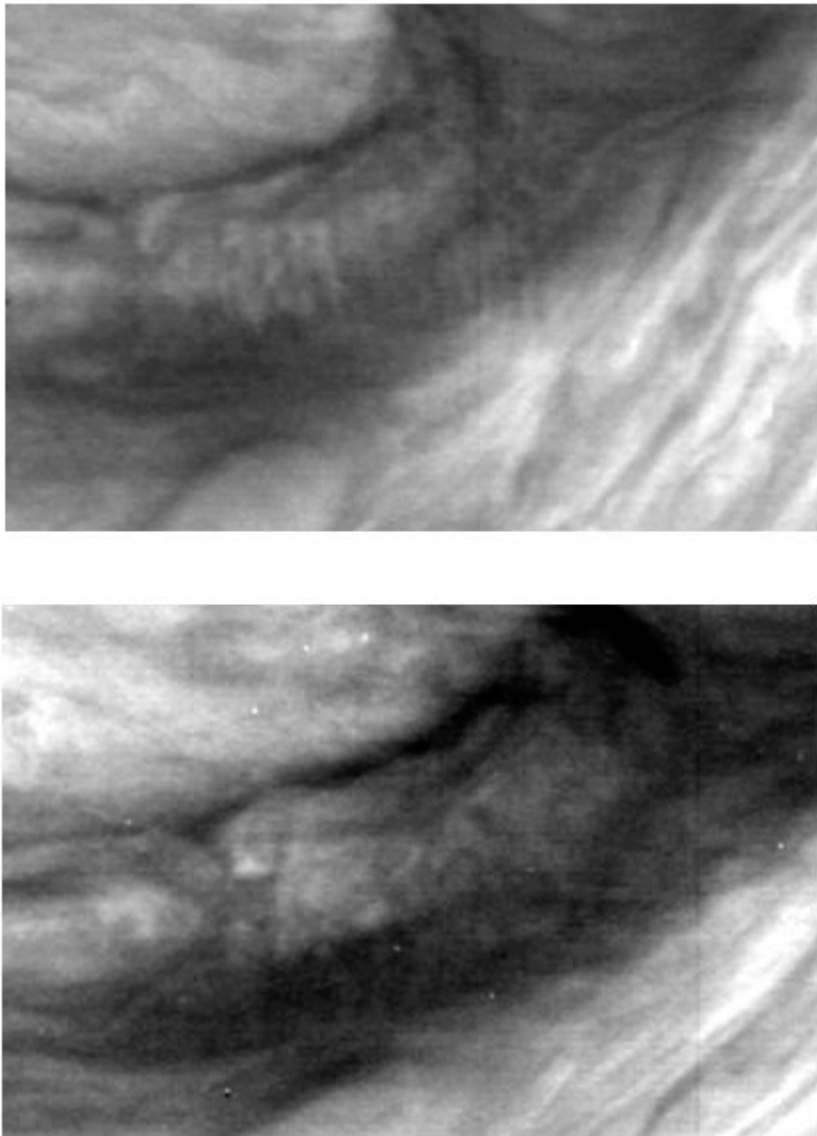


Figure 5.16 Two images of Jupiter's atmosphere recorded by *Galileo/SSI* with the 'violet' filter in 1996, centred at 15°S and 307°W . The pixel resolution is approximately 30 km. Mesoscale Kelvin–Helmholtz gravity waves can just be seen in the centre of the upper image where they appear as a series of about 15 nearly vertical north–south stripes. The combined wave packet is about 300 km long and is aligned in east–west direction. In the lower image, recorded 9 hours later, there is no indication of the waves, though the clouds appear to have been disturbed. Such waves were seen by the *Voyager* spacecraft in 1979.

Courtesy of NASA.

the 250-mbar temperatures found waves at 13°N in the NEB at the same time as the wave previously mentioned in the stratosphere near 20°N. Both disturbances appeared to have a zonal group velocity of -5.5 m s^{-1} with respect to System III longitude and there appeared to be some correlation with height implying vertical propagation of a Rossby wave. A more recent study by Deming *et al.* (1997) found such waves to be ubiquitous at near-equatorial latitudes with wavenumbers anywhere between 2 and 15. The amplitude of thermal waves in the lower stratosphere (20 mbar) sounded at 7.8 μm was found to be roughly 3 times greater than thermal waves in the upper troposphere (250 mbar), sounded at 18 μm. The waves at these two altitudes appear to be correlated and the amplitude growth is consistent with a $\rho^{-1/2}$ -dependence expected for vertically propagating Rossby–gravity waves. By analysing the amplitude of these stationary Rossby waves, Deming *et al.* (1997) infer latitudinal deflections of only 1° which may arise from interaction with the interior ‘banana cell’ convective structure or through interaction with vortices which themselves are slowly moving with respect to System III, sandwiched between easterly and westerly flow regions.

Waves have also now been detected in ground-based images of Jupiter recorded at 5 μm, a wavelength sensitive to the total cloud opacity above the warm 5–8 bar pressure regions and thus sensitive to the opacity of the expected water, ammonium hydrosulphide, and ammonia cloud decks. A number of waves were discovered at many latitudes (Harrington *et al.*, 1996) including near-stationary wavenumber-10 features between 7–8°N and eastward propagating wavenumber-4 waves at the equator. The former wave appears to be associated with the 5-μm hot spots at the southern edge of the NEB which appear to be distributed semi-uniformly with longitude, and are interspersed by highly reflective ‘equatorial plumes’ lying between the hot spots and slightly to the south. These hot spots were studied by Ortiz *et al.* (1998) who concluded that they were manifestations of equatorially-trapped Rossby waves. The 5-μm hot spots are regions of very low cloud cover which makes them appear very bright at IR wavelengths, and dark at visible wavelengths and although they only cover 0.1–0.5% of Jupiter’s surface, they dominate the 5-μm emission. For some time these features were interpreted as being regions of rapid downdraft which would explain their low cloud cover and also the observed depletion of volatiles such as ammonia and water. However, such models required excessive downdraft velocities and also predicted that the abundance of volatiles such as ammonia, water vapour, and hydrogen sulphide should all return to their ‘deep’ abundances at roughly the same pressure level. In fact, the *Galileo* entry probe, which sampled just such a 5-μm hot spot, found that the abundance of ammonia increased first as the probe descended, then H₂S, then H₂O which was still increasing at 20 bar when communication with the probe was lost. More recently the alternative theory that these hot spots are associated with a planetary wave system which alternately compresses and expands the vertical air column has been developed and extended with non-linear modelling (Friedson, 1999; Showman and Dowling, 2000). This is currently the favoured explanation. In this model, the bright anticyclonic regions (equatorial plumes) appear on the upward portion of the planetary wave, concentrating volatiles at high altitudes where they condense to

form bright white clouds. The 5- μm hot spots then appear on the downward portion of the wave where the statically stable air column is vertically stretched, increasing the base pressure by almost a factor of 2. The accompanying adiabatic heating forces the clouds to sublimate and reduces the apparent volatile abundances but retains the relative abundances of H_2O , H_2S , and NH_3 which increase towards their deep values at the different rates observed by the *Galileo* probe. Showman and Dowling (2000) found that their modelled waves were only stable if large initial pressure perturbations were assumed, suggesting that non-linear effects are central to the stability of this wave. Furthermore, the authors found that the zonal wind profile measured by the *Galileo* entry probe (Atkinson *et al.*, 1998) which implies static stability in the troposphere consistent with the probe's atmospheric temperature experiment (Seiff *et al.*, 1998) may in fact be a local effect. The vertical negative wind shear (winds decreasing with height) was reproduced by Showman and Dowling's model at the southern edge of their simulated hot spots (where the probe entered), but was zero in the centre and positive at the northern edge implying that the measured wind profile may owe more to local dynamical effects than to the general zonal wind structure. Recently the spectral signature of pure ammonia ice has been observed in these equatorial plumes (and in localized thunderstorm clouds seen in other cyclonic regions (Baines *et al.*, 2002)), which is not generally seen elsewhere. This is interpreted as being due to the rapid condensation of new 'fresh' ammonia crystals in these regions which are then subsequently degraded, or coated with chromophores after a few days. A link between these waves and upper tropospheric properties was observed by *Cassini*/ISS and can be seen on Figure 5.13 where a wavenumber-16 wave is clearly seen at 9–19°N in both the strong methane absorbing band at 0.89 μm and in the accompanying UV image. Hence the wave clearly extends into the upper troposphere and has an effect on either the abundance or reflecting properties of the haze particles (Porco *et al.*, 2003).

One of the most striking features of the stratospheric temperatures observed by Orton *et al.* (1991) was a periodic, approximately 4-year variation of the zonal temperatures at 20 mbar, the Quasi-Quadrennial Oscillation (QQO). This feature, which has been continuously observed since 1978 takes the form of a periodic warming of the equator and simultaneous cooling of latitudes between $\pm(15\text{--}30)$, followed by a cooling of the equator and warming of the $\pm(15\text{--}30)$ latitude band with a period of between 2 and 5 years. The amplitude of the oscillation is approximately 1–2 K. During the cool equatorial phase, longitudinal structures were observed in the northern band which were the thermal waves mentioned earlier. The oscillation was also observed in the upper troposphere (250 mbar) at equatorial latitudes by Orton *et al.* (1994) where the temperature oscillation was found to be roughly 180° out of phase with the stratosphere. Leovy *et al.* (1991) likened this variability to the variation in the Earth's equatorial stratosphere known as the QBO discussed in Section 5.3.2. However, Friedson (1999) found that this analysis underestimated the vertical and horizontal averaging of the ground-based observations and that Leovy's identification of the driving waves as alternating equatorially-trapped Kelvin and mixed Rossby–gravity waves was not able to account for the amplitude of the oscillation observed. Instead, Friedson considered a wide range of

equatorially-trapped modes and found that forcing of the upper tropospheric and lower stratospheric flow by smaller-scale internal gravity waves produced temperature variations much closer to that seen. However, Li and Read (2000) also modelled the QJO and found that the effect was sufficiently well modelled by alternating wavenumber-8–11 waves with an equatorial Rossby mode moving eastwards at around 100 m s^{-1} (or perhaps a Kelvin mode) and a mixed Rossby–gravity wave stationary with respect to System III, apparently excited by a wave source moving with the zonal wind in the deep atmosphere. While these studies appear inconsistent, Li and Read did find that the identification of wave mode depended substantially on the model assumptions and thus that more detailed non-linear modelling might be necessary. Hence while it seems likely that Jupiter’s QJO is substantially like the Earth’s QBO, the precise identification of the wave motions forcing it remains elusive.

5.6 METEOROLOGY OF SATURN

5.6.1 General circulation and zonal structure

Saturn emits 1.78 times more energy than it receives from the Sun, but compared to Jupiter the overall energy emission is much less (only one-third that of Jupiter). Hence it might be expected that Saturn should have a commensurately less vigorously overturning atmosphere. However, the atmosphere appears just as energetic as Jupiter’s with strong zonal winds that reach speeds of 400 m s^{-1} in the eastward flowing equatorial jet. Although the atmosphere is very dynamic, the appearance of Saturn is generally much more subdued than that of Jupiter, with the belt/zone structure being much less clear. The tropospheric cloud structure appears to be much more masked by tropospheric and stratospheric haze layers due both to the expected ammonia ice cloud deck condensing at deeper levels than in Jupiter’s atmosphere and also due to the greater scale height of the Saturnian atmosphere as outlined in Chapter 4. The belts and zones have similar names to those of Jupiter and the universally accepted naming convention is shown in Figure 5.17.

The obliquity of Saturn (26.7°) means that it is much more prone to seasonal effects (Figure 5.18) than Jupiter and the *Voyager* spacecraft found in 1980 and 1981 (corresponding roughly to the northern spring equinox) that the upper tropospheric temperature at the 210 mbar level was approximately 10 K warmer in the southern hemisphere than the northern hemisphere (Hanel *et al.*, 1981, 1982), decreasing at higher pressures. The thermal response of the atmosphere at this level is estimated from the radiative time constant (Gierasch and Goody, 1969) to be roughly 5 years or equivalently $\pi/2$ out of phase with the solar forcing, which corresponds well to the observations. Like Jupiter, the variations in temperature with latitude were used to calculate the thermal wind shear which again was well correlated with the cloud-top zonal winds, indicating that the jets decay with height (Smith *et al.*, 1981, 1982; Pirraglia *et al.*, 1981). A similar north–south asymmetry in stratospheric temperature has recently been reported by Karkoschka (1998a) from visible and near-IR observations. In this study the northern hemisphere was warmer which is as expected since

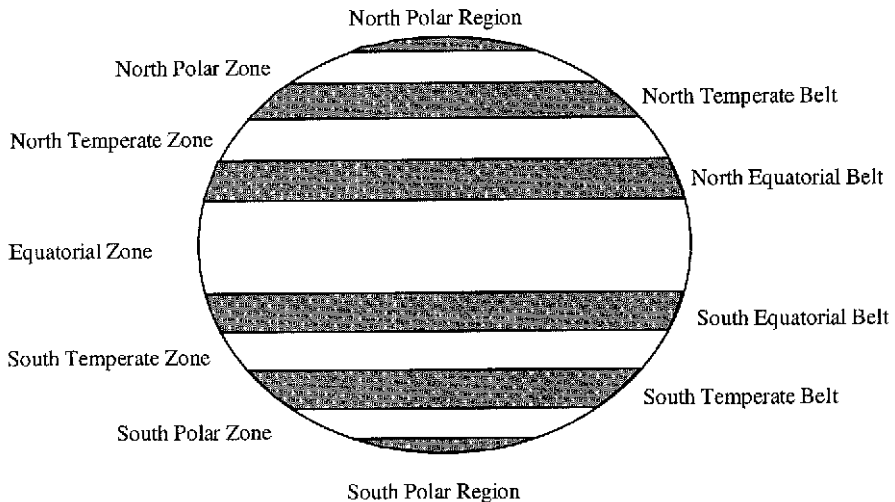


Figure 5.17 Standard Saturnian zonal nomenclature.

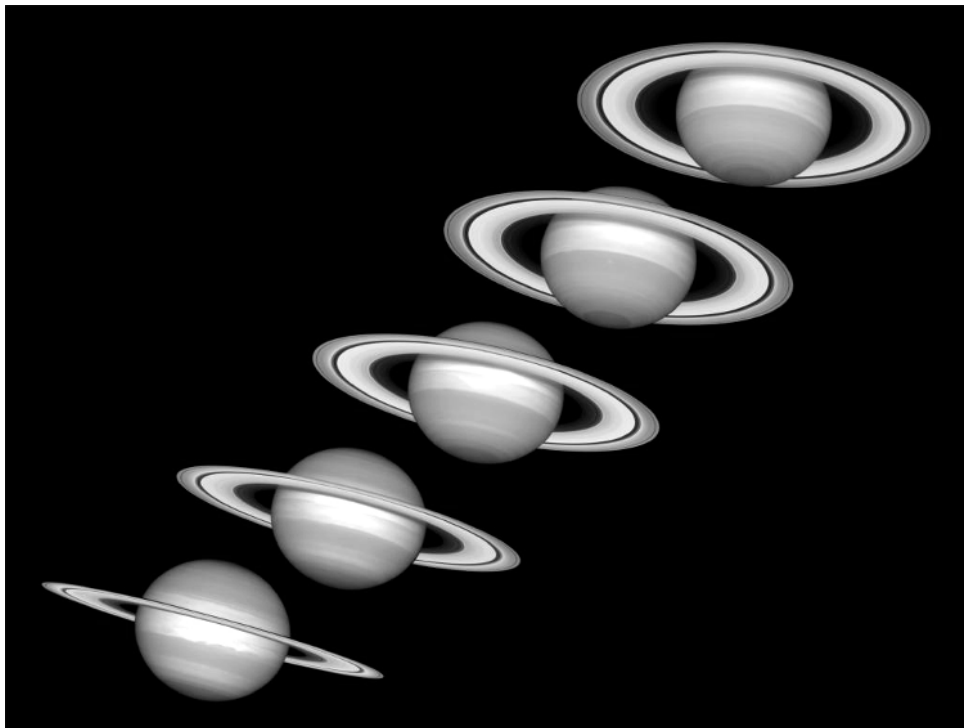


Figure 5.18 Mosaic of five HST images of Saturn recorded between 1996 and 2000, showing Saturn's rings opening up from just past edge-on to nearly fully open as it moves from autumn towards winter in its northern hemisphere during its orbit about the Sun.

Courtesy of NASA.

Saturn was approaching its northern autumnal equinox. Although seasonal effects are observed in the stratospheric temperatures, the north–south symmetry of the zonal wind pattern observed at the cloud tops suggests that the tropospheric circulation is most influenced by rotational forces and perhaps internal energy sources.

5.6.2 Storms and vortices

Cloud features which are visible on Saturn appear to be the tops of active convection systems which push their way up into the overlying semi-transparent region. While generally less active than Jupiter’s atmosphere, a number of spots have been observed in Saturn’s atmosphere from ground-based observations over many years (Sanchez-Lavega, 1982). While most features are small, large white spots occasionally form in one of the planet’s zones which rapidly expand (day timescales) in the east–west direction until they girdle the whole planet before gradually subsiding (month timescales). Such Great White Spots (GWS) have now been observed from the ground in all zones except the STZ. Although no such storm was observed during the *Voyager* encounters, an equatorial storm (or ‘Equatorial Disturbance’) was observed by HST in September 1990 at 4°N (Westphal *et al.*, 1992) which had almost completely disappeared by June 1991. Subsequently a new storm was observed by HST in September 1994 which had not changed much by December 1994 (Figure 1.5) but has now disappeared. Although the origin of these storms remains unknown, detailed observations suggest that they result from a sudden outburst of convective activity, presumably originating from disturbances deep below the visible cloud tops which trigger rapid vertical convection and resultant ammonia cloud condensation (with possible thunderstorm-style deep vertical convection). These localized, thick, bright, high clouds then spread latitudinally and are subsequently torn apart by the high-latitudinal wind shear observed in Saturn’s atmosphere and are spread right around the planet before eventually settling. Previous storms in the EZ were observed in 1876 and 1933, and at a first glance these major equatorial storms would seem separated by approximately 57 years (2 Saturn years) and appear correlated with the northern hemisphere summer suggesting a link with solar forcing. If this is true then the next equatorial disturbance may be expected around the year 2047 (Beebe, 1997).

While the *Voyager* spacecraft did not observe a GWS, numerous anticyclonic ovals were observed in Saturn’s atmosphere including, amongst others, Brown Spots 1, 2, and 3 at 42°N, ‘Anne’s Spot’ (which had a reddish colour) at 55°S shown in Figure 5.19 (colour plate), and the ‘UV Spot’ at 27°N. A North Polar Spot (sometimes called ‘Big Bertha’) was also observed at 75°N whose interaction with the North Polar Hexagon feature will be discussed in the next section. These features were generally found to have the highest contrast in green-filtered images although as the name suggests, the UV Spot was most prominent at UV wavelengths. In addition to these regular ovals, a number of convective regions were also seen near 39°N (Figure 5.20, colour plate), a region of cyclonic vorticity, which have a similar appearance to the plumes that appear in Jupiter’s NEB (Smith *et al.*, 1981, 1982; Sromovsky *et al.*, 1983). It is possible that the convective events observed were

triggered by the passage of a cyclonic white spot immediately to the south of the outbreaks.

Recent ground-based imaging of Saturn in the 5- μm window (Yanamandra-Fisher *et al.*, 2001) has shown the main thermal emission to originate between 38° and 49°S, a region of westward zonal winds. Discrete dark (cold) features are apparent in this latitude band, with lengths of 30,000–50,000 km. These features are quite unlike anything that has been observed in Jupiter's atmosphere.

5.6.3 Waves

Two major planetary-scale waves have been observed in Saturn's atmosphere: the 'Ribbon Wave' at 46°N, and the North Polar Hexagon at 76°N shown in Figure 5.21.

The 'Ribbon Wave' was first detected by the *Voyager 2* spacecraft in 1981 (Smith *et al.*, 1982) and appears at visible wavelengths as a thin wavy line within the bright zone at 46°N, coincident with the first major eastward jet in Saturn's atmosphere north of the equatorial jet (Figure 5.22). The wavelength of the Ribbon Wave is of the order of 5,000 km and the phase speed is approximately 140 m s⁻¹. The wave feature was Fourier-analysed by Sromovsky *et al.* (1983) and later Godfrey and Moore (1986), who found that the dominant wavenumbers were 8 and 20. Although both sides of the zone are equally bright in green and red filters, the southern side appears brighter in violet images. However this contrast is completely reversed in UV where the southern side appears almost black. These observations point to the existence of high-altitude haze consisting of small particles to the south of the wave and low haze opacity to the north. This would suggest that air is rising to the south of the Ribbon Wave and sinking to the north and indeed cloud tracking of features shows the northern edge to be cyclonic and the southern edge to be anti-cyclonic which is the general association found in the Jovian atmosphere, although not generally in the Saturnian atmosphere as we have seen. Various attempts have been made to model these waves and Sromovsky *et al.* (1983) derived a dispersion relation which they argued showed that the wave was fundamentally a barotropic Rossby wave. However, Godfrey and Moore (1986) pointed out that the zonal wave curvature d^2u/dy^2 (for which high values are expected to lead to barotropic instability) was at a minimum at the central latitude of the wave and this appeared to be inconsistent with the barotropic wave hypothesis. Instead they favoured a baroclinic Rossby wave explanation since the *Voyager/IRIS* measurements showed the temperature at 150 mbar (Hanel *et al.*, 1982) to have a sharp gradient at this latitude with temperatures to the south being roughly 6 K cooler than the north. This is again consistent with the picture of rising air to the south and descending air to the north. The position of the wave at UV wavelengths (where we only see high in the atmosphere) is identical to that in visible wavelengths indicating little vertical shear in the feature. The ribbon wave was recently observed again by HST (Sanchez-Lavega, 2002) with the same wavelength and phase speed and would thus appear to be a long-lived feature.

Although the *Voyager* flybys of Saturn occurred in 1980 and 1981, the second

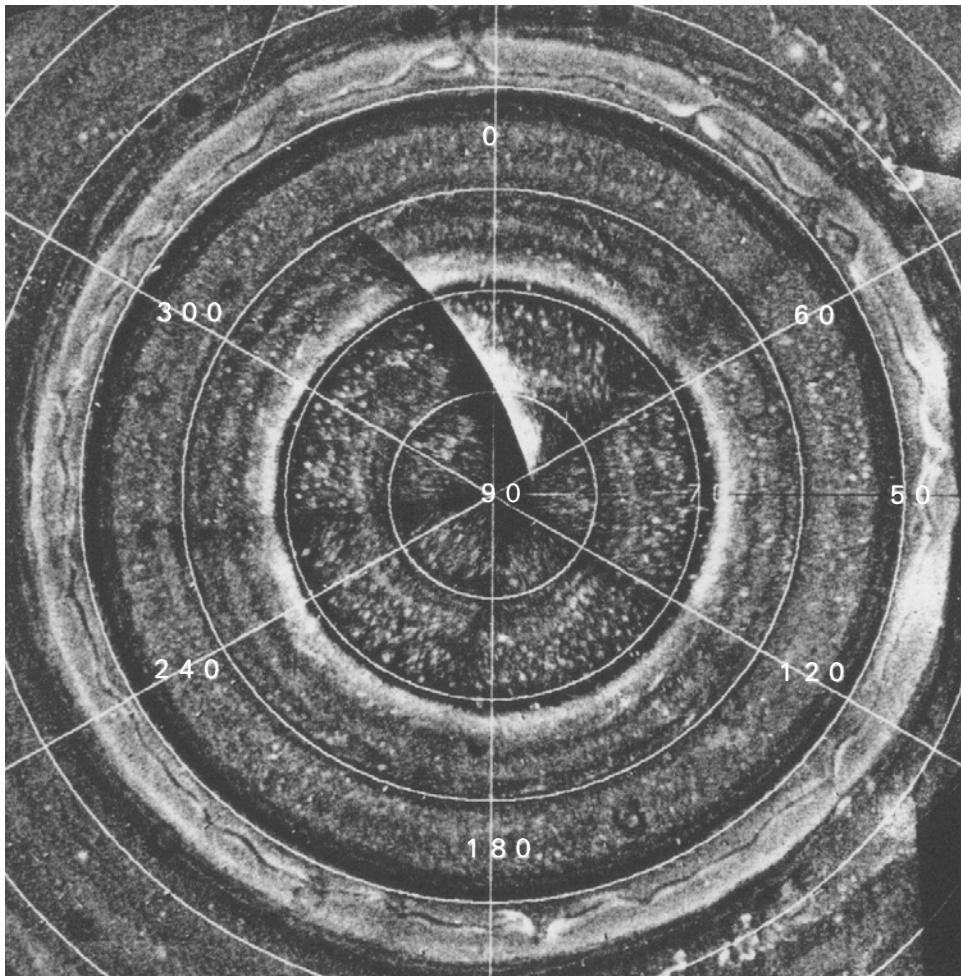


Figure 5.21 Saturn's North Polar Hexagon, North Polar Spot, and the 'Ribbon Wave'. Polar stereographic projection after Godfrey and Moore (1986). The Ribbon Wave at 47°N is clearly visible. The Hexagon Wave is not so clear but is visible at latitude $\sim 78^{\circ}\text{N}$. The North Polar Spot is at latitude 75°N and longitude (planetographic) of 320°W .

major wave system, the 'North Polar Hexagon' was not discovered until 1988, when *Voyager* images were re-projected to produce polar maps (Godfrey, 1988). This feature is a very regular wavenumber-6 wave centred in a 100 m s^{-1} eastward jet at 76°N . On the southern edge of one of the Hexagon's faces is the NPS. What is most remarkable about these features is that they are found to remain almost static with respect to System III longitudes, which is defined by the rotation of the magnetic field and thus the bulk interior. It seems unlikely that the magnetic field itself could be exerting such an influence on the motion of the observable

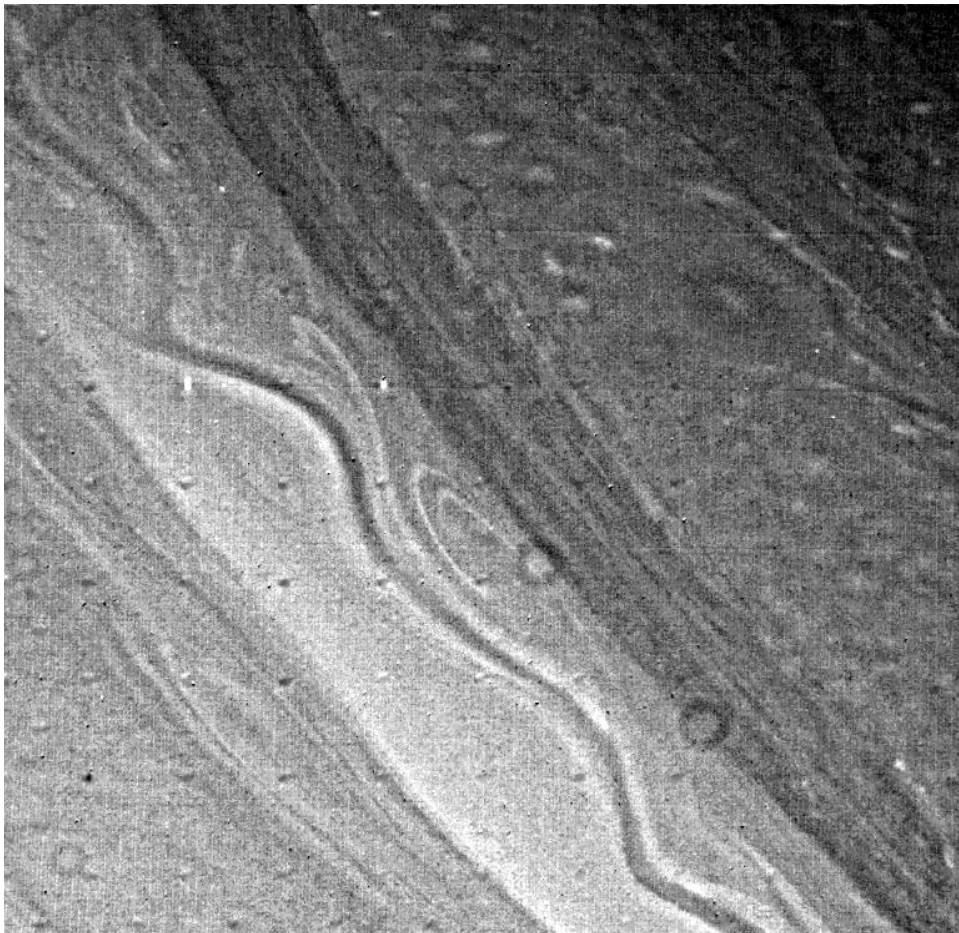


Figure 5.22 The ‘Ribbon Wave’ cloud structure in Saturn’s atmosphere observed by *Voyager 2* with a ‘green’ filter.

Courtesy of NASA.

troposphere and it would thus appear that both the NPS and the Hexagon are linked in some way to the deep interior. It has been suggested (Allison *et al.*, 1990) that the Hexagon is a stationary Rossby wave forced by interaction between the eastward jet and the adjacent NPS and meridionally trapped by the strong relative vorticity gradient of the flow itself. Both the NPS and hexagon were observed 10 years later by ground-based observations (Sanchez-Lavega *et al.*, 1993) although the scattering properties of the NPS appeared to have changed. In 1990, the NPS was observable from yellow to red wavelengths and was particularly bright in the near-IR methane bands indicating a high cloud top of ~ 90 mbar. However the *Voyager* NPS had greatest contrast at 419 nm but was barely visible at 566 nm. An additional difference is that while the *Voyager* and 1990 NPS had similar drift rates, extrapolat-

ing the position of the *Voyager* NPS forward to 1990 predicted a position approximately 60° away from the NPS's actual observed position. Sanchez-Lavega *et al.* suggested that an explanation for all the observed differences between the 1981 and 1990 NPS might be that there may in fact be *two* spots, on two adjacent sides of the Hexagon which alternately brighten and fade. Putting this last difference aside, the NPS and Hexagon system would appear to be extraordinarily long-lived considering their location at polar latitudes where the solar flux variations are extreme. Long-term monitoring of the upper troposphere and stratospheric temperatures by thermal-IR measurements show them to be in radiative equilibrium with the solar forcing. Hence it is suggested that the system arises from a deep-rooted wind field, insensitive to solar flux variations which supports a large anticyclonic eddy at the latitude observed (Sanchez-Lavega *et al.*, 1993). This oval then deflects the eastward jet at that latitude forcing a near-stationary wavenumber-6 Rossby wave. Why the wave should be wavenumber-6 and not any other is unclear, although it is interesting to note that the wavelength is very similar to the mean distance between Saturn's belts and zones and may be a 'preferred length' of the atmosphere.

No wave features have yet been observed in the southern hemisphere. A simple belt is seen at 48°S and a south polar belt has been regularly observed between 74.5° and 81.4°S (Sanchez-Lavega *et al.*, 1993). A small polar cap of only 2,000 km diameter has been seen in the most recent HST observations, although this appears to be highly variable and in 1998 was not distinguishable. However, by 2001 it was clearly visible together a bright ring around it (Sanchez-Lavega, 2002).

Much has already been observed about these waves on Saturn, but much remains unknown, particularly their vertical aerosol and thermal structure which will be a major goal of the *Cassini* mission. In addition, it will be very interesting to search for previously undiscovered wave activity in the southern hemisphere.

5.7 METEOROLOGY OF URANUS

5.7.1 General circulation and zonal structure

The amount of energy emitted by Uranus is at most only 1.06 times that received from the Sun indicating that Uranus has a very low internal heat source and, one might suspect, a sluggish circulation system driven primarily by latitudinal variations of the solar flux which at Uranus' distance from the Sun is a meagre 3.7 W m^{-2} . Another difference between Uranus and Jupiter/Saturn is Uranus' extremely large obliquity which means that Uranus receives direct sunlight over both poles as well as the equator during the course of a Uranian year (NB, even though both poles experience a night lasting half a Uranian year long, they receive annually 50% more sunlight per unit area than the equator). The final difference between Uranus and Jupiter/Saturn is that the visible hydrogen–helium atmosphere is only a small fraction of the total planet mass and thus the Taylor–Proudman column hypothesis is unlikely to apply due to the boundary between the hydrogen–helium outer atmosphere and the denser icy-rock interior occurring at a depth of just

5,000 km below the visible cloud tops. During the *Voyager 2* flyby mission, when Uranus' South Pole was facing almost directly towards the Sun, the dominant circulation must have been one which efficiently redistributed relatively warm polar air over the planet. Modelling the planet as a black sphere in radiative equilibrium with the received insolation, the expected equator-to-pole temperature difference would be of the order of 10 K. However, almost no thermal variation has been found in the 0.5–1 bar pressure levels by *Voyager 2* (Hanel *et al.*, 1986), and indeed in the stratosphere the equator was found to be actually warmer than the pole (Baines, 1997). However, estimates of the para-H₂ fraction and the eddy mixing coefficients suggest that vertical and meridional circulation of Uranus is indeed very sluggish. How such an apparently sluggish atmosphere can have such small temperature gradients given its differential radiative forcing is very unclear.

Although Uranus has very little visible belt/zone structure (Smith *et al.*, 1986, and Figure 1.6, colour plate), with only a very slight north–south asymmetry apparent in broad-band visible images (South Polar latitudes appear slightly brighter due to thicker methane haze) enough variable features do exist to allow cloud tracking and thus determination of the cloud-top winds. This was achieved by the *Voyager 2* cameras and further wind speed data has since been deduced from more recent HST observations (Hammel *et al.*, 2001). Thermal wind shears calculated from the retrieved temperature fields of *Voyager 2* suggest that the zonal winds decay with height with a vertical scale of ~ 10 scale heights or 300 km.

The most recent images of Uranus recorded by the HST (Karkoschka, 1998b, 2001) (Figure 5.23, colour plate) reveal a ‘zone’ at 40–50°S, and that the polar regions are slightly brighter than mid-latitudes. Hence most of the variation in Uranus’ total albedo measured since 1982 is attributed to apparent changes in reflectivity due to Uranus’ varying illumination angle (Uranus reaches its northern spring equinox in 2007) rather than physical changes in cloud structure. However, some north–south asymmetry is seen with southern mid-latitudes appearing brighter than equivalent northern latitudes, even after allowing for limb-darkening. There is also some indication that the optical thickness of the south polar haze has decreased in recent years. With the equinox rapidly approaching, the solar forcing of the Uranian atmosphere is about to change dramatically and it is quite possible that the cloud structure observed will rapidly change. Photographic plates of the previous equinox show a very different zonal appearance (Karkoschka, 2001).

5.7.2 Storms and vortices

Although Uranus exhibits a clear zonal wind structure, no regular cyclonic or anti-cyclonic eddies have been observed. Small white clouds are occasionally observed at mid-latitudes (at approximately $\pm 30^\circ$) which have been interpreted as localized methane clouds forming in restricted areas of rapid upwelling, rather like the equatorial brightenings seen on Saturn. Recent observations of these clouds (Figure 5.24) with the HST have been reported by Karkoschka (1998b, 2001) and Sromovsky *et al.* (2000). Such clouds, if associated with vigorous enough convection may help to transport methane through the cold trap of the tropopause and on into the strato-

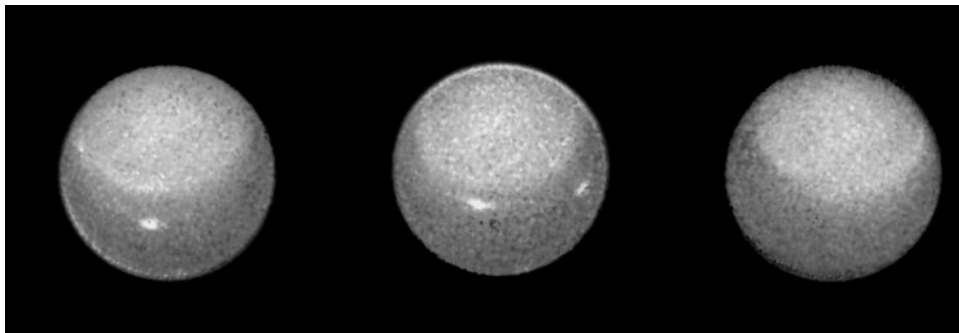


Figure 5.24 Three HST/WFPC-2 images of Uranus recorded in 1994 in a methane absorption band, revealing the motion of a pair of bright clouds in the planet's southern hemisphere, and a high altitude haze that forms a 'cap' above the planet's South Pole. The two high-altitude clouds are 4,300 and 3,100 km across, respectively. Three hours have elapsed between the first two images, and five hours have elapsed between the second pair of observations.

Courtesy of NASA.

sphere. However estimates of the abundance of methane in the stratosphere lie close to the 'cold trap' value at the tropopause. The recent HST data suggest that the northern mid-latitudes just coming into view as Uranus approaches equinox are considerably more convectively active than southern mid-latitudes.

5.7.3 Waves

No wave structures have been observed in the Uranian atmosphere.

5.8 METEOROLOGY OF NEPTUNE

5.8.1 General circulation and zonal structure

The atmosphere of Neptune is powered by extremely low energy fluxes. The internal heat energy flux is estimated to be 0.45 W m^{-2} (Table 3.2) while the absorbed solar flux is estimated to be 0.27 W m^{-2} , compared with values of 0 and 205.5 W m^{-2} respectively for the Earth. However, the cloud top zonal winds on Neptune are found to be very high with an extremely fast westward retrograde equatorial jet reaching speeds of 400 m s^{-1} gradually decreasing in the poleward direction and becoming eastward and prograde at latitudes poleward of 50° . It has been postulated that such high winds are allowed because the atmosphere of Neptune has low turbulence and thus low eddy viscosity. The general zonal wind structure is similar to that of Uranus. Why the equatorial jets of both planets should be blowing in the opposite direction to that of Jupiter and Saturn is unclear. In some ways it is easier to see how a retrograde equatorial jet is driven than a prograde, super-rotating jet.

Air rising from deep levels at the equator, and initially rotating at the internal rotation rate would be expected to slow at higher levels (and thus greater distance from the centre) due simply to conservation of angular momentum, giving rise to a westward blowing air stream. Similarly, fast flowing air at the equator which moves polewards would be expected to acquire additional eastward momentum via the same mechanism, giving prograde jets near the poles. Alternatively, air rising at mid-latitudes and then travelling both polewards and equatorwards would give rise to a similar wind structure. This view may be supported by the observation of upwelling at mid-latitudes described below.

Thermal wind shears calculated from *Voyager 2* thermal-IR measurements (Conrath *et al.*, 1989) show that like all the other giant planets the zonal winds decay with height. It is also of great interest, as we have seen, to determine how deep the zonal winds extend into the interior. This may be answered unequivocally for both Neptune and Uranus by determination of the J_4 gravitational constant. If the zonal currents were superficial such that virtually all the planetary mass rotates with the deep period, then calculations suggest that J_4 should be negative and have a value close to that given in Table 2.4. If however the zonal currents are surface expressions of internal differentially-rotating cylinders then J_4 is predicted to be positive and have an absolute value roughly twice as big as that observed (Hubbard, 1997). Hence, at least for the case of Uranus and Neptune, the zonal winds appear to be restricted to the upper levels of the atmosphere, although the Thermal Wind Equation suggests they must still be reasonably deep given the small latitudinal variation in temperature at pressures greater than approximately 1 bar.

Another curious feature of Neptune's atmosphere is that, while some banding is observed (more so than Uranus), the relationship between visible albedo and vorticity appears to be the opposite of that observed for Jupiter and Saturn with the anticyclonic, mid-latitude regions appearing generally darker, and the equator and poles appearing generally bright. Unfortunately the flux at $5\text{ }\mu\text{m}$ is too low to determine if these albedo variations are due to total cloud opacity changes or to some other effect. In addition to these general banded features, transitory white clouds are often observed on Neptune, and these clouds remain bright in the methane bands, indicating high cloud tops. The most plausible explanation of these features is that they are convectively produced methane clouds, although how they are initiated is unclear since the zonal wind flow is apparently stable everywhere to baroclinic and barotropic instabilities according to the *Charney–Stern* criterion. These convective clouds are observed at a number of latitudes, but they usually appear at mid-latitudes (i.e., in the cyclonic vorticity regions just as they do for all of the other giant planets). This interpretation is strengthened by the *Voyager 2/IRIS* observations that the coolest tropopause temperatures, indicating divergence at the tropopause and thus convection from below, are found at mid-latitudes. The rapid overturning of Neptune's atmosphere is also indicated by the detection of disequilibrium species such as CO and the modelled possible presence of N₂. The background banded appearance of Neptune is thus probably due to variations in either the depth or colour of the lower H₂S cloud and it would appear that this cloud deck responds counter-intuitively to the convective motion of the atmo-

sphere above by appearing darker or being depressed to deeper levels where upper level convection occurs.

On a historical note, the high equatorial wind speeds on Neptune led to early confusion about its internal structure. As we discussed in Chapter 2, for a body in hydrostatic equilibrium rotating with a single period P , the oblateness, J_2 , and P are uniquely related. Prior to the arrival of *Voyager 2* at Neptune in 1989, the rotational period was estimated from observation of the variation of Neptune's disc-averaged albedo caused by the transition of distinct cloud features which occur at mid- and equatorial-latitudes. Since these clouds lie in a strong retrograde zonal flow, the rotational period was estimated to be 18 hours which was found to be incompatible with the observed oblateness and J_2 . However, *Voyager 2* measured the rotational period of the magnetic field (and thus the interior) to be just over 16 hours which is consistent with the other data.

5.8.2 Storms and vortices

The atmosphere of Neptune is observed to be highly dynamic and convective with numerous storm and eddy features which allowed early estimates of the planet's rotation rate due to diurnal variations of the planets observed reflectivity. More recently, in the last twenty years, ground-based images in the 0.89- μm methane band have revealed distinct high-altitude cloud features from Earth on scales of 10,000 km or more (Baines, 1997). The distribution of these features has been found to be highly variable.

The arrival of *Voyager 2* at Neptune in 1989 heralded an enormous development in our understanding of clouds and storm systems in Neptune's atmosphere (Smith *et al.*, 1989). *Voyager 2* observed four large features that persisted for the duration of the *Voyager* observations (from January to August, 1989). The largest of these was the Great Dark Spot (GDS) and its white companion immediately to the south which together drifted from 26°S to 17°S during the period of observation, or equivalently drifted polewards at a rate of 15° year⁻¹ (Figure 5.25). At first glance, the GDS appeared similar to the GRS of Jupiter since they both rotated anti-cyclonically, and were of comparable size. However in other respects they were very different. For a start the GDS appears to have been a short-lived disturbance, which by the time new HST observations were made in 1994 had completely disappeared, only to be subsequently replaced by a new dark spot at 32°N (NGDS32) which has not been observed to drift latitudinally since (Sromovsky *et al.*, 2001c, d). Secondly, the GRS is believed to be a region of rapid updraft and the cloud cover is particularly thick and high, whereas the dark colour of the GDS may be attributed either to a low methane ice, and stratospheric haze abundance above the GDS or, more likely, that the main 3.8 bar cloud itself is somehow darker, or deeper. The wispy white clouds associated with the companion to the GDS were observed to move at a different speed to the GDS and companion, suggesting that these features form and evaporate high above the GDS as they pass through a local pressure anomaly, perhaps a standing wave caused by flow around the GDS (West, 1999). The second dark spot (DS2) was observed at 55°S in the dark circumpolar band and

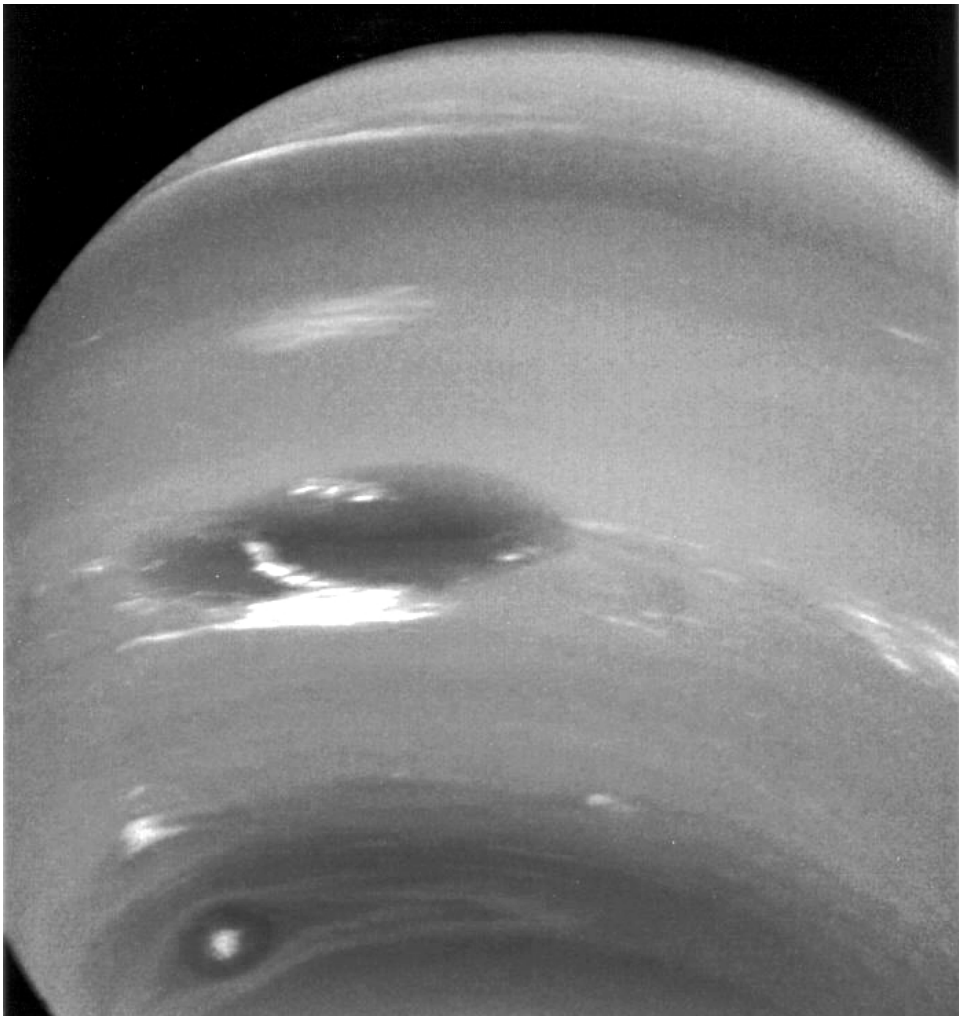


Figure 5.25 Detail of the GDS and DS2 observed by *Voyager 2* in 1989.

Courtesy of NASA.

appeared to be roughly 180° in longitude away from transient bright clouds seen at 70°S , called the South Polar Feature (SPF) (Sromovsky *et al.*, 1993). An additional bright cloud was seen near 42°S and acquired the name ‘scooter’.

A striking feature of Neptune’s dark spots, discovered by *Voyager 2*, was that they wobbled! The longitudinal and latitudinal widths of the GDS were found to vary sinusoidally and in antiphase, with a period of approximately 200 hours and with amplitudes of 7.4° longitude and 1.5° latitude (Sromovsky *et al.*, 1993). While the shape of DS2 did not undergo such oscillations, its position was found to vary sinusoidally with a period of 36 days and amplitude of 2.4° latitude and 47.5°

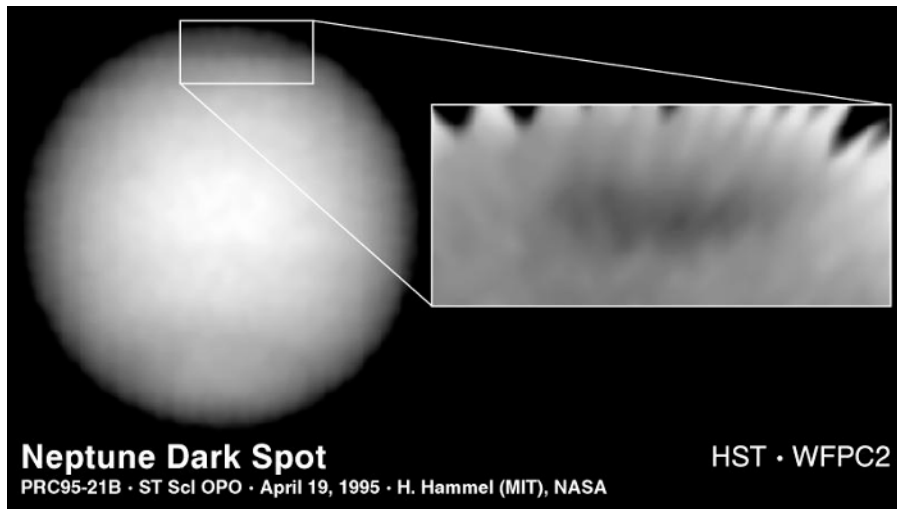


Figure 5.26 HST image of a new ‘Great Dark Spot’, located at a latitude of 32°N in the northern hemisphere of the planet Neptune recorded in 1994. By this time the *Voyager* GDS found in the southern hemisphere had completely disappeared.

Courtesy of NASA.

longitude (relative to the mean drift longitude). These positional variations were accompanied by a variation in the area of the bright core of the DS2 which had maximum area when the DS2 was furthest north.

After the *Voyager 2* encounter, high-resolution imaging of Neptune did not begin again until HST observed the planet in 1994. All of the discrete atmospheric features observed by *Voyager 2* were found to have disappeared with the exception of the SPF which is still seen to come and go. More recently, advances in deconvolution of ground-based images (Sromovsky *et al.*, 2001a) have allowed the resolution of discrete cloud features at near-IR wavelengths and have thus greatly improved the spectral sampling of the Neptunian clouds. The *Voyager 2* GDS appeared to have disappeared by 1994 (Hammel *et al.*, 1995) only to be replaced by a new dark spot at 32°N (NGDS32) which has apparently remained fixed in latitude ever since (Figure 5.26). An additional dark spot was observed at 15°N in 1996 but by 1998 this had apparently disappeared (Sromovsky *et al.*, 2001d). Numerous clouds have now been recorded in Neptune’s atmosphere over a number of years (Figure 5.27, colour plate). Transient clouds generally appear between 29° and 45°S, and 29° and 39°N (this is the furthest north that can currently be seen due to Neptune’s obliquity and season). These latitudes correspond to cooler tropopause temperatures indicative of upwelling and divergence at high altitudes. The zonal stability of Neptune’s winds imply any small-scale disturbances will rapidly cascade into large eddies such as the Dark Spots, and it may be that NGDS32 is an ‘adolescent’ spot that has recently formed (Sromovsky *et al.*, 2001c). These spots are predicted by non-linear modelling to drift down the potential vorticity gradient towards the equator (LeBeau and Dowling, 1998). The fact that NGDS32 is currently fixed at 32°N may be due to

the fact that since the spot has only recently formed, the potential vorticity gradient has not yet had a chance to re-establish itself. As soon as it does, NGDS32 may be lured towards the equator, much like the *Voyager GDS* was, where it is predicted to rapidly dissipate through conversion into planetary waves (Sromovsky *et al.*, 2001c).

5.8.3 Waves

The main apparent wave features observable in Neptune's atmosphere are the South Polar Wave (SPW), and possibly transient cloud features known as 'Outbursts'. Other examples include the observed oscillation of discrete cloud features which was discussed in the previous section.

A dark apparently axisymmetric feature was detected near Neptune's South Pole by *Voyager 2* in 1989 (Figure 5.28, colour plate). The band extended between planetocentric latitudes of 65° S and 40° S. However, within this band was a narrower, darker region which appeared as a wavenumber-1 planetary wave. The poleward excursion of the inner band was bordered on the north by a dark anticyclone (DS2) centred at 55° S, while the longitude of maximum equatorial excursion was marked by an outbreak of bright clouds at 70° S, the SPF. This wave appears in many respects to be analogous to the North Polar Hexagon in Saturn's atmosphere which is generally believed to be a planetary wave forced by interaction with its own equator-side anticyclone, the NPS. However, while the North Polar Hexagon is quasi-stationary with respect to System III, suggesting a link with the rotation of the bulk interior, Neptune's SPW drifts significantly with respect to the interior rotation (Sromovsky *et al.*, 1993). More recent observations of Neptune by HST and ground-based telescopes between 1994 and 1996 (Sromovsky *et al.*, 2001c) have shown that while the SPW was still clearly visible, the latitudinal extent of the band had shrunk to between 55° S and 65° S. In addition the SPF were rarely apparent and DS2 had completely disappeared. Dynamically, Sromovsky *et al.* (2001c) suggested that it is hard to see how such a wave could still be present in the absence of a forcing anticyclone and suggested that DS2 may have in fact still been present, but was too faint to observe.

While the *Voyager GDS* had disappeared by 1994–1996, a new dark feature NGDS32 had appeared at 32° N, which remained fixed in latitude during the observation campaign. In 1994 many bright clouds were observed extending from 30° N to the equator at roughly the same longitude as NGDS32 (Sromovsky *et al.*, 2001c). Furthermore, the zonal velocity of these clouds was substantially less than the average zonal velocity at the equator, and instead the speed seemed locked to the zonal velocity at the NGDS32 latitude. This sudden appearance of bright equatorial clouds (Sromovsky *et al.*, 2001b) would seem to be similar to the 'Outbursts' postulated to explain the increased disc-averaged albedo observed with ground-based telescopes between 1986 and 1987 by Hammel *et al.* (1992), and likened to the GWS of Saturn. A similar link between near equatorial Dark Spots and equatorial clouds was observed by *Voyager 2* where a bright 'smudge' was observed just past the equator at the same longitude as the GDS and apparently co-rotating with it. This co-rotation suggests some sort of wave interaction and since the phase speed of the wave would appear to be eastward the most likely candidate is an equatorially-

trapped Kelvin wave (Sromovsky *et al.*, 2001c). However the equatorial confinement of such a wave with an estimated phase speed of 210 m s^{-1} is calculated from the equatorial deformation radius to be 17° of latitude whilst the observed clouds actually extended to 30°N . The nature of this interaction hence clearly warrants further study.

5.9 REFERENCES

- Allison, M. (1990) Planetary waves in Jupiter's equatorial atmosphere. *Icarus*, **83**, 282–307.
- Allison, M., D. Godfrey, and R. F. Beebe (1990) A wave dynamical interpretation of Saturn's polar hexagon. *Science*, **247**, 1061–1063.
- Andrews, D. G., J. R. Holton, and C. B. Leovy (1987) *Middle Atmosphere Dynamics*. Academic Press, San Diego, CA.
- Andrews, D. G. (2000) *An Introduction to Atmospheric Physics*. Cambridge University Press, Cambridge, UK.
- Atkinson, D. H., J. B. Pollack, and A. Seiff (1998) The Galileo Probe Doppler Wind Experiment: Measurement of the deep zonal winds on Jupiter. *J. Geophys. Res.*, **103**, 22911–22928.
- Baines, K. H. (1997) Uranus: Atmosphere. *Encyclopaedia of the Planetary Sciences* (edited by J. H. Shirley, and R. W. Fairbridge). Chapman & Hall, London.
- Baines, K. H., R. W. Carlson, and L. W. Kamp (2002) Fresh ammonia ice clouds in Jupiter: Spectroscopic identification, spatial distribution, and dynamical implications. *Icarus*, **159**, 79–94.
- Banfield, D., P. J. Gierasch, M. Bell, E. Ustinov, A. P. Ingersoll, A. R. Vasavada, R. A. West, and M. J. Belton (1998) Jupiter's cloud structure from Galileo imaging data. *Icarus*, **135**, 230–250.
- Beebe, R. (1997) Saturn: Atmosphere. *Encyclopaedia of the Planetary Sciences* (edited by J. H. Shirley and R. W. Fairbridge), Chapman & Hall, London.
- Beebe, R. F., A. P. Ingersoll, G. E. Hunt, J. L. Mitchell, and J.-P. Muller (1980) Measurements of wind vectors, eddy momentum transports, and energy conversions in Jupiter's atmosphere from Voyager 1 images. *Geophys. Res. Lett.*, **7**, 1–4.
- Busse, F. H. (1976) A simple model of convection in the Jovian atmosphere. *Icarus*, **29**, 255–260.
- Chamberlain, J. W. and D. M. Hunten (1987) *Theory of Planetary Atmospheres* (2nd Edition). Academic Press, San Diego, CA.
- Charney, J. G. (1971) Geostrophic turbulence. *J. Atmos. Sci.*, **28**, 1087–1095.
- Conrath, B. J., F. M. Flasar, R. Hanel, V. Kunde, W. Maguire, J. Pearl, J. Pirraglia, R. Samuelson, P. Gierasch, A. Weir, B. Bézard, D. Gautier, D. Cruikshank, L. Horn, R. Springer, and W. Shaffer (1989) Infrared observations of the Neptunian system. *Science*, **246**, 1454.
- Conrath, B. J., P. J. Gierasch, and S. S. Leroy (1990) Temperature and circulation in the stratosphere of the outer planets. *Icarus*, **83**, 255–281.
- Conrath, B. J., P. J. Gierasch, and E. A. Ustinov (1998) Thermal structure and para hydrogen fraction on the outer planets from Voyager IRIS measurements. *Icarus*, **135**, 501–517.
- Deming, D., M. J. Mumma, F. Espenak, D. E. Jennings, T. Kostiuk, G. Wiedemann, R. Loewenstein, and J. Priscitelli (1989) A search for *p*-mode oscillations on Jupiter: Serendipitous observations of non-acoustic thermal wave structure. *Astrophys. J.*, **343**, 456–467.

- Deming, D., D. Reuter, D. Jennings, G. Bjaraker, G. McCabe, K. Fast, and G. Wiedemann (1997) Observations and analysis of longitudinal thermal waves on Jupiter. *Icarus*, **126**, 301–312.
- Dowling, T. E. (1997) Jupiter. *Encyclopaedia of the Planetary Sciences* (edited by J. H. Shirley and R. W. Fairbridge). Chapman & Hall, London.
- Dowling, T. E. and A. P. Ingersoll (1988) Potential vorticity and layer thickness variations in the flow around Jupiter's Great Red Spot and White Oval. *J. Atmos. Sci.*, **45**, 1380–1396.
- Dowling, T. E. and A. P. Ingersoll (1989) Jupiter's Great Red Spot as a shallow water system. *J. Atmos. Sci.*, **46**, 3256–3278.
- Dowling, T. E., A. S. Fischer, P. J. Gierasch, J. Harrington, R. L. LeBeau, and C. M. Santori (1998) The explicit planetary isentropic-coordinate (EPIC) atmospheric model. *Icarus*, **132**, 221–238.
- Flasar, F. M. and P. J. Gierasch (1986) Mesoscale waves as a probe of Jupiter's deep atmosphere. *J. Atmos. Sci.*, **43**, 2638–2707.
- Fouchet, T., E. Lellouch, and H. Feuchtgruber (2003) The hydrogen ortho-to-para ratio in the stratospheres of the giant planets. *Icarus*, **161**, 127–143.
- Friedson, A. J. (1999) New observations and modelling of a QBO-like oscillation in Jupiter's stratosphere. *Icarus*, **137**, 34–55.
- Friedson, A. J., R. A. West, A. K. Hronek, N. A. Larsen, and N. Dalal (1999) Transport and mixing in Jupiter's stratosphere inferred from Comet S-L9 dust migration. *Icarus*, **138**, 141–156.
- Gierasch, P. J. and R. M. Goody (1969) Radiative time constants in the atmosphere of Jupiter. *J. Atmos. Sci.*, **26**, 979–980.
- Gierasch, P. J. and B. J. Conrath (1993) Dynamics of the atmospheres of the outer planets: Post-Voyager measurement objectives. *J. Geophys. Res.*, **98**, 5459–5469.
- Gierasch, P. J., A. P. Ingersoll, D. Banfield, S. P. Ewald, P. Helfenstein, A. Simon-Miller, A. Vasavada, H. H. Breneman, D. A. Senske, and the Galileo Imaging Team (2000) Observation of moist convection in Jupiter's atmosphere. *Nature*, **403**, 628–630.
- Gill, A. E. (1982) *Atmosphere–Ocean Dynamics*. Academic Press, San Diego, CA.
- Godfrey, D. A. (1988) A hexagonal feature around Saturn's north pole. *Icarus*, **76**, 335–356.
- Godfrey, D. A. and V. Moore (1986) The Saturnian ribbon feature – a baroclinically unstable model. *Icarus*, **68**, 313–343.
- Hammel, H. B., S. L. Lawson, J. Harrington, G. W. Lockwood, D. T. Thompson, and C. Swift (1992) An atmospheric outburst on Neptune from 1986 through 1989. *Icarus*, **99**, 363–367.
- Hammel, H. B., G. W. Lockwood, J. R. Mills, and C. D. Barnet (1995) Hubble Space Telescope imaging of Neptune's cloud structure in 1994. *Science*, **268**, 1740–1742.
- Hammel H. B., K. Rages, G. W. Lockwood, E. Karkoschka, and I. de Pater (2001) New measurements of the winds on Uranus. *Icarus*, **153**, 229–235.
- Hanel, R. A., B. Conrath, F. M. Flasar, V. Kunde, P. Lowman, W. Maguire, J. Pearl, J. Pirraglia, R. Samuelson, D. Gautier, P. Gierasch, S. Kumar, and C. Ponnampерuma (1979a) Infrared observations of the Jovian system from Voyager 1. *Science*, **204**, 972–976.
- Hanel, R. A., B. Conrath, F. M. Flasar, L. Herath, V. Kunde, P. Lowman, W. Maguire, J. Pearl, J. Pirraglia, and L. Horn (1979b) Infrared observations of the Jovian system from Voyager 2. *Science*, **206**, 952–956.
- Hanel, R. A., B. Conrath, F. M. Flasar, V. Kunde, W. Maguire, J. C. Pearl, J. Pirraglia, R. Samuelson, L. Herath, M. Allison, D. P. Cruikshank, D. Gautier, P. J. Gierasch, L. Horn, R. Koppany, and C. Ponnampерuma (1981) Infrared observations of the Saturnian system from Voyager 1. *Science*, **212**, 192–200.
- Hanel, R. A., B. Conrath, F. M. Flasar, V. Kunde, W. Maguire, J. C. Pearl, J. Pirraglia, R. Samuelson, D. P. Cruikshank, D. Gautier, P. J. Gierasch, L. Horn and C. Ponnamp

- uma (1982) Infrared observations of the Saturnian system from Voyager 2. *Science*, **215**, 544–548.
- Hanel, R. A., B. Conrath, F. M. Flasar, V. Kunde, W. Maguire, J. Pearl, J. Pirraglia, R. Samuelson, L. Horn, and P. Schulte (1986) Infrared observations of the Uranian system. *Science*, **233**, 70–74.
- Harrington, J., T. E. Dowling, and R. L. Baron (1996) Jupiter's tropospheric thermal emission. II: Power spectrum analysis and wave search. *Icarus*, **124**, 32–44.
- Hart, J. E., J. Toomre, A. E. Deane, N. E. Hurlbert, G. A. Glatzmaier, G. H. Fichtl, F. Leslie, W. W. Fowlis, and P. A. Gilman (1986) Laboratory experiments on planetary and stellar convection performed on Spacelab 3. *Science*, **234**, 61–234.
- Holton, J. R. (1992) *An Introduction to Dynamical Meteorology* (3rd Edition). Academic Press, San Diego, CA.
- Houghton, J. T. (1986) *The Physics of Atmospheres* (2nd Edition). Cambridge University Press, Cambridge, UK.
- Hubbard, W. B. (1997) Neptune. *Encyclopaedia of the Planetary Sciences*, (edited by J. H. Shirley and R. W. Fairbridge). Chapman & Hall, London.
- Hubbard, W. B. (1999) Gravitational signature of Jupiter's deep zonal flows. *Icarus*, **137**, 357–359.
- Ingersoll, A. P., R. F. Beebe, J. L. Mitchell, G. W. Garneau, G. M. Yagi, and J. P. Müller (1981) Interaction of eddies and mean zonal flow on Jupiter as inferred from Voyager 1 and 2 images. *J.Geophys. Res.*, **86**, 8733–8743.
- Ingersoll, A. P. and D. Pollard (1982) Models of the interiors and atmospheres of Jupiter and Saturn: Scale analysis, anelastic equations, barotropic stability criterion. *Icarus*, **52**, 61–80.
- Ingersoll, A. P. (1990) Atmospheric dynamics of the outer planets. *Science*, **248**, 308–315.
- Ingersoll, A. P., P. J. Gierasch, D. Banfield, A. R. Vasavada, and the Galileo Imaging Team (2000) Moist convection as an energy source for the large-scale motions in Jupiter's atmosphere. *Nature*, **403**, 630–632.
- Irwin, P. G. J., A. L. Weir, F. W. Taylor, S. B. Calcutt, and R. W. Carlson (2001) The origin of belt/zone contrasts in the atmosphere of Jupiter and their correlation with 5-micron opacity. *Icarus*, **149**, 397–415.
- Karkoschka, E. (1998a) Methane, ammonia, and temperature measurements of the Jovian planets and Titan from CCD-spectrophotometry. *Icarus*, **133**, 134–146.
- Karkoschka, E. (1998b) Clouds of high contrast on Uranus. *Science*, **280**, 570–572.
- Karkoschka, E. (2001) Uranus' apparent seasonal variability in 25 HST filters. *Icarus*, **151**, 84–92.
- Lellouch, E., B. Bézard, J. I. Moses, G. R. Davis, P. Drossart, H. Feuchtgruber, E. A. Bergin, R. Moreno, and T. Encrenaz (2002) The origin of water vapour and carbon dioxide in Jupiter's stratosphere. *Icarus*, **159**, 112–131.
- Leovy, C. B., A. J. Friedson, and G. S. Orton (1991) The quasiquadrennial oscillation of Jupiter's equatorial stratosphere. *Nature*, **354**, 380–382.
- LeBeau, R. P. and T. E. Dowling (1998) EPIC simulations of time-dependent three-dimensional vortices with application to Neptune's Great Dark Spot. *Icarus*, **132**, 239–265.
- Leovy, C. (1986) Eddy processes in the general circulation of the Jovian atmospheres. *NASA GISS: The Jovian atmospheres*, pp. 177–196.
- Lewis, S. R. (1988) Long-lived eddies in the atmosphere of Jupiter, D.Phil. Thesis, University of Oxford.
- Li, X. and P. L. Read (2000) A mechanistic model of the quasi-quadrennial oscillation of Jupiter's stratosphere. *Plan. Space Sci.*, **48**, 637–669.
- Little, B., C. D. Anger, A. P. Ingersoll, A. R. Vasavada, D. A. Senske, H. H. Breneman, W. J. Borucki, and the Galileo SSI team (1999) Galileo images of lightning on Jupiter. *Icarus*, **142**, 306–323.

- Magalhães, J. A., A. L. Weir, B. J. Conrath, P. J. Gierasch, and S. S. Leroy (1989) Slowly moving features on Jupiter. *Nature*, **337**, 444–447.
- Magalhães, J. A., A. L. Weir, B. J. Conrath, P. J. Gierasch, and S. S. Leroy (1990) Zonal motion and structure in Jupiter's upper troposphere from Voyager infrared and imaging observations. *Icarus*, **88**, 39–72.
- Moreno, F. and J. Sedano (1997) Radiative balance and dynamics in the stratosphere of Jupiter: Results from a latitude-dependent aerosol heating model. *Icarus*, **130**, 36–48.
- Ortiz, J. L., G. S. Orton, A. J. Friedson, S. T. Stewart, B. M. Fisher, and J. R. Spencer (1998) Evolution and persistence of 5-μm hot spots at the Galileo Probe entry latitude. *J. Geophys. Res.*, **103**, 23051–23069.
- Orton, G. S., A. J. Friedson, J. Caldwell, H. B. Hammel, K. H. Baines, J. T. Bergstrahl, T. Z. Martin, M. E. Malcom, R. A. West, W. F. Golisch, D. M. Griep, C. D. Kaminski, A. T. Tokunaga, R. Baron, and M. Shure (1991) Thermal maps of Jupiter: Spatial organization and time dependence of stratospheric temperatures, 1980 to 1990. *Science*, **252**, 537–542.
- Orton, G. S., A. J. Friedson, P. A. Yanamandra-Fisher, J. Caldwell, H. B. Hammel, K. H. Baines, J. T. Bergstrahl, T. Z. Martin, R. A. West, G. J. Veeder Jr, D. K. Lynch, R. Russell, M. E. Malcom, W. F. Golisch, D. M. Griep, C. D. Kaminski, A. T. Tokunaga, T. Herbst, and M. Shure (1994) Spatial organization and time dependence of Jupiter's tropospheric temperatures, 1980–1993. *Science*, **265**, 625–631.
- Pirraglia, J. A., B. J. Conrath, M. D. Allison, and P. J. Gierasch (1981) Thermal structure and dynamics of Saturn and Jupiter. *Nature*, **292**, 677–679.
- Porco, C. C., R. A. West, A. McEwen, A. D. Del Genio, A. P. Ingersoll, P. Thomas, S. Squyres, L. Donas, C. D. Murray, T. V. Johnson, J. A. Burns, A. Brahic, G. Neukum, J. Everka, J. M. Barbara, T. Denk, M. Evans, J. J. Ferrier, P. Geissler, P. Helfenstein, T. Roatsch, H. Throop, M. Tiscareno and A. R. Vasavada (2003) Cassini imaging science at Jupiter. *Science*, **299**, 1541–1547.
- Read, P. L. (1986) Stable, baroclinic eddies on Jupiter and Saturn: A laboratory analogue and some observational tests. *Icarus*, **65**, 304–334.
- Read, P. L. and R. Hide (1984) An isolated baroclinic eddy as laboratory analogue of the Great Red Spot. *Nature*, **308**, 45–48.
- Read, P. L. and R. Hide (1983) Long-lived eddies in the laboratory and in the atmospheres of Jupiter and Saturn. *Nature*, **302**, 126–129.
- Rhines, P. B. (1973) Observations of energy-containing oceanic eddies and theoretical models of waves and turbulence. *Bound.-Layer Meteor.*, **4**, 345–360.
- Rhines, P. B. (1975) Waves and turbulence on a beta plane. *J. Fluid Mech.*, **69**, 417–443.
- Rogers, J. H. (1995) *The Giant Planet Jupiter*. Cambridge University Press, Cambridge, UK.
- Roos-Serote, M., A. R. Vasavada, L. Kamp, P. Drossart, P. Irwin, C. Nixon, and R. W. Carlson (2000) Proximate humid and dry regions in Jupiter's atmosphere indicate complex local meteorology. *Nature*, **405**, 158–160.
- Sanchez-Lavega, A. (1982) Motions in Saturn's atmosphere: Observations before Voyager. *Icarus*, **49**, 1–16.
- Sanchez-Lavega, A., J. Leacheux, F. Colas, and P. Laques (1993) Ground-based observations of Saturn's North Polar Spot and Hexagon. *Science*, **260**, 329–332.
- Sanchez-Lavega, A., J. Rojas, and P. Sada (2000) Saturn's zonal winds at cloud level. *Icarus*, **147**, 405–420.
- Sanchez-Lavega, A. (2002) Observations of Saturn's Ribbon wave 14 years after its discovery. *Icarus*, **158**, 272–275.
- Seiff, A., D. B. Kirk, T. C. D. Knight, R. E. Young, J. D. Mihalov, L. A. Young, F. S. Milos, G. Schubert, R. C. Blanchard, and D. Atkinson (1998) Thermal structure of Jupiter's atmosphere near the edge of a 5-μm hot spot in the north equatorial belt. *J. Geophys. Res.*, **103**, 22857–22889.

- Showman, A. P. and T. E. Dowling (2000) Nonlinear simulations of Jupiter's 5-micron hotspots. *Science*, **289**, 1737–1740.
- Simon-Miller, A. A., P. J. Giersch, R. F. Beebe, B. Conrath, F. M. Flasar, R. K. Achterberg, and the Cassini CIRS Team (2002) New observational results concerning Jupiter's Great Red Spot. *Icarus*, **158**, 249–266.
- Smith, B. A., L. A. Soderblom, T. V. Johnson, A. P. Ingersoll, S. A. Collins, E. M. Shoemaker, G. E. Hunt, H. Masursky, M. H. Carr, M. E. Davies, A. F. Cook, J. M. Boyce, T. Owen, G. E. Danielson, C. Sagan, R. F. Beebe, J. Veverka, J. F. McCauley, R. G. Strom, D. Morrison, G. A. Briggs and V. E. Suomi (1979a) The Jupiter system through the eyes of Voyager 1. *Science*, **204**, 951–957, 960–972.
- Smith, B. A., L. A. Soderblom, R. Beebe, J. Boyce, G. Briggs, M. Carr, S. A. Collins, T. V. Johnson, A. F. Cook, G. E. Danielson, and D. Morrison (1979b) The Galilean satellites and Jupiter: Voyager 2 imaging science results. *Science*, **206**, 927–950.
- Smith, B. A., L. Soderblom, R. Beebe, J. Boyce, G. Briggs, A. Bunker, S. A. Collins, C. J. Hansen, T. V. Johnson, J. L. Mitchell, R. J. Terrile, A. F. Cook, J. Cuzzi, J. B. Pollack, G. E. Danielson, A. P. Ingersoll, M. E. Davies, G. E. Hunt, H. Masursky, E. Shoemaker, D. Morrison, T. Owen, C. Sagan, J. Veverka, R. Strom, and V. E. Suomi (1981) Encounter with Saturn: Voyager 1 imaging science results. *Science*, **212**, 163–191.
- Smith, B. A., L. Soderblom, R. Batson, P. Bridges, J. Inge, H. Masursky, E. Shoemaker, R. Beebe, J. Boyce, G. Briggs, A. Bunker, S. A. Collins, C. J. Hansen, T. V. Johnson, J. L. Mitchell, R. J. Terrile, A. F. Cook, J. Cuzzi, J. B. Pollack, G. E. Danielson, A. P. Ingersoll, M. E. Davies, G. E. Hunt, D. Morrison, T. Owen, C. Sagan, J. Veverka, R. Strom, and V. E. Suomi (1982) A new look at the Saturn system: The Voyager 2 images. *Science*, **215**, 504–537.
- Smith, B. A., L. A. Soderblom, R. Beebe, D. Bliss, R. H. Brown, S. A. Collins, J. M. Boyce, G. M. Briggs, A. Brahic, J. N. Cuzzi, and D. Morrison (1986) Voyager 2 in the Uranian system: Imaging science results. *Science*, **233**, 43–64.
- Smith, B. A., L. A. Soderblom, D. Banfield, C. Barnet, R. F. Beebe, A. T. Bazilevskii, K. Bollinger, J. M. Boyce, G. A. Briggs, and A. Brahic (1989) Voyager 2 at Neptune: Imaging science results. *Science*, **246**, 1422–1449.
- Sromovsky, L. A., H. E. Revercomb, V. E. Suomi, S. S. Limaye, and R. J. Kraus (1982) Jovian winds from Voyager 2. II: Analysis of eddy transports. *J. Atmos. Sci.*, **39**, 1433–1445.
- Sromovsky, L. A., H. E. Revercombe, R. J. Kraus, and V. E. Suomi (1983) Voyager 2 observations of Saturn's northern mid-latitude cloud features: Morphology, motions and evolution. *J. Geophys. Res.*, **88**, 8650–8666.
- Sromovsky, L. A., S. S. Limaye, and P. M. Fry (1993) Dynamics of Neptune's major cloud features. *Icarus*, **105**, 110–141.
- Sromovsky, L. A., J. Spencer, K. Baines, and P. Fry (2000) Ground-based observations of cloud features on Uranus. *Icarus*, **146**, 307–311.
- Sromovsky, L. A., P. M. Fry, K. H. Baines, S. S. Limaye, G. S. Orton, and T. E. Dowling (2001a) Coordinated 1996 HST and IRTF imaging of Neptune and Triton. I: Observations, navigation, and differential deconvolution. *Icarus*, **149**, 416–434.
- Sromovsky, L. A., P. M. Fry, T. E. Dowling, K. H. Baines, and S. S. Limaye (2001b) Coordinated 1996 HST and IRTF imaging of Neptune and Triton. II: Implications of disk-integrated photometry. *Icarus*, **149**, 435–458.
- Sromovsky, L. A., P. M. Fry, K. H. Baines, and T. E. Dowling (2001c) Coordinated 1996 HST and IRTF imaging of Neptune and Triton. III: Neptunes's atmospheric circulation and cloud structure. *Icarus*, **149**, 459–488.
- Sromovsky, L. A., P. M. Fry, T. E. Dowling, K. H. Baines, and S. S. Limaye (2001d) Neptune's atmospheric circulation and cloud morphology: Changes revealed by 1998 HST imaging. *Icarus*, **150**, 244–260.

- Stone, P. H. (1976) The meteorology of the Jovian atmosphere. *Jupiter* (edited by T. Gehrels). University of Arizona Press, Tucson, AZ.
- Vasavada, A. (2002) private communication.
- West, R. A., A. J. Friedson, and J. K. Appleby (1992) Jovian large-scale stratospheric circulation. *Icarus*, **100**, 245–259.
- West, R. A. (1999) Atmospheres of the giant planets. *Encyclopaedia of the Solar System*, (edited by P. R. Weissman, L.-A. McFadden, and T. V. Johnson). Academic Press, San Diego, CA.
- Westphal, J. A., W. A. Baum, A. P. Ingersoll, C. D. Barnet, E. M. De Jong, G. E. Danielson, and J. Caldwell (1992) Hubble Space Telescope observations of the 1990 equatorial disturbance on Saturn: Images, albedoes and Limb-darkening. *Icarus*, **100**, 485–498.
- Williams, G. P. (1986) Jovian and comparative atmospheric modelling. *Adv. Geophys.*, **28A**, 381–429.
- Williams, G. P. (1978) Planetary circulations. 1: Barotropic representation of Jovian and terrestrial turbulence. *J. Atmos. Sci.*, **35**, 1399–1426.
- Williams, G. P. (1979) Planetary circulations. 2: The Jovian quasi-geostrophic regime. *J. Atmos. Sci.*, **36**, 932–968.
- Williams, G. P. and J. B. Robinson (1973) Dynamics of a convectively unstable atmosphere: Jupiter. *J. Atmos. Sci.*, **30**, 684–717.
- Yanamandra-Fisher, P. A., G. S. Orton, B. M. Fisher, and A. Sanchez-Lavega (2001) Saturn's 5.2-micron cold cold spots: Unexpected cloud variability. *Icarus*, **150**, 189–193.
- Young, A. T. (1985) What color is the solar system? *Sky and Telescope*, **69**, 399–403.

5.10 BIBLIOGRAPHY

- Andrews, D. G., J. R. Holton, and C. B. Leovy (1987) *Middle Atmosphere Dynamics*. Academic Press, San Diego, CA.
- Andrews, D. G. (2000) *An Introduction to Atmospheric Physics*. Cambridge University Press, Cambridge, UK.
- Beatty, J. K. and A. Chaikin (eds) (1998) *The New Solar System* (4th Edition). Sky Publishing, Cambridge, MA.
- Bergstrahl, J., E. D. Miner, and M. S. Matthews (eds) (1991) *Uranus*. University of Arizona Press, Tucson, AZ.
- Cruikshank, D. P., M. S. Matthews, and A. M. Schumann (eds) (1995) *Neptune and Triton*. University of Arizona Press, Tucson, AZ.
- Gehrels, T. (ed.) (1976) *Jupiter*. University of Arizona Press, Tucson, AZ.
- Gehrels, T. and M. S. Matthews (eds) (1984) *Saturn*. University of Arizona Press, Tucson, AZ.
- Holton, J. R. (1992) *An Introduction to Dynamical Meteorology* (3rd Edition). Academic Press, San Diego, CA.
- Houghton, J. T. (1986) *The Physics of Atmosphere* (2nd Edition). Cambridge University Press, Cambridge, UK.
- Jones, B. W. (1999) *Discovering the Solar System*. John Wiley & Sons, Chichester, UK.
- Rogers, J. H. (1995) *The Giant Planet Jupiter*. Cambridge University Press, Cambridge, UK.
- Shirley, J. H. and R. W. Fairbridge (eds) (1997) *Encyclopaedia of the Planetary Sciences*. Chapman & Hall, London.
- Weissman, P. R., L.-A. McFadden, and T. V. Johnson (eds) (1999) *Encyclopaedia of the Solar System*. Academic Press, San Diego, CA.

NASA Planetary images in this chapter were mostly downloaded from:

<http://photojournal.jpl.nasa.gov/>

6

Radiative transfer processes in outer planetary atmospheres

6.1 INTRODUCTION

With the exception of Jupiter, none of the atmospheres of the giant planets has been directly sampled. Even with Jupiter the only *in situ* measurements that are available were made from the *Galileo* entry probe which sampled a single, probably not very representative, region of the planet, namely a 5- μm hotspot. Hence the bulk of our knowledge of the composition, cloud structure, and dynamics of these planets has not come from direct measurements but instead has come indirectly from analysing features in their electromagnetic spectrum, measured by ground-based telescopes, Earth-orbiting telescopes, and from specific flyby and orbiting spacecraft missions. There are two main components of the observed spectra which provide atmospheric information: reflected sunlight from the cloud and haze layers and thermal emission from the atmosphere itself.

In this chapter we will examine how electromagnetic radiation interacts with molecules and aerosols and thus how the spectra of these planets are formed through the process of *radiative transfer*. Once a satisfactory radiative transfer model has been developed (sometimes called a *forward model*), synthetic spectra of the planets may be generated from initial assumptions of the mean atmospheric vertical profile and compared with observations. Differences between the observed and modelled spectra may be then used to revise the atmospheric profile assumptions used to generate the synthetic spectra and thus improve the fit. The process of revising the atmospheric profiles to improve the spectral fit is known as the *inverse model* or *retrieval model* and will be discussed in Chapter 7.

6.2 INTERACTION BETWEEN ELECTROMAGNETIC RADIATION AND PARTICLES

6.2.1 Fermi's golden rule

From quantum mechanics, the time-dependent Schrödinger equation governing the wavefunction Ψ of a particle is

$$i\hbar \frac{\partial \Psi}{\partial t} = \hat{H}\Psi \quad (6.1)$$

where $\hat{H} = -\hbar^2/2m \nabla^2 + V(\mathbf{r}, t)$ is the Hamiltonian operator representing the total energy of the system. If the potential V is time independent, then Schrödinger's equation may be separated into time and space factors with the wavefunctions written as $\Psi(\mathbf{r}, t) = \psi(\mathbf{r})e^{-iEt/\hbar}$, and where the separation constant E and time-independent wavefunction ψ satisfy the time-independent Schrödinger equation

$$-\frac{\hbar^2}{2m} \nabla^2 \psi + V(\mathbf{r})\psi = E\psi. \quad (6.2)$$

It may be shown that there are a number of possible time-independent wavefunctions, or stationary states ψ_m , satisfying Equation 6.2 and thus a number of possible separation constants E_m . Furthermore it may be shown that these stationary states form an orthonormal basis. Hence the general time-dependent wavefunction Ψ may be represented as a linear combination of the stationary states as

$$\Psi(\mathbf{r}, t) = \sum_m c_m(t) \psi_m(\mathbf{r}) e^{-iE_m t/\hbar} \quad (6.3)$$

where the c_m are coefficients to be determined and where the probability of finding a particle in the m th stationary state is $|c_m|^2$.

Suppose now that a photon interacts with the particle to promote a change between two such stationary states. Let us assume that the transition between two energy levels is caused by a time-dependent influence, which we represent by a small additive potential $v(\mathbf{r}, t)$. Suppose also that at time $t = 0$ we know that the particle is in a certain stationary state ψ_n . The coefficients c_m some time later (where $m \neq n$) may be shown from perturbation theory (Rae, 1985) to be

$$c_m \approx \frac{1}{i\hbar} \int_0^t H'_{mn} e^{i\omega_{mn} t} \quad (6.4)$$

where $H'_{mn}(t) = \int \psi_m^* v(\mathbf{r}, t) \psi_n d\tau$ is the integral over volume with $d\tau$ representing an element of volume, and $\omega_{mn} = (E_m - E_n)/\hbar$. For an interaction between a particle and an electromagnetic field of angular frequency ω , the time-dependent perturbation varies, to a first approximation, sinusoidally with time as

$$v(\mathbf{r}, t) = v'(\mathbf{r}) \cos \omega t. \quad (6.5)$$

Substituting this into the previous equations and defining $H_{mn}^* = \int \psi_m^* v'(\mathbf{r}) \psi_n d\tau$ we find that the probability that the particle will be in state m some time t after being in state n is given by

$$|c_m|^2 \approx \frac{|H_{mn}^*|^2}{4\hbar^2} \frac{\sin^2[(\omega_{mn} - \omega)t/2]}{[(\omega_{mn} - \omega)/2]^2}. \quad (6.6)$$

This probability is negligible except when ω is close to ω_{mn} , provided that the time t is long compared to the period of the perturbation and thus it can be seen that the absorption or emission of a photon of appropriate frequency may change the state of a particle. In reality, various broadening effects such as Doppler broadening mean that there are a number of pairs of energy levels which have an energy difference $\hbar\omega_{mn}$ and thus we need an additional term, known as the density of states $g(\omega_{mn})$, where $g(\omega_{mn}) d\omega_{mn}$ is defined as the number of pairs of energy levels with energy difference between $\hbar\omega_{mn}$ and $\hbar(\omega_{mn} + d\omega_{mn})$. The total probability for the transition to take place is then

$$P(t) = \frac{|H_{mn}^*|^2}{4\hbar^2} \int \frac{\sin^2[\omega_{mn} - \omega)t/2]}{[(\omega_{mn} - \omega)/2]^2} g(\omega_{mn}) d\omega_{mn}. \quad (6.7)$$

In general the density of states function $g(\omega_{mn})$ is much more slowly varying than the \sin^2 term in Equation 6.7, which may thus be well approximated by

$$P(t) \approx \frac{\pi |H_{mn}^*|^2}{2\hbar^2} g(\omega) t. \quad (6.8)$$

Hence the observed *transition rate* W is given by

$$W = \frac{dP}{dt} = \frac{\pi |H_{mn}^*|^2}{2\hbar^2} g(\omega). \quad (6.9)$$

This formula is known as Fermi's golden rule.

6.2.2 Electric and magnetic moments

In Section 6.2.1 we considered a general sinusoidal perturbation of the Hamiltonian of a particle introduced by interaction with an electromagnetic wave. To be more specific about spectral transitions we must consider the detailed interaction of an atom or molecule with an electromagnetic wave.

An electromagnetic wave has an electric field whose strength varies with time and position as $\mathbf{E} = \mathbf{E}_0 \cos(\omega t - \mathbf{k} \cdot \mathbf{r})$, where ω is the angular frequency and \mathbf{k} is the wavevector ($|\mathbf{k}| = 2\pi/\lambda$). The wave also has an associated magnetic field $\mathbf{B} = (\mathbf{E}_0/c) \cos(\omega t - \mathbf{k} \cdot \mathbf{r})$ and thus the total force acting on each electron and nucleus in the molecule is given by $\mathbf{F}_i = q_i(\mathbf{E} + \mathbf{v}_i \times \mathbf{B})$ where q_i is the electric charge of the i th particle and \mathbf{v}_i is its velocity. The energy of interaction between the wave and the molecule is then defined as $v(\mathbf{r}, t) = \sum_i \mathbf{F}_i \cdot \mathbf{r}_i$.

Since the electric field strength is greater than the magnetic field strength by a factor of c , and since particle velocities are in general small compared to c , the electric field terms in the perturbation potential tend to completely dominate the

magnetic ones. However, since the electric field varies with position, there are different ways in which the electric interaction can take place. The electric field of the wave may be expanded as the following power series

$$\mathbf{E} = \mathbf{E}_0 \cos(\omega t - \mathbf{k} \cdot \mathbf{r}) = \mathbf{E}_0 [\cos \omega t + (\mathbf{k} \cdot \mathbf{r}) \sin \omega t - \frac{1}{2} (\mathbf{k} \cdot \mathbf{r})^2 \cos \omega t + \dots] \quad (6.10)$$

and the molecule may be considered to interact with different terms independently. Interaction with the first term, where the amplitude of the field is constant over the molecule, leads to *electric dipole* transitions. Interaction with the second, much weaker term leads to *electric quadrupole* transitions, interaction with the third even weaker term leads to *electric octopole* transitions, and so on. Although small, the magnetic field interactions may similarly be resolved as *magnetic dipole* transitions, *magnetic quadrupole* transitions etc. For most molecules, the electric dipole transitions completely dominate everything else and thus it is these transitions which are usually considered. However, some molecules such as H₂ do not have a dipole moment and thus may not engage in electric dipole transitions although they do have an electric quadrupole moment and hence may engage in electric quadrupole transitions. Such transitions are clearly observable in giant planet spectra. Magnetic transitions are very weak and difficult to observe in giant planet spectra and may be neglected except for the effect of magnetic dipole O₂ absorption in Earth's atmosphere discussed in Chapter 7.

6.3 MOLECULAR SPECTROSCOPY: VIBRATIONAL-ROTATIONAL TRANSITIONS

At visible wavelengths, most transitions that are observed in the laboratory are due to electronic transitions within atoms, where electrons move between different atomic energy levels in atoms. However, at infrared (IR) wavelengths, photons have insufficient energy to interact directly with atoms. Instead, at these lower energies molecular absorption mechanisms come into play which are the core processes in forming the observed IR spectra of planets. Depending on temperature and molecular structure, molecules possess both rotational and vibrational degrees of freedom and absorption of IR photons can promote transitions between these different rotational-vibrational states as will now be described.

6.3.1 Molecular vibrational energy levels

The bonds between the atoms in a molecule are subject to stretching and (sometimes) bending degrees of freedom that may contribute to IR spectra. The simplest case is for a diatomic molecule composed of atoms of mass m_1 and m_2 . To a first approximation we may consider the binding forces between the atoms to be similar to a spring of stiffness k . Such a system, for which the restoring force is proportional to the displacement, will vibrate with simple harmonic motion and we may use

quantum mechanics to show that the allowed energy levels of such an oscillator are (Rae, 1985)

$$E_\nu = \left(\nu + \frac{1}{2} \right) \hbar \sqrt{\frac{k}{\mu}} \quad (6.11)$$

where μ is the reduced mass $\mu = m_1 m_2 / (m_1 + m_2)$ and ν is the vibrational integer quantum number.

6.3.2 Molecular rotational energy levels

In addition to the vibrational degrees of freedom, molecules also have rotational degrees of freedom which lead to discrete energy levels. Consider a molecule which has moments of inertia I_a, I_b, I_c about its three *principal axes* a, b, c , which are aligned along lines of rotational or reflectional symmetry of the molecule, where the moment of inertia is defined as

$$I = \sum_i m_i r_i^2. \quad (6.12)$$

By convention the axes are ordered such that $I_a \leq I_b \leq I_c$. For the molecule to have a rotational degree of freedom about a certain axis, the moment of inertia must be non-zero. Hence linear molecules, for which the moment of inertia is zero along one axis, have two degrees of rotational freedom, while non-linear molecules for which the moment of inertia is non-zero along all three axes has three degrees of rotational energy. Depending on their moments of inertia, molecules may be categorized as *linear rotors*, *symmetric rotors* (oblate or prolate), *asymmetric rotors*, and *spherical tops* as defined in Table 6.1 and discussed below. From quantum mechanics, the square of the total angular momentum is quantized as

$$L^2 = L_a^2 + L_b^2 + L_c^2 = \hbar^2 J(J+1) \quad (6.13)$$

Table 6.1. Symmetry classifications of molecules relevant to giant planets.

Name	Definition	Examples
Linear rotor	$I_a = 0, I_b = I_c$	$\text{CO}_2, \text{C}_2\text{H}_2$ (acetylene)
Symmetric rotor or top	Prolate: $I_a = I_A, I_b = I_c = I_B$	$\text{CH}_3\text{C}_2\text{H}$ (methyl acetylene), C_2H_6 (ethane), C_2H_4 (ethylene), CH_3D
	Oblate: $I_c = I_C, I_a = I_b = I_B$	$\text{NH}_3, \text{AsH}_3, \text{PH}_3$
Asymmetric rotor or top	$I_a < I_b < I_c$	$\text{H}_2\text{O}, \text{O}_3, \text{C}_3\text{H}_8$ (propane), H_2S
Spherical top	$I_a = I_b = I_c$	$\text{CH}_4, \text{GeH}_4$

NB, diatomic molecules are by definition linear rotors.

where J is an integer quantum number, and the allowed components of angular momentum along a symmetry axis are given by

$$L_\alpha = \hbar K \quad (6.14)$$

where K is a quantum number which satisfies $|K| \leq J$.

The classical rotational energy is defined as

$$E = \frac{L_a^2}{2I_a} + \frac{L_b^2}{2I_b} + \frac{L_c^2}{2I_c} \quad (6.15)$$

and from this expression, and the quantum mechanical expressions for the angular momenta, we may calculate the rotational energy levels for the four different molecule types as follows.

- (i) *Linear rotors.* For linear rotors $I_a = 0$, $I_b = I_c = 1$, and the energy levels may be found from simple quantum theory to be

$$E_J = \frac{\hbar^2}{2I} J(J+1) \quad (6.16)$$

where since $-J \leq K \leq J$, the energy levels have a degeneracy of $2J+1$.

- (ii) *Spherical tops.* For these molecules $I_a = I_b = I_c = I$, and the energy levels are found to be essentially the same as Equation 6.16 although in this case the degeneracy of the rotational energy levels is found to be partially lifted.
- (iii) *Symmetric rotors.* For prolate symmetric rotors where $I_a = I_A$, $I_b = I_c = I_B$, the classical rotational energy may be written as

$$E = \frac{L_a^2}{2I_A} + \frac{L_b^2 + L_c^2}{2I_B} = \frac{L^2}{2I_B} + \left(\frac{1}{2I_A} - \frac{1}{2I_B} \right) L_a^2 \quad (6.17)$$

from which the quantum mechanical expression may be derived

$$E_J = \frac{\hbar^2}{2I_B} J(J+1) + \frac{\hbar^2}{2} \left(\frac{1}{I_A} - \frac{1}{I_B} \right) K^2. \quad (6.18)$$

Similarly for the oblate case where $I_a = I_b = I_B$, $I_c = I_C$, the energy levels are found to be

$$E_J = \frac{\hbar^2}{2I_B} J(J+1) + \frac{\hbar^2}{2} \left(\frac{1}{I_C} - \frac{1}{I_B} \right) K^2. \quad (6.19)$$

Hence the rotational energy levels of symmetric rotors are considerably more complex than those of linear rotors and spherical tops since the energies depend on both J and K .

- (iv) *Asymmetric rotors.* Although the total angular momentum for molecules of this type is well defined, there is no principal axis along which the component L_α may be defined, which greatly complicates the calculation of the energy levels as is discussed further by Hanel *et al.* (1992). Water is a typical example of an asymmetric rotor, and the rotational energy levels are found to be so complex that they have an apparently random distribution of energy levels.

At higher moments of inertia, the bonds between the atoms of all molecular types become stretched due essentially to centrifugal forces. This stretching increases the moment of inertia and thus lowers the rotational energy levels. Including centrifugal effects the rotational energy levels of, for example, a simple linear rotor are modified as

$$E_J = \frac{\hbar^2}{2I} J(J+1) - DJ^2(J+1)^2 \quad (6.20)$$

where D is a small constant. The rotational energy levels of other molecular types are similarly adjusted.

6.3.3 Rotational transitions

The spacing of rotational energy levels is very much less than that between vibrational energy levels. At long wavelengths, electric dipole rotational transitions may be promoted by the absorption or emission of a photon provided, as mentioned earlier, that the molecule has an electric dipole moment defined as

$$\mathbf{M} = \sum_i q_i \mathbf{r}_i. \quad (6.21)$$

For homonuclear diatomic molecules such as H_2 , and symmetric linear polyatomic molecules such as CO_2 , the electric dipole moment \mathbf{M} is zero and thus pure rotational transitions are forbidden. However, heteronuclear diatomic molecules and all polyatomic molecules other than symmetric linear ones do have an electric dipole moment and thus may absorb photons subject to the selection rule $\Delta J = 1$, and may emit a photon provided $\Delta J = -1$ (Hanel *et al.*, 1992). Hence a molecule in the J th rotational energy level may only absorb a photon with an energy needed to promote it to the $(J+1)$ th energy level. This required energy, known as the *transition energy* is given by the difference between the $(J+1)$ th and J th rotational energy levels, i.e.,

$$\Delta E = E_{J+1} - E_J = \frac{\hbar^2}{2I} [(J+1)(J+2) - J(J+1)] = \frac{\hbar^2}{I} (J+1). \quad (6.22)$$

Thus, since the transition energy is proportional to the total angular momentum J of the lower state, the frequencies of the rotational absorption lines are to a first approximation all equally spaced. In reality, effects such as centrifugal distortion lead to the rotational energy levels becoming more closely spaced at higher J .

The strength of a rotational absorption, or the *line strength* depends both on the transition probability derived earlier from quantum mechanics and also on the number of molecules which are in the J th rotational energy level at any particular time. For *rotation bands* it is found that the dominant factor affecting the line strengths is the population of the lower rotational state. Assuming thermodynamic equilibrium, the population of states varies with energy according to the Boltzmann distribution

$$N = N_0 g_J \exp\left(-\frac{E_J}{k_B T}\right) \quad (6.23)$$

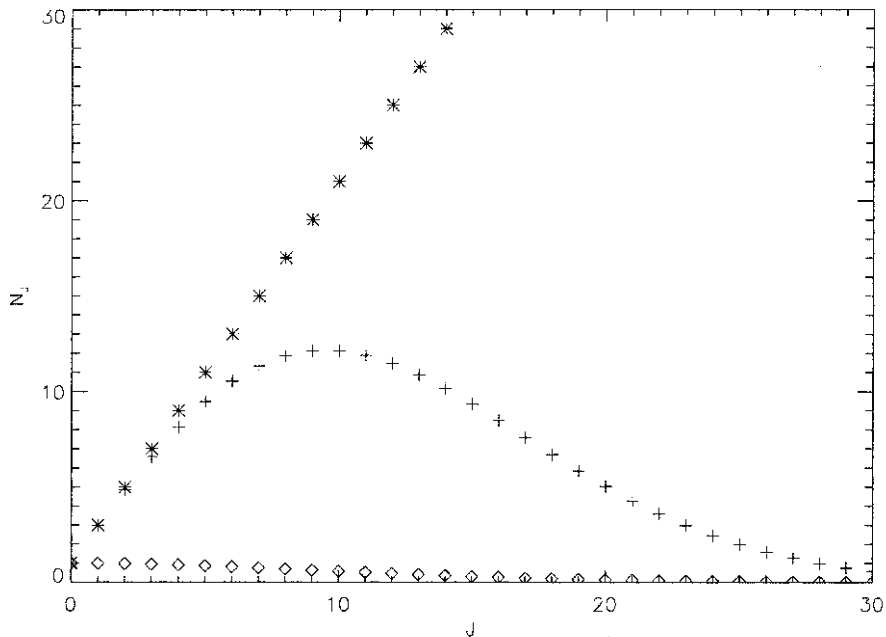


Figure 6.1 Population of rotational energy states. Diamond symbols indicate a typical Boltzmann distribution, while the asterisk symbols indicate the degeneracy $2J + 1$. The product of the two is shown by the cross symbols.

where k_B is the Boltzmann constant, E_J is the energy of the J th energy level, and g_J is the degeneracy of the J th level (i.e., the number of individual states with the same energy E_J). Hence for linear rotors, substituting for the energy E_J from Equation 6.16, and setting the degeneracy g_J equal to $2J + 1$, the number of molecules actually in the J th rotational energy state is given by:

$$N_J = (2J + 1)N_0 \exp(-J(J + 1)\hbar^2/2Ik_B T) \quad (6.24)$$

which has a distribution as shown in Figure 6.1. The measured line strengths of the rotation band of the heteronuclear linear rotor CO are shown in Figure 6.2 and it can be seen that the variation in strength closely resembles the population curve of Figure 6.1 and that the lines are equally spaced as expected.

6.3.4 Vibration–rotation bands

At shorter wavelengths, individual photons carry more energy and may thus excite transitions between vibrational states. The transition rule for molecules changing their vibrational state through an electric dipole transition is simply $\Delta\nu = \pm 1$ (Hanel *et al.*, 1992). Now since the vibrational and rotational degrees of freedom of a molecule are (more or less) independent, at wavelengths where vibrational transitions are excited, they may also be associated with rotational level changes giving rise

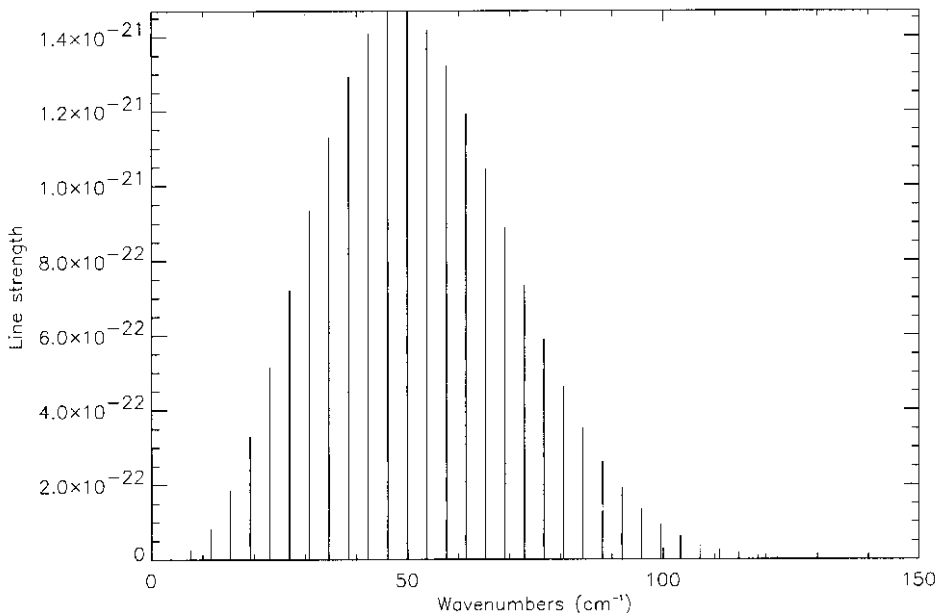


Figure 6.2 Measured line strengths at 296 K in the rotation band of CO (line strengths measured in units of cm^{-1} ($\text{molecule}\cdot\text{cm}^{-2}$) $^{-1}$).

to combined rotation–vibration spectra. The form of these *vibration–rotation bands* depends on the symmetry of the molecule as follows.

- (i) *Diatom*ic molecules. Diatomic molecules have a single vibrational mode and thus a single set of vibration–rotation bands centred at frequencies $n\nu_1$ where n is an integer and ν_1 is the fundamental frequency given (from Equation 6.11) by

$$\nu_1 = \frac{1}{2\pi} \sqrt{\frac{k}{\mu}} \quad (6.25)$$

Just as for rotational transitions, only heteronuclear diatomic molecules may engage in electric dipole transitions and during each vibrational transition, the rotational energy level may also change for which the selection rule is $\Delta J = \pm 1$. Hence each vibration–rotation band actually consists of 2 branches, the ‘P-branch’ at frequencies below the central vibrational frequency for which $\Delta J = -1$ and the ‘R-branch’ at frequencies above the central vibrational frequency for which $\Delta J = +1$. The shape of the R-branch is identical to the pure rotational band since the population and degeneracy of the rotational states are not affected by the vibrational state. The shape of the P-branch is the mirror image of the R-branch.

- (ii) *Linear polyatomic molecules and spherical tops*. For these molecules, the main vibration–rotation bands are actually composed of *three* bands which again incorporate the possible simultaneous changes in the rotational energy levels.

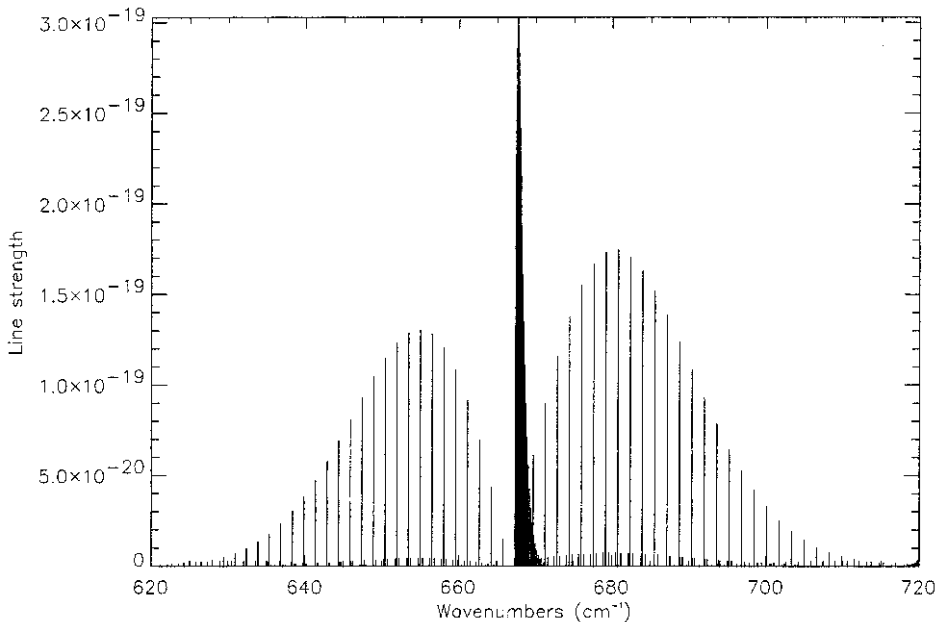


Figure 6.3 Measured line strengths at 296 K in the ν_2 vibration–rotation band of CO₂ (line strengths measured in units of cm^{-1} ($\text{molecule}\cdot\text{cm}^{-2}$) $^{-1}$).

Just as for heteronuclear diatomic molecules, rotational energy changes governed by $\Delta J = \pm 1$ give rise to the P- and R-branches. However, for linear polyatomic and spherical top molecules, an additional ‘Q-branch’ arises since transitions for which $\Delta J = 0$ are also allowed. For an ideal molecule all the possible transitions in the Q-branch would perfectly overlap but since the rotational transitions are not perfectly equally spaced, a tight collection of transitions are seen at the central vibrational frequency. A good example of a classic P, Q, R vibration–rotation band is the 15-μm ν_2 band of CO₂ shown in Figure 6.3.

- (iii) *Symmetric rotors*. The situation for symmetric rotors is a little more complicated since additional structure arises from possible variations in the K angular momentum quantum number. Two types of bands arise. Transitions for which $\Delta K = 0$ have a very similar appearance to the classic P, Q, R structure of linear and symmetric top molecules just described and are called *parallel* bands. However, a second type of band arises from transitions for which $\Delta K = \pm 1$, known as *perpendicular* bands. These have the appearance of a number of P, Q, R branches superimposed on each other with a small frequency shift between each central Q-branch giving rise to a regularly spaced series of Q-branches and associated P- and R-branches. The vibration–rotation band of ethane at 800 cm $^{-1}$ (NB, wavenumbers are often used to describe frequency in visible/infrared spectroscopy and are defined as the reciprocal of wavelength, usually expressed in cm) is a good example of a perpen-

dicular band which is clearly seen at certain emission angles and latitudes in the thermal emission spectra of Jupiter, Saturn, and Neptune.

- (iv) *Asymmetric rotors.* The vibration–rotation bands of asymmetric rotors are even more complex and appear similar to either the parallel or perpendicular bands of symmetric rotors depending on the values of the three principal moments of inertia. Water molecules are asymmetric rotors and the spectrum of each band is so complex that they have the appearance of a random jumble of line positions and strengths.

Vibrational modes

A molecule composed of N atoms has by definition $3N$ degrees of freedom comprising translation, rotation, and vibration. Of these, 3 degrees of freedom define the mean translational position of the molecule. In addition, linear molecules have 2 degrees of rotational freedom and all other molecules have 3 degrees of rotational freedom. Hence a linear molecule has $3N - 5$ vibrational degrees of freedom while a non-linear molecule has $3N - 6$ vibrational degrees of freedom. Substituting for N it can be seen that a diatomic molecule has a single vibrational degree of freedom, a molecule with three atoms (such as CO_2 or H_2O) has either 3 or 4 vibrational modes depending on its linearity, a molecule with four atoms has 6 or 7 vibrational modes, and so on. Clearly the number of possible vibrational modes increases rapidly with the number of atoms, although not all will contribute to the observable vibration–rotation spectra since not all will be able to interact with electric dipole radiation as we shall now see.

Consider a simple tri-atomic molecule such as CO_2 . Since this is a linear molecule, there are $3 \times 3 - 5 = 4$ vibrational modes which are shown in Figure 6.4. The first mode (ν_1) is called the symmetric stretch mode and the spacing of the vibrational energy levels is equivalent to a photon with frequency of approximately $1,100 \text{ cm}^{-1}$. However, the motion of the oxygen atoms associated with this mode do not change the centre of charge of the molecule and thus this mode may not interact with electric dipole radiation. The next two vibrational modes (ν_2) are the

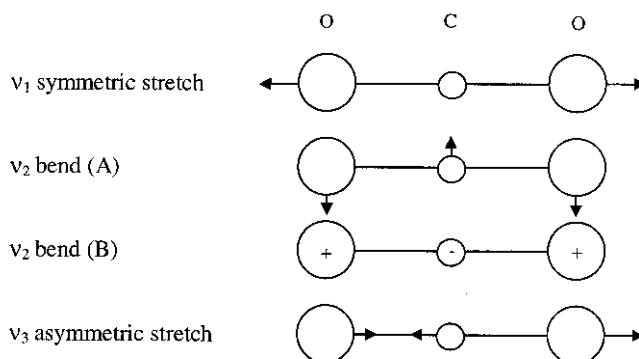


Figure 6.4 Vibrational modes of CO_2 .

bending modes which have identical frequencies and clearly vary the centre of charge of the molecule giving rise to the fundamental vibration–rotation band centred at 667 cm^{-1} (shown in Figure 6.3). The last mode (ν_3) is the asymmetric stretch mode and may also interact with electric dipole radiation giving rise to the fundamental vibration–rotation band at $2,350\text{ cm}^{-1}$.

Overtones and hot bands

The vibrational selection rule $\Delta\nu = \pm 1$ for electric dipole transitions is only absolute for a pure simple harmonic oscillator. The binding force between real molecules, while proportional to displacement for small oscillations, has non-negligible higher orders, or anharmonic elements for larger oscillations. These anharmonic elements relax the selection rules to $\Delta\nu = \pm 1, \pm 2, \pm 3, \dots$ giving rise to ‘overtone’ bands for which $|\Delta\nu| > 1$. The overtone bands are always far less intense than the fundamental for which $\Delta\nu = \pm 1$.

The population of vibrational energy states is also covered by a Boltzmann distribution and, at low temperatures, most molecules are in their lowest vibrational state and thus the absorption spectra of low temperature molecules are dominated by transitions from this ground state. However, as the temperature rises, so does the population of the higher vibrational states giving rise to so-called ‘hot bands’.

6.3.5 Inversion bands and inversion-doubling

Another type of band, relevant to microwave spectra, is the inversion band of ammonia. The arrangement of NH_3 has the N atom slightly above or below the plane of the three H atoms and the inversion band arises from symmetry considerations of whether the N atom is above or below the plane. This gives rise to a cluster of absorption lines centred at a wavelength of 1.3 cm which is the dominant feature of the microwave spectra of Jupiter and Saturn, although not Uranus and Neptune, which is how the low abundance of ammonia above $\sim 80\text{ bar}$ in these latter atmospheres is inferred. In addition to the microwave inversion band, this molecular structure also gives rise to a splitting of the rotational energy levels of ammonia, known as inversion-doubling (Herzberg, 1945).

6.3.6 Diatomic homonuclear molecules

Diatom homonuclear molecules do not interact with electromagnetic radiation via electric dipole transitions at all, since no vibrational or rotational change of state may induce an electric dipole in the molecule. Although such molecules may interact weakly with electromagnetic radiation in other ways they are usually effectively considered to be radiatively inactive in terrestrial atmospheres since their weak absorptions are totally dominated by the electric dipole transitions of other molecules. However, the atmospheres of the giant planets are dominated by molecular hydrogen, which is just such a diatomic homonuclear molecule, and in certain parts of the spectrum the more familiar electric dipole transitions of other

molecules are themselves so negligible that it becomes necessary to consider in detail how such diatomic molecules may interact with electromagnetic radiation.

Electric quadrupole transitions

We saw earlier that in addition to electric dipole transitions, there are a number of less likely, and thus weaker interaction mechanisms between a molecule and radiation. While diatomic homonuclear molecules may not engage in electric dipole transitions they may engage in the much weaker electric quadrupole transitions. For these electric quadrupole transitions the selection rules are $\Delta J = \pm 2$, and $\Delta\nu = \pm 1, \pm 2, \pm 3, \dots$. Thus instead of having a P, Q, R-branch structure, electric quadrupole transitions are confined to the O-branch($\Delta J = -2$) and S-branch($\Delta J = 2$).

In the atmospheres of the giant planets, which are dominated by molecular hydrogen, the electric quadrupole lines of H₂ are detectable for a number of vibrational transitions. In the far-IR, the S(0) and S(1) lines associated with the (1-0) vibrational transitions are observable where ‘S’ means $\Delta J = 2$, and the numbers refer to the total angular momentum J of the lower state. In the visible, the S(0) and S(1) transitions associated with the (3-0) and (4-0) vibrational energy changes are visible. Electric quadrupole transitions have similar line widths to electric dipole transitions described later in Section 6.3.7.

Collision-induced dipole transitions

In the gas phase, collisions and interactions with other molecules can lead to transitory dipole moments being induced on homonuclear diatomic molecules that may then interact with IR light. Although the absorption is weak, the abundance of H₂ in the giant planet atmospheres is so high that the far-IR spectra of the giant planets is dominated by H₂–H₂ and H₂–He pressure- or collision-induced absorptions (CIA). Another example is N₂–N₂ and N₂–CH₄ collision-induced absorption in Titan’s atmosphere. These pressure-induced dipole absorptions have $\Delta J = 2$ (i.e., S(0) and S(1)) and are thus found near the wavelengths of the pure quadrupole lines just discussed. However, the temporary induced dipoles have very short lifetimes, and thus from Heisenberg’s uncertainty principle their line shape is extremely broad. For more detailed information on H₂–H₂ and H₂–He collision-induced absorptions, the reader is referred to Birnbaum *et al.* (1996).

6.3.7 Line-broadening

We have now discussed a number of different absorption mechanisms of molecules and have also outlined that the strength of an absorption line depends both on the transition probability and on the population of the lower energy level. However, these transitions are not infinitely thin, but instead have a finite width as we have alluded to previously and which arise from a number of possible mechanisms which we shall now describe.

Natural broadening

In any transition, there is a natural line width that arises due to the finite time over which a photon is absorbed or emitted by an atom or molecule. From Heisenberg's uncertainty principle we know that $\Delta E \Delta t \approx h$, or $\Delta\nu \Delta t \approx 1$ since $E = h\nu$. This may be further refined to give the width of an absorption line in terms of wavenumbers (cm^{-1})

$$\Delta\tilde{\nu} \approx \frac{1}{c\Delta t}. \quad (6.26)$$

In practice natural broadening is usually negligible compared to the following mechanisms. As an order of magnitude, the natural broadened line width is of the order of 10^{-7} cm^{-1} (Hanel *et al.*, 1992).

Collision- or pressure-broadening

In a gas, molecules suffer repeated collisions with other molecules and there is a certain probability that such a collision may occur while molecules are absorbing or emitting photons. This effectively shortens the length of the absorbed or emitted wavetrains, and thus from the uncertainty principle increases the spread of wavelengths. This process is known as *collision-broadening* or sometimes *pressure-broadening* since this effect becomes dominant at high pressures. The absorption coefficient $k_{\tilde{\nu}}$ (usually defined in units of molecules per m^2) at wavenumber $\tilde{\nu}$ due to a collision-broadened line centred at $\tilde{\nu}_0$ is given by the Lorentz lineshape

$$k_{\tilde{\nu}} = \frac{s\gamma_L}{\pi((\tilde{\nu} - \tilde{\nu}_0)^2 + \gamma_L^2)} \quad (6.27)$$

where $s = \int_0^\infty k_{\tilde{\nu}} d\tilde{\nu}$ is the line strength and $\gamma_L = (2\pi tc)^{-1}$ is the line width (cm^{-1}). The parameter t is the mean time between collisions which depends on density and thus for atmospheres, mostly on pressure. We may thus rewrite γ as

$$\gamma_L = \gamma_{L0} \frac{p}{p_0} \left(\frac{T_0}{T} \right)^n \quad (6.28)$$

where γ_{L0} is the line width at a reference pressure of p_0 . The temperature coefficient n is by simple theory equal to 0.5, although in reality it varies slightly from molecule to molecule. At a pressure of 1 bar, and room temperature, a typical collision-broadened line width is of the order of 0.1 cm^{-1} .

Doppler broadening

This arises due the line of sight motion of the emitting/absorbing molecules in the gas which is due to the molecules moving with a Maxwell–Boltzmann distribution of speeds. This distribution depends upon the temperature of the gas and the molecular weight of the molecules. Molecules approaching the observer will absorb at slightly

higher frequencies than receding molecules due to the Doppler effect, and the absorption spectrum of a Doppler-broadened line is given by

$$k_{\tilde{\nu}} = \frac{s}{\gamma_D \pi^{1/2}} \exp\left(-\left(\frac{\tilde{\nu} - \tilde{\nu}_0}{\gamma_D}\right)^2\right) \quad (6.29)$$

where

$$\gamma_D = \frac{\tilde{\nu}_0}{c} \left(\frac{2RT}{M_r}\right)^{1/2} = \gamma_{D0} \left(\frac{T}{T_0}\right)^{1/2}$$

is the Doppler line width and M_r is the molecular weight. For example, for methane, for which $M_r = 16$ g, the Doppler width at room temperature (293 K) and a wave-number of 1300 cm^{-1} is 0.002 cm^{-1} .

Voigt broadening

Considering the previous two mechanisms it is found that pressure-broadening dominates at high pressures in an atmosphere, whereas Doppler broadening dominates at low pressures since pressure-broadening is directly proportional to pressure which falls exponentially with height in an atmosphere, while Doppler broadening is proportional to \sqrt{T} which decreases much less rapidly. At intermediate temperatures and pressures both mechanisms are significant and thus the lineshape of an observed absorption line is due to a combination of both pressure-broadening and Doppler broadening giving rise to the Voigt lineshape

$$k_{\tilde{\nu}} = \frac{sy}{\gamma_D \pi^{3/2}} \int_{-\infty}^{\infty} \frac{\exp(-t^2)}{(x-t)^2 + y^2} dt \quad (6.30)$$

where $x = (\tilde{\nu} - \tilde{\nu}_0)/\gamma_D$ and $y = \gamma_L/\gamma_D$. Unfortunately this equation does not have an analytical solution and so must be integrated numerically.

6.3.8 Giant planet gas transmission spectra

The absorption of gases in planetary atmospheres has been seen to be due to both vibration–rotation bands and collision-induced absorptions and to demonstrate the absorptions of different gases Figure 6.5 shows the transmission of a typical path in an atmosphere of approximately solar composition between 0 and $2,500\text{ cm}^{-1}$. Here we can see the basic properties outlined above. The various vibration–rotation bands, and pure rotation bands if allowed, can be seen for the main gases of interest in the tropospheres of the giant planets. Together with the line spectra, the importance of $\text{H}_2\text{--H}_2$ and $\text{H}_2\text{--He}$ collision induced absorption at long wavelengths is clearly seen. Figure 6.5 also shows transmission spectra for various hydrocarbons observed in the giant planet stratospheres.

At shorter wavelengths, Figure 6.6 shows the calculated transmission between 0.4 and $5.5\text{ }\mu\text{m}$ for the same solar composition path used in Figure 6.5 where further vibration–rotation bands can be seen. The absorption of methane, ammonia, and

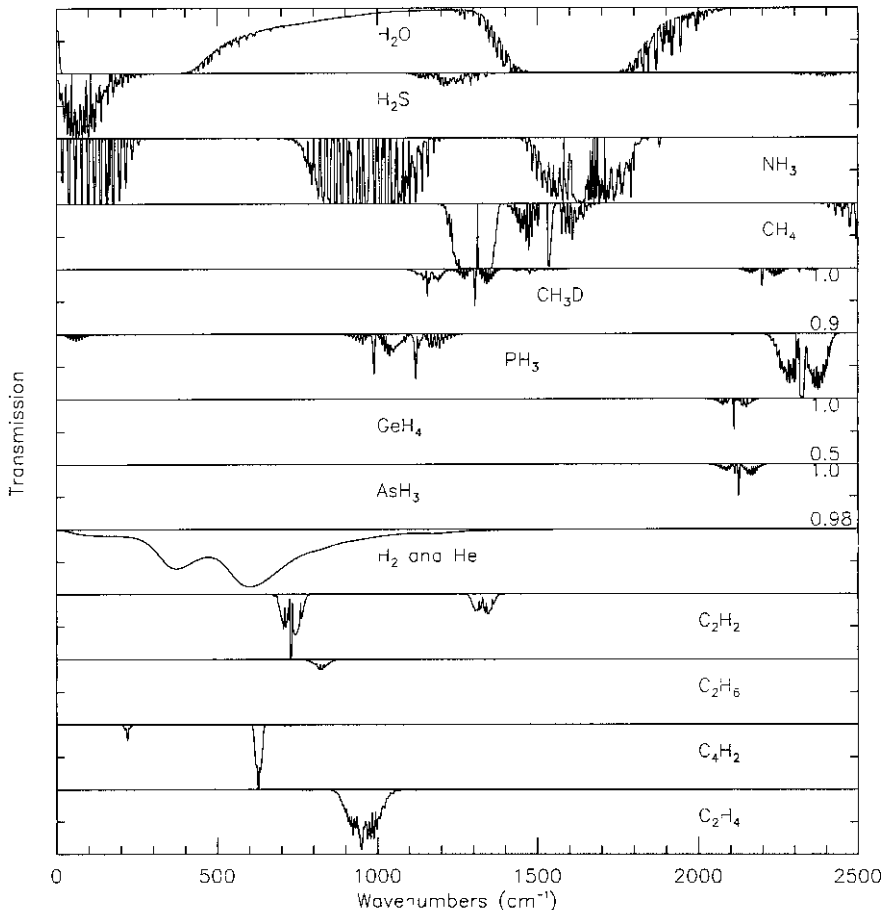


Figure 6.5 Mid to far-IR transmission of tropospheric and stratospheric gases for a solar composition path with $p = 0.3$ bar, $T = 127\text{ K}$, and path length = 10 km. Calculated transmissions are between 0 and 1 unless indicated otherwise. (The stratospheric hydrocarbon abundances have been set to give clear absorption spectra.)

again $\text{H}_2\text{--H}_2$ and $\text{H}_2\text{--He}$ CIA are most important in this region. Although water vapour also has strong absorptions, the abundance of water vapour at the cloud tops of the giant planets is so low that water vapour is not detectable at these wavelengths.

6.4 RADIATIVE TRANSFER IN A GREY ATMOSPHERE

Now we have discussed the mechanisms by which gases may absorb IR radiation we will now consider how the thermal emission spectra of planets are generated.

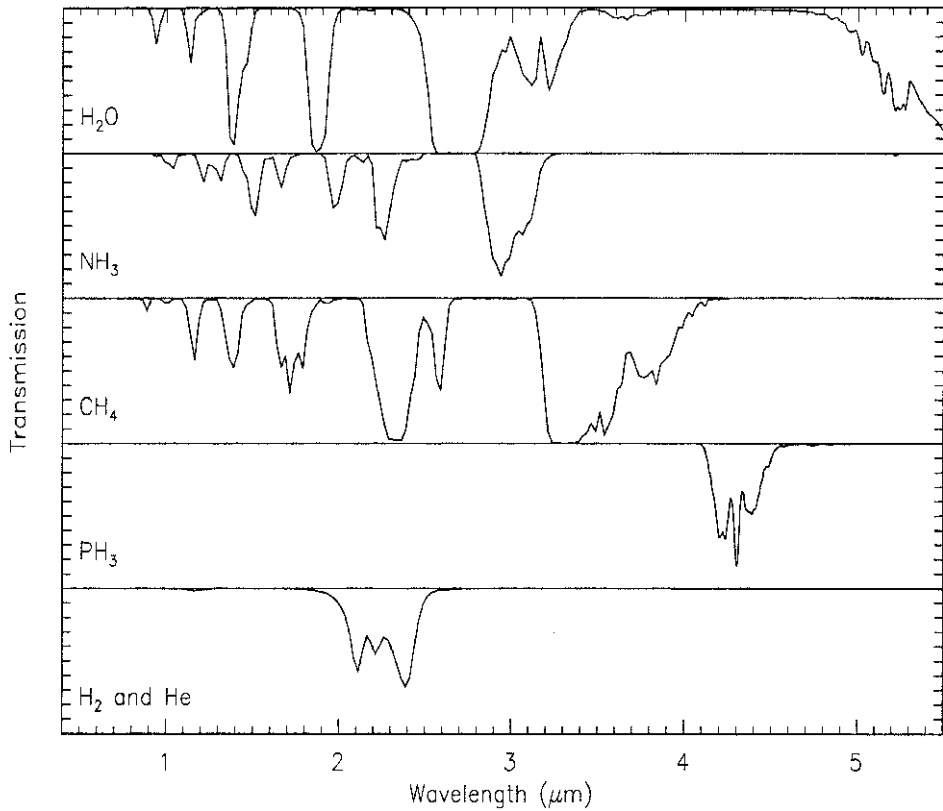


Figure 6.6 Near-IR transmission of tropospheric gases for a solar composition path with $p = 0.3$ bar, $T = 127$ K, and path length = 10 km.

6.4.1 Nadir viewing

When considering radiation that is emitted to space at angles reasonably close to the vertical, it is a very good approximation to consider the atmosphere as being effectively plane-parallel. This approximation breaks down at very high emission angles such as when the limb of the planet is observed (but even then the radiative transfer equations turn out to be rather similar). Consider such a plane-parallel atmosphere as shown in Figure 6.7. Lambert's law of absorption states that the absorption of radiation of *radiance* $I_{\bar{\nu}}$ (typically measured in units of $\text{W cm}^{-2} \text{sr}^{-1} (\text{cm}^{-1})^{-1}$) travelling at a *zenith angle* θ to the vertical, through a path of vertical thickness dz (m), mean number density n (molecules/m³) containing material with absorption coefficient $k_{\bar{\nu}}$ (molecules/m²) is given by

$$dI_{\bar{\nu}} = -Ik_{\bar{\nu}}n dz / \cos \theta. \quad (6.31)$$

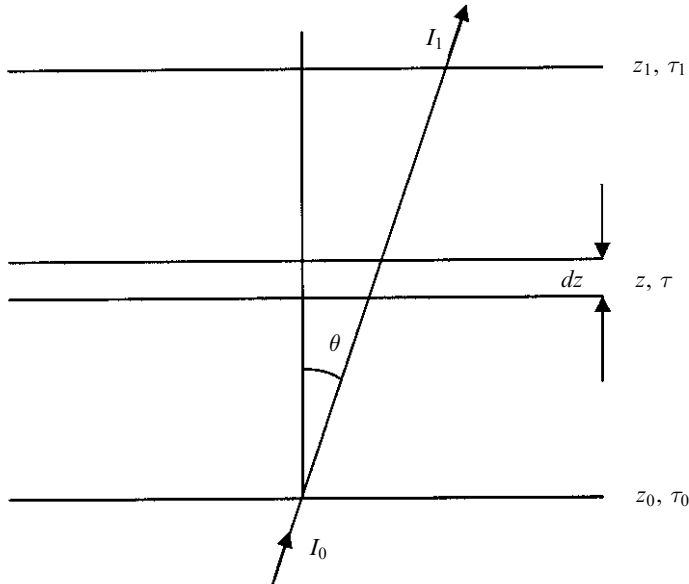


Figure 6.7 Radiative transfer in a grey plane-parallel atmosphere.

In other words the element layer of thickness dz has absorption along the slant path equal to $\alpha = k_{\tilde{\nu}} n dz / \mu$, where $\mu = \cos \theta$. Consider a thick slab of atmosphere between levels z_0 and z_1 , with radiant intensity $I_{\tilde{\nu}0}$ incident upwards at z_0 at an angle θ . This radiation will be attenuated before reaching z_1 and thus the upward radiation at the top of the atmosphere from the base is given by

$$I_{\tilde{\nu}1} = I_{\tilde{\nu}0} \exp\left(-\int_{z_0}^{z_1} \frac{k_{\tilde{\nu}}(z)n(z)}{\mu} dz\right) \quad (6.32)$$

which may be re-expressed as

$$I_{\tilde{\nu}1} = I_{\tilde{\nu}0} \exp(-\tau_{\tilde{\nu}}(z_0, z_1)/\mu) = I_{\tilde{\nu}0} T_{\tilde{\nu}}(\mu, z_0, z_1) \quad (6.33)$$

where $\tau_{\tilde{\nu}}(z_0, z_1)$ is the *optical thickness* (or *optical depth*) if measured downwards from the top of the atmosphere between z_0 and z_1 for a vertical path and $T_{\tilde{\nu}}(\mu, z_0, z_1)$ is the transmission from z_0 to z_1 at angle θ .

Now the thin slab at altitude z of thickness dz will also emit thermal radiation, and from Kirchoff's law the emissivity of the layer is equal to its absorptivity. Hence the radiance emitted by this layer at angle θ is equal to

$$dI_{\tilde{\nu}} = k_{\tilde{\nu}}(z)n(z)B(\tilde{\nu}, T(z)) dz / \mu. \quad (6.34)$$

where $T(z)$ is the temperature at altitude z and $B(\tilde{\nu}, T(z))$ is the Planck function at wavenumber $\tilde{\nu}$ and temperature $T(z)$. This radiance is itself attenuated by overlying

layers before reaching the top of the atmosphere and thus the contribution to $I_{\bar{\nu}1}$ from this slab is

$$dI_{\bar{\nu}1} = \frac{k_{\bar{\nu}}n(z)B_{\bar{\nu}}(z)dz}{\mu} \exp\left(-\int_z^{z_1} k_{\bar{\nu}}(z')n(z')dz'/\mu\right) \quad (6.35)$$

or

$$dI_{\bar{\nu}1} = B_{\bar{\nu}}(z)dT_{\bar{\nu}}(\mu, z, z_1). \quad (6.36)$$

Thus summing the thermal emission from all the layers, the total radiance reaching the top of the atmosphere at z_1 (where the optical depth is zero) is

$$I_{\bar{\nu}1}(\mu) = I_{\bar{\nu}0}T_{\bar{\nu}}(\mu, z_0, z_1) + \int_{T_{\bar{\nu}}(z_0, z_1)}^1 B_{\bar{\nu}}(z)dT_{\bar{\nu}}(\mu, z, z_1) \quad (6.37)$$

or alternatively

$$I_{\bar{\nu}1}(\mu) = I_{\bar{\nu}0}T_{\bar{\nu}}(\mu, z_0, z_1) + \int_{z_0}^{z_1} B_{\bar{\nu}}(z) \frac{dT_{\bar{\nu}}}{dz} dz \quad (6.38)$$

which can be written as

$$\begin{aligned} I_{\bar{\nu}1}(\mu) &= I_{\bar{\nu}0}T_{\bar{\nu}}(\mu, z_0, z_1) + \int_{z_0}^{z_1} B_{\bar{\nu}}(z)K_{\bar{\nu}}(z)dz \\ &= I_{\bar{\nu}0}T_{\bar{\nu}}(\mu, z_0, z_1) + \int_{z_0}^{z_1} C_{\bar{\nu}}(z)dz \end{aligned} \quad (6.39)$$

where $K_{\bar{\nu}}(z) = dT_{\bar{\nu}}/dz$ is the *transmission weighting function*, and $C_{\bar{\nu}}(z) = B_{\bar{\nu}}(z)K_{\bar{\nu}}(z)$ is commonly known as the *contribution function*. The transmission weighting function for nadir viewing (for which the zenith angle $\theta = 0$) is a smoothly varying function as can be seen from Figure 6.8 which shows the calculated weighting function at 600 cm^{-1} and $1,300\text{ cm}^{-1}$ for Jupiter's atmosphere. Also shown in Figure 6.8 is the variation of transmission to space with height. It can be seen that the weighting function peaks roughly where the optical depth is unity, or equivalently where the transmission to space is 0.368. Since the transmission of the atmospheric gases varies with wavelength as was shown in Figures 6.5 and 6.6, the altitude of the peak of the weighting function varies correspondingly. Hence in spectral regions of high absorption (such as at $1,300\text{ cm}^{-1}$ in Figure 6.8), the weighting function peaks high in the atmosphere and thus most of the radiation observed is emitted from high levels, whereas in spectral regions of low absorption (such as at 600 cm^{-1}), the weighting functions peak at low altitudes and thus most of the radiation comes from deep levels. Figure 6.9 shows how the altitude of the peak of the calculated weighting function varies with wavelength for the Jovian atmosphere assuming no clouds. At $2,000\text{ cm}^{-1}$ (or 5-μm) gas absorption is particularly low and thus the radiation is mostly emitted from the deep troposphere. At 1300 cm^{-1} , in the middle of a strong CH_4 absorption, most of the radiation is emitted from the stratosphere. Similar variation of weighting function peak with wavelength is found for the other giant planets. Clearly if we have good models for the absorption spectra of gases we may use the observed thermal emission spectra

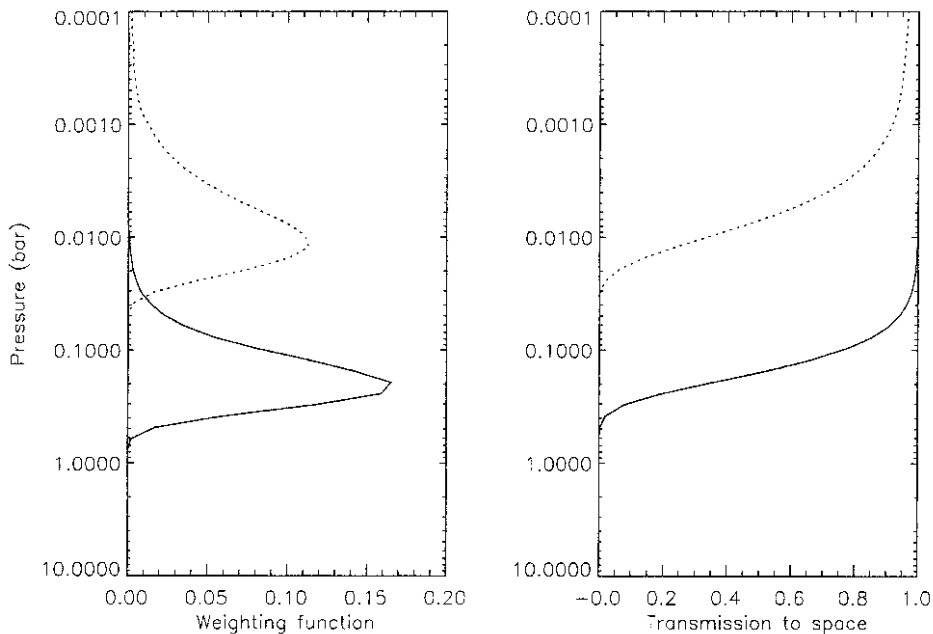


Figure 6.8 Calculated transmission weighting functions (nadir) for Jupiter at 600 cm^{-1} and $1,300\text{ cm}^{-1}$ respectively.

to infer the variation of both temperature and composition with height in the giant planet atmospheres.

6.4.2 Net flux and disc-averaging

The radiative transfer equation (Equation 6.37) very successfully models the IR observations of the giant planets made by passing spacecraft instruments such as *Voyager IRIS* which have a small field of view and thus sample only a small range of positions and zenith angles. Ground-based observations of the planets historically have poorer spatial resolution and thus often (especially for planets such as Uranus and Neptune which have a small angular size) the spectrum measured is that averaged over the whole planet and thus samples not only all visible parts of the disc, but also all zenith angles between 0 and 90° . If we assume that the temperature and composition profiles are the same all over the planet, then the disc-averaged spectrum is directly proportional to the averaged spectrum emitted by a single location on the planet into a hemisphere. Hence to calculate the disc-averaged spectrum, all we need to do is integrate Equation 6.37 over all zenith angles and then multiply by the total surface area of the planet. The radiance emitted

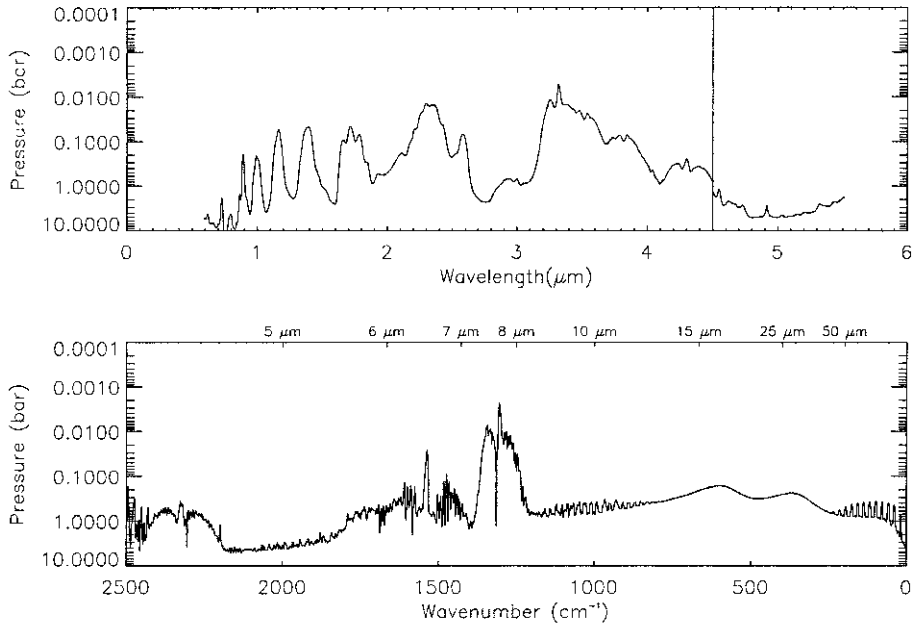


Figure 6.9 Variation of peak of calculated transmission weighting function with wavelength for Jupiter. Below 4.5 μm, the pressure level where the transmission to and from space is 0.5, has been plotted.

upwards at the top of the atmosphere at zenith angle θ (Equation 6.37) may be rewritten as

$$I_{\tilde{\nu}1}(\mu) = I_{\tilde{\nu}0} e^{-\tau_0/\mu} + \int_0^{\tau_0} B_{\tilde{\nu}}(\tau) e^{-\tau/\mu} \frac{d\tau}{\mu} \quad (6.40)$$

where the vertical coordinate is now the optical depth of the atmosphere τ . This expression is valid for $0 < \mu \leq 1$ and gives us the radiance emitted in any given direction. To calculate the total flux leaving the atmosphere, we need to integrate Equation 6.40 over the solid angle of a hemisphere. The total upward spectral flux ($\text{W m}^{-2} (\text{cm}^{-1})^{-1}$) is then given by

$$F_{\tilde{\nu}1} = \int I_{\tilde{\nu}1} \mu d\Omega = 2\pi \int_0^1 I_{\tilde{\nu}1}(\mu) \mu d\mu \quad (6.41)$$

where $d\Omega = 2\pi \sin \theta d\theta = -2\pi d\mu$ is the element of solid angle and where the extra factor of μ arises since it is assumed that the emitting surfaces are horizontal. Substituting for $I_{\tilde{\nu}1}(\mu)$ in Equation 6.41 we find

$$F_{\tilde{\nu}1} = 2\pi I_{\tilde{\nu}0} \int_0^1 e^{-\tau_0/\mu} \mu d\mu + 2\pi \int_0^{\tau_0} B_{\tilde{\nu}}(\tau) \left(\int_0^1 e^{-\tau/\mu} d\mu \right) d\tau \quad (6.42)$$

or

$$F_{\bar{\nu}1} = 2\pi I_{\bar{\nu}0} E_3(\tau_0) + 2\pi \int_0^{\tau_0} B_{\bar{\nu}}(\tau) E_2(\tau) d\tau \quad (6.43)$$

where $E_n(x) = \int_1^\infty e^{-wx}/w^n dw = \int_0^1 \mu^{n-2} e^{-x/\mu} d\mu$, known as an *exponential integral*, is a standard tabulated integral (Goody and Yung, 1989) which has a number of properties including $E'_n(x) = -E_{n-1}(x)$. Using this last property the net flux (Equation 6.43) may be re-expressed as

$$F_{\bar{\nu}1} = 2\pi I_{\bar{\nu}0} E_3(\tau_0) + 2\pi \int_{E_3(\tau_0)}^{0.5} B_{\bar{\nu}}(\tau) dE_3(\tau) \quad (6.44)$$

where we have substituted $E_3(0) = 0.5$. The total power emitted by a planet is then $4\pi R^2 F_{\bar{\nu}1}$ where R is the radius of the planet and hence the measured spectral flux or irradiance of the disc-averaged spectrum seen at a distance D is given by

$$I_{\bar{\nu}} = F_{\bar{\nu}1} \left(\frac{R}{D} \right)^2. \quad (6.45)$$

The spectral irradiance may be measured in units such as $\text{W cm}^{-2} (\text{cm}^{-1})^{-1}$, $\text{W m}^{-2} \mu\text{m}^{-1}$, or sometimes in *Janskys* (for Earth-based observations) which have rather unusual units of $1 \text{Jy} = 10^{-26} \text{W m}^{-2} \text{Hz}^{-1}$. To obtain the disc-averaged radiance of a planet, we then divide this irradiance by the solid angle projected by the planet which is equal to $\pi(R/D)^2$. Hence the disc-averaged radiance is given by

$$\bar{I}_{\bar{\nu}1} = 2I_{\bar{\nu}0} E_3(\tau_0) + 2 \int_{E_3(\tau_0)}^{0.5} B_{\bar{\nu}}(\tau) dE_3(\tau) \quad (6.46)$$

which is similar to the nadir radiative transfer equation, Equation 6.37. In Figure 6.10 the nadir transmission and transmission weighting function for Jupiter at 600 cm^{-1} is compared to $2E_3(\tau)$ and $2dE_3(\tau)/dz$. As can be seen the curves are very similar with the only real difference being that the disc-averaged weighting function peaks at slightly higher altitudes, roughly at the altitude of the transmission weighting function calculated for a zenith angle of $\sim 50^\circ$, and is slightly broader.

6.4.3 Limb-viewing

We saw in Section 6.4.1 that for nadir, or near-nadir, viewing geometries the weighting functions are rather broad. This low vertical resolution can be a problem when the spectra are used to assess the vertical profiles of gases whose abundances vary rapidly with altitude. One way to increase the vertical resolution is to view the limb of the planet. The radiative transfer equation is very similar to Equation 6.39 but instead of integrating over height we instead integrate directly along the path l

$$I_{\bar{\nu}1} = \int_{l_0}^{l_1} B_{\bar{\nu}}(l) \frac{dT_{\bar{\nu}}}{dl} dl = \int_{z_0}^{z_1} B_{\bar{\nu}}(z) K'_{\bar{\nu}} dz \quad (6.47)$$

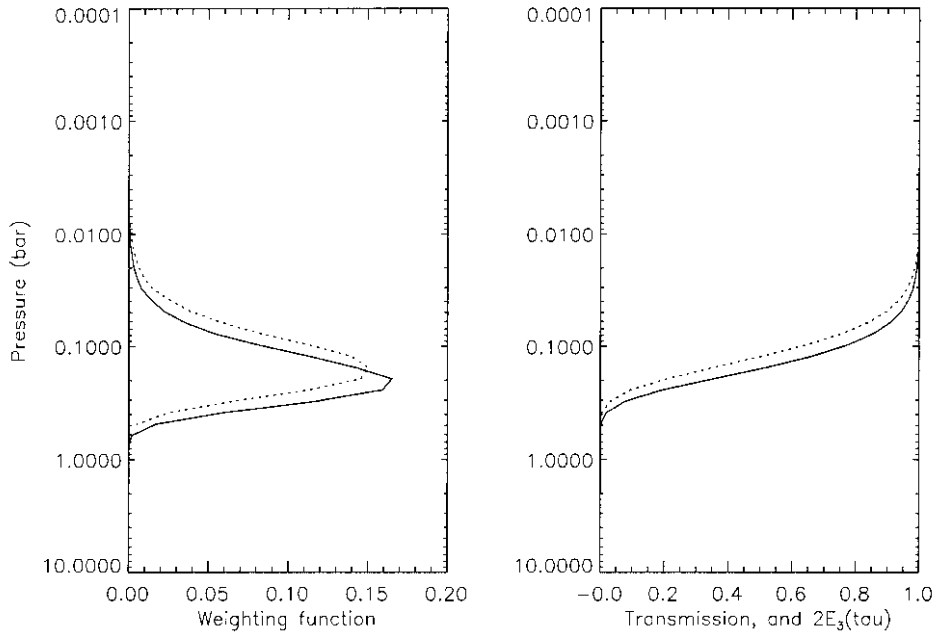


Figure 6.10 Calculated weighting functions for Jupiter at 600 cm^{-1} for nadir viewing (solid line), and for disc-averaged (dotted line) conditions.

where

$$K'_{\tilde{\nu}} = \frac{dT_{\tilde{\nu}}}{dl} \frac{dl}{dz}. \quad (6.48)$$

Since density varies exponentially with height in an atmosphere, the density of the slant path is highest near the tangent altitude and thus at wavelengths where the gas absorption is low, the transmission weighting function is an exponential shape function with a sharp base at the tangent altitude z_0 . As the gas absorption becomes stronger, more and more emission comes from molecules between the observer and the tangent point and the weighting function becomes broader. Example limb weighting functions are shown for Jupiter at 600 cm^{-1} in Figure 6.11. At a tangent pressure of $\sim 10\text{ mbar}$, the weighting function can be seen to be very narrow with a sharp lower boundary. However as the tangent pressure increases, and the absorption increases, the weighting function becomes broader as can be seen in the second weighting function of Figure 6.11 where the pressure at the tangent altitude is $\sim 0.38\text{ bar}$.

In addition to increased vertical resolution, limb-sounding also provides greater sensitivity to the detection of trace atmospheric constituents by providing much longer path lengths. For an atmosphere whose number density varies with height as $n = n_0 \exp(-(z - z_0)/H)$, above some reference altitude z_0 , where H is the scale height, it may easily be shown that the column amount (i.e., molecules/m²) of molecules above this altitude for nadir viewing is $A_N = n_0 H$. However, if

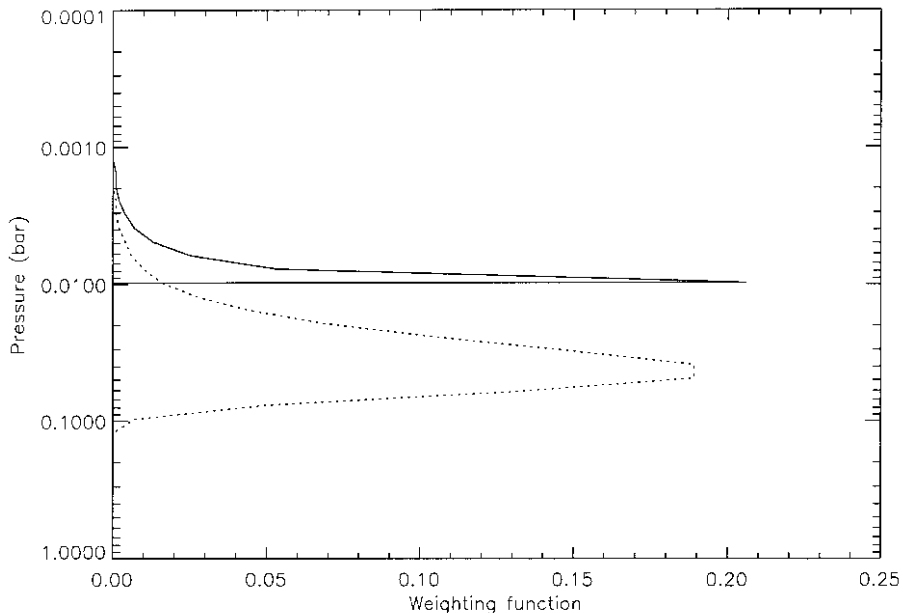


Figure 6.11 Calculated limb weighting functions for Jupiter at 600 cm^{-1} and tangent height pressures of 9.7 mbar (solid lines) and 387 mbar (dotted line).

limb-viewing the atmosphere with a tangent altitude at z_0 , the total amount of molecules in the path may be shown to be well-approximated by $A_L = n_0(2\pi RH)^{1/2}$, where R is the planetary radius at the tangent altitude z_0 . Since the radius of all planets is very large compared to H , the limb path contains much greater amounts, and thus absorption features of trace constituents are much easier to observe in limb paths than in nadir ones. For the giant planets, the increase in path amount A_L/A_N is of the order of 100.

The disadvantage of limb-viewing is that it places considerably tighter constraints on the telescope field of view and pointing accuracy and is hence much more difficult to achieve in practice. However the possible improvement in vertical resolution and sensitivity to trace species makes it a very attractive technique and it is widely used in terrestrial remote sensing. The field of view of the *Voyager* IRIS spectrometers was too broad to allow limb-sounding of the giant planets, although it was achieved for Titan. The *Cassini* CIRS instrument however, has been specifically designed with limb-viewing in mind and will be able to make limb-sounding observations of both Titan and Saturn when it arrives in the Saturnian system in 2004.

6.4.4 Radiative balance

The balance between radiative heating and cooling affects the temperature profile in upper tropospheres and stratospheres of the giant planets and thus affects the

circulation of air at these altitudes. At an altitude z , or optical depth τ , in the atmosphere, the upward spectral flux of radiation is, from Equation 6.44 equal to

$$F_{\tilde{\nu}}(\uparrow) = 2\pi I_{\tilde{\nu}0} E_3(\tau_0 - \tau) + 2\pi \int_{E_3(\tau_0 - \tau)}^{0.5} B_{\tilde{\nu}}(\tau') dE_3(\tau' - \tau) \quad (6.49)$$

and the downward spectral flux is

$$F_{\tilde{\nu}}(\downarrow) = 2\pi \int_{E_3(\tau)}^{0.5} B_{\tilde{\nu}}(\tau') dE_3(\tau - \tau'). \quad (6.50)$$

If the fluxes are then integrated over all wavelengths, the difference between the two may be used to calculate the heating rate as

$$\rho c_p \frac{dT}{dt} = \frac{d \left(\int_0^{\infty} (F_{\tilde{\nu}}(\uparrow) - F_{\tilde{\nu}}(\downarrow)) d\tilde{\nu} \right)}{dz} \quad (6.51)$$

where ρ is the mass density and c_p is the specific heat capacity at constant pressure. In the stratospheres of the giant planets it is of particular interest to know how long it takes for temperature perturbations introduced by effects such as dynamics to relax back to zero (i.e., for the temperature profile to return to its equilibrium radiative balance state). Near the emitting level, a simple estimate of the radiative time constant is (Allison *et al.*, 1991)

$$t_R \approx \frac{c_p p T}{g \sigma T_e^4} \quad (6.52)$$

where T_e is the effective radiating temperature. This expression is basically the heat stored per unit area of the atmosphere above the level at pressure p divided by the outgoing thermal radiation flux. Once an estimate for the radiative time constant has been derived, the local heating rates \dot{Q} implied by local departures of temperature from equilibrium can be estimated from (Conrath *et al.*, 1990)

$$\frac{\dot{Q}}{c_p T} = \frac{1}{T} \frac{T - T_{eqm}}{t_R}, \quad (6.53)$$

where T_{eqm} is the local radiative equilibrium temperature.

6.4.5 Local thermodynamic equilibrium

For radiative transfer calculations, we normally assume that the atmosphere is in local thermodynamic equilibrium (LTE). This means that we can use the Planck function $B(\tilde{\nu}, T)$ as we have done in our previous equations. However, at very low pressures the time between collisions becomes equal to, or greater than, the time of interaction of the molecules with photons, and thus the population density of states deviates from a simple Boltzmann distribution (Goody and Yung, 1989). Under these conditions of non-LTE, the calculation of the *source* function, used instead of the Planck function in the previous radiative transfer equations, becomes very complicated and is a whole research area in its own right (Lopez-Puertas and Taylor, 2001).

6.4.6 Transmission calculations

Given the absorption coefficients of the various gases and aerosols in a planetary atmosphere, it can be seen that the emerging radiance for a real atmosphere may be calculated. Since the line strengths and line widths are functions of temperature and pressure, and since atmospheres are extremely inhomogeneous in both respects, the monochromatic transmission at wavenumber $\tilde{\nu}$ of a path through an atmosphere between two levels z_1 and z_2 at zenith angle θ is given by

$$T_{12}(\tilde{\nu}) = \exp\left(-\frac{1}{\mu} \int_{z_1}^{z_2} n(z) \left(\sum_j q_j(z) \sum_i k_{ij}(\tilde{\nu}, p(z), T(z)) \right) dz\right) \quad (6.54)$$

where $n(z)$ is the number density of the atmosphere at altitude z (molecules/m³), $p(z)$ and $T(z)$ are the atmospheric pressures and temperatures, $q_j(z)$ is the mole fraction of gas j at altitude z , and the summation over i is over all the absorption lines of gas j which contribute to the optical depth at this wavenumber. There are a number of databases available which list the molecular absorption lines of important gases including HITRAN (Rothman *et al.*, 1998) which is extensively used for terrestrial atmospheric calculations and GEISA (Husson *et al.*, 1992, 1994) which includes lines of exotic gases only found in the atmospheres of the giant planets. For each line of each gas, the absorption coefficient k_{ij} must be calculated from the line strength s and line shape, both of which are functions of temperature and pressure. Since thousands of absorption lines may contribute to the absorption at a particular wavelength, it can easily be seen that such *line-by-line* calculations are computationally expensive and thus slow, although they are clearly the most accurate method available.

In most cases, spectral calculations are made to compare to real measured spectra which have limited spectral resolution. Hence the transmissions used in the radiative transfer equation must be integrated over the instrument function. While it is still most accurate to convolve line-by-line calculated spectra to the required spectral resolution, there are alternative methods of simulating finite-resolution spectra which are much faster and only slightly less accurate. Since the line parameters used to generate line-by-line spectra are themselves sometimes accurate to only 10% in some cases, the use of these lower-accuracy models is very common and perfectly defendable. There are two main approaches, band models and correlated- k models which will now be discussed.

Band model approximation

A number of possible band models exist including Goody–Lorentz, Godson–Lorentz, Malkmus–Lorentz, and Goody–Voigt band models. A full discussion of these models is beyond the scope of this book, but they are discussed in detail in a number of more general radiative transfer books such as Goody and Yung (1989). The basic idea of such models is that if we have an atmosphere of fixed temperature, pressure, and composition, and if we then measure (or calculate with a line-by-line model) the mean transmission over the wavenumber range $\tilde{\nu}$ to $\tilde{\nu} + \Delta\tilde{\nu}$ of a number

of paths of different lengths through this atmosphere, then the mean transmission as a function of the path amount m (molecules/m²), due to individual gases, may be well-approximated by a smoothly varying analytical function of just a few parameters. For example, the *band transmission* as a function of path amount for the Goody–Voigt approximation due to a certain gas of mole fraction q is given by

$$\bar{T}(m) = \exp\left(-2k_{\bar{\nu}}(T)m \int_0^{\infty} \frac{V(x,y)}{1 + k_{\bar{\nu}}(T)mV(x,y)(\delta/\alpha_D^0)\sqrt{T}} dx\right) \quad (6.55)$$

where $V(x,y)$ is the Voigt function and where

$$y = \frac{\alpha_L}{\alpha_D} = \frac{\alpha_L^0 p}{\alpha_D^0 p_0} \frac{\sqrt{T_0}}{T} \left(q + \frac{1-q}{SFB}\right) = y_0 \frac{p}{p_0} \frac{\sqrt{T_0}}{T} \left(q + \frac{1-q}{SFB}\right) \quad (6.56)$$

where T_0 and p_0 are reference temperatures and pressures and SFB is a factor to be fitted or calculated (see below). The mean absorption coefficient $k_{\bar{\nu}}$ may be expanded as

$$k_{\bar{\nu}}(T) = k_{\bar{\nu}}(T_0) \left(\frac{T_0}{T}\right)^{q_r} \exp\left[1.439E_l\left(\frac{1}{T_0} - \frac{1}{T}\right)\right] \quad (6.57)$$

where q_r is 1.0 for linear molecules and 1.5 for non-linear molecules. There are thus 5 independent parameters in the Goody–Voigt model: $k_{\bar{\nu}}(T_0)$, y_0 , δ/α_D^0 , E_l , and SFB which may either be fitted to laboratory transmission spectra, or alternatively derived from tabulated line listings such as HITRAN and GEISA. These parameters, while usually fitted directly to the measured spectra, are related to the properties of the real absorption lines in the spectral band: $k_{\bar{\nu}}(T_0)$ is the integrated line strength of all the lines in the band at the standard temperature; y_0 is the mean ratio of pressure-broadened to Doppler broadened line widths at STP (standard temperature and pressure); δ/α_D^0 is the mean line spacing divided by the Doppler broadened width at STP; E_l is the mean energy of the lower states; and SFB is the mean self- to foreign-broadening ratio of the absorption lines.

Once band data have been tabulated, the transmission of homogeneous paths may be rapidly and accurately calculated. However, real atmospheres are inhomogeneous in that pressure and temperature vary rapidly with position. How then may band models be applied? It may be shown that the mean transmission of a path through an inhomogeneous atmosphere at zenith angle θ may be well approximated by the mean transmission of an equivalent homogeneous path whose path amount, mean pressure, and mean temperature are given by:

$$m = \frac{1}{\mu} \int_{z_1}^{z_2} n(z) dz, \quad \bar{p} = \frac{\frac{1}{\mu} \int_{z_1}^{z_2} n(z)p(z) dz}{m}, \quad \bar{T} = \frac{\frac{1}{\mu} \int_{z_1}^{z_2} n(z)T(z) dz}{m}. \quad (6.58)$$

This is known as the *Curtis–Godson* approximation. Hence to use band models to calculate thermal emission spectra, the inhomogeneous atmosphere is represented by a series of equivalent Curtis–Godson paths from space to progressively deeper levels in the atmosphere, and the difference between the band-calculated mean transmissions used to find the mean transmission weighting function. Fortunately, since the

absorption lines of different molecules are rarely correlated with each other, the total transmission of the Curtis–Godson paths is simply found by multiplying the individual gas transmissions together, or equivalently by summing the optical thicknesses. The band model approach is very fast but is found to be useless for scattering calculations and hence is mostly used in the mid- to far-IR where scattering is less generally important, as we shall see in Section 6.5.2.

Correlated-k approximation

An alternative approach to calculating finite resolution spectra is to use *k*-distributions. For a path of absorber amount m in an atmosphere of uniform pressure p and temperature T , the mean transmission is given by

$$\bar{T}(m) = \frac{1}{\Delta\tilde{\nu}} \int_{\tilde{\nu}}^{\tilde{\nu} + \Delta\tilde{\nu}} \exp(-k(\tilde{\nu})m) d\tilde{\nu} \quad (6.59)$$

where the absorption coefficient at a particular wavelength is the summation of all the individual line contributions. Since the absorption coefficient $k(\tilde{\nu})$ is a rapidly varying function of wavenumber, in order to numerically calculate the mean transmission accurately, a very fine wavenumber step must be chosen. However, when calculating the mean transmission in a spectral interval it does not matter which parts of the interval are actually highly or poorly absorbing. All we need to know is what fraction of the interval has low absorption, what fraction has high absorption, and so on. In other words, if we calculate a high resolution absorption coefficient spectrum using a regularly spaced high resolution grid, and then shuffle the absorption coefficients into order starting with the low absorption coefficients first and then working monotonically through to the high absorption coefficients, the resulting integral of the shuffled spectrum is identical to that of the original. The advantage of the technique is that the reshuffled spectrum, known as the *k*-distribution $k(g)$, is a *smoothly varying* function which is usually expressed in terms of the fraction of the interval g which varies between 0 and 1. Since $k(g)$ is a smoothly varying function, the integral may be accurately integrated with far fewer quadrature points and thus the calculation of the mean transmission is very much faster. In practice, ten quadrature points are usually found to be satisfactory and the mean transmission may be approximated by

$$\bar{T}(m) \equiv \int_0^1 \exp(-k(g)m) dg \simeq \sum_{i=1}^N \exp(-k_i m) \Delta g_i \quad (6.60)$$

where k_i is the *k*-distribution calculated at each of the N quadrature points, and Δg_i are the quadrature weights. The *k*-distributions may be pre-calculated for each gas for a range of temperatures and pressures found in the real atmospheres, and then stored in look-up tables for rapid interpolation and calculation of the mean transmission. Again since the absorption lines of different gases may be assumed to be uncorrelated, it is reasonably straightforward to combine *k*-distributions together (Lacis and Oinas, 1991). The *k*-distribution look-up tables may be calculated either directly from line data, or indirectly from band data using the technique of expo-

nential sums (Irwin *et al.*, 1996). While we can see that k -distributions can speed up transmission calculations for homogeneous paths, how can they help us for inhomogeneous paths? For monochromatic calculations, the transmission of an inhomogeneous path is found by splitting the path into small sub-paths, calculating the transmission and then multiplying all the transmissions together. However, for band-averaged transmissions such as those used by band models this multiplication is not possible and thus the Curtis–Godson approximation must be used. The Curtis–Godson approximation may also be used with k -distributions but there is then no advantage over the band model approach. Instead, it is found that regions of high and low absorption within the spectral band are correlated between various sub-paths within the inhomogeneous path. This correlation exists between the k -distributions also (Lacis and Oinas, 1991; Goody *et al.*, 1989). Hence the k -distributions may effectively be multiplied together almost as though they were monochromatic to achieve the mean transmission of the inhomogeneous path

$$\bar{T} \simeq \sum_{i=1}^N \exp\left(-\sum_{j=1}^M k_{ij} m_j\right) \Delta g_i \quad (6.61)$$

where the inhomogeneous path has been split into M sub-paths. This is the correlated- k approximation and is found to have an accuracy similar to that of the Curtis–Godson approximation. The great advantage however lies in the fact that thermal emission, and in particular scattering calculations discussed in Section 6.6, may also be summed in exactly the same way. Hence the technique of correlated- k allows for rapid calculation of spectra in scattering atmospheres and is used extensively to simulate the near-IR reflectance spectra of the giant planets.

6.5 SCATTERING OF LIGHT BY PARTICLES

We have seen in Section 6.4 that the equations for radiative transfer in a non-scattering ‘grey’ atmosphere are relatively simple. However, these equations are not applicable to the analysis of sunlight reflected by clouds in planetary atmospheres and are hence only of use in modelling the thermal-IR spectra of the planets. Even in the thermal-IR however, neglecting the scattering effects of atmospheric aerosols can sometimes lead to errors, especially if cloud particles are of a size approximately equal to or greater than the wavelength. The scattering effect of aerosols greatly complicates the equations of radiative transfer as we shall see in Section 6.6. However, before we can investigate the effects of scattering, we must first introduce the basic definitions of scattering parameters, and how the scattering properties of individual particles may be calculated.

Consider a single photon of wavelength λ incident on a particle which is then scattered forward at an angle θ to the original direction (Figure 6.12). This angle is defined as the *scattering angle* and in an experiment where light is incident upon such a particle, the numbers of photons scattered into different directions will be a function of this scattering angle. The function, which gives the probability that a

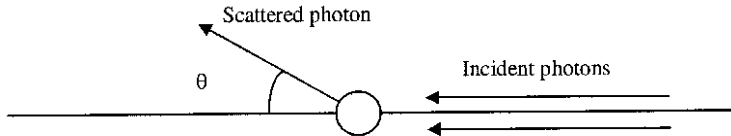


Figure 6.12 Scattering angle definition.

photon will be scattered into an element of solid angle $d\Omega$ and scattering angle θ is known as the *phase function* $p(\theta)$ and by convention is normalized such that

$$\int_0^{4\pi} p(\theta) d\Omega = \int_{\phi=0}^{2\pi} \int_{\theta=0}^{\pi} p(\theta) \sin \theta d\theta d\phi = 4\pi. \quad (6.62)$$

Note that in some schemes this integral is normalized to unity which can lead to confusion! The phase function itself is a function of wavelength, particle composition, mean particle radius, and particle shape.

The probability that a photon will actually be absorbed or scattered by a particle, regardless of direction, depends upon the *absorption* and *scattering cross sections*, σ_{abs} and σ_{sca} respectively. These cross sections also depend on the wavelength, particle composition, mean particle radius, and shape. The *extinction cross section* is defined as $\sigma_{ext} = \sigma_{sca} + \sigma_{abs}$, and the *single-scattering albedo* ϖ_0 is defined as the ratio

$$\varpi_0 = \frac{\sigma_{sca}}{\sigma_{ext}}. \quad (6.63)$$

The absorption, scattering, and extinction scattering *efficiencies* Q_{abs} , Q_{sca} , and Q_{ext} are defined as the ratios of the respective cross sections to the geometric cross-sectional area of the particles.

6.5.1 Rayleigh or dipole scattering

When the wavelength is very much bigger than the particle size, the scattering particles tend to behave as simple dipoles and we have the condition for *Rayleigh scattering* which we referred to in Chapter 4. The phase function for Rayleigh scattering may be shown from standard electromagnetic theory to be (Goody and Yung, 1989)

$$p(\theta) = \frac{3}{4}(1 + \cos^2 \theta) \quad (6.64)$$

and thus the probability that photons will be scattered at a scattering angle between θ and $\theta + d\theta$ is

$$P(\theta) d\theta = \frac{3}{8}(1 + \cos^2 \theta) \sin \theta d\theta. \quad (6.65)$$

Such dipole scatterers are purely scattering and thus have zero absorption cross section. Their scattering cross section varies with wavelength as $1/\lambda^4$ as described in Chapter 4 (Equation 4.34) and the most familiar example of such scattering is in the Earth's atmosphere, where the molecules of N_2 and O_2 scatter a fraction of the incident sunlight in all directions. Clearly from Equation 4.34, blue light is scattered

more effectively than red light leading to the familiar blue sky seen from the surface of the Earth (in the absence of cloud!).

Raman scattering and fluorescence

Quantum mechanically, an atom or molecule Rayleigh-scatters a photon by first absorbing it and becoming excited to an intermediate or virtual state whereupon it immediately relaxes back to its initial state releasing a photon with the same wavelength in a direction governed by Equation 6.64. However, it is also possible that the atom or molecule relaxes back to a different state, thus releasing a photon of either greater or lesser wavelength than the original photon. *Stokes Transitions* lead to scattered photons with longer wavelengths than the incident light, while *Anti-Stokes Transitions* lead to scattered photons with shorter wavelengths. The phenomenon is called *Raman* scattering and is usually rather weak compared to Rayleigh scattering and thus may usually be neglected. The exception to this is in the case of the giant planets (occurring in the UV spectra) of Uranus and Neptune where distinct solar spectrum features appear shifted to long wave in the observed albedoes of these planets by Raman scattering associated mainly with the rotational S(0) transition of hydrogen molecules (giving a wavenumber shift of 354 cm^{-1}) and to a much lesser extent the S(1) and Q₁(1) transitions (shifted by 587 cm^{-1} and $4,161\text{ cm}^{-1}$ respectively). Raman scattering in the outer planet atmospheres is described in detail by Karkoschka (1994).

Should the scattered photons have considerably less energy than the incident photons, and thus significantly longer wavelengths, but be released quickly (within roughly 10^{-7} s), then the effect is sometimes also known as *fluorescence*. It is observed that many household materials glow, or fluoresce, under UV illumination (Hecht and Zajac, 1974). If there is an appreciable delay in the release of the lower-energy photons, sometimes several hours, then the effect is known as *phosphorescence*.

6.5.2 Mie theory

For particles that have a non-negligible size compared to the wavelength, Rayleigh scattering no longer applies, and the calculation of the phase function and extinction cross section becomes more complicated. However, provided the aerosol particles are spherical (and are thus liquid), and provided that the complex refractive index ($n_r + i n_i$) as a function of wavelength is known, Maxwell's equations may be solved analytically via a method known as Mie theory to calculate the scattering properties. This method deals with the classical case of a dielectric sphere interacting with a plane electromagnetic wave, and is too complex to be covered in detail here. The reader is referred to a number of more detailed references for further information: Hanel *et al.* (1992); Goody and Yung (1989); and Hansen and Travis (1974). Using Mie theory, Q_{ext} , ϖ_0 , and $p(\theta)$ may all be calculated as a function of wavelength. The typical variation of Q_{ext} with wavelength is shown in Figure 6.13. From this figure,

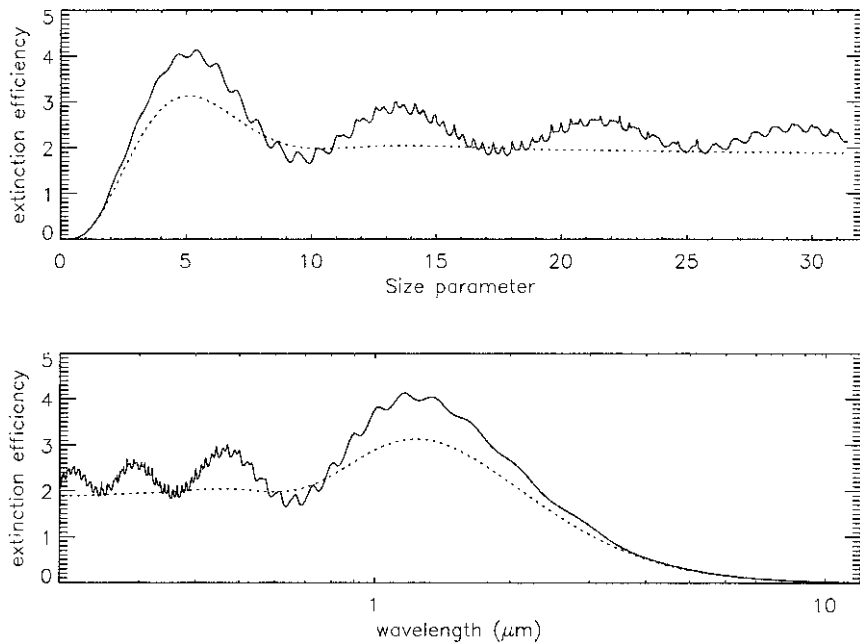


Figure 6.13 Mie scattering calculation of Q_{ext} as a function of wavelength for particles with refractive index (1.4, 0). The solid line shows the properties of particles with a single radius of 1 μm while the dotted line shows the properties if there is a small distribution of particle size with about 1 μm . The spectra are plotted as a function of both wavelength and size parameter, defined as $2\pi r/\lambda$, where r is the radius and λ the wavelength.

together with the calculated phase functions, the bulk scattering properties of spherical liquid aerosols are found to be:

- (1) For particles which are small compared to the wavelength, the extinction cross section tends to $1/\lambda^4$, and phase function tends towards the Rayleigh or dipole scattering case discussed earlier.
- (2) A particle is most efficient at scattering light with a wavelength approximately equal to its own radius.
- (3) For particles that are large compared to the wavelength, it is found that the amount of light diffracted is equal to the amount striking the particle (independent of particle shape and refractive index) and thus $Q_{ext} = 2$. It is also found that the phase function becomes more and more forward scattering, and in the limit where the particle is very much greater than the wavelength of the incident light, $p(\theta) = \delta(\theta)$, where $\delta(\theta)$ is the Dirac-delta function.

6.5.3 Non-spherical particles

A number of analytical/numerical methods exist for calculating the scattering behaviour of non-spherical scatterers (i.e., ice crystals) with electromagnetic

radiation. This adds a further layer of complexity. Fortunately, the non-spherical nature of real ice crystals may often be ignored since a set of randomly orientated crystals is, to a first approximation, indistinguishable from a set of spheres with the same mean radius. However, if crystals become aligned in some way through dynamics or other effects, the difference can become significant. The general case of non-spherical particles is outlined by Goody and Yung (1989).

6.5.4 Analytical forms of phase functions

The phase functions calculated for both spherical particles (using Mie theory) and non-spherical particles do not have a simple analytical expression. However, it is sometimes useful to have a more simple parameterized form of the phase function to use in radiative transfer models that can reasonably well approximate the real phase functions of particles. One such representation is the double Henyey–Greenstein representation

$$p(\theta) = \left\{ f \frac{1 - g_1^2}{(1 + g_1^2 - 2g_1 \cos \theta)^{3/2}} + (1 - f) \frac{1 - g_2^2}{(1 + g_2^2 - 2g_2 \cos \theta)^{3/2}} \right\} \quad (6.66)$$

where g_1 is the asymmetry of the forward scattering lobe (varying between 0 and 1), g_2 is the asymmetry of the backscattering lobe (varying between 0 and –1), and f is the fractional contribution (between 0 and 1) of the forward scattering part. The calculated Henyey–Greenstein phase functions for a range of parameters are shown in Figure 6.14. An example of the use of Henyey–Greenstein phase functions is that scattering radiative transfer models may be optimized to use them. Hence by approximating real phase functions by Henyey–Greenstein functions, great reductions in computation times may be achieved.

6.6 RADIATIVE TRANSFER IN SCATTERING ATMOSPHERES

The radiative transfer equations of Section 6.4 for a grey atmosphere must be substantially modified to deal with atmospheres that contain substantial abundances of scattering particles as we shall shortly see. These modifications greatly increase the computation time and thus scattering calculations are notoriously difficult and slow. There are two main ways of approaching the problem. The simplest is to ignore the curvature of the planetary atmosphere and approximate the problem by a stack of plane-parallel layers. Using this approach, a number of good approximations may be made which considerably reduce the computation time. Most calculations are made with this *plane-parallel approximation*. However, under certain conditions, such as for limb observations, the plane-parallel approximation no longer applies and thus much slower, but more general purpose techniques such as *Monte Carlo* calculations must be used. In this section we will outline how the scattering

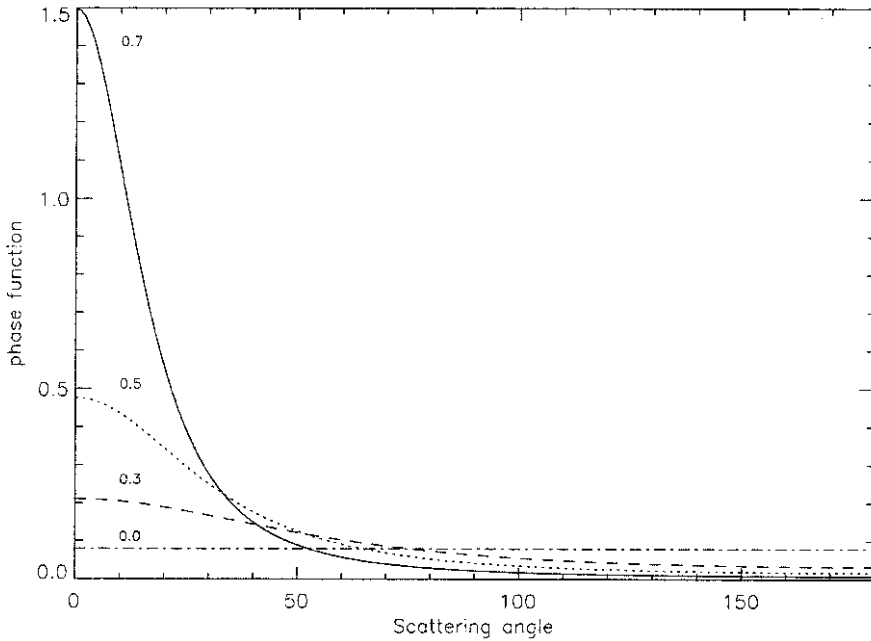


Figure 6.14 Examples of different Henyey–Greenstein phase functions depending on f , g_1 , g_2 . Here $f = 1$, $g_2 = 0$, and $g_1 = 0.7$ (solid), 0.5 (dots), 0.3 (dashes) and 0.0 (dot–dash).

properties of particles, just discussed, may be used in radiative transfer models to calculate synthetic spectra of the giant planets.

6.6.1 Plane-parallel approximation

In Section 6.4.1 we found that the thermal contribution of a thin slab to the vertical upwelling radiance at z_1 in a plane-parallel atmosphere is given by

$$dI_{\bar{\nu}1} = B_{\bar{\nu}}(z) d\tau_{\bar{\nu}}(z, z_1) \quad (6.67)$$

where $\tau_{\bar{\nu}}$ is the optical depth of the atmosphere which is zero at the top of the atmosphere and increases steadily as we move to deeper levels. Considering the intensity $I_{\bar{\nu}}$ of radiation at altitude z , radiating in a direction specified by the zenith angle θ and azimuth angle ϕ , the radiative transfer equation may be expressed as

$$\mu \frac{dI_{\bar{\nu}}(\tau_{\bar{\nu}}, \mu, \phi)}{d\tau_{\bar{\nu}}} = I_{\bar{\nu}}(\tau_{\bar{\nu}}, \mu, \phi) - B_{\bar{\nu}}(\tau_{\bar{\nu}}) \quad (6.68)$$

where $\mu = \cos \theta$. For scattering atmospheres, the equations become more complicated in that particles may scatter light out of a beam, and also scatter light into the

beam which was initially travelling in other directions. The equation of transfer under these conditions becomes (Hanel *et al.*, 1992)

$$\begin{aligned} \mu \frac{dI_{\bar{\nu}}(\tau_{\bar{\nu}}, \mu, \phi)}{d\tau_{\bar{\nu}}} &= I_{\bar{\nu}}(\tau_{\bar{\nu}}, \mu, \phi) \\ &- \frac{\varpi_0}{4\pi} \int_0^{2\pi} \int_{-1}^1 p(\mu, \phi; \mu', \phi') I_{\bar{\nu}}(\tau_{\bar{\nu}}, \mu', \phi') d\mu' d\phi' \\ &- (1 - \varpi_0) B_{\bar{\nu}}(\tau_{\bar{\nu}}) \end{aligned} \quad (6.69)$$

where $p(\mu, \phi; \mu', \phi')$ is the phase function. The single scattering albedo ϖ_0 here is the ratio of $\sigma_{sca}/\sigma_{ext}$ for both aerosols *and* gas (i.e., it includes the scattering of aerosols and Rayleigh scattering of the gas together with absorption by both the aerosols and gas). This equation clearly reduces to the thermal emission form for non-scattering atmospheres, where $\varpi_0 = 0$.

The scattering second term of Equation 6.69 contains both the scattered diffuse field and the scattering of direct sunlight that has reached a particular optical depth. It is very useful to be able to discriminate between the two. Suppose that the incident sunlight (considered to be a beam of collimated radiation) carries a spectral flux F_0 ($\text{W m}^{-2} (\text{cm}^{-1})^{-1}$) normal to its direction, and suppose that the cosine of the zenith angle of the Sun is μ_0 . The magnitude of the flux directly vertically downwards is $\mu_0 F_0$ and Equation 6.69 may be re-expressed as

$$\begin{aligned} \mu \frac{d[e^{-\tau_{\bar{\nu}}/\mu} I_{\bar{\nu}}(\tau_{\bar{\nu}}, \mu, \phi)]}{d\tau_{\bar{\nu}}} &= -\frac{\varpi_0}{4\pi} e^{-\tau_{\bar{\nu}}/\mu} \int_0^{2\pi} \int_{-1}^1 p_0(\mu, \phi; \mu', \phi') I_{\bar{\nu}}(\tau_{\bar{\nu}}, \mu', \phi') d\mu' d\phi' \\ &- \frac{\varpi_0 F_0(\tilde{\nu})}{4\pi} \exp \left[-\left(\frac{1}{\mu} + \frac{1}{\mu_0} \right) \tau_{\bar{\nu}} \right] p_0(\mu, \phi; -\mu_0, \phi_0) \\ &- (1 - \varpi_0) e^{-\tau_{\bar{\nu}}/\mu} B_{\bar{\nu}}(\tau_{\bar{\nu}}). \end{aligned} \quad (6.70)$$

Here the first term contains scattered diffuse light, the second term contains directly scattered sunlight, and the third term contains thermally emitted radiation. Equation 6.70 may not be solved analytically but must instead be solved numerically. There are a number of ways of doing this and one of the most common is the Matrix-Operator (or the Doubling-Adding) method. This technique basically applies a Gaussian Quadrature technique to the integration over zenith angle and the Fourier method to the integration over azimuth angle and is well described by Plass *et al.* (1973), Hansen and Travis (1974), and Goody and Yung (1989). Alternative techniques include Discrete Ordinates (Hanel *et al.*, 1992) and Successive Orders (Hansen and Travis, 1974). A particularly useful technique for cases where the scattering optical depth is small is the *single-scattering approximation* which assumes that thermal emission is negligible and that the probability of a photon being scattered more than once is so small that only the second term on the

right-hand side of Equation 6.70 need be considered. This leads to the directly integrable equation

$$I_{\tilde{\nu}}(\mu, \phi) = \frac{\varpi_0 F_0(\tilde{\nu})}{4\pi} \int_0^\infty p_0(\mu, \phi; -\mu_0, \phi_0) \exp \left[-\left(\frac{1}{\mu} + \frac{1}{\mu_0} \right) \tau_{\tilde{\nu}} \right] \frac{d\tau_{\tilde{\nu}}}{\mu}. \quad (6.71)$$

A further particularly simple approximation to scattering, which is applicable for atmospheres with thin cloud layers, is the so-called *reflecting layer approximation*. Here the gas absorption spectra are used to calculate the transmission of a path from the Sun, to a particular level in the atmosphere and back to the observer. If a thin cloud exists at that pressure level, then the observed spectrum may be approximated by multiplying this transmission by the effective reflectivity of the cloud layer. Several clouds may be approximated by summing the ‘reflections’ from a number of levels. The technique is closely related to the single scattering approximation.

6.6.2 Spherical atmospheres and limb-viewing: Monte Carlo simulations

The scattering equations just derived relate to plane-parallel atmospheres and thus are only applicable when the zenith angles are not too near to 90° . For limb-viewing geometries, the equations are unusable and thus a more basic numerical technique known as the *Monte Carlo* method must be used.

As the name suggests, the Monte Carlo technique basically ‘fires’ a large number of model photons into an atmosphere and tracks where they go using the scattering probability functions and a random number generator. The technique is computationally expensive and thus slow to converge. However, if enough photon paths are simulated, the accuracy is as good as the more conventional techniques, and the technique has the advantage of being able to model any geometry.

From Beer’s law of absorption we know that the probability that a photon will pass through a slab of optical thickness τ is given simply $\exp(-\tau)$. Hence by inversion we know that the optical thickness travelled by a random photon before absorption or scattering is given simply by

$$\tau = -\log(R) \quad (6.72)$$

where R is a random number between 0 and 1. From a given starting position and direction we may thus calculate the new position of the photon given this random optical thickness. At the new position, the probability of scattering is simply the single scattering albedo ϖ , and thus the photon is scattered if $\varpi > R$, where R is a new random number between 0 and 1. If the photon is scattered, then the new photon direction may be calculated from the phase function where the scattering angle θ_0 is given by

$$\int_{\theta=0}^{\theta_0} p(\theta) \sin \theta d\theta = 2R \quad (6.73)$$

where R is another random number between 0 and 1 and where the rotation of the new direction around the old direction is governed by a further random angle between 0 and 360° . The new optical thickness for the next photon path is then

calculated and the process iterated until either the photon is absorbed or it leaves the atmosphere.

For cases where scattered sunlight dominates, the most efficient way of proceeding is to fire a sequence of photons at the planet from the direction of the Sun and track the proportion that are reflected by the atmosphere at different angles. For cases where thermal emission dominates, the most efficient way of proceeding is to fire a sequence of photons at the planet from the observer's position, calculate where in the atmosphere they are absorbed, and then average the Planck functions from the absorption regions. Monte Carlo thermal emission calculations converge much faster than reflected sunlight calculations.

6.7 GIANT PLANET SPECTRA

6.7.1 General features of giant planet spectra: UV to microwave

At UV wavelengths, the atmospheres of the giant planets are optically thick due to Rayleigh scattering. Hence at these wavelengths most of the light we see is Rayleigh-scattered sunlight, modified by the absorption of high altitude haze layers. Towards the poles, auroral glow is also seen, especially for Jupiter. Superimposed on this spectrum are the absorption features of several gases which suffer photolysis in the upper atmosphere and which were discussed in Chapter 4. As can be seen in Table 4.4, as the wavelength increases, Rayleigh scattering rapidly becomes less important and thus at visible wavelengths sunlight may penetrate to, and be reflected from, the deeper cloud layers at several bar pressures. Towards the red end of the visible spectrum, weak vibration–rotation bands of methane (and also ammonia) appear, which become increasingly strong in the near-IR. In the centre of these bands, the atmosphere is optically thick and thus any light that is detected must be reflected from the upper cloud and haze layers of the atmosphere. Between the bands, the atmosphere is optically thin and thus sunlight may be reflected from both upper and deeper cloud layers. Hence the analysis of the near-IR reflection spectrum is very important in determining the vertical cloud structure. The solar spectrum diminishes at longer wavelengths and thus in the mid-IR the spectrum is dominated by thermal emissions from the atmosphere itself, modulated by the presence of numerous vibration–rotation (Section 6.3.4) absorption bands of several molecules. In the far-IR the thermal emission spectra of the giant planets becomes dominated by collision-induced H₂–H₂ and H₂–He absorption (see the subsection 'Collision-induced dipole transitions' in Section 6.3.6) together with the rotational bands of several molecules (Section 6.3.3). At sub-millimetre and microwave wavelengths these sources of absorption become increasingly weak and thus thermal emission from the deep levels of the atmospheres may be detected at wavelengths other than near 1.3 cm, where ammonia has an inversion band.

6.7.2 Near-IR and visible reflectance spectra

Estimates of the disc-averaged geometric albedoes of the giant planets are shown in Figure 6.15. Data below 1 μm is taken directly from the ground-based observations of Karkoschka (1994, 1998). Above 1 μm , data are scarcer and the spectra are estimated from a variety of sources including Fink and Larson (1979), Kerola *et al.* (1997), Irwin *et al.* (1998), and Sromovsky *et al.* (2001). These spectra are formed by sunlight scattering off aerosol particles at different altitudes in the atmosphere. Sunlight scattering from deep clouds passes through a longer path of methane (and for Jupiter and Saturn, ammonia) before reaching the observer than sunlight scattering from haze layers in the upper troposphere. In the near-IR the absorption of methane (and ammonia) is significant and thus only wavelengths close to the methane absorption minima at 1.05, 1.3, 1.6, 2.0, and 3.0 μm may be scattered from deeper clouds leading to a series of narrow reflection peaks at these wavelengths. Sunlight scattering off higher clouds suffers less methane absorption and thus the reflection peaks are broader, whilst sunlight scattering off upper tropospheric and lower stratospheric hazes suffer very little absorption and thus have very broad reflection peaks. Hence by analysing the shape of the observed reflection

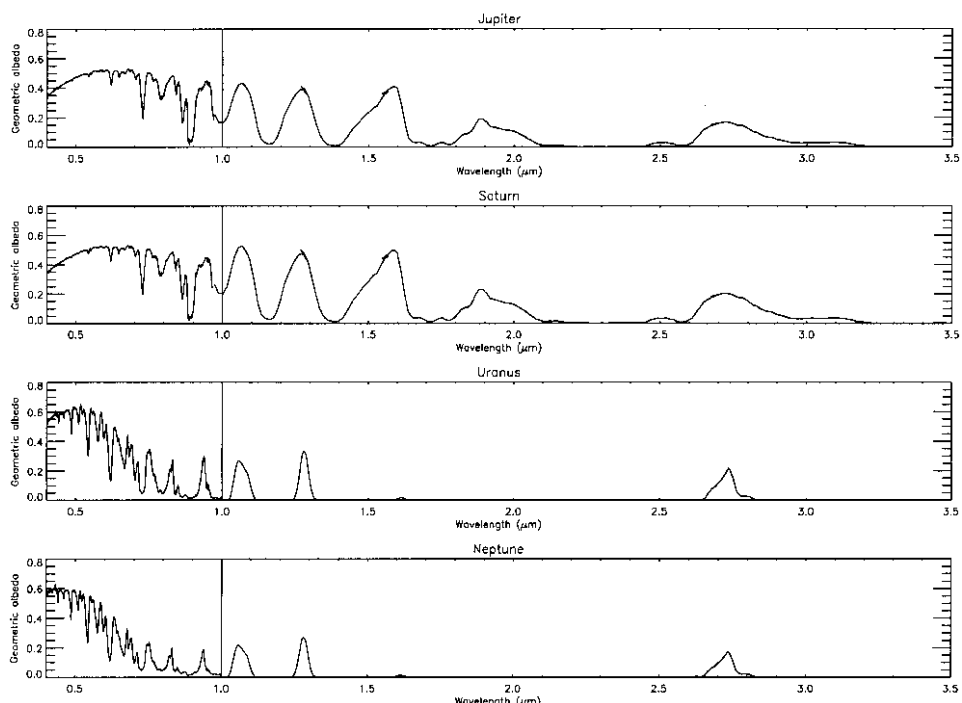


Figure 6.15 Measured and calculated geometric albedo spectra of the giant planets. Below 1 μm , the spectra are those measured from ground-based observations of Karkoschka (1994, 1998). The spectra above 1 μm are rough calculations and estimations from other sources.

spectra, we can deduce the vertical cloud structure of the giant planet atmospheres. In addition, the particle size of clouds may be estimated from analysing how the reflectivity of the cloud layers vary with wavelength since we saw in Section 6.5.2 that the extinction cross section of particles tends to zero at long wavelengths.

The main absorption bands of methane (shown previously in Figure 6.6) are clearly seen in Figure 6.15 for all four planets. At wavelengths greater than 1 μm , the shape of the spectra tell us immediately that the reflection spectra of Jupiter and Saturn are formed from reflections from a vertically extended cloud system, since a combination of reflections from deep, middle, and high cloud layers is required to simulate the observed spectra. In contrast, the reflection spectra of Uranus and Neptune have narrow peaks near the main methane pass bands indicating that the dominant reflection comes from the main clouds at ~ 3 bar, and that little sunlight is reflected from the tropospheric hazes. In addition to being deeper in the atmosphere than the main reflecting clouds of Jupiter and Saturn, the abundance of methane on Uranus and Neptune is also much greater, leading to substantial methane absorption. Towards the visible, the absorption of methane rapidly decreases, and the reflectivity of the small particles found in the tropospheric hazes increases leading to the increase in albedo observed for all four planets. The visible spectra of both ice giants can be seen to be significantly weighted towards the blue end, especially Neptune, which gives these planets their characteristic blue colours. Although this coloration arises partly from the red-absorbing nature of methane, which can be clearly seen, it is found that in addition, the main cloud deck at ~ 3 bar must also be significantly blue-absorbing as was mentioned in Chapter 4.

The variation of reflectivity of the planets across the visible disc may also tell us something about the scattering properties and vertical distribution of the cloud particles. The most precise definition of reflectivity is the *bidirectional reflectivity function* or BDRF defined as

$$R = \frac{\pi I}{\mu_0 F_0 / D^2}. \quad (6.74)$$

Here I is the measured reflected radiance, μ_0 is the cosine of the solar zenith angle, F_0 is the solar flux at the distance of the Earth, and D is the distance of the planet from the Sun in AU (Hanel *et al.*, 1992). This formulation correctly approximates the fact that the flux of sunlight arriving per unit area of a horizontal surface depends on the cosine of the zenith angle. For a *Lambertian* reflecting surface (where the BDRF is the same in all directions) Equation 6.74 may be rearranged as $I = R\mu_0 F_0 / D^2$ or $I = I_0\mu_0$ where I_0 is the maximum reflected radiance viewed then the Sun is directly overhead ($\mu_0 = 1$). Hence for a single Lambertian cloud layer, the observed reflectivity is expected to be limb-darkened with the reflectivity decreasing towards the limb of the planet as μ_0 tends to zero.* However, the extended vertical distribution of clouds in the giant planets together with significant gaseous atmospheric absorption means that sometimes significant departures to this simple limb-darkening rule

* A planet completely covered by Lambertian cloud layer would actually appear on a uniformly lit disc since although the reflectivity varies on μ_0 toward the limb, the area observed on $1/\mu_0$ and thus the two effects cancel.

are sometimes observed. A common approximation to the observed limb-darkening curve for these non-Lambertian cases is the semi-empirical *Minnaert* limb-darkening equation (Minnaert, 1941)

$$I = I_0 \frac{(\mu_0 \mu)^k}{\mu} \quad (6.75)$$

where μ is the cosine of the observer's zenith angle and where k is a constant between 0 and 1 which may be fitted to the experimental data. For a Lambert reflector $k = 1$. The measured limb-darkening curves may be fitted with scattering models to determine the vertical distribution of particles and their scattering properties.

6.7.3 Thermal-IR spectra

The calculated thermal emission spectra of the giant planets are shown in Figure 6.16 for nadir viewing geometry, and for the case of zero cloud opacity for Jupiter and Saturn, and deep thick cloud for Uranus and Neptune, with an optical depth of unity at ~ 3 bar for all wavelengths. For reference, the Planck function for a number of temperatures has also been plotted. Thermal emission diminishes rapidly with temperature and wavenumber and thus the emission of the ice giants is significantly

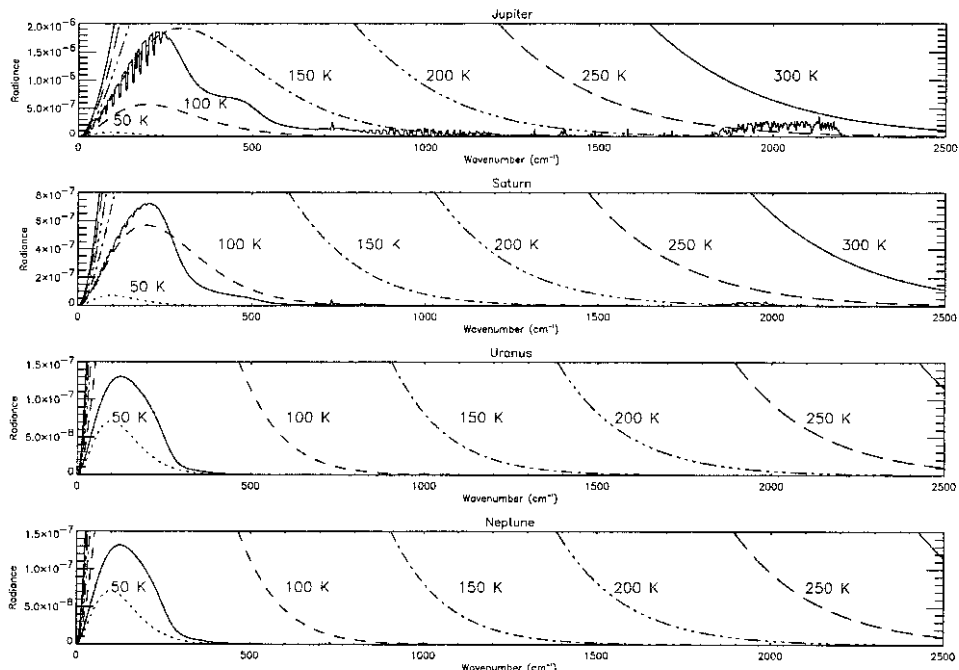


Figure 6.16 Calculated thermal emission spectra of the giant planets for nadir viewing. Note that the scales are different since the integrated flux from the planets decreases as T^4 , where T is the mean emission temperature. The Planck functions at temperatures: 50, 100, 150, 200, 250, and 300 K have also been plotted for reference. Radiance units are $\text{W cm}^{-2} \text{ sr}^{-1} (\text{cm}^{-1})^{-1}$.

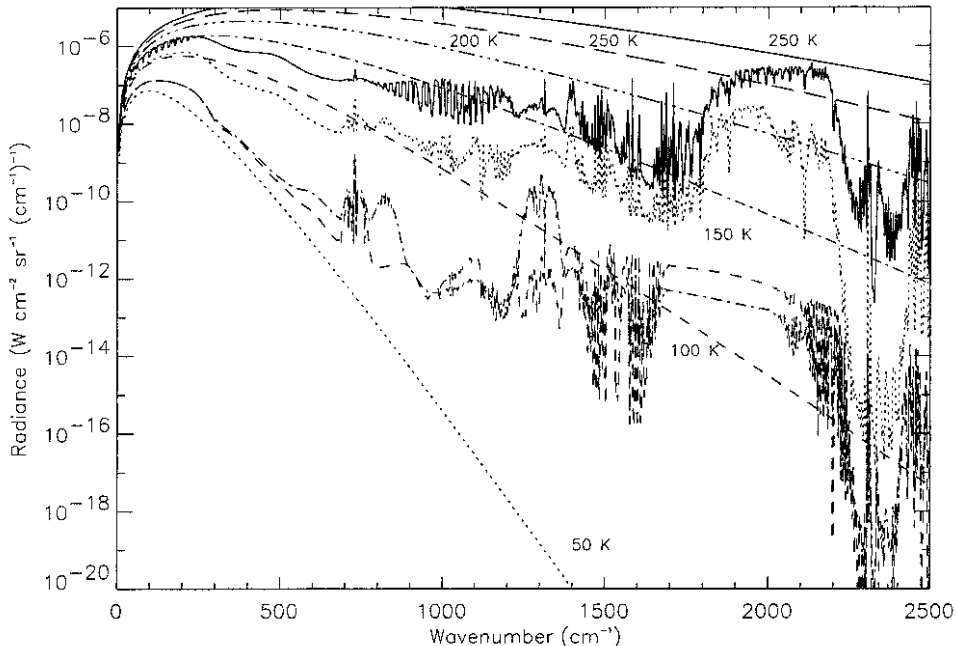


Figure 6.17 Calculated thermal emission spectra of the giant planets on a log scale. The rapid decrease in brightness, due to the decrease in mean thermal temperature is clearly seen, as is the disappearance of spectral features due to ammonia and water vapour as we go outwards through the Solar System. Absorption of methane is clearly visible for all planets as is the emission of hydrocarbons such as ethane and acetylene from the stratospheres. The Planck functions at temperatures: 50, 100, 150, 200, 250, and 300 K have also been plotted for reference. The spectra of Jupiter and Saturn have been calculated for cloud-free conditions while deep ‘H₂S’ clouds have been assumed for Uranus and Neptune with optical depth of unity at ~ 3 bar.

smaller than for the gas giants as can be seen by the vertical scales of Figure 6.16 and by the steady diminishment of 5-μm and mid-IR radiance as we go from Jupiter to Neptune. Hence it can immediately be seen that it is very much more difficult to measure the thermal emission spectra of the ice giants than the gas giants since the radiance levels are so much lower. An alternative way of comparing the thermal spectra of the giant planets is to instead plot the log of the radiance as shown in Figure 6.17, or to plot their *brightness temperature* spectra as has been done in Figure 6.18. The brightness temperature is defined as the temperature of a black body which emits the same radiance as that observed at a given wavenumber.

Jupiter

To interpret the spectrum shown in Figure 6.16, it is useful to consider also the peak levels of the weighting functions for this planet shown earlier in Figure 6.9. Starting

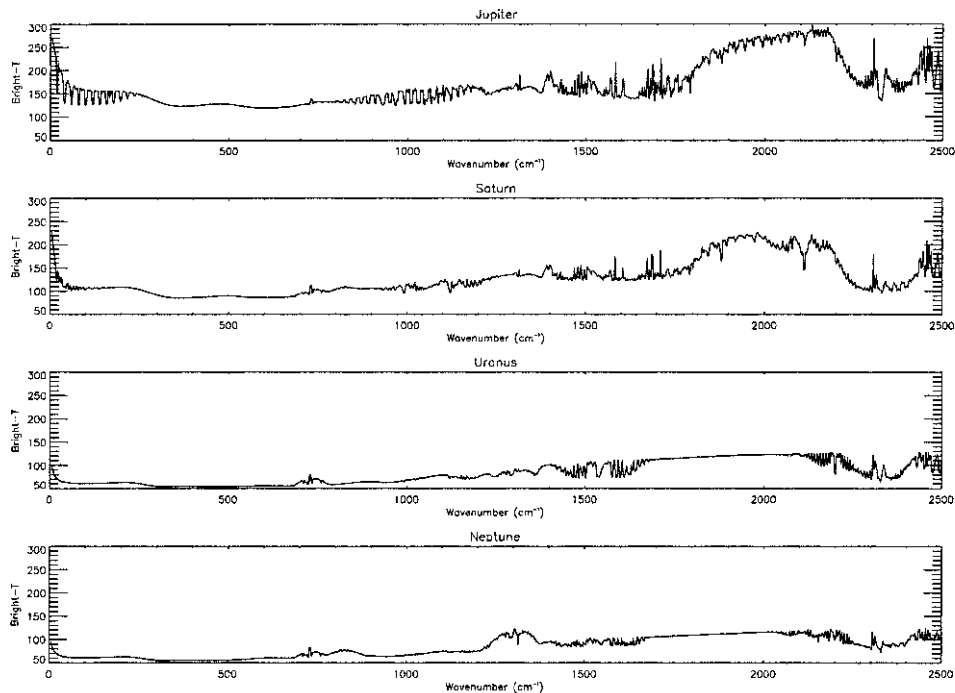


Figure 6.18 Calculated brightness temperature spectra of the giant planets.

in the far-IR, the weighting function at $\sim 5\text{ cm}^{-1}$ peaks fairly deeply, but the Planck function for all temperatures tends to zero in this region leading to a small radiance. As the wavenumber increases, the opacity increases due to H₂-H₂ and H₂-He CIA, and also rotational absorption lines of mainly NH₃, and to a lesser extent PH₃ and CH₄. Although the weighting functions move upwards to cooler levels, the Planck function increases rapidly and thus the spectrum peaks at $\sim 210\text{ cm}^{-1}$. Between 220 and 600 cm⁻¹ the spectrum is smooth and arises due to H₂-H₂ and H₂-He CIA only. As the weighting function continues to drift slowly upwards, the decreasing temperature and the decay of the Planck function causes the radiance to decrease. Between 600 and 700 cm⁻¹ the weighting function starts to drift downwards again until the 729 cm⁻¹ vibration-rotation band of stratospheric acetylene appears, which in the central Q-branch, introduces a second peak to the weighting function at $\sim 1 \times 10^{-5}$ bar, not shown in Figure 6.9. Since the stratosphere is warm at this altitude, the acetylene Q-branch introduces the characteristic ‘spike’ seen in the spectrum at this wavelength. A perpendicular band of ethane next appears at $\sim 820\text{ cm}^{-1}$, although this is more apparent at higher zenith angles. The spectrum between 800 and 1,200 cm⁻¹ is mostly dominated by vibration-rotation transitions of upper tropospheric ammonia, and to a lesser extent phosphine and CH₃D. Between 1,200 and 1,400 cm⁻¹ there appears one of the main vibration-rotation

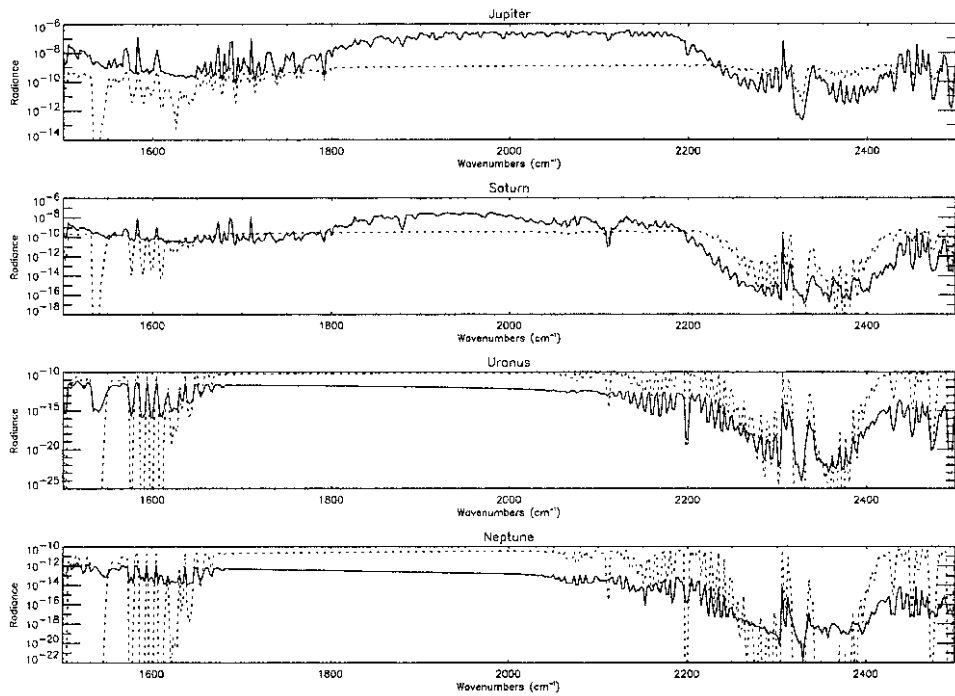


Figure 6.19 Overlap spectral regions between thermal emission (solid) and reflected sunlight (dotted) for the giant planets. Calculated reflection is from a Lambertian layer with albedo 0.1 placed at 1 bar for Jupiter and Saturn, and 3 bar for Uranus and Neptune. Radiance units are again $\text{W cm}^{-2} \text{sr}^{-1} (\text{cm}^{-1})^{-1}$.

bands of methane. The high absorption of methane pushes the weighting function high into the stratosphere and the characteristic P-, Q-, and R-branch system is visible. The spectrum between $1,400$ and $1,800\text{ cm}^{-1}$ is composed of ammonia, CH_3D , and weaker bands of methane. The strength of these absorptions decreases rapidly after $1,800\text{ cm}^{-1}$ and thus between $1,800$ and $2,100\text{ cm}^{-1}$ the weighting functions peak deep in the atmosphere, providing there are no clouds. The absorption features seen in this 5- μm window arise from deep H_2O , NH_3 , CH_3D , CO , AsH_3 , GeH_4 , and PH_3 absorptions and thus allow for abundance determinations of these molecules in the 5–8 bar pressure region. Above 2100 cm^{-1} , a strong vibration–rotation band of phosphine appears which pushes the weighting function back up to approximately the 1 bar level. At higher wavenumbers, the spectrum becomes dominated by reflected sunlight on the day side. There is a small contribution of reflected sunlight in the 5- μm window, although this is usually negligible provided that the clouds are not too thick as can be seen in Figure 6.19 where the thermal emission from $1,500$ – $2,500\text{ cm}^{-1}$ has been overplotted with the calculated reflected solar radiance from a cloud layer at 1 bar with albedo 0.1.

Saturn

The thermal emission spectrum of Saturn is in many respects rather similar to that of Jupiter but of significantly lower overall brightness. Spectral features are formed from similar gas absorptions, with the main differences in the observed spectra coming from the lower mean atmospheric temperatures and the greater scale height of Saturn's atmosphere. Between 0 and 600 cm^{-1} , the overall shape of the spectrum is similar to that of Jupiter's with the exception that the low abundance of ammonia above 1 bar leads to greatly reduced rotational absorption lines at wavenumbers less than 200 cm^{-1} . Stratospheric emission from acetylene is again seen at 729 cm^{-1} , together with the clear appearance of the ethane perpendicular band at 820 cm^{-1} . The absorption bands of ammonia between 750 and $1,100\text{ cm}^{-1}$ are much less strong, and instead the absorption features of phosphine are more prominent in this region. The strong vibration–rotation band of methane is again seen between $1,200$ and $1,400\text{ cm}^{-1}$ and the radiation in this region again comes mostly from the stratosphere. Between $1,400$ and $1,800\text{ cm}^{-1}$, the spectrum looks similar to Jupiter's (but colder) until we arrive at the $5\text{-}\mu\text{m}$ window. The weighting functions here peak at slightly lower pressures than for Jupiter, both because of the extra opacity introduced by significantly supersolar abundances of gases like phosphine and ammonia, and also because of Saturn's greater scale height. Combined with Saturn's lower tropospheric temperatures, the thermal emission in the $5\text{-}\mu\text{m}$ window is substantially smaller than that of Jupiter. In fact, the thermal emission is so low that reflected sunlight is found to be a substantial component in the $5\text{-}\mu\text{m}$ spectrum at longer wavenumbers (Figure 6.19) and thus must be carefully modelled for day side observations. At wavenumbers greater than $2,100\text{ cm}^{-1}$, the strong absorption of PH_3 pushes the weighting function back up into the upper troposphere and the thermal emission drops to levels insignificant compared to reflected sunlight.

Uranus and Neptune

The thermal emission spectra of Uranus and Neptune are both very similar and both very weak. The spectra are formed in the same way as for Jupiter and Saturn, but since the atmospheres of these planets are so cold, the power of the spectra is extremely low which makes them experimentally very difficult to measure. Between 200 and 400 cm^{-1} , the spectrum has been fairly well measured by the IRIS instrument on *Voyager 2*, and has the appearance shown in Figures 6.16 and 6.17. Ground-based microwave observations indicate very low abundances of ammonia in the observable troposphere and thus the rotational absorption lines of this gas are predicted to be completely lacking at all wavenumbers as shown. The acetylene spike at 729 cm^{-1} has been detected on both planets, but ethane has only been positively identified in Neptune's atmosphere. This may be understood from Figure 6.17 in that although ethane has been included with a peak volume mixing ratio (v.m.r.) of 3×10^{-6} at 0.1 mbar (as modelled by Encrenaz *et al.*, 1998) its spectral features are not apparent due to the lower stratospheric temperatures of Uranus compared to Neptune. By contrast, although the estimated ethane abundance in Neptune's stratosphere is lower at 1.5×10^{-6} (Bézard and Romani,

1991), the higher stratospheric temperatures make the ethane band clearly visible. A similar effect can be seen in the centre of the methane vibration–rotation band between $1,200\text{ cm}^{-1}$ and $1,400\text{ cm}^{-1}$, where Neptune shows enhanced stratospheric emission compared to the neighbouring tropospheric emissions, while Uranus shows little contrast. While there are expected to be no ammonia absorption features between 750 and $1,200\text{ cm}^{-1}$ as shown, but there may conceivably be phosphine absorption features observable. We have assumed a solar abundance in these calculations, although to date the abundance of phosphine in both planets' atmospheres has not been well measured. Additional absorption features in this region are due to CH_3D and $\text{H}_2\text{--H}_2$, $\text{H}_2\text{--He CIA}$. In the range between $1,400$ and $1,800\text{ cm}^{-1}$, absorption features of CH_3D and CH_4 dominate, but then the absorption becomes due effectively to $\text{H}_2\text{--H}_2$, $\text{H}_2\text{--He CIA}$ alone since the abundance of the strong 5- μm absorbing gases, water vapour, and ammonia, is estimated to be zero and the abundance of other 5- μm absorbing gases is unknown (although we have assumed solar abundances of GeH_4 and AsH_3 in addition to PH_3). Hence the calculated 5- μm spectra appear rather smooth. Unfortunately the real 5- μm spectra of these planets is observationally not at all well known due to the very low power of the emitted radiance in this spectral region. However, the spectra from regions on the sunlit side of these planets are expected to be dominated by reflected sunlight, as can be seen in Figure 6.19, where the reflection from a Lambertian layer placed at 3 bar and with an albedo of 0.1 has also been plotted. To date only one ground-based measurement of Uranus' 5- μm spectrum has been made by Orton and Kaminski (1989). The 5- μm spectrum was found to be very different in character to that of Jupiter or Saturn but the data were not of sufficient accuracy to allow unambiguous conclusions of composition and cloud structure. The 5- μm spectrum of Neptune has not been measured at all.

6.7.4 Microwave spectra

Although the Planck function tends to zero at longer wavelengths, the thermal emission signal is measurable with ground-based microwave telescopes and has proved extremely useful since the opacity of any aerosols, and most of the atmospheric gases becomes small, allowing the weighting function to probe down to almost 100 bar in some cases. For Jupiter the spectrum is complicated by synchrotron emission radiated by relativistic particles trapped in Jupiter's strong magnetic field which dominates at decametric wavelengths. The wavelength where thermal emission from the atmosphere and synchrotron emission from the radiation belts are equal is approximately 7 cm (Berge and Gulkis, 1976). Fortunately the thermal and synchrotron components of Jupiter's microwave spectrum have different polarization, and other properties which make them separable. Synchrotron emission from the radiation belts of the other giant planets is negligible.

The microwave spectra of all four giant planets are well-reviewed by de Pater and Massie (1985), de Pater and Mitchell (1993), and de Pater and Lissauer (2001) and the mean spectral observations are shown in Figure 6.20. The main gaseous absorber in this region is ammonia which has an inversion band at 1.3 cm, and the

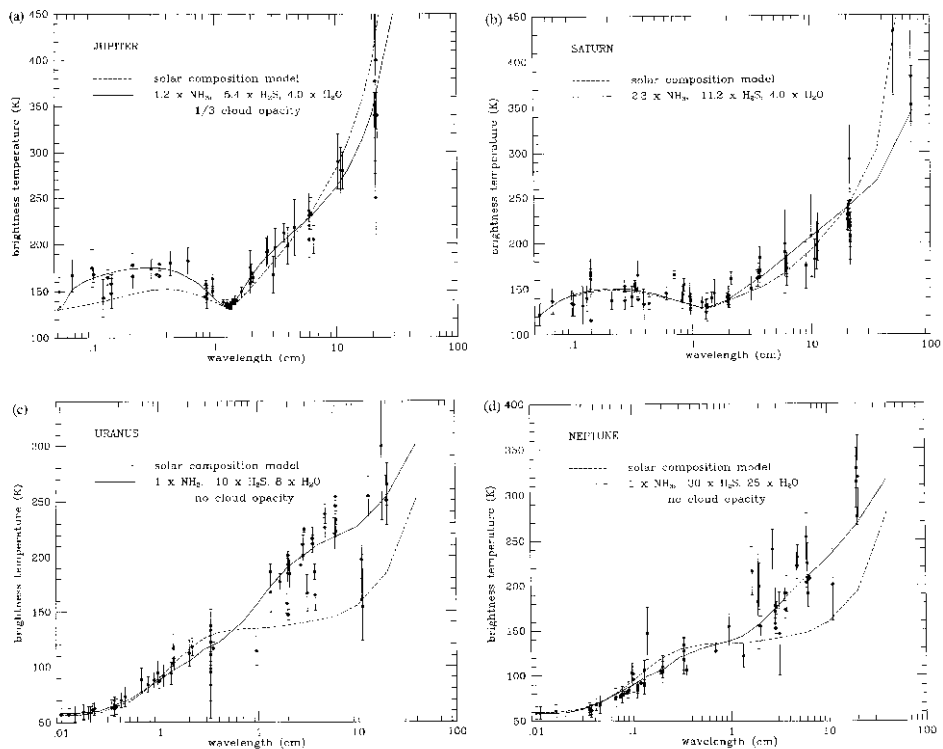


Figure 6.20 Microwave and radio-emission disc-averaged spectra of the giant planets (from de Pater and Lissauer, 2001; de Pater and Mitchell, 1993).

Courtesy of Cambridge University Press.

absorption of ammonia is clearly visible in ground-based microwave spectra of Jupiter and Saturn. In fact, since Jupiter subtends a relatively large angle at the Earth, microwave telescopes have been able to map the abundance of ammonia across the planet and it is found that belts are regions of depleted ammonia and zones regions of enhanced ammonia (de Pater, 1986; de Pater and Dickel, 1986) (Figure 6.21) as is expected from the generally accepted view that zones are regions of upwelling, moist air, and belts are regions of downwelling, desiccated air. By contrast the microwave spectra of Uranus and Neptune are completely lacking in the ammonia absorption feature indicating depletion of this species at great depth. Carbon monoxide has been detected at these wavelengths for both Uranus and Neptune, whilst HCN has been detected on Neptune.

6.8 APPENDIX

6.8.1 Planck function

The Planck function defines the radiance emitted by a surface of unit emissivity as a

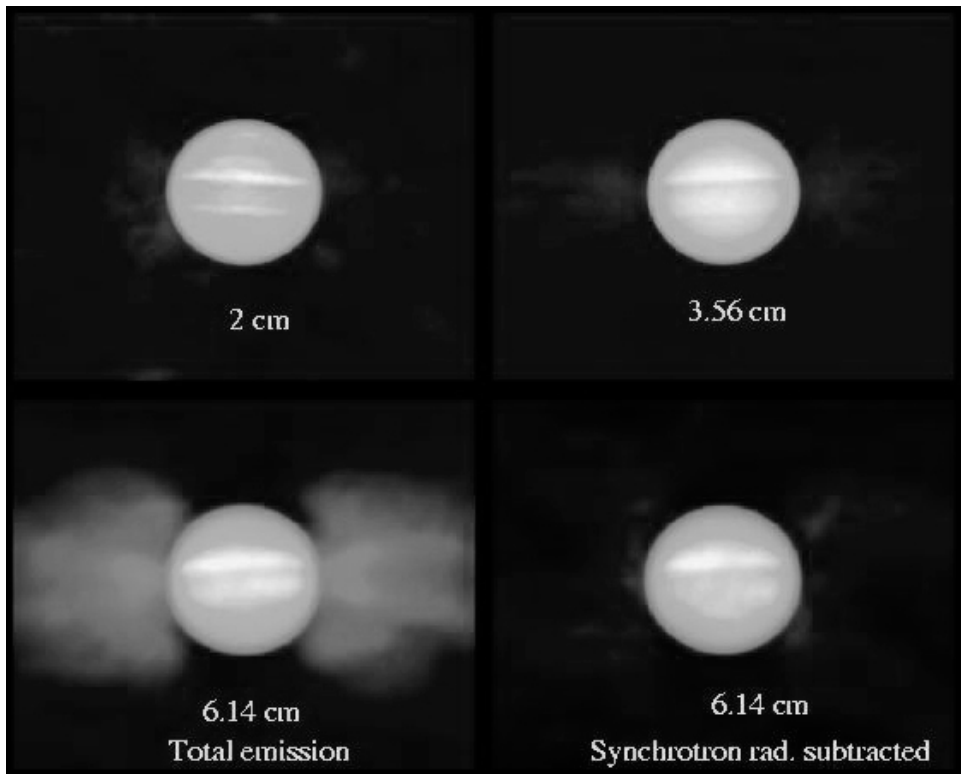


Figure 6.21 Appearance of Jupiter at 2.0, 3.56, and 6.14 cm as observed by the VLA (courtesy of Imke de Pater). The increasing contribution of synchrotron emission from the radiation belts with wavelength is clear.

function of wavelength. There are two forms that are commonly used in IR spectroscopy depending on the unit of wavelength.

In terms of wavenumbers (cm^{-1}), the Planck function is defined as

$$B(\tilde{\nu}, T) d\tilde{\nu} = \frac{1.1911 \times 10^{-12} \tilde{\nu}^3}{\exp(1.439\tilde{\nu}/T) - 1} d\tilde{\nu} \quad (\text{A1})$$

where the units of $B(\tilde{\nu}, T)$ are $\text{W cm}^{-2} \text{sr}^{-1} (\text{cm}^{-1})^{-1}$. In terms of wavelength (μm), the Planck function is defined as

$$B(\lambda_{\mu\text{m}}, T) d\lambda_{\mu\text{m}} = \frac{1.1911 \times 10^4}{(\exp(14,390/\lambda T) - 1)\lambda_{\mu\text{m}}^5} d\lambda_{\mu\text{m}} \quad (\text{A2})$$

where the units are $\text{W cm}^{-2} \text{sr}^{-1} \mu\text{m}^{-1}$.

6.9 REFERENCES

- Allison, M., R. F. Beebe, B. J. Conrath, D. P. Hinson, and A. P. Ingersoll (1991) Uranus atmospheric dynamics and circulation. *Uranus* (edited by J. Bergstrahl, E. D. Miner and M. S. Matthews). University of Arizona Press, Tucson, AZ.
- Andrews, D. G. (2000) *An Introduction to Atmospheric Physics*. Cambridge University Press.
- Berge, G. L. and S. Gulkis (1976) Earth-based radio observations of Jupiter: Millimeter to meter wavelengths. *Jupiter* (edited by T. Gehrels). University of Arizona Press, Tucson, AZ.
- Bézard, B. and P. Romani (1991) Hydrocarbons in Neptune's stratosphere from Voyager infrared observations. *J. Geophys. Res.*, **96**, 18961–18975.
- Birnbaum, G., A. Borysow, and G. S. Orton (1996) Collision-induced absorption of H₂–H₂ and H₂–He in the rotational and fundamental bands for planetary applications. *Icarus*, **123**, 4–22.
- Conrath, B. J., P. J. Gierasch, and S. S. Leroy (1990) Temperature and circulation in the stratosphere of the Outer planets. *Icarus*, **83**, 255–281.
- de Pater, I. and J. J. Lissauer (2001) *Planetary Sciences*. Cambridge University Press, Cambridge, UK.
- de Pater, I. and D. L. Mitchell (1993) Radio observations of the planets: The importance of laboratory measurements. *J. Geophys. Res.*, **98**, 5471–5490.
- de Pater, I. (1986) Jupiter's zone-belt structure at radio wavelengths. *Icarus*, **68**, 344–365.
- de Pater, I. and J. R. Dickel (1986) Jupiter's zone-belt structure at radio wavelengths. I: Observations. *Astrophys. J.*, **308**, 459–471.
- de Pater, I. and S. Massie (1985) Models of the millimeter–centimeter spectra of the giant planets. *Icarus*, **62**, 143–171.
- Encrenaz, Th., H. Feuchtgruber, S. K. Atreya, B. Bézard, E. Lellouch, J. Bishop, S. Edgington, Th. de Graauw, M. Griffin, and M. F. Kessler (1998) ISO observations of Uranus: The stratospheric distribution of C₂H₂ and the eddy diffusion coefficient. *Astron. Astrophys.*, **333**, L43–L46.
- Fink, U. and H. P. Larson (1979) The infrared spectra of Uranus, Neptune, and Titan from 0.8 to 2.5 microns. *Astrophys. J.*, **233**, 1021–1040.
- Goody, R. M. and Y. L. Yung (1989) *Atmospheric Radiation. Theoretical Basis* (2nd Edition). Oxford University Press, Oxford, UK.
- Goody, R. M., R. West, L. Chen, and D. Crisp (1989) The Correlated-*k* method for radiation calculations in nonhomogeneous atmospheres. *J. Quant. Spectrosc. Rad. Trans.*, **42**, 539–550.
- Hanel, R. A., B. J. Conrath, D. E. Jennings, and R. E. Samuelson (1992) *Exploration of the Solar System by Infrared Remote Sensing*. Cambridge University Press, Cambridge, UK.
- Hansen, J. E. and L. D. Travis (1974) Light scattering in planetary atmospheres. *Space Sci. Rev.*, **16**, 527–610.
- Hecht, E. and A. Zajac (1974) *Optics*. Addison-Wesley, Reading, MA.
- Herzberg, G. (1945) *Molecular Spectra and Molecular Structure II. Infrared and Raman Spectra of Polyatomic Molecules*. Van Nostrand Reinhold Company, New York.
- Houghton, J. T. (1986) *The Physics of Atmospheres* (2nd Edition). Cambridge University Press, Cambridge, UK.
- Husson, N., B. Bonnet, N. A. Scott, and A. Chedin (1992) Management and study of spectroscopic information: The GEISA program. *J. Quant. Spectrosc. Rad. Trans.*, **48**, 509–518.

- Husson, N., B. Bonnet, A. Chedin, N. A. Scott, A. A. Chursin, V. F. Golovko, and V. G. Tyuterev (1994) The GEISA data bank in 1993: A PC/AT compatible computer's version. *J. Quant. Spectrosc. Rad. Trans.*, **52**, 425–438.
- Irwin, P. G. J., S. B. Calcutt, F. W. Taylor, and A. L. Weir (1996) Calculated k coefficients for hydrogen- and self-broadened methane in the range 2000–9500 cm $^{-1}$ from exponential sum fitting to band modelled spectra. *J. Geophys. Res.*, **101**, 26137–26154.
- Irwin, P. G. J., A. L. Weir, S. E. Smith, F. W. Taylor, A. L. Lambert, S. B. Calcutt, P. J. Cameron-Smith, R. W. Carlson, K. Baines, G. S. Orton, P. Drossart, T. Encrenaz, and M. Roos-Serote (1998) Cloud structure and atmospheric composition of Jupiter retrieved from Galileo near-infrared mapping spectrometer real-time spectra. *J. Geophys. Res.*, **103**, 23001–23021.
- Karkoschka, E. (1994) Spectrophotometry of the Jovian planets and Titan at 300- to 1000-nm wavelength: The methane spectrum. *Icarus*, **111**, 174–192.
- Karkoschka, E. (1998) Methane, ammonia, and temperature measurements of the Jovian planets and Titan from CCD-spectrophotometry. *Icarus*, **133**, 134–146.
- Kerola, D. X., H. P. Larson, and M. G. Tomasko (1997) Analysis of the near-IR spectrum of Saturn: A comprehensive radiative transfer model of its middle and upper troposphere. *Icarus*, **127**, 190–212.
- Lacis, A. A. and V. Oinas (1991) A description of the correlated- k distribution method for modelling nongray gaseous absorption, thermal emission, and multiple scattering in vertically inhomogeneous atmospheres. *J. Geophys. Res.*, **96**, 9027–9063.
- Lopez-Puertas, M. and F. W. Taylor (2001) *Non-LTE Radiative Transfer in the Atmosphere* (3rd Edition). World Scientific, Singapore.
- Minnaert, M. (1941) The reciprocity principle in lunar photometry. *Astrophys. J.*, **93**, 403–410.
- Orton, G. S. and C. D. Kaminski (1989) An exploratory 5-micron spectrum of Uranus. *Icarus*, **77**, 109–117.
- Plass, G. N., G. W. Kattawar, and F. E. Catchings (1973) Matrix operator method of radiative transfer. 1: Rayleigh scattering. *Appl. Opt.*, **12**, 314–329.
- Rae, A. I. M. (1985) *Quantum Mechanics*. Adam Hilger, Bristol.
- Rothman, L. S., C. P. Rinsland, A. Goldman, S. T. Massie, D. P. Edwards, J-M. Flaud, A. Perrin, C. Camy-Peyret, V. Dana, J-Y. Mandin, J. Schroeder, A. McCann, R. R. Gamache, R. B. Wattson, K. Yoshino, K. Chance, K. Jucks, L. R. Brown, V. Nemtchinov and P. Varanasi (1998) The HITRAN molecular spectroscopic database and HAWKS (HITRAN atmospheric workstation): 1996 Edition. *J. Quant. Spectrosc. Rad. Trans.*, **60**, 665–710.
- Sromovsky, L. A., P. M. Fry, K. H. Baines, and T. E. Dowling (2001) Coordinated 1996 HST and IRTF imaging of Neptune and Triton. II: Implications of disc-integrated photometry. *Icarus*, **149**, 435–458.

6.10 BIBLIOGRAPHY

- Andrews, D. G. (2000) *An Introduction to Atmospheric Physics*. Cambridge University Press.
- Goody, R. M. and Y. L. Yung (1989) *Atmospheric Radiation. Theoretical Basis* (2nd Edition). Oxford University Press, Oxford, UK.
- Hanel, R. A., B. J. Conrath, D. E. Jennings, and R. E. Samuelson (1992) *Exploration of the Solar System by Infrared Remote Sensing*. Cambridge University Press, Cambridge, UK.

- Herzberg, G. (1945) *Molecular Spectra and Molecular Structure II. Infrared and Raman Spectra of Polyatomic Molecules*. Van Nostrand Reinhold Company, New York.
- Hollas, J. M. (1992) *Modern Spectroscopy* (2nd edition). John Wiley & Sons, New York.
- Houghton, J. T. (1986) *The Physics of Atmospheres* (2nd Edition). Cambridge University Press, Cambridge, UK.

7

Sources of remotely sensed data on the giant planets

7.1 INTRODUCTION

In the previous chapter we saw how the ultraviolet (UV), visible, infrared (IR) and microwave spectra of the giant planets are formed, and how the absorption features of different gases (and theoretically aerosols) are visible in these spectra. Clearly much can be learnt about the atmospheres from observing the spectra of these planets and in this chapter we will review the measurements that have been made to date and how they may be used.

In this chapter we will review some of the technical details of measuring the UV–microwave spectra of the planets and in Section 7.2 we will briefly review how such radiation is detected and how spectra are measured. Prior to 1973, the only measurements of the giant planets that were available were telescope observations from the surface of the Earth in visible, IR, and microwave wavelengths. Such observations have the obvious attraction that they are relatively easy to do, and have a number of other advantages, although there are drawbacks as we shall see in Section 7.3. We shall also see that the technology of detection and data processing has improved dramatically over the years and thus ground-based observations continue to be a rich source of information on the giant planets to this day. In Sections 7.4 and 7.5 we will look at some of the major ground and airborne visible/IR telescope facilities around the world that are engaged in outer planet observations, and in Section 7.6 will look at ground-based microwave observations. Many of the problems encountered by ground-based visible/IR telescopes are negated by placing the telescope in orbit around the Earth and thus in Section 7.7 we will look at recent space telescopes such as the Hubble Space Telescope (HST) and the Infrared Space Observatory (ISO).

In 1973, the first spacecraft mission arrived at Jupiter and since then a number of spacecraft have flown past the giant planets, and more recently have been placed in orbit to conduct extended campaigns. These missions have enormous advantages

over ground- and space-based telescopes but are of course immensely expensive and difficult to achieve. In Section 7.8 we will review the flyby missions of the giant planets and then in Section 7.9 we will consider the orbiting missions of *Galileo* and *Cassini/Huygens*. Finally we will discuss retrieval methods in Section 7.10 where we will see how remotely sensed observations are actually used to infer atmospheric properties.

7.2 MEASUREMENT OF VISIBLE, IR, AND MICROWAVE SPECTRA

Before going on to look at the current sources of spectral data on the giant planets and how these data are reduced to infer atmospheric properties, we will briefly look at how the spectra of these planets are actually measured from visible through to microwave wavelengths.

7.2.1 Detection of IR radiation

For all remote sensing instruments, the radiance incident must first be collected and focused onto detecting elements in order to record a signal. In any detection system there are sources of noise, and the design of remote sensing instruments aims to minimize these in order to achieve a high signal-to-noise ratio. Suppose that radiance B ($\text{W m}^{-2} \text{ sr}^{-1} (\text{cm}^{-1})^{-1}$) is incident upon a remote sensing system. The power P (W) incident on the detector is given by

$$P = A\Omega \int F(\tilde{\nu})B(\tilde{\nu}) d\tilde{\nu} + E \quad (7.1)$$

where $F(\tilde{\nu})$ is the spectral transmission of the optical system and the $A\Omega$ product is given either by the area of the entrance aperture multiplied by the solid angle of the field of view (FOV) observed by the instrument, or equivalently by the area of the detector multiplied by the solid angle of the cone of radiation condensed onto the detector by the instrument optics. The quantity E in Equation 7.1 refers to thermal radiation self-emitted by the telescope and optics which is incident on the detector. The signal detected by the instrument (e.g., volts or amps) is then given by

$$S = A\Omega \int F(\tilde{\nu})R(\tilde{\nu}, T)B(\tilde{\nu}) d\tilde{\nu} + E' \quad (7.2)$$

where $R(\tilde{\nu}, T)$ is the *Spectral Responsivity* of the detector, and has units of V/W or A/W. In the detection and pre-amplification stages of instruments there are numerous sources of noise such as Johnson noise (or voltage noise, which appears across resistances), Shot noise (or current noise, arising from the fact that a ‘steady current’ is actually composed of a stream of individual electrons), noise arising from the incident radiation itself and radiation from the optical elements if we are considering the thermal-IR (Hanel *et al.*, 1992). The Shot noise associated with a current I_0 is given by $I_S^2 = 2eI_0 \Delta f$, where Δf is the bandwidth, and e is the electron charge, and is clearly minimized by limiting the currents in the detection stages of amplifica-

tion. Johnson noise however, given by $V_f^2 = 4k_B T R \Delta f$, where R is the resistance and k_B is the Boltzmann constant, depends on the temperature, as does the noise of radiation thermally emitted by the optics and filters. Hence to maximize the signal-to-noise ratio of the detected radiance, especially when working in the thermal-IR, the detectors, filters, and as much of the telescope optical system as is possible must be cooled to low temperatures. Adding all sources of noise together, a common figure of merit of the instrument is the Noise Equivalent Power (NEP) which is defined as the power of incident radiation which when viewed in a 1 Hz bandwidth gives a signal equivalent to all the sources of noise. Another very useful figure of merit for comparing the sensitivities of a detector is D^* which is defined as

$$D^* = \frac{(A \Delta f)^{1/2}}{\text{NEP}} \quad (7.3)$$

where A is the area of the detector. Highly sensitive detectors have a high D^* . Finally, for thermal-IR observations, all the sources of noise may be analysed in terms of their Noise Equivalent Radiance (NER) defined as the incident spectral radiance which gives a signal-to-noise ratio of unity.

There are two main ways of detecting radiation: (1) photon detectors which detect individual photons; and (2) thermal detectors, or *bolometers*, which detect the temperature rise of elements exposed to radiation. Examples of photon detectors are: photovoltaic cells where absorbed photons promote the production of an electron-hole pair in a *p–n* junction and thus produce a transient voltage; and photoconductive detectors where absorbed photons again promote the production of an electron-hole pair in an element of semiconductor material which temporarily alters its conductivity. Examples of thermal conductors include: thermopiles which are basically a stacked array of bimetallic junctions which produce a voltage dependent on their temperature via the thermocouple effect, and pyroelectric detectors which use a dielectric material with a temperature-sensitive dipole moment sandwiched between the plates of a capacitor. Absorption of thermal radiation modifies the permittivity and thus the capacitance. The choice of detector depends on many things: cost, required signal-to-noise, and response time. The reader is referred to more specialized texts for further information (Hanel *et al.*, 1992; Houghton and Smith, 1966; Smith *et al.*, 1968).

7.2.2 Radiometers/photometers

Many remote sensing instruments simply record the incident radiation received within a bandwidth defined by a set of spectral filters, and most imaging cameras operate in this way. Photometers record accurately the flux level of visible or near-IR light within narrow spectral channels, while radiometers perform a similar function at thermal-IR wavelengths. Such an instrument design is cheap, reliable, and ideally suited to imaging although it does require *a priori* knowledge of the planetary spectrum in order to place the channel filters at suitable wavelengths.

Where the planetary spectrum is less well known, spectrometers must be used of which in the visible/IR there are two main types: grating spectrometers and

interferometers. For really high-resolution visible/IR work, Fabry–Pérot interferometers may also be used, usually in conjunction with a grating spectrometer which limits the range of wavelengths that are passed through the Fabry–Pérot.

7.2.3 Grating spectrometers

Grating spectrometers are often used for IR spectroscopy, particularly at near-IR wavelengths and have the advantage of relative simplicity. Light is collected from the planet via a telescope system and then the collimated light is used to illuminate a reflecting diffraction grating which disperses a spectrum onto the focal plane (Figure 7.1). The grating is ‘blazed’ to maximize the throughput at the central wavelength of the region of interest. In its simplest form, there is a single IR detector at the focal plane, and the spectrum is measured by recording the detector signal as the grating is scanned through a small angle. Since IR detectors are usually sensitive to a wide range of wavelengths, an ‘order-sorting’ filter must in practice also be added to limit the range of wavelengths that can be detected so that the spectrometer only operates in the spectral order desired.

While such a design is simple, only a small range of wavelengths are recorded at a time, and so much of the radiation that is dispersed by the grating is wasted. Also it takes a certain length of time to scan the grating through the angular range required to build up a spectrum, and this can be particularly problematic from an observational point of view when the instrument is observing a planet whose spectrum alters significantly with position. During the time the grating is scanned, the spectrometer

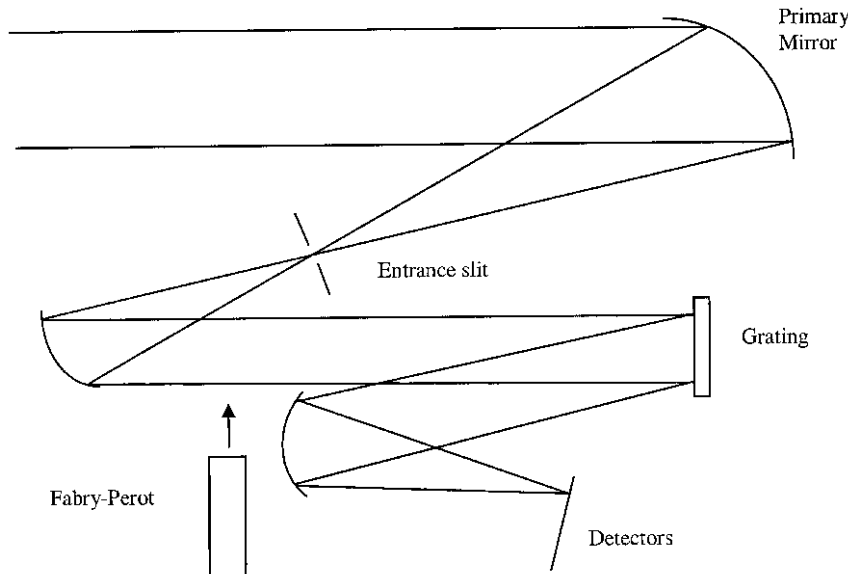


Figure 7.1 Grating spectrometer layout.

may be looking at a very different region at the end of the scan to that observed at the beginning, and thus the recorded spectrum may be very hard to interpret. An alternative approach, sometimes called a spectrograph, is to have a whole array of closely spaced, contiguous detectors in the focal plane, each recording different wavelengths, and thus leave the grating angle fixed. While such instruments are much harder, and more expensive to build, a spectrum is recorded much more quickly, and if the region of the planet observed should vary, all parts of the recorded spectrum are equally affected. An intermediate approach is to use fewer detectors, spaced further apart on the focal plane and then scan the grating over a short range, such that the final spectrum is built up from a number of sub-spectra recorded by each individual detector. This design is easier to build and records a spectrum in a reasonably short space of time, but can suffer from variable scene problems which reveal themselves as mismatches between the individual detector sub-spectra where they overlap.

Clearly for planetary work, it is of great interest to record the spectrum at a number of positions in order to build up a multispectral image. This can be achieved by scanning the instrument in both ‘x’ and ‘y’ directions, but in more recent years it has been possible to construct imaging spectrographs where a two-dimensional array of detectors is placed in the focal plane, and thus multiple spectra are simultaneously recorded from a small range of viewing angles perpendicular to the grating dispersion direction. The instrument then need only be scanned in one direction (the grating dispersion direction), not two, in order to construct a multispectral image.

The spectral resolution of a grating spectrometer is fixed by the size of the entrance aperture to the collimator, the dispersion of the grating, and by the physical dimensions of the detectors. For higher resolution spectroscopy, some instrument designs allow for a Fabry-Pérot interferometer to enter the beam as indicated in Figure 7.1. This allows very high-resolution spectrometry to be conducted over a small spectral range with a resolving power ($\lambda/\Delta\lambda$) of the order of 10,000.

7.2.4 Michelson interferometers

While grating spectrometers perform spectroscopy by ‘division of wavefront’ interferometers are also often used at mid- to far-IR wavelengths which operate by division of amplitude. The simplest example is a Michelson interferometer where light is split into two beams by a beam-splitting mirror and then recombined onto a detector as in Figure 7.2. For monochromatic light of intensity I_0 , the intensity at the detector varies with scanning mirror position x as (Hecht and Zajac, 1974)

$$I(\Delta) = \frac{I_0}{2}(1 + \cos k\Delta) \quad (7.4)$$

where $k = 2\pi/\lambda$, and $\Delta = 2x$. For incident light with a spread of wavelengths, and spectral density $I(k) dk$, Equation 7.4 must be modified to

$$I(\Delta, k) dk = \frac{I(k)}{2}(1 + \cos k\Delta) dk \quad (7.5)$$

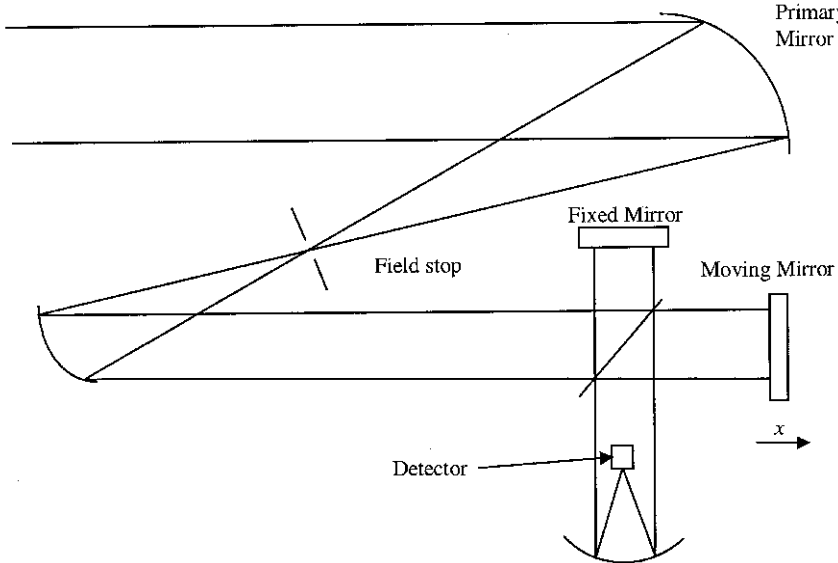


Figure 7.2 Michelson interferometer layout.

and since IR detectors are typically sensitive to a wide range of wave numbers $\Delta\tilde{\nu}$, the detected intensity must be integrated over all wavelengths in this range:

$$I(\Delta) = \frac{1}{2} \int_{\Delta\tilde{\nu}} I(k)(1 + \cos k\Delta) dk = \frac{I_0}{2} + \frac{1}{2} \int_{\Delta\tilde{\nu}} I(k) \cos k\Delta dk. \quad (7.6)$$

Hence in the limit that $\Delta\tilde{\nu}$ is large it can be seen that the intensity detected is equal to a mean value plus the Fourier–cosine transform of the incident spectrum. The signal $I(\Delta)$, recorded as a function of mirror position, is called an *interferogram* and the incident spectrum may then theoretically be perfectly reconstructed by the inverse Fourier–cosine transform as

$$I(k) = \frac{2}{\pi} \int_0^\infty [I(\Delta) - I_0/2] \cos k\Delta d\Delta. \quad (7.7)$$

Such instruments are thus often referred to as Fourier-Transform Spectrometers (FTS). Consider the case where the interferometer views monochromatic light of wavevector k_0 . From Equation 7.4, the resulting interferogram is a pure cosine wave and substituting this into Equation 7.7 we find

$$I(k) = \frac{2}{\pi} \int_0^\infty (I_0/2) \cos k_0 \Delta \cos k\Delta d\Delta \equiv I_0 \delta(k - k_0) \quad (7.8)$$

where $\delta(k - k_0)$ is the Kronecker-delta function, and thus the reconstructed spectrum is found to be purely monochromatic as expected. However in reality, the path length $2x$ may be scanned up to a maximum value of Δ_m , and this limits the spectral resolution of the interferometer. If we limit Δ to Δ_m in Equation 7.8 then

the reconstructed spectrum is no longer monochromatic but instead has finite width since

$$\begin{aligned}
 I(k) &= \frac{2}{\pi} \int_0^{\Delta_m} (I_0/2) \cos k_0 \cos k \Delta d\Delta \\
 &= \frac{I_0}{\pi} \int_0^{\Delta_m} \frac{1}{2} [\cos (k_0 + k) \Delta + \cos (k_0 - k) \Delta] d\Delta \\
 &= \frac{I_0}{2\pi} \left\{ \frac{\sin (k_0 + k) \Delta_m}{(k_0 + k)} + \frac{\sin (k_0 - k) \Delta_m}{(k_0 - k)} \right\}.
 \end{aligned} \tag{7.9}$$

Since k_0 is typically large (except for the very long wavelengths) this may usually be approximated as

$$I(k) \approx \frac{I_0}{2\pi} \frac{\sin (k_0 - k) \Delta_m}{(k_0 - k)} \tag{7.10}$$

and thus the reconstructed spectrum has a finite spread of wavelengths, although this becomes more monochromatic as Δ_m is increased since $I(k) \rightarrow \delta(k - k_0)$ as $\Delta_m \rightarrow \infty$, as expected. Hence an interferogram which is truncated with a maximum path difference of Δ_m , has an effective spectral resolution of $\Delta\tilde{\nu} = 1/\Delta_m$. Because of this feature, the spectral resolution of a Fourier-Transform Spectrometer is easily adjustable by simply recording longer, or shorter interferograms and thus the same instrument may record spectra with multiple resolutions. In addition, the shape of the spectral instrument function may also be adjusted through the process of *apodization*. We can see in Equation 7.10 that the instrument function when an interferogram is transformed directly with a hard cut-off at Δ_m is essentially a sinc function. Suppose that there was a weak feature in the true spectrum very close to a strong feature. Because the sinc function has non-negligible ripples next to it, the weak feature might easily get lost in the ‘feet’ of the strong feature in the reconstructed spectrum, especially if noise was also present. To avoid this, the interferogram may first be multiplied by an apodizing function $A(\Delta)$, which instead of imposing a hard cut-off at Δ_m , instead forces the interferogram to decay smoothly to zero at Δ_m . It may easily be shown that this changes the effective shape of the instrument function and if applied correctly may completely remove the ripples from strong features at the expense of slightly lowering the overall spectral resolution. This technique is thus called apodization which derives from Greek words literally meaning ‘removal of feet’!

Another factor to consider in real Fourier-Transform Spectrometers is *aliasing*. In practice the interferogram is sampled at a finite resolution of the path difference $\Delta = 2x$. Higher frequencies in the observed spectrum can be seen from Equation 7.5 to appear as higher and higher frequency components in the interferogram. If the minimum sampling path difference is Δ_s , then the maximum frequency in the incident spectrum that may unambiguously be reconstructed, according to the Nyquist sampling theorem, is $\nu_0 = 1/(2\Delta_s)$ (James and Stern, 1969; Vanasse, 1983). Hence if any higher frequencies are detectable by the system then they may artificially appear at lower and incorrect frequencies between 0 and ν_0 . This

phenomenon is known as aliasing and may be removed by ensuring that the frequency response of the actual detection system is limited to the frequency range defined by the sampling limit.

Together with allowing variable instrument functions, one of the major advantages of interferometers over spectrometers is that they simultaneously record data over a wide wavelength range and thus little radiation that is collected by the telescope system is wasted. This property also means that interferometers suffer less from FOV variations that may occur during an interferogram scan than grating spectrometers. One possible drawback of the classic Michelson interferometer design for space operation is that the flat mirrors need to be very precisely aligned in order that the central spot of the interference pattern falls on the detector. Such a precise alignment can easily be destroyed during the vibrations which accompany the launch of spacecraft, although the IRIS instruments on *Voyager* (and previous Earth and Mars missions) which had simple Michelson designs were successful. More recently, the CIRS interferometer on the *Cassini* spacecraft (Section 7.9.2) uses corner reflectors, and roof reflectors which are much less sensitive to misalignment.

7.2.5 Detection of microwave radiation

The microwave emission of the giant planets is extremely weak and difficult to detect but technology is rapidly improving. Two main types of receivers are currently used: (1) bolometers; and (2) heterodyne receivers.

Bolometers

With bolometers the radiation is again collected in a tiny absorber, whose temperature changes are converted to electrical signals which are then amplified and measured. Bolometers can detect broadband radiation, for example within the microwave atmospheric windows described in Section 7.3.1, with high sensitivity, but cannot give information on the detailed spectral energy distribution within that band.

Heterodyne receivers

Heterodyne receivers of microwave radiation operate by first converting the microwave signals to a lower frequency by non-linear mixing with a local oscillator signal. The converted lower frequency signal may then be amplified and measured with conventional electronics. At the heart of such receivers is the heterodyne mixer and the most sensitive receivers at present use the strong heterodyne mixing provided by superconductor-insulator-superconductor (or SIS) tunnel junctions. A SIS junction consists of two superconducting electrodes separated by a very thin insulating barrier. Electrons tunnelling across this barrier give rise to a very non-linear current-voltage characteristic which is the key to heterodyne mixing. Such junctions need to operate at very cold temperatures in order to achieve superconductivity depending on the material used in their construction, typically the

temperature of liquid helium (4.2 K). As an example, the SIS junctions currently used by IRAM (Section 7.6.1) consist of a superposition of a thin layer (of the order 4 μm) of aluminum oxide between two layers of the superconducting metal niobium. However, SIS junctions are still very much under development and thus a number of different superconducting alloys and insulating layer materials are currently under investigation all over the world. Apart from low-noise characteristics, the other main advantage of heterodyne receivers is their capability to provide high-resolution spectroscopy which is very important for detecting the absorption lines of microwave absorbers such as CO and HCN, and determining their abundance by accurately measuring the line depth.

7.3 GROUND-BASED OBSERVATIONS OF THE GIANT PLANETS

There are a number of extremely large and sensitive telescopes across the world which may be used for planetary observations, each of which are equipped with a range of instruments for recording images, or spectra, of the giant planets. There are enormous advantages in ground-based observations including: (1) long-term monitoring of slow changes (such as for example the decadal variation in the disc-averaged albedo of Neptune); (2) the flexibility of being able to record with variable spectral resolutions, in particular very high resolution and thus discriminate between individual gaseous absorption lines; and (3) the ability to observe at short notice should something unusual and unexpected occur on the planet in question. However there are also disadvantages in that the available observing time for these telescopes is very limited, and any time that might be allocated for investigating a particular question may be foiled by weather conditions. In addition there are also other significant problems of observing the giant planets from the surface of the Earth including terrestrial atmospheric absorption, angular resolution, and brightness, which will now be discussed.

7.3.1 Terrestrial atmospheric absorption

From the UV through to microwave wavelengths the absorption of the Earth's atmosphere makes some regions of the giant planet spectra completely unobservable from the ground. This can be seen in Figure 7.3 where the vertical transmission to space from the ground has been calculated from UV to microwave wavelengths both from sea level in a standard atmosphere, and from an altitude of 4,000 m in a dry atmosphere. A number of strong absorptions throughout can be seen. At UV wavelengths below 0.3 μm , the Earth's atmosphere is effectively opaque due to photolysis of ozone (O_3) and molecular oxygen (O_2) in the stratosphere. In the visible/near-IR most of the absorption below 3 μm is due to water vapour. At 4.3 μm a strong absorption band of CO_2 appears, but then between 6 and 9 μm (1,600 to 1,100 cm^{-1}) most of the absorption is again due to water vapour. At 9.6 μm (1,040 cm^{-1}) there appears a strong absorption band of ozone, while at 15 μm (667 cm^{-1}) the strong ν_2 absorption band of CO_2 appears. At even longer wavelengths, the absorption is dominated by the rotational absorption lines of water

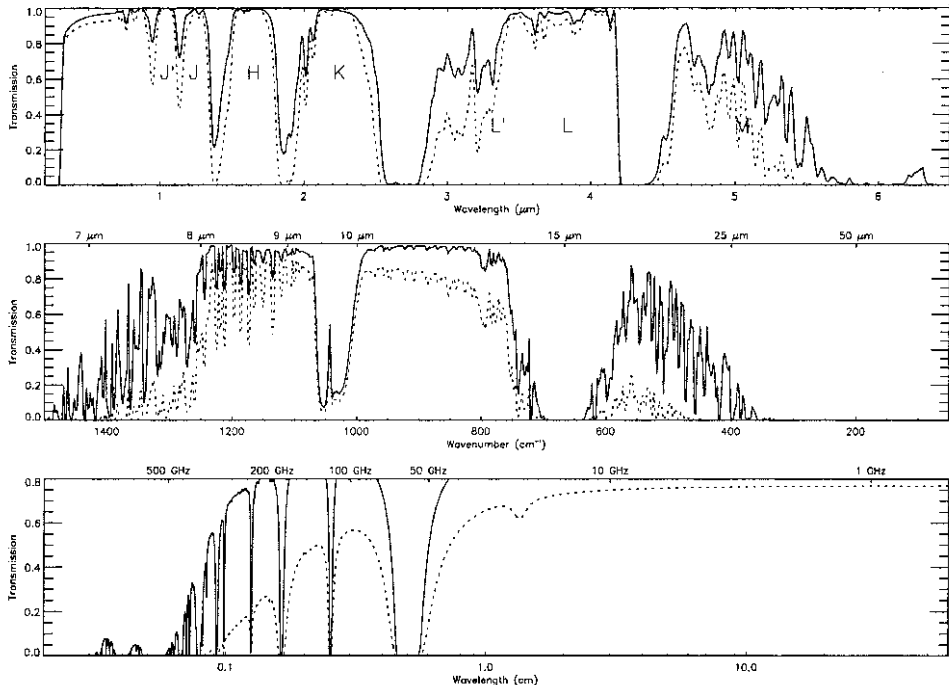


Figure 7.3 Transmission of Earth's atmosphere from ground to space (vertical path). The dotted line is the calculated transmission from sea level in a nominal standard atmosphere while the solid line is from an altitude of 4,000 m in a mid-latitude summer atmosphere. The spectral advantage of placing telescopes on mountain tops is clear. In addition, since most of the absorption features are due to water vapour, telescopes are preferentially located in the driest regions of the world. In the near-IR range the spectral regions where atmospheric absorption is minimum, known as spectral ‘windows’, are commonly called by the letter indicated. Hence, for example, the 2.1–2.4 μm window is commonly known as the K-band and so on.

vapour which then tends to zero towards microwave and radio wavelengths. At millimetre wavelengths, in addition to water vapour, O_2 is also strongly absorbing at 2.5 mm and 5 mm due to magnetic dipole absorptions. At longer wavelengths, the atmosphere is effectively transparent up to wavelengths of approximately 30 m, where it then becomes opaque again due to ionospheric effects.

Clearly the absorption features of water vapour are a major problem for terrestrial observatories, but fortunately most of the water vapour is held in the lower, warmer levels in the atmosphere and thus by placing the telescope at higher altitudes, and/or in desert regions, the absorption of water vapour can be greatly diminished as can be seen in Figure 7.3. In addition, since the pressure of the atmosphere, and thus column abundance of overlying air falls exponentially with height, the absorption of the other gases such as O_2 and CO_2 is also reduced, together with any absorption due to dust or haze. The regions of low atmospheric absorption, between the main

absorption bands, are known as spectral ‘windows’. In the near-IR range these spectral ‘windows’ are often called by the designations shown in Figure 7.3. Hence the 2.1–2.4 μm window is often referred to as the K-band, and so on. Clearly, even on dry mountain tops, the absorption of the terrestrial atmosphere means that several very interesting regions of the giant planet spectra are unobservable. In addition, where the atmosphere is partially clear, the absorption depends on the abundance of highly variable atmospheric constituents such as water vapour and dust. Hence whenever the spectrum of a planet is recorded, the spectrum of a standard reference source such as the Moon, or Mars must also be recorded so that the terrestrial absorption may be determined and corrected for. This correction leads inexorably to additional errors in the final recorded spectra.

7.3.2 Angular resolution

The second historical problem with ground-based observations is the achievable angular resolution. Figure 7.4 compares the physical sizes of all the giant planets and the Earth. However, for ground-based telescopes and Earth-orbiting space telescopes, the apparent angular size of the planets decreases greatly as we go from Jupiter to Neptune, and Figure 7.5 compares the apparent sizes of the planets as they appear at opposition where, for reference, the apparent diameter of Jupiter is $\sim 40''$ (i.e., 40 arcsec). Clearly the apparent size of Neptune is very

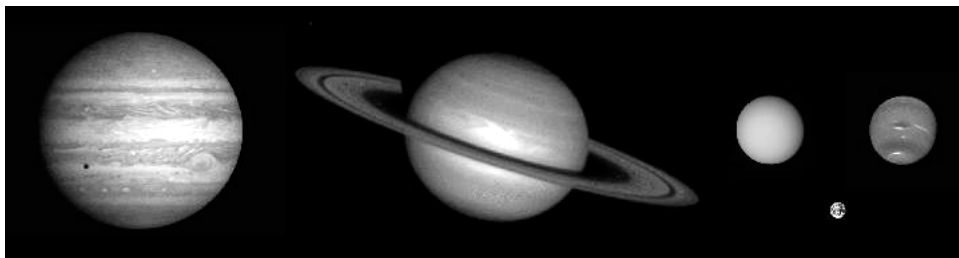


Figure 7.4 Comparative sizes of the giant planets (Jupiter, Saturn, Uranus and Neptune) and the Earth.

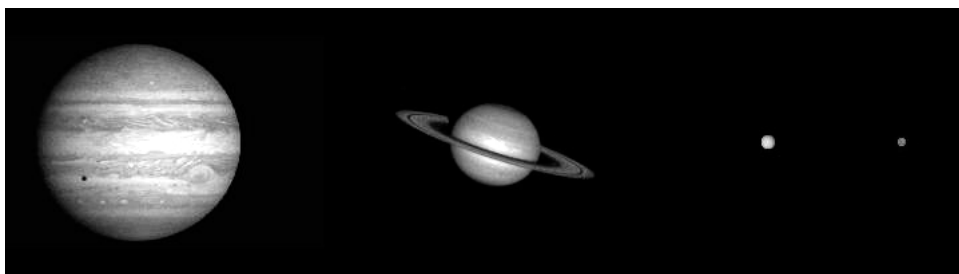


Figure 7.5 Relative apparent sizes of the giant planets as seen at opposition from the Earth with a telescope of ‘perfect’ resolution.

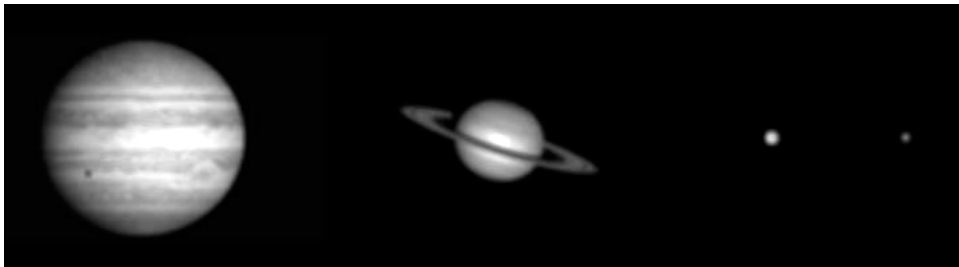


Figure 7.6 Relative appearance of the giant planets as seen at opposition from the Earth with good ‘seeing’ of approximately 1 arcsec resolution.

small, making it very difficult to discern variable cloud features, although the disc-averaged brightness is easier to determine and has been monitored from the ground for decades (Lockwood and Thompson, 2002). While the angular resolution of space-based telescopes depends on aperture and optical quality alone, the angular resolution of ground-based telescopes is severely limited by the turbulence of the overlying atmosphere. The strength of this turbulence depends on local atmospheric conditions and is particularly noticeable in winter giving rise to the ‘twinkling’ of the stars. Typically the ‘seeing’ is limited to approximately 1" and in Figure 7.6, the images have been blurred to this approximate resolution. While considerable cloud detail can still be seen on Jupiter the effect on the other planets becomes increasingly severe as the apparent angular diameter decreases.

The blurring of ground-based telescope images caused by atmospheric turbulence arises due to refractive index variations in the column of air between the telescope and the object. Light from a distant source, such as a star, arrives at the top of the Earth’s atmosphere effectively as a plane wave. However, after passing through the Earth’s atmosphere to reach the telescope, variations in temperature introduced by turbulence, introduce small variations in the refractive index of the air which in turn introduce randomly changing phase variations that continuously distort the wavefront and make it impossible to form a diffraction-limited image. The typical correlation time of the distortions is of the order of a few milliseconds and the problem is most evident at visible wavelengths but becomes progressively smaller at longer wavelengths due to the variations in the flatness of the wavefront becoming smaller and smaller compared to the wavelength of the light observed. This problem severely affected terrestrial astronomical observations for many years but recently, technology has developed to such an extent that new techniques have been developed that go a long way to negating this problem.

Adaptive optics

The most ambitious technique for correcting the problem of ‘seeing’ is *adaptive optics* which attempts to remove the distortions from the wavefront before the image is formed. This is achieved by simultaneously observing either a bright star close to the target, or if no such star is available, observing a simulated star formed

by light scattered back from sodium atoms in the upper atmosphere from a powerful laser situated at the telescope facility. The important thing is to observe the ‘star’ and the target through as nearly the same column of air as possible. Light from the guide star is collimated by the telescope and the flatness of the wavefront sensed. Data from the wavefront sensor is then used, via a suitable control algorithm to modify a corrector plate which attempts to null the atmospheric distortions before the image is formed. The wavefront sensor and corrector plate operate in a closed loop and when operating correctly can effectively fully flatten the wavefront from the guide star. An image simultaneously recorded of the nearby target will be similarly corrected and will thus have an angular resolution much closer to the diffraction limit of the telescope depending on the sensitivity and resolution of the wavefront sensor and corrector plate, the correlation time of the distortions, and the efficiency of the control algorithm. Complex adaptive optics systems use correcting plates which can fully flatten the wavefront, while the simplest use a straightforward tip-tilt system: simply a flat mirror whose mean angle is continually adjusted to keep the centroid of the guide star fixed.

Speckle imaging

A simpler method of image correction is *speckle imaging*. Since the correlation time of the variations is of the order of a few milliseconds, images recorded with shorter exposures will each have a constant, non-varying distortion. If thousands of short-exposure images are recorded, they can be analysed and then suitably averaged to reconstruct near-diffraction limited images. Obviously this technique will work best for bright images due to the low signal-to-noise ratio of short-exposure images.

Deconvolution

The final method of improving the angular resolution is *deconvolution*. In its simplest form, the atmospheric turbulence blurs the image of the object by convolving the true image with an effective point spread function (PSF). If we have a blurred image and we know the PSF, then theoretically we can simply deconvolve the measured image to recover the original image. Unfortunately in practice things are not that simple since both the PSF and the blurred image include random noise, and with the simplest deconvolution methods this noise can propagate through to yield enormous errors in the deconvolved image. This phenomenon is known as *ill-conditioning*, and is also encountered when trying to retrieve vertical atmospheric profiles from measured IR spectra as we shall see in Section 7.10. Practical deconvolution routines must somehow constrain the deconvolved solution to prevent noise error building. A commonly used technique is the Richardson–Lucy (RL) deconvolution algorithm (Sromovsky *et al.*, 2001). If we represent the PSF as $P(i|j)$ (where the PSF represents the fraction of light from true pixel j which gets scattered into pixel i) then the noiseless blurred image $I(i)$ is formed from the unblurred image $O(j)$ as

$$I(i) = \sum_j P(i|j)O(j). \quad (7.11)$$

The RL algorithm then takes the n th estimate of the unblurred image and improves it by the iteration equation

$$O_{n+1}(j) = O_n(j) \frac{\sum_i P(i|j) \frac{D(i)}{I_n(i)}}{\sum_i P(i|j)} \quad (7.12)$$

where $D(i)$ is the observed image and $I_n(i)$ is the n th fit to the blurred image constructed using $O_n(j)$ in Equation 7.11.

Interferometry

Interferometry is a technique routinely used in radio astronomy, and more recently microwave observations, which is currently under development at several optical/IR observatories also. Assuming that the effects of atmospheric turbulence are negated by the use of adaptive optics at visible wavelengths, or by observing at much longer wavelengths, the angular resolution of a single telescope is diffraction-limited by the diameter of the entrance aperture as

$$\theta_d = \frac{1.22\lambda}{D} \quad (7.13)$$

where D is the diameter of the entrance aperture, and λ is the wavelength. The 1.22 factor comes from the fact that the entrance aperture is assumed to be circular and θ_d is specifically the angle between the centre and first minimum of the *Airy* function. Hence as we go to longer wavelengths, the aperture size required to achieve a specific angular resolution increases linearly with wavelength which means that it is simply impractical to build a single-dish radio telescope with the same angular resolution as optical telescopes. However, an alternative approach is to use several telescopes, spaced over large distances and combine their signals together with the appropriate phase delay to simulate, in effect, a giant mirror of diameter equal to the maximum separation of the individual telescopes. The details of the recombination of the signals is complex, but as a simple example, two telescopes of diameter D placed a distance L apart, would have an effective angular resolution in the direction parallel to the line connecting the telescopes of λ/L , and an angular resolution of λ/D perpendicular to this direction. To achieve high resolution at all angles, interferometers usually have several telescopes arranged in a ‘T’ or ‘Y’ shape and the telescopes may usually be placed at a variety of separations in order to increase the sensitivity. The imaging properties of such arrangements are complicated but effectively such interferometers have an angular resolution of λ/L , where L is the maximum baseline, and a field-of-view of λ/D .

7.3.3 Brightness

We saw in Section 6.7 that the thermally-emitted radiance ($\text{W m}^{-2} \text{sr}^{-1} (\text{cm}^{-1})^{-1}$) of the giant planets decreases rapidly as we go out through the Solar System due to the

decreasing atmospheric temperatures. What was not explicitly stated however is that the reflected solar radiance also drops rapidly as $1/D^2$ where D is the distance of the planet from the Sun, due to these planets' greater and greater distance from the Sun. This decrease in the reflected and thermally-emitted radiance affects all remote-sensing observations, not just ground-based ones, and makes remote observation increasingly difficult as we go from Jupiter to Neptune. However some ground-based observations of the giant planets, such as microwave observations or some thermal-IR spectroscopic observations, which have limited angular resolution, are unable to resolve the discs of these planets, especially Uranus and Neptune. Where this is the case there is a further factor decreasing the measured disc-averaged irradiance of the giant planets due to the rapidly decreasing projected solid angle of these planets as we go out through the Solar System. At opposition, when the Earth is closest to the planet, the solid angle is given by

$$\Delta\Omega = \frac{\pi R^2}{((D - 1)D_{AU})^2} \quad (7.14)$$

where D is the planet's distance to the Sun in AU, D_{AU} is one AU, and R is the planetary radius. Hence the observed irradiance is given by the calculated disc-averaged radiance multiplied by the above solid-angle and so drops even more rapidly as we go from Jupiter to Neptune due both to the increase in D , and to the decrease in R . For example, at visible wavelengths the visible opposition magnitudes of Jupiter, Saturn, Uranus, and Neptune are, respectively, -2.7 , 0.67 , 5.52 , and 7.84 where the magnitude m (designed to formalize the observing convention of a 100-fold decrease in irradiance when going from magnitude 1 to magnitude 6 stars) is defined as

$$m = 2.512 \log(B/B_0) \quad (7.15)$$

where B is the measured irradiance from the source, and B_0 is a reference irradiance approximately equal to $B_0 = 7 \times 10^{10} \text{ W m}^{-2} \text{ nm}^{-1}$ at visible wavelengths. The calculated disc-averaged spectral irradiances of the giant planets at the Earth in the visible/near-IR, and mid- to far-IR spectral ranges are shown in Figures 7.7 and 7.8 where the spectral irradiance has been expressed in terms of Janskys, a unit often used in ground-based IR spectroscopy and defined as $1 \text{ Jy} = 10^{-26} \text{ W m}^{-2} \text{ Hz}^{-1}$. The rapid decrease in irradiance with distance is clearly apparent in both spectral ranges.

7.4 GROUND-BASED VISIBLE/IR OBSERVATORIES

We saw earlier that the problems of atmospheric absorption, especially due to water vapour, may be limited by placing telescopes at high altitudes and thus limiting the mass of air above the telescope. In addition, it helps to place telescopes in regions where the air is statically stable and thus atmospheric turbulence is minimal. Very good regions for ground-based telescopes are thus near the tropics of Cancer and Capricorn since these are latitudes where air which has risen near the equator at the Intertropical Convergence Zone (ITCZ) and travelled towards the poles in the

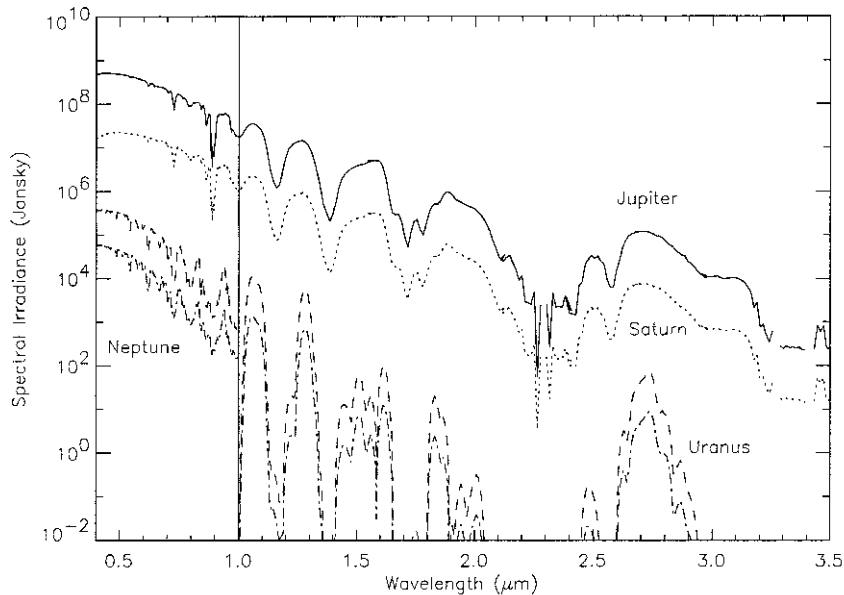


Figure 7.7 Calculated disc-integrated irradiance spectra of the giant planets in the visible and near-IR as seen from the Earth at opposition, in Janskys ($1\text{ Jy} = 10^{-26}\text{ W m}^{-2}\text{ Hz}^{-1}$). Jupiter: solid line, Saturn: dotted line, Uranus: dashed line, Neptune: dot-dashed line.

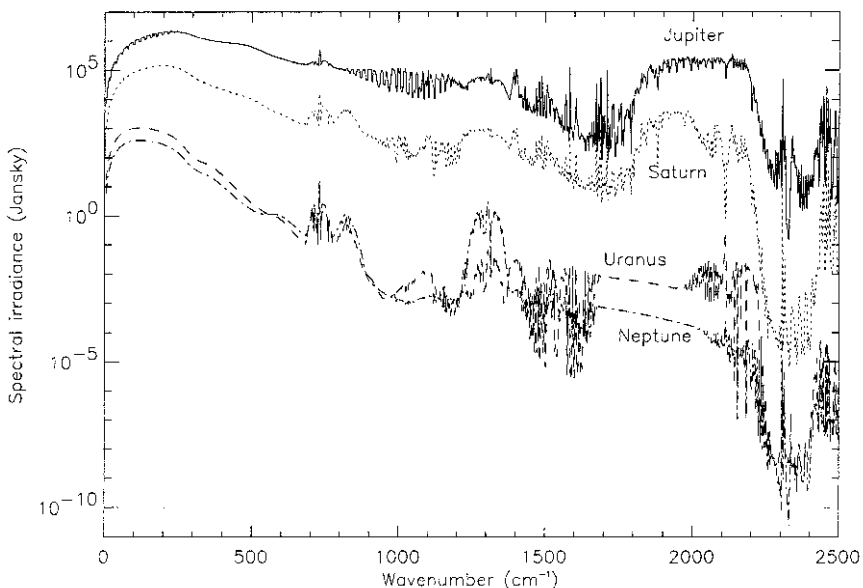


Figure 7.8 Calculated disc-integrated irradiance spectra of the giant planets in the mid- to far-IR as seen from the Earth at opposition (in Janskys). Jupiter: solid line, Saturn: dotted line, Uranus: dashed line, Neptune: dot-dashed line.

terrestrial equatorial Hadley cell circulation then descend and heat adiabatically forming a particularly stable air column. The air is also very dry which has additional advantages for ground-based telescopes as we have just seen, and is also the reason why the Earth's major deserts are found to lie at these latitudes. Such regions are clearly relatively free of clouds, an obvious advantage for visible/IR astronomy! It is thus no accident that most of the major telescope sites on the Earth: Hawaii, Canary Islands, Chile, South-west USA, etc. are near these desert latitudes. In this section we will review some of the major astronomical observatories that, amongst many other things, are currently undertaking observations of the giant planets.

7.4.1 European Southern Observatory (ESO) – Very Large Telescope (VLT)

The ESO is an intergovernmental organization of ten member states which operates two astronomical observatories in the Atacama desert of Chile, one of the driest places on Earth. The La Silla observatory ($29^{\circ} 15' S$, $70^{\circ} 44' W$) at an altitude of 2,400 m is the elder of the two ESO observatories and comprises a number of optical telescopes of diameter between 0.6 and 3.6 m, together with the 15-m Swedish ESO Submillimetre Telescope (SEST), which is the largest submillimetre telescope in the southern hemisphere. The telescopes are listed in Table 7.1. The Paranal Observatory ($24^{\circ} 40' S$, $70^{\circ} 25' W$) at an altitude of 2,645 m is home to ESO's new Very Large Telescope (VLT) facility and was chosen for its excellent atmospheric conditions and remoteness ensuring that its operation is not disturbed by the effects of human settlement such as dust and light from roads and mines.

The VLT is the world's largest and most advanced astronomical observatory (Figure 7.9). It comprises four 8.2-m reflecting Unit Telescopes which may operate individually or in a combined mode providing the total light-collecting power of a single 16-m telescope. In addition the telescopes will eventually be used in an interferometric mode together with three movable 1.8-m Auxiliary Telescopes to form the VLT Interferometer (VLTI). The four large telescopes, initially designated UT1–UT4, have recently been renamed in the indigenous Mapuche language as Antu (The Sun), Kueyen (The Moon), Melipal (The Southern Cross), and Yepun (Venus). A schematic of the observatory showing the telescopes and instruments

Table 7.1. La Silla telescopes.

ESO operated telescopes	National telescopes
3.6 m	DENIS 1 m
2.2 m	MARLY 1 m (EROS project)
ESO 1.5 m	Geneva 1.2 m
Danish 1.5 m	
New Technology Telescope 3.5 m	
SEST 15 m	



Figure 7.9 The European Southern Observatory Very Large Telescope (VLT) at La Paranal, Chile.

Courtesy of ESO.

that will eventually be available is shown in Figure 7.10. To save weight, the primary mirrors of the Unit Telescopes are rather thin and thus flexible. Hence their shape is dynamically controlled using *active optics* to apply correcting forces to the primary mirror and move the secondary mirror in order to cancel out the errors. The active optics system was originally developed for the ESO 3.5-m New Technology Telescope (NTT) at La Silla. The VLT telescopes use the Ritchey–Chrétien optical design and each telescope may operate in either the Cassegrain, Nasmyth, or Coudé focus. The image quality of the VLT telescopes is very impressive with a record angular resolution of $0.18''$. More usually, the seeing is in the $0.5\text{--}1.0''$ range, but the VLT may also use adaptive optic techniques to achieve near-diffraction limited observations of angular resolution $0.05''$. Should no guide star be available then UT4 (Yepun) incorporates a laser system to generate a Laser Guide Star. UT1 (Antu) achieved first light on 25 May 1998, and the most recently completed

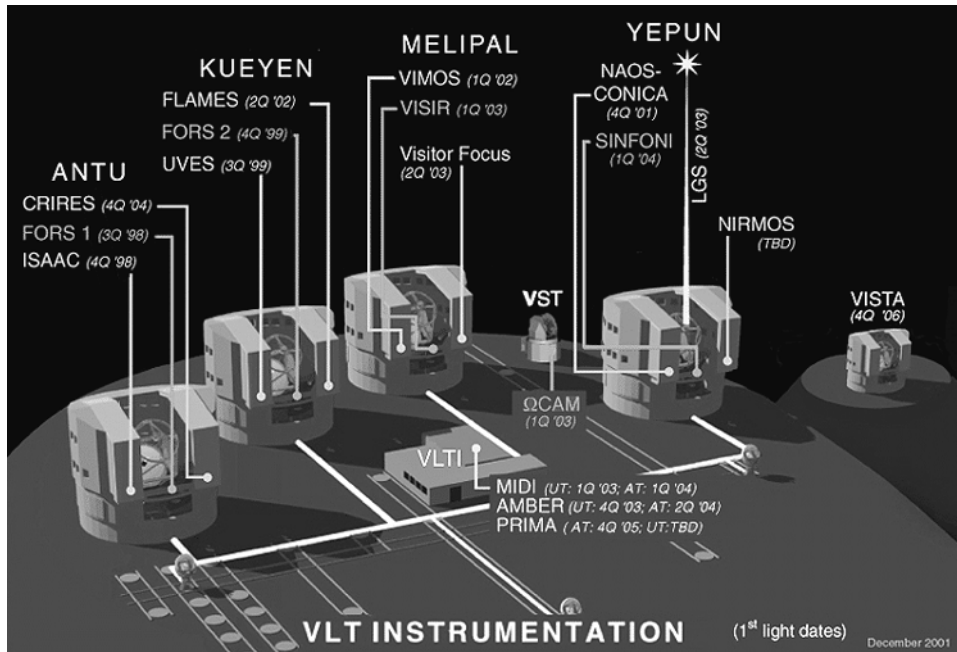


Figure 7.10 Schematic design of VLT site.

Courtesy of ESO.

telescope, UT3 (Melipal), achieved first light on 26 January 2000. The VLT is already providing excellent new data on the giant planets due to its high angular resolution, and is equipped with a number of instruments for imaging and spectroscopy from the UV to approximately 25 μm .

7.4.2 The Mauna Kea observatories

The Mauna Kea volcano on Big Island, Hawaii is an excellent place for astronomical observations due to its high altitude of 4,200 m, and its dry, stable atmospheric conditions. Hence the site is currently home to the world's largest, and most powerful telescopes (Figure 7.11). The largest of these are the twin Keck telescopes (Figure 7.12) which have primary mirrors that are 10 m in diameter and are composed of 36 individual, actively controlled, hexagonal elements that operate together as a single, high precision mirror. The Keck observatory is jointly operated by NASA and the California Institute of Technology (Caltech). The Keck I telescope began operations in May 1993, while Keck II began observing in October 1996.

Other telescopes which are situated on the Mauna Kea site are listed in Table 7.2 and of particular note are the Japanese Subaru 8.2-m telescope, the Gemini North 8.1-m telescope, and the NASA Infrared Telescope Facility (IRTF). The Subaru 8.2-m telescope incorporates the largest single-piece, or monolithic,

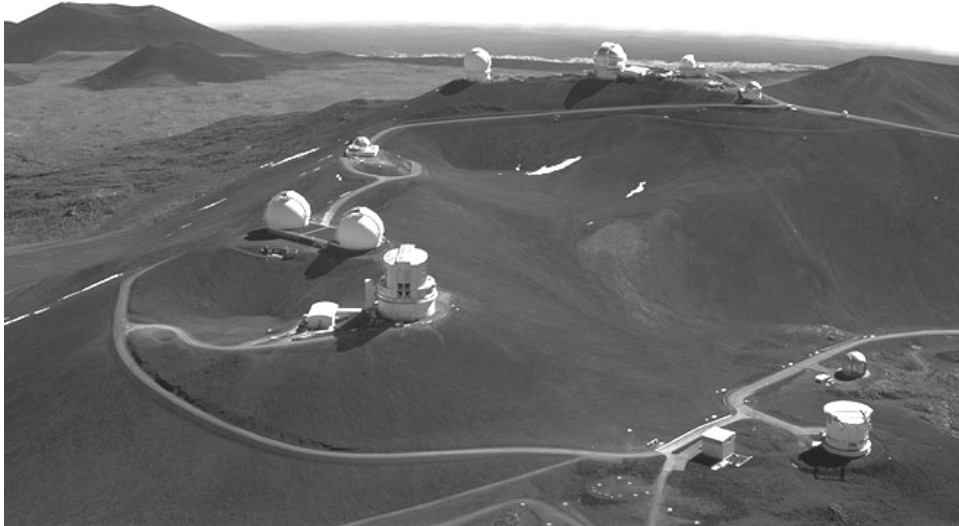


Figure 7.11 Mauna Kea site in Hawaii. The Keck telescopes are the twin domes seen at centre left. The 8-m Subaru Telescope (with a cylindrical dome) is in front of the Kecks and behind it are (left to right): the NASA IRTF, the Canada–France–Hawaii Telescope (CFHT), the Gemini North 8-m telescope (in this picture still under construction), the University of Hawaii 2.2-m telescope, and the 3.8-m United Kingdom Infrared Telescope (UKIRT). In the lower foreground are (left to right): the Smithsonian–Taiwan submillimeter array, the James Clerk Maxwell 15-m submillimeter telescope, and the Caltech 10-m submillimeter telescope.

Courtesy of Keck Observatory, California Institute of Technology and Richard Wainscoat/ILA.

mirror ever built and achieved ‘first light’ in January 1999. The Gemini project is an international collaboration between seven countries (USA, UK, Canada, Chile, Australia, Argentina, and Brazil) to place two identical telescopes in both northern and southern hemispheres to allow unobstructed observation of both northern and southern skies simultaneously. While Gemini North is located on Mauna Kea, its identical brother, Gemini South, is located at Cerro Pachon in Chile (2,737 m). The Gemini Telescope mirrors are single-piece thin mirrors whose shape is continuously adjusted by an active optics system using 120 actuators at the back of the mirror to maintain the mirror shape. Gemini North was dedicated on 25 June 1999, and Gemini-South was dedicated on 18 January 2002. The NASA IRTF is a 3-m infrared telescope operated and managed for NASA by the University of Hawaii. Observing time is open to the entire astronomical community, and 50% of the IRTF observing time is reserved for studies of Solar System objects.

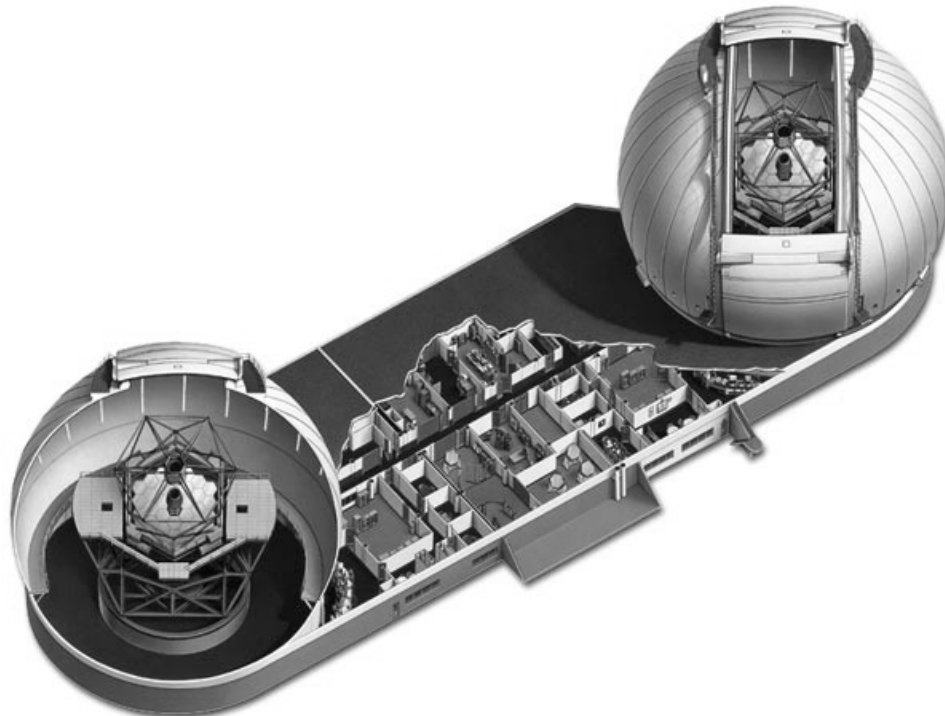


Figure 7.12 Schematic design of the Keck Observatory, Hawaii.

Courtesy of Keck Observatory, Institute of Technology.

Table 7.2. Mauna Kea telescopes.

Telescope	Mirror diameter	Operator
Subaru	8.2 m	National Astronomical Observatory of Japan (NAOJ)
NASA Infrared Telescope Facility (IRTF)	3 m	NASA and University of Hawaii
Canada–France–Hawaii Telescope (CFHT)	3.6 m	Canada and France
Gemini North	8.1 m	International Gemini Consortium
University of Hawaii 2.2 m	2.2 m	University of Hawaii
United Kingdom Infrared Telescope (UKIRT)	3.8 m	Joint Astronomy Centre (JAC) UK, Holland, Canada
James Clark Maxwell submillimetre Telescope (JCMT)	15 m	Joint Astronomy Centre (JAC) UK, Holland, Canada
Caltech submillimetre Telescope	10 m	California Institute of Technology
Smithsonian–Taiwan Submillimeter Array	6 × 8 m	Smithsonian Institute and Taiwan

7.4.3 Other major observatories

There are a number of other major observatories across the world, many of which are involved in giant planet observations. In this section we will briefly list some of the largest, and most famous of these observatories and outline the telescopes available.

- (1) *Calar Alto*. This observatory, sited at an altitude of 2,168 m in Andalucia, Spain, is operated by the Max-Planck-Institut für Astronomie, Heidelberg, Germany, and has been used extensively for planetary observations. Three main telescopes are provided with apertures of 1.23 m, 2.2 m, and 3.5 m, together with a 1.5-m telescope operated by the Observatory of Madrid.
- (2) *AAO*. The Anglo–Australian Observatory is situated in northern New South Wales, Australia, and operates the 3.9-m Anglo–Australian telescope and the 1.2-m UK Schmidt telescope. The AAO is not currently involved in giant planet observations but is involved in the search for extrasolar planets, by the ‘Doppler wobble’ technique.
- (3) *Pic-du-Midi*. The Pic-du-Midi Observatory is situated at an altitude of 2,872 m in the French Pyrenees. The observatory operates a 1- and 2-m telescope and has undertaken numerous investigations of the giant planets.
- (4) *La Palma*. The La Palma Observatory, run by the Isaac Newton Group of Telescopes (ING), operates the 4.2-m William Herschel Telescope, the 2.5-m Isaac Newton Telescope and the 1.0-m Jacobus Kapteyn Telescope on behalf of British, Dutch, and Spanish research agencies. The La Palma Observatory does not currently undertake giant planet observations.
- (5) *Kitt Peak National Observatory*. The Kitt Peak National Observatory is located high above the Sonoran Desert in Arizona and is home to 22 optical and two radio telescopes representing eight astronomical research institutions. The largest of these telescopes are the Mayall 4-m telescope, the 3.5-m WIYN telescope, and 2.1- and 0.9-m telescopes. The Kitt Peak National Observatory is also involved in the search for extrasolar planets.
- (6) *Palomar*. The Palomar Observatory in California is owned and operated by the California Institute of Technology. Its principal instruments are the 200-inch (5-m) Hale Telescope, the 48-inch (1.2-m) Oschin Telescope, the 18-inch (0.45-m) Schmidt telescope, and the 60-inch (1.5-m) reflecting telescope. For many years the Hale telescope was the largest in the world.
- (7) *Las Campanas*. The Las Campanas Observatory, at an altitude of 2,438 m in the Chilean Andes, is operated by the Observatories of the Carnegie Institution of Washington (OCIW). The site includes the two 6.5-m Magellan telescopes which began operations in September 2000 and September 2002 respectively.

7.5 AIRBORNE VISIBLE/IR OBSERVATIONS

We saw earlier that IR astronomy from ground-based telescopes is severely hampered by the absorption of gases in the Earth’s atmosphere, especially water

vapour. Most of this water vapour lies in the lower, warmer parts of the atmosphere and thus as mentioned earlier, most ground-based IR facilities are placed at high altitudes, in climatically dry parts of the world. However, the number of locations on the Earth that satisfy these requirements are limited, and they are often also remote, making the construction and operation of these telescopes rather difficult. An alternative approach to Earth-based IR astronomy is to mount an infrared telescope on to an aircraft and observe in-flight at high altitude almost anywhere in the world. At the high altitudes attainable by jet aircraft, the obscuration by overlying water vapour is reduced by a factor of one thousand compared to observations at sea level. In addition, airborne observations are unaffected by cloud obscuration and such observatories may be used to observe both the southern and northern skies. A further advantage is that an airborne observatory is ideal for observing stellar occultation events since it can fly to the optimum position in the world to observe them.

7.5.1 Kuiper Airborne Observatory

The first airborne observations were made in the 1960s, but airborne IR observations really came of age with the commission of NASA's Kuiper Airborne Observatory (KAO) named after the American planetary scientist Gerard P. Kuiper (1905–1973). The KAO aircraft (Figure 7.13) was a Lockheed C-141A jet transport plane with a range of 6,000 nautical miles and was capable of conducting research operations to 45,000 ft (14 km). The aircraft was modified to carry a 0.91-m aperture Cassegrain IR



Figure 7.13 The Kuiper Airborne Observatory (KAO) aircraft.

Courtesy of NASA.

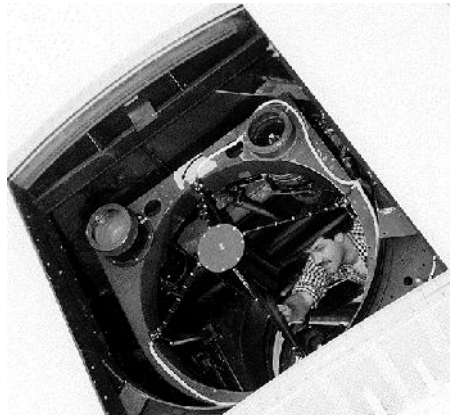


Figure 7.14 The KAO telescope looking through the aperture in the aircraft's side.

Courtesy of NASA.

telescope operating in the 1–500 μm spectral range and which observed through a hole cut in the side of the aircraft at an elevation of between 35 and 75° (Figure 7.14). The KAO flew out of NASA Ames Research Center, at Moffett Field, California, and began operating in 1971, finally finishing service in October 1995.

The telescope was mounted such that it moved independently from the aircraft and an automatic system kept the telescope pointed at the selected target even when the aircraft moved in turbulence. The telescope mirrors were cooled with liquid nitrogen and other cryogenic liquids to reduce their background IR emission.

7.6 GROUND-BASED MICROWAVE OBSERVATORIES

The submillimetre to microwave part of the giant planets' thermal emission spectra is a very interesting one since it allows for the probing of the deep pressure levels of these planets with weighting functions extending down to almost 100 bar for Uranus and Neptune. The spectral range contains absorption features of ammonia, CO, HCN, and other constituents and thus the deep abundance of these molecules may be determined. The transmission of the Earth's atmosphere at microwave wavelengths was shown in Figure 7.3 and hence ground-based microwave observations are limited to the spectral windows between these main absorption bands. Since the main absorber is once again water vapour, microwave observatories are, like visible/IR observatories, preferentially located at high altitudes in dry regions of the world. Observing the giant planets at microwave wavelengths poses considerable problems, not least of which is the very low power of microwave emission radiated by these planets which means that antennas must be very large, and detectors must be very sensitive. A second problem, for Jupiter observations, is that synchrotron emission is also observed from the radiation belts, which needs to be subtracted for wavelengths longer than about 4 cm. The final problem is that at these long wavelengths, it is

technically very difficult to make antennas large enough to resolve structure on the surfaces of these planets. For example, an antenna able to resolve down to 1 arcsec at the wavelength of the inversion absorption band of ammonia at 1.3 cm needs to be 3.2 km across! For this very reason, microwave and radio observatories have led the way in developing interferometric arrays to increase their angular resolution. There are currently several large millimetre arrays in the world which have been used for giant planet observations which will now be reviewed.

7.6.1 The Institut de RadioAstronomie Millimétrique (IRAM)

IRAM is an international institute for research in millimetre astronomy founded in 1979 by the Centre National de la Recherche Scientifique (CNRS), France, and the Max Planck Gesellschaft (MPG), Germany. The organisation was joined by the Instituto Geográfico Nacional (IGN), Spain, in September 1990. IRAM operates two major facilities: a 30-m radio telescope on Pico Veleta in the Sierra Nevada (southern Spain), and an array of six 15-m radio telescopes on the Plateau de Bure in the French Alps. The IRAM telescopes observe in the microwave ‘windows’ at 0.85 mm, 1.3 mm, 2 mm, and 3 mm.

The Pico Veleta observatory is located at an altitude of 2,920 m on the second highest mountain of the Iberian peninsula. Its high altitude, southern location and its dry climate are extremely favourable for millimetric observations due to the low column abundances of water vapour which, on cold, dry winter days, can drop to as low as 1 precipitable-mm. The 30-m Cassegrain telescope at Pico Veleta is currently the world’s largest telescope operating at wavelengths between 0.8 and 3.5 mm (350 to 80 GHz), with a collection area of 700 m^2 , and received its first millimetric ‘light’ in May 1984. The angular resolution of the Pico Veleta observatory is purely diffraction limited and thus depends inversely on wavelength, with an angular resolution of $10''$ at a wavelength of 1.3 mm. Radio telescopes have historically operated with a single receiver (or pixel) and thus an image was built up by scanning the entire telescope across the sky. More recently, multiple detectors are located in imaging arrays at the focal plane of these telescopes to provide instant imaging of objects.

The Plateau de Bure observatory is located at an altitude of 2,552 m in the French Alps. Atmospheric conditions are good for millimetric observations and the column amount of water vapour can drop below 2 precipitable-mm on dry winter days. Work on the construction of the site began in 1985, and the first interferometric fringes were obtained in 1988. The site consists of six 15-m antennas operating between 2.6 and 3.7 mm (81 to 115 GHz) and also between 1.2 and 1.4 mm (205 to 245 GHz), which can move on rail tracks up to a maximum separation of 408 m in the E–W direction and 232 m in the N–S direction (Figure 7.15). Each dish has a collecting area of 175 m^2 and thus the combined collecting area of the six telescopes is $1,050\text{ m}^2$ which makes this one of the most sensitive, and high angular resolution interferometers in the world. As mentioned earlier, for an interferometer the field of view is defined by the ratio of wavelength to



Figure 7.15 The IRAM millimetre array at the Plateau de Bure Observatory, France

Courtesy of IRAM.

diameter for each antenna, while the resolution is determined by the ratio of the wavelength to the maximum separation between antennas. Hence, for example at 1.3 mm, the field of view of the interferometer is 20" while the best angular resolution is 0.5".

7.6.2 Very Large Array (VLA)

The VLA is one of the world's greatest astronomical radio observatories. It consists of twenty-seven 25-m radio antennas in a Y-shaped configuration on the plains of San Agustin in New Mexico at an altitude of 2,124 m. Each arm is 21 km in length (Figure 7.16) and the data from the antennas may be combined interferometrically to give the resolution equivalent to an antenna 36 km across in the facility's highest resolution configuration. Each antenna has a collecting area of 491 m^2 , giving a total facility collection area of $13,250\text{ m}^2$, equivalent to a single 130-m diameter dish. Construction of the VLA began in 1973, and the facility was formally dedicated in 1980.

The radio-dishes of the VLA may be moved on a rail system to take up one of 4 positions with different maximum separations: A (36 km), B (10 km), C (3.6 km), and D (1 km). The configuration is typically switched every four months or so. The reason for changing the separations is that although configuration A has the highest resolution, it also has the lowest sensitivity to faint objects. Conversely, configuration D has the highest sensitivity, but the lowest angular resolution. Hence the optimal configuration depends on the use to which the VLA is to be put. The VLA can observe in various bands between 75 MHz (400 cm) and 43 GHz (0.7 cm), summarized in Table 7.3, and the beam size and angular resolution

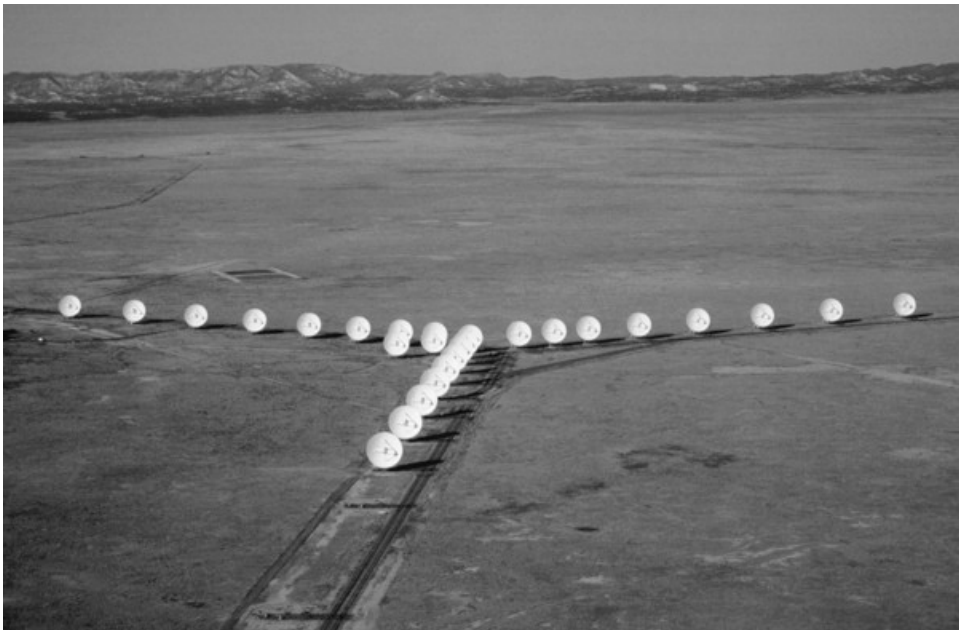


Figure 7.16 The Very Large Array (VLA) in New Mexico.

Courtesy of NRAO/AUI.

Table 7.3. Receivers available at the VLA.

	4 Band	P Band	L Band	C Band	X Band	U Band	K Band	Q Band
Frequency (GHz)	0.073–0.0745	0.30–0.34	1.34–1.73	4.5–5.0	8.0–8.8	14.4–15.4	22–24	40–50
Wavelength (cm)	400	90	20	6	3.6	2	1.3	0.7
Primary beam (arcmin)	600	150	30	9	5.4	3	2	1
Highest resolution (arcsec)	24.0	6.0	1.4	0.4	0.24	0.14	0.08	0.05

in configuration A vary inversely with wavelength between 11° and $1'$, and $24''$ and $0.05''$ respectively.

7.6.3 Very Large Baseline Array (VLBA)

The VLBA is a series of ten 25-m diameter radio antennas located at sites across the continental U.S. and on Mauna Kea, Hawaii, and St. Croix in the U.S. Virgin Islands. Work on its construction began in 1985, and the last VLBA station on Mauna Kea was completed in 1993. Because of its extremely long baseline, and large collecting area, the VLBA has a maximum angular resolution of less than

one-thousandth of an arcsecond (at $\lambda = 7\text{ mm}$), and covers the wavelength range from 7 mm to 90 cm in nine bands. The wavelength range is currently being extended downwards to 3.5 mm. Clearly to achieve its high resolution, the data from the antennas must be combined interferometrically, but since the sites are so far apart this is not easy to do in real time. Instead, each site records its data onto magnetic tape and the data ‘time-tagged’ with a reference signal generated by a hydrogen maser at each site. The tapes are then sent to the VLBA station in Sorroco, USA, where the tapes from each station are read and combined with the appropriate time delays consistent with the station’s different positions across the globe to form a single interferometric device.

7.6.4 Berkeley Illinois Maryland Association (BIMA)

The BIMA is a consortium consisting of the University of California, Berkeley, the University of Illinois, Urbana, and the University of Maryland and operates a millimetre-wave radio interferometer at Hat Creek, California.

The BIMA array dates back to the 1970s and originally consisted of just three antennas. Currently there are ten operational 6.1-m dishes which may be moved to one of three configurations (depending on the required sensitivity and angular resolution) along a ‘T’-shaped concrete track 305 m long in the E–W direction, and 183 m long in the N–S direction (Figure 7.17).

7.6.5 Owens Valley Radio Observatory (OVRO)

The OVRO is the largest university-operated radio observatory in the world and is located near Bishop, California, on the east side of the Sierra Nevada at an altitude



Figure 7.17 The Berkeley Illinois Maryland Association (BIMA) millimetre array at Hat Creek, California.

Courtesy of BIMA.



Figure 7.18 The Owens Valley Radio Observatory (OVRO) millimetre array in Bishop, California.

Courtesy of California Institute of Technology.

of 1,222 m. The site is managed by the California Institute of Technology and includes a 40-m telescope used primarily for studies of the cosmic microwave background radiation, a solar array for microwave observations of the Sun between 1 and 18 GHz, and a millimeter array.

The newly completed millimeter-wavelength array consists of six 10.4-m radio telescopes where the individual telescopes may be moved to various observing stations along a 'T'-shaped rail track which is 440 m long in the N–S direction and 400 m long in the E–W direction (Figure 7.18). There are again a number of possible arrangement configurations for the telescopes depending on the required sensitivity and angular resolution. Each telescope has receivers covering the ranges 86–116 GHz (2.5–3.5 mm) and 210–270 GHz (1.1–1.4 mm). The array has made significant new observations of protoplanetary and circumstellar discs.

7.6.6 Nobeyama Millimeter Array (NMA)

The NMA in Japan consists of 6 transportable 10-m antennas, equipped with cryogenically cooled SIS receivers, covering 3 wavelength bands: 3 mm (85–116 GHz), 2 mm (126–152 GHz), and 1 mm (213–237 GHz), respectively (Figure 7.19). A 45-m dish is also at the site. There are 30 antenna stations



Figure 7.19 The Nobeyama Millimeter Array (NMA) in Japan.

Courtesy of NMA.

located along two tracks, one extending 560 m in the E–W direction, and another 520 m long inclined at an angle of 33° from the N–S direction. The antennas may again be arranged in a number of configurations.

7.7 SPACE-BASED TELESCOPES

Space-based visible/IR telescopes offer considerable advantages over ground-based and airborne telescopes in that the effects of the terrestrial atmosphere are almost completely eliminated (although even the HST at an altitude of 600 km experiences some sensitivity to terrestrial UV airglow). Hence the complete, unobscured spectra of the giant planets may be observed and the angular resolution is, if the telescope and detection system are correctly constructed, diffraction limited. Of course the angular diameters of the planets are unchanged and so very fine resolution, highly sensitive instruments are still required to image the furthest giant planet, Neptune. Although a number of space observatories have now been launched, only three have been used for planetary observations: the HST, the ISO, and the Submillimeter Wave Astronomy Satellite (SWAS) which will now be described.



Figure 7.20 The Hubble Space Telescope in orbit about the Earth.

Courtesy of NASA/ESA.

7.7.1 HST

The HST is a collaborative ESA/NASA mission and was launched on 25 April 1990 by the space shuttle *Discovery* (STS-31) into a low-Earth 600-km-altitude orbit. The telescope is 13.2 m long, 4.2 m in overall diameter, and weighs 11,110 kg (Figure 7.20). With a primary mirror of diameter 2.5 m, the theoretical angular resolution of HST is approximately $0.1''$ in the visible and near-IR, which is ten times better than can be achieved with most ground-based observations without adaptive optics. Unfortunately, soon after launch, the primary mirror was discovered to have been ground incorrectly and thus the telescope initially suffered from spherical aberration which significantly impaired its performance. Some of these defects were dealt with by corrective optics installed by the December 1993 shuttle servicing mission (STS-61, *Endeavor*), and subsequent servicing missions have now completely replaced the original instruments launched on HST such that they all now correct for the aberration of the primary. The instruments currently onboard HST will now be reviewed.

Wide Field/Planetary Camera 2

The Wide Field/Planetary Camera 2 (WF/PC2) was a replacement for the original Wide Field/Planetary Camera (WF/PC1) launched on HST and was installed by the December 1993 shuttle servicing mission to negate the aberration in the primary

mirror. WF/PC2 records high-resolution images of astronomical objects over a relatively wide FOV and a broad range of wavelengths (115 to 1,100 nm), which are defined by a large selection of filters. WF/PC2 is composed of 4 cameras, each of which has an 800×800 element silicon CCD array. Three of the cameras make up the wide field camera (WFC) and operate at f/12.9 giving a pixel size of 0.1" and a FOV of $150'' \times 150''$. The pointing of these cameras is arranged to form a projected 'L' shape in the sky. The fourth camera, known as the Planetary Camera (PC), operates at f/28.3 and thus covers a FOV of $35'' \times 35''$ with a pixel size of 0.046". This camera points in the gap left by the WFC.

Space Telescope Imaging Spectrograph (STIS)

The STIS covers a similar spectral range to WF/PC2 (115–1,000 nm) and uses three detector arrays. The spectral regions 115–170 nm, and 165–310 nm each use a Multi-Anode Microchannel Array (MAMA), while a CCD array covers the 305 to 1,000 nm range. All three arrays have $1,024 \times 1,024$ elements and the FOV is $25'' \times 25''$ for each MAMA (0.024"/pixel), and $50'' \times 50''$ for the CCD (0.05"/pixel). Although STIS covers a smaller region of the sky than WF/PC2, it has higher angular resolution and other advantages at UV wavelengths.

Near-IR Camera and Multi-Object Spectrometer (NICMOS)

The IR NICMOS covers the wavelength range of 0.8 and 2.5 μm , and its highly sensitive HgCdTe detector arrays must be cooled to liquid nitrogen temperatures for optimum sensitivity. Initially the cooling was provided by an onboard exhaustible liquid-nitrogen supply and it operated as such between February 1997 and November 1998 yielding exciting new results on the giant planets, amongst many other things. However, the cryogen was eventually exhausted and thus the detectors warmed up, reducing the usefulness of the instrument. More recently NICMOS has been revived by the shuttle servicing mission 3B (STS-109) in March 2002 which installed an active cooling system for the instrument called the NICMOS Cooling System (NCS). The performance of NICMOS is now again as designed.

NICMOS is composed of three cameras: NIC1, NIC2, and NIC3 which form 3 adjacent FOV at different angular resolutions. Each camera has a 256×256 detector array and 19 different combinations of filters, gratings, and prisms. NIC1 covers a $11'' \times 11''$ region of the sky at a resolution of 0.043", NIC2 covers a $19.2'' \times 19.2''$ region at resolution of 0.075", and NIC3 covers a $51.2'' \times 51.2''$ region at an angular resolution of 0.2". Most of the filters of NIC1 cover the short wavelength end of the NICMOS range, while NIC2 has more filters covering the long wavelength end. NIC3 has yet another selection of filters across the range, and can also operate as a spectrometer with resolving power of 200 and three spectral ranges of 0.8–1.2, 1.1–1.9, and 1.4–2.5 μm respectively. In addition, NIC1 and NIC2 can also measure the mean polarization at 0° , 120° , and 240° between 0.8–1.3 μm for NIC1, and 1.9–2.1 μm for NIC2.

Advanced Camera for Surveys (ACS)

The newly-installed ACS provides HST with: (1) a deep, wide-field survey capability from the visible to near-IR; (2) high-resolution imaging from the near-UV to the near-IR; and (3) solar blind far-UV imaging. The primary ACS design goal is to achieve a factor of 10 improvement in the discovery efficiency of new objects, compared to WF/PC2, where discovery efficiency is defined as the product of imaging area and instrument throughput. ACS was installed by the March 2002 shuttle servicing mission and is composed of three cameras: (1) a Wide Field Camera (WFC) which covers the spectral range 350–1,100 nm, and a $202'' \times 202''$ region of the sky at an angular resolution of $0.049''$; (2), a High-Resolution Camera (HRC) which covers the spectral range of 200–1,100 nm, and a $29.1'' \times 26.1''$ region of the sky at an angular resolution of $0.028'' \times 0.025''$; and (3) a Solar Blind Camera (SBC) which covers the spectral range of 115–170 nm, and a $34.6'' \times 30.8''$ region of the sky at an angular resolution of $0.033'' \times 0.030''$.

7.7.2 ISO

The ESA ISO was launched on 17 November 1995 by an *Ariane 44P* launcher from Kourou, French Guiana into a highly elliptical orbit with a perigee altitude of 1,000 km, an apogee altitude of 70,500 km, and a period of approximately 24 hr (Figure 7.21). The design of the orbit allowed for very long integration times to

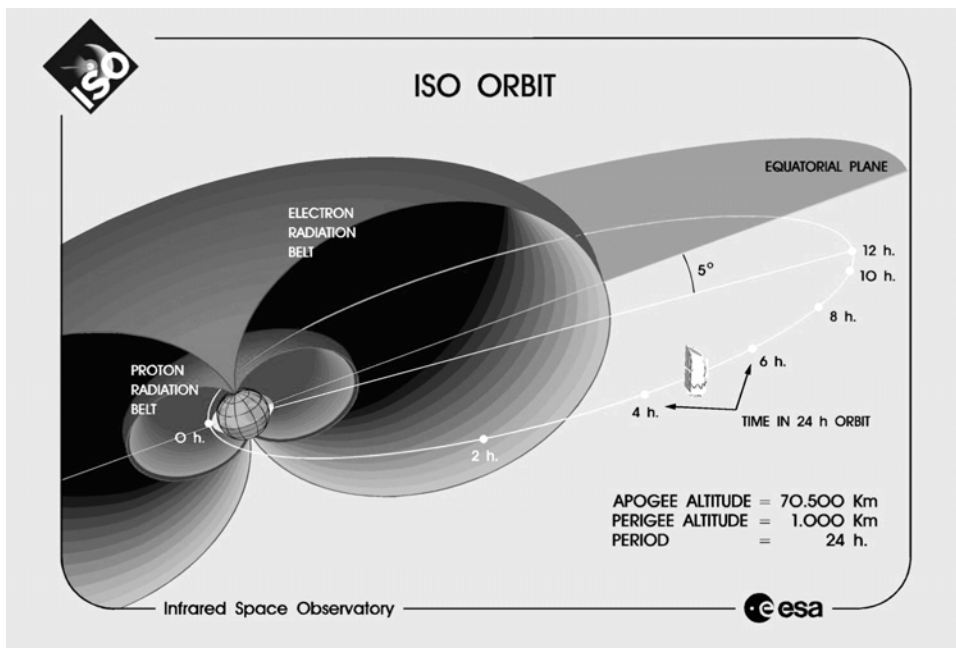


Figure 7.21 Orbit of the Infrared Space Observatory (ISO) about the Earth.

Courtesy of ESA.

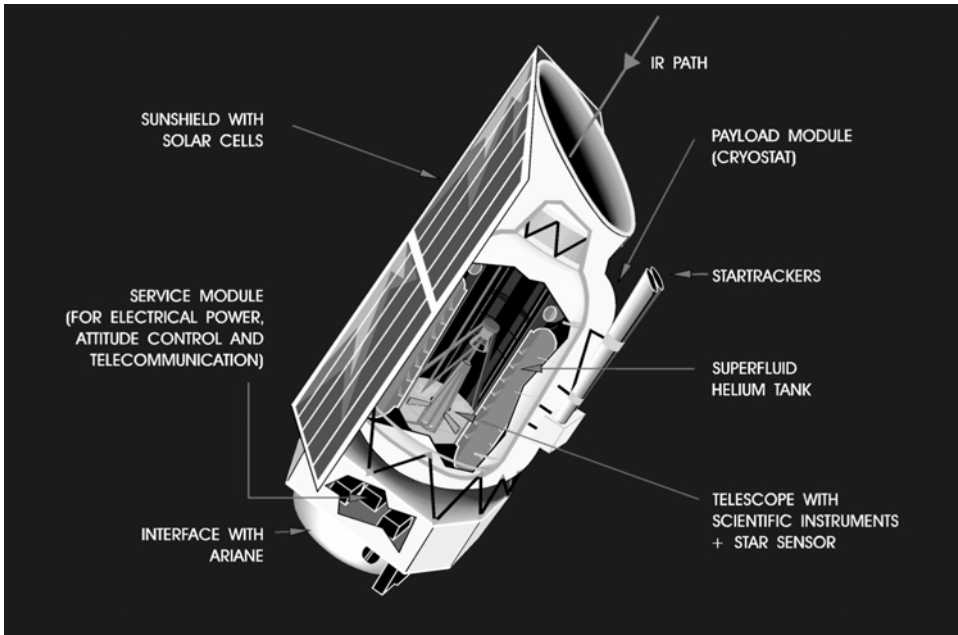


Figure 7.22 Schematic design of ISO.

Courtesy of ESA.

record extremely faint objects and also ensured that ISO minimized its time within the Earth's radiation belts which interfere with the operation of its detectors. The orbit chosen allowed 17 hr of continuous telescope operation per orbit.

Although the physical size of ISO is large ($5.3 \times 3.6 \times 2.8$ m), the telescope itself is relatively small with a primary mirror diameter of only 0.6 m (Figure 7.22). Most of the volume was filled up with liquid helium which cooled the entire optical system to a temperature of 4 K reducing the noise of the detectors to their minimum theoretical values, and allowing the measurement of images and spectra of extremely cold objects over the spectral range of $2.3\text{--}240\,\mu\text{m}$ ($41\text{--}4,300\,\text{cm}^{-1}$). ISO was originally planned to be operational for 20 months, but eventually the working life was stretched to more than 28 months and ISO operated until May 1998. ISO had four main instruments which will now be reviewed.

Infrared camera: ISOCAM

The ISO camera provided imaging in the spectral range $2.5\text{--}17\,\mu\text{m}$. The instrument was split into a short wavelength (SW) channel covering $2.5\text{--}5.2\,\mu\text{m}$, and a long wavelength (LW) channel covering $4\text{--}17\,\mu\text{m}$. Each channel contained a 32×32 pixel IR detector array, fixed filters, continuous variable filters (CVF) with a resolving power of $\lambda/\Delta\lambda = 40$, and a set of magnification lenses giving angular resolutions of 1.5, 3, 6, and $12''$ respectively. These effective pixel sizes, however, neglect diffraction effects which can become very significant at longer wavelengths.

for a telescope with this small mirror size. The calculated diffraction limited resolution is $2''$ at $2.5\text{ }\mu\text{m}$, and $13.6''$ at $17\text{ }\mu\text{m}$.

Photo-polarimeter: ISOPHOT

The ISO imaging photo-polarimeter (PHOT) was composed of 3 subsystems optimized for specific photometric modes. These were: (1) PHT-P, a multi-band, multi-aperture photometer with three single detectors covering the wavelength range $3\text{--}120\text{ }\mu\text{m}$ from the near-IR to the far-IR; (2) PHT-C, two photometric far-IR cameras for the wavelength range $50\text{--}240\text{ }\mu\text{m}$; and (3) PHT-S, two grating spectrophotometers, operated simultaneously, for the wavelength ranges of about $2.5\text{--}5\text{ }\mu\text{m}$ and $6\text{--}12\text{ }\mu\text{m}$. In addition, ISOPHOT was equipped with two sets of three polarizers, one set for the PHT-P detector group and one for the PHT-C detectors, covering the whole wavelength region from 3 to $240\text{ }\mu\text{m}$, although during the mission polarization observations were actually only ever done at $25\text{ }\mu\text{m}$ and $170\text{ }\mu\text{m}$. The instrument design incorporated a number of design features to maximize the performance of the instrument including the fact that a range of apertures ($5''\text{--}180''$) could be selected to match the point spread function at each selected filter wavelength and thus optimize the source-to-background contrast.

Short-Wave Spectrometer: SWS

The ISO Short-Wavelength Spectrometer (SWS) provided medium- and high-spectral-resolution spectrometry in the wavelength region $2.4\text{--}45.2\text{ }\mu\text{m}$. It consisted of two largely independent grating spectrometers operating in the SW range of $2.4\text{--}12\text{ }\mu\text{m}$, and the LW range of $12\text{--}45\text{ }\mu\text{m}$, and had a spectral resolving power of $R = \lambda/\Delta\lambda \approx 1,000\text{--}2,000$. By inserting Fabry–Pérot (FP) interferometers into the beam, one for the range $11\text{--}26\text{ }\mu\text{m}$ and the other for the region $26\text{--}45\text{ }\mu\text{m}$, the spectral resolving power could be increased to $R \approx 30,000$.

The SW and LW parts of the spectrometer each had two sets, or blocks, of 12 detectors (photoconductive and photodiode), and by the switching in of different order-sorting filters each block recorded the spectrum in a ‘band’ of wavelengths covering approximately half of the SW and LW spectral ranges respectively when the gratings were scanned. Hence in grating mode, the SW and LW spectra are each made up of 24 individual sub-spectra from each of the 24 detectors which are then overlapped. In addition, the FP interferometers each had 2 double detectors (only one of each pair being used to gather valid data) giving a total of 52 detectors in all.

The aperture size of the spectrometer in grating mode was $14'' \times 20''$ for $\lambda < 12\text{ }\mu\text{m}$ (detector blocks 1 and 2), $14'' \times 27''$ or $20'' \times 27''$ (depending on order-sorting filter) for $\lambda > 12\text{ }\mu\text{m}$ in detector block 3, and $20'' \times 33''$ in detector block 4. In the FP mode, the aperture size was $10'' \times 39''$ for $\lambda < 26\text{ }\mu\text{m}$, and $17'' \times 40''$ for $\lambda > 26\text{ }\mu\text{m}$.

ISO/SWS recorded many spectra of the giant planets and averaged spectra are shown in Figure 7.23. For Uranus and Neptune, whose angular diameters are much less than the FOV, these are pure disc-averaged spectra. However, the spectra for

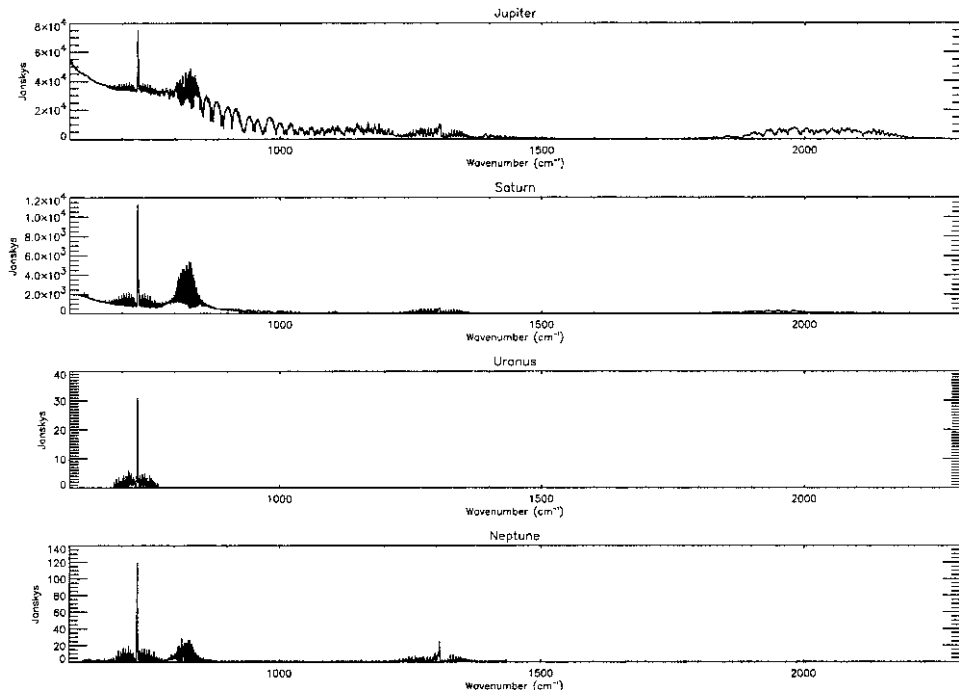


Figure 7.23 Disc-integrated irradiance spectra of the giant planets recorded by ISO/SWS measured in Janskys. In fact, the spectra for Jupiter and Saturn are not quite disc-averaged as is described in the text.

Courtesy of T. Encrenaz and T. Fouchet.

Saturn and Jupiter are not quite disc-averaged since Saturn's apparent diameter was comparable to the FOV, and Jupiter completely filled it. Although there are some gaps in the spectra as we go from Jupiter to Neptune, the spectra that were measured are in good agreement with the synthetic spectra shown in Figure 7.8 and in Chapter 6.

Long-Wave Spectrometer: LWS

The ISO Long-Wave Spectrometer (LWS) covered the long wavelength spectral range between 43 and 197 μm with a single grating operating in either 1st or 2nd order, and a block of ten order sorting filters and photoconductive detectors each covering approximately 1/10th of the total spectral range when the grating was scanned. Hence, like SWS, the spectrum recorded by LWS was composed of ten sub-spectra from the ten individual detectors which were then overlapped. The resolving power varied between $\lambda/\Delta\lambda = 150-200$ in the individual sub-spectra but, again like SWS, this could be greatly increased to $\lambda/\Delta\lambda = 6,800-9,700$ by the addition of one or two FP interferometers placed in the beam.

The aperture size of the instrument was set to be approximately equal to the diffraction-limited angular resolution of the ISO telescope at 200 μm , the longest

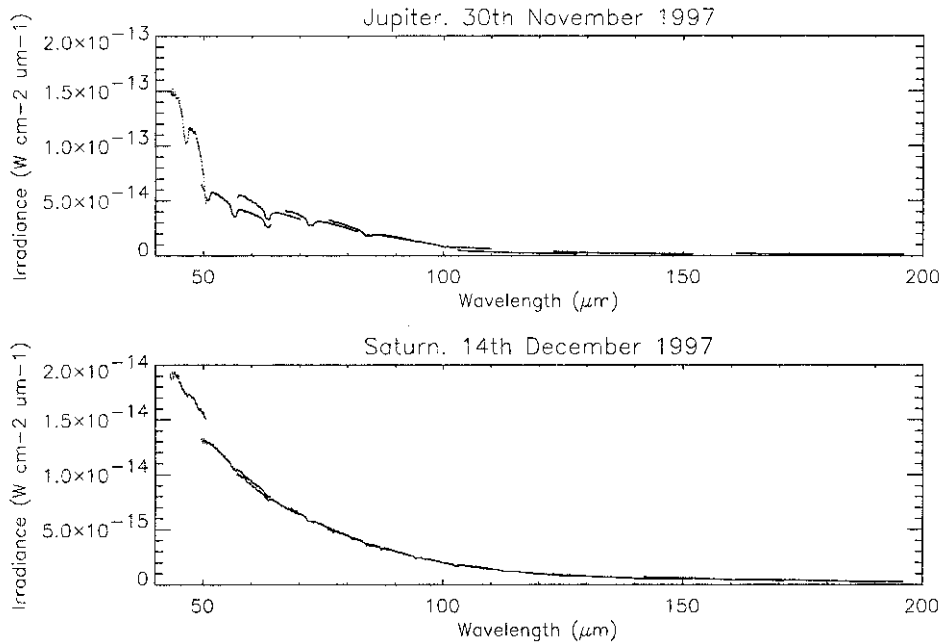


Figure 7.24 Disc-integrated irradiance spectra of Jupiter and Saturn recorded by ISO/LWS in units of $\text{W cm}^{-2} \mu\text{m}^{-1}$.

Courtesy of G. Davies, JAC, Hawaii.

operating wavelength of LWS, and during in-flight operation the FOV was observationally determined to be $80''$.

Observed disc-averaged LWS spectra of Jupiter and Saturn are shown in Figure 7.24. It proved in practice somewhat difficult to radiometrically calibrate this instrument, and thus the detector sub-spectra here do not overlap well. However, individual sub-spectra are correct relative to themselves and thus the depths of the ammonia absorption lines are reliable. The available LWS and SWS spectra of the giant planets have been combined in Figure 7.25 to give near-complete disc-averaged spectra. The gap between 16 and 45 μm which should nominally have been recorded by SWS was not reliably measured. The ISO instruments were designed primarily to observe very cold, distant astronomical objects and it was found that Jupiter SWS observations suffered saturation effects in this spectral range.

7.7.3 Submillimeter Wave Astronomy Satellite (SWAS)

The NASA SWAS was launched in 1998 on a two-year mission to observe mainly interstellar dust clouds at submillimetre wavelengths from 487–557 GHz (0.62 to 0.54 mm). The wavelength region was chosen to search for emission lines of water vapour and SWAS detected water in almost every dust cloud that it observed, a key

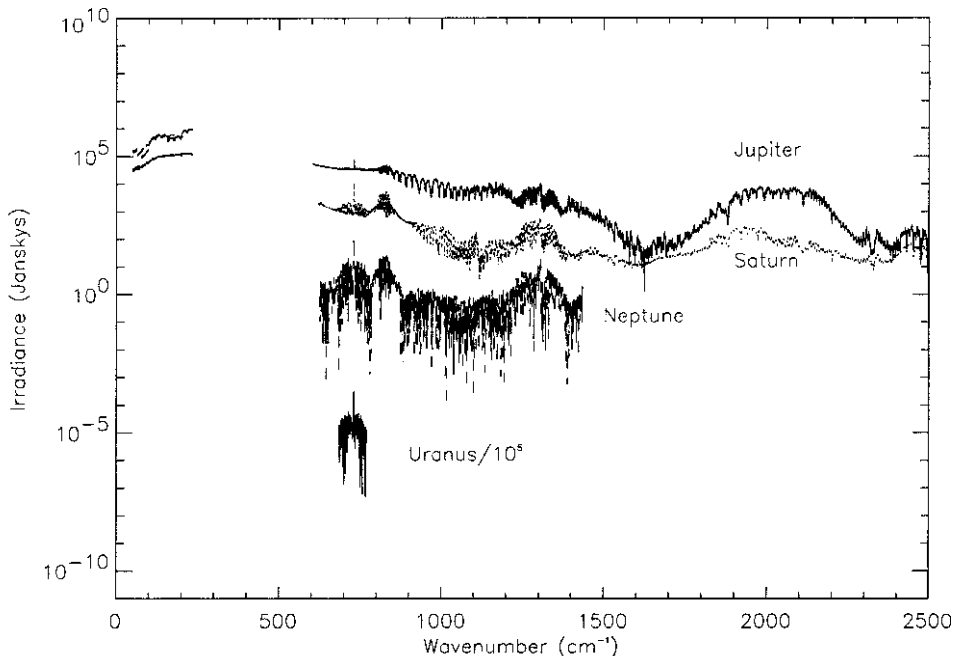


Figure 7.25 Disc-integrated irradiance spectra of the giant planets recorded by both ISO/SWS and ISO/LWS, plotted together on a log-scale. Jupiter: solid line, Saturn: dotted line, Uranus: dashed line, Neptune: dot-dashed line. The SWS Uranus spectrum has been divided by 10^5 in order to distinguish it from the SWS Neptune spectrum. The spectra can be seen to be in good agreement with the synthetic spectra shown previously in Figure 7.8.

indicator in the cooling process of these clouds that eventually leads to their collapse to form stars. In addition to these observations, SWAS also observed water vapour emission lines from Jupiter (Lellouch *et al.*, 2002).

SWAS was launched into a 600-km-altitude near-polar orbit. Its primary mirror was $0.68\text{ m} \times 0.58\text{ m}$ in size, and its total mass was 288 kg. Hence SWAS was a reasonably small spacecraft but provided a valuable precursor to future far-IR/submillimetre missions such as the Herschel Space Observatory.

7.8 FLYBY SPACECRAFT

While ground- and Earth-orbiting telescopes have recorded a wealth of information concerning the giant planets, the vast majority of what we know about these worlds comes from remote observations of flyby, and more recently, orbiting spacecraft. The advantages of spacecraft observations for understanding the atmospheres of the giant planets are enormous. By recording the strength of the radio signal from the spacecraft as it travels behind the planet (or emerges from behind), the number

density of molecules in the atmosphere may be almost directly determined, and using simple assumptions, the temperature–pressure profiles may be extracted with a high degree of precision. Such *radio-occultation* measurements have been made for all the giant planets and provide the bedrock of the models of atmospheric structure. Another advantage is that the spacecraft can get very close to the planets and thus record images at much higher spatial resolution than can usually be achieved from the ground, or indeed from Earth-orbit, especially for the more distant worlds of Neptune and Uranus. Reflectance and thermal emission spectra may be recorded either at high spatial resolution, allowing studies of the spatial variation of atmospheric constituents or, by averaging a large number of spectra or averaging over large solid angles, with high sensitivity at the expense of spatial resolution. In addition, these thermal emission spectra can be recorded at a wide range of emission angles, thus allowing for much better determination of the vertical profiles by increasing the vertical spread of the weighting functions. Similarly, reflectance spectra can be measured with a wide range of incident solar, and reflected zenith angles, which not only allows for much better vertical discrimination of cloud structure, but also allows for better estimates of the aerosol properties since the reflected intensity and polarization may be sampled over a wide range of phase angles (the angle between the incident, and reflected beams). By contrast, ground-based and Earth-orbiting telescope observations are limited to phase angles close to zero. A final advantage is that if the FOV of the instruments are small enough, limb-sounding may be performed which offers significant advantages in terms of vertical resolution, and enhanced sensitivity to trace species as we saw in Chapter 6.

A number of spacecraft have now visited the giant planets, each armed with a wide selection of remote sensing instruments which will now be reviewed. The angular resolution of these instruments is typically not as fine as that of terrestrial instruments, but since they are so much closer to their targets, both their spatial resolution and sensitivity are usually significantly better. In order to compare between the spatial resolutions quoted in the following sections and the terrestrial observations described previously, Table 7.4 converts the possible angular resolutions of terrestrial and space-based observatories to spatial resolution (at opposition) at the four giant planets. Table 7.5 converts a range of possible angular resolutions

Table 7.4. Spatial resolutions of terrestrial and earth-orbiting telescopes at the giant planets.

Angular resolution	Jupiter		Saturn		Uranus		Neptune	
	km	f_D	km	f_D	km	f_D	km	f_D
10''	30,460	0.213	61,650	0.511	132,000	2.582	211,057	4.261
1''	3,046	0.021	6,165	0.051	13,200	0.258	21,105	0.426
0.5''	1,523	0.011	3,082	0.026	6,600	0.129	10,552	0.213
0.1''	305	0.002	616	0.005	1,320	0.026	2,110	0.043

NB. f_D is the fraction of the disc covered by the spatial resolution.

Table 7.5. Conversion of angular resolution (in km) to spatial resolution as a function of distance.

Angular resolution	Distance (km)			
	25,000	75,000	750,000	1,500,000
10 µrad	0.25	0.75	7.5	15
0.5 mrad	12.5	37.5	375	750
1 mrad	25	75	750	1,500
10 mrad	250	750	7,500	15,000

for fly-by and orbiting spacecraft observations to spatial resolution, dependent on the distance from the target.

7.8.1 *Pioneer*

The first spacecraft to visit some of the giant planets were the *Pioneer 10* and *11* spacecraft managed by the NASA Ames Research Center. The spacecraft were designed as low cost, simple missions to demonstrate the viability of sending spacecraft through the Asteroid Belt to these planets, before more sophisticated and expensive spacecraft were flown (Figure 7.26). The spacecraft weigh 270 kg each and the diameter of the main radio dish is 2.7 m. The spacecraft are spin stabilized, spinning at 5 rpm and are powered by 4 radioisotope thermoelectric generators (RTGs), each of which provided 40 W power at launch.

Pioneer 10 was launched on 2 March 1972 and flew past Jupiter on 3 December 1973 at an altitude of only $1.82 R_J$ (130,354 km). It was then directed to the outer reaches of the Solar System and is now heading in the direction of the star Aldabaran as can be seen in Figure 7.27. *Pioneer 10* remained in radio contact until January 2003 and it may have been deflected in 1999 by an encounter with a Kuiper belt object. In addition, detailed tracking of the *Pioneer 10* spacecraft (and other spacecraft now at great distance from the Sun) has revealed a tiny unexplained acceleration towards the Sun. The nature of this mysterious anomaly has so far defied analysis and it has been conjectured that it may even indicate a small discrepancy in gravitational theory itself! As the mission has proceeded, the power generated by the RTGs has steadily fallen, partially because of the 92 year half-life of the Plutonium-238 isotope used, but mainly due to degradation of the thermocouple junctions which convert the heat to electricity. *Pioneer 10* is expected to run out of power sometime in the next 20 years.

Pioneer 11 was identical to *Pioneer 10* except that a Flux-Gate Magnetometer was also added. The spacecraft was launched on 5 April 1973 and flew past Jupiter on 2 December 1974 at an even lower altitude of $0.6 R_J$ (43,000 km). *Pioneer 11* arrived from south of Jupiter's equator and left from above, allowing imaging of Jupiter's North Polar Region. Its trajectory then took it across the Solar System to then fly past Saturn on 1 September 1979 at an altitude of $0.21 R_S$ (13,000 km). Since

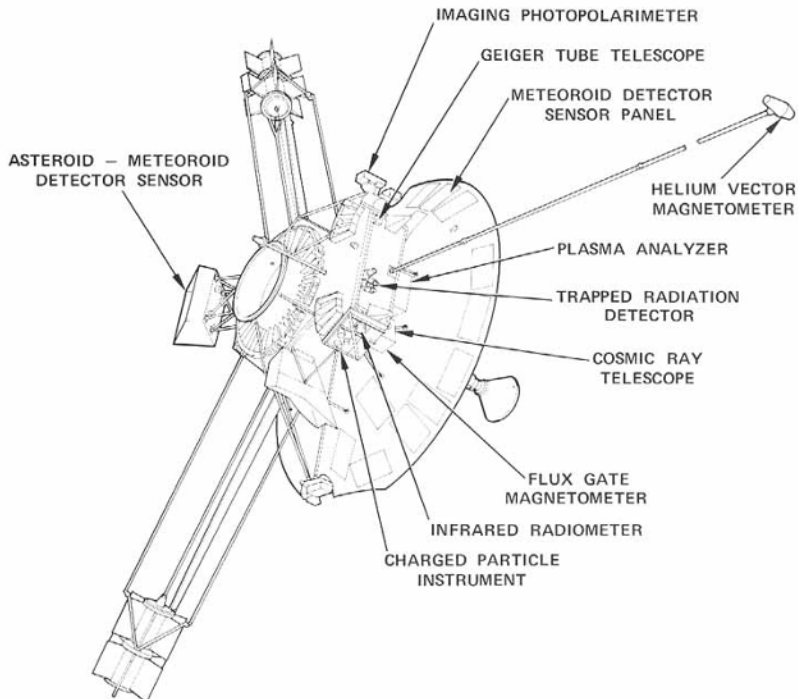


Figure 7.26 *Pioneer 10 and 11 spacecraft.*

Courtesy of NASA.

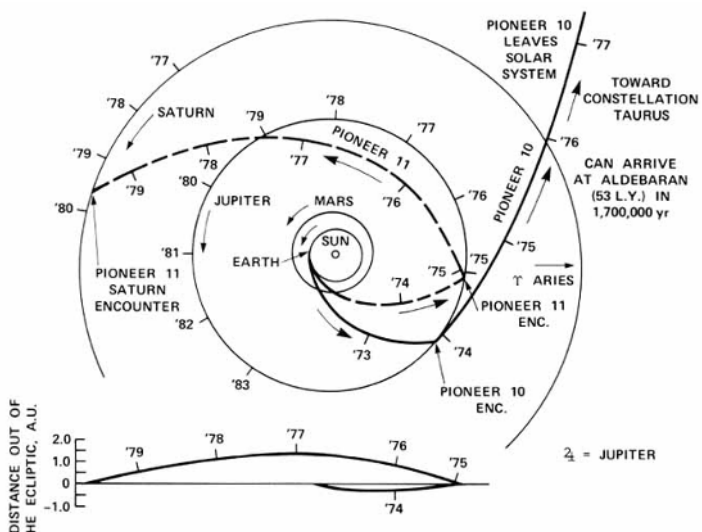


Figure 7.27 *Pioneer 10 and 11 trajectories.*

Courtesy of NASA.

then it has been heading out of the Solar System and contact with the spacecraft was lost in November 1995. It is not known if *Pioneer 11* is still transmitting.

Pioneer 10 and *11* both carried three remote sensing instruments useful for atmospheric studies: a UV photometer, an imaging photopolarimeter, and an IR radiometer.

UV photometer

This was a very simple, two-channel photometer which recorded the UV reflectivity of the giant planets at 1216 Å (Hydrogen- α) and 584 Å (Helium). The instrument made the first detection of Helium on Jupiter and enabled the first estimation of the H₂/He ratio.

Imaging photopolarimeter

The Imaging Photopolarimeter had a single 0.5 mrad FOV and used the spinning motion of the spacecraft to build up images. Each rotation of the spacecraft provided one line of the image, and a pointing mirror was then adjusted before the next line was recorded, and so on. The pointing mirror allowed the instrument to view at angles between 27° and 170° of the rotation axis. The Imaging Photopolarimeter could record images in two spectral channels: red (595–720 nm) and blue (390–500 nm), and could also determine the polarization of the light.

IR radiometer

The IR radiometer had a FOV of 17.4 × 5 mrad and had two channels covering the spectral ranges (14–25 μm) and (30–56 μm) respectively. Since both spectral regions are dominated by the collision-induced absorption of hydrogen and helium, temperature sounding was achieved by viewing a location on the planet at multiple emission angles, generating a range of weighting functions peaking at different altitudes.

7.8.2 Voyager

Once the *Pioneer 10* and *11* spacecraft had demonstrated that spacecraft missions to the giant planets were possible, and of high scientific interest, more sophisticated spacecraft were built. The *Voyager* spacecraft were managed by the NASA Jet Propulsion Laboratory (JPL) and were considerably larger, and more complex than *Pioneer 10* and *11* (Figure 7.28). The spacecraft weigh 825 kg each and the main communications dish is 3.7 m in diameter. The spacecraft are 3-axis stabilized and are powered by 3 RTGs which together generated 470 W at launch.

Voyager 1 was launched from Cape Canaveral on 5 September 1977 and flew past Jupiter on 5 March 1979 at an altitude of 2.9 R_J (206,700 km). The spacecraft then flew by Saturn on 12 November 1980 at an altitude of 1.1 R_S (64,200 km). The trajectory also provided *Voyager 1* with a close encounter with Titan. Subsequently, *Voyager 1* left the ecliptic plane and is now heading out to interstellar space at an

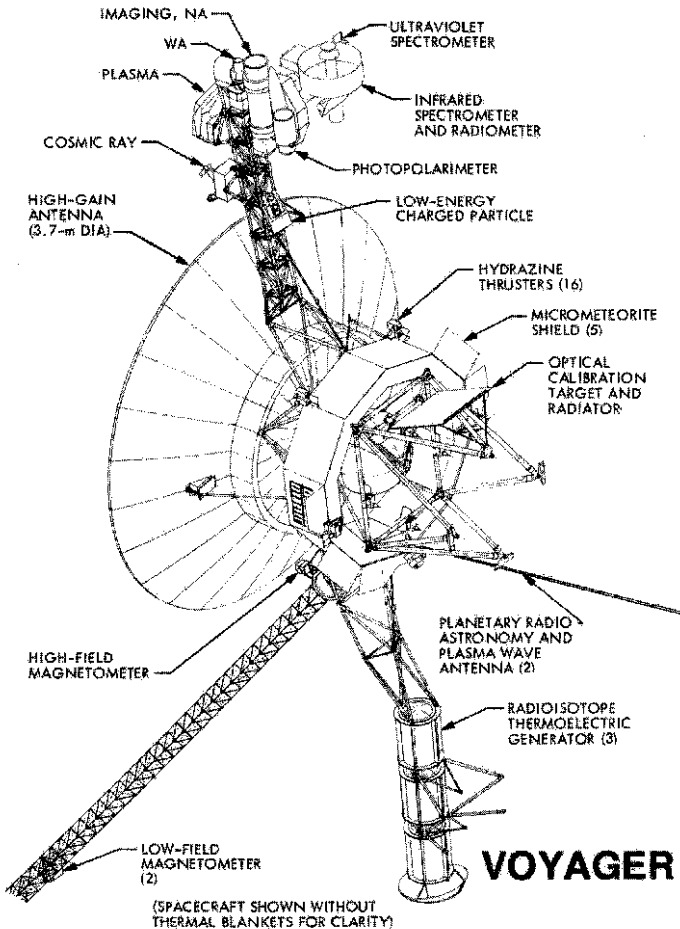


Figure 7.28 *Voyager 1* and *2* spacecraft.

Courtesy of NASA.

angle of 35° to that plane (Figure 7.29). On 17 February 1998, *Voyager 1* passed *Pioneer 10* to become the most distant man-made object in space (Figure 7.30).

Voyager 2 was actually launched before *Voyager 1* on 20 August 1977 from Cape Canaveral and subsequently made the ‘Grand Tour’ of all four giant planets. *Voyager 2* flew past Jupiter on 9 July 1979 at an altitude of $8 R_J$ (570,000 km) and then flew on to Saturn, which it passed on 25 August 1981 at an altitude of $0.7 R_S$ (41,000 km). The flyby of Uranus took place on 24 January 1986 at an altitude of $3.2 R_U$ (81,500 km) and *Voyager 2* made a very close flyby of Neptune on 25 August 1989 at an altitude of just $0.2 R_N$ (5,000 km). The resulting trajectory is taking *Voyager 2* south out of the ecliptic plane at an angle of 48° . Both spacecraft have sufficient power (currently ~ 315 W/spacecraft) and attitude control propellant to keep them operational until probably 2020.

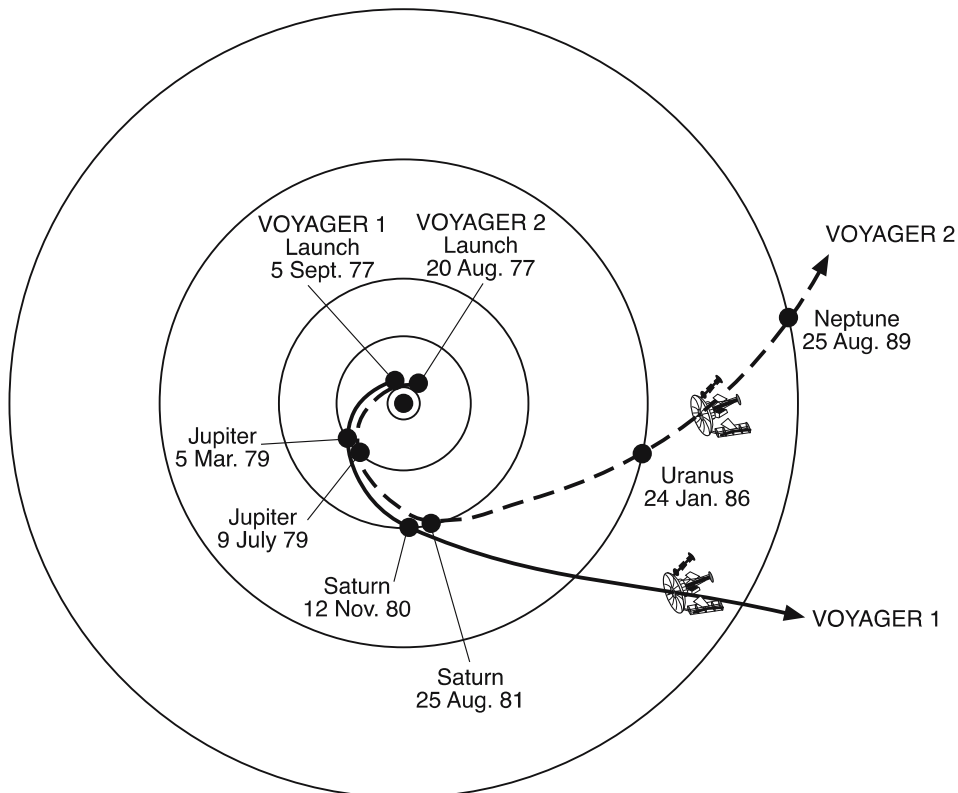


Figure 7.29 *Voyager 1* and *2* trajectories.

Courtesy of NASA.

The *Voyager* spacecraft carried 4 instruments of relevance to atmospheric remote sensing.

Imaging Science Subsystem (ISS)

The *Voyager* ISS consisted of a high-resolution narrow angle (NA) video camera, and a more sensitive, lower resolution wide angle (WA) camera. Each camera had an 800×800 detecting array and the FOV was 7.4×7.4 mrad for the narrow angle camera, and 55.31×55.31 mrad for the wide angle camera, giving pixel sizes of $10 \mu\text{rad}$ and $70 \mu\text{rad}$ respectively. Each camera was equipped with a set of 8 filters covering various wavelengths across the visible and UV.

Ultraviolet Spectrometer (UVS)

The UVS was a reflection diffraction grating spectrometer which dispersed the spectrum from 50 to 170 nm onto an array of 128 adjacent detectors. Hence the spectral resolution of the instrument was 1 nm. The instrument had two fields of

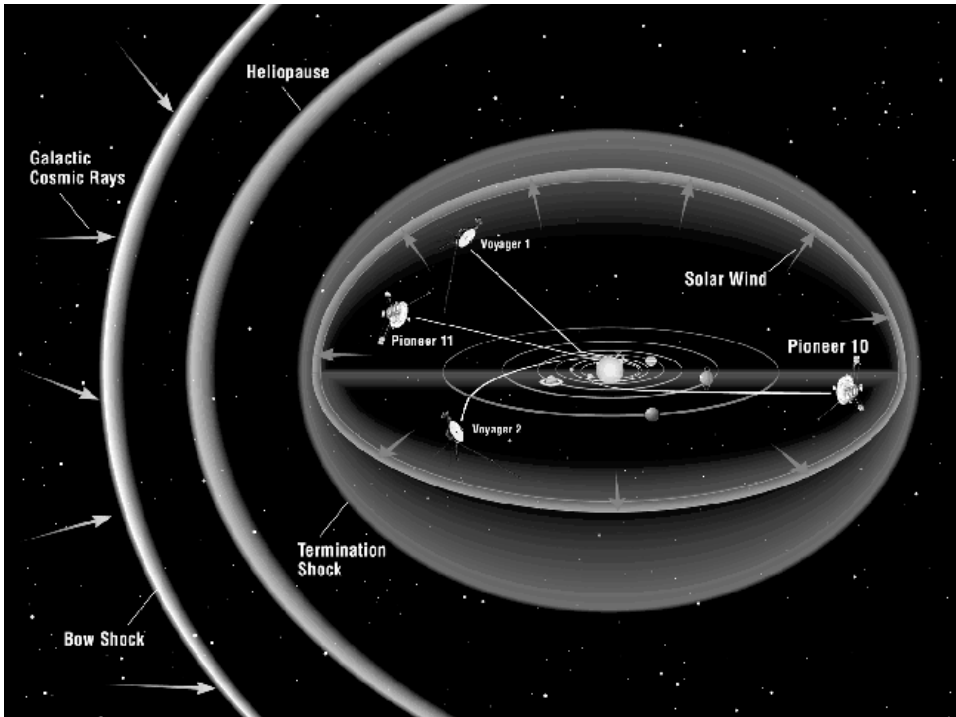


Figure 7.30 Current position of *Pioneer* and *Voyager* spacecraft.

Courtesy of NASA.

view: (1) 1.7×15 mrad boresighted with the camera (ISS); and (2) 4.4×15 mrad offset from the boresight by 20° .

Photopolarimeter Subsystem (PPS)

The PPS was a photoelectric photometer and used a 15-cm telescope and a set of 8 filters between 235 and 750 nm, 8 polarizers, and 4 field stop apertures, each located on a separate wheel to allow any combination of filter, polarizer, and field stop. The allowed FOVs had diameters of 2.1, 5.8, 17, and 61 mrad respectively.

Infrared Interferometer Spectrometer (IRIS)

The IRIS comprised two instruments sharing a single large aperture telescope system and is shown in Figure 7.31. The large primary mirror of diameter 0.5 m was needed to record the extremely low thermal emission and reflected flux from the more distant giant planets. Short wave radiation ($0.3\text{--}2\,\mu\text{m}$) was monitored by a simple radiometer utilizing a thermopile detector, while the longer wavelength radiation passed to a Michelson interferometer which recorded the IR spectrum from 180 to $2500\,\text{cm}^{-1}$ at a spectral resolution of up to $4.3\,\text{cm}^{-1}$. Both halves of the instruments shared the same 4.4-mrad diameter circular FOV, which was boresighted with the

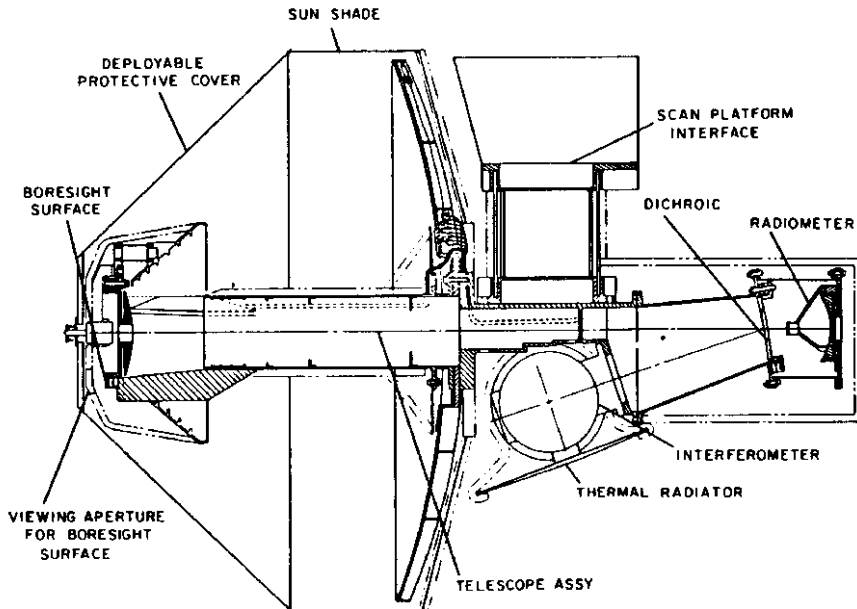


Figure 7.31 *Voyager/IRIS* instrument.

Courtesy of NASA.

ISS camera system. The mean nadir spectra of the giant planets recorded by IRIS are shown in Figures 7.32 and 7.33 and have yielded a wealth of information on the temperature and composition of these planets' atmospheres.

7.8.3 *Ulysses*

The *Ulysses* spacecraft was built by ESA and was not intended for planetary observations. However, it did record data covering fields and particles about Jupiter in the early 1990s and so is included here for completeness. *Ulysses* was launched on 6 October 1990 by the space shuttle *Discovery* (STS-41). Its mission was to observe the magnetic field and plasma environment in the solar wind from above the poles of the Sun. To achieve this viewing position, *Ulysses* flew first to Jupiter and made a gravity assist flyby manoeuvre on 8 February 1992 which placed it into a high-inclination, highly eccentric orbit about the Sun. It passed over the Sun's South Pole in 1994 and then its North Pole in 1995. The most recent passes over the Sun's South and North Poles took place in 2000 and 2001 respectively. The spacecraft is still operating.

7.9 ORBITING SPACECRAFT

7.9.1 *Galileo*

The *Galileo* mission to Jupiter was the first space mission designed to place a spacecraft in orbit about a giant planet, and also the first space mission to deploy an entry

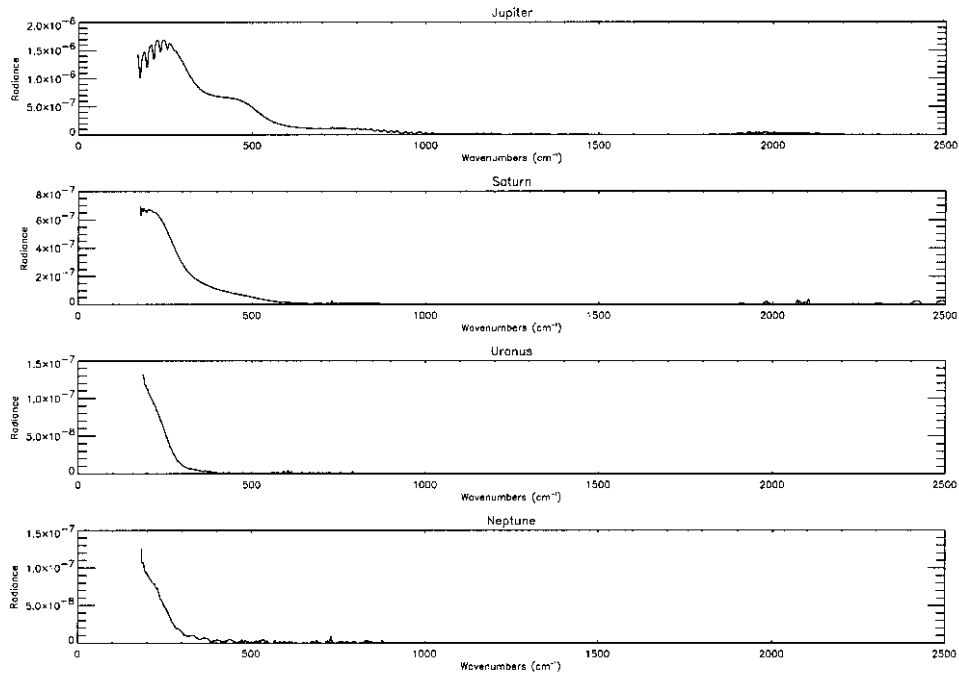


Figure 7.32 Voyager/IRIS radiance spectra of the giant planets (in units of $\text{W cm}^{-2} \text{sr}^{-1} (\text{cm}^{-1})^{-1}$). Averages of all spectra with emission angle less than 20° .

probe directly into the atmosphere of such a planet. The *Galileo* spacecraft, managed by JPL, was a huge structure with a mass of 2,223 kg and was over 6 m tall (Figure 7.34). The spacecraft used a novel ‘dual-spin’ design with a top section, incorporating the communications systems, booms, and other systems, spinning at 3 rpm and a lower three-axis stabilized section, upon which the remote sensing instruments were placed on a pointable platform allowing them to stop and look in almost any direction. The *Galileo* entry probe was stowed at the bottom of the spacecraft until it was deployed on approach to Jupiter. The spacecraft is named after Galileo Galilei (1564–1642) who first observed Jupiter’s major moons: Io, Europa, Ganymede, and Callisto, now known as the Galilean satellites, in January 1610.

The spacecraft was launched on 18 October 1989 from Cape Canaveral onboard the space shuttle *Atlantis*, and embarked upon an extended Venus–Earth–Earth–Gravity–Assist (VEEGA) trajectory to Jupiter as shown in Figure 7.35, before going into orbit about that planet on 7 December 1995. Six months prior to its arrival, the probe was deployed, proceeding purely under its own momentum and the pull of Jupiter’s gravity, before entering the atmosphere just prior to the entry of the main part of the spacecraft into Jupiter orbit.

The orbital design of *Galileo*’s tour primary is shown in Figure 7.36. The distance at each perijove was typically $15 R_J$. The high eccentricity of the orbits allowed *Galileo* to not only pass close to Jupiter on each revolution, but also to

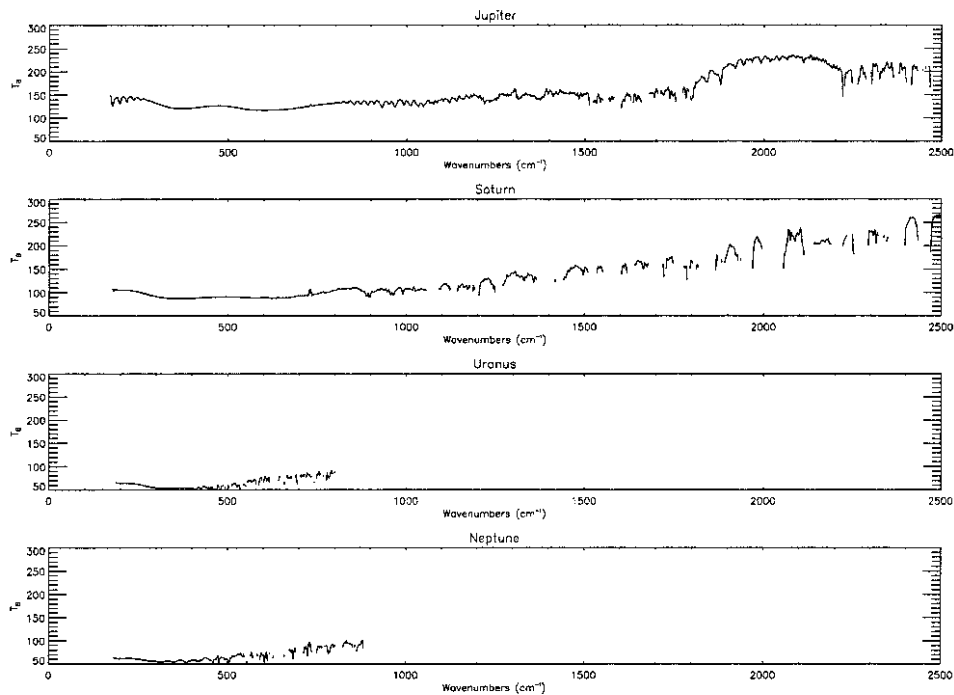


Figure 7.33 *Voyager/IRIS* average spectra of the giant planets expressed as brightness temperatures.

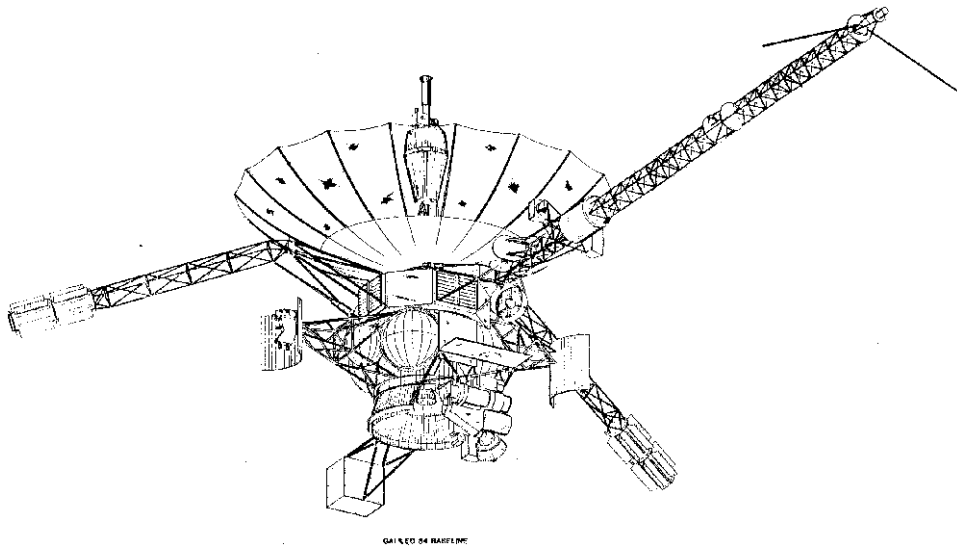


Figure 7.34 *Galileo* spacecraft.

Courtesy of NASA.

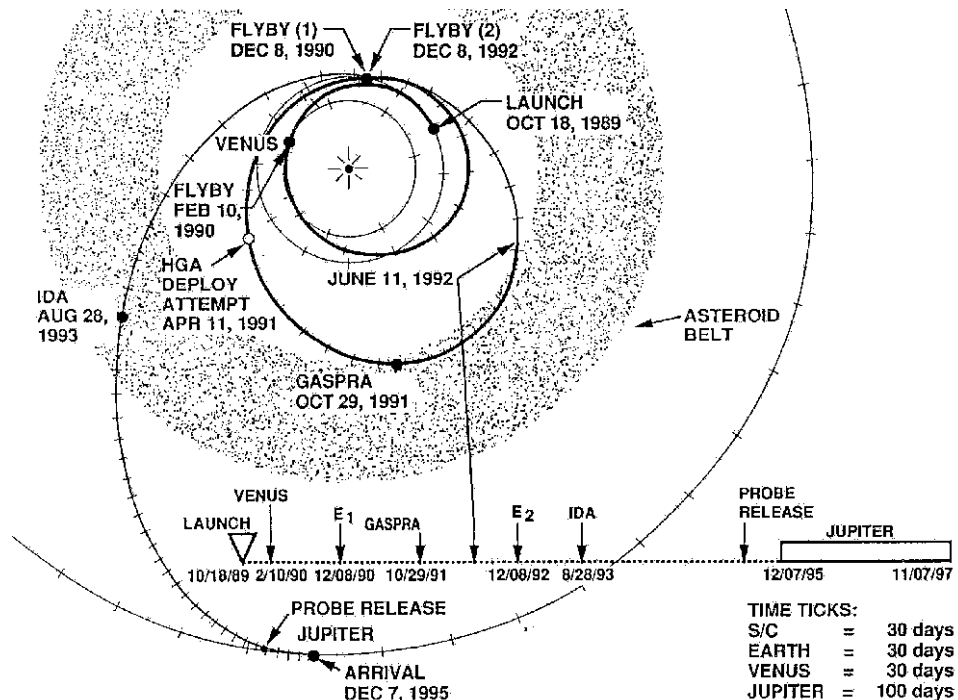


Figure 7.35 Galileo interplanetary trajectory.

Courtesy of NASA.

pass close by one of the four Galilean satellites either on the inward or outward legs. The orbital design also minimized the time that *Galileo* spent close to Jupiter, and thus within its highly energetic and damaging radiation belts. The orbital design however had a further, unforeseen and wholly serendipitous advantage. The main communications High Gain Antenna (HGA) of *Galileo* had a novel, lightweight, deployable design, rather like an umbrella. Unfortunately when this was commanded to open some time after launch, it became stuck and could not subsequently be moved. This meant that *Galileo* had to communicate with Earth via its much smaller low gain antenna which, at Jupiter's distance from Earth, limited the communication speed to initially only 10 bits/second! It was feared that this would greatly reduce the amount of data that could be returned and thus the scientific value of the mission. However, since each orbit lasted approximately two months, and encounters with Jupiter and the satellites took only a few days, the spacecraft was comparatively idle for most of the time. Hence data was recorded onto an onboard tape recorder during each encounter and then subsequently 'trickled' back to Earth on the relatively inactive parts of the orbit at the low data rate. This solution, together with the use of sophisticated data compression techniques and improvements in the Deep Space Network receiving stations meant that the *Galileo* mission achieved scientifically almost everything it set out to achieve.

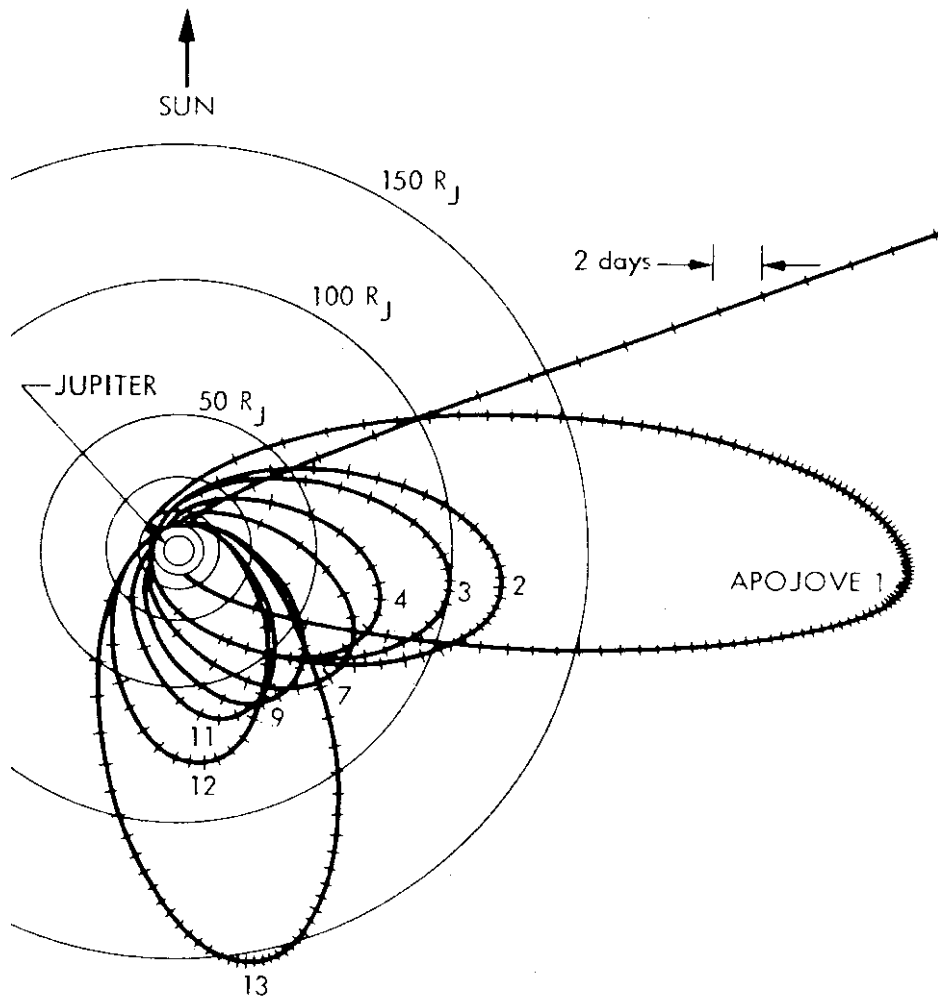


Figure 7.36 *Galileo* prime mission orbital design.

Courtesy of NASA.

The *Galileo* orbiter operated for many years longer than was originally planned. However, the spacecraft and its instruments gradually became more and more damaged by particle impacts from passing through Jupiter's radiation belts, and the spacecraft slowly ran out of attitude-control fuel. Hence, it was finally decided to terminate the mission by crashing the spacecraft into Jupiter's atmosphere where it burned-up and vaporized in September 2003. The advantage of destroying *Galileo* in this way rather than leaving it in orbit about Jupiter was to avoid collision with the Galilean satellites and thus contamination of those worlds with any organic matter. This is of particular importance with respect to Europa, which is believed

to have a substantial salty ocean beneath its icy crust and could thus, as some researchers suggest, have possibly evolved its own forms of life!

The *Galileo* orbiter had four remote sensing instruments suitable for atmospheric study placed on its remote sensing platform and a further instrument mounted on the spinning section which will now be reviewed, together with the probe mission.

Solid State Imaging (SSI)

The SSI used a 17.6 cm Cassegrain telescope to form an image on a 800×800 pixel solid-state CCD array. The harsh nature of Jupiter's radiation belt meant that this CCD array had to be shielded by a 1 cm thick shroud of tantalum. The device contained an eight-position filter wheel which had narrow-band filters covering various wavelengths between 400 and 1100 nm. The central filter wavelengths were: 611, 404, 559, 671, 734, 756, 887, and 986 nm and the overall FOV of the camera was 8.1×8.1 mrad, which converts to $10.16 \times 10.16 \mu\text{rad}/\text{pixel}$. Both the optical system and the filter wheel were inherited from the *Voyager*/ISS narrow angle camera. At closest approach the spatial resolution was 11 km.

Ultraviolet Spectrometer (UVS) and Extreme Ultraviolet Spectrometer (EUV)

Galileo carried two instruments for measuring UV radiation, the UVS and the EUV. The UVS was mounted on the scan platform and could thus be freely pointed. The EUV however, was on the spun-section and thus observed only a narrow ribbon of space perpendicular to the spin axis.

The UVS was a grating spectrometer utilizing a 25-cm-diameter Cassegrain telescope. There were three photomultiplier detectors which, by scanning the grating, covered the spectral ranges of 113 to 192 nm, 282 to 432 nm, and 162 to 323 nm respectively, at a spectral resolution of 0.7 nm below 190 nm and 1.3 nm above. The FOV was 17.4×1.7 mrad ($1 \times 0.1^\circ$) for the first two detectors, and 7×1.7 mrad ($0.4 \times 0.1^\circ$) for the third detector.

The EUV also had a 25-cm-aperture telescope system, but had a fixed grating and array of 128 contiguous detecting elements. Hence the design was very similar to the *Voyager* UVS. The spectral range is 54–128 nm and thus each detector had a theoretical resolution of 0.59 nm. However, other instrumental effects meant that the resolution was 3.5 nm for extended sources and 1.5 nm for point sources. The instrument FOV was 3×15 mrad ($0.17 \times 0.87^\circ$).

Photopolarimeter Radiometer (PPR)

The PPR used a 10-cm-aperture Cassegrain telescope to observe a 2.5-mrad-diameter circular FOV in a number of photometric, polarimetric, and radiometric channels. Polarimetry was done in three spectral channels at 410, 678, and 945 nm, while photometry was done in 7 narrowband channels at 619, 633, 648, 789, 829, 840, and 892 nm, which covered various important methane and ammonia absorption features. PPR also had seven radiometry bands. One of these used no filters and

observed all the radiation, both solar and thermal, while another let only solar radiation through (i.e., wavelengths less than $4\text{ }\mu\text{m}$). The difference between the solar-plus-thermal and the solar-only channels gave the total thermal radiation emitted. Five further broadband channels were included at 17, 21, 27, 36, and $>42\text{ }\mu\text{m}$. Unfortunately, for a substantial part of the mission the PPR filter wheel became stuck which somewhat limited the data return from this instrument.

Near-IR Mapping Spectrometer (NIMS)

The NIMS was a single grating spectrometer utilizing a 22.8-cm mirror telescope system (Figure 7.37). Light diffracted from the grating was focused onto an array of 15 InSb detectors cooled to 64 K by passive radiative cooler, each covering just over 1/15th of the spectral range $1\text{--}5.2\text{ }\mu\text{m}$ (in 1st order), and two Si detectors covering the sub-micron range $0.7\text{--}1\text{ }\mu\text{m}$ (in 2nd order). The spectral resolution was $0.0125\text{ }\mu\text{m}$ below $1\text{ }\mu\text{m}$, and $0.025\text{ }\mu\text{m}$ above. The angular resolution was $0.5 \times 0.5\text{ mrad}$ corresponding to approximately $500 \times 500\text{ km}$ at perijove.

A spectrum was constructed by scanning the grating over a small angular range such that 17 sub-spectra are recorded by the individual detectors which were then overlapped. In addition to the grating scan, the secondary mirror of the telescope could also be scanned over 20 contiguous positions in the cross-dispersion direction. Hence by scanning the grating for each mirror position, a single line of a spectral image could be constructed with 20 individual spectra of 408 wavelengths (24 grating steps \times 17 detectors). To record an image, the whole instrument was simultaneously

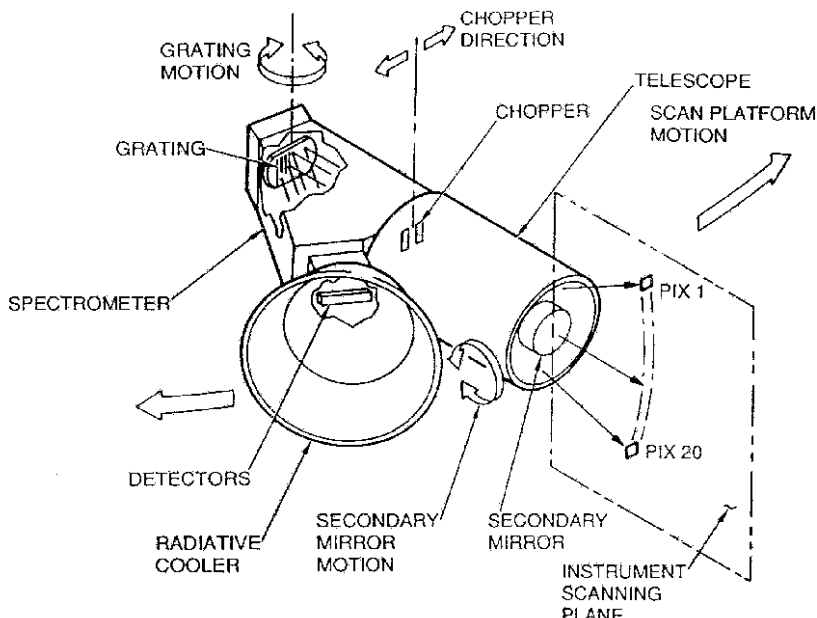


Figure 7.37 Near-IR Mapping Spectrometer (NIMS).

Courtesy of NASA.

scanned by the remote sensing platform in the grating dispersion direction, as is shown in Figure 7.37, building up an image with 20 rows (secondary mirror scan) \times a variable number of columns (remote sensing platform scan) \times up to 408 wavelengths (grating scan). The format of the NIMS data were thus referred to as ‘cubes’ composed of a number of two-dimensional images recorded at multiple wavelengths. In practice, the instrument could be operated with a variable number of grating steps, and to reduce data volume not all detectors were read during a particular observation. The instrument could thus very flexibly trade-off between spatial and spectral coverage. This was particularly fortunate given *Galileo*’s communications difficulties and meant that NIMS could adapt to fit in with whatever observation time/data storage was available.

Galileo entry probe

The 340 kg *Galileo* entry probe entered the atmosphere of Jupiter on 7 December 1995 at a speed of 170,000 km hr⁻¹ and at a shallow entry angle as shown in Figure 7.38. The probe was ‘aero-captured’ by Jupiter’s atmosphere (experiencing a maximum deceleration of 230 g), and once it had slowed sufficiently, its heat shield

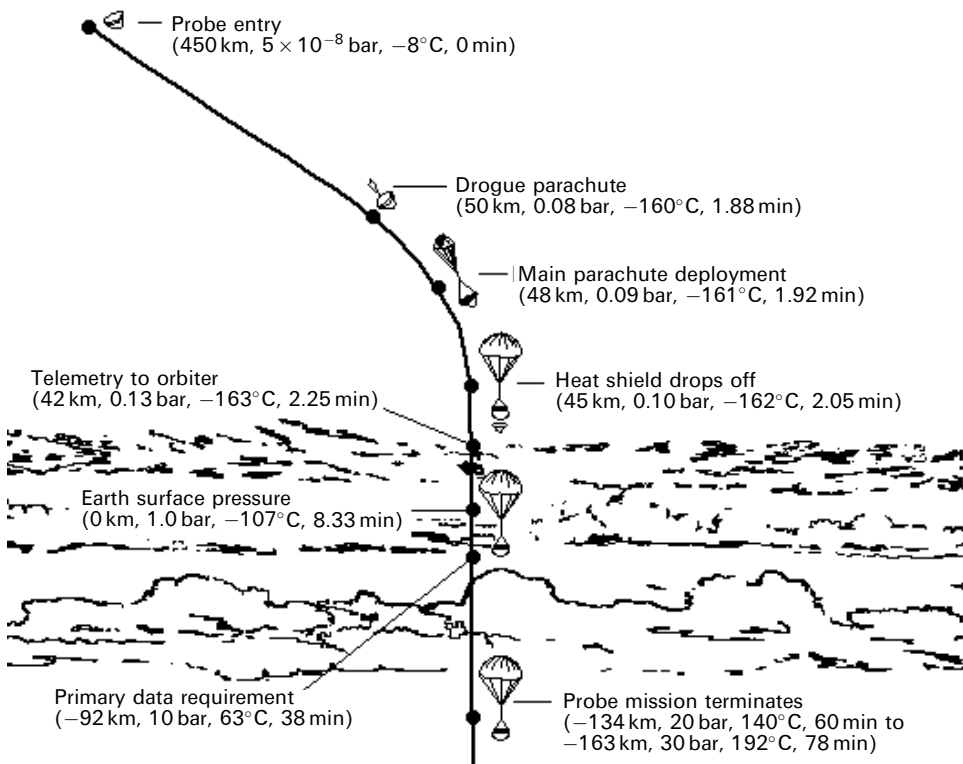


Figure 7.38 *Galileo* probe descent trajectory.

Courtesy of NASA.

was jettisoned, a parachute deployed, and the probe then descended slowly down through the atmosphere recording information with several instruments on the way. Instruments included a particle nephelometer (Ragent *et al.*, 1998), a mass spectrometer (Niemann *et al.*, 1998), a net flux radiometer (Sromovsky *et al.*, 1998), and a host of thermometers and accelerometers to record vertical structure (Seiff *et al.*, 1998). In addition to the *in situ* observations, the probe signal was also tracked from the orbiter, and the Doppler shifting of the signal used to deduce the horizontal winds speeds down to depths of nearly 20 bar, and the strength of the signal used to determine the deep NH₃ abundance.

The probe collected data for 58 minutes as it descended through Jupiter's atmosphere, with the transmission terminating at a pressure level of \sim 20 bar. The findings of the probe have already been discussed in Chapters 4 and 5, and the probe data is the only 'ground truth' we have for conditions in the Jovian atmosphere. However, as discussed previously, it was somewhat unfortunate that the probe entered the atmosphere at a rather unrepresentative 5- μ m hotspot region and it would be highly desirable to fly further multiple probe missions to explore other regions.

7.9.2 Cassini/Huygens

Cassini/Huygens is the first space mission dedicated to the study of the Saturnian system. *Cassini* is a NASA-led spacecraft designed to orbit Saturn and observe the planet and its moons with a range of remote sensing instruments. The *Cassini* orbiter is named after Jean-Dominique Cassini (1625–1712) who made many early observations of Saturn, and discovered the major gap in its ring system now known as the Cassini division. *Cassini* also carried an ESA-led entry probe called *Huygens* which parachuted through, and directly sampled, the atmosphere of Titan in January 2005. *Huygens* was named after Christiaan Huygens (1629–1695) who discovered Titan in 1655.

The *Cassini* spacecraft was launched from Cape Canaveral on 15 October 1997 by a *Titan IV* launcher into a similar multiple-gravity-assist trajectory (Venus–Venus–Earth–Jupiter–Gravity-Assist [VVEJGA]) taken by the *Galileo* spacecraft (Figure 7.39). The spacecraft flew past Jupiter on 30 December 2000 at a distance of 136 R_J (9,700,000 km), and went into orbit about Saturn in July, 2004. During *Cassini*'s flyby of Jupiter, its remote sensing instruments were activated to record a huge amount of information regarding the Jupiter satellites and Jupiter's atmosphere. During this 'Millennium Mission' data were also simultaneously recorded by the *Galileo* spacecraft, already in orbit, and the combined data from two different positions has proved to be very useful for studies of the magnetic field and the particle environment.

The *Cassini* spacecraft is a truly huge three-axis stabilized spacecraft. It stands over 6.7 m tall (Figure 7.40), weighs 2,175 kg, and has a HGA with a diameter of 4 m. The spacecraft is powered by three RTGs developing a total of 630 W. Unlike *Voyager* and *Galileo*, for financial reasons there is no pointable remote sensing platform. Instead the remote sensing instruments are hard-bolted onto the side of the spacecraft and pointing is achieved mainly by using the attitude control system of

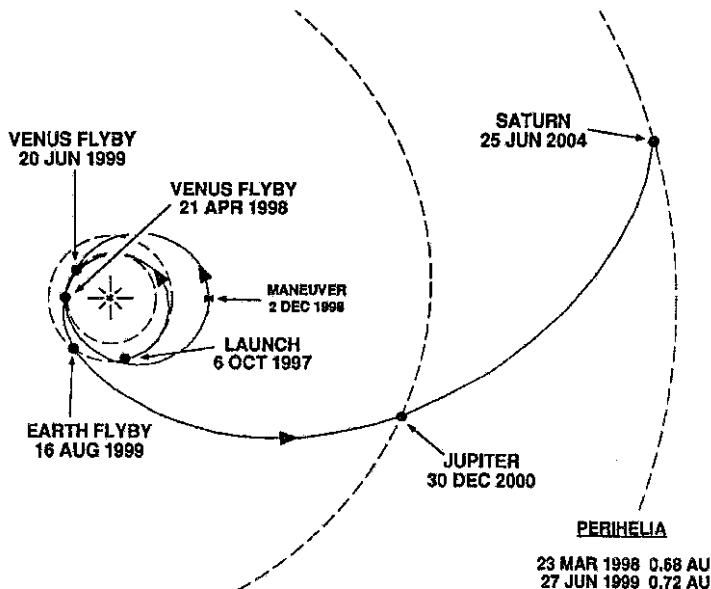


Figure 7.39 Cassini interplanetary trajectory.

Courtesy of NASA.

the spacecraft. Hence during observations the HGA may not point at earth and thus data recorded are temporarily stored on a solid-state recorder until such time as wide-band communications with the spacecraft are re-established and the data can be relayed to Earth. *Cassini* comprises a number of remote sensing instruments.

Imaging Science Subsystem (ISS)

The *Cassini* ISS includes a narrow angle camera (NAC) and a wide angle camera (WAC), each focusing images onto a 1024×1024 CCD array. The WAC FOV is 61×61 mrad (60×60 μ rads per pixel) and the NAC FOV is 6.1×6.1 mrad (6×6 μ rads per pixel). The WAC has 18 filters between 380 and 1100 nm, and the NAC has 24 filters between 200 and 1100 nm. The CCD arrays are cooled to 180 K by a passive radiative cooler to improve the signal-to-noise ratio.

Ultraviolet Imaging Spectrograph (UVIS)

The *Cassini* UVIS has two main channels: the extreme ultraviolet channel (EUV) and the far ultraviolet channel (FUV), together with a high-speed photometer channel and a hydrogen-deuterium absorption cell channel.

The EUV and FUV channels are of similar construction and use a grating to form a spectrum on to a 60×1024 array of detecting elements with the 1024 element dimension in the spectral direction. The EUV records from 55.8 to 118 nm, and the FUV from 110 to 190 nm. In addition, the FOV has three settings for each spectrograph: $(1, 2, 6) \times 64$ mrad for the EUV and $(0.75, 1.5, 6) \times 64$ mrad for the FUV.

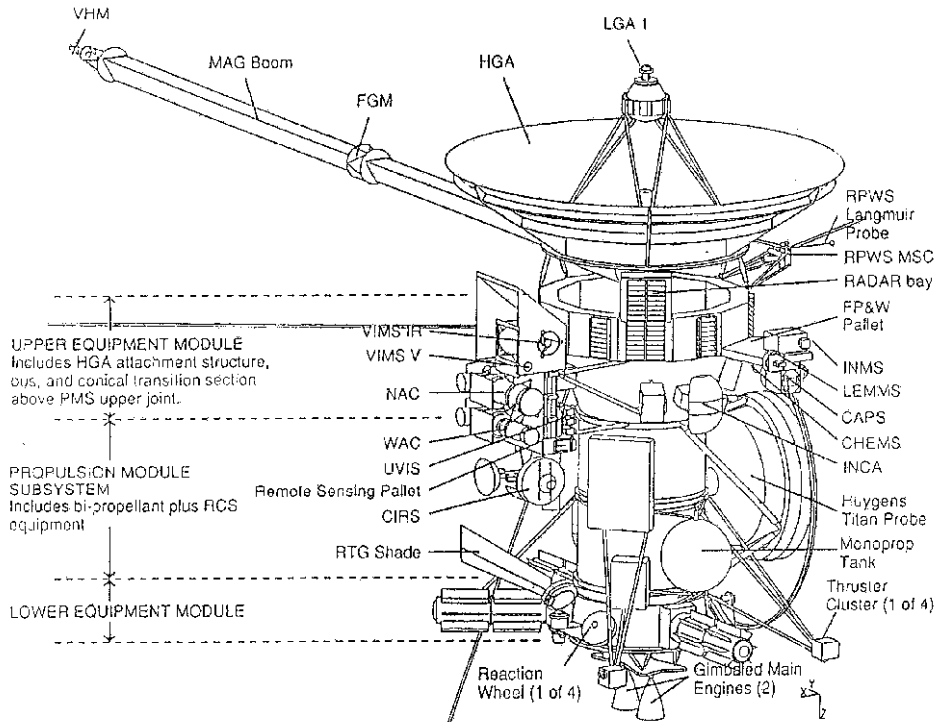


Figure 7.40 Cassini spacecraft.

Courtesy of NASA.

The photometer channel is a wideband channel recording between 115 and 185 nm, with a FOV of 6×6 mrad and an integration time of 2 msec. It is designed to perform stellar occultation measurements of Saturn's ring system. The hydrogen-deuterium absorption channel will view the Saturnian system through onboard hydrogen, deuterium, and oxygen gas absorption cells to measure the abundances of hydrogen and deuterium.

Visible and Infrared Mapping Spectrometer (VIMS)

The VIMS is a development of the NIMS instrument flown on *Galileo*. It actually consists of two instruments: a visible channel (VIMS-V) recording the spectrum in 96 channels between 0.35 and 1.07 μm , and an IR channel (VIMS-IR) recording the spectrum in 256 channels between 0.85 and 5.1 μm . The FOV of both channels is 32×32 mrad and both focal planes are cooled by a passive radiative cooler to 190 K for VIMS-V and as low as 56 K for VIMS-IR.

In the visible section (VIMS-V), light collected by a 4.5-cm Shafer telescope is dispersed by a holographic grating onto a 256×512 silicon CCD array. The data are averaged into 96 spectral channels and 64 cross-dispersion pixels giving a pixel size of 0.5 mrad. Imaging is then achieved by a single-axis scanning mirror.

The IR section (VIMS-IR) consists of a 23-cm Cassegrain telescope and a linear array of 256 cooled InSb detectors. During the time VIMS-V makes an exposure, VIMS-IR must record 64 individual spectra by stepping its two-axis scan mirror in the cross-dispersion direction which, together with the fact that the reflected radiance of Jupiter decreases with wavelength, is why the entrance aperture of VIMS-IR has to be so much larger. Imaging is then achieved by stepping the scan mirror in the dispersion direction in the same way as VIMS-V.

Composite Infrared Spectrometer (CIRS)

The CIRS is a development of the IRIS spectrometers flown on *Voyagers 1* and *2* (Calcutt *et al.*, 1992). Light is gathered by a 50-cm telescope and fed to two interferometers, one working in the mid-IR range from $600\text{--}1400\text{ cm}^{-1}$ and the other operating in the far-IR from $10\text{--}600\text{ cm}^{-1}$ (Figure 7.41). Both sections share the same mirror drive assembly and the maximum path difference that can be introduced is 2 cm. Hence the spectral resolution is a maximum of 0.5 cm^{-1} which is almost a factor of ten better than that achieved by *Voyager* IRIS. In addition, the mid-IR detectors are cooled to 80 K by a passive radiative cooler which gives them much higher sensitivity than the IRIS detectors.

The mid-IR section is itself split into two parts. The spectrum from $600\text{--}1100\text{ cm}^{-1}$ is recorded by the FP3 array of ten mercury–cadmium–telluride (HgCdTe) detectors of 0.273×0.273 mrad FOV arranged as shown in Figure 7.42. Similarly the spectrum from $1100\text{--}1400\text{ cm}^{-1}$ is recorded by the FP4 array, of similar fabrication and FOV. The mirror system of the mid-IR interferometer utilizes corner-cube reflectors, and the far-IR interferometer uses rooftop reflectors to make the combined spectrometer more rugged and less prone to misalignment.

The far-IR section uses a polarizing interferometer and a pair of bolometer detectors. The polarizing beamsplitter and polarizing plates are formed from finely etched metal grids, and the use of polarization grids allows for the cancellation of the offset term in the interferogram (Equation 7.6) by subtracting the signals recorded by the detector pair. This makes the spectrometer far less susceptible to instrumental drifts and increases the measurement precision. The far-IR FOV is 4.3 mrad in diameter, just like *Voyager* IRIS.

7.10 RETRIEVALS

We have seen in Chapter 6 how the electromagnetic spectra of the planets have many absorption and reflection features which are unique to particular constituents. Using measured and estimated absorption coefficients, and assumed atmospheric profiles of temperature, cloud, and composition, radiative transfer models may be constructed which can simulate the spectrum of a planet as seen from the Earth or a passing spacecraft. These synthetic spectra may then be compared to measured spectra and any differences interpreted in terms of how much we need to modify the assumed profiles in order to achieve the best possible fit between the two. This is the essence of

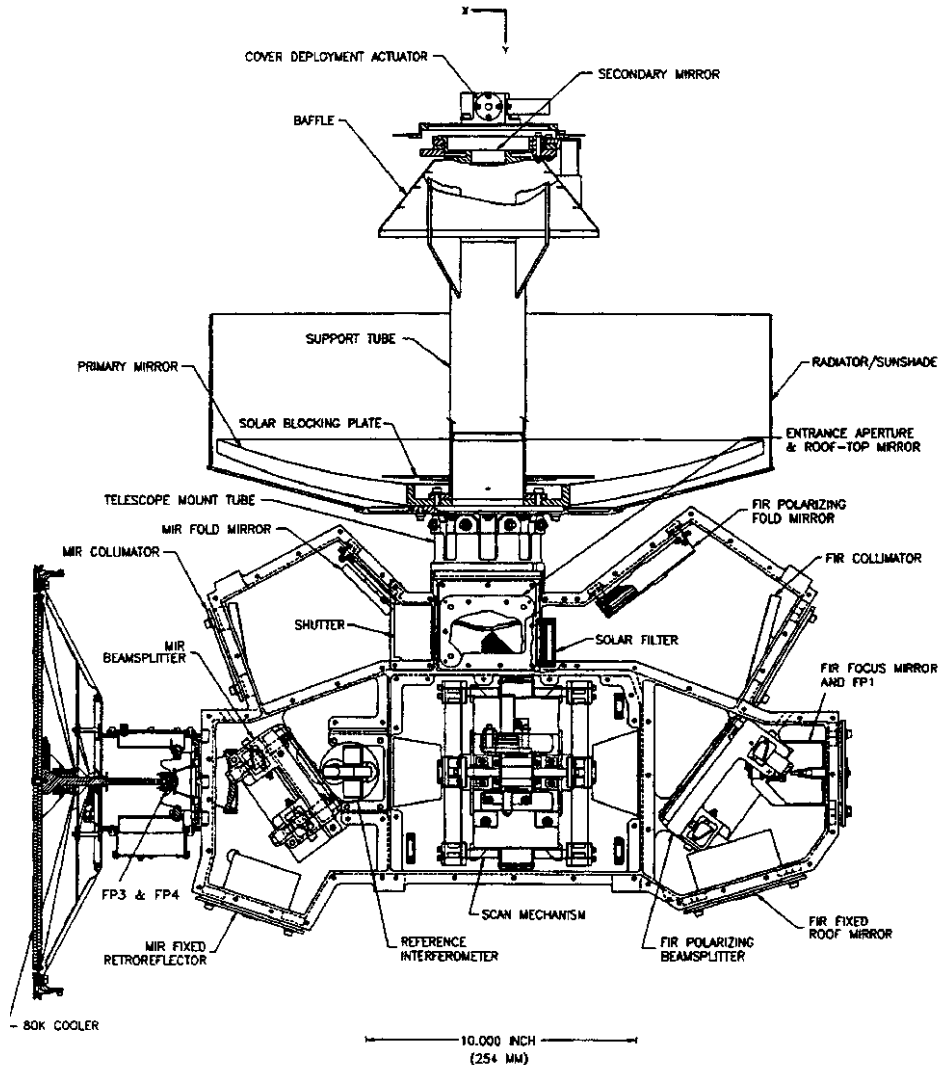


Figure 7.41 CIRS instrument. The mid-IR section is to the left and is cooled by the passive radiative cooler. The far-IR polarizing interferometer is to the right.

Courtesy of NASA.

the *retrieval theory*, and at first sight appears relatively straightforward. For example, consider a region of the thermal-IR where the atmospheric absorption is due only to a well-mixed gas. The $600\text{--}700\text{ cm}^{-1}$ spectrum of the giant planets is a good example of such a region since the absorption here is due almost entirely to $\text{H}_2\text{--H}_2$ and $\text{H}_2\text{--He}$ collision-induced absorption. Suppose our simulated spectrum was too bright at some wavelength in this range, then we would correctly deduce that our assumed, or *a priori*, temperature profile was too warm around about

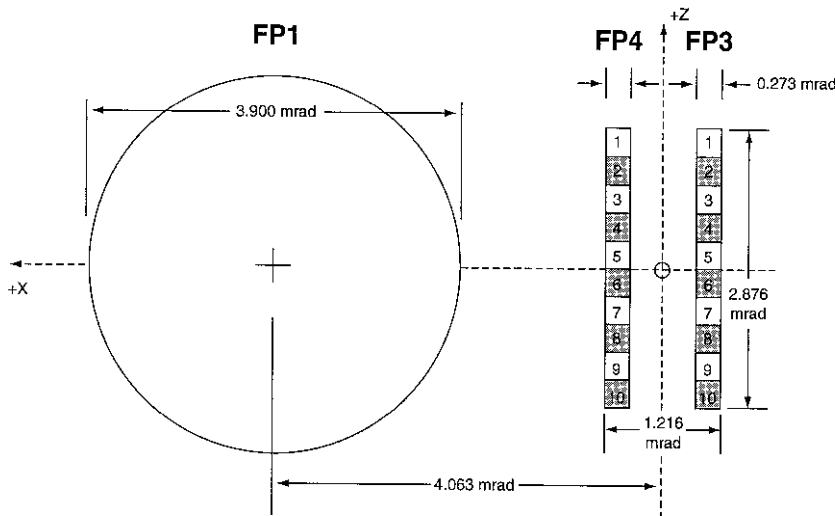


Figure 7.42 CIRS focal plane pointing and FOV.

Courtesy of NASA.

where the weighting function peaked. Hence we would need to slightly ‘cool’ our model profile at this level in order to improve the fit between the synthetic and measured spectra.

Although this seems straightforward it is in fact very difficult for a number of reasons. First of all, it can be seen from the radiative transfer equation (Section 6.4.1 and Equation 6.39) that the radiance at any particular wavelength is the weighted average of the thermal emission from a continuous range of altitudes governed by the transmission weighting function. The width of the transmission weighting function for nadir viewing is approximately one scale height and hence it can be seen that the information on the vertical temperature structure is considerably vertically smoothed. Hence there are an infinitely wide range of possible temperature profiles whose synthetic spectra will fit the measured spectrum equally well! Fortunately, using spectral data from a range of wavelengths (or a range of emission angles, such that the peaks of the weighting functions cover a certain vertical span) reduces this ambiguity somewhat, but even here it must be remembered that the spectra are measured at a finite set of wavelengths (or emission angles) whereas an atmospheric profile is a continuous function. Hence the retrieval problem is in effect one of attempting to calculate an infinite set of parameters using a finite set of measurements which is known as an *ill-posed* problem. While there are techniques for solving such ill-posed problems, retrievals also suffer from the fact that they are *ill-conditioned* which means that without care, any experimental error in the measured spectrum may become greatly amplified when calculating the best-fit atmospheric profile leading to wholly unreliable solutions!

Since there are literally an infinite number of possible atmospheric profiles whose simulated spectra will fit a measured spectrum to within the measurement

error, how then may we hope to extract any meaningful information from measurements of the planets' electromagnetic spectra? Fortunately nature comes to our rescue since, although atmospheric properties such as temperature are continuous functions of height, we know that in practice they are also generally *smoothly varying* functions. Hence if we make the reasonable assumption that the function may be represented by a finite set of parameters, and we ensure that this number is less than, or equal to the number of points in a measured spectrum, then we may hope to be able to extract meaningful information.

7.10.1 Exact, least squares, and Backus–Gilbert solution

Suppose that we represent a set of measurements (channel radiances, or a whole spectrum measured at a set of discrete wavelengths) by the vector \mathbf{y} of m elements known as the *measurement vector*. We may also represent the atmospheric conditions with the *state vector* \mathbf{x} of n elements, which may contain the temperature, composition, and cloud abundances at appropriate levels in the atmosphere, etc. We may represent the radiative transfer model by a forward model $\mathbf{F}(\mathbf{x})$, from which we may calculate the synthetic spectrum \mathbf{y}_c

$$\mathbf{y}_c = \mathbf{F}(\mathbf{x}). \quad (7.16)$$

Retrievals of properties such as temperature may be linearized by expanding the state vector \mathbf{x} (in this case containing a smoothed representation of the temperature at n levels) about an initial first guess, or *a priori*, solution \mathbf{x}_0 and hence

$$\mathbf{y}_c = \mathbf{y}_0 + \Delta\mathbf{y} = \mathbf{F}(\mathbf{x}_0) + \mathbf{K}(\mathbf{x} - \mathbf{x}_0) \quad (7.17)$$

where \mathbf{K} is a matrix, not a function, and contains the rate of range of each element of \mathbf{y}_c with each element of \mathbf{x} , and \mathbf{y}_0 is the spectrum calculated with the *a priori* state vector. If we choose the number of elements n of the state vector to be equal to the number of measured spectral radiances m , then the \mathbf{K} -matrix is square and may be inverted. Hence substituting the measured spectrum \mathbf{y}_m for the calculated spectrum \mathbf{y}_c in Equation 7.17, and solving for \mathbf{x} we find

$$\mathbf{x} = \mathbf{x}_0 + \mathbf{K}^{-1}(\mathbf{y}_m - \mathbf{y}_0). \quad (7.18)$$

This so-called ‘exact’ solution provides a perfect fit to the measured spectrum but does so at a very heavy price. Such solutions are extremely ill conditioned and small errors in the measured spectrum may lead to huge errors in \mathbf{x} and hence it is difficult to assess the reliability of the derived solution. In cases where noise is present, the usual thing to do is to represent the atmospheric profile with fewer points than the number of measurements and solve for \mathbf{x} using a ‘least squares’ fitting algorithm which minimizes the difference between the measured and calculated spectra by minimizing the ‘cost function’ ϕ

$$\phi = (\mathbf{y}_m - \mathbf{y}_0)^T(\mathbf{y}_m - \mathbf{y}_0) \quad (7.19)$$

where ϕ is simply the sum of the squares of the differences between the measured and calculated spectra. Such least squares solutions are better behaved, but in practice

still suffer from serious drawbacks. In order to retrieve meaningful atmospheric data from measured spectra it is found that we need to apply some *a priori* assumptions in order to prevent meaningless solutions. There are a number of approaches to the problem which are discussed at length by Hanel *et al.* (1992), Houghton *et al.* (1984), and Rodgers (2000). However all methods basically arrive at the same conclusion, namely that the precision of a retrieval depends on the vertical averaging applied or assumed. Hence remotely sensed spectra may be inverted to yield very accurate smoothed perturbations to the assumed profile, but increasingly less accurate retrievals as less and less vertical smoothing is applied. There is thus essentially a trade-off between error and vertical resolution which is formalized by the approach of Backus and Gilbert (1970) and further discussed by Hanel *et al.* (1992) and Rodgers (2000). A particularly widespread approach when interpreting giant planet spectra is thus to parameterize the atmospheric temperature and composition profiles with far fewer parameters than the number of spectral points. For example, the abundance of hydrocarbons in the stratosphere is so little known that often all that can be meaningfully retrieved from the data is the approximate mean mole fraction. Assuming a temperature profile derived either from previous radio-occultation measurements, or from radiances measured in the nearby 1300 cm^{-1} methane band, synthetic spectra may be generated for a range of mole fractions likely to be consistent with photochemical models and compared with the measured spectrum to find the best fit. Another example is ammonia retrievals for Jupiter and Saturn, where the ammonia profile may be represented by a mean fixed value up to the condensation level whereupon it follows either some relative humidity curve, or alternatively decreases at a fixed fractional scale height.

In cases where more vertical resolution is required, or where the spectra are particularly noisy it is useful to approach the problem from a more statistical point of view in order to find the most appropriate solution. Such an approach is adopted by the technique of optimal estimation.

7.10.2 Linear optimal estimation

Optimal estimation was developed for use with terrestrial retrievals where satellite observations are used to improve upon the measurements already provided by other sources. Although it is not explicitly used so much in planetary retrievals, it is relatively easy to understand and it turns out that the solution is identical to a number of other advanced retrieval methods which are commonly used.

Suppose that we can again represent a set of measurements by the measurement vector \mathbf{y} and the atmospheric conditions with the state vector \mathbf{x} . In most cases, the properties of the atmosphere are not a complete mystery and from models and previous measurements, we have some *a priori* knowledge of the state of the atmosphere to within some initial error. For example, in the lower troposphere we know that the temperature profile will be close to the dry or saturated adiabatic lapse rate and at other altitudes we can apply some assumption on how rapidly the temperature is likely to vary with height. We may then use this profile, and the assumed

constraints on it, as the first guess and find the solution to the state vector \mathbf{x} which minimizes the modified cost function

$$\phi = (\mathbf{y}_m - \mathbf{F}(\mathbf{x}))^\top \mathbf{S}_\varepsilon^{-1} (\mathbf{y}_m - \mathbf{F}(\mathbf{x})) + (\mathbf{x} - \mathbf{x}_0)^\top \mathbf{S}_x^{-1} (\mathbf{x} - \mathbf{x}_0) \quad (7.20)$$

where:

- \mathbf{y}_m is the measured spectrum.
- $\mathbf{F}(\mathbf{x})$ is the spectrum calculated with the forward model.
- \mathbf{S}_ε is the measurement covariance matrix, which contains both the estimated random and systematic measurement errors, as well as forward-modelling errors.
- \mathbf{x} is the model state vector.
- \mathbf{x}_0 is the *a priori* state vector.
- \mathbf{S}_x is the *a priori* covariance matrix, which contains the assumed errors on the *a priori* state vector, together with the assumed vertical smoothing which is represented by non-zero off-diagonal elements which are commonly set as

$$S_{ij} = S_{ii} S_{jj} \exp(-((z_i - z_j)/l)^2) \quad (7.21)$$

where l is known as the correlation length.

The cost function is simply a measure of how closely the synthetic spectrum matches the measured spectrum and how far the solution deviates from the assumed *a priori* state vector. The optimal solution to the state vector is thus found which maximizes the closeness of fit to the measured spectrum without deviating too greatly from the *a priori* state vector. The degree to which the final solution will depart from the *a priori* solution will depend upon the relative size of the errors contained within the *a priori* and measurement covariance matrices. For linear models, such as temperature retrievals, for which the synthetic spectrum is calculated as $\mathbf{y}_c - \mathbf{y}_0 = \mathbf{K}(\mathbf{x} - \mathbf{x}_0)$, the optimal solution is found to be (Rodgers, 2000)

$$\hat{\mathbf{x}} = \mathbf{x}_0 + \mathbf{S}_x \mathbf{K}^\top (\mathbf{K} \mathbf{S}_x \mathbf{K}^\top + \mathbf{S}_\varepsilon)^{-1} (\mathbf{y}_m - \mathbf{y}_0 - \mathbf{K}(\mathbf{x}_0 - \mathbf{x})). \quad (7.22)$$

For cases where the errors on the measured spectrum are high (i.e., the elements of \mathbf{S}_ε are large), the optimal solution lies close to \mathbf{x}_0 , whereas for cases where the measurement errors are negligible compared to the *a priori* error, the solution tends to the ‘least squares’ or ‘exact’ solutions (depending on m and n) which are ill-conditioned and thus prone to error. Hence to ensure reliable operation, the sufficient constraint must be placed on the *a priori* solution to ensure smooth, realistic retrievals. The tuning of the *a priori* constraint is thus one of the ‘dark arts’ of retrievals! The error covariance matrix of the optimal solution to the state vector is found to be

$$\hat{\mathbf{S}} = \mathbf{S}_x - \mathbf{S}_x \mathbf{K}^\top (\mathbf{K} \mathbf{S}_x \mathbf{K}^\top + \mathbf{S}_\varepsilon)^{-1} \mathbf{K} \mathbf{S}_x \quad (7.23)$$

which is equal to the *a priori* error covariance matrix for the case when the measurement errors are large. The method of optimal estimation is closely related, and under certain assumptions identical, to the method of *constrained linear inversion* described by Hanel *et al.* (1992).

7.10.3 Non-linear optimal estimation

The linearity of temperature retrievals comes from the fact that the elements of the \mathbf{K} -matrix (the rate of change of the spectral radiances with temperature) are not strongly dependent on the temperature profile. Hence, once the \mathbf{K} -matrix is calculated, the best-fit temperature profile is found in a single step. This situation does not apply for composition retrievals, since small changes in the composition profile strongly affect the atmospheric transmission, and thus the \mathbf{K} -matrix. Hence composition retrievals are highly non-linear and computationally expensive since they must be performed iteratively, and the \mathbf{K} -matrix recalculated at every step in the worst case.

Extending the principles of optimal estimation to such non-linear cases, the $(n+1)$ th estimate of the state vector is found to be

$$\mathbf{x}_{n+1} = \mathbf{x}_0 + \mathbf{S}_x \mathbf{K}_n^T (\mathbf{K}_n \mathbf{S}_x \mathbf{K}_n^T + \mathbf{S}_\varepsilon)^{-1} (\mathbf{y}_m - \mathbf{y}_n - \mathbf{K}_n (\mathbf{x}_0 - \mathbf{x}_n)) \quad (7.24)$$

where \mathbf{K}_n is the \mathbf{K} -matrix calculated for the n th state vector \mathbf{x}_n . Once the solution has converged to within errors, the final error covariance matrix is calculated from Equation 7.23. A full description of this method is described in Chapter 7 of Houghton *et al.* (1984) and by Rodgers (2000).

7.10.4 Joint retrievals

Consider a region of the thermal IR where the weighting functions peak in the upper troposphere and where, say, ammonia is strongly absorbing. Suppose that the simulated spectrum is less bright than the measured spectrum. This would suggest that the abundance of ammonia in our first simulated spectrum is too high near the peak of the weighting function and should thus be reduced. However, it could also mean that the assumed atmospheric temperatures are too low and must be increased, or, that the abundance of some other constituent such as aerosols needs to be modified! It could also conceivably mean that all three need to be modified in some way!

In such cases, a spectral region could first be selected which is sensitive only to well-mixed absorbers and a linear temperature retrieval conducted to give the ‘true’ temperature profile. This temperature profile could then be used in an ammonia composition non-linear retrieval, using another spectral region dependent on both temperature and ammonia. However, in some cases it is found to be more effective to consider both spectral regions together and retrieve both ammonia and temperature simultaneously in a non-linear joint retrieval. Such an approach is useful in cases where the number of spectral points is limited or where there is significant noise.

7.11 REFERENCES

- Backus, G. and F. Gilbert (1970) Uniqueness in the inversion of inaccurate gross earth data. *Phil. Trans. Royal. Soc. London*, **A266**, 123–192.

- Calcutt, S., F. Taylor, P. Ade, V. Kunde, and D. Jennings (1992) The composite infrared spectrometer. *J. British Interplan. Soc.*, **45**, 811–816.
- Hanel, R. A., B. J. Conrath, D. E. Jennings, and R. E. Samuelson (1992) *Exploration of the Solar System by Infrared Remote Sensing*. Cambridge University Press, Cambridge, UK.
- Hecht, E. and A. Zajac (1974) *Optics*. Addison-Wesley, Reading, MA..
- Houghton, J. T., F. W. Taylor, and C. D. Rodgers (1984) *Remote Sounding of Atmospheres*. Cambridge University Press, Cambridge, UK.
- Houghton, J. T. and S. D. Smith (1966) *Infrared Physics*. Oxford University Press, Oxford, UK.
- James, J. F. and R. S. Stern (1969) *The Design of Optical Spectrometers*. Chapman and Hall, London.
- Lellouch, E., B. Bézard, J. I. Moses, G. R. Davis, P. Drossart, H. Feuchtgruber, E. A. Bergin, R. Morenón and T. Encrenaz (2002) The origin of water vapor and carbon dioxide in Jupiter's stratosphere. *Icarus*, **159**, 112–131.
- Lockwood, G. and D. Thompson (2002) Photometric variability of Neptune, 1972–2000. *Icarus*, **156**, 37–51.
- Niemann, H. B., S. K. Atreya, G. R. Carignan, T. M. Donahue, J. A. Haberman, D. N. Harpold, R. E. Hartle, D. M. Hunten, W. T. Kasprzak, P. R. Mahaffy, T. C. Owen, and S. H. Way (1998) The composition of the Jovian atmosphere as determined by the Galileo probe mass spectrometer. *J. Geophys. Res.*, **103**, 22831–22845.
- Ragent, B., D. S. Colburn, K. A. Rages, T. C. D. Knight, P. Avrin, G. S. Orton, P. A. Yanamandra-Fisher, and G. W. Grams (1998) The clouds of Jupiter: Results of the Galileo Jupiter Mission Probe Nephelometer Experiment. *J. Geophys. Res.*, **103**, 22891–22909.
- Rodgers, C. D. (2000) *Inverse Methods for Atmospheric Sounding: Theory and Practice*. World Scientific, Singapore.
- Seiff, A., D. B. Kirk, T. C. D. Knight, R. E. Young, J. D. Mihalov, L. A. Young, F. S. Milos, G. Schubert, R. C. Blanchard, and D. Atkinson (1998) Thermal structure of Jupiter's atmosphere near the edge of a 5-μm hotspot in the north equatorial belt. *J. Geophys. Res.*, **103**, 22857–22890.
- Smith, R. A., F. E. Jones, and R. P. Chasmus (1968) *The Detection and Measurement of Infrared Radiation* (2nd Edition). Oxford University Press, Oxford, UK.
- Sromovsky, L. A., A. D. Collard, P. M. Fry, G. S. Orton, M. T. Lemmon, M. G. Tomasko, and R. S. Freedman (1998) Galileo probe measurements of thermal and solar radiation fluxes in the Jovian atmosphere. *J. Geophys. Res.*, **103**, 22929–22977.
- Sromovsky, L. A., P. M. Fry, K. H. Baines, S. S. Limaye, G. S. Orton, and T. E. Dowling (2001) Coordinated 1996 HST and IRTF imaging of Neptune and Triton. I: Observations, navigation, and differential deconvolution. *Icarus*, **149**, 416–434.
- Vanasse, G. A. (ed.) (1983) *Spectrometric Techniques, Volume III*. Academic Press, San Diego, CA.

7.12 BIBLIOGRAPHY

- Hanel, R. A., B. J. Conrath, D. E. Jennings, and R. E. Samuelson (1992) *Exploration of the Solar System by Infrared Remote Sensing*. Cambridge University Press, Cambridge, UK.
- Hecht, E. and A. Zajac (1974) *Optics*. Addison-Wesley, Reading, MA.

- Houghton, J. T., F. W. Taylor, and C. D. Rodgers (1984) *Remote Sounding of Atmospheres*. Cambridge University Press, Cambridge, UK.
- Houghton, J. T. and S. D. Smith (1966) *Infrared Physics*. Oxford University Press, Oxford, UK.
- James, J. F. and R. S. Stern (1969) *The Design of Optical Spectrometers*. Chapman and Hall, London.
- Rodgers, C. D. (2000) *Inverse Methods for Atmospheric Sounding: Theory and Practice*. World Scientific, Singapore.
- Vanasse, G. A. (ed.) (1983) *Spectrometric Techniques, Volume III*. Academic Press, San Diego, CA.

Much of the information presented in this chapter has been extracted from various very useful public websites which are listed.

Useful public NASA websites for mission information include:

NASA Jet Propulsion Laboratory: <http://www.jpl.nasa.gov/>

NASA Ames Research Center: <http://www.arc.nasa.gov/>

NASA Goddard Space Flight Center: <http://www.gsfc.nasa.gov/>

General NASA missions: <http://history.nasa.gov/>

General ESA missions: <http://sci.esa.int/home/ourmissions/index.cfm>

Ground-based visible/IR telescope sites include:

European Southern Observatory: <http://www.eso.org/>

Palomar Observatory: <http://www.astro.caltech.edu/palomarpublish/overview.html>

NASA IRTF: http://irtf_ifa.hawaii.edu/

Anglo–Australian Observatory: <http://www.aao.gov.au/>

Joint Astronomy Centre (JCMT, UKIRT): <http://www.jach.hawaii.edu/JACpublic/index.html>

Kitt Peak National Observatory: <http://www.noao.edu/kpno/>

Pic-du-Midi Observatory: <http://www.omp.obs-mip.fr/omp/pic/>,
<http://www.bdl.fr/s2p/>

Keck Telescopes: <http://www.astro.caltech.edu/mirror/keck/index.html>

Gemini: <http://www.gemini.edu/>

Ground-based microwave telescope sites include:

BIMA: <http://bima.astro.umd.edu/>

IRAM: <http://www.iram.fr/>

Nobeyama Millimetre Array: <http://www.nro.nao.ac.jp/~nma/index-e.html>

VLA: <http://www.aoc.nrao.edu/vla/html/VLAhome.shtml>

VLBA: <http://www.aoc.nrao.edu/vlba/html/VLBA.html>

OVRO: <http://www.ovro.caltech.edu/>

Kuiper Airborne Observatory:

[http://spacelink.nasa.gov/NASA.Projects/Space.Science/Solar.System/
Kuiper.Airborne.Observatory/](http://spacelink.nasa.gov/NASA.Projects/Space.Science/Solar.System/Kuiper.Airborne.Observatory/)

Earth-orbiting space telescope sites include:

HST: <http://www.stsci.edu/hst/>

ISO: <http://www.iso.vilspa.esa.es/>

SWAS: <http://sunland.gsfc.nasa.gov/smex/swas/>

Fly-by and orbiting mission sites include:

Cassini-Huygens: <http://saturn.jpl.nasa.gov/index.cfm>

Galileo: <http://galileo.jpl.nasa.gov/>

Millennium Mission: <http://www.jpl.nasa.gov/jupiterflyby/>

Pioneer: http://spaceprojects.arc.nasa.gov/Space_Projects/pioneer/PNhome.html

Voyager: <http://voyager.jpl.nasa.gov/>

Ulysses: <http://ulysses.jpl.nasa.gov/>

Index

- a priori* constraints, 305
accretion discs, circumplanetary, 12, 32
accretion discs, circumstellar, 12, 23, 30, 35
 angular momentum, 23–25
 bipolar jets, 25
 Keplerian disc, 27
 T-tauri phase, 25, 29
 turbulence, 25
acetylene, 71, 72, 80, 87, 88
active optics, 264
Adams, John Couch, 1
adaptive optics, 13, 258
adiabatic lapse rate (dry and saturated), 69–70
airborne observatories, 268–270
Airy function, 260
aliasing, 253
ammonia, 80, 86
ammonium hydrosulphide, 70, 89–90
amorphous ice, 37
Anglo-Australian Observatory (AAO), 268
angular momentum of Solar System, 3, 24–25
apodization, 253
arsine, 82
asymmetric rotors, 201
auroral H₃⁺ emission, 30
Backus–Gilbert retrievals, 306–307
backwards energy cascade, 6, 147–148
banana cell, 159, 175
band-model approximation, 222
Barnard 68
molecular cloud, 21
baroclinic instability, 151
barotropic, 10, 134, 162, 147
barotropic instability, 150, 158
belts/zone structure, 5, 6, 10, 77, 141–147, 164–166
Berkeley Illinois Maryland Association (BIMA), 274
beta parameter (β), 148, 151
bidirectional reflectivity (BDRF), 235
Big Bang, 17, 33
bolometers, 249
bolometric temperature, 4, 62
Bond Albedo, 60, 61
Brewer–Dobson circulation, 164
brightness temperature, 237
Brunt–Väisälä frequency, 153
buoyancy frequency, 153
Calar Alto Observatory, 268
Callisto, 12, 32
Cassini, Jean-Dominique, 7, 170
Cassini mission, 5, 9, 14, 98, 108, 144, 183, 215, 300
Composite Infrared Spectrometer (CIRS), 100, 104, 220, 303

- Cassini mission (*cont.*)
- Imaging Science Subsystem (ISS), 160, 168, 169, 172, 173, 176, 301
 - Ultraviolet Imaging Spectrograph (UVIS), 301
 - Visible and Infrared Mapping Spectrometer (VIMS), 302
- Chandra X-Ray Telescope, 173
- characteristic escape time, 55
- characteristic radius, 43
- Charon, 13
- Charney–Stern instability criterion, 151, 186
- chromophores, 87, 115, 123, 145, 167, 171
- clathrate-hydrates, 38, 62
- Clausius–Clapeyron equation, 89
- clouds, 5, 69
- collision broadening, 210
- collision-induced absorption (CIA), 83, 209
- comets, 28, 30, 36, 37, 98
 - Hale–Bopp, 37, 39
 - Halley, 37
 - Hyakutake, 37
 - Shoemaker–Levy 9, 30, 59, 92, 164
- composition of giant planets, 33–39
- condensation, 89–91
- condensation line, 25
- contribution functions, 215
- constrained linear inversion, 308
- core accretion model, 28
- Coriolis parameter (f), 137
- coronograph, 343
- correlated- k approximation, 224
- correlation length, 308
- Coriolis force, 136
- Cosmic Background Explorer (COBE)
 - spacecraft, 18
- cosmic microwave background radiation, 18
- covariance matrices, 308
- Cowling theorem, 42
- cross-sections (absorption, extinction, scattering), 226
- Curtis–Godson approximation, 223
- cyclones and anticyclones, 146
- deconvolution, 13, 259
- deep models, 158–161
- Deep Space Network, 295
- detector D^* , 249
- deuterium (${}^2\text{H}$)
 - primordial D/H abundance, 17–18
 - D/H ratio in Solar System objects, 19, 33–38
- diabatic circulation, 164
- diffusion *see* molecular diffusion and eddy diffusion
- disc-averaging, 216
- disc-averaged visible brightness, 260
- disequilibrium species, 77, 81–84
- Doppler broadening, 210
- dust
 - ISM, 21
 - circumstellar discs, 27, 28
- Earth
 - atmospheric absorption, 13–14, 255–257
 - atmospheric near-IR absorption band names, 256–257
 - atmospheric turbulence, 258
 - cyclones and anticyclones, 146
 - eddy–mean interactions, 162–163
 - eddy mixing, 77–81, 154
 - eddy mixing coefficient, 78–80
 - eddy diffusion, 78
 - Edgeworth, Kenneth Essex, 30
 - effective radiating temperature, 4, 60–62
 - electric dipole transitions, 200
 - electric quadrupole transitions, 83, 111, 115, 116, 123, 145, 200, 209
 - embryos, planetary, 28
 - equatorial deformation radius, 154
 - equatorially-trapped waves, 152, 175, 176
 - Equilibrium Cloud Condensation Model (ECCM), 90–91, 92, 99
 - Ertl’s potential vorticity, 141
 - escape velocity, 54
 - ethane, 71, 72, 80, 88
 - Europa, 12, 32
 - European Southern Observatory (ESO), 263
 - exact retrievals, 306
 - expansion velocity, 55
 - exponential integrals, 218
 - extraplanetary sources, 91
 - extrasolar planets, 47–48
- Fabry–Pérot interferometers, 250
- feeding zone, 28
- Fermi’s golden rule, 198
- fluorescence, 227

- formation of the planets, 14
 core accretion model, 28, 44, 46
 gravitational instability model, 32
- formation of satellites, 12, 32
- formation of the stars, 18
- Fourier-transform spectrometers, 252
- Galactic Cosmic Rays (GCR), 119
- Galilean satellites, 7, 12, 32, 295
- Galileo, Galilei, 7
- Galileo* orbiter, 14, 94, 99, 103, 292
 Extreme Ultraviolet Spectrometer
 (EUV), 297
 Near-Infrared Mapping Spectrometer
 (NIMS), 298
 Photopolarimeter Radiometer (PPR),
 297
 Solid State Imaging (SSI), 172, 297
 Ultraviolet Spectrometer (UVS), 297
- Galileo* probe, 14, 62, 92, 95, 99, 158, 172,
 173, 175, 176, 299
- Galileo Probe Mass Spectrometer
 (GPMS), 95
- nephelometer, 99
- Net Flux Radiometer (NFR), 95
- Galle, Johann Gottfried Galle, 1
- Ganymede, 9, 12, 32
- Geisa, 222
- Gemini Telescopes, 265
- Geometric Albedo, 61
- geostrophic approximation, 137
- germane, 82
- gradient wind approximation, 156
- grating spectrometers, 250
- gravitational collapse, 21
- gravitational J -coefficients, 40, 92
 dependence on deep winds, 161, 186
- gravity waves, 53, 73, 145, 152–154
 breaking, 78, 124, 144, 154, 163
- Greenhouse Effect, 61
- ground-based microwave observatories,
 270–276
- ground-based visible/IR observatories,
 261–268
- Hadley cell, 136, 145, 263
- heat capacity, 69, 73
 of ortho/para hydrogen, 73–75
- helium abundance, 18
- Henyey–Greenstein phase function, 229
- Herschel, Sir William, 1
- heterodyne receivers, 254
- HITRAN, 222
- homopause, 78
- homosphere, 79
- Hooke, Robert, 6, 171
- hot bands, 208
- Hot Jupiters, 32, 48
- Hubble Space Telescope (HST), 11, 13, 108,
 145, 164, 184, 172, 179, 277
 Advanced Camera for Surveys (ACS),
 279
 Near-IR Camera and Multi-Object
 Spectrometer (NICMOS), 278
 Space Telescope Imaging Spectrograph
 (STIS), 278
 Wide Field/Planetary Camara 2
 (WF/PC2), 277
- Huygens* entry probe, 9, 13, 300
- hydrazine, 86
- hydrocarbon hazes, 6, 88
- hydrodynamic escape, 58
- hydrostatic equilibrium, 67
- Iapetus, 9
- ice line, 28, 38
- ill-conditioning, 259, 305
- ill-posed, 305
- impact escape, 59
- inertial instability, 150
- inertio-gravity waves, 152–153
- infrared detectors, 248
- Infrared Space Observatory (ISO) 13, 145,
 279
- ISOCAM (camera), 280
- ISO-LWS (Long Wave Spectrometer),
 282
- ISOPHOT (photo-polarimeter), 281
- ISO-SWS (Short Wave Spectrometer),
 281
- Infrared Telescope Facility (IRTF), NASA,
 265
- instabilities
- baroclinic, 151
 - barotropic, 150, 158
 - inertial, 150
- Kelvin–Helmholtz, 150

- instabilities (*cont.*)
 - static, 148
 - radiative, 151
- Institute de RadioAstronomie Millimétrique (IRAM), 271
- Interplanetary dust (IPD), 91, 122
- interior models, 37
- interferogram, 252
- interferometry, 260
- intermediate hydrogen, 76
- internal differentiation, 5, 59, 61, 63
- internal heat, 4
- internal structure, 13
- Interstellar Medium (ISM), 19, 21, 33, 35
 - D/H ratio, 19, 33
 - $^{15}\text{N}/^{14}\text{N}$ ratio, 19
- Intertropical Convergence Zone (ITCZ), 261
- inversion bands (NH_3), 208, 242
- inversion doubling, 208
- Io, 12, 32, 45
- ionospheres, 72–73
- Jansky, 218, 261
- Jeans, Sir James, 21
- Jean's flux, 53–55
- Jean's theory of collapse, 21
- Johnson noise, 248
- joint retrievals, 309
- Jupiter
 - abundance profiles, 92–99
 - acetylene, 173
 - albedo variations and 5- μm correlation, 142, 167
 - ammonia ice absorption, 100, 171, 176
 - Brown Barges, 7, 157, 169
 - clouds, 6, 94, 99–103
 - equatorial plumes, 171, 175
 - Equatorial Zone, 169
 - general circulation, 164–169
 - general vortices, 169–173
 - Great Red Spot (GRS) 6, 87, 101, 150, 156–157, 166, 169
 - colour, 170
 - comparison with terrestrial hurricane, 170
 - stability, 171
 - internal heat, 4, 62, 164
 - internal structure, 42–45
 - hazes, 6, 100, 101–103, 164
 - hot spots, 94, 99, 175
 - lightning, 101, 171–172
 - magnetic field, 44
 - magnetosphere, 45
 - North Equatorial Belt (NEB), 7, 78, 101, 169, 175
 - North Temperate Belt (NTB), 169
 - North Tropical Zone (NTropZ), 7
 - polar auroral oval, 173
 - quasi-quadrennial oscillation (QJO), 156, 176
 - ring, 7
 - satellites, 7, 12
 - South Equatorial Belt (SEB), 6, 101, 166, 170
 - South Temperate Belt (STB), 7, 166, 169, 171
 - South Temperate Zone (STZ), 7, 166
 - South Tropical Zone (STropZ), 166
 - spectrum
 - microwave, 241
 - near-IR and visible reflectance, 234
 - thermal-IR, 237
 - thunderstorms, 101, 171–172
 - ultraviolet spots, 172
 - waves, 173–177
 - White Ovals, 7, 157, 169, 171
 - X-ray polar emission, 173
 - zonal structure, 6, 164–166
 - zonal winds, 7, 141–147, 168
- k*-distributions, 224
- Keck Observatory, 265
- Kelvin waves, 145, 154, 176, 191
- Kelvin–Helmholtz instability, 150, 173
- Kelvin–Helmholtz mechanism, 4, 61, 62, 63, 64, 133
- Keplerian disc, 27
- Kirchoff's Law, 214
- Kitt Peak National Observatory, 268
- Kuiper, Gerard Peter, 30, 269
- Kuiper Airborne Observatory, 269
- Kuiper Belt Objects (KBO), 13, 31
- Kuiper–Edgeworth belt, 30–31, 48
- Lambertian reflecting surface, 61, 235
- La Palma Observatory, 268

- Las Campanas Observatory, 268
 Le Verrier, Urbain Jean Joseph, 1
 least-squares retrievals, 305
 limb-darkening, 184, 236
 limb-viewing, 218
 line-by-line calculations, 222
 line broadening, 209
 line strengths, 203
 linear rotors, 201
 linear wave theory, 152
 local thermodynamic equilibrium (LTE), 221
 magnetic dipole transitions, 200
 magnetic fields, 42
 Mars, 72
 Mauna Kea Observatory, 265
 metallic-hydrogen 44
 meteorites, 36
 Michelson interferometers, 251
 Mie theory, 227
 microwave remote sensing, 10, 11
 microwave spectra (giant planets), 241
 microwave absorption (terrestrial), 256
 microwave band definitions, 273
 Millennium Mission, 300
 Milne–Eddington equation, 70
 migration, 32, 37, 47–48, 119
 Minnaert limb-darkening equation, 236
 mixing length theory (Prandtl), 78
 molecular clouds, 19, 21
 molecular diffusion, 55, 57, 78, 80
 molecular weight, 75–76.
 moment of inertia, 41
 momentum equations, 137
 Monte Carlo scattering models, 232
 natural broadening, 210
 nadir-viewing, 213
 Navier–Stokes equation, 135
 near-infrared reflectance spectra, 243
 net-flux radiative calculations, 216
 Neptune
 abundance profiles, 116–122
 clouds, 11, 122–125
 cloud shadows, 122
 dark spots, 156, 187–190
 general circulation, 185–187
 general vortices, 187–190
 Great Dark Spot (GDS), 11, 187
 hazes, 77, 124–125, 164
 correlation with solar activity, 124
 internal heat, 4, 64, 119, 185
 internal structure, 45–47
 migration, 119
 Outbursts, 190
 satellites, 12
 Second Dark Spot (DS2), 187, 190
 South Polar Feature (SPF), 188
 South Polar Wave (SPW), 190
 spectrum
 microwave, 241
 near-IR and visible reflectance, 234
 thermal-IR, 240
 tanning of stratospheric haze, 124
 waves, 190–191
 zonal structure, 185–187
 zonal winds, 11–12, 141–147, 185–186
 New Technology Telescope (NTT), 264
 nitrogen
 $^{15}\text{N}/^{14}\text{N}$ ratio in ISM, 19, 39
 $^{15}\text{N}/^{14}\text{N}$ ratio in Jupiter, 39
 Nobeyama Millimeter Array (NMA), 275
 noise, 248
 Noise Equivalent Power (NEP), 249
 Noise Equivalent Radiance (NER), 249
 non-LTE, 221
 one-and-a-half-layer models, 161–162
 Oort cloud, 19, 28, 30
 Oort, Jan Hendrick, 30
 optical depth, 71, 214
 optimal estimation
 linear, 307
 non-linear, 309
 ortho/para hydrogen, 73–77, 83, 145
 Orion Nebula, 23
 overtone bands, 208
 Owens Valley Radio Observatory (OVRO), 274
 Palomar Observatory, 268
 para-hydrogen *see* ortho/para hydrogen
 parallel bands, 206
 Paranal Observatory, 263
 Penzias, Arno, 18

- perpendicular bands, 206
 phase angle, 14
 phase functions, 226
 phosphine, 80, 82, 86
 photochemistry, 71, 77
 photoconductive detectors, 249
 photodissociation, 85–86
 photolysis, 79, 84–89
 photometers, 249
 photon detectors, 249
 photovoltaic detectors, 249
 Pic-du-Midi Observatory, 268
 Pioneer spacecraft, 7, 13, 45, 170, 286
 - Imaging Photopolarimeter, 288
 - IR Radiometer, 288
 - UV Photometer, 288
 planetary densities, 4
 planetary waves *see* Rossby waves
 planetesimals, 12, 28, 30, 32
 planetocentric latitude, 40
 planetographic latitude, 40
 Planck function, 72, 242
 plutinos, 48
 Pluto, 13, 30–31, 48
 Point Spread Function (PSF), 259
 potential temperature, 149
 potential vorticity, 141
 P-branch, 205
 P, Q, R bands, 206
 Prandtl's mixing length theory *see* mixing length theory
 protostars, 23
 pyroelectric detectors, 249
 pyrolysis, 6, 88, 116
- Q-branch, 206
 quadrupoles *see* electric quadrupole transitions
 Quasi-Biennial Oscillation (QBO), 155
 Quasi-Quadrennial Oscillation (QQO), 156, 176
 quenching, 77, 81
- R-branch, 205
 radiative balance, 220
 radiative–convective boundary, 71
 radiative heating and cooling, 71
 radiative transfer (grey atmosphere), 213
 radiative transfer (scattering atmosphere), 229
 radiative instability, 151
 radio occultation, 14, 111, 116, 119, 284–285
 radioisotope heating, 61
 radiometers, 249
 radius of deformation, 148, 153
 Raman scattering, 227
 Rayleigh scattering, 84, 226
 Rayleigh–Kuo instability criterion, 150
 reflecting layer approximation, 232
 relative vorticity, 140
 residual mean circulation, 164
 retrieval theory, 303
 Reynold's stress, 163
 Rhea, 9
 Rhines length, 148
 Richardson number (Ri), 147
 Richardson–Lucy (RL) deconvolution, 259
 Rossby number (Ro), 138
 Rossby radius, 153
 Rossby waves, 140, 145, 152, 154–156
 Rossby–gravity waves, 156, 175, 176
 rotation bands, 203
 rotational energy levels, 201
 rotational partition function, 73
 rotational temperature, 73, 74
 rotational transitions, 203
- Saturn
 abundance profiles, 103–105
 Brown Spots, 179
 clouds, 8, 105–110
 cold spots, 180
 Equatorial Disturbances *see* Great White Spots
 Equatorial Zone (EZ), 110, 179
 general circulation, 177–179
 general vortices, 179–180
 Great White Spots (GWS), 110, 179
 hazes, 8, 108–110, 142, 164, 177
 internal differentiation, 63
 internal heat, 4, 8, 63, 177
 internal structure, 42–45
 North Polar Spot (NPS), 157, 179, 181
 North Polar Hexagon Wave, 157, 179–181
 Ribbon wave, 180
 rings, 8, 9, 91, 105

- satellites, 9
- spectrum
 - microwave, 241
 - near-IR and visible reflectance, 234
 - thermal-IR, 240
- UV spot, 179
- waves, 180–183
- zonal structure, 178
- zonal winds, 8, 141–147
- scale height
 - cloud, 91
 - number density, 57
 - pressure, 57, 67
- scattering, 225
 - non-plane parallel scattering, 232
 - plane-parallel approximation, 231
 - single-scattering approximation, 230
- selection rules
 - rotational transitions, 203
 - rotational–vibrational transitions, 204
- self-exciting dynamo, 42
- shallow-layer models, 158
- Shot noise, 248
- single-scattering albedo, 226
- single-scattering approximation, 231
- SIS junctions, 254
- solar system abundances, 19, 33
- space-based telescopes, 276–284
- Spacelab 3, 159
- speckle imaging, 13, 259
- spectra of giant planets (general), 233
- spectral responsivity (of detectors), 248
- spherical tops, 201
- spin–orbit resonances, 31
- static stability, 148
- stellar occultation, 13
- stratosphere, 70–71, 76–77
- stratospheric circulation, 163–164
- stratospheric heating, 76–77
- stratospheric temperature, 70–72, 76–77
- Subaru Telescope, 265
- Submillimeter Wave Astronomy Satellite (SWAS), 283
- supernovae, 18, 39
- super-rotation, 7, 8, 145
- Swedish ESO Submillimetre Telescope (SEST), 263
- symmetric rotors, 201
- synchrotron radio emission, 44, 241
- synoptic scale, 153
- synthetic Uranus models, 45
- System I, II and III longitudes, 7
- tanning, 115, 116, 124
- Taylor–Proudman Theorem, 141, 159, 168, 183
- thermal detectors, 249
- thermal escape, 53–55
 - characteristic escape time, 55
 - expansion velocity, 55
 - limiting flux, 55
- thermal-infrared spectra, 236
- thermal winds, 144
- Thermal Wind Equation, 138
- Titan, 9, 14, 55, 145, 209, 215, 220, 300
- transition energy, 203
- transition rates, 199
- transmission weighting function, 215
- trans-Neptunian objects, 31, 48
- Triton, 12, 13, 31, 47, 55, 122, 124
- tropopause, 71, 76, 79
 - cold-trap, 90
- troposphere, 68, 71, 76
- tropospheric circulation, 158–163
- T-Tauri phase, 25, 29, 46
- turbulence, 77, 78, 145, 147–151
 - three-dimensional, 6, 147
 - turbulence, two-dimensional, 6, 147
- ultraviolet reflectance spectra, 234
- Ulysses* spacecraft, 292
- Uranus
 - abundance profiles, 110–115
 - clouds, 10, 115–116, 184–185
 - general circulation, 183–184
 - hazes, 77, 115–116, 164
 - internal heat, 4, 11, 64, 183, 314
 - internal structure, 45–47
 - migration, 119
 - obliquity, 10, 31–32, 64, 134
 - retrograde spin, 41
 - rings, 11
 - satellites, 11
 - spectrum
 - microwave, 241
 - near-IR and visible reflectance, 234
 - thermal-IR, 240

- Uranus (*cont.*)
 zonal structure, 184
 zonal winds, 10, 141–147, 185–186
- VEEGA trajectory (*Galileo*), 293
- Venus, 41, 72, 136, 145
- Very Large Array (VLA), 272
- Very Large Baseline Array (VLA), 273
- Very Large Telescope (VLT), 263
- Very Large Telescope Interferometer (VLTI), 263
- vibrational energy levels, 200
- vibrational modes, 207
- vibration–rotation bands, 204
- diatomic molecules, 205
- linear polyatomic and spherical tops, 205
- symmetric rotors, 206
- asymmetric rotors, 207
- visible reflectance spectra, 234
- Voigt broadening, 211
- vortices, 156–157
- cyclonic/anticyclonic asymmetry, 156
- stability, 157
- Vorticity equation, 139
- Voyager* spacecraft, 7, 9, 10, 11, 12, 14, 47, 65, 94, 101, 108–109, 111, 116, 119, 122, 144, 145, 159, 160, 163, 168, 169, 171, 177, 180–190, 288
- Imaging Science System (ISS), 290
- Infrared Spectrometer and Radiometer (IRIS), 145, 180, 216, 220, 240, 291, 303
- Photopolarimeter Subsystem (PPS), 291
- Ultraviolet Spectrometer (UVS), 290
- VVEJGA trajectory (*Cassini*), 300
- wavenumbers (cm^{−1}), 206
- waves, 151–156
- weighting function *see* transmission weighting function
- Wilson, Robert, 18
- Young Stellar Objects (YSO), 23, 25
- zonal winds, 7, 141–147
- stability, 158–159

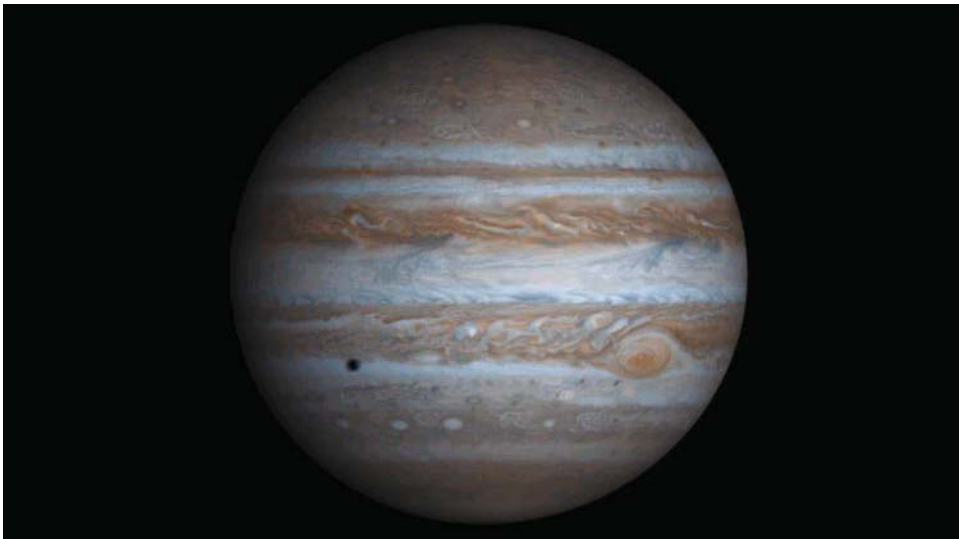


Figure 1.3 Jupiter as observed by *Cassini* in December 2000. The dark spot on the lower left is the shadow of Europa, one of the Galilean satellites. The Great Red Spot (GRS) is clearly visible as is the prominent banding, and the highly turbulent cloud structure.

Courtesy of NASA.

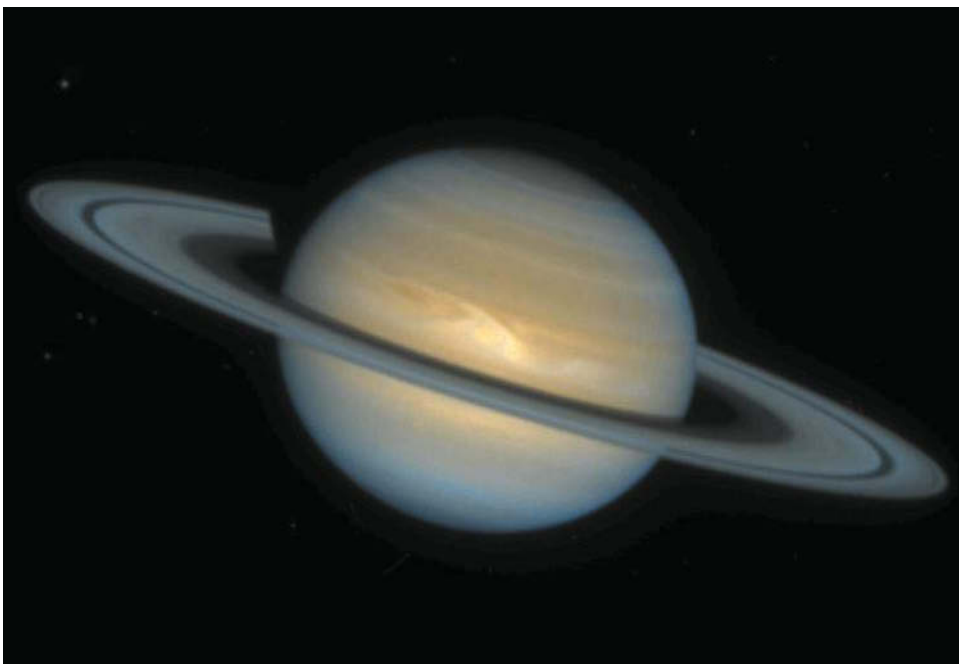


Figure 1.5 Saturn as observed by the Hubble Space Telescope (HST) in December 1994. A large bright feature, known as a Great White Spot (GWS), is clearly visible at the centre of Saturn's disc.

Courtesy of NASA.



Figure 1.6 Uranus observed by *Voyager 2* in 1986. More recent observations of Uranus will be discussed in Chapters 4–5.

Courtesy of NASA.

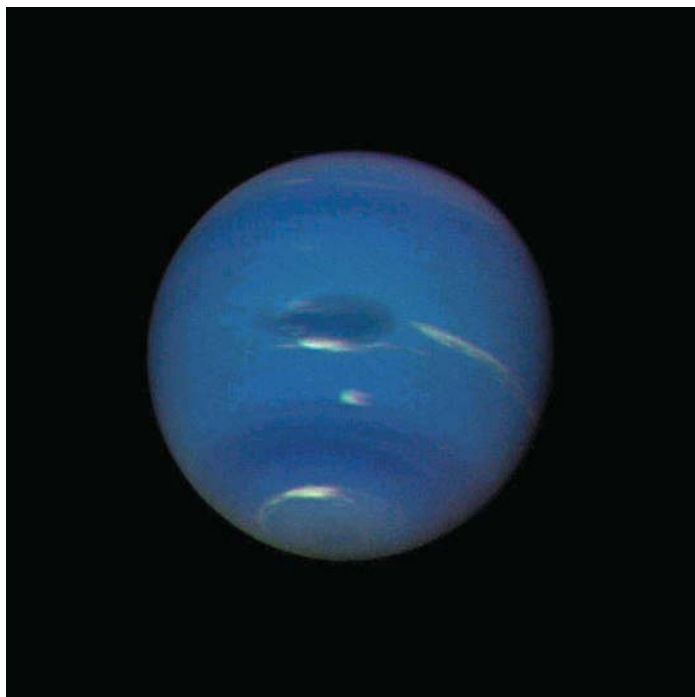


Figure 1.7 Neptune as observed by *Voyager 2* in 1989. The Great Dark Spot (GDS) is clearly visible at the centre of the disk together with the darker mid-latitude bands, and various small, convectively-generated white methane clouds.

Courtesy of NASA.

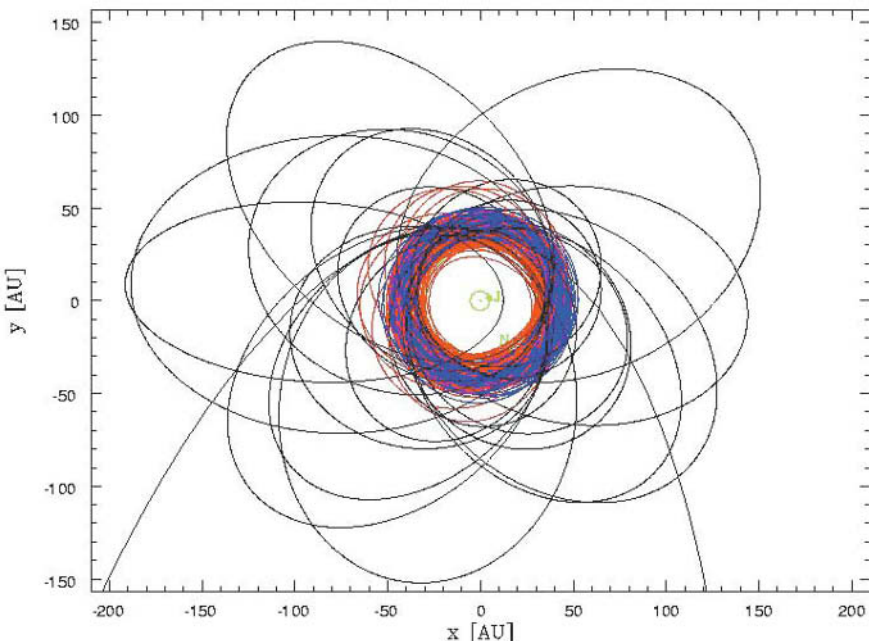


Figure 2.6 Plan view of known trans-Neptunian object orbits in the Kuiper–Edgeworth belt. Red orbits relate to ‘Plutinos’, objects which are in a 3 : 2 orbital resonance with Neptune. Blue orbits relate to classical Kuiper belt objects (KBOs) which do not have an orbital resonance with Neptune and typically orbit slightly further from the Sun. Black orbits relate to scattered KBOs whose orbits have high eccentricity.

Courtesy of David Jewitt, Institute for Astronomy, University of Hawaii.

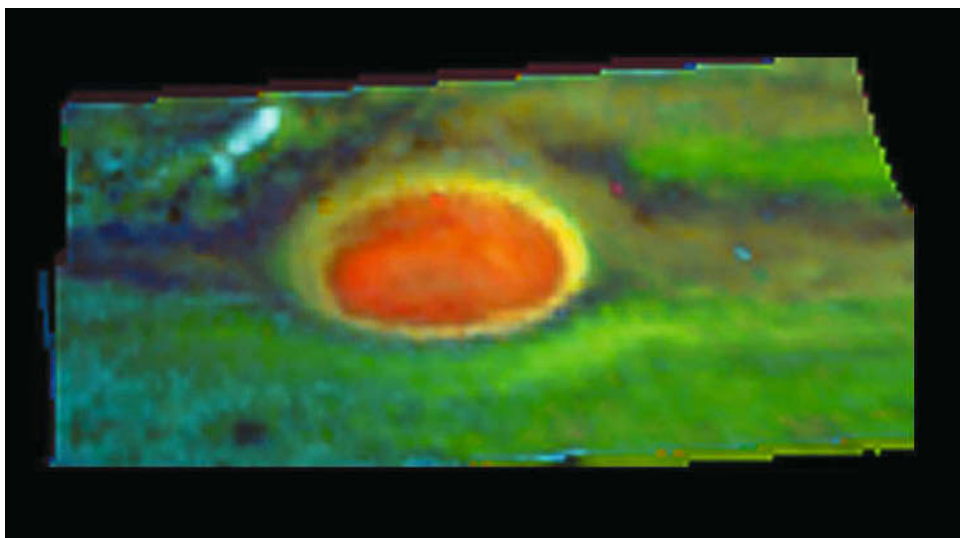


Figure 4.10 False colour image of the GRS constructed from near-IR data recorded in 1996 by *Galileo/NIMS*. Reddish-orange areas show regions of high-level clouds, yellow areas depict mid-level clouds, and green areas depict lower-level clouds. The darker areas are cloud-free regions. The light blue region to the north-west of the GRS has been identified as middle-to-high-level ammonia ice clouds.

From Baines *et al.* (2002). Courtesy of NASA.

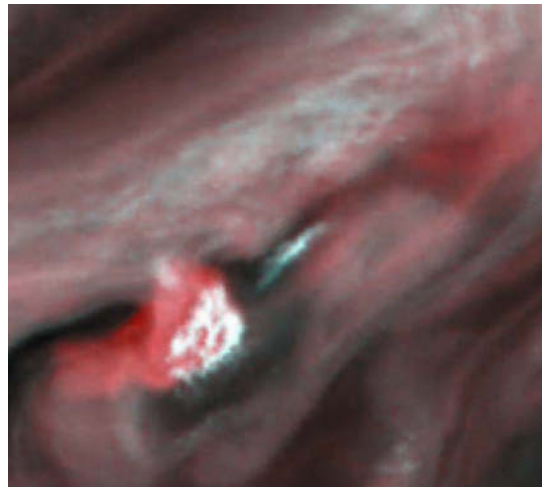


Figure 4.11 False colour picture of a convective thunderstorm 10,000 km (6,218 miles) northwest of the GRS recorded by *Galileo/SSI* in June 1996 (Banfield *et al.*, 1998). The picture is constructed of images recorded at wavelengths of 756 nm (red), 889 nm (blue), and 727 nm (green). The central thick white cloud is over 1,000 km across, and is estimated to be standing almost 25 km higher than the surrounding clouds. Its base, extending off to the left, appears red in this representation, indicating a pressure of almost 4 bar. Hence the base of this cloud is almost certainly composed of water.

Courtesy of NASA.

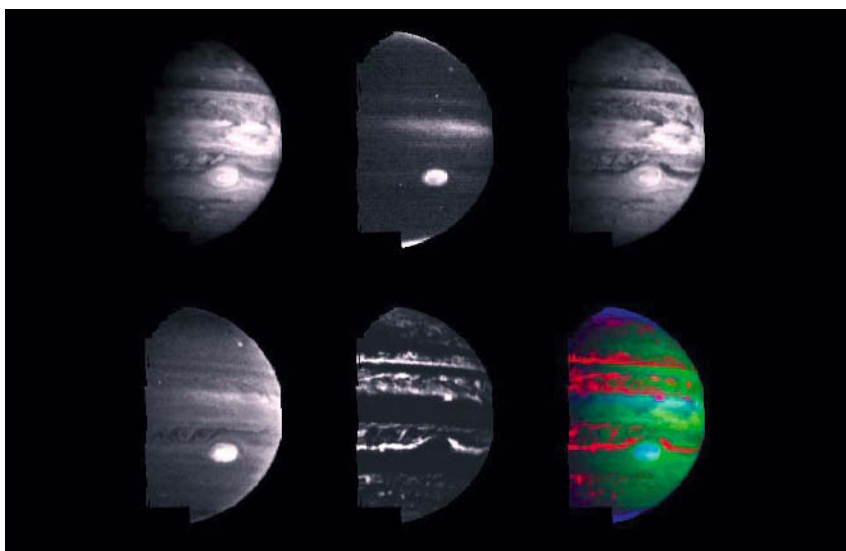
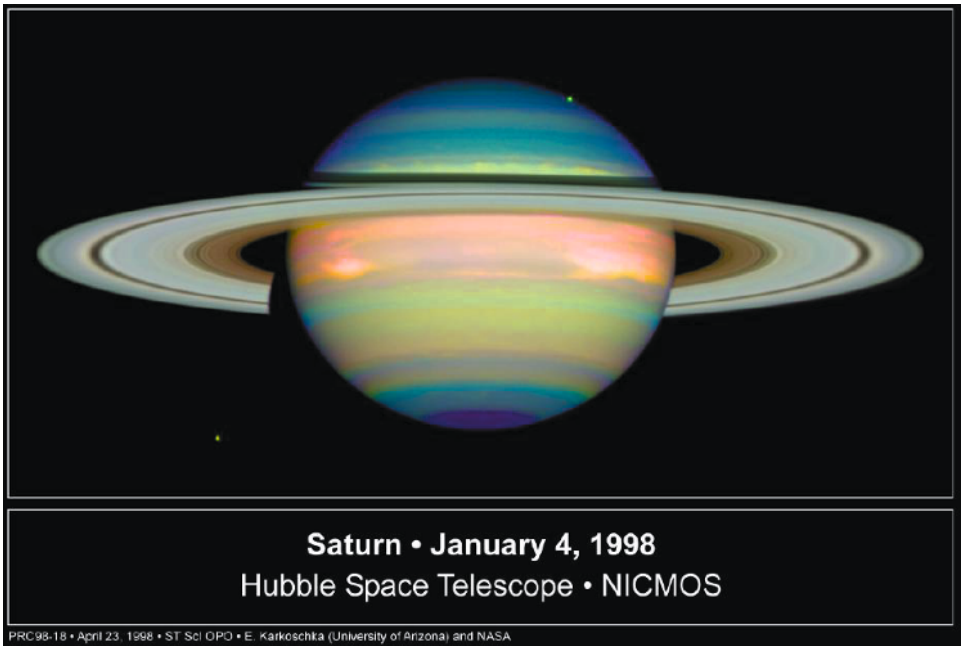


Figure 4.14 *Galileo NIMS* images of Jupiter recorded in September 1996. The five greyscale images are recorded at 1.61, 2.17, 2.73, 3.01, and 4.99 μm , and the false colour image is made up of images recorded at 4.99 μm (red), 1.61 μm (green), and 2.17 μm (red) respectively. The Jovian atmosphere is relatively transparent at 1.61 and 2.73 μm and thus the well-known pattern of belts and zones, familiar from visible light images, is seen. At 2.17 μm , strong absorptions of methane and hydrogen mean that only light reflected from the upper haze layers is visible and these are clearly seen over the GRS and the northern edge of the Equatorial Zone (EZ), while at 3.01 μm , where ammonia gas also absorbs, the features seen are due to both haze and ammonia. The 4.99 μm image records thermal emission from the 5–8 bar region and the general anticorrelation between visible/near-IR albedo and thermal emission is clear. The GRS is clearly visible in this image, and its great height means that it appears bright in all of the near-IR reflected-sunlight images, and is correspondingly dark in the 5- μm image where it can be seen to be surrounded by a cloud-free annulus.

Courtesy of NASA.



Saturn • January 4, 1998
Hubble Space Telescope • NICMOS

PRC 98-18 • April 23, 1998 • ST Scl OPO • E. Karkoschka (University of Arizona) and NASA

Figure 4.18 False colour image of Saturn composed of images recorded at $1.0\text{ }\mu\text{m}$ (low gaseous absorption) (blue), $1.8\text{ }\mu\text{m}$ (medium gaseous absorption) (green), and $2.1\text{ }\mu\text{m}$ (high gaseous absorption) (red), in 1998 by the HST/Near Infrared and Multi-Object Spectrometer (NICMOS) instrument. In this representation the blue colours indicate a clear atmosphere down to the main, presumed ammonia cloud deck. The dark region around the south pole indicates a large hole in the main cloud layer here. The green and yellow regions indicate haze layers above the main cloud deck with thin hazes appearing green and thick hazes yellow. The red and orange regions indicate clouds reaching high up into the atmosphere. Thick clouds are seen at equatorial latitudes, while the southern hemisphere at this time appears to have higher abundances of upper tropospheric haze than the northern hemisphere.

Courtesy of NASA.

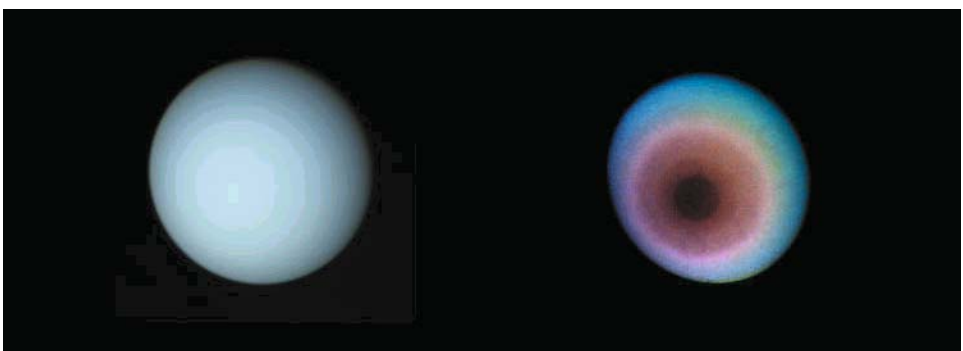


Figure 4.19 Uranus observed by *Voyager 2* in 1986. The left-hand frame shows a true colour image while the right-hand frame shows a false colour image where the original ultraviolet-, violet-, and orange-filtered images are displayed, respectively, as blue, green, and red (greatly stretched to improve contrast). Ultraviolet wavelengths are sensitive to the abundance of upper tropospheric and stratospheric haze, and during the *Voyager 2* flyby, when the South Pole of Uranus was pointed almost directly towards the Sun, the increased abundance of haze over the South Pole was clearly visible.

Courtesy of NASA



Figure 5.11 Cloud features on Jupiter. Cylindrical map of Jupiter observed by *Cassini/ISS* extending from 60°S to 60°N. The GRS is clearly visible towards the centre of the image, as is the single remaining White Oval to the south, and approximately 180° to the east. Several smaller white ovals are seen further to the south. The equatorial plumes at the northern edge of the equatorial zone are apparent, interspersed by darker regions which appear bright at 5 µm and are thus known as the 5-µm hotspots. The dark cyclonic ovals at the northern edge of the NEB are the Brown Barges. Several small thunderstorm clouds can be seen erupting in the NEB.

Courtesy of NASA.



Figure 5.19 False colour image of Saturn recorded by *Voyager 1* in 1980 showing the unique red oval cloud feature located at 55°S, sometimes known as ‘Anne’s Spot’.

Courtesy of NASA.

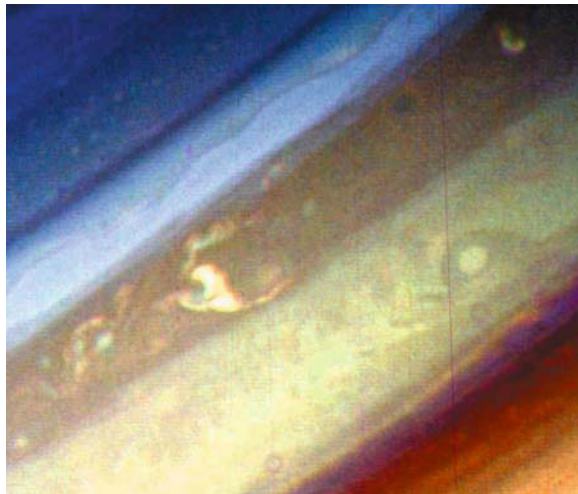
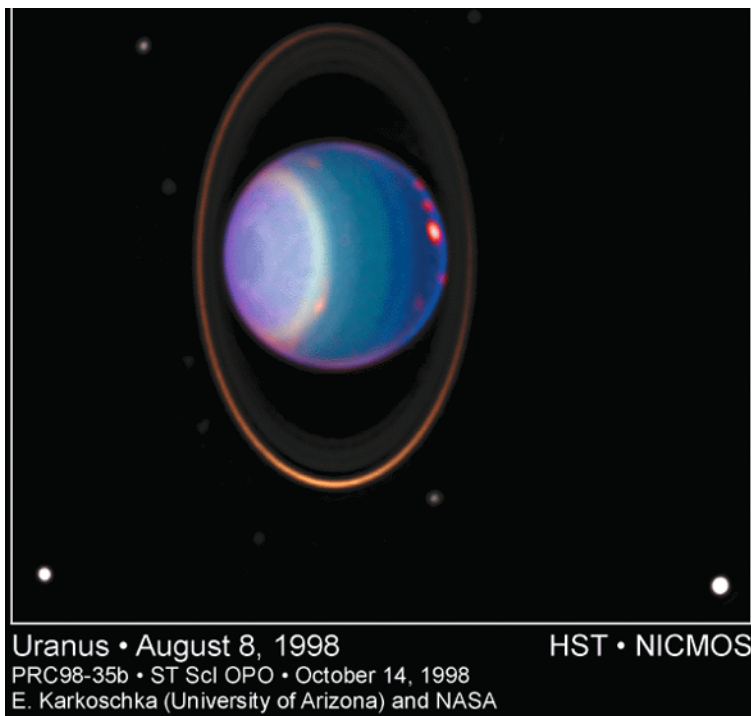


Figure 5.20 Highly enhanced image of Saturn's cloud features observed by *Voyager 2*. The ribbon wave is visible at the top left in the bright zone centred at 47°N in the North Polar Zone (NPZ). A bright convective cloud is seen to the south at a latitude ~38°N in the North Temperate Belt. Further south is the North Temperate Zone, the North Equatorial Belt, and the edge of the Equatorial Zone at the bottom right of the image. These convective clouds appear to erupt and then shear apart in the zonal wind flow, much like very similar features in Jupiter's NEB.

Courtesy of NASA.



Uranus • August 8, 1998
PRC98-35b • ST Scl OPO • October 14, 1998
E. Karkoschka (University of Arizona) and NASA

HST • NICMOS

Figure 5.23 HST/NICMOS false colour image of Uranus where the blue, green, and red components correspond to the real near-IR wavelengths of 0.9, 1.1, and 1.7 μm respectively. The increased haze opacity at 40–50°S is clearly seen as is the generally increased reflection over the South Pole. Individual methane clouds appear red in this image since they are most apparent at 1.7 μm (shown here as red) where the methane absorption is strong. The ring system plus several satellites are also clearly visible.

Courtesy of NASA.

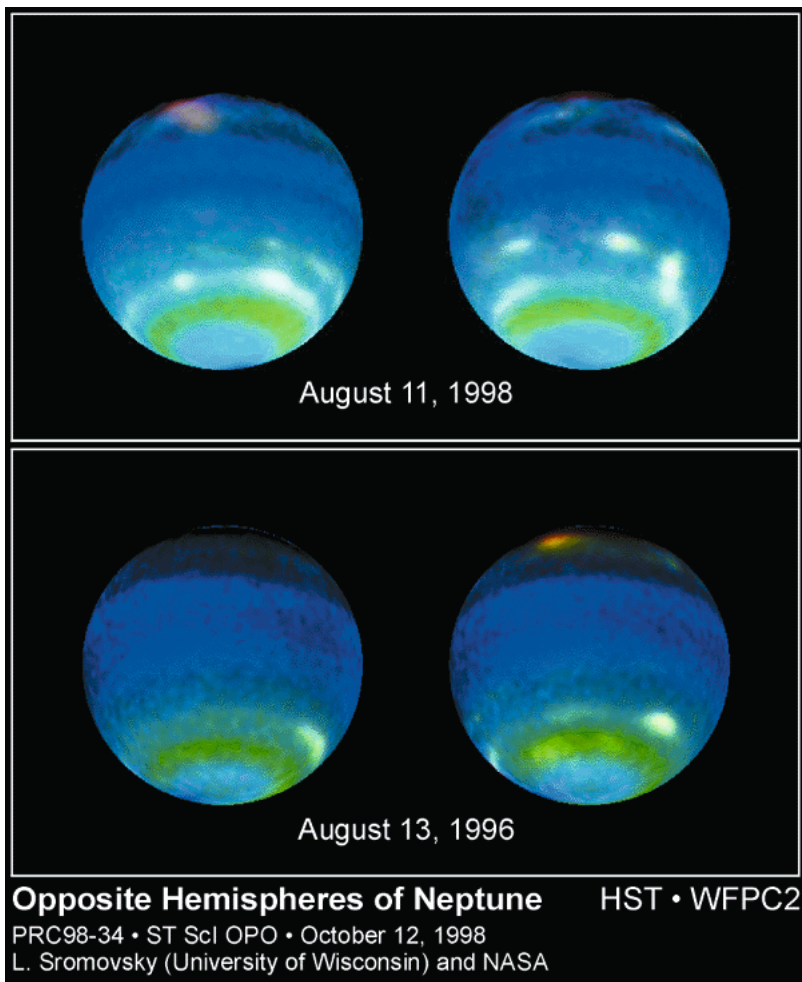


Figure 5.27 False colour images of Neptune observed by HST/Wide Field Planetary Camera 2 (WFPC2) in 1998.

Courtesy of NASA.

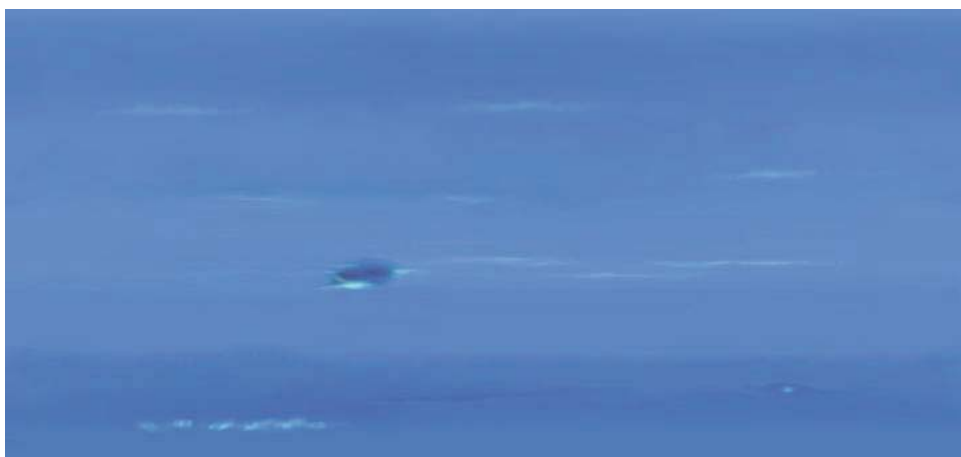


Figure 5.28 Cylindrical map of Neptune between 90°S and 90°N from *Voyager 2* data, showing GDS, DS2, SPF, and a trace of the South Polar Wave (SPW).

Courtesy of NASA and James Hastings-Trew.